NASA TECHNICAL NOTE

NASA TN D-8423 c.1

NASA TN D-8423

COMPARISON OF JET MACH NUMBER DECAY DATA WITH A CORRELATION AND JET SPREADING CONTOURS FOR A LARGE VARIETY OF NOZZLES

Donald E. Groesbeck, Ronald G. Huff, and Uwe H. von Glahn

Lewis Research Center
Cleveland, Ohio 44135

NATIONAL AERONAUTICS AND SPACE ADMINISTRATION • WASHINGTON, D. C. • JUNE 1977

Quality Deficiencies In Original Document

_____ Missing Pages

_____ Bleed Through Pages

_____ Poor Quality Text/Image

1. Report No. NASA TN D-8423	2. Government Accession No.
4. Title and Subtitle COMPARISON OF JET MACH NUMBER DECAY DATA WITH A CORRELATION AND JET SPREADING CONTOURS FOR A LARGE VARIETY OF NOZZLES	5. Report Date June 1977
	6. Performing Organization Code
7. Author(s) Donald E. Groesbeck, Ronald G. Huff, and Uwe H. von Glahn	8. Performing Organization Report No. E-8561
9. Performing Organization Name and Address Lewis Research Center National Aeronautics and Space Administration Cleveland, Ohio 44135	10. Work Unit No. 505-03
	11. Contract or Grant No.
12. Sponsoring Agency Name and Address National Aeronautics and Space Administration Washington, D. C. 20546	13. Type of Report and Period Covered Technical Note
	14. Sponsoring Agency Code
15. Supplementary Notes	

16. Abstract

Small-scale circular, noncircular, single- and multielement nozzles with flow areas as large as 122 cm^2 were tested with cold airflow at exit Mach numbers from 0.28 to 1.15. The effects of multielement nozzle shape and element spacing on jet Mach number decay were studied in an effort to reduce the noise caused by jet impingement on externally blown flap (EBF) STOL aircraft. The jet Mach number decay data are well represented by empirical relations. Jet spreading and Mach number decay contours are presented for all configurations tested.

17. Key Words (Suggested by Author(s))		18. Distribution Statement
Short takeoff aircraft	Jet aircraft noise	Unclassified - unlimited
Exhaust nozzles	Noise reduction	STAR Category 02
Mach number	Mixer nozzles	
Velocity decay		

19. Security Classif. (of this report)	20. Security Classif. (of this page)	21. No. of Pages	22. Price*
Unclassified	Unclassified	299	A13

* For sale by the National Technical Information Service, Springfield, Virginia 22161

CONTENTS

COMPARISON OF JET MACH NUMBER DECAY DATA WITH A CORRELATION AND JET SPREADING CONTOURS FOR A LARGE VARIETY OF NOZZLES

by Donald E. Groesbeck, Ronald G. Huff, and Uwe H. von Glahn

Lewis Research Center

SUMMARY

Axial jet Mach number decay data were obtained for a large variety of cold-flow, small-scale nozzles (flow areas to 122 cm^2), including single- and multielement and bypass types. Nozzle-exit jet Mach numbers ranged from 0.28 to 1.15. The effects of multielement nozzle shape and element spacing on jet Mach number decay were studied in an effort to reduce the noise caused by jet impingement on externally blown flap (EBF) short takeoff and landing (STOL) aircraft.

The axial jet Mach number decay data for the nozzles tested are well represented by the empirical relations included herein.

Contours of jet (or multijet) spreading and Mach number decays are presented as determined from crossplots of total pressure surveys taken downstream of the nozzles. The contours are all for a nominal jet-exit Mach number of 0.99.

INTRODUCTION

Short takeoff and landing (STOL) aircraft are expected to become a significant part of the commercial air transportation system. At present, externally blown flaps (EFB), figure 1, are being considered for the lift augmentation required for STOL aircraft. However, the impingement of the engine exhaust jet on the extended flaps causes an unacceptable increase in the noise level (refs. 1 to 3). The noise level increase is a function of the jet impingement velocity to the sixth power and the impingement area (determined from the width of the velocity profile curve where the velocity is 80 percent of the peak jet impingement velocity) to the first power (ref. 1). The jet impingement noise can be lowered by reducing the impingement velocity on the flaps (refs. 1 and 2) within the distance specified by the engine-flap design.

The impinging jet velocity can be reduced (1) by using a large-bypass fan engine with a lower exhaust velocity; (2) by increasing the distance from the nozzle to the flaps, if feasible; or (3) by mixing the jet with ambient air more rapidly by using a multielement nozzle of the same total flow area as a single-element nozzle. The last means results in a large overall-size nozzle. The multielement nozzle should be designed to achieve the same thrust coefficient as a single-element nozzle. For the same nozzle-exit velocity, the individual smaller jets of a multielement nozzle will decay in less actual distance than a single larger jet. Consequently, their impingement velocity is less; however, the impingement area may increase enough to negate any decrease in noise obtained from the velocity reduction. A compromise is required, therefore, among the number, shape, and spacing of the nozzle elements of a multielement nozzle in order to give the velocity reduction desired with a minimum spreading of the jets.

This report summarizes the results of an experimental cold-flow, small-scale study conducted at the NASA Lewis Research Center on the decay of the peak axial Mach number obtained with a large variety of single-element, multielement, and bypass nozzles. Nozzle total flow areas ranged from 4.4 to 122 square centimeters. Nozzle shapes tested included circular, rectangular, triangular, trapezoidal, "Y" shaped, and annular. Nozzle-exit jet Mach numbers ranged from 0.28 to 1.15. Jet Mach numbers were surveyed from the nozzle exit to a downstream distance of over 100 single-element nozzle diameters. Some of these data were previously reported in preliminary form (refs. 4 and 5). The empirical Mach number decay correlation equations of reference 6 are used herein for comparison with the data. Jet Mach number decay and spreading contours for all configurations tested are presented in appendix A.

APPARATUS

Test Stand

The test stand used in the present work is illustrated in figure 2(a). Pressurized air at ambient temperature (approx. 289 K) is supplied to a 15.41-centimeter-inside-diameter pipeline by two diametrically opposed 10.23-centimeter-inside-diameter supply lines (section A-A, fig. 2(a)). Flexible couplings in each of the twin supply lines isolate the air supply system from a thrust measuring system. However, in the present study no thrust measurements were made. The test nozzles were attached to a flange at the downstream end of the 15.41-centimeter-inside-diameter pipeline. Airflow through the overhead main air supply line was measured with a calibrated orifice. The nominal nozzle-inlet total pressure was measured by a single centerline probe near the nozzle inlet. Figure 2(b) shows the supply lines. In the foreground is the traverse cart with the pitot-static probe used to survey the nozzle jets.

Nozzle Configurations

Axial Mach number decay data were obtained by using single-element nozzles with the following cross sections:

(1) Circular: constant-diameter tube; sharp- or round-edge orifice; convergent nozzle

(2) Rectangular: sharp- or round-edge orifice; convergent nozzle; aspect ratios from 1.5 to 13.3

(3) Triangular: sharp-edge orifice

(4) Trapezoidal: flat- or round-end constant-area nozzle

(5) "Y" shape: sharp-edge orifice

(6) Annular: sharp- or round-edge orifice; convergent nozzle

Data were also obtained for coplanar-exit multielement nozzles that included the following:

(1) Six to 24 constant-diameter tubes and/or orifices (sharp and round edge). A designation, such as a 1-6-6, 0-6-0, etc., is used to define a multitube or multiorifice configuration. The first number denotes whether or not a center element is used, and the second and third numbers denote the number of elements in the first and second rings, respectively. Figures 3(a) to (e) show some of the multitube nozzles tested. For multitube or multiorifice nozzles, the spacings between elements and between circumferential rings of elements were varied to evaluate the geometry effects on the axial Mach number decay.

(2) Three-slot convergent nozzles (fig. 3(f))

(3) Four-slot sharp-edge orifices; single-element aspect ratios of 2.22 to 11.25

(4) Six-slot convergent nozzles (fig. 3(g))

(5) Six- and 12-lobe, flat-end, trapezoidal, constant-area nozzles (figs. 3(h) to (j))

(6) Seven- or eight-lobe, round-end, trapezoidal, constant-area nozzles, with all lobes at 0° to the nozzle axis and with alternate lobes canted at 5° or 10° to the nozzle axis (fig. 3(k))

Data were obtained also for noncoplanar-exit, multielement bypass nozzles. Typical nozzles tested are shown in figures 3(l) to (o). The core (primary) of these nozzles consisted either of tubes, orifices, a single slot, or a convergent nozzle. The bypass (secondary) of these nozzles consisted either of circular orifices, round- or sharp-edge annuli, or a convergent annulus with the exit some distance upstream of the core nozzle exit. Various mesh screens, placed in the bypass passages, were used to vary the ratio of secondary to primary Mach number M_b/M_j from 0.44 to 1.0. All symbols are defined in appendix B. These noncoplanar-exit nozzles were tested to determine the effect of the secondary flow on the axial jet Mach number decay of the primary flow. Some of the exhaust nozzle configurations are typical of high-bypass, fan-jet engines.

Tables I to III summarize the detailed dimensions of all nozzle configurations tested as well as those of nozzles from other references. The configurations are listed in the order in which the decay data are discussed. The original-run column gives the original sequence of configurations. The symbols C_n, $Z_{\textcircled{1}}$, and D_x denote calculated values that are discussed in later sections. The symbol A_n denotes the total nozzle area with an equivalent circular diameter of $D_{e,T}$, D_e is the equivalent circular diameter of a single element of any nozzle, and D_h is the hydraulic diameter of a single element. The axial length l is the length of a nozzle tube (or tubes) or the thickness of an orifice plate. For other than the circular tube or orifice multielement nozzles, nozzle dimensions (i.e., spacings and areas) were determined from measurements of the nozzles as tested, and averaged values have been tabulated. Many of the multielement nozzle areas were determined with an integrating polar planimeter, while others were calculated from measured dimensions. The tabulated spacings, r's and s's, are actual jet spacings (i.e., wall thicknesses are included in the spacing dimensions).

TEST PROCEDURE

A traversing pitot-static probe was first positioned approximately 0.32 centimeter downsteam of each nozzle assembly exit and a pressure traverse was made on the centerline of the pertinent element dimension (i.e., the diameter of a circular element, the altitude of a triangular element, the width of a rectangular element, etc.). Surveys were taken at screened bypass exits also. Pressure measurements were obtained at nozzle-inlet gage pressures of 5.27, 14.1, 31.0, 52.4, 86.9, and 129.5 kN/m^2. These pressures correspond to nominal nozzle pressure ratios of 1.05, 1.15, 1.31, 1.53, 1.87, and 2.30 and to nozzle-exit jet Mach numbers M_j of 0.28, 0.45, 0.64, 0.80, 0.99, and 1.15, respectively. The survey procedure was repeated at nominal downstream distances of 12.7, 25.4, 38.1, and 50.8 centimeters. For most of the program, a single pitot-static probe was moved manually on the nozzle axial centerline to various locations beyond the 50.8-centimeter survey limit, to nearly 300 centimeters downstream of the nozzle exit; and the single-pressure-probe data were recorded.

Near the end of the program (original-run configuration 95 and after), the traversing probe carriage was rebuilt (fig. 2(b)) and the carriage track was extended to cover the full range of axial distances.

The pressures at the traversing probe acted upon pressure transducers on the carriage, and the electrical signals from the transducers were transmitted to a plotter that made graphic traces of the total and static pressure distribution radially across the jet. Other pressure data were recorded from water or mercury manometers.

DATA REDUCTION

Figure 4 is a typical copy of a total pressure survey made with the traversing probe and the plotter. For nearly all the data runs, an amplifier at a gain of 2 was used to increase the reading accuracy of the total pressure trace. The static pressure survey trace is not included as it was normally a straight line at the atmospheric pressure level. Plots like figure 4 were obtained for each nozzle tested. The linear total pressure scale was converted to a Mach number scale by assuming the local ambient static pressure p_0 to be a constant value of 100 kN/m^2. This assumption was maintained for all the nozzle-inlet pressures run. Because gage pressures were used to set the nozzle-inlet total pressure, an assumption of constant atmospheric pressure could introduce an error in the nozzle-exit jet Mach number M_j. If it was assumed that the median p_0 is a good representative value, the maximum error in the calculated M_j was only ±0.004, which is considered insignificant. Even at the highest nozzle-inlet total pressure, the error in the calculated M_j was only ±0.01, using the maximum and minimum values of p_0 recorded for all the configurations tested.

Figure 5 is a nondimensional plot showing the effect of four nozzle-exit jet Mach numbers on the local jet Mach number profiles (M_l/M) at the nozzle-exit plane and at three stations downstream of the nozzle exit. Plotted are (1) the downstream local Mach number M_l at each station divided by the downstream peak Mach number M at the survey station and (2) the radius r of M_l divided by r_{max}, the radius of the jet defined as the point where M_l was zero at the survey station. These jet Mach number profiles are reasonably similar over the range of nozzle-exit jet Mach numbers M_j of 0.63 to 1.15. The similarity of these profiles is also evident in figure 4, since increasing M_j simply raises the level of M_l without altering the general shape of the profile at any given survey station. Because of the similarity of velocity profiles, a nominal M_j of 0.99 was used for the jet Mach number decay and spreading contours presented in appendix A for all the configurations investigated.

Tables IV to VI list M as a function of survey axial distance X for all the configurations investigated. Also tabulated for most of the configurations are the measured values of M_j and nozzle mass flow rate W_n divided by their respective calculated ideal values ($M_{j,id}$ and $W_{n,id}$).

JET MACH NUMBER DECAY CORRELATIONS

Data Variations

The peak axial jet Mach number decay data from the configurations previously described were used to develop nondimensional graphs similar to the ones shown in figure 6. In this figure, the downstream peak Mach number M is divided by the nozzle-exit jet Mach number M_j and the ratio is plotted as a function of an axial distance parameter $X/\left(C_n D_e \sqrt{1 + M_j}\right)$.

According to references 7 to 9, the axial-decay ratio of M/M_j downstream of a single-element jet nozzle exit varies from a function of X^{-1} for circular nozzles to a function of $X^{-1/2}$ for finite- or large-aspect-ratio rectangular (slot) nozzles (fig. 6(a)). For other single-element shapes the Mach number decay also varies between these exponents. The axial distance is nondimensionalized by the equivalent diameter of the single element (i.e., X/D_e (ref. 6)).

The peak Mach number ratio M/M_j at a given axial survey station has been found to increase with increasing M_j (refs. 10 and 11). In general, the exit Mach number effect was correlated by dividing the axial distance parameter X/D_e by $\sqrt{1 + M_j}$ (ref. 6). The Mach number factor applies to the entire decay curve. The axial distance parameter $X/\left(D_e \sqrt{1 + M_j}\right)$ is then divided by a empirical normalizing coefficient C_n $\left(\text{i.e., } X/\left(C_n D_e \sqrt{1 + M_j}\right) \text{(ref. 6)}\right)$. The coefficient C_n accounts for the nonideal conditions of flow and exit velocity for the test nozzle. For an ideal nozzle, C_n would be equal to 1.0. This coefficient is discussed and compared with a kinetic energy ratio in a later section.

For multielement nozzles, the initial axial decay of M/M_j (fig. 6(b)) is the same as that for a single element. At some downstream distance, departure point (1) defined by an axial distance parameter of $Z_{(1)}$, the individual jets coalesce sufficiently to form a large-diameter coalescing core; and a very slow decay of the peak axial Mach number occurs. Once the coalescing core has fully formed into a new large-diameter jet, departure point (2), normal mixing again takes place with a rapid Mach number decay. The coalesced-core decay thus becomes a distance- or diameter-adjusted extension of the single-element decay and is displaced from the single-element decay curve by D_x.

In references 10 and 11 the multielement-nozzle jet velocity decay distance was nondimensionalized by use of an equivalent diameter $D_{e,T}$ based on the total nozzle-exit area. For the wide range of multielement configurations covered in this investigation, it was determined that an equivalent diameter D_e based on a single-element area was more useful for practical applications.

The next section presents the jet Mach number decay correlation equations from reference 6.

Correlation Equations

The peak Mach number ratio M/M_j is a function of the axial distance parameter $X\Big/\left(C_n D_e \sqrt{1 + M_j}\right)$, figure 6(b). For all nozzle shapes except rectangular, the following empirical equation predicts the single-element, peak Mach number ratio:

$$\frac{M}{M_j} = \left[1 + \left(\frac{0.15\ X}{C_n D_e \sqrt{1 + M_j}}\right)^a\right]^{-1/a} \tag{1}$$

where

$$a = 4\left(2 - \frac{w_s}{w_l}\right)\left[1 + \frac{8}{3}\left(\frac{D_e}{D_h} - 1\right)\right]^{-1} \tag{2}$$

For a circular nozzle, the exponent a reduces to 4.

<u>For rectangular nozzles only</u>, because of an aspect ratio effect, the exponent a should be replaced by a', where

$$a' = a\left\{1 + \left[\frac{\frac{8}{3}}{(1 + 0.0001)(AR)^3\left(\frac{X}{C_n D_e \sqrt{1 + M_j}}\right)}\right]^3\right\} \tag{3}$$

Rewriting equation (1) with the exponent given by equation (3) results in the following correlation for rectangular nozzles:

$$\frac{M}{M_j} = \left[1 + \left(\frac{0.15\ X}{C_n D_e \sqrt{1 + M_j}}\right)^{a'}\right]^{-1/a'} \tag{3a}$$

For multijet Mach number decay, the axial distance parameter at departure point (1) (fig. 6(b)) is calculated from the geometric and operating characteristics of the nozzles by the equation

$$Z_{(1)} = \left(\frac{X}{C_n D_e \sqrt{1 + M_j}}\right)_{(1)} = 12\left[1 + \frac{1}{4} f\left(\frac{s}{d}\right)\right]^{2/3} f\left(\frac{s}{d}\right)^{1/3} f\left(\frac{D_e}{D_h}\right) f\left(\frac{r}{s}\right) \tag{4}$$

where

$$f\left(\frac{D_e}{D_h}\right) = \left[1 + \frac{\frac{8}{3}\left(\frac{D_e}{D_h} - 1\right)}{1 + 5\left(1 - \frac{w_s}{w_l}\right)^8}\right]^{-1} \tag{5}$$

and

$$f\left(\frac{r}{s}\right) = \left\{1 + 0.33\,\frac{r}{s}\,[f(d)]^3\left(\frac{M_b}{M_j}\right)^2\right\}^{-1} \tag{6}$$

The following table summarizes the necessary ratios of f(s/d), (r/s), and f(d) to use in equations (4) and (6):

Nozzle	f(s/d)	r/s	f(d)
Circular center element with one or two rings of elements	s_1/d_1	r_1/s_1	d_1/d_0
Two rings of circular elements; no center element	s_1/d_1	r_2/s_2	d_2/d_1
Multielement rectangular	s_1/w	r_1/s_1	1.0

Good correlation can be achieved for large-aspect-ratio, rectangular, multislot nozzles by dividing $Z_{(1)}$ (eq. (4)) by the following aspect-ratio relation:

$$\left[1 + \frac{1}{0.8 + \dfrac{10^5}{(AR)^4}}\right] \tag{7}$$

The displacement distance of the fully coalesced, multielement core from the single-element curve (D_x, fig. 6(b)) is calculated from the following equation:

$$D_x = 1 + \left[\sqrt{\frac{A_c + A_b\left(\dfrac{M_b}{M_j}\right)^2}{A_e}} - 1\right]\left\{1 + f\left(\frac{s}{d}\right)\left[\frac{1}{1 + 50\left(\dfrac{D_e}{D_h} - 1\right)^{5/3}}\right]\right\}^{-1/2} \tag{8}$$

by using f(s/d) from the preceding table. If M_b/M_j equals 1.0, the term

$$\left[\sqrt{\frac{A_c + A_b\left(\frac{M_b}{M_j}\right)^2}{A_e}} - 1\right]$$

in equation (8) reduces to $\left[(D_{e,T}/D_e) - 1\right]$.

The Mach number decay ratio in the coalescing-core region, ① → ②, is given by the following relation:

$$\left|\frac{M}{M_j}\right|_{①\to②} = \left[\left(\frac{M}{M_j}\right)_{①}\left(\frac{Z_{①}}{\frac{X}{C_n D_e \sqrt{1 + M_j}}}\right)^{1/5}\right]_{①\to②} \tag{9}$$

In the coalesced-core region, ② → ⊚, the Mach number decay ratio is given by

$$\left|\frac{M}{M_j}\right|_{②\to\infty} = \left\{\left[1 + \left(\frac{0.15\,X}{D_x C_n D_e \sqrt{1 + M_j}}\right)^a\right]^{-1/a}\right\}_{②\to\infty} \tag{10}$$

The intersection of the curves calculated from equations (9) and (10) will give the location of point ② in figure 6(b). For rectangular nozzles only, $Z_{①}$ in equation (9) should be divided by the relation (7), and the exponent a in equation (10) should be replaced by the exponent a' in equation (3).

The rectangular single-slot nozzles of reference 10 and some of the rectangular four-slot nozzles of reference 11 had divergent walls (narrow side) in which the divergent wall angle β was varied from 0^o to 30^o. The Mach number decay data for these "β" nozzles were correlated (see ref. 5) by including β in the axial distance parameter as follows:

$$\frac{X(1 + \sin^2\beta)}{C_n D_e \sqrt{1 + M_j}} \tag{11}$$

The term $(1 + \sin^2\beta)$ should be used wherever the axial distance parameter appears in any of the empirical equations for this type of nozzle.

Normalizing Coefficient

An empirical normalizing coefficient C_n was used to adjust the jet Mach number decay data of any nozzle in the downstream direction so that the data fall on a calculated decay curve. The calculated decay curve assumes a C_n of 1.0 and was determined from many small-scale nozzle jet Mach number decay data. For any given nozzle it is impossible to predict what the value of C_n will be. But for a well-built large-scale nozzle, it should be safe to assume a C_n somewhere between 0.95 and 1.0. Sometime after the correlation was developed, unpublished large-scale data confirmed a C_n between 0.95 and 1.0. The real C_n can be determined only by measuring the jet Mach number decay of the actual nozzle, large or small scale. At present, it is not known exactly why the jet Mach number decay with axial distance is different for nozzles of the same size and type. For example, for two different 7.62-centimeter-diameter circular convergent nozzles, the C_n's were 0.85 and 0.91, and for a 3.58-centimeter-diameter circular convergent nozzle, the C_n was 0.82. Comparing the internal geometry of the two 7.62-centimeter-diameter nozzles (see sketches in table I(a)) suggests that the internal approach to the nozzle exit or the way the pressure energy is converted into velocity head affects the jet Mach number decay distance. The internally contoured nozzle from references 10 and 11 required a C_n of 0.91 to correlate the data, whereas the straight conical nozzle (configurations 5 and 6) required a C_n of 0.85. In other words the lower the value of C_n, the less the actual distance that is required for the Mach number to decay to a given value.

It can be speculated that the C_n is attributable to the initial amount of kinetic energy in the nozzle jet. The kinetic energy of the jet is reduced to zero as the jet Mach number decays to zero. For the majority of circular nozzles reported herein, the rate of jet Mach number decay with axial distance is constant; the only difference is the axial distance required to achieve any given jet Mach number. For two jets of the same size, assuming the same rate of energy dissipation with axial distance, the jet with the lower initial kinetic energy would dissipate that energy in the shorter distance.

It can also be speculated that the nozzle-exit boundary layer condition and/or magnitude is the main influence on the distance required for the dissipation of the kinetic energy, since jet mixing occurs at the periphery of the jet. With a very large nozzle the boundary layer is extremely small compared with the total jet. On the other hand, for a small nozzle the boundary layer, although still relatively small, comprises a larger portion of the jet.

A C_n determined from decay data and a kinetic energy ratio for a nozzle that was used for the decay data are now compared. The kinetic energy ratio is defined as

$$\text{K.E. ratio} = \frac{\text{Actual K.E.}}{\text{Ideal K.E.}} = \left(\frac{W_n}{W_{n,id}}\right)\left(\frac{M_j}{M_{j,id}}\right)^2$$

The nozzle-exit Mach number profiles of figure 4 were integrated with a polar planimeter to determine an average flat-peaked total pressure (Mach number) profile. The Mach number ratios calculated from the integration by using an atmospheric pressure p_0 of 100 kN/m^2 are given in the following table:

Measured nozzle-exit jet Mach number, M_j	Ratio of integrated average M_j to ideal, $M_j/M_{j,id}$	Ratio of nozzle mass flow rate to ideal, $W_n/W_{n,id}$	Kinetic energy ratio
0.26	-----	0.869	----
.44	0.913	.896	0.75
.63	.931	.887	.77
.80	.951	.902	.82
.99	.959	.924	.85
1.14	.957	.927	.85
			0.81 (Average)

The nozzle coefficient C_n determined from the decay data was 0.83, very close to the average kinetic energy ratio of 0.81. The C_n values used in this report are based on estimates made from the decay data - not on the kinetic energy ratio concept.

Correlation Summary

The following table lists the correlation equations used to calculate each regime of the Mach number decay curve for each type of nozzle reported herein. Included are the specific ratios listed in tables I to III that were used in the equations.

Nozzle type	Equations to use for –			Table	Values for for $Z_{①}$, eq. (4)						
	M/M_j	$Z_{①}$	D_x		For a, eq. (2) and $f(D_e/D_h)$, eq. (5)		For a', eq. (3)	f(s/d)	For f(r/s), eq. (6)		
					W_s/W_l	D_e/D_h	AR		r/s	f(d)	M_b/M_j
Single element:											
Circular[a]	1, 2	-------	---	I(a)	1.0	1.0	---	------	---------	------	---------
Rectangular	2, 3, 3a	-------	---	I(b)	1.0	(b)	(b)	------	---------	------	---------
Rectangular with β exit	2, 3, 3a, 11	-------	---	I(b)	1.0	↓	(b)	------	---------	------	---------
Triangular	1, 2	-------	---	I(c)	0	↓	---	------	---------	------	---------
Trapezoidal	↓	-------	---	I(d)	(b)	↓	---	------	---------	------	---------
Y-shape	↓	-------	---	I(e)	1.0	↓	(b)	------	---------	------	---------
Annular[c]	↓	-------	---	I(f)	1.0	1.0	---	------	---------	------	---------
Multielement - coplanar:											
Circular											
0-x-0	1, 2	4, 5, 6	8	II(a)	1.0	1.0	---	s_1/d_1	0	1.0	1.0
0-x-x	↓	↓	↓	↓	↓	↓	---	↓	r_2/s_2	d_2/d_1	↓
1-x-0	↓	↓	↓	↓	↓	↓	---	↓	$r_1/s_1 = 1.0$	d_1/d_0	↓
1-x-x	↓	↓	↓	↓	↓	↓	---	↓	$r_1/s_1 = 1.0$	d_1/d_0	↓
Rectangular array	↓	↓	↓	↓	↓	↓	---	↓	$r_1/s_1 = 1.0$	1.0	↓
Rectangular											
Three slots (configurations 70 and 71)[d]	2, 3, 3a	4+7, 5, 6	8	II(b)	1.0	(b)	(b)	s_1/W	$r_1/s_1 = 0$	1.0	1.0
Three slots	2, 3, 3a	↓	↓	↓	↓	↓	↓	↓	↓	↓	↓
Four slots	2, 3, 3a	↓	↓	↓	↓	↓	↓	↓	↓	↓	↓
Four slots (ref. 11)	2, 3, 3a, 11	↓	↓	↓	↓	↓	↓	↓	↓	↓	↓
Six slots	2, 3, 3a	↓	↓	↓	↓	↓	↓	↓	r_1/s_1	↓	↓
Triangular	1, 2	4, 5, 6	↓	II(c)	0	↓	---	s_1/W_l	s_1/W_l	↓	↓
Trapezoidal	1, 2	4, 5, 6	↓	II(d)	(b)	↓	---	s_1/W_l	1.0	W_s/W_l	↓
Multielement - noncoplanar:											
Core, tubes or orifices; bypass, tubes or orifices	1, 2 (core flow)	4, 5, 6	8	III	1.0	1.0	---	s_1/d_1	r_2/s_2	d_2/d_1	Use average values
Core, tubes or orifices; bypass, annulus	(e)	(e)	(e)	↓	---	---	---	------	---------	------	---------
Core, slot; bypass, annulus	(e)	(e)	(e)	↓	---	---	---	------	---------	------	---------
Core, conical nozzle; bypass, annulus	(e)	(e)	(e)	↓	---	---	---	------	---------	------	---------

[a]Eq. (2) = a = 4.
[b]Values listed in tables I to III.
[c]$D_e = \sqrt{4A_n/\pi}$; eq. (2) = a = 4.
[d]Use D_e/D_h of center slot.
[e]No equations available.

SINGLE-ELEMENT NOZZLES AND ORIFICES

The following nozzle shapes are described in this section:

(1) Circular; various diameters

(2) Rectangular; various aspect ratios

(3) Triangular

(4) Trapezoidal; flat and round ends

(5) "Y"; three rectangular legs

(6) Annuli; sharp edge, round edge, and converging

Circular Elements

The peak axial Mach number decay of a jet from a circular tube, a round- or sharp-edge orifice, and a circular convergent nozzle is shown in figure 7. All decay data were collapsed onto the calculated correlation curve by using an appropriate C_n. The scatter in the data at large values of the axial distance parameter is possibly a result of not having the manually positioned pitot-static tube at the maximum velocity location in the downstream ($0.9\ m < X < 1.5\ m$), low-velocity jet.

The Mach number decay of a 3.58-centimeter-diameter circular convergent nozzle is shown in figure 8. The data are well correlated by the calculated curve.

In figure 9, the decay data (from ref. 10) for a 7.62-centimeter-diameter convergent nozzle are compared with the calculated decay. The data vary from the calculated curve perhaps because the value of C_n was too high; however, the variation in the data at an M_j of 1.179 cannot be accounted for.

Rectangular Elements

The axial Mach number decay of six rectangular slot orifices is presented in figures 10 to 14. All had sharp edges, except the round-edge rectangular orifice of figure 14(b). The rounding of the inlet edge of the orifice in figure 14(b) had a significant effect on increasing the decay distance; C_n was increased from 0.67 (fig. 14(a)) for the sharp-edge orifice to 0.81 (fig. 14(b)) for the round-edge orifice. As stated previously, the lower the value of C_n, the more rapid the actual decay with distance. For most of the configurations tested, tables IV to VI give ratios of the actual nozzle mass flow rate W_n to the calculated ideal mass flow rate $W_{n,id}$. The ratio of the average $W_n/W_{n,id}$ for the configuration of figure 14(b) divided by that of figure 14(a) is 1.175, and the ratio of the C_n's is 1.209. Since these ratios are so close, the difference in the C_n between the sharp- and round-edge orifices could be attributed mostly to the reduced weight flow for the sharp-edge orifice (i.e., less kinetic energy in the jets).

Figures 15 to 19 present the axial Mach number decay for the single elements of five four-slot, sharp-edge, rectangular orifice nozzles. (All multielement nozzle decay data are discussed in a later section.) In general, the calculated curves predict the data trends. The Mach number decay for the single elements of two six-slot convergent rectangular nozzles are shown in figures 20 and 21.

A round-end rectangular slot (AR = 4.76) was used as the primary or core by a bypass nozzle. In figure 22, the Mach number decay of this core nozzle is well represented by the calculated decay curve.

The convergent rectangular-slot nozzle used for the data of figure 23 was one of three identical nozzles that were used on two three-slot nozzle configurations to study the effect of nozzle spacing. The same single-slot nozzle was tested with 15° end plates with side walls (fig. 24). The peak axial Mach number decay was affected by the end plates to the extent that the C_n was reduced from 0.94 to 0.88.

Mach number decay data taken from reference 10 for five convergent nozzles with aspect ratios from 1 to 6 and wall divergence angles β from 0° to 30° are shown in figures 25 to 29. The "β" correction factor has been included in the axial distance parameter.

The decay data from reference 8 for a 21.7-aspect-ratio slot nozzle are shown in figure 30. According to reference 8, great care was applied in building the nozzle and air supply system. This is shown by the fact that the nozzle coefficient C_n is 1.0.

Triangular Elements

The axial Mach number decay data for three triangular sharp-edge orifices are shown in figures 31 to 33. Good agreement of the data with the predicted curves is apparent for the three nozzles, which have length-to-base ratios from 1.5 to 6.0.

Trapezoidal Elements

Figures 34 to 36 give the Mach number decay data for three different flat-end trapezoidal nozzles; figure 37 presents the decay of a round-end trapezoidal nozzle. All four nozzles were single elements of multielement nozzles. Again the data agree well with the predicted curves. Rounding the short sides of the trapezoidal nozzle (fig. 37) did not appear to affect the Mach number decay.

"Y" Shape

The Mach number decay data of figure 38 are for a three-leg, "Y"-shape, sharp-edge orifice. The peak axial Mach number was dominated by the jet on the orifice centerline. Except at large distances downstream of the nozzle-exit plane, the data correlated well with the predicted curve.

Annuli

The axial Mach number decay for three different annuli is shown in figures 39 to 41. The decay of an annulus can be predicted by converting the annular flow area to an equivalent circular flow area with a diameter of D_e. The jet from the sharp-edge annulus of figure 39 evacuated the surface of the inside diameter of the annulus (appendix A). Since the inner surface of the jet was exhausting to a pressure lower than atmospheric, the jet overexpanded. As a result the decay was much more rapid; hence the low value of 0.32 for C_n. Rounding the inlet edge of an annulus and adding an afterbody (fig. 40) improved the flow conditions, and the decay data are well correlated. The data in figure 41 for a converging annulus are also well predicted by the calculated curve.

MULTIELEMENT NOZZLES

(NOMINALLY COPLANAR EXITS)

Nozzle configurations to be discussed in this section include

(1) Multielement circular arrays; single and double rings of elements, with and without an element on the nozzle centerline

(2) Rectangular elements; 3, 4, and 6 slots

(3) Triangular elements; 2-, 4-, and 12-lobe convergent nozzles from reference 10

(4) Trapezoidal elements; 6- and 12-lobe flat-end elements, and 2-, 4-, 7-, or 8-lobe round-end elements.

Circular Elements

For the circular tube or orifice multielement nozzles, a designation such as 0-6-0 is used to describe the number of elements in the nozzle. As previously stated, the first digit (1 or 0) denotes whether or not a center tube was used, the second digit represents the number of elements in the first ring, and the third digit represents the number of elements in the second ring.

Configuration 0-6-0. - Figures 42 to 45 present the Mach number decay data of six-tube (0-6-0) nozzles with spacing ratios s_1/d_1 from 0.345 to 1.825. The spacing dimension s_1 and the jet width d_1 are determined from the tube inside diameters and therefore represent actual jet spacing dimensions.

Orifice inlet condition: The effect of the orifice inlet condition (round or sharp edge) on the Mach number decay of a 0-6-0 multiorifice nozzle can be seen in figures 46 and 47. The previous discussion about a sharp- or round-edge rectangular orifice (figs. 14(a) and (b)) would apply for these nozzles also. However, for these nozzles, the average weight flow ratio $W_n/W_{n,id}$ (tables IV to VI) and C_n for the round-edge orifices are 1.270 and 1.127 times the corresponding values for the sharp-edge orifices. The calculated coalesced-core decay distance for both nozzles underpredicts the actual data somewhat at large axial distances.

Figure 48 is a composite plot of the calculated decay curves for the 0-6-0 multitube nozzles just discussed. As the spacing s_1 between the tubes (or orifices) is increased, the departure point of the coalescing jets from the single-element decay curve occurs further downstream. The symbols represent points (1) and (2) in figure 6(b). For these six-jet nozzles the coalesced-core decay is a weak function of the nozzle spacing.

Swirl inducer: Figure 49 presents the Mach number decay of the multitube nozzle of figure 44 with a swirl-inducing tape in each tube (approx. 110° twist in 10.16-cm length). The purpose of the swirl in each jet was to increase the decay and coalescing of the individual jets. However, no significant results were obtained. The initial single-element decay data are a few percentage points below the calculated curve, but the overall results are the same as for figure 44. The C_n is 0.78 for both nozzles. Similar negligible results were obtained in reference 10 for a circular convergent nozzle with a vortex generator insert (short vanes around the inside of the nozzle) and also for turbulence rings at the nozzle inlet.

Configuration 0-8-0. - Shown in figure 50 are Mach number decay data for a 0-8-0 multitube nozzle. The data are well correlated by the calculated decay curves. This nozzle was used as the core nozzle for several noncoplanar bypass nozzles that are discussed later.

Configuration 0-6-6. - Figures 51 to 56 present Mach number decay data for several 0-6-6 multiorifice and multitube nozzles. Increasing the radial spacing between the first and second rings of sharp-edge orifices (figs. 51 to 53) had a minimal effect on the overall decay for the range of r_2/s_2 covered. The departure point from the single-element decay curve is controlled by the spacing ratio s_1/d_1 of the inner ring of jets. The differences in the C_n's required to correlate the data for these three orifice nozzles is attributed to the coalescing of any two radially adjacent jets. Comparing the peak Mach number ratios for these configurations (appendix A) at an X/D_e of 10 shows that the closely spaced jets of figure 51 almost immediately coalesce but those of figures 52 and 53 remain somewhat separated. To collapse the Mach number decay ratios onto a single curve, the distance has to be adjusted by the C_n.

The data in figures 54 to 56 are for the 0-6-6 multitube nozzles. Because of the small spacing ratio s_1/d_1 of the inner ring, the departure point in figure 54 is at a relatively high value of M/M_j. The multitube nozzle used for the data of figure 55 had the same centerline radii as the orifices used for figure 53. The calculated decay curves for both configurations are identical, except for the slight effect of the different spacing ratio s_1/d_1 on the coalescing-core region. The orifice data (fig. 53) are not predicted nearly as well at the departure point and in the coalescing-core region as are the tube data (fig. 55). Again, the effect on the coefficient C_n is seen by comparing sharp-edge orifices to tubes, as in the case previously discussed, where a round-edge and a sharp-edge rectangular slot were compared. The nozzle used for the data in figure 56 had the same inner-ring radius as that for figure 55, but the outer-ring radius was increased to 10.16 centimeters. The effect of this radius increase was minimal in both the decay data and the calculated curves.

Configuration 0-6-12. - Adding six more tubes to the outer ring of the 0-6-6 nozzle of figure 56 created the 0-6-12 nozzle of figure 57. The departure point is at a slightly higher M/M_j than for the 0-6-6 nozzle; and because more kinetic energy was added by the six additional jets, the coalesced-core decay region occurred further downstream than for the 0-6-6 nozzle.

Configuration 0-6-18. - Figure 58 presents the peak axial Mach number decay of a 0-6-18 sharp-edge orifice nozzle. Because the spaces between the orifices were pumped to below atmospheric rates by the exiting jets (appendix A), the initial single-element velocity decay was much more rapid than would be predicted. (Similar results were shown in fig. 39.) As a result the coalescing-core region was also at a lower Mach number than predicted. The coefficient C_n was chosen by assuming that the coalesced-core region would decay as predicted.

Configuration 1-6-0. - Mach number decay data for three 1-6-0 multitube nozzles are presented in figures 59 to 61. For figures 59 and 61, the exposed tube length was 1.27 centimeters. The nozzle tubes were always 10.16 centimeters long, but an adjustable baffle with holes matching the nozzle tube base was positioned to vary the external length of tube exposed to the atmosphere. The space between the baffle and the nozzle base was covered and sealed with a sheet metal cylinder. The nozzle radii of the six tube rings of these three nozzles are the same as those of the 0-6-0 nozzles shown in figures 43 to 45, respectively. The result of adding a jet to the center of a six-tube ring was that the jets began coalescing sooner and at a higher Mach number ratio because of reduced atmospheric ventilation area surrounding each jet.

The additional jet caused the coalesced-core regions to move downstream a slight amount when compared with the 0-6-0 nozzles.

Configuration 1-6-6. - Figures 62 and 65 show the axial Mach number decay of three radially symmetric 1-6-6 multitube nozzles; figures 66 to 69 present variations of one radially nonsymmetric 1-6-6 multitube nozzle. In general, all the decay data are well predicted by the calculated correlation equations.

Exposed tube length had a negligible effect on the axial decay of a 1-6-6 nozzle (fig. 63). Essentially no difference in the decay was observed (fig. 66) when the exposed tube length was reduced from 10.16 centimeters to 1.27 centimeters at the two survey stations of 12.7 and 50.8 centimeters. Screens were also placed at the inlets of the six outer tubes to reduce their exit velocity (fig. 67). No difference in the peak axial decay was observed, as the seven full-velocity jets dominated the velocity field. When the six outer tubes were shortened from 10.16 centimeters to 3.81 centimeters (fig. 68), again the jets from the seven full-length tubes dominated the velocity field. The decay was affected (fig. 69) when the nozzle center tube was shortened to 1.27 centimeters, the inner tubes were shortened to 6.35 centimeters, and the six outer tubes were 10.16 centimeters long. The jets from the full-length outer tubes were affected by the decaying and spreading jets of the seven shortened tubes. The peak Mach number at the first survey station came from the outer jets but was at a lower level because of the mixing with the inner jets. Hence, the data are below the single-element calculated decay curve. The actual (not calculated) coalescing-core distance was also longer (jet coalescing began sooner) than for the nozzle of figure 66, wherein all the tubes were the same length.

Configuration 1-6-12. - Figure 70 shows Mach number decay data for a 1-6-12 multitube nozzle. The calculated decay curve and C_n are the same as for the 0-6-12 nozzle with the same tube spacing (fig. 57), except that the coalesced-core region is slightly further downstream because of the additional energy from the nozzle centerline jet.

Rectangular array. - The Mach number decay data in figure 71 are for a 12-tube rectangular-array nozzle (4 tubes by 3 tubes). The data and the calculated curves are essentially identical to the data and the calculated curves for the 1-6-6 nozzles of figures 64 and 66, the main difference being the C_n's required to correlate the data. The 1-6-6 nozzles were used for a comparison since they had the same spacing ratio s_1/d_1. Figure 71 required a C_n of 0.83; both figures 64 and 66 required a C_n of 0.91. Also, the extra jet in the nozzles of figures 64 and 66 moved their coalesced-core region slightly downstream.

Rectangular Elements

Three slots; round ends. - Figures 72 and 73 present Mach number decay data for round-end, three-slot nozzles. For the data in figure 72 all three slots were parallel to the nozzle axis; for the data in figure 73 the two smaller outer slots were canted outward 10° to the nozzle axis. The space between the slot exits was nominally the same for both nozzles. For the data in figure 72, coalescing of the individual jets began just downstream of the 12.7-centimeter survey station - the result of the jets pumping the space between the slots to slightly below atmospheric pressure (appendix A). Therefore the data do not fall on the decay curves calculated for the nozzle geometry. Just the opposite can be said for the data in figure 73 for the nozzle with 10° canted slots. Very little coalescing of the three jets was evident even at the 50.8-centimeter survey station. The decay follows the prediction even though the correlation equations do not include an allowance for the 10° canted jets.

Three slots; flat ends; convergent. - Figures 74 to 76 show the Mach number decay of two, three-slot, convergent nozzle configurations. Comparing figures 74 and 75 shows that as the space between the nozzles is increased the departure point is moved downstream and is at a lower peak Mach number ratio M/M_j. The same nozzles, mounted on different bases, were used for the data in figures 74 and 75. The nozzles had a 1.02-centimeter-long internal structural support web (knife-edge fore and aft) at their exits. From unpublished exit surveys across the long dimension of the nozzles, an appreciable wake from the support web was apparent. At a survey distance of 12.7 centimeters a significant effect on the velocity was noted. This wake probably caused the single jets to begin coalescing sooner than would be predicted, hence the disagreement between the data and the calculated curves in figures 74 and 75. For figure 76, the configuration of figure 75 was rerun with a hemispherical afterbody flush with the nozzle exits. No difference in the Mach number decay was observed for surveys taken as far downstream as 50.8 centimeters.

Four slots; orifices. - Data shown in figures 77 to 81 were taken with four-slot, sharp-edge-orifice nozzles. The spacing ratio s_1/w for all the nozzles was 2.0, but the single-slot aspect ratio was varied from 2.22 to 11.25. In figure 77, the last three sets of decay data are well below the predicted curve. These data were taken with the manually positioned pitot-static tube; and because of the small jets of the configuration, the pitot-static tube apparently was not placed at the maximum velocity location in the downstream jet. The effect of the jets pumping the surface space between the slots to below atmospheric pressure is seen again in figure 78. The data do not show any obvious departure point, but rather a fairly continuous smooth decay. The data in figure 79 are well predicted by the calculated curves. For the configuration of figure 80, the nozzle-exit survey revealed slightly subatmospheric pressure between the slots (appendix A), and this is possibly the reason that the 12.7-centimeter data are somewhat below the predicted values. The balance of the data follow the prediction. In figure 81, two calculated Mach number decay curves are shown. Considering the fact that the subatmospheric pressure was observed (appendix A), between the jets at the nozzle exit as well as at the 2.54-centimeter survey station, the dashed curve ($C_n = 0.80$) in figure 81 is probably the more correct curve. It shows that the initial single-element decay is more rapid than would be predicted. This condition would exist with the subatmospheric pumping (jet overexpansion) occurring between the jets.

Four slots; convergent. - The Mach number decay data from reference 11 for four-slot rectangular convergent nozzles are shown in figures 82 to 84. Many of these nozzles had divergent walls (narrow side); the divergent wall angle β for each side was either 0^o, 5^o, 15^o, or 30^o. The effect of β on the decay data was correlated by including $(1 + \sin^2\beta)$ in the axial distance parameter. The effect of aspect ratio h/w is shown in figure 82; in figure 83 the effect of wall-divergence angle β is shown; in figure 84 the effect of the nozzle spacing ratio s_1/w on the peak axial decay is presented. In general, the decay data are well correlated by the calculated decay equations, except the data for $s_1/w = 0.5$ in figure 84.

Six slots; flat ends; convergent. - The decay data for two six-slot ventilated (split element) convergent nozzles are presented in figures 85 and 86. Centerbodies either 3.81 or 6.35 centimeters long were inserted into the middle of each element of the three-slot nozzle of figure 75 with an element spacing of 6.35 centimeters. The centerbodies made second spacing ratios r_1/h of 0.46 and 0.91, respectively. For both configurations, decay data were taken on the centerlines of three elements for the first 50.8 centimeters and also on the six-element nozzle centerline. The data taken on the nozzle centerlines show that a gradual mixing or energizing of the air between the nozzles occurs with increasing distance downstream. It appears that for the shorter centerbody (fig. 85) the separation of the two jets in a common slot is not adequate to maintain separate jets that energize the air between them, and the slope of the Mach number ratio increase is less than 0.2. With a longer centerbody (fig. 86) the slope of the Mach number increase is nearer 0.2. It seems reasonable to assume that the jets would energize the ambient air between them at the same rate that the jets would decay in the coalescing-core regime. It is in the coalesced-core regime that the velocity ratio on the nozzle centerline becomes the dominant peak value. As the centerbody length r_1 is decreased toward zero, the decay will approach that of figure 75. The previously used hemispherical afterbody (flush with the nozzle exits) was installed on the configuration of figure 86, and no difference in the data was observed at survey distances of 25.4 and 50.8 centimeters.

Triangular Elements

Mach number decay data from reference 10 for 2-, 4-, and 12-lobe triangular convergent nozzles are shown in figures 87, 88, and 89, respectively. The single-element decays for all three nozzles are fairly well predicted, but only the 12-lobe nozzle decay (fig. 89) is well correlated over all three decay regimes.

Trapezoidal Elements

Flat ends. - Three flat-end trapezoidal nozzles with nominally the same total area were tested to determine the effect of element spacing and element number on the peak axial Mach number decay. Data obtained with these nozzles are shown in figures 90 to 92 together with calculated decay curves. The calculated decay curves for these three nozzles are compared in figure 93. It is evident that doubling the number of elements while keeping the radial height and the circumferential spacing ratio constant resulted in only a small increase in the Mach number ratio at the departure point from the single-element curve. Increasing the circumferential spacing ratio from 1 to 3 (by increasing the element radial height and reducing its width) for the six-element nozzle resulted in a significantly lower Mach number ratio at the departure point.

Round ends. - The Mach number decay data for nozzles with round-end trapezoidal elements are presented in figures 94 to 100. The data in figures 94 and 95 for a two-lobe and a four-lobe nozzle, respectively, agree well with predicted trends. Decay data shown in figure 96 are for an eight-lobe nozzle with a 10° conical afterbody. Essentially no difference in the peak Mach number ratio was detected by a survey taken at 50.8 centimeters with no afterbody on the nozzle. As the number of lobes is decreased, the values of M/M_j at departure point (1) are significantly lowered.

To promote a greater single-element decay of the peak axial Mach number by maintaining separate jets for a longer time, alternate lobes of the eight-lobed nozzle were canted outward from the nozzle centerline. Decay data achieved with an eight-lobe nozzle with alternate lobes canted 5° and 10° are shown in figures 97 and 98, respectively. The correlation used to predict the decay did not include any allowance for canted nozzles (or jets); therefore, the dashed decay curves beyond the single-element curves are estimated curves through the data. The effect of nozzle cant angle is shown in figure 99. As the nozzle cant angle is increased, the jets maintain their individuality for a greater distance downstream, and lower values of M/M_j are achieved before coalescing of the jets begins.

The eight-lobe nozzle with four 10° lobes was modified by plugging one 10° lobe. Decay data were taken on this seven-lobe nozzle and are presented in figure 100. As discussed in reference 2, this modification reduced the scrubbing noise generated by jet attachment to the underside of the wing in a 1/2-scale externally blown flap (EBF) installation. Although surveys were not taken beyond 50.8 centimeters, the data in figure 100(a) are essentially the same as those in figure 98(a) (no plugged lobe). The survey across the plugged lobe (fig. 100(b)) shows the same slope of Mach number ratio increase (0.2) as did the multislot configuration of figure 86.

MULTIELEMENT BYPASS NOZZLES

(NOMINALLY NONCOPLANAR EXITS)

Nozzle types discussed in this section are typical of high-bypass, fan-jet engine nozzles insofar as the bypass exit plane is some distance upstream of the core exit plane. For some configurations, screens were placed in the bypass portion of a nozzle to vary the bypass-to-core velocity ratio.

Eight-Tube Primary and Eight-Orifice Secondary

In figure 101, data taken with and without screens in the secondary orifices are compared to show the effect of a reduced secondary (bypass) jet Mach number on the peak axial Mach number decay of a nozzle consisting of eight tubes for the primary and eight round-edge orifices for the secondary. By reducing the velocity of the secondary jets, the departure point for figure 101(b) is at a lower value of the ratio M/M_j than that for figure 101(a). For both configurations the data are well represented by the calculated decay curves.

Eight-Orifice Primary and Eight-Orifice Secondary

A planar sharp-edge multiorifice nozzle with the same element location dimensions as in the tube/round-edge orifice nozzle was tested to compare its decay characteristics with that nozzle. The calculated curves in figure 102 were based on the D_e of the secondary (large diameter) orifices since these jets had a higher kinetic energy and therefore supplied the peak velocities at each survey station. The effect of the sharp-edge orifice flow can be seen in the C_n required to correlate the data; -0.60 for figure 102 compared with 0.83 for figure 101(a). Also in figure 102, the departure point is not sharply defined and the coalescing-core region is nonlinear.

Three-Tube Primary and Eight-Orifice Secondary

The configuration for which data are shown in figure 103 had the same secondary (eight round-edge orifices) as the configuration of figure 101, but the eight-tube primary was replaced by three larger tubes. The actual departure point was unaffected by reducing the secondary flow velocity for this nozzle, the calculated departure point being below the data. However, the coalesced-core data show the result of the reduced total energy in the combined jets.

Eight-Tube Primary and Annular Orifice Secondary

In figure 104, decay data are shown for a nozzle configuration consisting of an eight-tube primary surrounded by a 1.02-centimeter-wide sharp-edge annulus. The nozzle was tested with and without a centerbody (see sketch in table III) inside the bundle of eight tubes and with and without a screen in the annulus. Without a screen in the annulus, the presence of a centerbody (compare figs. 104(a) and (b)) makes a significant difference in the Mach number decay rate in the coalescing-core region. In figure 104(b), the annulus flow was attached to the centerbody and retarded the decay rate in the coalescing-core region. However, the departure point appears to be about the same for both configurations. With a screen in the annulus (the screen mesh and wire size were not the same for the two configurations (figs. 104(c) and (d)) - hence, the difference in the annulus Mach number ratio, $M_{b,av}/M_j$), the effect of a centerbody in the eight-tube bundle again shows up. With a centerbody between the tubes (fig. 104(d)) the departure point is at a higher M/M_j than without a centerbody (fig. 104(c)). Just the opposite should have occurred in the location of the departure point considering that the bypass-to-core Mach number ratio M_b/M_j is lower in figure 104(d) than in figure 104(c). Therefore, it is concluded that the centerbody caused an earlier coalescing of the primary and secondary flows. The correlation used for the decay prediction did not include any terms for the effect of an annular jet surrounding a core nozzle. Therefore, the Mach number decay curves are estimated through the data in the coalescing-core and coalesced-core regimes.

Three-Tube Primary and Annular Orifice Secondary

For the data in figure 105, the primary nozzle was again changed from eight tubes to three tubes with the same sharp-edge annulus as for figure 104. No centerbody was used for this configuration. Comparing figures 105(a) and (b) shows that a reduced secondary flow velocity delayed the departure point and that, with less total energy in the coalesced-core regime, the Mach number ratio was less at the same downstream distance.

Round-End Slot Primary and Annular Orifice Secondary

The nozzle of figure 106 had a round-end slot (AR = 4.76) for the primary and a 1.664-centimeter-wide, round-edge annular orifice for the secondary. A smoothed fairing of plaster of paris was used from the inside edge of the annulus to the exit of the slot nozzle (see sketch in table III). Screens of various blockages were used to reduce the velocity of the jet from the annulus. Figures 106(a) to (c) present the decays for three different bypass-to-core nominal Mach number ratios M_b/M_j. The calculated decay curves are based on the calculated (ideal) decay curve for the primary (slot) nozzle. The C_n for the primary nozzle was 0.47 (fig. 22). By increasing the C_n to 0.89, 0.96, and 1.08 for figures 106(a), (b), and (c), respectively, the data correlated very well. Increasing the C_n toward 1.0 and/or greater than 1.0 accounts for the jet energy added to the primary flow by the secondary flow. In figure 106(d), the data are correlated on the calculated decay curve for the annulus only (fig. 40) by using a C_n of 1.2. The secondary (annulus) area is over three times the core (slot) area, and without any velocity reduction in the annulus it is reasonable to expect the annulus jet to dominate the velocity field downstream of the nozzle.

The decay data of figure 106 are normalized in figure 107 by dividing the axial distance parameter by $\left(1 + M_b/M_j\right)^{1.41}$ and using the decay curve of the core (slot) nozzle of figure 22. The data in figures 107(a) to (c) are well predicted; but as mentioned in regard to figure 106(d), the data in figure 107(d) would not be expected to follow the predicted decay of the core (slot) nozzle.

Convergent Circular Primary and Convergent Annulus Secondary

Figure 108 shows the decay data for a bypass nozzle consisting of a 3.58-centimeter-diameter circular convergent nozzle for the primary (core) and a 1.15-centimeter-wide convergent annulus for the secondary (bypass). Screens were placed in the annulus to vary the bypass-to-core Mach number ratio M_b/M_j. The support struts for the core nozzle assembly were splayed and located upstream of the screen location to minimize wake effects (see sketch in table III). Figure 108(a) is a repeat of figure 8 for convenience and shows the axial Mach number decay of the core nozzle only, with a C_n of 0.82. Figures 108(b) to (d) show the decay data for nominal M_b/M_j of

0.50, 0.73, and 1.0, respectively. Using the diameter of the core nozzle, the calculated decay curves required C_n's of 1.27, 1.33, and 1.50, respectively, to account for the jet energy added to the core-only flow.

Normalization of the effect of the secondary flow ratio for the data of figure 108 is shown in figure 109. For this nozzle, the data are normalized by dividing the axial distance parameter by $\left(1 + M_b/M_j\right)^{0.875}$, using the calculated decay curve of the core nozzle.

A slightly larger bypass nozzle with a core nozzle diameter of 5.18 centimeters and an annulus width of 1.60 centimeters was also tested. This nozzle had radial support struts (for the core nozzle assembly) (see sketch in table III) located immediately downstream of the screen location and was built and tested before the nozzle of figure 108. Axial Mach number decay data for this larger nozzle are shown in figures 110(a), (b), and (c) for nominal M_b/M_j ratios of 0.46, 0.69, and 1.0, respectively. For these ratios, C_n's of 1.35, 1.45, and 1.53, respectively, were required to account for the increased jet energy from the bypass flow.

In figure 111 the data of figure 110 are normalized by the same parameter as the smaller bypass nozzle data (fig. 109). Except for the no-screen configuration (fig. 111(c)), the data are not correlated as well as for the smaller bypass nozzle data of figure 109.

JET-INDUCED MACH NUMBER RATIOS BETWEEN ELEMENTS OF MULTIELEMENT NOZZLES

For the data in figure 112 several small-diameter, four-hole, stream-static-pressure tubes were mounted off the nozzle base parallel to the tubes and at various distances upstream of the tube exits. Two static probes were laid flat on the nozzle base (i.e., at 10.16 cm upstream of the tube exits). An induced Mach number M_s was calculated by using atmospheric pressure p_0 (for total pressure) and static pressure p_s (read on a water manometer board referenced to atmospheric pressure) in the following isentropic relation:

$$M_s = \sqrt{5\left[\left(\frac{p_0}{p_s}\right)^{(\gamma-1)/\gamma} - 1\right]}$$

where the ratio of specific heats γ is 1.4 and $(\gamma - 1)/\gamma = 0.2857$. The calculated induced

Mach number M_s was ratioed to the nozzle-exit Mach number M_j. The range of M_j was from 0.64 to 1.15. As shown in figure 112(a), with all nozzle tubes 10.16 centimeters long, the induced Mach number ratio ranged from nominally 7 percent at a point 1.27 centimeters upstream of the nozzle exit to nominally 2 percent on the nozzle base. When the exposed tube length was reduced to 1.27 centimeters by using an adjustable baffle (described previously in the discussion of figs. 59 and 61), the induced Mach number ratio was increased to nominally 10 percent. As shown in figure 112(b), essentially no difference in the ratio M_s/M_j (compared with fig. 112(a)) was noted when the six outer-tube exit velocities were reduced to about 75 percent of the seven inner-tube exit velocities. An increase of up to 0.025 in the ratio M_s/M_j was noted when the six outer tubes were shortened to 3.81 centimeters (fig. 112(c)). It appears the expanding jets from the six outer tubes increased the induced flow between the seven inner tubes.

Figure 113 presents the effect of exposed nozzle tube length on the Mach number M_s induced at the base of the exposed tube. Two of the four-hole stream static pressure tubes were attached flat on the surface of the adjustable baffle at radii of 1.75 and 4.92 centimeters. With the baffle flush with the tube exits (zero tube length), a Mach number M_s as high as 23 percent of the nozzle-exit Mach number was induced between the tubes (1.75 cm radius). For the full-length tubes (10.16 cm), 2.5 percent of the nozzle-exit Mach number was induced at both locations on the nozzle base.

As shown in figure 114, one outside surface of the center slot of the two three-slot nozzles (figs. 74 and 75) was instrumented with surface static pressure taps. Depending on the spacing between the nozzles, the induced surface Mach number M_s ranged between 5 and 9.5 percent of the nozzle-exit Mach number. The closer nozzle spacing consistently gave the higher ratio.

CONCLUDING REMARKS

Correlation equations were developed to predict the peak axial jet Mach number decay of a multitude of single- and multielement (mixer) nozzles. Prediction of multitube (nonorifice) nozzle jet decay data was very good over all three decay regimes (i.e., single element, coalescing core, and coalesced core). Prediction of multiorifice nozzle jet decay generally was not as good as for the multitube nozzles.

In using a mixer nozzle for reducing the jet-flap interaction noise from an externally blown flap for STOL aircraft applications, we must consider not only the effect of the reduction of the impinging velocity on the flap, but also the larger jet impingement area on the flap. This increased area is caused primarily by the larger overall dimensions of the mixer-nozzle jet compared with a conventional circular-nozzle jet. Thus, the full jet-flap interaction noise benefits resulting from the velocity decay associated with a mixer nozzle may be significantly reduced by the larger jet impingement area (determined from the width of the velocity profile curve where the velocity is down to 80 percent of the peak jet impingement velocity). Also the mixer-nozzle jets may create a new location of jet-flap interaction noise, such as a flap leading edge or wing scrubbing because of the increased size and location of the mixer nozzle.

For a given Mach number decay requirement, the minimum number of elements for a multielement nozzle appears to be obtained when the design value of $X/\left(C_n D_e \sqrt{1 + M_j}\right)$ for the nozzle is at the departure point of the coalescing core from the single-element curve. This design criterion could be achieved by only a small number of elements for a given nozzle application. And it should cause minimum internal flow losses and external drag increases.

On the basis of the preceding brief remarks, there are obvious performance tradeoffs and compromises that can be exercised in the design of mixer nozzles for specific applications. The empirical relations for predicting peak Mach number decay curves for jets presented herein are a step in establishing rational design procedures for mixer nozzles. Use of present technology for predicting internal nozzle-flow loses and aerodynamic penalties associated with the larger mixer-nozzle surfaces and cross-sectional profiles can provide the additional necessary information to achieve optimum mixer-nozzle configurations.

Lewis Research Center,
National Aeronautics and Space Administration,
Cleveland, Ohio, April 27, 1976,
505-03.

TABLE I. - NOZZLE DIMENSIONS AND CALCULATED VALUES FOR SINGLE-ELEMENT NOZZLES OR ORIFICES

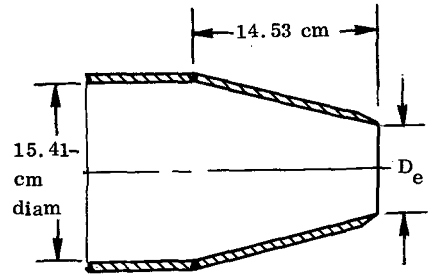

Configurations 5 and 6

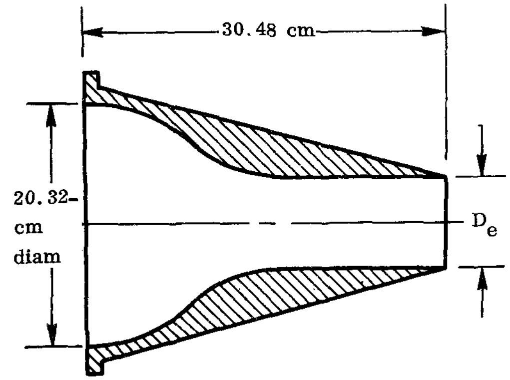

Configuration 8

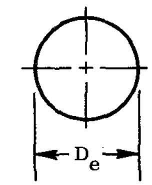

(a) Circular elements

	Configuration							
	a1	2	3	4	b5	c6	d7	e8
Figure	7	7	7	7	7	7	8.108(a)	9
Original run	3	50	51	82	105	106	119	------
Normalizing coefficient, C_n	0.91	0.77	0.91	0.80	0.85	0.85	0.82	0.91
Type	Tube	Orifice	Orifice	Orifice	Nozzle	Nozzle	Nozzle	Nozzle
Inlet	82° Countersunk	Sharp edge	Round edge	Sharp edge	------	------	------	------
Nozzle axial length, l, cm	10.16	0.318	0.318	0.635	------	------	------	------
Total nozzle area, A_n, cm^2	4.38	4.75	4.75	5.08	45.60	45.60	10.10	45.60
Nozzle diameter, D_e, cm	2.36	2.46	2.46	2.54	7.62	7.62	3.58	7.62

[a] 1.27 cm of tube exposed to atmosphere.
[b] 15° Half-angle convergent (0.318-cm lip).
[c] 15° Half-angle convergent (0.079-cm lip).
[d] 4.4° Half-angle convergent (sharp lip).
[e] Nozzle 1 (refs. 10 and 11).

TABLE I. - Continued.

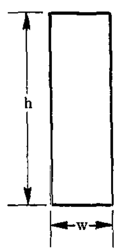

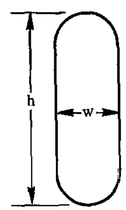

Configuration 22

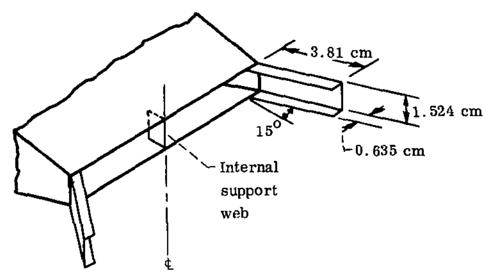

Configuration 24

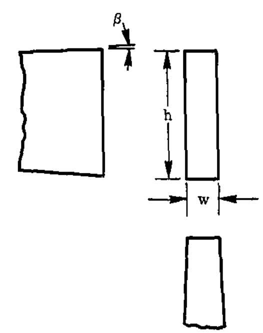

Nozzles 5 to 9 of ref. 10

(b) Rectangular elements

	Configuration																					
	9	10	11	12	13	14	[f]15	[g]16	[h]17	[i]18	[j]19	[k]20	[l]21	[m]22	[n]23	[o]24	[p]25	[q]26	[r]27	[s]28	[t]29	[u]30
Figure	10	11	12	13	14a	14b	15	16	17	18	19	20	21	22	23	24	25	26	27	28	29	30
Original run	40	41	42	43	44	52	80	70	87	89	74	101	104	109	98	99	-------	-------	-------	-------	-------	-------
Normalizing coefficient, C_n	0.71	0.63	0.60	0.60	0.67	0.81	0.70	0.84	0.63	0.67	0.59	0.81	0.78	0.47	0.94	0.88	0.93	0.33	0.50	0.31	0.73	1.00
Type	Orifice	Orifice	Orifice	Orifice	Orifice	Orifice	Orifice	Orifice	Orifice	Orifice	Orifice	Convergent nozzle	Convergent nozzle	Convergent nozzle	Convergent nozzle	Convergent nozzle	Convergent nozzle	Convergent nozzle	Convergent nozzle	Convergent nozzle	Convergent nozzle	Convergent nozzle
Inlet	Sharp edge	Sharp edge	Sharp edge	Sharp edge	Sharp edge	Round edge	Sharp edge	Sharp edge	Sharp edge	Sharp edge	Sharp edge	-------	-------	-------	-------	-------	-------	-------	-------	-------	-------	-------

Thickness of orifice plate, *t*, cm	0.318	0.318	0.318	0.318	0.318	0.318	0.635	0.318	0.635	0.635	0.318	-------	-------	-------	-------	-------	-------	-------	-------	-------	-------	-------
Total nozzle area, A_n, cm^2	38.70	77.50	58.00	38.70	19.35	19.35	11.61	11.61	26.10	17.41	11.61	10.64	12.58	22.20	30.97	30.97	45.60	45.60	45.60	45.60	45.60	195.00
Equivalent diameter, D_e, cm	7.03	9.94	8.60	7.03	4.96	4.96	3.84	3.84	5.76	4.71	3.84	3.68	4.00	5.32	6.28	6.28	7.62	7.62	7.62	7.62	7.62	15.75
Hydraulic diameter, D_h, cm	6.100	7.620	6.100	4.350	2.340	2.340	3.150	2.540	3.810	2.690	1.866	2.500	2.570	3.900	2.830	2.830	6.750	6.370	5.030	5.030	4.700	5.740
Diameter ratio, D_e/D_h	1.152	1.302	1.410	1.615	2.120	2.120	1.220	1.516	1.512	1.750	2.059	1.471	1.558	1.365	2.220	2.220	1.130	1.198	1.515	1.515	1.620	2.750
Noncircular element width, w, cm	5.080	5.080	3.810	2.540	1.270	1.270	2.286	1.524	2.286	1.524	1.020	1.524	1.524	2.290	1.524	1.524	6.750	4.775	3.020	3.020	2.740	3.000
Noncircular element height, h, cm	7.62	15.24	15.24	15.24	15.24	15.24	5.08	7.62	11.43	11.43	11.43	6.99	8.25	10.30	20.32	20.32	6.75	9.55	15.10	15.10	16.55	65.00
Aspect ratio, AR = h/w (except as noted)	1.50	3.00	4.00	6.00	12.00	12.00	2.22	5.00	5.00	7.50	11.25	4.51	5.42	[v]4.76	13.33	13.33	1.00	2.00	5.00	5.00	6.00	21.70

[f]*Single slot of four-slot configuration* 75.
[g]Single slot of four-slot configuration 76.
[h]Single slot of four-slot configuration 77.
[i]Single slot of four-slot configuration 78.
[j]Single slot of four-slot configuration 79.
[k]Single slot of six-slot configuration 90.
[l]Single slot of six-slot configuration 89.
[m]*Core nozzle of* bypass-nozzle configurations 114 to 117.
[n]Single nozzle of three-slot configurations 72 to 74.
[o]Configuration 23 with 15° end plates.
[p]Reference 10; nozzle 5; wall divergence angle, β, 0°.
[q]Reference 10; nozzle 7; wall divergence angle, β, 30°.
[r]Reference 10; nozzle 8; wall divergence angle, β, 5°.
[s]Reference 10; nozzle 9; wall divergence angle, β, 30°.
[t]*Reference* 10; *nozzle 6; wall divergence* angle, β, 0°.
[u]Reference 8.
[v]$AR = h^2/A_e$.

TABLE I. - Continued.

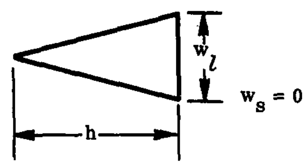

(c) Triangular elements (sharp-edge orifices, 0.318 cm thick)

	Configuration		
	31	32	33
Figure	31	32	33
Original run	46	47	48
Normalizing coefficient, C_n	0.71	0.65	0.67
Total nozzle area, A_n, cm^2	19.35	38.70	19.35
Equivalent diameter, D_e, cm	4.96	7.03	4.96
Hydraulic diameter, D_h, cm	3.66	4.30	2.34
Diameter ratio, D_e/D_h	1.360	1.635	2.120
Larger width of variable-width element, w_l, cm	5.08	5.08	2.54
Noncircular element height, h, cm	7.62	15.24	15.24

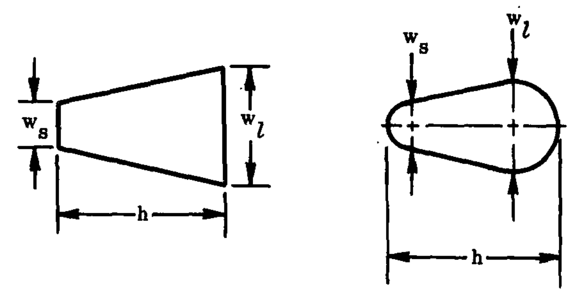

(d) Trapezoidal elements (round inlet; constant flow area)

	Configuration			
	[w]34	[x]35	[y]36	[z]37
	Flat end		Round end	
Figure	34	35	36	37
Original run	54	56	58	22
Normalizing coefficient, C_n	0.77	0.83	0.81	0.71
Nozzle axial length, l, cm	7.62	7.62	7.62	5.08
Total nozzle area, A_n, cm^2	8.00	7.67	3.80	11.40
Equivalent diameter, D_e, cm	3.190	3.125	2.200	3.810
Hydraulic diameter, D_h, cm	2.350	2.690	1.736	3.050
Diameter ratio, D_e/D_h	1.36	1.16	1.27	1.25
Smaller width of variable-width element, w_s, cm	0.915	1.575	0.838	1.194
Larger width of variable-width element, w_l, cm	2.130	3.30	1.575	2.510
Noncircular element height, h, cm	5.23	3.15	3.15	6.22

[w]Single nozzle of configuration 94.
[x]Single nozzle of configuration 95.
[y]Single nozzle of configuration 96.
[z]Single nozzle of configurations 97 to 102.

TABLE I. - Concluded.

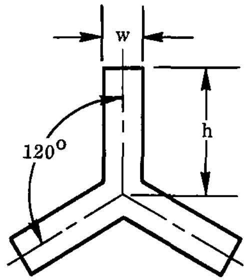

(e) Y-shape (sharp-edge orifice, 0.318 cm thick)

	Configuration 38
Figure	38
Original run	45
Normalizing coefficient, C_n	0.93
Total orifice:	
Throat nozzle area, A_n, cm^2	55.4
Equivalent diameter, D_e, cm	8.41
Hydraulic diameter, D_h, cm	4.51
One leg:	
Noncircular element width, w, cm	2.54
Noncircular element height, h, cm	7.62
Aspect ratio, $AR = h^2/(A_n/3)$	3.14

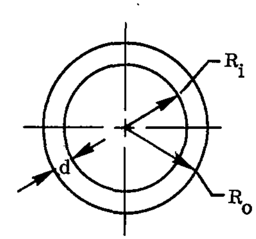

(f) Annuli

	Configuration		
	aa39	bb40	cc41
Figure	39	40	41
Original run	90	111	120
Normalizing coefficient, C_n	0.32	0.82	0.85
Type	Orifice 0.476 cm thick	Orifice 0.476 cm thick	Convergent
Inlet	Sharp edge	Round edge	-------
Total nozzle area, A_n, cm^2	38.7	69.0	32.9
Inner radius, R_i, cm	5.588	5.715	3.962
Outer radius, R_o, cm	6.604	7.379	5.118
Annulus height, d, cm	1.106	1.664	1.156
Equivalent diameter, D_e, cm	7.050	9.370	6.472
Hydraulic diameter, D_h, cm	2.03	3.33	2.31
Diameter ratio, D_e/D_h	3.470	2.815	2.803

[aa]Used on configurations 108 to 113.
[bb]Used on configurations 114 to 117.
[cc]Used on configurations 118 to 120.

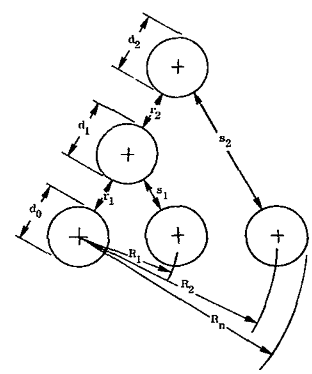

CE - Circular array, equal number of tubes per ring

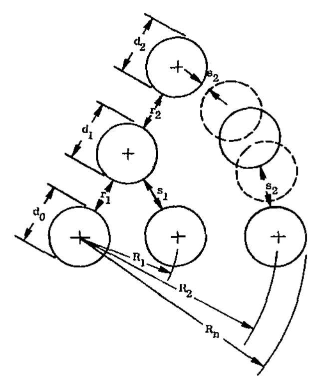

CU - Circular array; unequal number of tubes per ring

(a) Circular element

	Configuration												
	42	43	44	45	46	47	[a]48	[b]49	50	51	52	53	54
Figure	42	43	44	45	46	47	49	50	51	52	53	54	55
Original run	14	13	11	16	59	49	96	65	85	84	83	18	92
Normalizing coefficient, C_n	0.83	0.78	0.78	0.83	0.71	0.63	0.78	0.83	0.77	0.70	9.63	0.89	0.80
Value of axial distance parameter $X/C_nD_e\sqrt{1+M_j}$ at departure point of coalescing core from single-element decay curve, $Z_{①}$	9.45	12.03	16 04	20.14	15.44	15.44	16.04	16.37	14.85	14.47	14.07	8.86	14.94
Analytical displacement parameter, D_x	2.25	2.14	1.99	1.86	2.01	2.01	1.99	2.23	2.74	2.74	2.74	3.13	2.69
Designation[j]	0-6-0	0-6-0	0-6-0	0-6-0	0-6-0	0-6-0	0-6-0	0-8-0	0-6-6	0-6-6	0-6-6	0-6-6	0-6-6
Array[k]	CE	CE	CE	CE	CE	CE	CE	CE	CE	CE	CE	CE	CE
Type	Tubes	Tubes	Tubes	Tubes	Orifices	Orifices	Tubes	Tubes	Orifices	Orifices	Orifices	Tubes	Tubes
Inlet	82° Counter sunk	Sharp edge	82° Counter sunk	82° Counter sunk	Round edge	Sharp edge	37° Flared	82° Counter sunk	Sharp edge	Sharp edge	Sharp edge	82° Counter sunk	37° Flared
Nozzle axial length, l, cm	10.160	10.160	10.160	10.160	0.318	0.318	10.160	10.160	0.635	0.635	0.635	10.160	10.160
Equivalent diameter, $D_{e,T}$, cm	5.79	5.79	5.79	5.79	6.03	6.03	5.66	3.99	8.80	8.80	8.80	8.20	8.20
Equivalent diameter,[l] D_e, cm	2.36	2.36	2.36	2.36	2.46	2.46	2.31	1.41	2.54	2.54	2.54	2.30	2.36
Equivalent diameter ratio, $D_{e,T}/D_e$	2.449	2.449	2.449	2.449	2.449	2.449	2.449	2.828	3.464	3.464	3.464	3.464	3.464
Centerline radius of first ring of tubes, R_1, cm	3.18	3.81	5.08	6.67	5.08	5.08	5.08	4.06	5.08	5.08	5.08	3.18	5.08
Centerline radius of second ring of tubes, R_2, cm	-------	-------	-------	-------	-------	-------	-------	-------	7.78	8.25	8.89	6.35	8.89
Overall nozzle radius R_n, cm	4.35	4.99	6.27	7.84	6.32	6.32	6.27	4.76	9.04	9.52	10.16	7.53	10.08
Actual radial and circumferential spacing between jets, cm:													
r_1	-------	-------	-------	-------	-------	-------	-------	-------	-------	-------	-------	-------	-------
s_1	0.813	1.450	2.720	4.300	2.620	2.620	2.720	1.698	2.540	2.540	2.540	0.813	2.720
r_2	-------	-------	-------	-------	-------	-------	-------	-------	0.159	0.635	1.270	0.813	1.450
s_2	-------	-------	-------	-------	-------	-------	-------	-------	5.24	5.71	6.35	3.99	6.53
Spacing ratios:													
r_1/s_1	-------	-------	-------	-------	-------	-------	-------	-------	-------	-------	-------	-------	-------
r_2/s_2	-------	-------	-------	-------	-------	-------	-------	-------	0.0304	0.1110	0.2000	0.2040	0.2220
r_1/d_1	-------	-------	-------	-------	-------	-------	-------	-------	-------	-------	-------	-------	-------
r_2/d_2	-------	-------	-------	-------	-------	-------	-------	-------	0.063	0.250	0.500	0.345	0.615
s_1/d_1	0.345	0.613	1.152	1.825	1.064	1.064	1.152	1.203	1.000	1.000	1.000	0.345	1.152
s_2/d_2	-------	-------	-------	-------	-------	-------	-------	-------	2.06	2.25	2.50	1.69	2.77

[a]Swirl inducers in tubes and deducted from flow area.
[b]Core nozzle for configurations 103, 104, and 108 to 111.
[c]Spaces between orifices pumped subatmospheric.
[d]Exposed tube length 1 27 cm
[e]Exposed tube lengths, 0, 5.08, and 10 16 cm.
[f]Exposed tube lengths, 1 27 and 10.16 cm
[g]Screens in six outer tubes
[h]Six outer tubes, 3.81 cm long, seven inner tubes 10.16 cm long.
[i]Tube lengths, cm center, 1.27, six inner, 6.35, six outer, 10.16.
[j]Denotes number of elements in center, first, and second rings respectively.
[k]See sketches.
[l]$D_e = d_0 - d_1 - d_2$.

…OZZLES WITH COPLANAR EXITS (UNLESS OTHERWISE SPECIFIED)

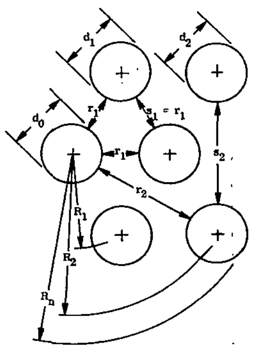

S - Staggered array

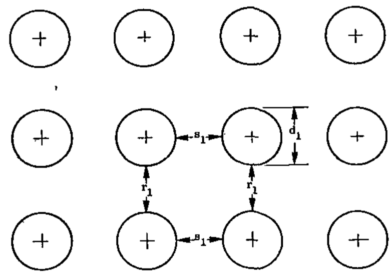

R - Rectangular array

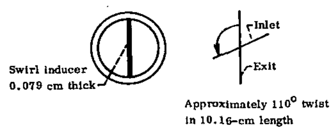

Configuration 48

…onstant flow area)

Configuration														
55	56	[c]57	[d]58	59	[d]60	[e]61	62	63	[f]64	[g]65	[h]66	[i]67	68	69
56	57	58	59	60	61	62	64	65	66	67	68	69	70	71
23	24	81	4	10	2	5	7	9	1	8	12	15	62	6
0.83	0.83	0.53	0.83	0.91	0.83	0.83	0.91	0.83	0.91	0.91	0.91	0.91	0.83	0.83
14.38	12.25	8.13	9.05	12.06	15.16	7.10	9.05	12.06	9.05	9.05	9.05	9.05	12.06	9 05
2.69	3.22	3.76	2.30	2.12	1.98	3.26	3.06	2.78	3.06	3.06	3.06	3.06	3.29	2.94
0-6-6	0-6-12	0-6-18	1-6-0	1-6-0	1-6-0	1-6-6	1-6-6	1-6-6	1-6-6	1-6-6	1-6-6	1-6-6	1-6-12	4 × 3
CE	CU	CU	CE	CE	CE	CE	CE	CE	S	S	S	S	CU	R
Tubes	Tubes	Orifices	Tubes	Tubes	Tubes	Tubes	Tubes	Tubes	Tubes	Tubes	Tubes	Tubes	Tubes	Tubes
…2° Counter sunk	82° Counter sunk	Sharp edge	82° Counter sunk	82° Counter sunk	82° Counter sunk	82° Counter sunk	Sharp edge	82° Counter sunk	82° Counter sunk	82° Counter sunk	82° Counter sunk	82° Counter sunk	82° Counter sunk	Sharp edge
10.160	10.160	0.635	10.160	10.160	10.160	10.160	10.160	10.160	10.160	10.160	(h)	(i)	10.160	10.160
8.20	10.03	12.45	6.25	6.25	6.25	8.53	8.53	8.53	8.53	8.53	8.53	8.53	10.30	8 16
2.36	2.36	2.54	2.36	2.36	2.36	2.36	2.36	2.36	2.36	2.36	2.36	2.36	2.36	2.36
3.464	4.243	4.899	2.646	2.646	2.646	3.606	3.606	3.606	3.606	3 606	3.606	3.606	4.359	3.464
5.08	5.08	5.08	3.81	5.08	6.67	3.18	3.81	5.08	3.81	3.81	3.81	3.81	5.08	------
10.16	10.16	10.16	--------	--------	--------	6.35	7.62	10.16	6.67	6.67	6.67	6 67	10.16	------
11.35	11.35	11.43	5.00	6.27	7.85	7.55	8.81	11.35	7.85	7 85	7.85	7 85	11 35	------
--------	--------	------	1.450	2.720	4.320	0.813	1.450	2.720	1.450	1.450	1.450	1 450	2.720	1 450
2.720	2.720	2.540	1.450	2.720	4.320	0.813	1.450	2.720	1.450	1 450	1 450	1.450	2.720	1.450
2.720	2.720	2.540	--------	--------	--------	0.813	1.450	2.720	4 320	4.320	4.320	4 320	2.720	------
7.80	2.90	0.99	--------	--------	--------	3.99	5.26	7.80	4.32	4.32	4.32	4 32	2.90	------
--------	--------	------	1.00	1.00	1.00	1.00	1.00	1.00	1.00	1.00	1.00	1.00	1.00	1.00
0.3490	0.9380	2.5600	--------	--------	--------	0.2040	0.2760	0.3480	1.0000	1.0000	1.0000	1.0000	0.937	------
--------	--------	------	0.613	1.152	1.830	0.345	0.613	1.152	0.613	0.613	0.613	0.613	1.152	0.613
1.152	1.152	1.0000	--------	--------	--------	0.345	0.613	1.152	1.830	1.830	1.830	1.830	1.152	------
1.152	1.152	1.000	0.613	1.152	1.830	0.345	0.613	1.152	0.613	0.613	0.613	0.613	1.152	0.613
3.31	1.23	0.39	--------	--------	--------	1.69	2.23	3.31	1.83	1.83	1.83	1.83	1.23	------

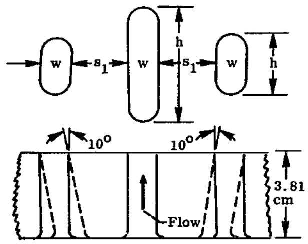

Configurations 70 and 71

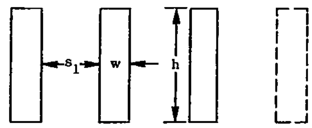

Three or four slots

(b) Rectangula[r]

	Configuration									
	$^{m}70$	$^{n}70$	$^{m}70$	$^{o}71$	$^{n}71$	$^{o}71$	72	73	$^{p}74$	$^{q}75$
Figure	72	72	72	73	73	73	74	75	76	77
Original run	25	25	25	31	31	31	95	97	102	7[illegible]
Normalizing coefficient, C_n	0.53	---------	---------	0.60	---------	---------	0.91	0.91	0.91	0.66
$\dfrac{Z_{①}(1 + \sin^2\beta)}{1 + \dfrac{1}{0.8 + \dfrac{10^5}{(AR)^4}}}$	8.78	---------	---------	8.37	---------	---------	4.78	5.97	5.97	13.26
Analytical displacement parameter, D_x	1.50	---------	---------	1.50	---------	---------	1.72	1.71	1.71	1.85
Type	Three-slot constant-area nozzle	Three-slot constant-area nozzle	Three-slot constant-area nozzle	Three-slot constant-area nozzle	Three-slot constant-area nozzle	Three-slot constant-area nozzle	Three-slot convergent nozzle	Three-slot convergent nozzle	Three-slot convergent nozzle	Four-slot orifice
Nozzle axial length, l, cm	3.81	3.81	3.81	3.81	3.81	3.81	10.16	10.16	10.16	0.635
Total nozzle area, A_n, cm^2	95.9	---------	---------	88.5	---------	---------	93.0	93.0	93.0	46.4
Area of single nozzle element, A_e, cm^2	$^{cc}26.8$	$^{cc}41.3$	$^{cc}27.8$	$^{cc}25.2$	$^{cc}38.1$	$^{cc}25.2$	31.0	31.0	31.0	11.6
Equivalent diameter, $D_{e,t}$, cm	11.07	---------	---------	10.60	---------	---------	10.88	10.88	10.88	7.70
Equivalent diameter, D_e, cm	5.85	7.25	5.94	5.66	6.96	5.66	6.27	6.27	6.27	3.85
Hydraulic diameter, D_h, cm	4.43	4.80	4.59	4.22	4.48	4.22	2.83	2.83	2.83	3.15
Equivalent diameter ratio, $D_{e,T}/D_e$	1.890	1.520	1.865	1.870	1.520	1.870	1.732	1.732	1.732	2.000
Diameter ratio, D_e/D_h	1.320	1.515	1.295	1.340	1.555	1.340	2.220	2.220	2.220	1.222
Noncircular element width, w, cm	2.540	2.540	2.540	2.540	2.540	2.540	1.520	1.520	1.520	2.290
Noncircular element height, h, cm	10.64	15.72	10.64	10.50	15.56	10.50	20.32	20.32	20.32	5.08
Aspect ratio AR = h/w (unless noted)	$^{dd}4.22$	$^{dd}5.97$	$^{dd}4.08$	$^{dd}4.36$	$^{dd}6.36$	$^{dd}4.36$	13.33	13.33	13.33	2.22
Actual spacing between jets, cm:										
Circumferential, s_1	5.080	5.080	5.080	5.080	5.080	5.080	4.320	6.350	6.350	4.570
Radial, r_1	0	0	0	0	0	0	0	0	0	0
Spacing ratio, s_1/w	2.00	2.00	2.00	2.00	2.00	2.00	2.83	4.17	4.17	2.00
Wall divergence angle, β, deg	0	0	0	0	0	0	0	0	0	0
Single-element configuration	---------	---------	---------	---------	---------	---------	23	23	23	15

[m]Outside slot at 0^o to nozzle axis.
[n]Center slot at 0^o to nozzle axis.
[o]Outside slot at 10^o to nozzle axis.
[p]Configuration 73 with hemispherical afterbody flush with nozzle exits.
[q]Sharp-edge inlets.
[r]Reference 11, nozzle 2.1.
[s]Reference 11, nozzle 2.2.
[t]Reference 11, nozzle 2.3.
[u]Reference 11, nozzle 2.4.
[v]Reference 11, nozzle 2.5.
[w]Reference 11, nozzle 2.6.
[x]Reference 11, nozzle 2.7.
[y]Reference 11, nozzle 2.8.
[z]Reference 11, nozzle 2.9.
[aa]Configuration 73 with 3.81-cm centerbody in each nozzle.
[bb]Configuration 73 with 6.35-cm centerbody in each nozzle.
[cc]Areas measured with planimeter.
[dd]$AR = h^2/A_e$.

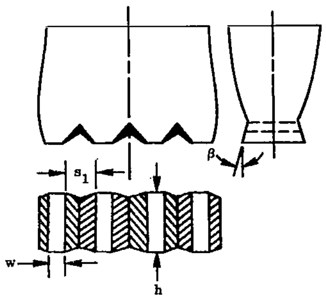

Reference 11 nozzles

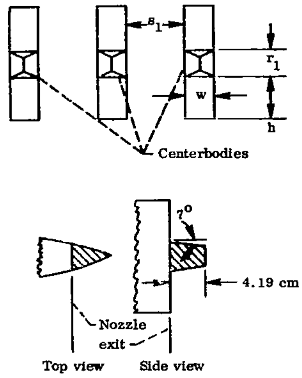

Six slots (fig. 3(l))

ments.

Configuration														
[q]76	[q]77	[q]78	[q]79	[r]80	[s]81	[t]82	[u]83	[v]84	[w]85	[x]86	[y]87	[z]88	[aa]89	[bb]90
78	79	80	81	83	83	84	84	82,83,84	84	83	82	82	85	86
69	86	88	73	----	----	----	----	----	----	----	----	----	103	100
0.54	0.34	0.56	0.40	0.58	0.58	0.55	0.55	0.50	0.45	0.53	0.45	0.63	0.75	0.75
8.83	8.87	6.81	4.81	8.81	8.74	4.31	5.86	8.26	10.28	7.05	10.93	5.08	10.61	10.57
1.95	1.95	1.97	1.98	1.95	1.95	1.99	1.97	1.95	1.93	1.95	1.89	1.98	2.32	2.29
our-slot orifice	Four-slot orifice	Four-slot orifice	Four-slot orifice	Four-slot convergent nozzle	Four-slot convergent nozzle	Four-slot convergent nozzle	Four-slot convergent nozzle	Four-slot convergent nozzle	Four-slot convergent nozzle	Four-slot convergent nozzle	Four-slot convergent nozzle	Four-slot convergent nozzle	Six-slot convergent nozzle	Six-slot convergent nozzle
0.318	0.635	0.635	0.318	30.48	30.48	30.48	30.48	30.48	30.48	30.48	30.48	30.48	10.16	10.16
46.4	104.4	69.6	46.4	45.6	45.6	45.6	45.6	45.6	45.6	45.6	45.6	45.6	75.5	63.5
11.6	26.1	17.4	11.6	11.4	11.4	11.4	11.4	11.4	11.4	11.4	11.4	11.4	12.59	10.59
7.70	11.52	9.42	7.70	7.62	7.62	7.62	7.62	7.62	7.62	7.62	7.62	7.62	9.80	9.00
3.85	5.76	4.71	3.85	3.81	3.81	3.81	3.81	3.81	3.81	3.81	3.81	3.81	4.00	3.67
2.54	3.81	2.69	1.865	2.51	2.51	2.51	2.51	2.51	2.51	2.51	2.92	1.94	2.58	2.50
2.000	2.000	2.000	2.000	2.000	2.000	2.000	2.000	2.000	2.000	2.000	2.000	2.000	2.450	2.450
1.516	1.512	1.752	2.065	1.518	1.518	1.518	1.518	1.518	1.518	1.518	1.303	1.962	1.555	1.470
1.520	2.290	1.520	1.020	1.510	1.510	1.510	1.510	1.510	1.510	1.510	1.950	1.068	1.520	1.520
7.62	11.43	11.43	11.43	7.55	7.55	7.55	7.55	7.55	7.55	7.55	5.84	10.68	8.26	6.99
5.00	5.00	7.50	11.25	5	5	5	5	5	5	5	3	10	5.42	4.58
3.050	4.570	3.050	2.030	3.020	3.020	0.755	1.510	3.020	4.540	3.020	3.890	2.135	6.350	6.350
0	0	0	0	0	0	0	0	0	0	0	0	0	3.81	6.35
2.00	2.00	2.00	2.00	2.00	2.00	0.50	1.00	2.00	3.00	2.00	2.00	2.00	4.17	4.17
0	0	0	0	0	5	15	15	15	15	30	15	15	0	0
16	17	18	19	----	----	----	----	----	----	----	----	----	21	20

TABLE II. - Continued.

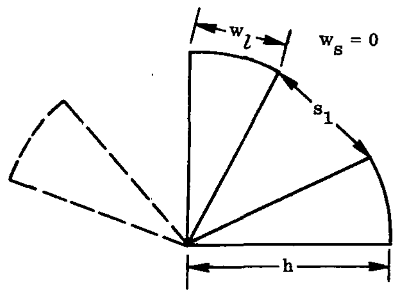

(c) Triangular elements (convergent nozzles)

	Configuration		
	ee$_{91}$	ff$_{92}$	gg$_{93}$
Figure	87	88	89
Original run	-----	-----	-----
Normalizing coefficient, C_n	0.73	0.75	0.90
Value of axial distance parameter $X/C_nD_e\sqrt{1+M_j}$ at departure point of coalescing core from single-element decay curve, $Z_{①}$	23.37	23.22	18.08
Analytical displacement parameter, D_x	1.355	1.933	3.422
Number of elements	2	4	12
Nozzle axial length, l, cm	30.48	30.48	30.48
Total nozzle area, A_n, cm^2	45.6	45.6	45.6
Area of single nozzle element, A_e, cm^2	22.8	11.4	3.8
Equivalent diameter, $D_{e,T}$, cm	7.62	7.62	7.62
Equivalent diameter, D_e, cm	5.40	3.81	2.20
Hydraulic diameter, D_h, cm	4.090	2.310	0.845
Equivalent diameter ratio, $D_{e,T}/D_e$	1.414	2.000	3.464
Diameter ratio, D_e/D_h	1.32	1.65	2.60
Larger width of variable-width element, w_l, cm	5.270	2.660	0.892
Noncircular element height, h, cm	8.51	8.51	8.51
Actual circumferential spacing between adjacent jets, s_1, cm	16.20	10.00	3.54
Spacing ratio, s_1/w_l	3.08	3.76	3.98

[ee]Reference 10, nozzle 10.
[ff]Reference 10, nozzle 11.
[gg]Reference 10, nozzle 12.

TABLE II. - Concluded.

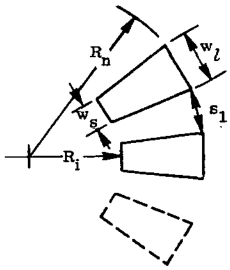

Flat end

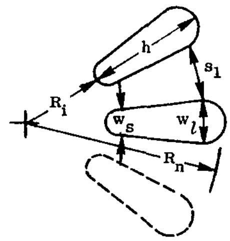

Round end

(d) Trapezoidal elements (round inlet; constant flow area)

	Flat end			Round end								
	Configuration											
	94	95	96	97	98	99	100[hh]	100[ii]	101[jj]	101[ii]	102[ii]	102[kk]
Figure	90	91	92	94	95	96	97(a)	97(b)	98(a)	98(b)	100(a)	100(b)
Original run	53	55	57	21	20	19	33	34	26	27	93	94
Normalizing coefficient, C_n	0.77	0.83	0.81	0.67	0.67	0.67	0.67	0.67	0.63	0.63	0.63, 0.67	0.63
Value of axial distance parameter $X/C_n D_e \sqrt{1 + M_j}$ at departure point of coalescing core from single-element decay curve, $Z_{①}$	13.76	10.27	8.92	23.43	17.07	10.20	[ll]10.20	[ll]10.20	[ll]10.20	[ll]10.20	[ll]10.20	[ll]10.20
Analytical displacement parameter, D_x	2.27	2.27	3.28	1.29	1.79	2.65	[ll]2.65	[ll]2.65	[ll]2.65	[ll]2.65	[ll]2.48	[ll]2.48
Number of lobes	6	6	12	2	4	8	8	8	8	8	7	7
Nozzle axial length, l, cm	10.16	10.16	10.16	5.08	5.08	5.08	5.08	5.08	5.08	5.08	5.08	5.08
Canted nozzle lobe angle, deg	0	0	0	0	0	0	4 at 0°, 4 at 5°	4 at 0°, 4 at 5°	4 at 0°, 4 at 10°	4 at 0°, 4 at 10°	4 at 0°, 3 at 10°	4 at 0°, 3 at 10°
Total nozzle area, A_n, cm^2	48.0	46.5	44.7	22.8	45.6	91.2	91.2	91.2	91.2	91.2	79.8	79.8
Area of single nozzle element, A_e, cm^2	8.00	7.75	3.74	11.4	11.4	11.4	11.4	11.4	11.4	11.4	11.4	11.4
Equivalent diameter, $D_{e,T}$, cm	7.825	7.700	7.550	5.38	7.62	10.78	10.78	10.78	10.78	10.78	10.04	10.04
Average equivalent diameter, D_e, cm	3.20	3.15	2.18	3.81	3.81	3.81	3.81	3.81	3.81	3.81	3.81	3.81
Hydraulic diameter, D_h, cm	2.34	2.72	1.73	3.05	3.05	3.05	3.05	3.05	3.05	3.05	3.05	3.05
Equivalent diameter ratio, $D_{e,T}/D_e$	2.453	2.452	3.463	1.414	2.000	2.828	2.828	2.828	2.828	2.828	2.646	2.646
Diameter ratio, D_e/D_h	1.355	1.159	1.270	1.250	1.250	1.250	1.250	1.250	1.250	1.250	1.250	1.250
Inner radius, R_i, cm	3.12	3.00	3.07	2.59	2.59	2.59	2.59	2.59	2.59	2.59	2.59	2.59
Overall nozzle radius, R_n, cm	8.40	6.22	6.32	8.77	8.77	8.77	8.77	8.77	8.77	8.77	8.77	8.77
Smaller width of variable-width element, w_s, cm	0.897	1.612	0.808	1.194	1.194	1.194	1.194	1.194	1.194	1.194	1.194	1.194
Larger width of variable-width element, w_l, cm	2.160	3.300	1.558	2.510	2.510	2.510	2.510	2.510	2.510	2.510	2.510	2.510
Noncircular element height, h, cm	5.23	3.15	3.15	6.22	6.22	6.22	6.22	6.22	6.22	6.22	6.22	6.22
Actual circumferential spacing between adjacent jets, s_1, cm	6.580	3.350	1.778	15.15	9.01	3.43	3.43	3.43	3.43	3.43	3.43	3.43
Width ratio, w_s/w_l	0.417	0.489	0.519	0.476	0.476	0.476	0.476	0.476	0.476	0.476	0.476	0.476
Spacing ratio, s_1/w_l	3.060	1.014	1.140	6.050	3.590	1.368	1.368	1.368	1.368	1.368	1.368	1.368
Single-element configuration	34	35	36	37	37	37	37	37	37	37	37	37

[hh]Surveyed across 5°-5° lobes.
[ii]Surveyed across 0°-0° lobes.
[jj]Surveyed across 10°-10° lobes.
[kk]Surveyed across plugged 10°-10° lobes.
[ll]Estimated.

TABLE III. - NOZZLE DIMENSIONS AND CALCULATED VALUES FOR MULTIELEMENT

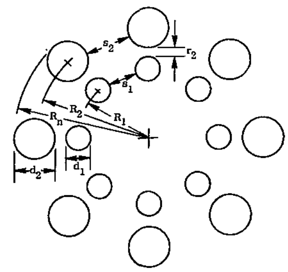

Configurations 103, 104, and 105

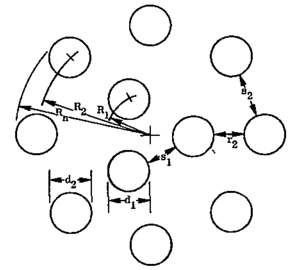

Configurations 106 and 107

	Configuration								
	103	[a]104	105	106	[a]107	[b]108	[c]109	[b,d]110	[e]111
Figure	101a	101b	102	103a	103b	104a	104b	104c	104d
Original run	64	63	66	77	76	68	71	67	72
Normalizing coefficient, C_n	0.83	0.83	0.60	0.86	0.86	0.83	0.83	0.83	0.83
Value of axial distance parameter $X/C_n D_e\sqrt{1+M_j}$ at departure point of coalescing core from single-element decay curve, $Z_{①}$	11.12	[i]13.60	11.44	10.88	12.17	[j]8.0	[j]8.0	[j]15.5	[j]16.0
Axial displacement parameter, D_x	4.25	[i]3.31	2.67	2.83	2.32	[j]3.85	[j]4.40	[j]2.50	[j]3.10
Number of elements:									
Core (primary)	8	8	8	3	3	8	8	8	8
Bypass (secondary)	8	8	8	8	8	1	1	1	1
Type of element:									
Core (primary)	[k]Tube	[k]Tube	[l]Orifice	[k]Tube	[k]Tube	[k]Tube	[k]Tube	[k]Tube	[k]Tube
Bypass (secondary)	[m]Orifice	[n]Orifice	[l]Orifice	[m]Orifice	[n]Orifice	[l]Annulus	[l]Annulus	[l,n]Annulus	[l,n]Annulus
Area of all elements, cm^2:									
Core	12.50	12.50	15.80	13.10	13.10	12.50	12.50	12.50	12.50
Bypass	40.50	40.50	40.50	40.50	40.50	38.90	38.90	38.90	38.90
Total	53.00	53.00	56.30	53.60	53.60	51.40	51.40	51.40	51.40
Area of single element, cm^2:									
Core	1.56	1.56	1.98	4.38	4.38	1.56	1.56	1.56	1.56
Bypass	5.06	5.06	5.06	5.06	5.06	38.9	38.9	38.9	38.9
Equivalent diameter (all elements), D_e, cm:									
Core	3.99	3.99	4.49	4.09	4.09	3.99	3.99	3.99	3.99
Bypass	7.19	7.19	7.19	7.19	7.19	7.05	7.05	7.05	7.05
Total	8.22	8.22	8.47	8.26	8.26	8.09	8.09	8.09	8.09
Equivalent diameter (single element), D_e, cm:									
Core	1.41	1.41	1.59	2.36	2.36	1.41	1.41	1.41	1.41
Bypass	2.54	2.54	2.54	2.54	2.54	7.05	7.05	7.05	7.05
Centerline radius of first ring of tubes, R_1, cm	4.06	4.06	4.06	2.54	2.54	4.06	4.06	4.06	4.06
Centerline radius of second ring of tubes, R_2, cm	6.67	6.67	6.67	6.67	6.67	5.59	5.59	5.59	5.59
Overall nozzle radius, R_n, cm	7.94	7.94	7.94	7.94	7.94	6.60	6.60	6.60	6.60
Nozzle axial length, l, cm	10.16	10.16	----	10.16	10.16	10.16	10.16	10.16	10.16
Actual circumferential spacing between adjacent jets, cm:									
s_1	1.698	1.698	1.520	2.040	2.040	1.698	1.698	1.698	1.698
s_2	2.55	2.55	2.55	2.55	2.55	-----	-----	-----	-----
Circular element diameter, cm:									
d_1	1.41	1.41	1.59	2.36	2.36	1.41	1.41	1.41	1.41
d_2	2.54	2.54	2.54	2.54	2.54	1.02	1.02	1.02	1.02
Actual radial spacing between adjacent jets, r_2, cm	0.628	0.628	0.539	1.678	1.678	0.818	0.818	0.818	0.818
Spacing ratios.									
s_1/d_1	1.203	1.203	0.955	0.865	0.865	1.203	1.203	1.203	1.203
s_2/d_2	1.01	1.01	1.01	1.01	1.01	-----	-----	-----	-----
r_2/d_1	0.445	0.445	0.339	0.711	0.711	0.580	0.580	0.580	0.580
Nominal ratio of bypass (secondary) flow exit Mach number to core (primary) flow exit Mach number, M_b/M_j	1.00	0.70	1.00	1.00	0.70	1.00	1.00	0.70	0.70

[a]Screens in orifices.
[b]No centerbody.
[c]Configuration 108 with centerbody.
[d]Screen in annulus.
[e]Configuration 110 with centerbody.
[f]Slot nozzle: AR = 4.76.
[g]No screen in annulus.
[h]Based on core nozzle.
[i]Average values.
[j]Estimated.
[k]82° Countersunk inlet.
[l]Sharp-edge inlet.
[m]Round-edge inlet.
[n]Screened.

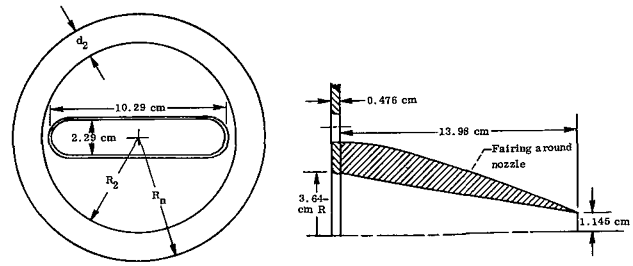

Configurations 114 to 117

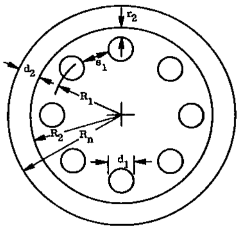

Configurations 108, 109, 110, and 111

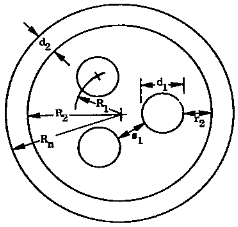

Configurations 112 and 113

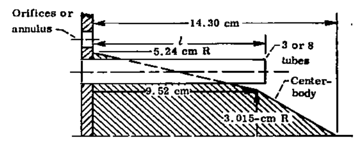

Configurations 103 to 113 (except 105) (centerbody used on configurations 109 and 111 only)

Configuration											
112	^{d}113	^{d,f}114	^{d,f}115	^{d,f}116	^{f,g}117	^{d}118	^{d}119	^{g}120	^{d}121	^{d}122	^{g}123
105a	105b	106a 107a	106b 107b	106c 107c	106d 107d	108b 109a	108c 109b	108d 109c	110a 111a	110b 111b	110c 111c
75	78	107	110	112	108	117	118	116	114	113	115
0.91	0.91	0.89	^{h}0.96	^{h}1.08	^{h}1.20	^{h}1.27	^{h}1.33	^{h}1.50	^{h}1.35	^{h}1.45	^{h}1.53
^{j}9.4	^{j}12.8	-----	-----	-----	-----	-----	-----	-----	-----	-----	-----
^{j}1.75	^{j}1.33	-----	-----	-----	-----	-----	-----	-----	-----	-----	-----
3	3	1	1	1	1	1	1	1	1	1	1
1	1	1	1	1	1	1	1	1	1	1	1
^{k}Tube ^{l}Annulus	^{k}Tube ^{l,n}Annulus	Convergent slot nozzle ^{m}Annulus	Convergent slot nozzle ^{m,n}Annulus	Convergent slot nozzle ^{m,n}Annulus	Convergent slot nozzle ^{m,n}Annulus	Convergent conical nozzle ^{n}Convergent annulus	Convergent conical nozzle ^{n}Convergent annulus	Convergent conical nozzle Convergent annulus	Convergent conical nozzle ^{n}Convergent annulus	Convergent conical nozzle ^{n}Convergent annulus	Convergent conical nozzle Convergent annulus
13.10	13.10	22.20	22.20	22.20	22.20	10.10	10.10	10.10	21.05	21.05	21.05
38.90	38.90	69.00	69.00	69.00	69.00	32.90	32.90	32.90	65.50	65.50	65.50
52.00	52.00	91.20	91.20	91.20	91.20	43.00	43.00	43.00	86.55	86.55	86.55
4.38	4.38	22.20	22.20	22.20	22.20	10.10	10.10	10.10	21.05	21.05	21.05
38.9	38.9	69.0	69.0	69.0	69.0	32.9	32.9	32.9	65.5	65.5	65.5
4.09	4.09	5.32	5.32	5.32	5.32	3.58	3.58	3.58	5.18	5.18	5.18
7.05	7.05	9.37	9.37	9.37	9.37	6.47	6.47	6.47	9.11	9.11	9.11
8.15	8.15	10.8	10.8	10.8	10.8	7.40	7.40	7.40	10.50	10.50	10.50
2.36	2.36	5.32	5.32	5.32	5.32	3.58	3.58	3.58	5.18	5.18	5.18
7.05	7.05	9.37	9.37	9.37	9.37	6.47	6.47	6.47	9.11	9.11	9.11
2.54	2.54	-----	-----	-----	-----	-----	-----	-----	-----	-----	-----
5.59	5.59	5.72	5.72	5.72	5.72	3.96	3.96	3.96	5.72	5.72	5.72
6.60	6.60	7.38	7.38	7.38	7.38	5.12	5.12	5.12	7.32	7.32	7.32
10.16	10.16	13.98	13.98	13.98	13.98	9.68	9.68	9.68	13.98	13.98	13.98
2.04	2.04	-----	-----	-----	-----	-----	-----	-----	-----	-----	-----
-----	-----	-----	-----	-----	-----	-----	-----	-----	-----	-----	-----
2.36	2.36	-----	-----	-----	-----	3.58	3.58	3.58	5.18	5.18	5.18
1.02	1.02	1.66	1.66	1.66	1.66	1.15	1.15	1.15	1.60	1.60	1.60
1.866	1.866	-----	-----	-----	-----	2.16	2.16	2.16	3.13	3.13	3.13
0.865	0.865	-----	-----	-----	-----	-----	-----	-----	-----	-----	-----
-----	-----	-----	-----	-----	-----	-----	-----	-----	-----	-----	-----
0.791	0.791	-----	-----	-----	-----	0.605	0.605	0.605	0.605	0.605	0.605
1.00	0.70	0.62	0.67	0.78	0.98	0.60	0.73	1.00	0.46	0.69	1.00

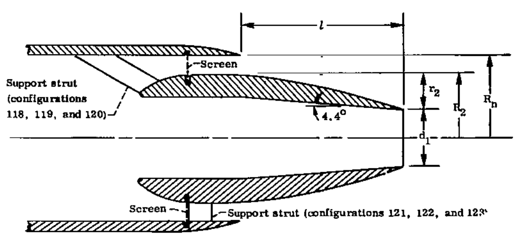

Configurations 118 to 123

TABLE IV. - PEAK AXIAL JET MACH NUMBER DECAY DATA FOR SINGLE-ELEMENT NOZZLES AND ORIFICES

(a) Configuration 1; nozzle-exit jet Mach number, M_j, 0.825

Axial distance, X, cm	Downstream peak Mach number, M
12.70	0.81
25.40	.60
38.10	.40
50.80	.28
93.98	.131
132.08	.075
Ratio of M_j to ideal, $M_j/M_{j,id}$	1.0
Ratio of nozzle mass flow rate to ideal, $W_n/W_{n,id}$	-----

(b) Configuration 2

Axial distance, X, cm	Nozzle-exit jet Mach number, M_j	
	0.802	0.985
	Downstream peak Mach number, M	
12.70	0.756	0.938
25.40	.51	.698
38.10	.34	.47
50.80	.25	.34
129.54	.082	-----
152.40	.069	.089
Ratio of M_j to ideal, $M_j/M_{j,id}$	0.999	0.995
Ratio of nozzle mass flow rate to ideal, $W_n/W_{n,id}$	-----	-----

TABLE IV. - Continued.

(c) Configuration 3

Axial distance, X, cm	Nozzle-exit jet Mach number, M_j	
	0.80	0.99
	Downstream peak Mach number, M	
12.70	0.780	0.967
25.40	.580	.765
38.10	.395	.52
50.80	.300	.37
152.40	.079	.102
Ratio of M_j to ideal, $M_j/M_{j,id}$	1.003	1.001
Ratio of nozzle mass flow rate to ideal, $W_n/W_{n,id}$	-----	-----

(d) Configuration 4

Axial distance, X, cm	Nozzle-exit jet Mach number, M_j	
	0.952	1.156
	Downstream peak Mach number, M	
12.70	0.93	1.105
25.40	.675	.87
38.10	.45	.58
46.99	.35	.47
101.60	-----	.191
139.70	.104	.132
Ratio of M_j to ideal, $M_j/M_{j,id}$	0.988	0.994
Ratio of nozzle mass flow rate to ideal, $W_n/W_{n,id}$	0.469	-----

TABLE IV. - Continued.

(e) Configuration 5

Axial distance, X, cm	Nozzle-exit jet Mach number, M_j				
	[a]0.780	0.985	[a]1.042	[a]1.195	[a]1.35
	Downstream peak Mach number, M				
7.62	0.780	0.985	1.049	1.190	1.343
15.24	.780	.981	1.043	1.185	1.318
22.86	.780	.975	1.040	1.188	1.300
30.48	.775	.980	1.041	1.181	1.290
38.10	.765	.970	1.035	1.188	1.280
45.72	.735	.945	1.015	1.170	1.285
53.34	.685	.895	.970	1.14	1.30
60.96	.640	.835	.915	1.095	1.270
68.58	.580	.770	.835	1.025	1.215
76.20	.540	.710	.770	.945	1.150
83.82	.490	.655	.715	.880	1.070
91.94	.455	.605	.665	.815	1.010
99.06	.425	.560	.610	.755	.920
106.68	.395	.525	.575	.705	.855
Ratio of M_j to ideal, $M_j/M_{j,id}$	0.991	0.995	0.989	0.992	0.996
Ratio of nozzle mass flow rate to ideal, $W_n/W_{n,id}$	------	-----	------	------	------

(f) Configuration 6

Axial distance, X, cm	Nozzle-exit jet Mach number, M_j				
	[a]0.785	0.985	[a]1.045	[a]1.195	[a]1.35
	Downstream peak Mach number, M				
7.62	0.785	0.982	1.048	1.190	1.342
15.24	.780	.980	1.040	1.182	1.320
22.86	.782	.990	1.042	1.190	1.302
30.48	.780	.977	1.040	1.175	1.290
38.10	.760	.973	1.037	1.185	1.280
45.72	.740	.950	1.015	1.170	1.290
53.34	.700	.900	.975	1.15	1.31
60.96	.640	.840	.915	1.100	1.275
68.58	.595	.780	.845	1.035	1.230
76.20	.550	.720	.780	.970	1.130
83.82	.500	.660	.720	.895	1.090
91.94	.470	.610	.665	.825	1.010
99.06	.425	.575	.615	.760	.935
106.68	.400	.525	.575	.710	.875
114.30	.375	.490	.530	.660	.760
Ratio of M_j to ideal, $M_j/M_{j,id}$	1.000	0.998	0.995	0.995	0.999
Ratio of nozzle mass flow rate to ideal, $W_n/W_{n,id}$	1.025	1.010	1.012	1.001	1.033

[a]Not plotted in fig. 7.

TABLE IV. - Continued.

(g) Configuration 7

Axial distance, X, cm	Nozzle-exit jet Mach number, M_j				
	0.465	0.638	0.805	0.991	1.158
	Downstream peak Mach number, M				
12.70	0.45	0.628	0.796	0.986	1.149
25.40	.375	.540	.700	.900	1.085
38.10	.270	.400	.525	.690	.874
50.80	.215	.315	.415	.540	.680
63.50	.170	.250	.330	.435	.540
76.20	.150	.220	.280	.350	.450
101.60	.105	.155	.210	.275	.335
Ratio of M_j to ideal, $M_j/M_{j,id}$	1.020	1.002	1.001	0.997	0.996
Ratio of nozzle mass flow rate to ideal, $W_n/W_{n,id}$	-----	-----	-----	-----	-----

(h) Configuration 9

Axial distance, X, cm	Nozzle-exit jet Mach number, M_j					
	0.26	0.458	0.635	0.805	0.990	1.160
	Downstream peak Mach number, M					
12.70	0.260	0.455	0.630	0.800	0.990	1.148
25.40	.260	.450	.628	.800	.990	1.147
38.10	.200	.380	.540	.710	.910	1.095
50.80	.150	.310	.440	.575	.755	.925
137.16	.067	.126	.180	.238	.314	.393
205.74	.047	.084	.117	.153	.203	.254
271.78	.040	.063	.092	.118	.151	.186
Ratio of M_j to ideal, $M_j/M_{j,id}$	0.959	1.004	0.998	1.002	0.997	0.998
Ratio of nozzle mass flow rate to ideal, $W_n/W_{n,id}$	0.657	0.646	0.657	0.696	0.746	0.793

TABLE IV. - Continued.

(i) Configuration 10

Axial distance, X, cm	Nozzle-exit jet Mach number, M_j					
	0.265	0.460	0.630	0.802	0.990	1.160
	Downstream peak Mach number, M					
12.70	0.265	0.450	0.630	0.800	0.988	1.142
25.40	.250	.420	.600	.772	.970	1.125
38.10	.220	.365	.530	.690	.890	1.040
50.80	.175	.320	.460	.600	.780	.935
137.16	.094	.168	.244	.319	.417	.530
218.44	.060	.103	.149	.197	.256	.328
304.80	.042	.071	.102	.135	.178	.230
Ratio of M_j to ideal, $M_j/M_{j,id}$	0.978	1.009	0.991	0.999	0.997	0.998
Ratio of nozzle mass flow rate to ideal, $W_n/W_{n,id}$	0.798	0.740	0.736	0.765	0.814	0.854

(j) Configuration 11

Axial distance, X, cm	Nozzle-exit jet Mach number, M_j					
	0.265	0.450	0.633	0.803	0.989	1.150
	Downstream peak Mach number, M					
12.70	0.265	0.450	0.62	0.795	0.983	1.147
25.40	.223	.370	.535	.705	.912	1.078
38.10	.175	.330	.450	.590	.770	.940
50.80	.150	.275	.380	.500	.650	.805
142.24	.076	.135	.195	.258	.335	.425
215.90	.053	.088	.127	.168	.222	.279
304.80	.034	.061	.087	.116	.150	.190
Ratio of M_j to ideal, $M_j/M_{j,id}$	0.978	0.987	0.995	1.000	0.996	0.990
Ratio of nozzle mass flow rate to ideal, $W_n/W_{n,id}$	0.922	0.764	0.727	0.760	0.802	0.841

TABLE IV. - Continued.

(k) Configuration 12

Axial distance, X, cm	Nozzle-exit jet Mach number, M_j					
	0.265	0.455	0.638	0.802	0.990	1.158
	Downstream peak Mach number, M					
12.70	0.250	0.420	0.580	0.760	0.970	1.100
25.40	.190	.320	.470	.600	.790	.895
38.10	.150	.275	.375	.495	.645	.720
50.80	.140	.240	.335	.430	.550	.630
144.78	.064	.109	.159	.208	.275	.341
210.82	.041	.074	.109	.143	.185	.236
'264.16	.030	.058	.084	.115	.147	.186
Ratio of M_j to ideal, $M_j/M_{j,id}$	0.981	1.000	1.003	1.000	0.998	0.997
Ratio of nozzle mass flow rate to ideal, $W_n/W_{n,id}$	0.646	0.662	0.690	0.735	0.786	0.830

(l) Configuration 13

Axial distance, X, cm	Nozzle-exit jet Mach number, M_j				
	0.455	0.635	0.805	0.994	1.155
	Downstream peak Mach number, M				
12.70	0.330	0.470	0.610	0.800	0.861
25.40	.225	.320	.420	.535	.635
38.10	.190	.270	.340	.435	.550
50.80	.170	.250	.300	.380	.485
114.30	.099	.144	.187	.241	.298
154.94	.070	.103	.140	.180	.222
228.60	.040	.065	.089	.118	.149
Ratio of M_j to ideal, $M_j/M_{j,id}$	1.000	0.998	1.002	1.002	0.995
Ratio of nozzle mass flow rate to ideal, $W_n/W_{n,id}$	0.708	0.690	0.726	0.769	0.818

TABLE IV. - Continued.

(m) Configuration 14

Axial distance, X, cm	Nozzle-exit jet Mach number, M_j				
	0.460	0.630	0.805	0.990	1.156
	Downstream peak Mach number, M				
12.70	0.360	0.520	0.670	0.860	[b]0.908
25.40	.260	.360	.466	.608	[b].668
38.10	.220	.300	.380	.475	.575
50.80	.190	.260	.330	.425	.520
132.08	.103	.145	.189	.240	.294
182.88	.075	.104	.138	.175	.212
218.44	.063	.088	.114	.146	.177
Ratio of M_j to ideal, $M_j/M_{j,id}$	1.011	0.992	1.004	0.998	0.996
Ratio of nozzle mass flow rate to ideal, $W_n/W_{n,id}$	0.825	0.835	0.855	0.907	0.940

(n) Configuration 15

Axial distance, X, cm	Nozzle-exit jet Mach number, M_j			
	0.640	0.800	0.985	1.156
	Downstream peak Mach number, M			
12.70	0.630	0.796	0.990	1.154
25.40	.490	.645	.84	.98
38.10	.330	.440	.580	.710
46.99	.275	.360	.480	.570
101.60	.129	.167	.216	.256
152.40	.085	.111	.144	.169
203.20	.063	.081	.109	.127
Ratio of M_j to ideal, $M_j/M_{j,id}$	1.006	0.996	0.992	0.995
Ratio of nozzle mass flow rate to ideal, $W_n/W_{n,id}$	0.704	0.730	0.768	0.768

[b]Uncertain value.

TABLE IV. - Continued.

(o) Configuration 16

Axial distance, X, cm	Nozzle-exit jet Mach number, M_j			
	0.644	0.803	0.990	1.155
	Downstream peak Mach number, M			
6.35	0.625	0.800	0.973	1.096
12.70	.573	.724	.905	.996
25.40	.475	.609	.761	.846
38.10	.380	.498	.640	.674
50.80	.275	.380	.500	[b].500
101.60	.137	.183	.244	[b].248
127.00	.096	.123	.162	.175
Ratio of M_j to ideal, $M_j/M_{j,id}$	1.011	0.999	0.996	0.992
Ratio of nozzle mass flow rate to ideal, $W_n/W_{n,id}$	0.698	0.732	0.752	0.765

(p) Configuration 17

Axial distance, X, cm	Nozzle-exit jet Mach number, M_j				
	0.450	0.625	0.785	0.970	1.133
	Downstream peak Mach number, M				
6.35	0.425	0.620	0.780	0.965	1.120
12.70	.390	.565	.730	.930	1.050
19.05	.350	.500	.660	.850	.955
25.40	.320	.450	.590	.770	.895
38.10	.270	.390	.500	.660	.800
46.99	.260	.370	.460	.590	.730
91.44	.145	.217	.287	.376	.448
152.40	.088	.123	.164	.218	.255
203.20	.062	.088	.115	.150	.179
Ratio of M_j to ideal, $M_j/M_{j,id}$	0.989	0.983	0.979	0.978	0.976
Ratio of nozzle mass flow rate to ideal, $W_n/W_{n,id}$	0.651	0.659	0.689	0.732	0.776

[b]Uncertain value.

TABLE IV. - Continued.

(q) Configuration 18

Axial distance, X, cm	Nozzle-exit jet Mach number, M_j			
	0.62	0.80	0.98	1.15
	Downstream peak Mach number, M			
6.35	0.610	0.780	0.975	1.135
12.70	.500	.660	.867	1.000
19.05	.430	.557	.735	.875
25.40	.375	.490	.640	.785
38.10	.320	.420	.525	.645
46.99	.300	.375	.480	.590
91.44	.177	.235	.306	.378
137.16	.114	.149	.196	.241
203.20	.078	.103	.132	.163
Ratio of M_j to ideal, $M_j/M_{j,id}$	0.972	0.994	0.985	0.988
Ratio of nozzle mass flow rate to ideal, $W_n/W_{n,id}$	0.681	0.702	0.764	0.795

(r) Configuration 19

Axial distance, X, cm	Nozzle-exit jet Mach number, M_j			
	0.650	0.805	0.990	1.155
	Downstream peak Mach number, M			
2.54	0.629	0.800	0.988	1.147
5.08	.600	.776	.970	1.080
6.35	.570	.734	.940	1.030
12.70	.410	.540	.722	.794
19.05	.330	.433	.568	.663
25.40	.290	.370	.480	.585
38.10	.260	.325	.405	.500
50.80	.225	.285	.360	.440
101.60	.120	.154	.195	.236
127.00	.098	.124	.156	.190
Ratio of M_j to ideal, $M_j/M_{j,id}$	1.020	1.001	0.996	0.993
Ratio of nozzle mass flow rate to ideal, $W_n/W_{n,id}$	0.728	0.730	0.748	0.794

TABLE IV. - Continued.

(s) Configuration 20

Axial distance, X, cm	Nozzle-exit jet Mach number, M_j			
	0.630	0.800	0.985	1.150
	Downstream peak Mach number, M			
12.70	0.590	0.750	0.940	1.060
25.40	.435	.560	.740	.860
38.10	.340	.435	.560	.695
50.80	.260	.350	.440	.550
76.20	.200	.250	.310	.380
101.60	.150	.190	.240	.290
Ratio of M_j to ideal, $M_j/M_{j,id}$	0.987	0.994	0.990	0.987
Ratio of nozzle mass flow rate to ideal, $W_n/W_{n,id}$	-----	-----	-----	-----

(t) Configuration 21

Axial distance, X, cm	Nozzle-exit jet Mach number, M_j				
	0.460	0.640	0.805	0.990	1.150
	Downstream peak Mach number, M				
12.70	0.420	0.600	0.750	0.945	1.065
25.40	.310	.440	.565	.750	.855
38.10	.230	.330	.430	.560	.700
50.80	.200	.275	.360	.450	.585
76.20	.140	.200	.260	.325	.410
101.60	.100	.140	.190	.250	.300
Ratio of M_j to ideal, $M_j/M_{j,id}$	1.011	1.008	1.005	1.000	0.992
Ratio of nozzle mass flow rate to ideal, $W_n/W_{n,id}$	1.011	0.971	0.956	0.983	1.032

TABLE IV. - Continued.

(u) Configuration 22

Axial distance, X, cm	Nozzle-exit jet Mach number, M_j				
	0.455	0.638	0.800	0.987	1.152
	Downstream peak Mach number, M				
12.70	0.420	0.595	0.750	0.958	1.130
25.40	.280	.395	.510	.665	.855
38.10	.220	.300	.380	.490	.615
50.80	.175	.250	.320	.400	.490
76.20	.140	.190	.240	.305	.355
Ratio of M_j to ideal, $M_j/M_{j,id}$	0.993	0.998	0.993	0.991	0.988
Ratio of nozzle mass flow rate to ideal, $W_n/W_{n,id}$	-----	-----	-----	-----	-----

(v) Configuration 23

Axial distance, X, cm	Nozzle-exit jet Mach number, M_j					
	0.290	0.455	0.638	0.803	0.990	1.152
	Downstream peak Mach number, M					
12.70	0.250	0.430	0.590	0.755	0.950	1.065
25.40	.200	.330	.460	.590	.755	.810
38.10	.160	.275	.385	.495	.615	.660
50.80	.140	.230	.330	.425	.520	.575
91.44	.110	.170	.230	.300	.360	.415
121.92	.100	.140	.200	.240	.290	.350
156.21	.070	.110	.150	.200	.230	.280
Ratio of M_j to ideal, $M_j/M_{j,id}$	1.074	0.998	1.002	1.000	0.997	0.991
Ratio of nozzle mass flow rate to ideal, $W_n/W_{n,id}$	0.985	0.965	0.973	0.987	1.000	1.027

TABLE IV. - Continued.

(w) Configuration 24

Axial distance, X, cm	Survey	Nozzle-exit jet Mach number, M_j					
		0.275	0.460	0.635	0.800	0.990	1.153
		Downstream peak Mach number, M					
12.70	2.72 Centimeters below centerline	0.250	0.410	0.560	0.715	0.935	1.055
25.40	↓	.175	.300	.410	.520	.695	.785
38.10	↓	.130	.245	.340	.440	.560	.655
50.80	↓	.125	.230	.300	.380	.485	.575
[c]12.70	On centerline	.275	.425	.595	.775	.960	1.090
[c]25.40	↓	[b].210	.330	.460	.610	.775	[b].795
[c]38.10	↓	[b].120	.270	.370	.505	.610	[b].635
[c]50.80	↓	[b].130	.225	.320	.420	.520	[b].580
76.20	↓	.100	.175	.230	.310	.390	.480
101.60	↓	.070	.125	.180	.240	.310	.370
127.00	↓	.060	.110	.150	.210	.260	.310
Ratio of M_j to ideal, $M_j/M_{j,id}$		1.022	1.013	1.002	1.000	1.001	0.996
Ratio of nozzle mass flow rate to ideal, $W_n/W_{n,id}$		0.976	0.983	0.982	0.997	1.000	1.023

(x) Configuration 31

Axial distance, X, cm	Nozzle-exit jet Mach number, M_j				
	0.450	0.635	0.805	0.990	1.160
	Downstream peak Mach number, M				
12.70	0.445	0.631	0.795	0.987	1.146
25.40	.405	.592	.763	.965	1.138
38.10	.300	.435	.590	.795	.990
50.80	.220	.330	.445	.600	.765
111.76	.112	.160	.215	.287	.363
157.48	.078	.112	.150	.198	.250
208.28	.059	.082	.112	.148	.186
Ratio of M_j to ideal, $M_j/M_{j,id}$	0.985	0.995	1.000	0.995	0.997
Ratio of nozzle mass flow rate to ideal, $W_n/W_{n,id}$	0.647	0.722	0.747	0.793	0.851

[b]Uncertain value.
[c]Not plotted in fig. 24.

TABLE IV. - Continued.

(y) Configuration 32

Axial distance, X, cm	Nozzle-exit jet Mach number, M_j					
	0.275	0.460	0.638	0.805	0.990	1.158
	Downstream peak Mach number, M					
12.70	0.270	0.460	0.640	0.805	0.990	1.151
25.40	.250	.420	.590	.770	.975	1.140
38.10	.220	.375	.520	.675	.890	1.080
50.80	.175	.290	.420	.570	.750	.940
132.08	.067	.118	.175	.232	.301	.374
152.40	.056	.103	.147	.201	.263	.323
233.68	.030	.061	.094	.126	.163	.204
Ratio of M_j to ideal, $M_j/M_{j,id}$	1.015	1.007	1.002	1.001	0.996	0.995
Ratio of nozzle mass flow rate to ideal, $W_n/W_{n,id}$	0.792	0.804	0.658	0.716	0.795	0.808

(z) Configuration 33

Axial distance, X, cm	Nozzle-exit jet Mach number, M_j				
	0.450	0.635	0.800	0.990	1.157
	Downstream peak Mach number, M				
12.70	0.430	0.610	0.780	0.980	1.130
25.40	.340	.490	.630	.835	.940
38.10	.250	.370	.490	.620	.740
50.80	.200	.300	.390	.500	.610
111.76	.106	.157	.205	.268	.328
142.24	.083	.120	.159	.203	.253
213.36	.054	.078	.104	.135	.168
Ratio of M_j to ideal, $M_j/M_{j,id}$	0.987	0.997	0.995	0.996	0.995
Ratio of nozzle mass flow rate to ideal, $W_n/W_{n,id}$	0.665	0.685	0.707	0.753	0.806

TABLE IV. - Continued.

(aa) Configuration 34

Axial distance, X, cm	Nozzle-exit jet Mach number, M_j			
	0.640	0.805	0.990	1.154
	Downstream peak Mach number, M			
12.70	0.620	0.780	0.965	1.090
25.40	.465	.605	.790	.860
38.10	.330	.430	.545	.652
50.80	.280	.340	.430	.520
121.92	.108	.137	.172	.205
149.86	.087	.110	.136	.164
203.20	.063	.081	.104	.121
Ratio of M_j to ideal, $M_j/M_{j,id}$	1.008	1.004	0.998	0.994
Ratio of nozzle mass flow rate to ideal, $W_n/W_{n,id}$	0.966	0.945	0.910	0.932

(bb) Configuration 35

Axial distance, X, cm	Nozzle-exit jet Mach number, M_j			
	0.638	0.805	0.990	1.155
	Downstream peak Mach number, M			
12.70	0.630	0.795	0.985	1.145
25.40	.510	.670	.875	1.010
38.10	.370	.480	.630	715
50.80	.290	.360	.470	.550
99.06	.144	.182	.233	.269
147.32	.092	.117	.146	.172
203.20	.065	.083	.105	.123
Ratio of M_j to ideal, $M_j/M_{j,id}$	1.005	1.004	0.998	0.995
Ratio of nozzle mass flow rate to ideal, $W_n/W_{n,id}$	0.994	0.976	0.938	0.935

TABLE IV. - Continued.

(cc) Configuration 36

Axial distance, X, cm	Nozzle-exit jet Mach number, M_j	
	0.810	0.990
	Downstream peak Mach number, M	
12.70	0.735	0.900
25.40	.47	.60
38.10	.320	.400
50.80	.225	.300
96.52	.123	-----
147.32	.073	.094
Ratio of M_j to ideal, $M_j/M_{j,id}$	1.002	0.992
Ratio of nozzle mass flow rate to ideal, $W_n/W_{n,id}$	-----	-----

(dd) Configuration 37

Axial distance, X, cm	Nozzle-exit jet Mach number, M_j			
	0.480	0.640	0.810	0.990
	Downstream peak Mach number, M			
12.70	0.470	0.630	0.795	0.970
25.40	.380	.510	.660	.830
38.10	.275	.380	.500	.630
50.80	.225	.300	.380	.500
126.37	.088	.115	.153	.192
250.83	.038	.060	.072	.088
Ratio of M_j to ideal, $M_j/M_{j,id}$	1.004	1.000	1.004	0.993
Ratio of nozzle mass flow rate to ideal, $W_n/W_{n,id}$	1.033	0.908	0.858	0.865

TABLE IV. - Continued.

(ee) Configuration 38

Axial distance, X, cm	Nozzle-exit jet Mach number, M_j					
	0.270	0.460	0.635	0.804	0.988	1.160
	Downstream peak Mach number, M					
12.70	0.270	0.450	0.630	0.802	0.990	1.149
25.40	.245	.415	.593	.778	.970	1.136
38.10	.210	.365	.525	.670	.885	1.060
50.80	.180	.320	.450	.595	.770	.930
127.00	.093	.168	.242	.321	.411	.502
213.36	.057	.100	.145	.190	.245	.301
264.16	.041	.077	.114	.151	.196	.240
Ratio of M_j to ideal, $M_j/M_{j,id}$	1.000	1.011	0.998	1.002	0.996	0.999
Ratio of nozzle mass flow rate to ideal, $W_n/W_{n,id}$	0.776	0.719	0.715	0.744	0.791	0.823

(ff) Configuration 39

Axial distance, X, cm	Nozzle-exit jet Mach number, M_j					
	0.260	0.440	0.625	0.790	0.978	1.135
	Downstream peak Mach number, M					
[d]6.35	0.175	0.315	0.443	0.583	0.800	1.020
[d]7.62	.175	.300	.425	.565	.760	.975
9.53	.175	.305	.435	.550	.720	.860
12.70	.200	.330	.462	.585	.740	.945
19.05	.185	.330	.460	.590	.755	.958
25.40	.170	.300	.430	.555	.745	.927
38.10	.115	.210	.330	.440	.630	.825
50.80	.090	.150	.230	.320	.470	.660
101.60	.041	.077	.116	.152	.211	.288
157.48	.023	.050	.066	.084	.114	.143
Ratio of M_j to ideal, $M_j/M_{j,id}$	0.959	0.963	0.980	0.981	0.983	0.975
Ratio of nozzle mass flow rate to ideal, $W_n/W_{n,id}$	0.662	0.666	0.683	0.730	0.784	0.841

[d]Center of jet subatmospheric.

TABLE IV. - Concluded.

(gg) Configuration 40

Axial distance, X, cm	Nozzle-exit jet Mach number, M_j				
	0.458	0.630	0.800	0.985	1.150
	Downstream peak Mach number, M				
6.99	0.445	0.628	0.798	0.983	1.141
14.45	.450	.625	.795	.980	1.124
20.32	.430	.610	.780	.972	1.130
25.40	.435	.610	.782	.981	1.138
38.10	.425	.600	.775	.980	1.154
45.72	.410	.580	.755	.955	1.130
63.50	.375	.535	.705	.886	1.058
101.60	.270	.400	.525	.685	.820
152.40	.180	.270	.350	.450	.550
203.20	.140	.200	.260	.330	.400
Ratio of M_j to ideal, $M_j/M_{j,id}$	1.004	0.989	0.996	0.992	0.990
Ratio of nozzle mass flow rate to ideal, $W_n/W_{n,id}$	-----	-----	-----	-----	-----

(hh) Configuration 41

Axial distance, X, cm	Condition of jets	Nozzle-exit jet Mach number, M_j				
		0.468	0.642	0.809	0.997	1.160
		Downstream peak Mach number, M				
[e]10.41	Separate	0.440	0.618	0.789	0.981	1.150
[e]22.23	Coalescing	.410	.570	.730	.930	1.110
34.93	Coalesced	.400	.562	.718	.905	1.074
47.63	↓	.370	.518	.668	.860	1.040
60.33	↓	.320	.467	.588	.770	.957
73.03	↓	.275	.400	.515	.670	.842
85.73	↓	.245	.345	.450	.588	.740
111.13	↓	.200	.275	.360	.470	.580
136.53	↓	.150	.225	.300	.375	.475
Ratio of M_j to ideal, $M_j/M_{j,id}$		1.026	1.009	1.007	1.004	0.998
Ratio of nozzle mass flow rate to ideal, $W_n/W_{n,id}$		-----	-----	-----	-----	-----

[e]Double peaks (average).

TABLE V. - PEAK AXIAL JET MACH NUMBER DECAY DATA FOR MULTIELEMENT NOZZLES WITH NOMINALLY COPLANAR EXITS

(a) Configuration 42

Axial distance, X, cm	Nozzle-exit jet Mach number, M_j					
	0.270	0.460	0.640	0.820	0.990	1.155
	Downstream peak Mach number, M					
12.70	0.250	0.410	0.560	0.730	0.930	1.110
25.40	.190	.300	.410	.540	.680	.840
38.10	.160	.280	.385	.485	.600	.730
50.80	.150	.250	.360	.455	.575	.685
147.32	.070	.117	.158	.210	.275	.341
294.64	.040	.056	.074	.094	.119	.149
Ratio of M_j to ideal, $M_j/M_{j,id}$	1.000	1.011	1.008	1.022	0.999	0.996
Ratio of nozzle mass flow rate to ideal, $W_n/W_{n,id}$	------	0.932	0.909	0.913	0.919	0.922

(b) Configuration 43

Axial distance, X, cm	Nozzle-exit jet Mach number, M_j					
	0.270	0.450	0.640	0.810	0.990	1.170
	Downstream peak Mach number, M					
12.70	0.250	0.410	0.570	0.755	0.940	1.110
25.40	.150	.260	.395	.500	.650	.830
38.10	.130	.225	.320	.410	.530	.650
50.80	.120	.210	.300	.380	.470	.575
147.32	.067	.108	.154	.197	.260	.325
297.18	.032	.048	.064	.086	.106	.133
Ratio of M_j to ideal, $M_j/M_{j,id}$	0.996	0.987	1.005	1.007	0.996	1.006
Ratio of nozzle mass flow rate to ideal, $W_n/W_{n,id}$	0.901	0.940	0.900	0.906	0.925	0.932

TABLE V. - Continued.

(c) Configuration 44

Axial distance, X, cm	Nozzle-exit jet Mach number, M_j					
	0.280	0.450	0.635	0.800	0.980	1.135
	Downstream peak Mach number, M					
12.70	0.250	0.410	0.590	0.750	0.935	1.110
25.40	.150	.275	.380	.490	.645	.810
38.10	.125	.200	.290	.360	.450	.570
50.80	.100	.175	.250	.320	.410	.485
132.08	.065	.091	.154	.203	.258	.310
299.72	.030	.046	.061	.084	.105	.129
Ratio of M_j to ideal, $M_j/M_{j,id}$	1.037	0.991	1.002	0.999	0.990	0.979
Ratio of nozzle mass flow rate to ideal, $W_n/W_{n,id}$	0.952	0.922	0.896	0.914	0.923	0.925

(d) Configuration 45

Axial distance, X, cm	Nozzle-exit jet Mach number, M_j					
	0.260	0.440	0.630	0.800	0.990	1.140
	Downstream peak Mach number, M					
12.70	0.230	0.410	0.580	0.745	0.945	1.120
25.40	.150	.270	.390	.470	.630	.830
38.10	.100	.180	.270	.340	.430	.560
50.80	.090	.150	.220	.270	.350	.430
92.71	.080	.135	.190	.240	.300	.360
148.27	.060	.097	.140	.184	.230	.290
321.95	.038	.050	.064	.082	.103	.125
Ratio of M_j to ideal, $M_j/M_{j,id}$	0.963	0.967	0.992	0.998	0.999	0.983
Ratio of nozzle mass flow rate to ideal, $W_n/W_{n,id}$	0.869	0.896	0.887	0.902	0.924	0.927

TABLE V. - Continued.

(e) Configuration 46

Axial distance, X, cm	Nozzle-exit jet Mach number, M_j					
	0.285	0.460	0.640	0.805	0.992	1.155
	Downstream peak Mach number, M					
12.70	0.230	0.430	0.580	0.750	0.966	1.105
25.40	.150	.250	.360	.470	[a].650	.720
38.10	.110	.190	.270	.350	.450	.530
50.80	.100	.170	.235	.320	.400	.470
121.92	.075	.122	.180	.236	.301	.358
203.20	.047	.080	.111	.146	.189	.225
243.84	.040	.061	.092	.117	.155	.184
Ratio of M_j to ideal, $M_j/M_{j,id}$	1.048	1.004	1.000	0.998	0.994	0.990
Ratio of nozzle mass flow rate to ideal, $W_n/W_{n,id}$	0.866	0.812	0.816	0.854	0.900	0.936

(f) Configuration 47

Axial distance, X, cm	Nozzle-exit jet Mach number, M_j					
	0.280	0.460	0.638	0.804	0.990	1.156
	Downstream peak Mach number, M					
12.70	0.210	0.400	0.570	0.730	0.950	1.076
25.40	.120	.225	.330	.435	.555	.655
38.10	.100	.175	.250	.320	.410	.490
50.80	.100	.160	.225	.275	.345	.420
127.00	.058	.108	.156	.204	.264	.314
157.48	.048	.087	.126	.166	.216	.258
213.36	.035	.065	.093	.124	.161	.196
Ratio of M_j to ideal, $M_j/M_{j,id}$	1.033	1.009	1.002	1.000	0.996	0.994
Ratio of nozzle mass flow rate to ideal, $W_n/W_{n,id}$	0.630	0.626	0.636	0.676	0.735	0.780

[a]Uncertain value.

TABLE V. - Continued.

(g) Configuration 48

Axial distance, X, cm	Nozzle-exit jet Mach number, M_j					
	0.265	0.440	0.620	0.790	0.975	1.140
	Downstream peak Mach number, M					
12.70	0.200	0.350	0.480	0.625	0.790	0.970
25.40	.130	.225	.320	.400	.510	.685
38.10	.100	.170	.250	.310	.400	.510
50.80	.100	.160	.230	.290	.370	.450
101.60	.060	.130	.190	.250	.310	.370
152.40	.050	.100	.140	.175	.220	.270
190.50	-----	-----	-----	.140	.180	.225
Ratio of M_j to ideal, $M_j/M_{j,id}$	0.978	0.963	0.972	0.981	0.980	0.979
Ratio of nozzle mass flow rate to ideal, $W_n/W_{n,id}$	0.891	0.886	0.894	0.907	0.915	0.923

(h) Configuration 49

Axial distance, X, cm	Nozzle-exit jet Mach number, M_j				
	0.460	0.630	0.800	0.987	1.150
	Downstream peak Mach number, M				
6.35	0.435	0.620	0.790	0.980	1.140
12.70	.320	.460	.610	.750	.910
19.05	.225	.305	.430	.530	.610
25.40	.170	.250	.315	.410	.480
31.75	.150	.225	.300	.365	.430
38.10	.150	.220	.275	.340	.405
50.80	.150	.210	.260	.330	.380
101.60	.101	.144	.184	.236	.283
139.70	.076	.108	.140	.176	.210
203.20	.051	.072	.095	.118	.141
Ratio of M_j to ideal, $M_j/M_{j,id}$	1.011	0.992	0.999	0.997	0.992
Ratio of nozzle mass flow rate to ideal, $W_n/W_{n,id}$	0.877	0.874	0.882	0.889	0.896

TABLE V. - Continued.

(i) Configuration 50

Axial distance, X, cm	Nozzle-exit jet Mach number, M_j					
	0.275	0.460	0.630	0.796	0.985	1.152
	Downstream peak Mach number, M					
12.70	0.225	0.390	0.555	0.733	0.927	1.105
25.40	.150	.275	.380	.530	.700	.856
38.10	.125	.200	.285	.380	.500	.615
46.99	.100	.170	.250	.330	.435	.520
101.60	.086	.146	.206	269	.347	.424
152.40	.068	.117	.169	.224	.291	.361
203.20	.056	.091	.133	.174	.231	.281
Ratio of M_j to ideal, $M_j/M_{j,id}$	1.015	1.007	0.987	0.989	0.990	0.990
Ratio of nozzle mass flow rate to ideal, $W_n/W_{n,id}$	0.650	0.657	0.683	0.719	0.775	0.819

(j) Configuration 51

Axial distance, X, cm	Nozzle-exit jet Mach number, M_j					
	0.275	0.455	0.630	0.800	0.984	1.150
	Downstream peak Mach number, M					
12.70	0.225	0.360	0.520	0.690	0.903	1.090
25.40	.140	.250	.350	.475	.590	.765
38.10	.125	.175	.270	.350	.455	.570
46.99	.100	.160	.225	.300	.365	.470
101.60	.075	.131	.188	.246	.315	.380
152.40	.062	.109	.158	.208	.269	.330
203.20	.050	.088	.127	.166	.217	.265
Ratio of M_j to ideal, $M_j/M_{j,id}$	1.015	0.996	0.987	0.994	0.989	0.987
Ratio of nozzle mass flow rate to ideal, $W_n/W_{n,id}$	0.651	0.657	0.682	0.717	0.772	0.812

TABLE V. - Continued.

(k) Configuration 52

Axial distance, X, cm	Nozzle-exit jet Mach number, M_j					
	0.270	0.450	0.630	0.800	0.984	1.155
	Downstream peak Mach number, M					
12.70	0.200	0.340	0.490	0.700	0.910	1.098
25.40	.130	.200	.300	.410	.530	.675
38.10	.120	.175	.250	.320	.420	.510
46.99	.080	.125	.220	.280	.375	.460
101.60	.077	.130	.183	.240	.308	.368
152.40	.061	.107	.154	.201	.262	.316
203.20	.052	.084	.124	.163	.214	.259
Ratio of M_j to ideal, $M_j/M_{j,id}$	0.993	0.983	0.986	0.991	0.987	0.991
Ratio of nozzle mass flow rate to ideal, $W_n/W_{n,id}$	0.651	0.653	0.672	0.707	0.761	0.808

(*l*) Configuration 53

Axial distance, X, cm	Nozzle-exit jet Mach number, M_j					
	0.270	0.470	0.640	0.800	0.990	1.150
	Downstream peak Mach number, M					
12.70	0.250	0.410	0.560	0.730	0.920	1.060
25.40	.200	.300	.425	.550	.700	.820
38.10	.200	.300	.400	.500	.630	.750
50.80	.180	.275	.380	.490	.610	.720
133.35	.113	.189	.265	.346	.440	-----
147.64	-----	-----	-----	-----	-----	.492
218.44	.066	.114	.162	.213	.268	.330
299.09	.046	.078	.109	.143	.185	.222
Ratio of M_j to ideal, $M_j/M_{j,id}$	0.996	1.031	1.005	0.996	0.997	0.990
Ratio of nozzle mass flow rate to ideal, $W_n/W_{n,id}$	0.920	0.909	0.913	0.920	0.931	0.937

TABLE V. - Continued.

(m) Configuration 54

Axial distance, X, cm	Nozzle-exit jet Mach number, M_j					
	0.270	0.460	0.630	0.795	0.980	1.150
	Downstream peak Mach number, M					
12.70	0.250	0.410	0.580	0.760	0.954	1.120
25.40	.150	.260	.372	.490	.659	.782
38.10	.120	.220	.300	.380	.480	.565
101.60	.109	.179	.251	.320	.393	.462
152.40	.077	.134	.188	.246	.305	.365
203.20	.062	.108	.156	.198	.245	.298
Ratio of M_j to ideal, $M_j/M_{j,id}$	0.996	1.009	0.989	0.989	0.986	0.989
Ratio of nozzle mass flow rate to ideal, $W_n/W_{n,id}$	0.924	0.927	0.935	0.952	0.961	0.971

(n) Configuration 55

Axial distance, X, cm	Nozzle-exit jet Mach number, M_j					
	0.280	0.460	0.640	0.800	0.980	1.140
	Downstream peak Mach number, M					
12.70	0.260	0.410	0.600	0.775	0.960	1.120
25.40	.160	.280	.380	.510	.640	.790
38.10	.125	.200	.300	.370	.480	.570
50.80	.100	.180	.270	.340	.420	.500
139.07	.080	.144	.201	.254	.321	.384
261.62	.048	.083	.117	.149	.186	.224
Ratio of M_j to ideal, $M_j/M_{j,id}$	1.033	1.009	1.005	0.996	0.987	0.981
Ratio of nozzle mass flow rate to ideal, $W_n/W_{n,id}$	0.894	0.869	0.881	0.890	0.897	0.906

TABLE V. - Continued.

(o) Configuration 56

Axial distance, X, cm	Nozzle-exit jet Mach number, M_j					
	0.275	0.460	0.640	0.805	0.993	1.146
	Downstream peak Mach number, M					
12.70	0.270	0.430	0.610	0.780	0.970	1.120
25.40	.160	.270	.390	.515	.665	.800
38.10	.130	.225	.320	.420	.520	.625
50.80	.125	.210	.300	.380	.480	.575
134.94	.106	.180	.255	.327	.411	.497
210.50	.074	.125	.175	.229	.287	.352
278.77	.055	.087	.125	.160	.204	.252
Ratio of M_j to ideal, $M_j/M_{j,id}$	1.019	1.011	1.008	1.004	1.002	0.988
Ratio of nozzle mass flow rate to ideal, $W_n/W_{n,id}$	0.956	0.885	0.895	0.899	0.908	0.910

(p) Configuration 57

Axial distance, X, cm	Nozzle-exit jet Mach number, M_j					
	0.275	0.460	0.650	0.815	1.000	1.150
	Downstream peak Mach number, M					
12.70	0.130	0.225	0.335	0.435	0.620	0.835
25.40	.120	.200	.275	.370	.490	.605
38.10	.100	.170	.270	.350	.450	.605
46.99	.100	.175	.225	.335	.440	.550
127.00	.087	.143	.206	.274	.364	.468
203.20	.058	.098	.141	.188	.250	.318
264.16	.044	.077	.112	.149	.196	.248
Ratio of M_j to ideal, $M_j/M_{j,id}$	1.015	1.009	1.020	1.014	1.006	0.989
Ratio of nozzle mass flow rate to ideal, $W_n/W_{n,id}$	0.754	0.718	0.726	0.758	0.794	0.840

TABLE V. - Continued.

(q) Configuration 58

Axial distance, X, cm	Exposed tube length, cm	Nozzle-exit jet Mach number, M_j					
		0.260	0.450	0.630	0.805	0.990	1.155
		Downstream peak Mach number, M					
12.70	1.27	0.260	0.430	0.590	0.750	0.960	1.130
25.40	↓	.200	.310	.440	.560	.720	.870
38.10		.190	.300	.400	.510	.650	.780
50.80		.180	.270	.380	.490	.620	.740
136.53		-----	-----	-----	.220	.288	-----
266.70		-----	-----	-----	.116	.147	-----
50.80	0	-----	-----	-----	.500	.625	-----
Ratio of M_j to ideal, $M_j/M_{j,id}$		0.963	0.989	0.992	1.004	0.999	0.996
Ratio of nozzle mass flow rate to ideal, $W_n/W_{n,id}$		0.914	0.878	0.888	0.894	0.903	0.914

(r) Configuration 59

Axial distance, X, cm	Nozzle-exit jet Mach number, M_j					
	0.290	0.455	0.635	0.805	0.970	1.140
	Downstream peak Mach number, M					
12.70	0.275	0.450	0.620	0.790	0.950	1.085
25.40	.175	.305	.420	.550	.685	.830
38.10	.145	.250	.340	.440	.540	.645
50.80	.130	.220	.310	.400	.500	.590
130.18	.080	.137	.193	.246	.310	.378
247.33	.042	.061	.084	.114	.144	.174
Ratio of M_j to ideal, $M_j/M_{j,id}$	1.078	1.004	1.005	1.009	0.983	0.986
Ratio of nozzle mass flow rate to ideal, $W_n/W_{n,id}$	0.915	0.903	0.911	0.917	0.924	0.928

TABLE V. - Continued.

(s) Configuration 60

Axial distance, X, cm	Nozzle-exit jet Mach number, M_j					
	0.260	0.450	0.630	0.805	0.990	1.155
	Downstream peak Mach number, M					
12.70	0.250	0.430	0.590	0.760	0.960	1.110
25.40	.160	.285	.380	.488	.670	.808
38.10	-----	.200	.280	.360	.460	.570
50.80	-----	.180	.250	.330	.400	.490
135.89	-----	-----	-----	.223	.290	-----
269.24	-----	-----	-----	.121	.154	-----
Ratio of M_j to ideal, $M_j/M_{j,id}$	0.959	0.985	0.987	1.000	0.995	0.992
Ratio of nozzle mass flow rate to ideal, $W_n/W_{n,id}$	0.863	0.876	0.881	0.892	0.903	0.913

(t) Configuration 61

Axial distance, X, cm	Exposed tube length, cm									
	0						5.08		10.16	
	Nozzle-exit jet Mach number, M_j									
	0.290	0.460	0.640	0.810	0.990	1.140	0.81	0.99	0.81	0.99
	Downstream peak Mach number, M									
12.70	0.260	0.420	0.580	0.740	0.905	1.03	0.730	0.910	0.740	0.912
25.40	.210	.350	.500	.640	.790	.930	.630	.785	.630	.790
38.10	.200	.340	.470	.605	.755	.890	.600	.745	.600	.745
50.80	.200	.320	.450	.570	.720	.850	-----	-----	-----	-----
132.72	-----	-----	-----	.367	.476	-----	-----	-----	-----	-----
291.47	-----	-----	-----	.163	.206	-----	.162	.210	.162	.210
Ratio of M_j to ideal, $M_j/M_{j,id}$	1.074	1.011	1.008	1.011	0.999	0.983	-----	-----	-----	-----
Ratio of nozzle mass flow rate to ideal, $W_n/W_{n,id}$	0.934	0.941	0.935	0.936	0.939	0.948	-----	-----	-----	-----

TABLE V. - Continued.

(u) Configuration 62

Axial distance, X, cm	Nozzle-exit jet Mach number, M_j					
	0.270	0.450	0.635	0.800	0.985	1.145
	Downstream peak Mach number, M					
12.70	0.250	0.415	0.590	0.770	0.950	1.080
25.40	.180	.300	.440	.555	.710	.845
38.10	.150	.280	.395	.505	.640	.760
50.80	.155	.270	.380	.490	.610	.725
132.72	.114	.187	.268	.345	.440	.530
291.78	.049	.081	.118	.154	.197	.241
Ratio of M_j to ideal, $M_j/M_{j,id}$	0.996	0.987	0.997	0.995	0.991	0.985
Ratio of nozzle mass flow rate to ideal, $W_n/W_{n,id}$	0.853	0.870	0.870	0.886	0.898	0.904

(v) Configuration 63

Axial distance, X, cm	Nozzle-exit jet Mach number, M_j					
	0.280	0.450	0.635	0.805	0.980	1.140
	Downstream peak Mach number, M					
12.70	0.275	0.440	0.620	0.785	0.960	1.120
25.40	.160	.290	.410	.540	.680	.790
38.10	.130	.230	.330	.430	.540	.630
50.80	.120	.220	.310	.405	.500	.580
130.81	.094	.163	.230	.299	.388	.460
297.82	.053	.073	.099	.123	.163	.199
Ratio of M_j to ideal, $M_j/M_{j,id}$	1.041	0.996	1.005	1.009	0.993	0.987
Ratio of nozzle mass flow rate to ideal, $W_n/W_{n,id}$	0.842	0.880	0.891	0.903	0.917	0.925

TABLE V. - Continued.

(w) Configuration 64

Axial distance, X, cm	Exposed tube length, cm	Nozzle-exit jet Mach number, M_j					
		0.270	0.450	0.640	0.770	0.990	1.150
		Downstream peak Mach number, M					
12.70	10.16	0.250	0.420	0.600	0.770	0.960	1.110
25.40	↓	.190	.300	.420	.560	.720	.850
38.10		.150	.270	.400	.510	.640	.760
50.80		.160	.280	.390	.500	.630	.740
116.80		-----	-----	-----	.390	.502	-----
169.55		-----	-----	-----	.292	.373	-----
238.76		-----	-----	-----	.205	.262	-----
12.70	1.27	.230	.390	.567	.750	.930	1.085
50.80	1.27	.190	.285	.400	.505	.630	.750
Ratio of M_j to ideal,[b] $M_j/M_{j,id}$		1.000	0.989	1.008	0.961	1.000	0.992
Ratio of nozzle mass flow rate to ideal,[b] $W_n/W_{n,id}$		0.824	0.881	0.892	0.909	0.913	0.920

(x) Configuration 65

Axial distance, X, cm	Nozzle-exit jet Mach number, M_j					
	0.280	0.450	0.635	0.805	0.990	1.155
	Nozzle-exit jet Mach number with screens, $M_{j,screens}$					
	0.210	0.340	0.475	0.610	0.775	0.930
	Downstream peak Mach number, M					
25.40	0.200	0.300	0.430	0.555	0.710	0.850
50.80	.180	.280	.390	.500	.620	.740
132.72	.112	.188	.267	.346	.444	.537
256.54	.056	.090	.132	.172	.220	.268
Ratio of M_j to ideal, $M_j/M_{j,id}$	1.033	0.985	0.997	1.001	0.996	0.992
Ratio of nozzle mass flow rate to ideal, $W_n/W_{n,id}$	0.838	0.805	0.815	0.820	0.833	0.841

[b]Apply to M_j values for exposed tube length of 10.16 cm only.

TABLE V. - Continued.

(y) Configuration 66

Axial distance, X, cm	Nozzle-exit jet Mach number, M_j					
	0.280	0.460	0.640	0.810	0.995	1.150
	Downstream peak Mach number, M					
12.70	0.240	0.400	0.580	0.760	0.950	1.085
25.40	.200	.310	.445	.560	.710	.840
38.10	.170	.305	.410	.530	.660	.790
50.80	.170	.290	.410	520	.655	.775
137.80	.109	.189	.270	.351	.450	-----
148.59	-----	-----	-----	-----	-----	.462
233.68	.063	.113	.164	.210	.265	.317
Ratio of M_j to ideal, $M_j/M_{j,id}$	1.033	1.009	1.005	1.009	1.002	0.990
Ratio of nozzle mass flow rate to ideal, $W_n/W_{n,id}$	0.964	0.927	0.931	0.937	0.947	0.952

(z) Configuration 67

Axial distance, X, cm	Nozzle-exit jet Mach number, M_j					
	0.230	0.440	0.620	0.790	0.980	1.135
	Downstream peak Mach number, M					
12.70	0.175	0.340	0.510	0.670	0.865	1.020
25.40	.130	.250	.370	.490	.580	.700
38.10	.130	.250	.360	.475	.570	.680
50.80	.130	.250	.350	.460	.570	.680
144.46	.096	.172	.246	.322	.405	.495
313.69	.048	.075	.111	.142	.181	.214
Ratio of M_j to ideal, $M_j/M_{j,id}$	0.849	0.963	0.972	0.981	0.985	0.975
Ratio of nozzle mass flow rate to ideal, $W_n/W_{n,id}$	0.853	0.890	0.901	0.912	0.919	0.926

TABLE V. - Continued.

(aa) Configuration 68

Axial distance, X, cm	Nozzle-exit jet Mach number, M_j					
	0.275	0.463	0.640	0.805	0.992	1.150
	Downstream peak Mach number, M					
12.70	0.260	0.430	0.610	0.775	0.962	1.105
25.40	.170	.275	.390	.510	.650	.770
38.10	.130	.225	.330	.415	.530	.625
50.80	.120	.210	.300	.387	.485	.580
137.16	.110	.190	.260	.340	.430	.520
203.20	.080	.140	.200	.250	.320	.390
330.20	.050	.080	.120	.160	.200	.240
Ratio of M_j to ideal, $M_j/M_{j,id}$	1.019	1.015	1.006	1.002	1.000	0.990
Ratio of nozzle mass flow rate to ideal, $W_n/W_{n,id}$	0.907	0.921	0.890	0.901	0.904	0.904

(bb) Configuration 69

Axial distance, X, cm	Nozzle-exit jet Mach number, M_j					
	0.280	0.460	0.645	0.805	0.985	1.140
	Downstream peak Mach number, M					
12.70	0.260	0.415	0.600	0.780	0.955	1.090
25.40	.190	.300	.410	.550	.690	.810
38.10	.150	.280	.380	.490	.610	.720
50.80	.150	.270	.370	.470	.590	.698
135.57	.106	.171	.244	.315	.404	.487
291.47	.050	.080	.113	.145	.186	.226
Ratio of M_j to ideal, $M_j/M_{j,id}$	1.037	1.011	1.016	1.004	0.993	0.982
Ratio of nozzle mass flow rate to ideal, $W_n/W_{n,id}$	0.994	0.844	0.907	0.920	0.920	0.933

TABLE V. - Continued.

(cc) Configuration 70

Axial distance, X, cm	Nozzle-exit jet Mach number, M_j					
	0.275	0.460	0.640	0.810	0.990	1.145
	Downstream peak Mach number, M					
12.70	0.260	0.430	0.614	0.788	0.970	1.125
25.40	.210	.360	.500	.650	.825	1.005
38.10	.180	.310	.440	.560	.715	.870
50.80	.175	.300	.420	.525	.670	.800
140.97	.129	.211	.300	.388	.480	-----
165.10	.110	.181	.260	.335	.413	.502
222.89	.083	.139	.199	.256	.318	.383
271.78	.059	.107	.162	.208	.259	.313
Ratio of M_j to ideal, $M_j/M_{j,id}$	1.015	1.009	1.005	1.009	0.997	0.985
Ratio of nozzle mass flow rate to ideal, $W_n/W_{n,id}$	0.968	0.942	0.940	0.935	0.921	0.936

(dd) Configuration 71

Axial distance, X, cm	Jet	Nozzle-exit jet Mach number, M_j					
		0.300	0.465	0.640	0.810	0.990	1.142
		Downstream peak Mach number, M					
12.70	Center	0.285	0.445	0.625	0.799	0.970	1.132
25.40	↓	.225	.370	.520	.680	.810	.960
38.10	↓	.185	.325	.450	.585	.670	.820
50.80	↓	.160	.285	.400	.515	.595	.740
142.24	↓	.090	.150	.210	.264	.322	.394
205.74	↓	.065	.108	.148	.184	.227	.278
281.94	↓	.050	.082	.116	.141	.172	.207
25.40	10^{o} Side	.175	.330	.460	.615	.790	.989
Ratio of M_j to ideal, $M_j/M_{j,id}$		1.107	1.018	1.003	1.006	0.995	0.981
Ratio of nozzle mass flow rate to ideal, $W_n/W_{n,id}$		1.022	0.966	0.942	0.935	0.918	1.918

TABLE V. - Continued.

(ee) Configuration 72

Axial distance, X, cm	Nozzle-exit jet Mach number, M_j					
	0.260	0.450	0.628	0.800	0.983	1.148
	Downstream peak Mach number, M					
12.70	0.230	0.410	0.595	0.770	0.948	1.100
25.40	.175	.320	.450	.595	.740	.825
38.10	.170	.290	.400	.515	.620	.695
50.80	.165	.280	.390	.490	.590	.675
101.60	.130	.240	.325	.420	.525	.610
152.40	.100	.175	.250	.320	.410	.485
203.20	.080	.140	.200	.260	.320	.370
Ratio of M_j to ideal, $M_j/M_{j,id}$	0.974	1.000	0.998	1.008	1.001	0.998
Ratio of nozzle mass flow rate to ideal, $W_n/W_{n,id}$	0.928	0.962	0.973	0.982	1.004	1.021

(ff) Configuration 73

Axial distance, X, cm	Nozzle-exit jet Mach number, M_j					
	0.280	0.460	0.640	0.803	0.990	1.155
	Downstream peak Mach number, M					
12.70	0.230	0.405	0.590	0.740	0.936	1.053
25.40	.175	.310	.450	.590	.730	.820
38.10	.160	.260	.370	.480	.580	.650
50.80	.150	.240	.340	.430	.530	.590
101.60	.125	.220	.310	.390	.475	.555
152.40	.100	.175	.250	.320	.400	.480
203.20	.070	.130	.200	.250	.320	.390
Ratio of M_j to ideal, $M_j/M_{j,id}$	1.029	1.004	1.002	0.995	0.993	0.990
Ratio of nozzle mass flow rate to ideal, $W_n/W_{n,id}$	1.004	0.975	0.969	0.973	0.999	1.007

TABLE V. - Continued.

(gg) Configuration 74; survey on nozzle centerline

Axial distance, X, cm	Nozzle-exit jet Mach number, M_j					
	0.290	0.460	0.635	0.805	0.985	1.160
	Downstream peak Mach number, M					
12.70	0.250	0.410	0.580	0.750	0.930	1.090
25.40	.180	.300	.440	.580	.720	.860
38.10	.150	.260	.365	.470	.570	.675
50.80	.140	.250	.340	.430	.520	.600
Ratio of M_j to ideal, $M_j/M_{j,id}$	1.074	1.011	1.000	1.004	0.994	1.000
Ratio of nozzle mass flow rate to ideal, $W_n/W_{n,id}$	-----	-----	-----	-----	-----	-----

(hh) Configuration 75

Axial distance, X, cm	Nozzle-exit jet Mach number, M_j					
	0.290	0.470	0.647	0.810	0.993	1.160
	Downstream peak Mach number, M					
12.70	0.305	0.460	0.625	0.802	0.990	1.155
25.40	.190	.320	.460	.614	.808	.950
38.10	.130	.230	.330	.450	.580	.680
46.99	.120	.200	.275	.370	.480	.575
101.60	.062	.102	.145	.187	.245	.299
152.40	.048	.073	.116	.151	.192	.234
205.74	.038	.065	.093	.123	.157	.191
Ratio of M_j to ideal, $M_j/M_{j,id}$	1.070	1.031	1.017	1.009	1.000	0.998
Ratio of nozzle mass flow rate to ideal, $W_n/W_{n,id}$	0.675	0.668	0.682	0.724	0.773	0.809

TABLE V. - Continued.

(ii) Configuration 76

Axial distance, X, cm	Nozzle-exit jet Mach number, M_j					
	0.280	0.455	0.632	0.800	0.990	1.155
	Downstream peak Mach number, M					
12.70	0.225	0.360	0.498	0.673	0.850	0.940
25.40	.180	.295	.405	.537	.655	.787
38.10	.140	.250	.340	.440	.560	.680
50.80	.120	.200	.300	.380	.505	.600
101.60	.080	.131	.185	.240	.310	.372
152.40	.061	.099	.140	.180	.231	.274
228.60	.041	.068	.099	.130	.166	.198
Ratio of M_j to ideal, $M_j/M_{j,id}$	1.033	0.998	0.992	0.995	0.996	0.993
Ratio of nozzle mass flow rate to ideal, $W_n/W_{n,id}$	0.676	0.655	0.678	0.716	0.765	0.807

(jj) Configuration 77

Axial distance, X, cm	Nozzle-exit jet Mach number, M_j					
	0.250	0.450	0.620	0.790	0.975	1.142
	Downstream peak Mach number, M					
12.70	0.175	0.300	0.440	0.620	0.820	1.000
25.40	.125	.220	.310	.400	.510	.640
38.10	.110	.200	.275	.360	.480	.560
46.99	.110	.220	.270	.350	.460	.560
127.00	.060	.105	.153	.207	.269	.326
203.20	.040	.075	.109	.149	.189	.235
266.70	.035	.062	.087	.121	.158	.188
Ratio of M_j to ideal, $M_j/M_{j,id}$	0.926	0.989	0.976	0.985	0.983	0.984
Ratio of nozzle mass flow rate to ideal, $W_n/W_{n,id}$	0.661	0.670	0.666	0.713	0.747	0.793

TABLE V. - Continued.

(kk) Configuration 78

Axial distance, X, cm	Nozzle-exit jet Mach number, M_j					
	0.275	0.450	0.630	0.800	0.984	1.145
	Downstream peak Mach number, M					
12.70	0.175	0.290	0.425	0.545	0.725	0.880
25.40	.140	.240	.340	.440	.550	.650
38.10	.130	.220	.320	.420	.520	.630
46.99	.120	.220	.300	.390	.505	.600
101.60	.095	.158	.230	.304	.385	.460
152.40	.068	.118	.171	.226	.292	.345
203.20	.054	.091	.132	.175	.224	.265
Ratio of M_j to ideal, $M_j/M_{j,id}$	1.011	0.985	0.987	0.994	0.989	0.983
Ratio of nozzle mass flow rate to ideal, $W_n/W_{n,id}$	0.675	0.685	0.713	0.746	0.797	0.841

(*ll*) Configuration 79

Axial distance, X, cm	Nozzle-exit jet Mach number, M_j					
	0.275	0.455	0.635	0.805	0.990	1.148
	Downstream peak Mach number, M					
2.54	0.265	0.455	0.620	0.800	0.986	1.135
5.08	.240	.370	.530	.715	.926	1.070
6.35	.220	.350	.480	.650	.849	.992
12.70	.160	.270	.370	.475	.620	.742
19.05	.150	.265	.370	.470	.600	.709
25.40	.150	.260	.360	.460	.580	.692
38.10	.150	.265	.365	.465	.580	.692
50.80	.140	.250	.340	.450	.570	.680
101.60	.098	.163	.235	.310	.407	.511
152.40	.065	.115	.168	.216	.284	.353
223.52	.049	.078	.116	.152	.198	.245
Ratio of M_j to ideal, $M_j/M_{j,id}$	1.015	0.996	0.997	1.001	0.996	0.986
Ratio of nozzle mass flow rate to ideal, $W_n/W_{n,id}$	0.681	0.686	0.714	0.744	0.788	0.825

TABLE V. - Continued.

(mm) Configuration 89

Axial distance, X, cm	Survey on -	Nozzle-exit jet Mach number, M_j					
		0.280	0.450	0.630	0.800	0.987	1.150
		Downstream peak Mach number, M					
12.70	Nozzle centerline (six slots)	0.090	0.140	0.220	0.270	0.385	0.445
25.40		.100	.170	.250	.335	.435	.475
38.10		.100	.175	.250	.320	.400	.455
50.80		.120	.180	.260	.325	.395	.445
101.60		.100	.175	.250	.320	.400	.475
152.40		-----	.140	.215	.270	.340	.410
203.20	↓	-----	.120	.160	.220	.270	.330
12.70	Centerline of three slots	.240	.390	.560	.720	.905	1.055
25.40		.180	.300	.420	.530	.665	.810
38.10		.160	.250	.350	.440	.545	.645
50.80	↓	.140	.225	.315	.400	.490	.575
Ratio of M_j to ideal,[c] $M_j/M_{j,id}$		1.037	0.989	0.992	0.998	0.996	0.991
Ratio of nozzle mass flow rate to ideal,[c] $W_n/W_{n,id}$		1.049	0.967	0.989	0.989	1.019	1.039

(nn) Configuration 90

Axial distance, X, cm	Survey on -	Nozzle-exit jet Mach number, M_j					
		0.275	0.460	0.630	0.800	0.990	1.150
		Downstream peak Mach number, M					
25.40	Nozzle centerline (six slots)	0.080	0.125	0.170	0.220	0.280	0.320
38.10		.090	.140	.200	.250	.300	.350
50.80		.100	.150	.220	.260	.315	.375
101.60		.100	.150	.225	.280	.360	.420
139.70		.070	.140	.200	.270	.330	.400
177.80	↓	.060	.125	.175	.230	.290	.350
12.70	Centerline of three slots	.240	.390	.560	.720	.920	1.060
25.40		.175	.300	.410	.540	.680	.810
38.10		.140	.225	.320	.420	.520	.610
50.80	↓	.125	.210	.290	.370	.460	.550
Ratio of M_j to ideal,[c] $M_j/M_{j,id}$		1.015	1.007	0.987	0.994	0.995	0.988
Ratio of nozzle mass flow rate to ideal,[c] $W_n/W_{n,id}$		1.004	1.001	1.000	1.010	1.024	1.047

[c]Apply to M_j values for survey on nozzle centerline only.

TABLE V. - Continued.

(oo) Configuration 94

Axial distance, X, cm	Nozzle-exit jet Mach number, M_j					
	0.275	0.460	0.640	0.803	0.990	1.156
	Downstream peak Mach number, M					
12.70	0.230	0.380	0.540	0.680	0.865	1.010
25.40	.160	.275	.390	.500	.640	.740
38.10	.135	.230	.320	.400	.500	.600
50.80	.120	.200	.280	.355	.445	.530
101.60	.108	.184	.256	.325	.404	.493
152.40	.084	.144	.201	.257	.319	.390
213.36	.061	.103	.148	.190	.239	.285
Ratio of M_j to ideal, $M_j/M_{j,id}$	1.015	1.009	1.005	0.999	0.996	0.994
Ratio of nozzle mass flow rate to ideal, $W_n/W_{n,id}$	0.949	0.960	0.962	0.965	0.964	0.970

(pp) Configuration 95

Axial distance, X, cm	Nozzle-exit jet Mach number, M_j					
	0.270	0.457	0.634	0.805	0.990	1.152
	Downstream peak Mach number, M					
12.70	0.270	0.440	0.613	0.795	0.972	1.133
25.40	.200	.330	.465	.615	.790	.930
38.10	.160	.275	.390	.510	.650	.750
50.80	.140	.250	.340	.440	.567	.665
114.30	.112	.192	.271	.354	.446	.534
152.40	.089	.147	.212	.273	.345	.415
223.52	.058	.105	.146	.191	.240	.288
Ratio of M_j to ideal, $M_j/M_{j,id}$	1.000	1.004	0.998	1.004	0.999	0.993
Ratio of nozzle mass flow rate to ideal, $W_n/W_{n,id}$	0.952	0.960	0.965	0.970	0.982	0.981

TABLE V. - Continued.

(qq) Configuration 96

Axial distance, X, cm	Nozzle-exit jet Mach number, M_j					
	0.270	0.460	0.633	0.802	0.988	1.151
	Downstream peak Mach number, M					
12.70	0.225	0.385	0.550	0.705	0.895	1.030
25.40	.175	.305	.425	.550	.688	.822
38.10	.150	.275	.375	.480	.609	.730
50.80	.140	.240	.340	.440	.555	.675
132.08	.098	.167	.238	.310	.400	.495
195.58	.065	.112	.159	.202	.264	.325
243.84	.050	.090	.127	.166	.213	.260
Ratio of M_j to ideal, $M_j/M_{j,id}$	0.993	1.004	0.989	0.994	0.991	0.986
Ratio of nozzle mass flow rate to ideal, $W_n/W_{n,id}$	0.979	0.989	0.996	1.001	1.011	1.019

(rr) Configuration 97

Axial distance, X, cm	Nozzle-exit jet Mach number, M_j				
	0.275	0.462	0.638	0.808	0.990
	Downstream peak Mach number, M				
12.70	0.260	0.450	0.620	0.785	0.960
25.40	.180	.340	.480	.625	.790
38.10	.140	.260	.360	.460	.590
50.80	.100	.200	.275	.360	.450
134.62	.058	.096	.131	.162	.193
254.00	.033	.052	.075	.096	.117
Ratio of M_j to ideal, $M_j/M_{j,id}$	1.011	1.009	0.998	1.001	0.993
Ratio of nozzle mass flow rate to ideal, $W_n/W_{n,id}$	0.906	0.904	0.884	0.889	0.875

TABLE V. - Continued.

(ss) Configuration 98

Axial distance, X, cm	Nozzle-exit jet Mach number, M_j					
	0.280	0.455	0.645	0.802	0.990	1.157
	Downstream peak Mach number, M					
17.70	0.240	0.400	0.580	0.755	0.945	1.120
25.40	.175	.310	.430	.570	.720	.915
38.10	.130	.240	.330	.430	.550	.690
50.80	.110	.200	.275	.360	.440	.540
134.62	.083	.140	.197	.251	.311	.374
254.00	.041	.080	.112	.145	.180	.218
Ratio of M_j to ideal, $M_j/M_{j,id}$	1.029	0.993	1.009	0.994	0.993	0.991
Ratio of nozzle mass flow rate to ideal, $W_n/W_{n,id}$	0.852	0.881	0.889	0.893	0.886	0.894

(tt) Configuration 99

Axial distance, X, cm	Conical afterbody	Nozzle-exit jet Mach number, M_j					
		0.270	0.450	0.630	0.805	0.987	1.152
		Downstream peak Mach number, M					
15.24	10^o	0.225	0.390	0.550	0.710	0.890	1.060
25.40	↓	.190	.320	.450	.580	.720	.900
38.10	↓	.170	.285	.390	.510	.630	.755
50.80	↓	.150	.270	.375	.480	.590	.700
201.30	↓	.093	.154	.216	.279	.349	.423
281.94	↓	.062	.106	.150	.196	.245	.296
50.80	None	.140	.260	.365	.475	.590	.695
Ratio of M_j to ideal, $M_j/M_{j,id}$		0.993	0.983	0.986	0.998	0.990	0.988
Ratio of nozzle mass flow rate to ideal, $W_n/W_{n,id}$		0.979	0.920	0.906	0.911	0.898	0.907

TABLE V. - Continued.

(uu) Configuration 100

Axial distance, X, cm	Survey across 0^{o} lobes					
	Nozzle-exit jet Mach number, M_j					
	0.265	0.450	0.625	0.798	0.980	1.145
	Downstream peak Mach number, M					
12.70	0.250	0.410	0.580	0.755	0.930	1.102
25.40	.175	.310	.440	.580	.740	.860
38.10	.140	.250	.350	.445	.560	.700
50.80	.125	.225	.330	.410	.510	.600
134.62	.107	.190	.267	.342	.420	.507
203.20	.080	.142	.198	.258	.319	.384
235.59	.072	.122	.174	.228	.280	.342
Ratio of M_j to ideal, $M_j/M_{j,id}$	0.978	0.985	0.980	0.991	0.985	0.984
Ratio of nozzle mass flow rate to ideal, $W_n/W_{n,id}$	0.916	0.908	0.901	0.898	0.904	0.905
Axial distance, X, cm	Survey across 5^{o} lobes					
	Nozzle-exit jet Mach number, M_j					
	0.265	0.450	0.630	0.805	0.989	1.150
	Downstream peak Mach number, M					
12.70	0.250	0.410	0.590	0.765	0.940	1.120
25.40	.180	.330	.470	.590	.730	.905
38.10	.150	.275	.370	.480	.580	.735
50.80	.125	.230	.335	.430	.515	.635
134.62	.109	.190	.267	.343	.424	.510
213.36	.079	.136	.193	.248	.306	.367
304.80	.050	.095	.139	.176	.219	.266
Ratio of M_j to ideal, $M_j/M_{j,id}$	0.978	0.987	0.989	1.001	0.995	0.989
Ratio of nozzle mass flow rate to ideal, $W_n/W_{n,id}$	0.949	0.889	0.901	0.892	0.903	0.903

TABLE V. - Continued.

(vv) Configuration 101

Axial distance, X, cm	Survey across 0^{o} lobes					
	Nozzle-exit jet Mach number, M_j					
	0.260	0.445	0.628	0.800	0.970	1.144
	Downstream peak Mach number, M					
12.70	0.235	0.400	0.570	0.750	0.918	1.102
25.40	.180	.320	.432	.565	.720	.850
38.10	.130	.220	.310	.420	.530	.640
50.80	.125	.210	.300	.380	.450	.545
142.24	.096	.165	.233	.298	.366	.444
198.12	.077	.135	.191	.244	.296	.358
281.94	.057	.098	.137	.177	.217	.261
Ratio of M_j to ideal, $M_j/M_{j,id}$	0.963	0.978	0.989	0.998	0.979	0.986
Ratio of nozzle mass flow rate to ideal, $W_n/W_{n,id}$	0.922	0.901	0.904	0.905	0.899	0.901
Axial distance, X, cm	Survey across 10^{o} lobes					
	Nozzle-exit jet Mach number, M_j					
	0.275	0.455	0.645	0.802	0.990	1.150
	Downstream peak Mach number, M					
12.70	0.260	0.425	0.600	0.770	0.948	1.127
25.40	.190	.335	.455	.595	.750	.955
38.10	.140	.250	.370	.455	.545	.730
50.80	.125	.220	.315	.390	.470	.590
139.70	.101	.172	.244	.310	.375	.454
203.20	.076	.125	.174	.222	.272	.326
269.24	.055	.098	.141	.176	.210	.255
Ratio of M_j to ideal, $M_j/M_{j,id}$	1.019	1.000	1.016	1.000	0.999	0.991
Ratio of nozzle mass flow rate to ideal, $W_n/W_{n,id}$	0.958	0.914	0.913	0.909	0.902	0.906

TABLE V. - Concluded.

(ww) Configuration 102

Axial distance, X, cm	Jet (fig. 100)	Survey across 0^{o} lobes					
		Nozzle-exit jet Mach number, M_j					
		0.250	0.445	0.620	0.800	0.980	1.150
		Downstream peak Mach number, M					
12.70	I	0.230	0.390	0.570	0.710	0.910	1.060
25.40	↓	.160	.280	.420	.540	.680	.810
38.10	↓	.130	.230	.320	.420	.510	.640
50.80	↓	.110	.200	.280	.350	.445	.525
12.70	II	.250	.430	.603	.760	.940	1.113
25.40	↓	.180	.330	.480	.620	.800	.953
38.10	↓	.150	.265	.365	.470	.605	.740
50.80	↓	.125	.220	.310	.400	.493	.592
Ratio of M_j to ideal, $M_j/M_{j,id}$		0.923	0.974	0.972	0.994	0.985	0.988
Ratio of nozzle mass flow rate to ideal, $W_n/W_{n,id}$		0.945	0.892	0.901	0.903	0.906	0.903
Axial distance, X, cm	Jet (fig. 100)	Survey across 10^{o} lobes					
		Nozzle-exit jet Mach number, M_j					
		0.275	0.450	0.630	0.800	0.984	1.140
		Downstream peak Mach number, M					
12.70	III	0.240	0.400	0.570	0.720	0.903	1.050
25.40	↓	.160	.300	.435	.575	.720	.848
38.10	↓	.120	.225	.325	.425	.515	.635
50.80	↓	.110	.180	.262	.340	.425	.500
12.70	IV	-----	-----	-----	-----	-----	-----
25.40	↓	.100	.150	.240	.270	.330	.380
38.10	↓	.100	.170	.240	.300	.370	.425
50.80	↓	.100	.170	.250	.310	.380	.445
Ratio of M_j to ideal, $M_j/M_{j,id}$		1.015	0.985	0.987	0.994	0.989	0.979
Ratio of nozzle mass flow rate to ideal, $W_n/W_{n,id}$		0.945	0.892	0.901	0.903	0.906	0.903

TABLE VI. - PEAK AXIAL JET MACH NUMBER DECAY DATA FOR MULTIELEMENT

BYPASS NOZZLES WITH NOMINALLY NONCOPLANAR EXITS

(a) Configuration 103; average bypass exit Mach number $M_{b,av} = M_j$

Axial distance from core exit, X, cm	Nozzle-exit jet Mach number, M_j					
	0.277	0.460	0.632	0.802	0.988	1.140
	Downstream peak Mach number, M					
6.35	0.250	0.410	0.578	0.741	0.940	1.080
12.70	.175	.290	.400	.510	.660	.770
19.05	.145	.240	.340	.455	.560	.680
25.40	.130	.220	.320	.420	.530	.630
31.75	.130	.225	.310	.390	.500	.600
38.10	.125	.220	.300	.380	.470	.580
50.80	.125	.200	.290	.370	.450	.545
106.68	.103	.178	.251	.327	.413	.496
203.20	.062	.108	.154	.200	.255	.311
Ratio of M_j to ideal, $M_j/M_{j,id}$	1.026	1.013	0.997	1.003	0.998	0.984
Ratio of nozzle mass flow rate to ideal, $W_n/W_{n,id}$	0.856	0.869	0.897	0.924	0.948	0.964

(b) Configuration 104

Axial distance from core exit, X, cm	Nozzle-exit jet Mach number, M_j					
	0.260	0.450	0.630	0.800	0.990	1.150
	Average bypass exit Mach number, $M_{b,av}$					
	0.190	0.300	0.400	0.510	0.650	0.800
	Downstream peak Mach number, M					
6.35	0.250	0.430	0.610	0.785	0.975	1.138
12.70	.175	.310	.450	.590	.753	.905
19.05	.130	.250	.350	.455	.580	.706
25.40	.125	.210	.304	.390	.500	.610
31.75	.120	.190	.275	.355	.453	.557
38.10	.120	.190	.270	.345	.425	.525
50.80	.100	.175	.250	.325	.395	.490
106.68	.084	.144	.203	.260	.332	.406
152.40	.062	.108	.154	.197	.252	.311
215.90	.046	.079	.114	.145	.186	.229
Ratio of M_j to ideal, $M_j/M_{j,id}$	0.963	0.989	0.992	0.999	1.000	0.992
Ratio of nozzle mass flow rate to ideal, $W_n/W_{n,id}$	0.631	0.640	0.650	0.651	0.657	0.663

TABLE VI. - Continued.

(c) Configuration 105; average bypass exit Mach number, $M_{b,av} = M_j$

Axial distance, from core exit, X, cm	Nozzle-exit jet Mach number, M_j					
	0.275	0.460	0.635	0.800	0.990	1.158
	Downstream peak Mach number, M					
6.35	0.250	0.430	0.610	0.782	0.977	1.135
12.70	.175	.335	.490	.685	.879	1.045
19.05	.140	.260	.390	.540	.705	.870
25.40	.130	.225	.330	.430	.540	.720
38.10	.110	.185	.275	.350	.450	.550
50.80	.090	.160	.220	.310	.380	.460
101.60	.090	.160	.220	.290	.370	.440
152.40	.070	.120	.170	.230	.290	.360
213.36	.050	.090	.130	.170	.210	.260
Ratio of M_j to ideal, $M_j/M_{j,id}$	1.019	1.011	1.000	0.998	0.999	0.998
Ratio of nozzle mass flow rate to ideal, $W_n/W_{n,id}$	0.662	0.695	0.730	0.772	0.823	0.870

(d) Configuration 106; average bypass exit Mach number, $M_{b,av} = M_j$

Axial distance from core exit, X, cm	Nozzle-exit jet Mach number, M_j					
	0.250	0.435	0.628	0.793	0.987	1.138
	Downstream peak Mach number, M					
12.70	0.230	0.420	0.580	0.745	0.926	1.040
25.40	.160	.300	.420	.530	.660	.780
38.10	.135	.250	.360	.470	.580	.694
50.80	.130	.250	.355	.450	.560	.670
127.00	.099	.174	.248	.322	.412	.504
223.52	.056	.103	.149	.195	.246	.301
Ratio of M_j to ideal, $M_j/M_{j,id}$	0.926	0.956	0.987	0.989	0.995	0.980
Ratio of nozzle mass flow rate to ideal, $W_n/W_{n,id}$	0.840	0.871	0.897	0.923	0.939	0.953

TABLE VI. - Continued.

(e) Configuration 107

Axial distance from core exit, X, cm	Nozzle-exit jet Mach number, M_j					
	0.270	0.440	0.625	0.802	0.989	1.142
	Average bypass exit Mach number, $M_{b,av}$					
	0.200	0.320	0.440	0.570	0.710	0.850
	Downstream peak Mach number, M					
12.70	0.250	0.430	0.610	0.775	0.955	1.053
25.40	.180	.310	.430	.560	.700	.800
38.10	.150	.255	.360	.460	.575	.700
50.80	.150	.250	.350	.430	.530	.630
101.60	.106	.182	.256	.332	.420	.510
152.40	.071	.126	.180	.232	.290	.355
223.52	.048	.086	.121	.158	.196	.239
Ratio of M_j to ideal, $M_j/M_{j,id}$	1.000	0.967	0.984	1.000	0.998	0.984
Ratio of nozzle mass flow rate to ideal, $W_n/W_{n,id}$	0.650	0.658	0.660	0.660	0.654	0.662

(f) Configuration 108; average bypass exit Mach number, $M_{b,av} = M_j$

Axial distance from core exit, X, cm	Peak Mach number determined by -	Nozzle-exit jet Mach number, M_j					
		0.260	0.440	0.625	0.795	0.980	1.150
		Downstream peak Mach number, M					
6.35	Jets from tubes	0.250	0.410	0.580	0.735	0.885	1.020
6.35	Jets from tubes	.260	.440	.605	.763	.930	1.070
12.70	Jets from tubes	.200	.320	.450	.570	.700	.830
12.70	Merged jets at nozzle centerline	.175	.300	.430	.560	.725	.870
19.05	↓	.175	.300	.420	.545	.700	.843
25.40	↓	.170	.285	.410	.530	.680	.818
31.75	↓	.150	.270	.390	.510	.660	.800
38.10	↓	.150	.270	.380	.500	.640	.780
50.80	↓	.130	.240	.350	.460	.600	.720
101.60	↓	.090	.160	.230	.300	.380	.480
152.40	↓	.060	.110	.160	.210	.260	.320
213.36	↓	.050	.080	.120	.150	.200	.240
Ratio of M_j to ideal, $M_j/M_{j,id}$		0.959	0.965	0.983	0.990	0.987	0.990
Ratio of nozzle mass flow rate to ideal, $W_n/W_{n,id}$		0.729	0.721	0.818	0.781	0.821	0.859

TABLE VI. - Continued.

(g) Configuration 109

Axial distance from core exit, X, cm	Peak Mach number determined by -	Nozzle-exit jet Mach number, M_j					
		0.275	0.460	0.634	0.805	0.990	1.150
		Average bypass exit Mach number, $M_{b,av}$					
		0.280	0.455	0.630	0.800	0.987	1.120
		Downstream peak Mach number, M					
6.35	Jets from tubes	0.250	0.425	0.600	0.755	0.940	1.087
12.70	Jets from tubes	.200	.330	.470	.596	.772	.915
19.05	Merged jets at nozzle centerline	.200	.330	.470	.595	.735	.870
25.40	↓	.200	.330	.468	.593	.740	.870
38.10	↓	.190	.325	.460	.585	.725	.855
50.80	↓	.175	.310	.440	.560	.700	.825
127.00	↓	.088	.149	.214	.280	.359	.430
213.36	↓	.058	.101	.145	.189	.242	.291
Ratio of M_j to ideal, $M_j/M_{j,id}$		1.019	1.011	0.998	1.004	0.998	0.991
Ratio of nozzle mass flow rate to ideal, $W_n/W_{n,id}$		0.770	0.761	0.791	0.805	0.835	0.865

(h) Configuration 110

Axial distance from core exit, X, cm	Nozzle-exit jet Mach number, M_j					
	0.260	0.430	0.620	0.800	0.985	1.150
	Average bypass exit Mach number, $M_{b,av}$					
	0.22	0.33	0.44	0.55	0.66	0.77
	Downstream peak Mach number, M					
6.35	0.250	0.430	0.613	0.782	0.973	1.135
12.70	.175	.320	.450	.592	.750	.898
19.05	.125	.230	.340	.470	.590	.730
25.40	.125	.210	.285	.380	.490	.600
31.75	.110	.190	.270	.340	.430	.515
38.10	.100	.175	.250	.320	.400	.475
50.80	.100	.160	.230	.310	.380	.450
101.60	.070	.110	.160	.210	.270	.310
142.24	.050	.080	.120	.150	.190	.230
203.20	.030	.050	.080	.110	.130	.160
Ratio of M_j to ideal, $M_j/M_{j,id}$	0.963	0.945	0.976	0.998	0.994	0.991
Ratio of nozzle mass flow rate to ideal, $W_n/W_{n,id}$	0.535	0.544	0.542	0.549	0.552	0.606

TABLE VI. - Continued.

(i) Configuration 111

Axial distance from core exit, X, cm	Nozzle-exit jet Mach number, M_j					
	0.270	0.451	0.630	0.802	0.989	1.153
	Average bypass exit Mach number, $M_{b,av}$					
	0.180	0.300	0.400	0.500	0.600	0.700
	Downstream peak Mach number, M					
6.35	0.275	0.450	0.610	0.780	0.960	1.132
12.70	.180	.310	.440	.560	.705	.875
19.05	.150	.250	.350	.440	.567	.690
25.40	.125	.225	.306	.390	.490	.600
38.10	.130	.220	.300	.370	.452	.536
50.80	.120	.200	.285	.360	.440	.521
127.00	.070	.120	.166	.213	.263	.317
210.82	.044	.074	.103	.130	.162	.195
Ratio of M_j to ideal, $M_j/M_{j,id}$	0.996	0.989	0.989	0.998	0.995	0.991
Ratio of nozzle mass flow rate to ideal, $W_n/W_{n,id}$	0.589	0.566	0.551	0.551	0.555	0.558

(j) Configuration 112; average bypass exit Mach number, $M_{b,av} = M_j$

Axial distance from core exit, X, cm	Nozzle-exit jet Mach number, M_j					
	0.265	0.455	0.630	0.800	0.975	1.135
	Downstream peak Mach number, M					
12.70	0.240	0.420	0.595	0.765	0.905	1.052
25.40	.175	.310	.430	.570	.720	.870
38.10	.150	.275	.380	.500	.640	.790
50.80	.130	.220	.320	.420	.570	.690
114.30	.067	.121	.178	.237	.319	.359
152.40	.048	.090	.133	.178	.241	.278
218.44	.034	.061	.096	.127	.171	.199
Ratio of M_j to ideal, $M_j/M_{j,id}$	0.981	1.000	0.992	0.999	0.984	0.978
Ratio of nozzle mass flow rate to ideal, $W_n/W_{n,id}$	0.718	0.720	0.745	0.774	0.809	0.844

TABLE VI. - Continued.

(k) Configuration 113

Axial distance from core exit, X, cm	Nozzle-exit jet Mach number, M_j					
	0.300	0.460	0.640	0.805	0.990	1.140
	Average bypass exit Mach number, $M_{b,av}$					
	0.200	0.330	0.440	0.540	0.600	0.730
	Downstream peak Mach number, M					
12.70	0.270	0.445	0.618	0.785	0.937	1.088
25.40	.175	.304	.422	.550	.685	.852
38.10	.140	.240	.350	.445	.560	.660
50.80	.125	.210	.300	.390	.500	.595
101.60	.067	.111	.158	.209	.269	.344
152.40	.041	.069	.100	.134	.172	.230
223.52	.026	.046	.068	.090	.118	.158
Ratio of M_j to ideal, $M_j/M_{j,id}$	1.111	1.011	1.008	1.004	0.998	0.983
Ratio of nozzle mass flow rate to ideal, $W_n/W_{n,id}$	0.588	0.560	0.564	0.565	0.565	0.565

(*l*) Configuration 114

Axial distance from core exit, X, cm	Nozzle-exit jet Mach number, M_j				
	0.455	0.630	0.800	0.988	1.150
	Average bypass exit Mach number, $M_{b,av}$				
	0.290	0.380	0.475	0.610	0.770
	Downstream peak Mach number, M				
12.70	0.445	0.628	0.795	0.983	1.145
25.40	.385	.560	.720	.920	1.103
38.10	.330	.475	.615	.805	.998
50.80	.275	.410	.525	.690	.890
76.20	.200	.290	.380	.505	.650
101.60	.140	.200	.280	.370	.480
152.40	.100	.150	.200	.250	.300
Ratio of M_j to ideal, $M_j/M_{j,id}$	0.993	0.984	0.991	0.991	0.985
Ratio of nozzle mass flow rate to ideal, $W_n/W_{n,id}$	-----	-----	-----	-----	-----

TABLE VI. - Continued.

(m) Configuration 115

Axial distance from core exit, X, cm	Nozzle-exit jet Mach number, M_j				
	0.455	0.630	0.800	0.984	1.152
	Average bypass exit Mach number, $M_{b,av}$				
	0.320	0.420	0.530	0.663	0.850
	Downstream peak Mach number, M				
12.70	0.448	0.625	0.793	0.984	1.145
25.40	.390	.565	.730	.930	1.098
38.10	.340	.485	.630	.842	1.020
45.72	.320	.450	.590	.795	.970
50.80	.290	.425	.550	.760	.930
76.20	.225	.325	.420	.575	.705
101.60	.170	.250	.320	.450	.540
152.40	.120	.160	.220	.280	.350
Ratio of M_j to ideal, $M_j/M_{j,id}$	1.000	0.991	0.998	0.992	0.992
Ratio of nozzle mass flow rate to ideal, $W_n/W_{n,id}$	-----	-----	-----	-----	-----

(n) Configuration 116

Axial distance from core exit, X, cm	Nozzle-exit jet Mach number, M_j			
	0.458	0.633	0.800	0.985
	Average bypass exit Mach number, $M_{b,av}$			
	0.350	0.490	0.620	0.773
	Downstream peak Mach number, M			
12.70	0.445	0.620	0.795	0.981
25.40	.390	.555	.715	.910
38.10	.355	.505	.665	.855
45.72	.335	.475	.630	.825
50.80	.320	.460	.605	.800
76.20	.250	.350	.470	.630
101.60	.190	.270	.365	.500
152.40	.130	.175	.240	.310
Ratio of M_j to ideal, $M_j/M_{j,id}$	1.002	0.992	0.994	0.990
Ratio of nozzle mass flow rate to ideal, $W_n/W_{n,id}$	-----	-----	-----	-----

TABLE VI. - Continued.

(o) Configuration 117

Axial distance from core exit, X, cm	Nozzle-exit jet Mach number, M_j			
	0.450	0.630	0.800	0.983
	Average bypass exit Mach number, $M_{b,av}$			
	0.440	0.616	0.783	0.972
	Downstream peak Mach number, M			
12.70	0.440	0.617	0.790	0.975
25.40	.425	.600	.765	.965
38.10	.415	.590	.760	.955
45.72	.405	.580	.750	.935
50.80	.385	.550	.730	.920
76.20	.300	.440	.580	.775
101.60	.230	.330	.445	.565
152.40	.150	.225	.300	.380
Ratio of M_j to ideal, $M_j/M_{j,id}$	0.983	0.986	0.993	0.987
Ratio of nozzle mass flow rate to ideal, $W_n/W_{n,id}$	-----	-----	-----	-----

(p) Configuration 118

Axial distance from core exit, X, cm	Nozzle-exit jet Mach number, M_j				
	0.467	0.640	0.805	0.995	1.160
	Average bypass exit Mach number, $M_{b,av}$				
	0.240	0.315	0.385	0.470	0.565
	Downstream peak Mach number, M				
12.70	0.467	0.639	0.804	0.995	1.151
25.40	.450	.625	.790	.986	1.149
38.10	.387	.550	.710	.903	1.085
50.80	.318	.455	.590	.765	.930
63.50	.257	.380	.495	.640	.780
76.20	.220	.325	.420	.545	.655
101.60	.155	.240	.320	.418	.508
Ratio of M_j to ideal, $M_j/M_{j,id}$	1.024	1.005	1.001	1.001	0.995
Ratio of nozzle mass flow rate to ideal, $W_n/W_{n,id}$	-----	-----	-----	-----	-----

TABLE VI. - Continued.

(q) Configuration 119

Axial distance from core exit, X, cm	Nozzle-exit jet Mach number, M_j				
	0.467	0.645	0.812	1.000	1.160
	Average bypass exit Mach number, $M_{b,av}$				
	0.340	0.460	0.570	0.700	0.910
	Downstream peak Mach number, M				
12.70	0.467	0.643	0.810	1.000	1.160
25.40	.450	.625	.795	.988	1.149
38.10	.400	.560	.722	.918	1.066
50.80	.330	.470	.613	.782	.918
63.50	.275	.400	.518	.665	.772
76.20	.235	.340	.450	.575	.670
101.60	.190	.270	.350	.450	.515
127.00	.145	.220	.290	.375	.425
Ratio of M_j to ideal, $M_j/M_{j,id}$	0.124	1.013	1.010	1.006	0.997
Ratio of nozzle mass flow rate to ideal, $W_n/W_{n,id}$	-----	-----	-----	-----	-----

(r) Configuration 120

Axial distance from core exit, X, cm	Nozzle-exit jet Mach number, M_j			
	0.475	0.652	0.822	1.010
	Average bypass exit Mach number, $M_{b,av}$			
	0.470	0.649	0.815	1.008
	Downstream peak Mach number, M			
12.70	0.470	0.650	0.820	1.008
25.40	.450	.630	.800	.995
38.10	.418	.580	.740	.945
50.80	.368	.510	.659	.849
63.50	.318	.450	.580	.745
76.20	.275	.395	.500	.645
101.60	.225	.320	.410	.515
127.00	.195	.265	.335	.425
Ratio of M_j to ideal, $M_j/M_{j,id}$	1.042	1.024	1.022	1.016
Ratio of nozzle mass flow rate to ideal, $W_n/W_{n,id}$	-----	-----	-----	-----

TABLE VI. - Continued.

(s) Configuration 121

Axial distance from core exit, X, cm	Nozzle-exit jet Mach number, M_j				
	0.450	0.580	0.800	0.990	1.151
	Average bypass exit Mach number, $M_{b,av}$				
	0.205	0.255	0.370	0.440	0.575
	Downstream peak Mach number, M				
12.70	0.450	0.570	0.800	0.988	1.151
25.40	.430	.570	.795	.987	1.150
38.10	.440	.570	.795	.988	1.151
50.80	.405	.535	.770	.969	1.145
63.50	.360	.480	.700	.905	1.095
76.20	.320	.420	.630	.805	1.010
101.60	.240	.325	.470	.620	.785
127.00	.200	.260	.370	.495	.620
177.80	.125	.175	.250	.320	.415
228.60	.090	.125	.175	.240	.300
Ratio of M_j to ideal, $M_j/M_{j,id}$	0.991	1.000	0.999	1.000	0.993
Ratio of nozzle mass flow rate to ideal. $W_n/W_{n,id}$	0.593	0.538	0.566	0.543	0.541

(t) Configuration 122

Axial distance from core exit, X. cm	Nozzle-exit jet Mach number, M_j				
	0.450	0.578	0.803	0.990	1.155
	Average bypass exit Mach number, $M_{b,av}$				
	0.310	0.390	0.542	0.671	0.839
	Downstream peak Mach number, M				
12.70	0.440	0.572	0.803	0.990	1.150
25.40	.450	.572	.800	.990	1.152
38.10	.435	.570	.800	.990	1.140
50.80	.420	.545	.765	.975	1.100
63.50	.380	.500	.715	.915	1.010
76.20	.340	.440	.640	.825	.885
101.60	.265	.350	.500	.650	.705
127.00	.220	.275	.400	.530	.585
177.80	.140	.200	.290	.375	.415
228.60	.120	.150	.220	.275	.320
Ratio of M_j to ideal, $M_j/M_{j,id}$	0.989	0.997	1.002	0.999	0.996
Ratio of nozzle mass flow rate to ideal. $W_n/W_{n,id}$	0.661	0.704	0.696	0.706	0.704

TABLE VI. - Concluded.

(u) Configuration 123

Axial distance from core exit, X, cm	Nozzle-exit jet Mach number, M_j			
	0.450	0.575	0.800	0.986
	Average bypass exit Mach number, $M_{b,av}$			
	0.445	0.572	0.798	0.985
	Downstream peak Mach number, M			
12.70	0.450	0.575	0.800	0.983
25.40	.450	.575	.795	.983
38.10	.440	.565	.790	.980
50.80	.425	.540	.765	.955
63.50	.390	.505	.715	.910
76.20	.360	.450	.650	.835
101.60	.290	.375	.530	.680
127.00	.240	.310	.440	.560
177.80	.160	.220	.310	.400
228.60	.125	.160	.230	.320
Ratio of M_j to ideal, $M_j/M_{j,id}$	0.989	0.990	0.998	0.994
Ratio of nozzle mass flow rate to ideal, $W_n/W_{n,id}$	0.928	0.950	0.955	0.962

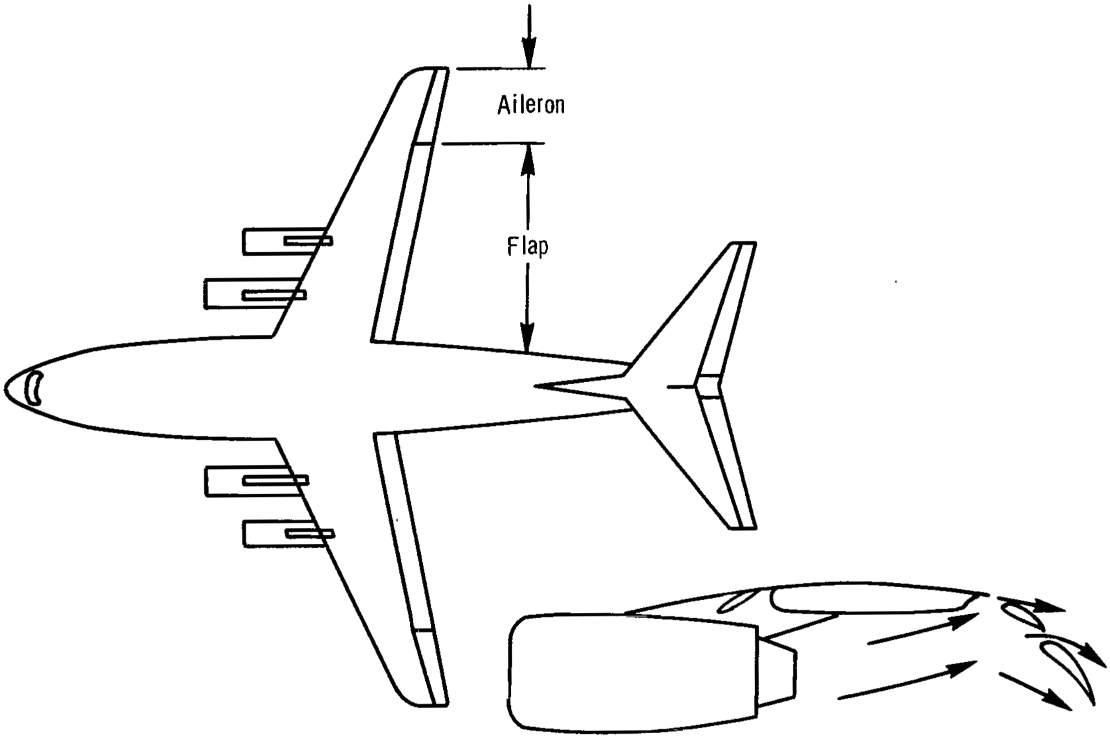

Figure 1. - Externally blown flap, short-takeoff-and-landing (STOL) airplane.

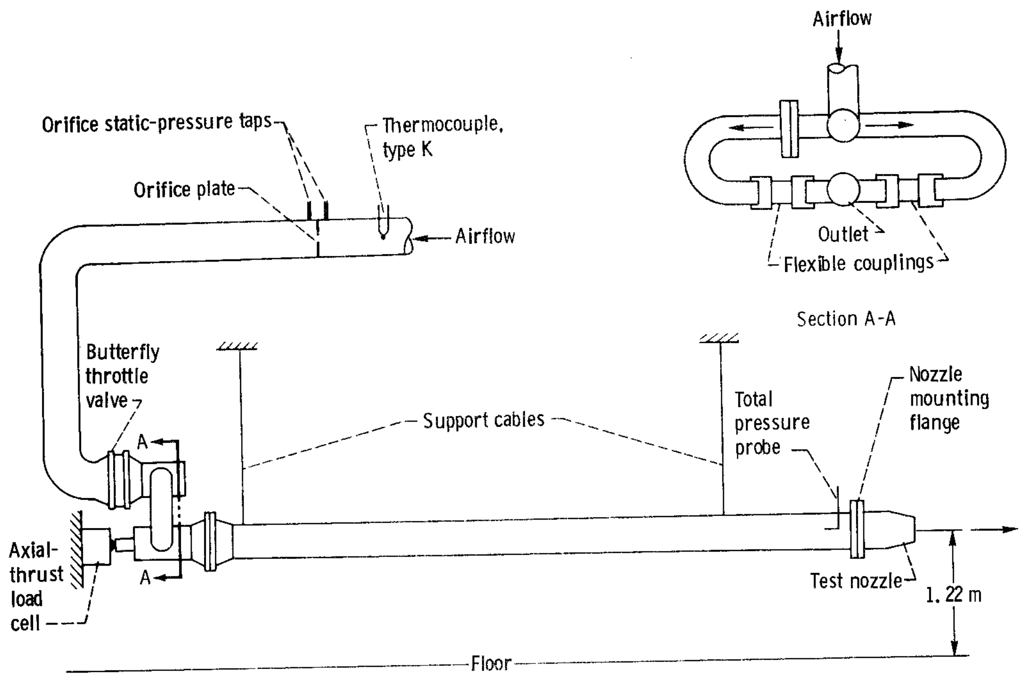

(a) Flow system.

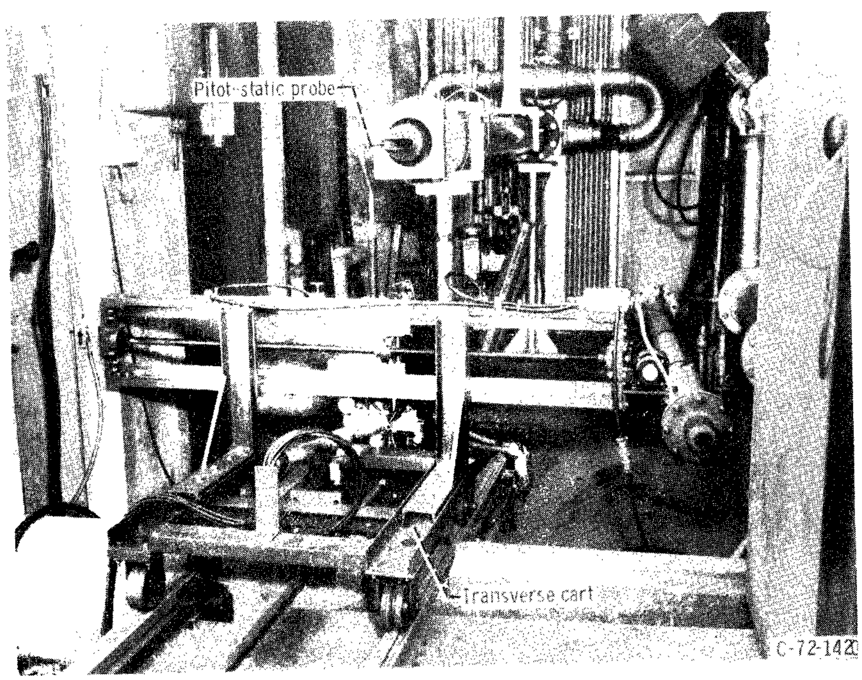

(b) Configuration 117 installed on air supply line.

Figure 2. - Nozzle test facility.

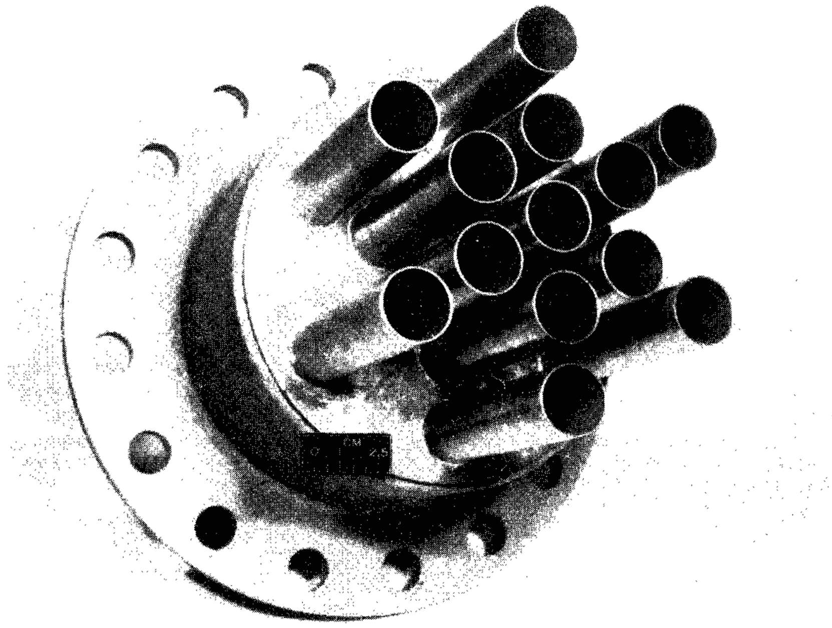

C-71-1405

(a) Radially symmetric multitube (1-6-6) nozzle, configuration 61.

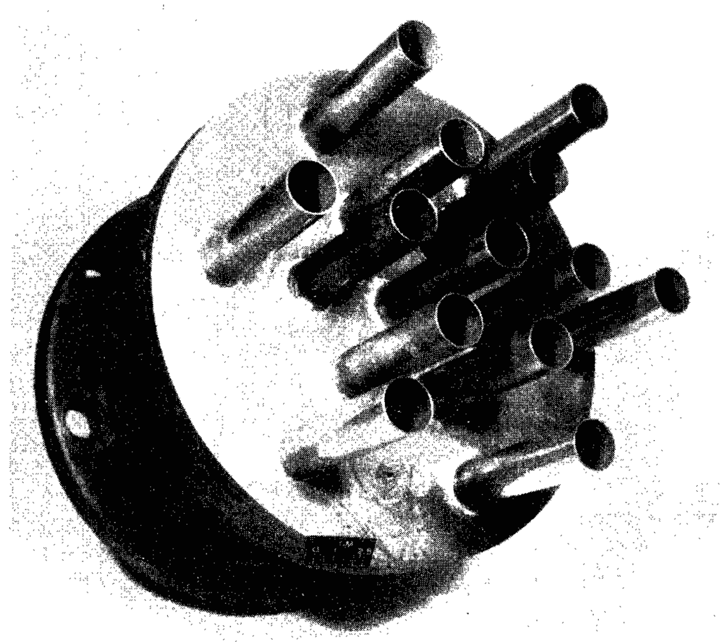

C-71-1403

(b) Radially symmetric multitube (1-6-6) nozzle, configuration 63.

Figure 3. - Multielement nozzles.

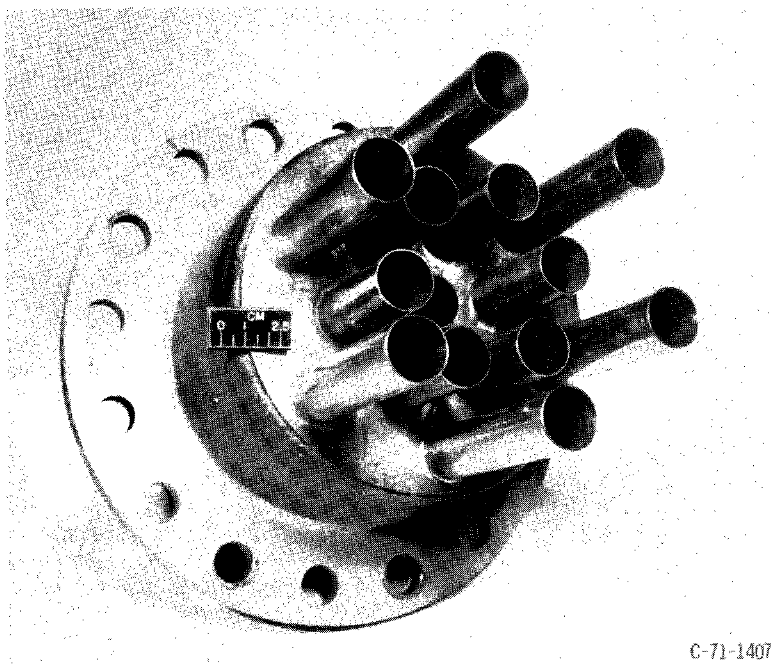

(c) Radially nonsymmetric multitube (1-6-6) nozzle, configuration 67.

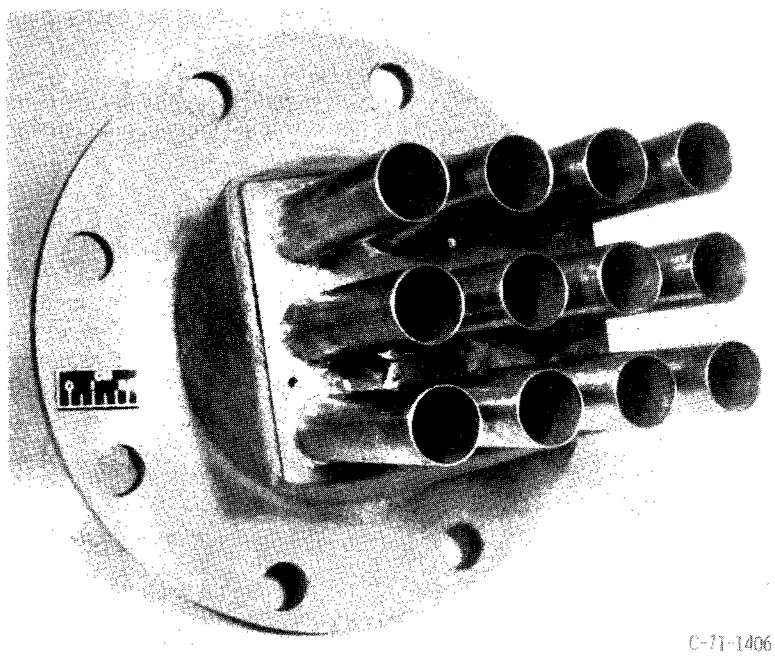

(d) Rectangular-array multitube nozzle, configuration 69.

Figure 3. - Continued.

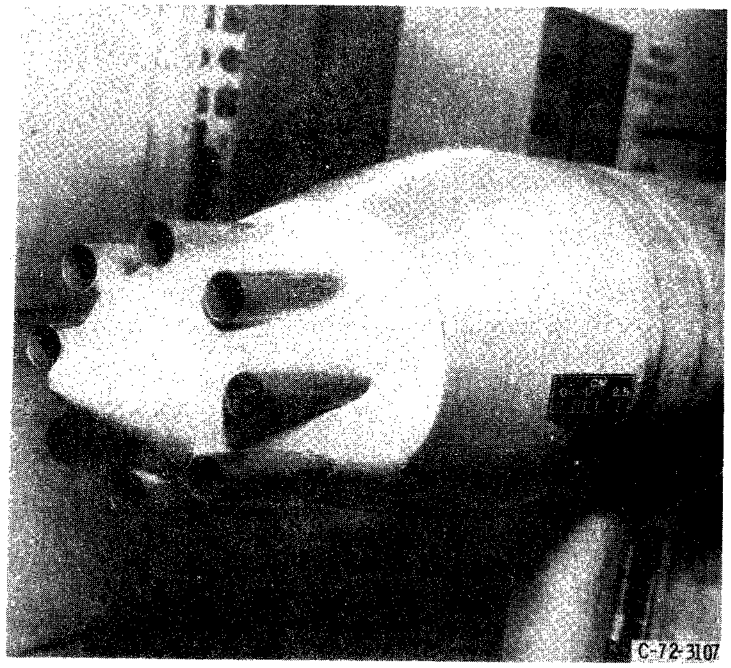

(e) Multitube (0-8-0) nozzle with centerbody, configuration 49.

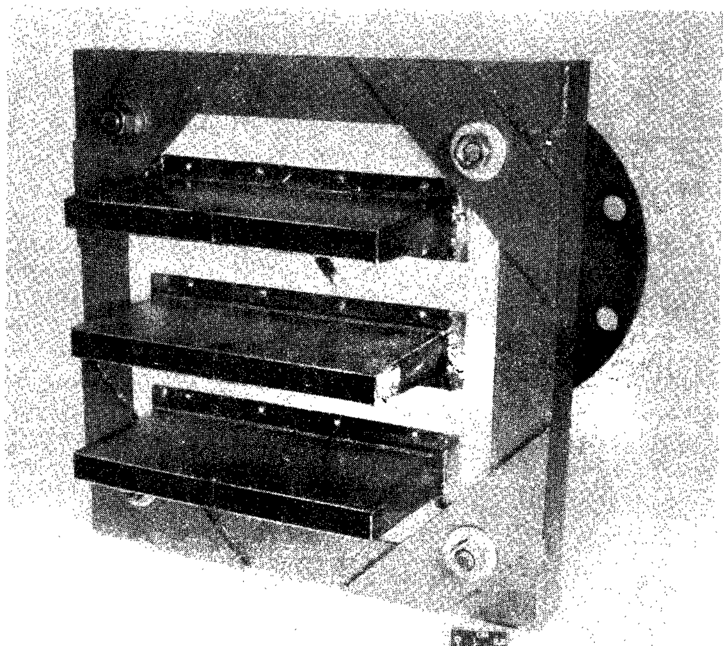

(f) Three-slot rectangular nozzle, configuration 73.

Figure 3. - Continued.

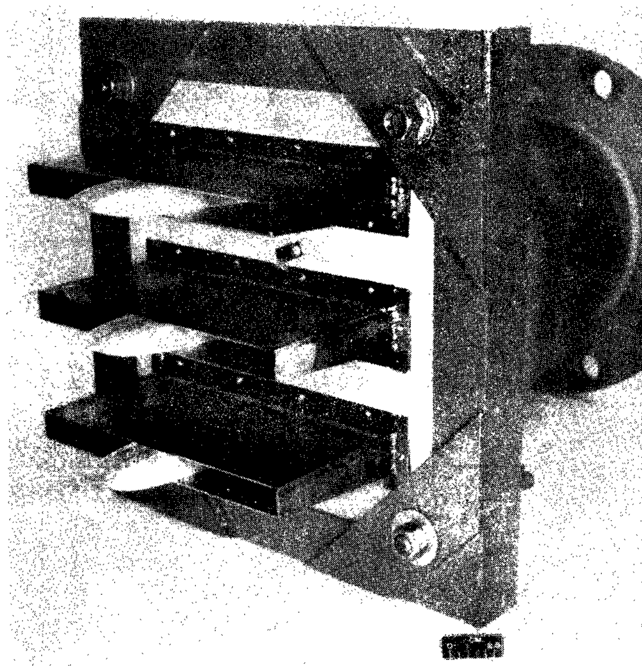

C-72-598

(g) Six-slot split-element nozzle, configuration 89.

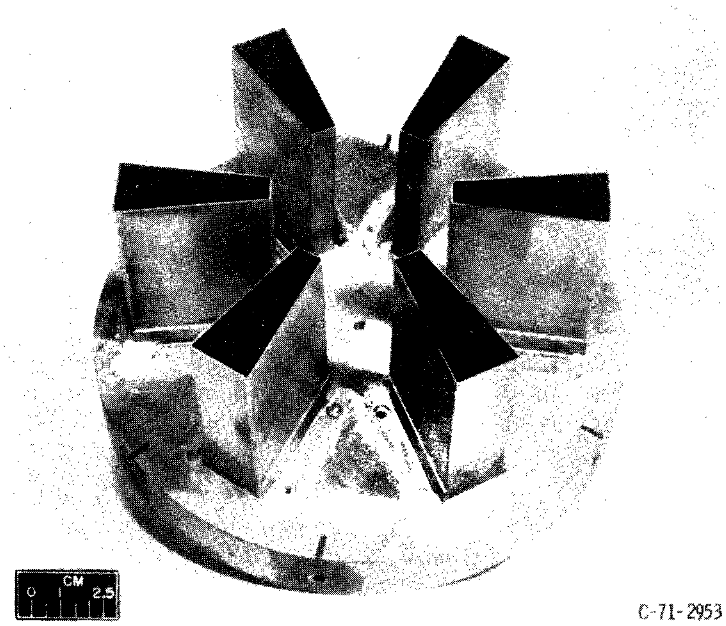

C-71-2953

(h) Flat-end trapezoidal nozzle, configuration 94.

Figure 3. - Continued.

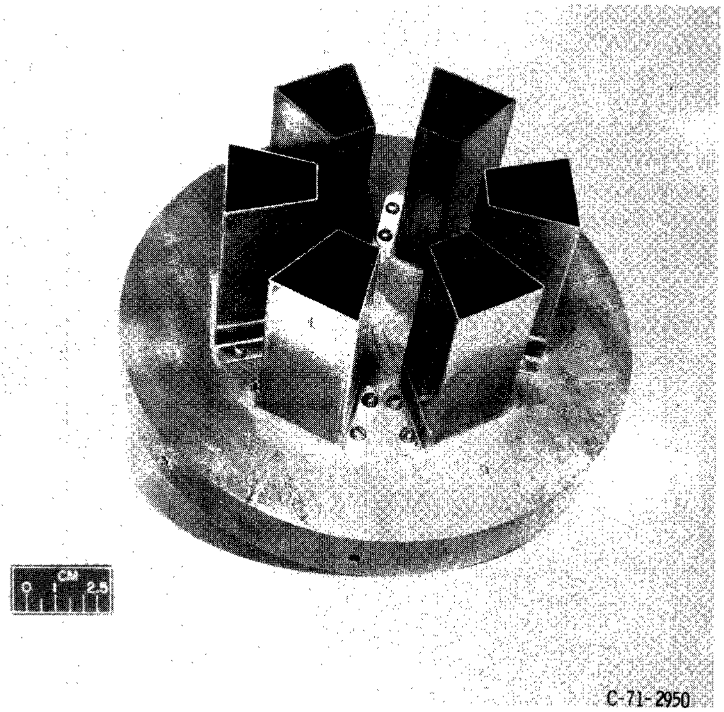

(i) Flat-end trapezoidal nozzle, configuration 95.

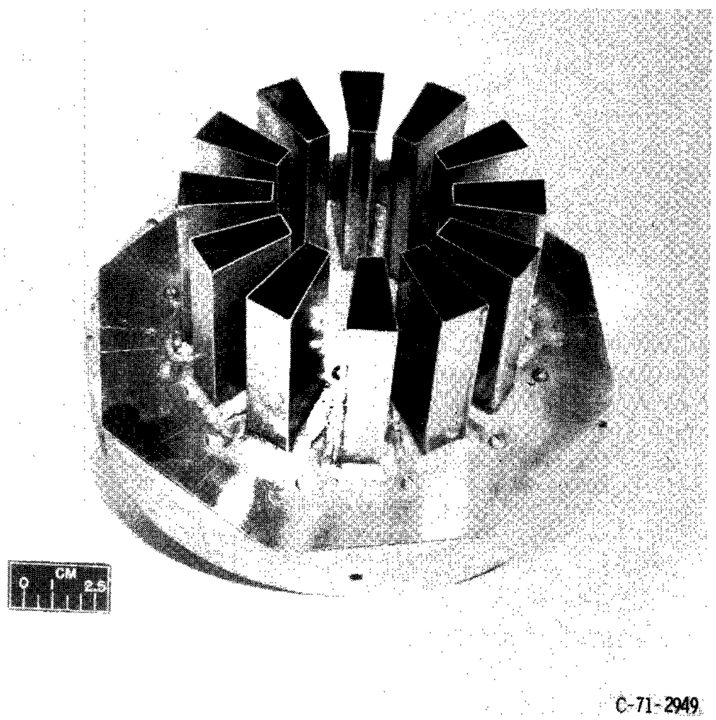

(j) Flat-end trapezoidal nozzle, configuration 96.

Figure 3. - Continued.

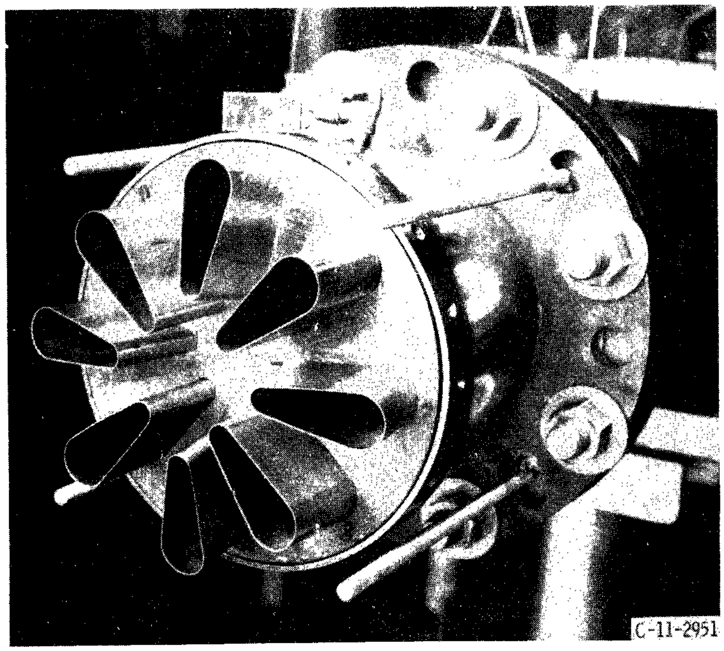

(k) Round-end trapezoidal nozzle with alternate lobes canted 10^0 outward from nozzle centerline, configuration 101.

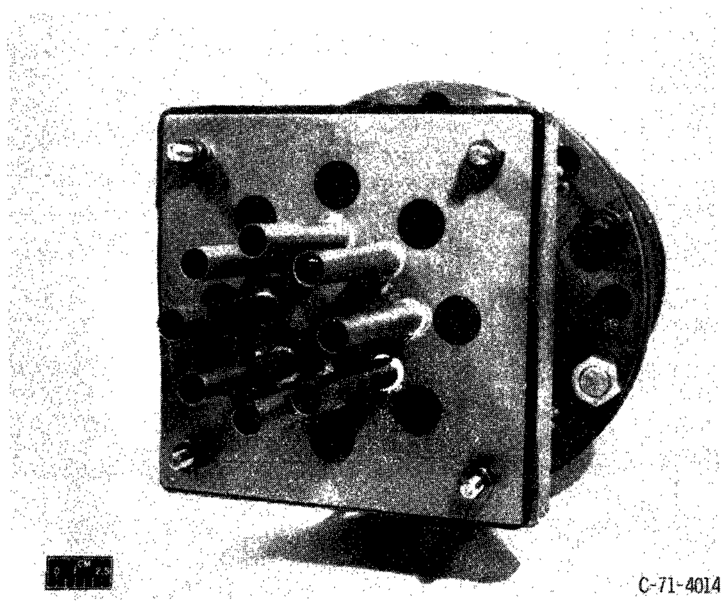

(l) Bypass nozzle with eight core tubes and eight secondary-flow orifices, configuration 103.

Figure 3. - Continued.

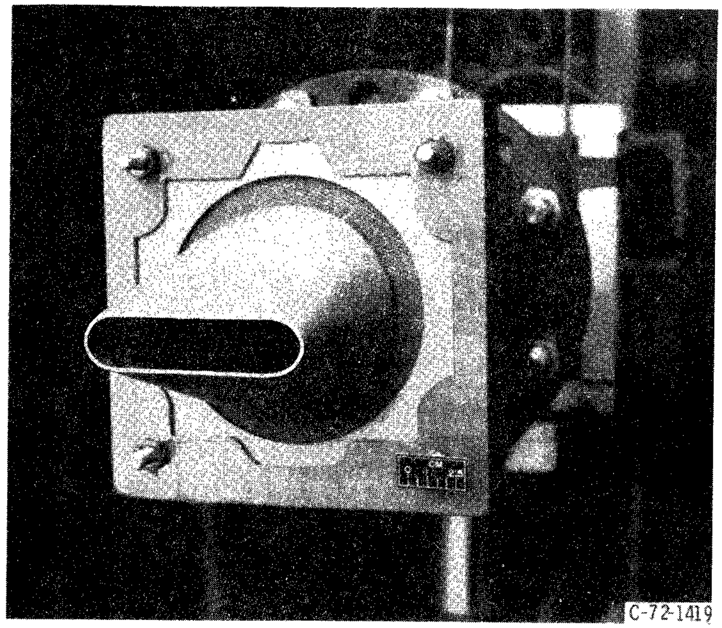

(m) Bypass nozzle with round-end slot core and screened annular secondary, configuration 116.

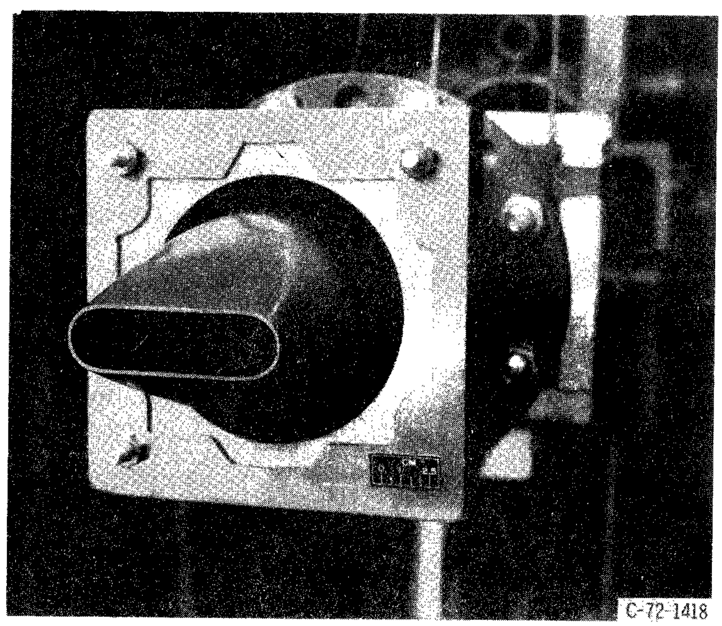

(n) Bypass nozzle with round-end slot core and annular secondary, configuration 117.

Figure 3. - Continued.

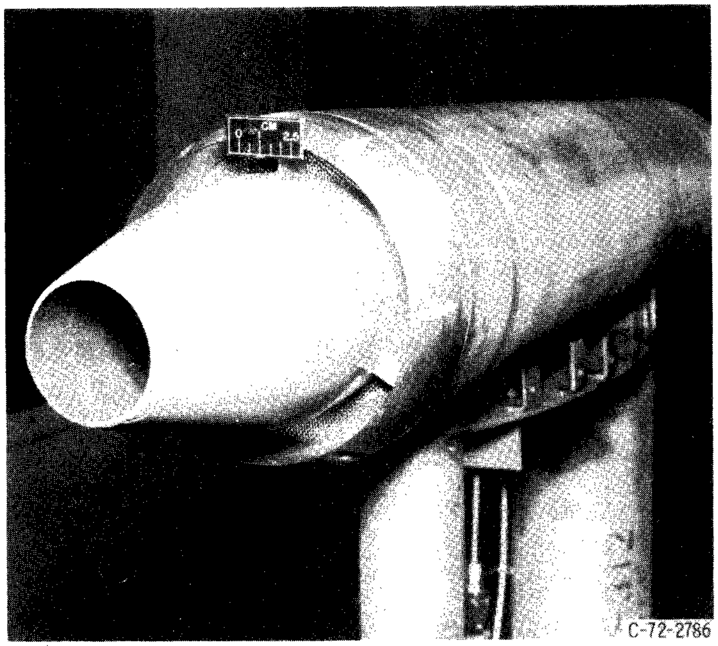

(o) Bypass nozzle with circular convergent core and screened annular secondary, configuration 121.

Figure 3. - Concluded.

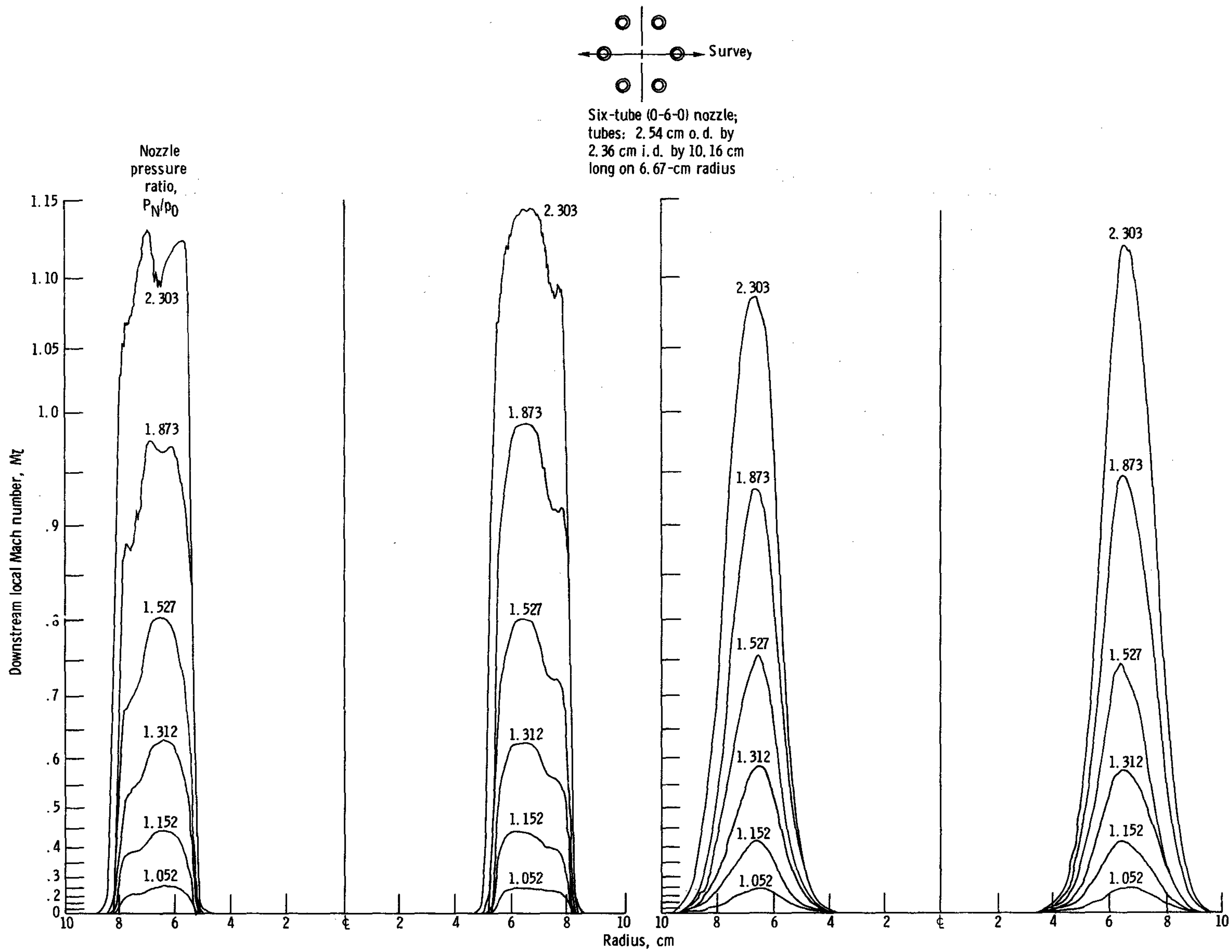

(a) Survey at 0.32 centimeter downstream of tube exits ($M_l = M_j$).

(b) Survey at 12.7 centimeters downstream of tube exits.

Figure 4. - Jet total pressure profiles converted to Mach numbers for various nozzle pressure ratios. Configuration 45.

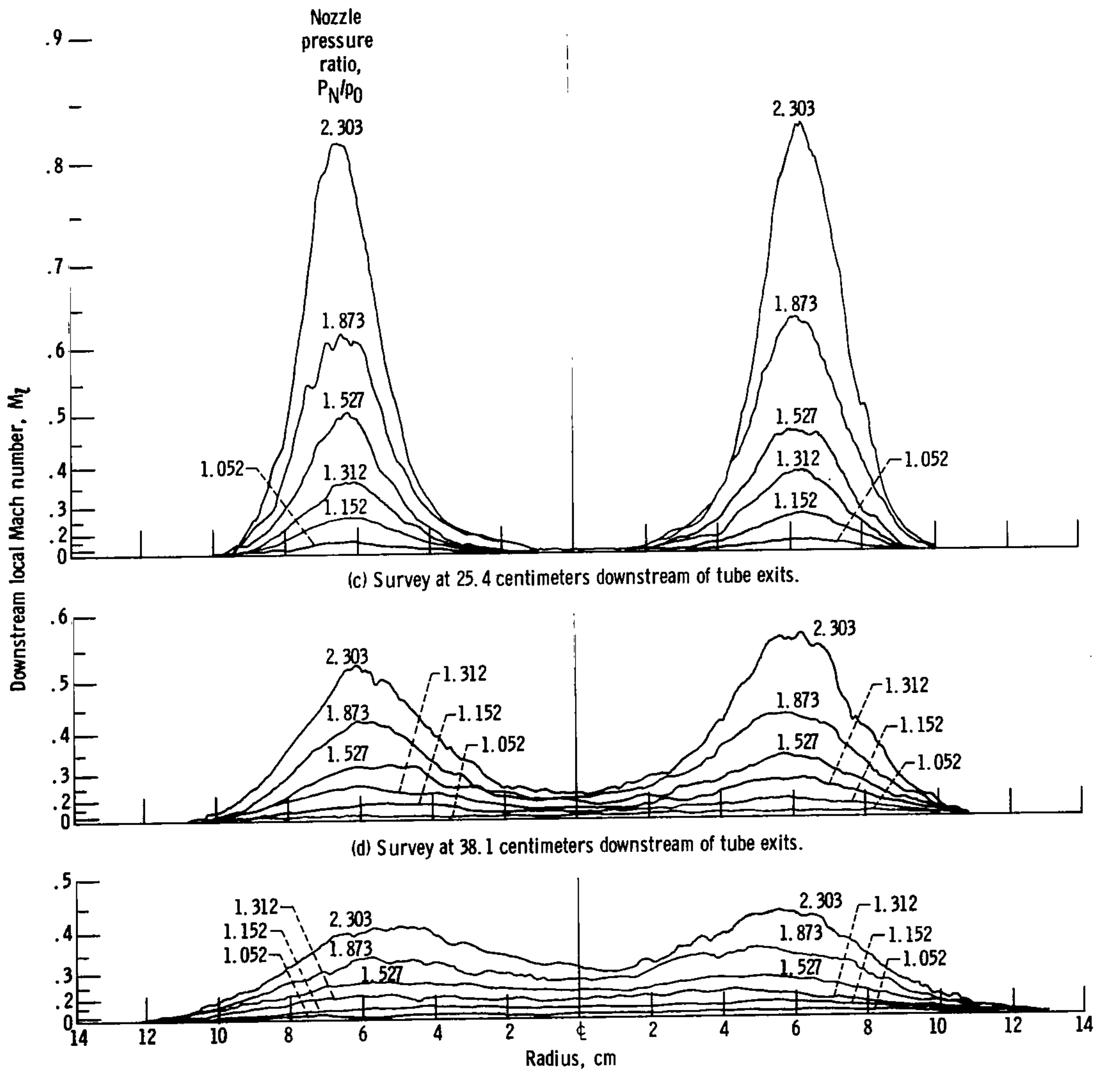

(c) Survey at 25.4 centimeters downstream of tube exits.

(d) Survey at 38.1 centimeters downstream of tube exits.

(e) Survey at 50.8 centimeters downstream of tube exits.

Figure 4. - Concluded.

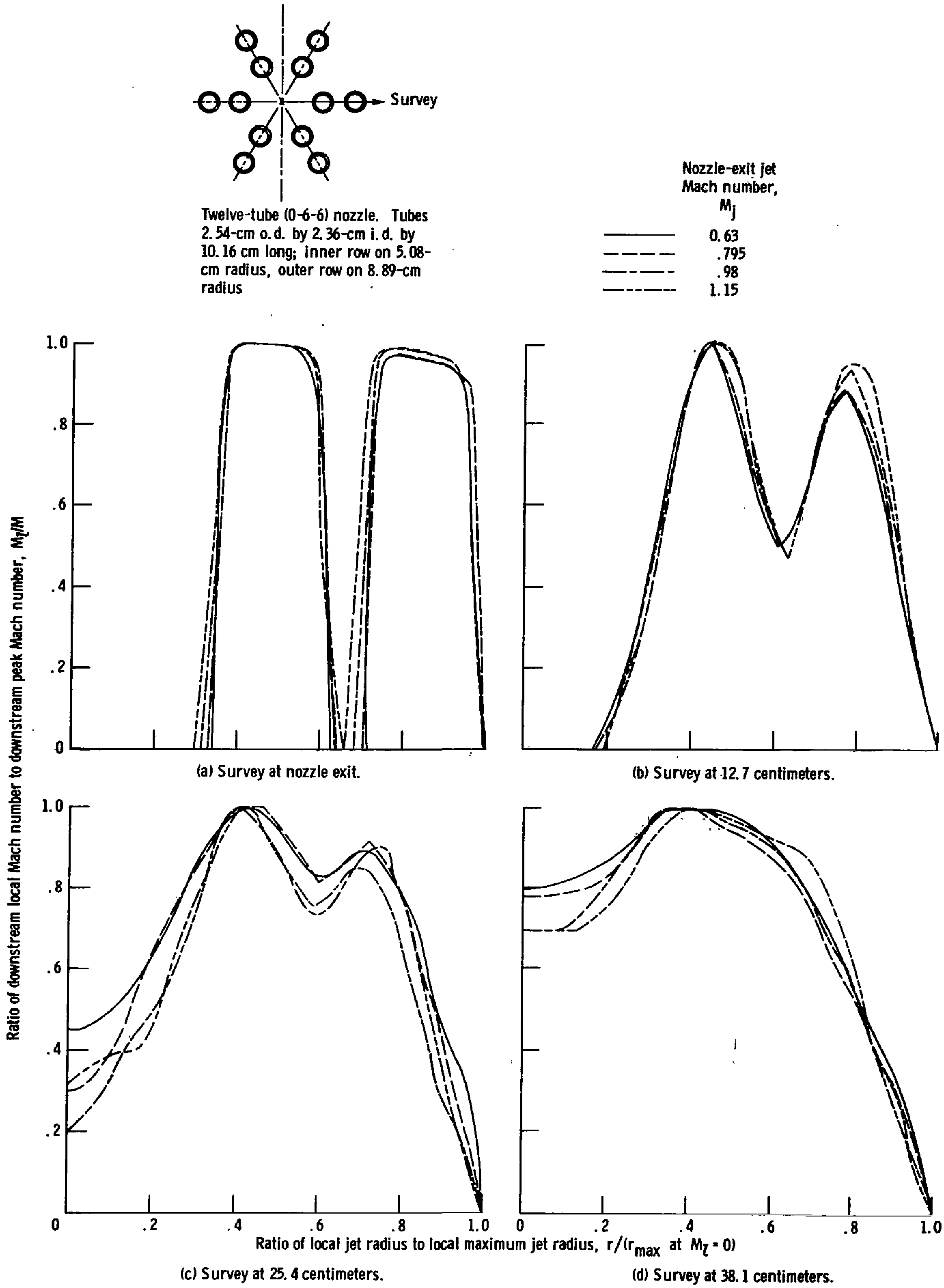

Figure 5. - Normalized nozzle-exit jet Mach number profiles. Configuration 54.

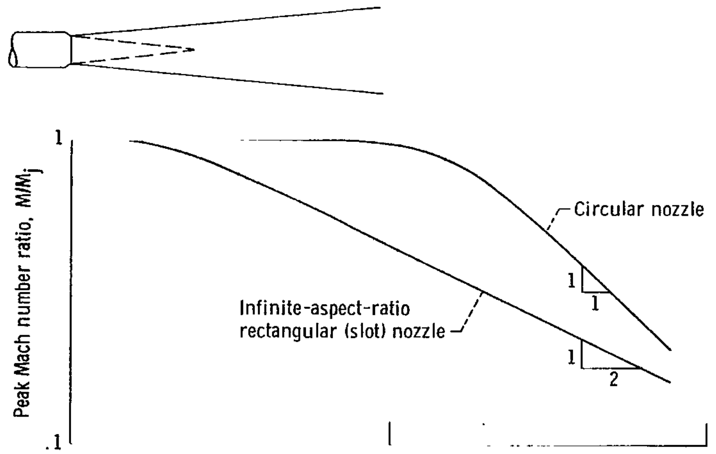

(a) Schematic diagram of single-element-nozzle peak axial Mach number decay.

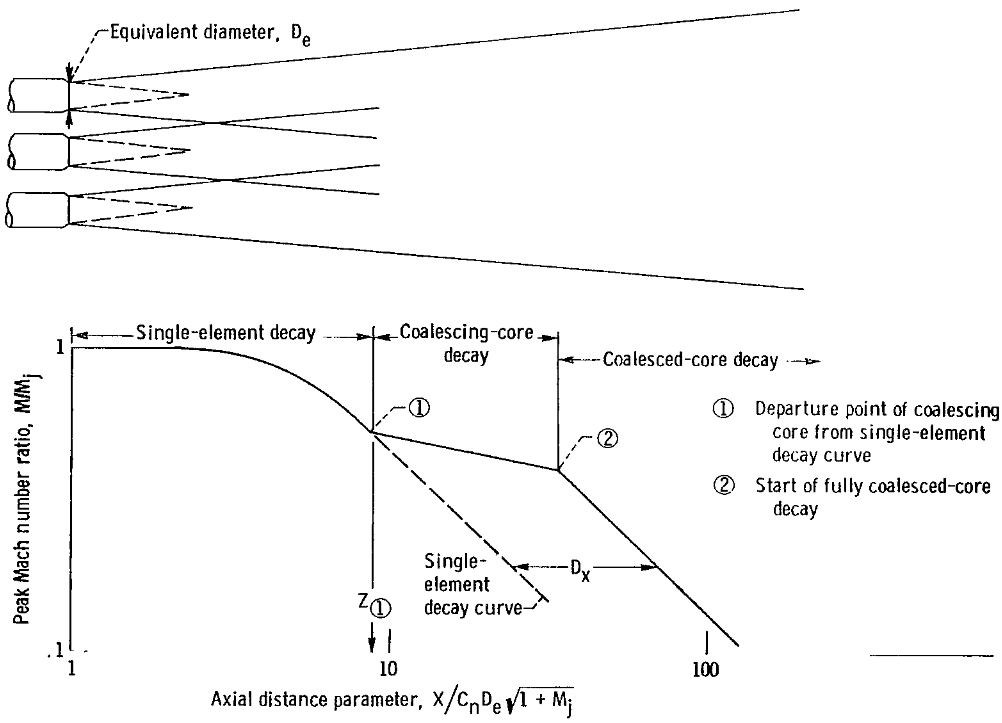

(b) Schematic diagram of multielement-nozzle peak axial Mach number decay regimes.

Figure 6. - Jet Mach number decay with axial distance.

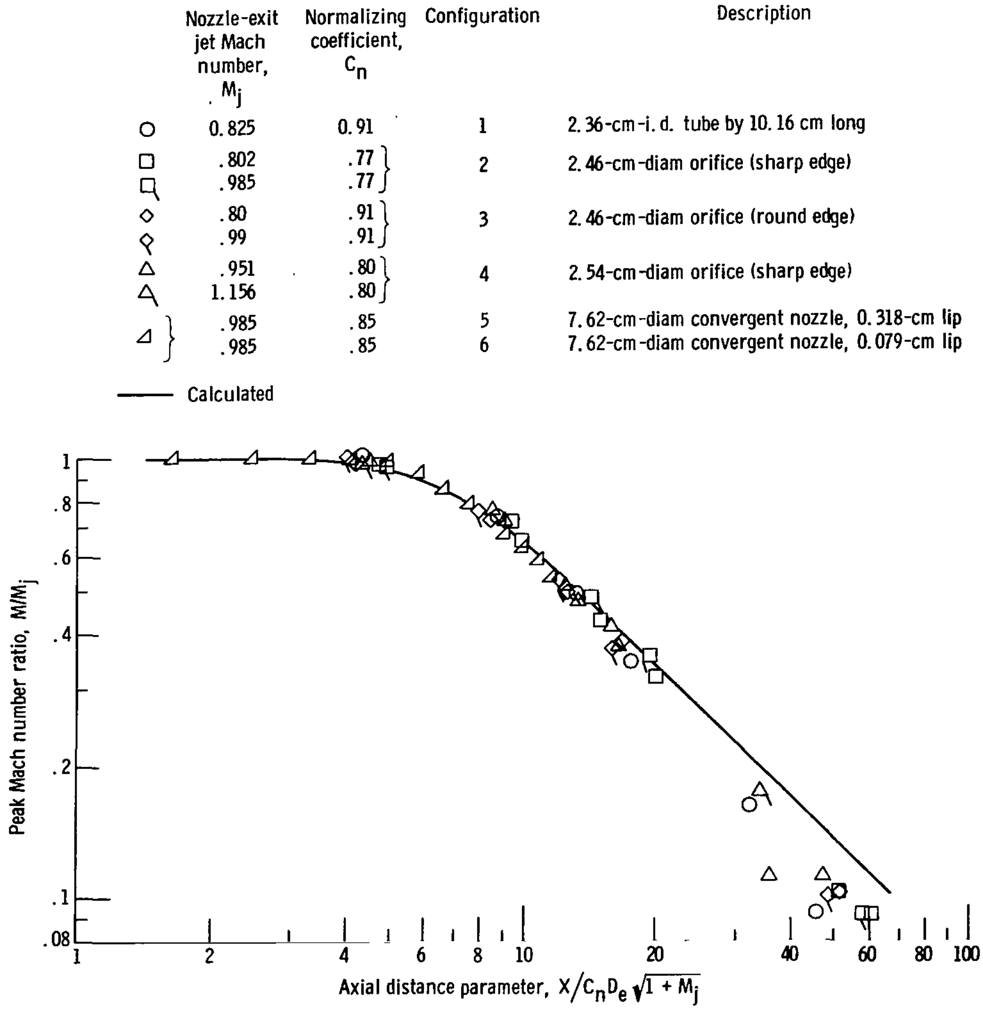

Figure 7. - Peak axial Mach number decay comparison of circular single-element nozzles, both tube and orifices (sharp and round edge), and a convergent (circular) nozzle.

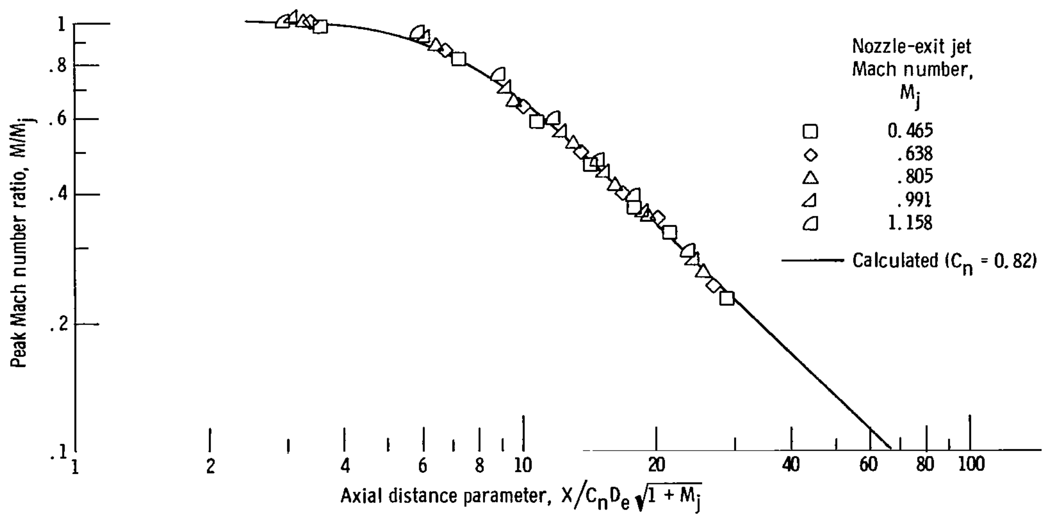

Figure 8. - Peak axial Mach number decay of 3.58-centimeter-diameter convergent nozzle. Configuration 7; equivalent diameter, D_e, 3.58 centimeters.

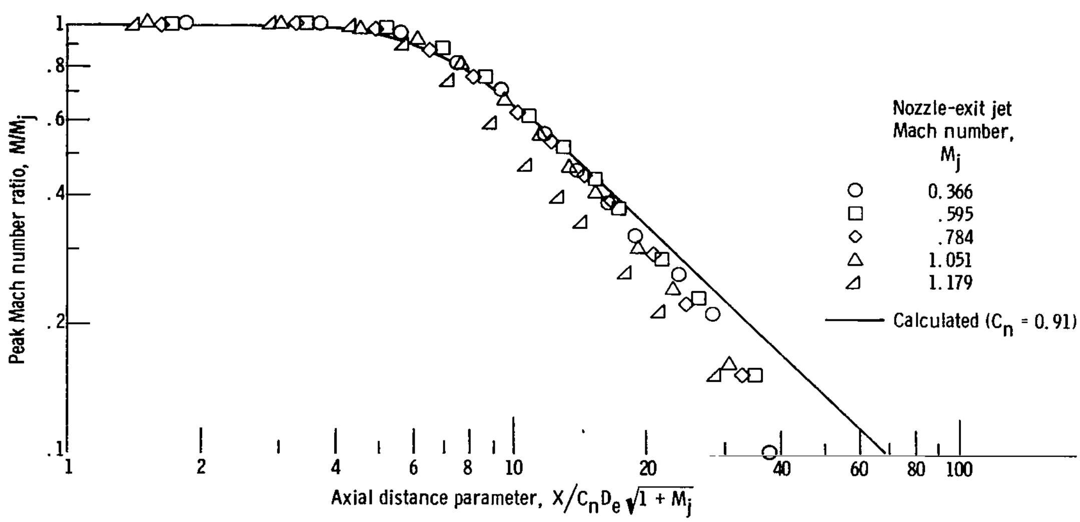

Figure 9. - Peak axial Mach number decay of 7.62-centimeter-diameter convergent nozzle (ref. 10). Configuration 8; equivalent diameter, D_e, 7.62 centimeters.

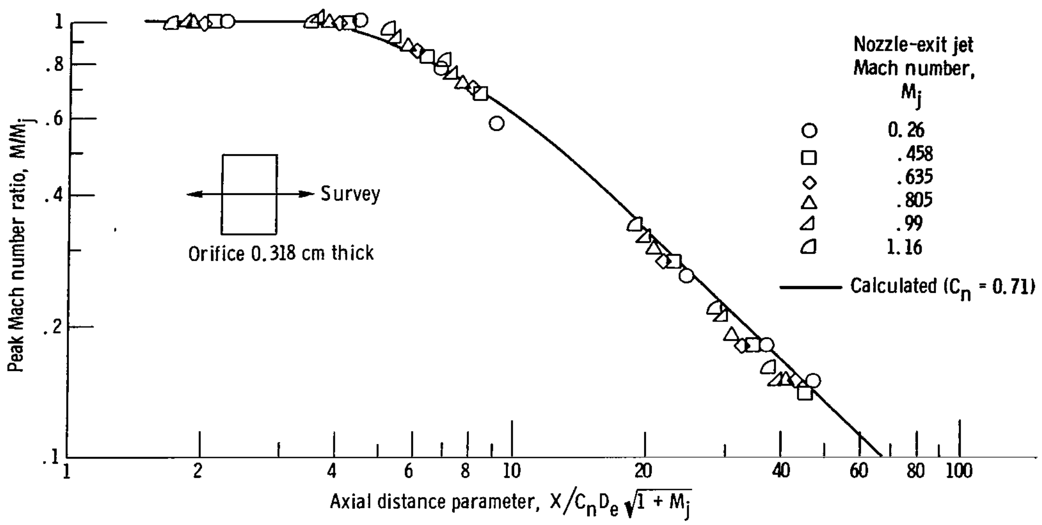

Figure 10. - Peak axial Mach number decay of 5.08-centimeter by 7.62-centimeter rectangular sharp-edge slot. Configuration 9; equivalent diameter, D_e, 7.03 centimeters.

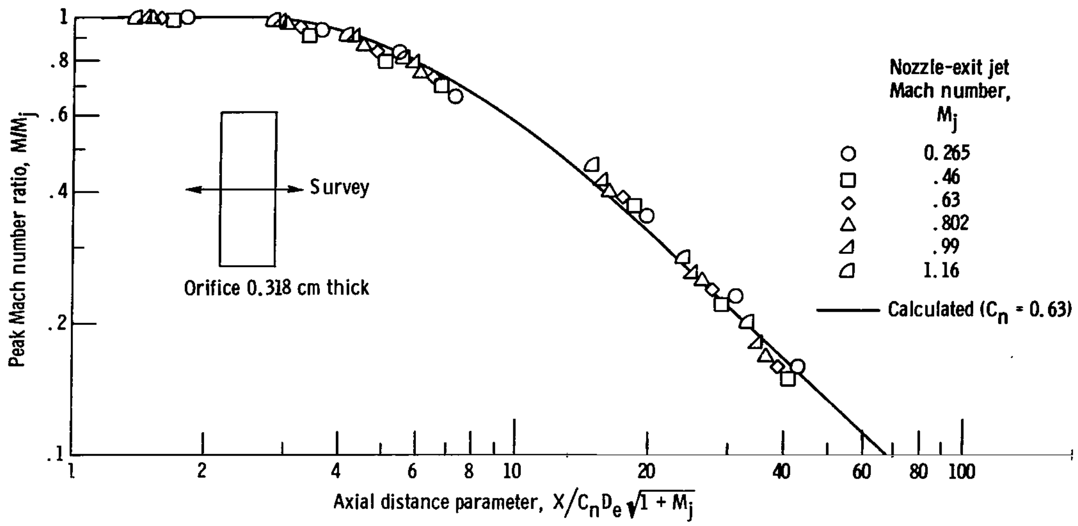

Figure 11. - Peak axial Mach number decay of 5.08-centimeter by 15.24-centimeter rectangular sharp-edge slot. Configuration 10; equivalent diameter, D_e, 9.94 centimeters.

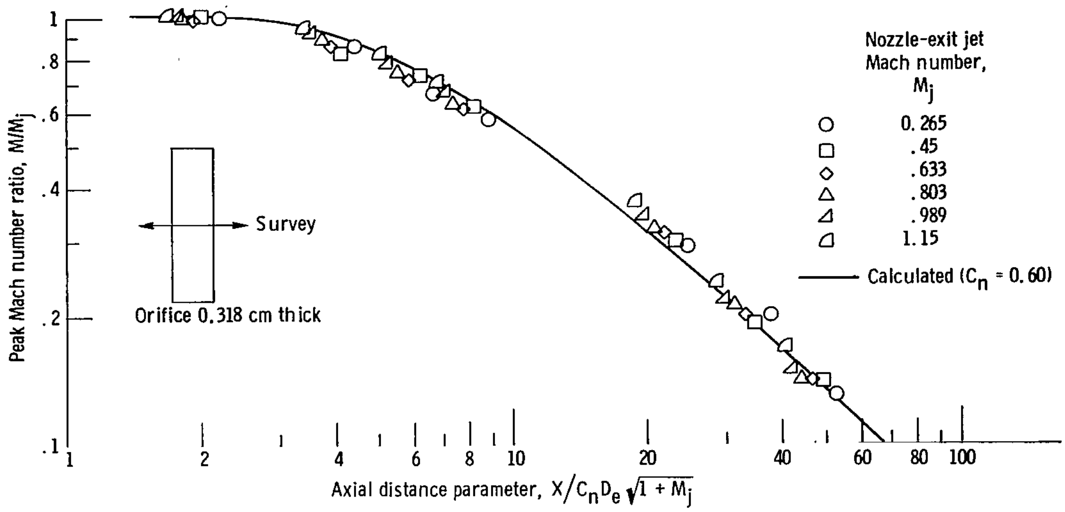

Figure 12. - Peak axial Mach number decay of 3.81-centimeter by 15.24-centimeter rectangular sharp-edge slot. Configuration 11; equivalent diameter, D_e, 8.6 centimeters.

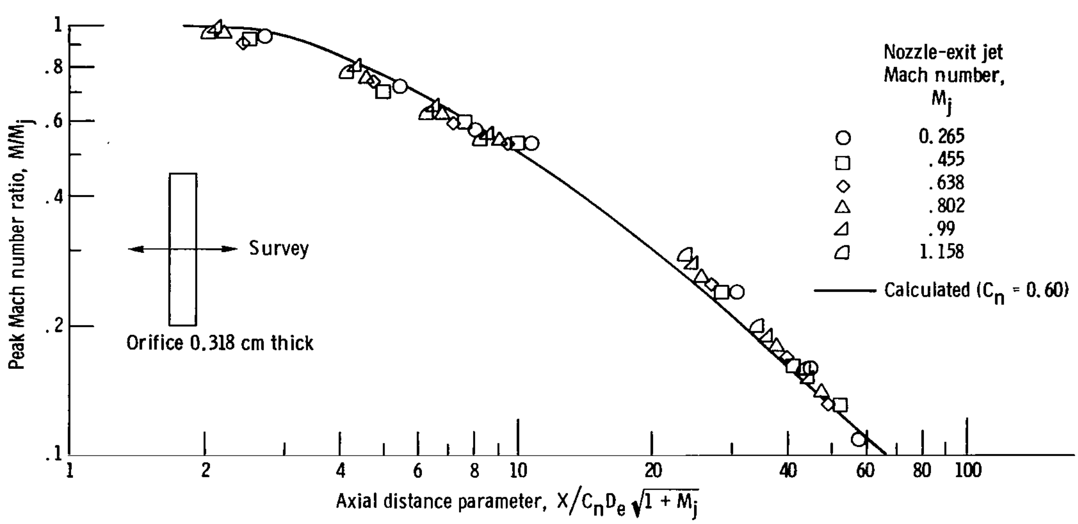

Figure 13. - Peak axial Mach number decay of 2.54-centimeter by 15.24-centimeter rectangular sharp-edge slot. Configuration 12; equivalent diameter, D_e, 7.03 centimeters.

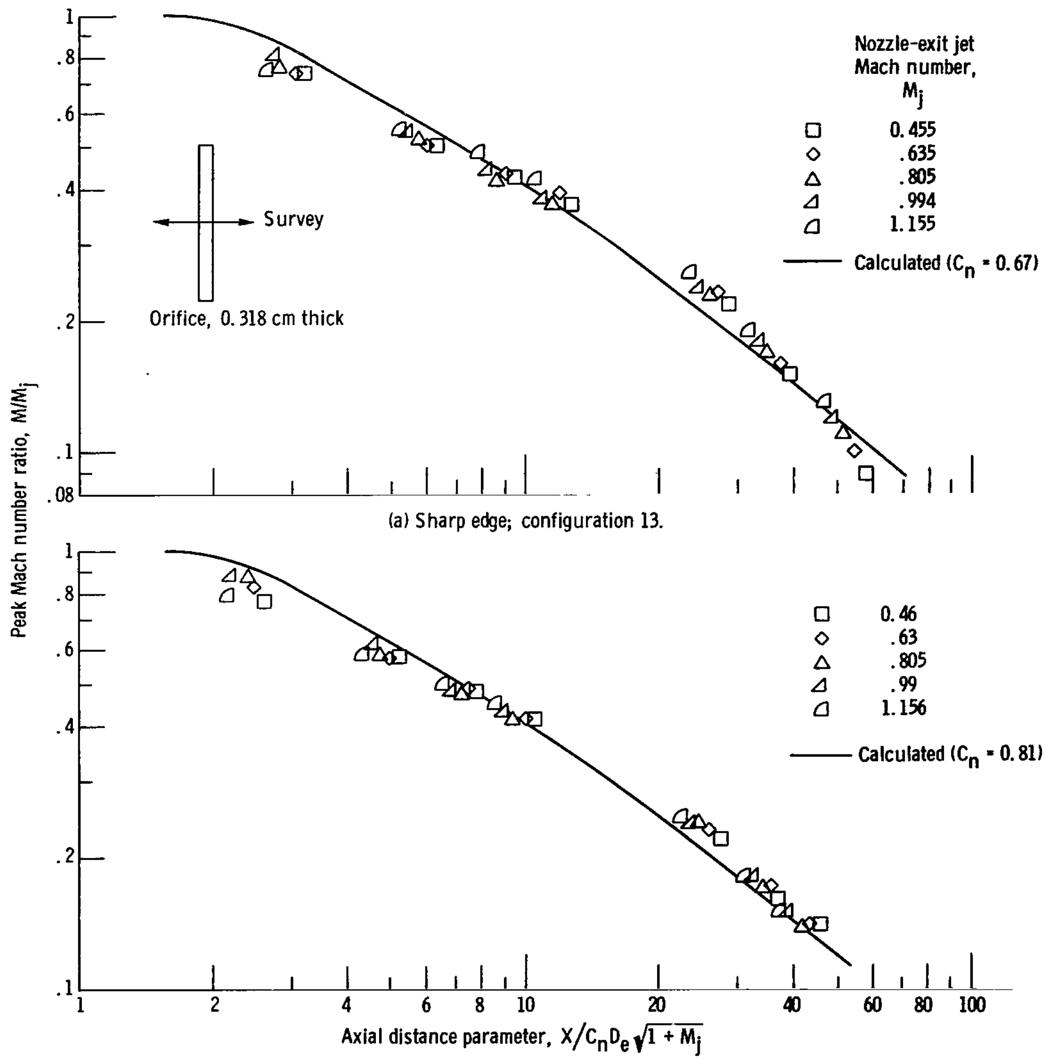

(b) Round edge; configuration 14.

Figure 14. - Peak axial Mach number decay of 1.27-centimeter by 15.24-centimeter rectangular slot. Equivalent diameter, D_e, 4.96 centimeters.

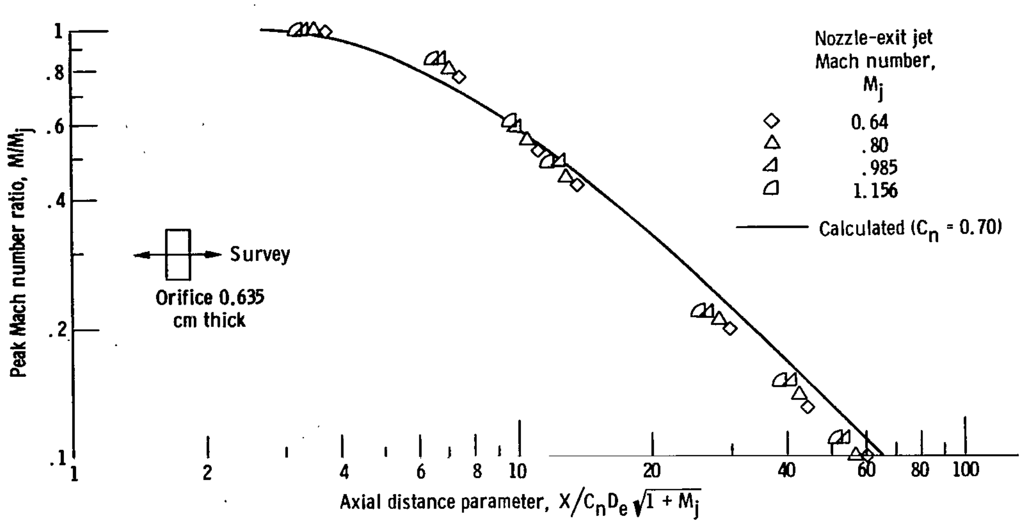

Figure 15. - Peak axial Mach number decay of 2.286-centimeter by 5.08-centimeter rectangular sharp-edge slot. Configuration 15 (single slot of configuration 75); equivalent diameter, D_e, 3.84 centimeters.

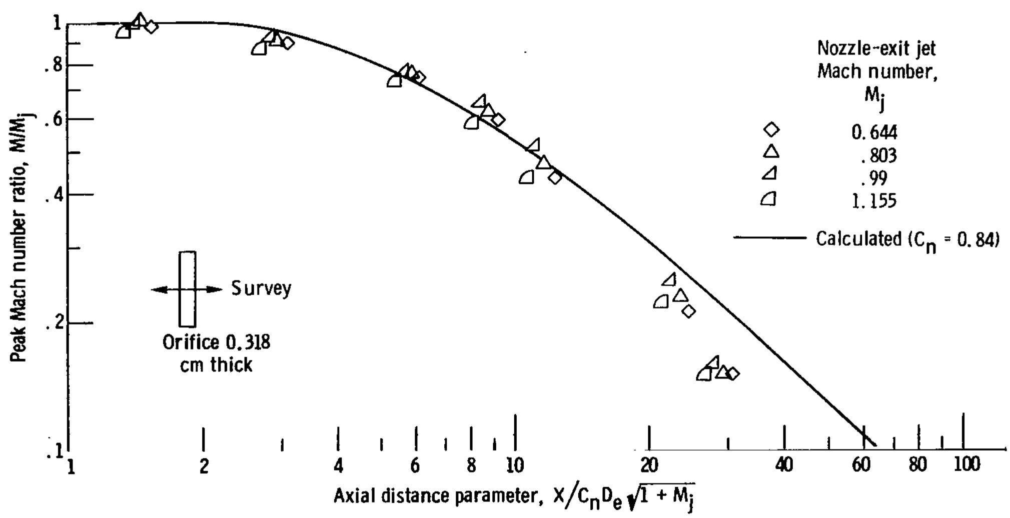

Figure 16. - Peak axial Mach number decay of 1.524-centimeter by 7.62-centimeter rectangular sharp-edge slot. Configuration 16 (single slot of configuration 76); equivalent diameter, D_e, 3.84 centimeters.

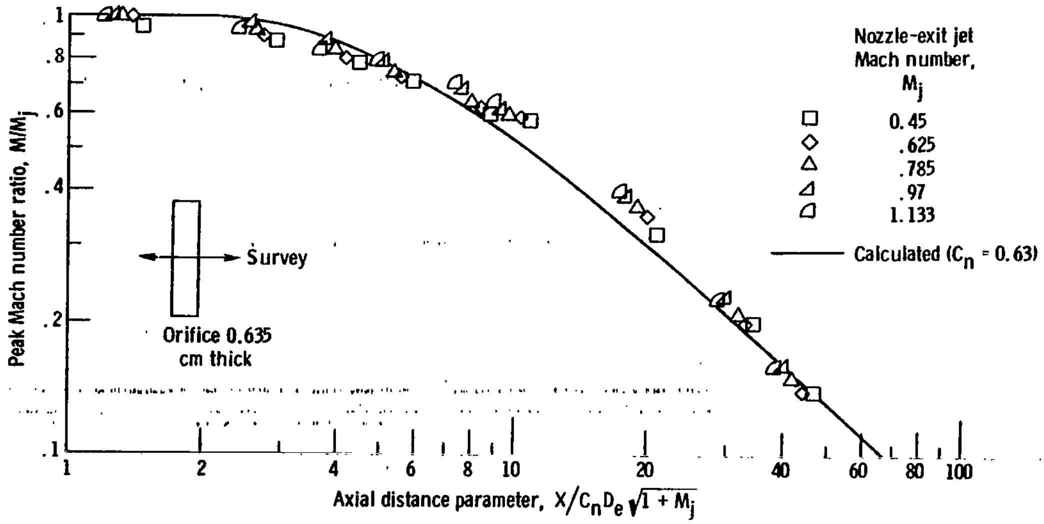

Figure 17. - Peak axial Mach number decay of 2.286-centimeter by 11.43-centimeter rectangular sharp-edge slot. Configuration 17 (single slot of configuration 77); equivalent diameter, D_e, 5.76 centimeters.

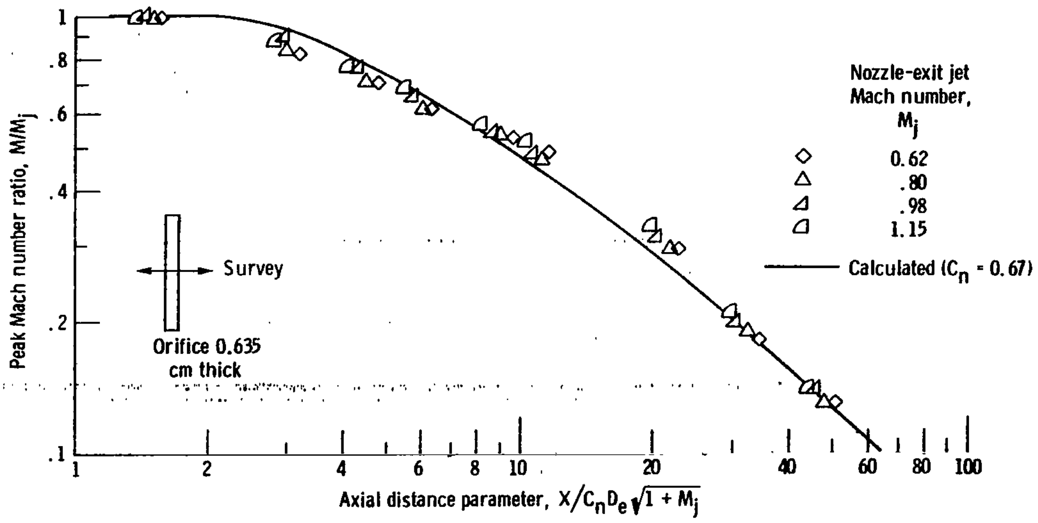

Figure 18. - Peak axial Mach number decay of 1.524-centimeter by 11.43-centimeter rectangular sharp-edge slot. Configuration 18 (single slot of configuration 78); equivalent diameter, D_e, 4.71 centimeters.

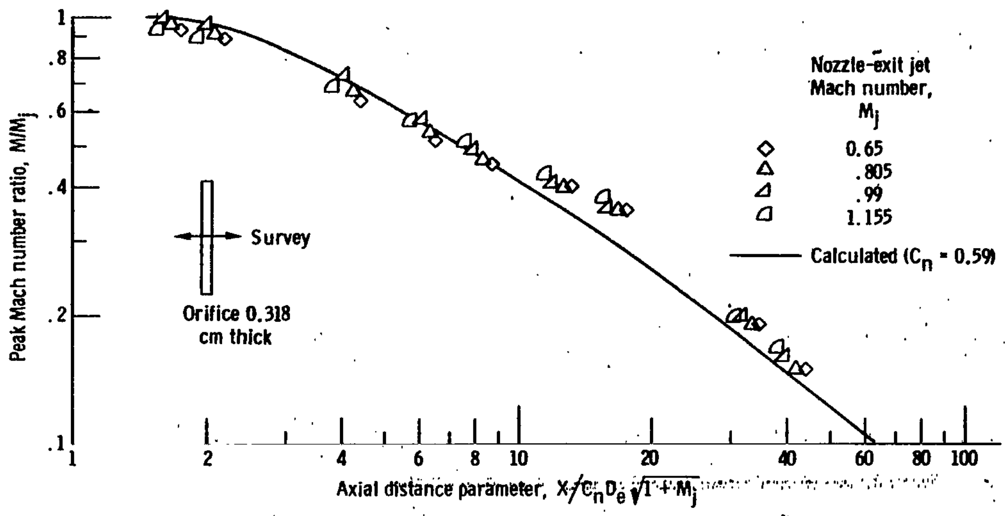

Figure 19. - Peak axial Mach number decay of 1.02-centimeter by 11.43-centimeter rectangular sharp-edge orifice. Configuration 19 (single slot of configuration 79); equivalent diameter, D_e, 3.84 centimeters.

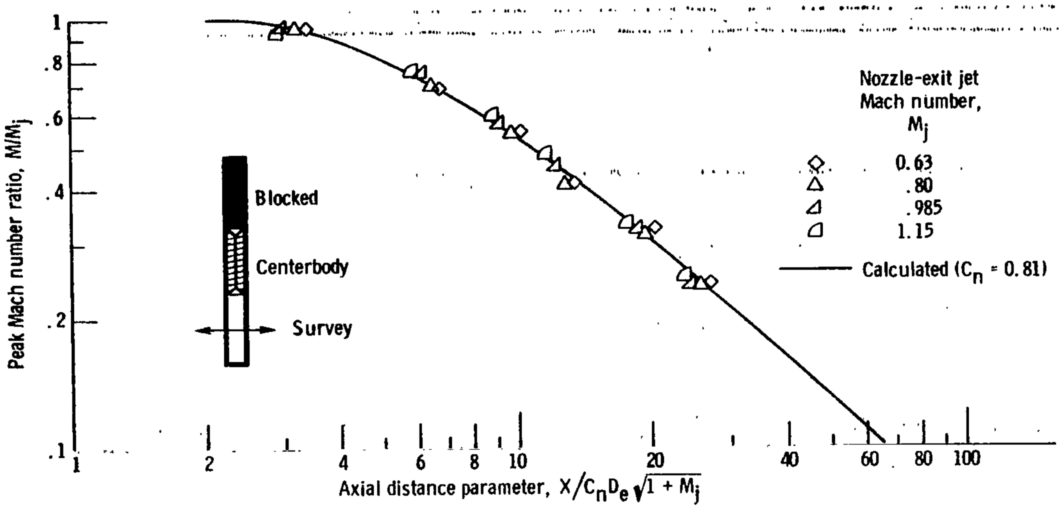

Figure 20. - Peak axial Mach number decay of 1.524-centimeter by 6.99-centimeter rectangular convergent nozzle. Configuration 20 (single nozzle of configuration 90); equivalent diameter, D_e, 3.68 centimeters.

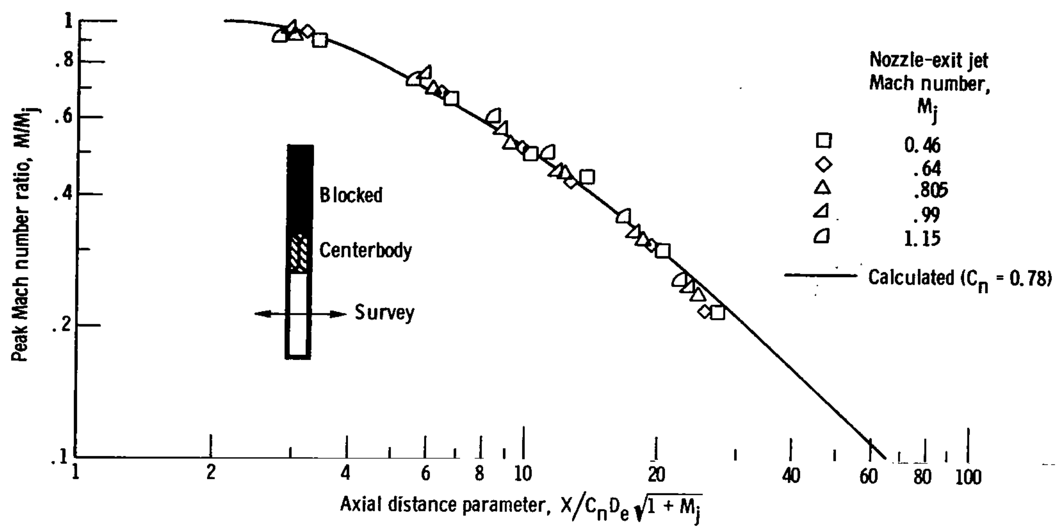

Figure 21. - Peak axial Mach number decay of 1.524-centimeter by 8.25-centimeter rectangular convergent nozzle. Configuration 21 (single nozzle of configuration 89); equivalent diameter, D_e, 4.00 centimeters.

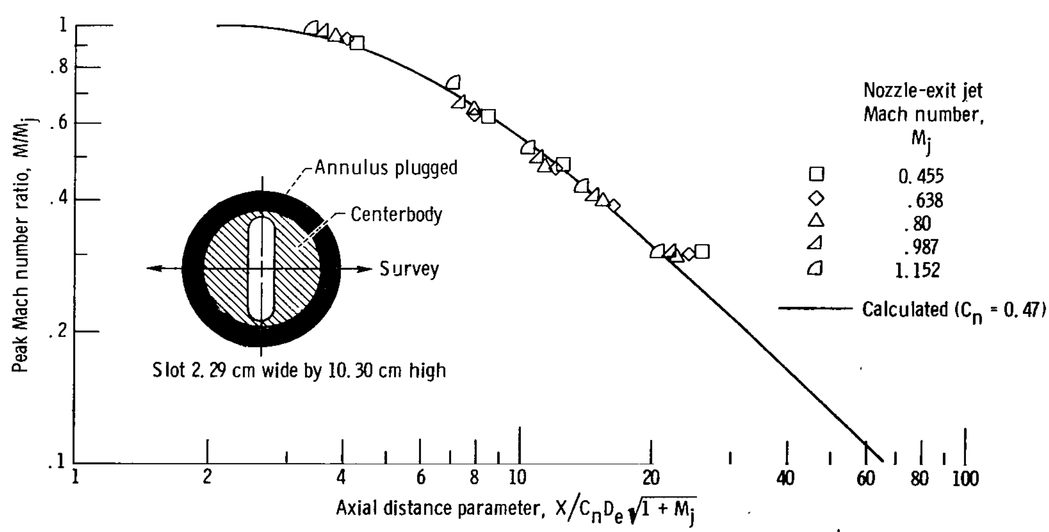

Figure 22. - Peak axial Mach number decay of round-end rectangular nozzle. Configuration 22 (core nozzle of configurations 114, 115, 116, and 117); equivalent diameter, D_e, 5.32 centimeters; aspect ratio, AR, 4.76

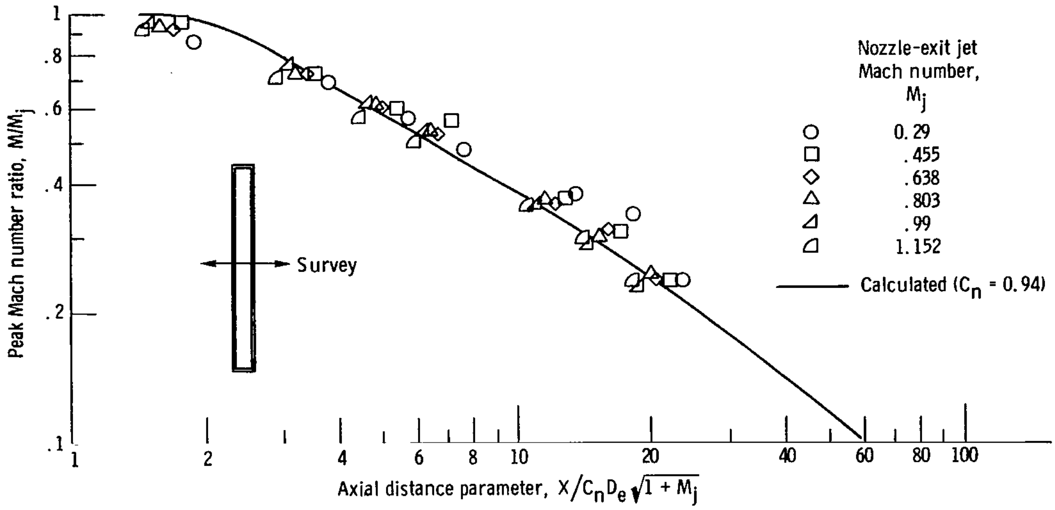

Figure 23. - Peak axial Mach number decay of 1.524-centimeter by 20.32-centimeter rectangular convergent nozzle. Configuration 23 (single nozzle of configurations 72, 73, and 74); equivalent diameter, D_e, 6.28 centimeters.

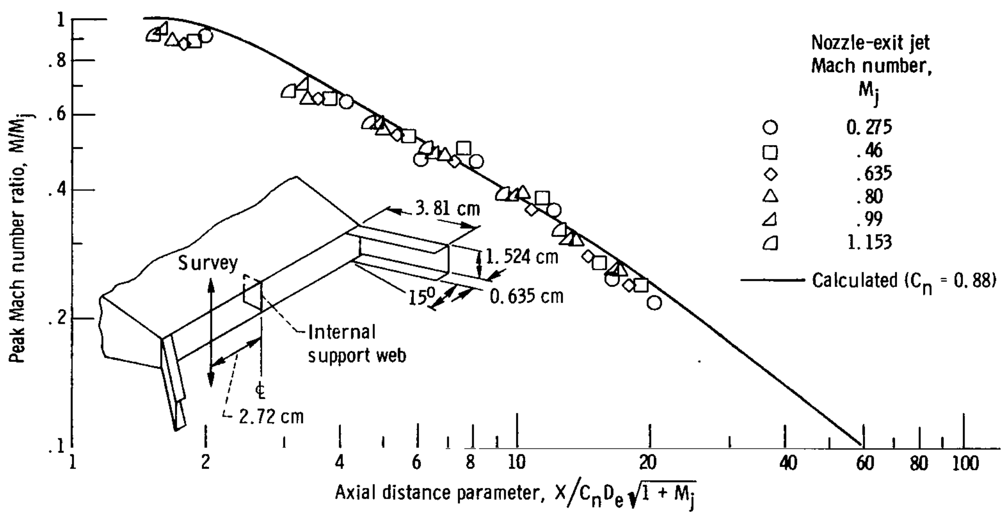

Figure 24. - Peak axial Mach number decay of 1.524-centimeter by 20.32-centimeter rectangular convergent nozzle with 15° end plates. Configuration 24 (same basic nozzle as configuration 23); equivalent diameter, D_e, 6.28 centimeters.

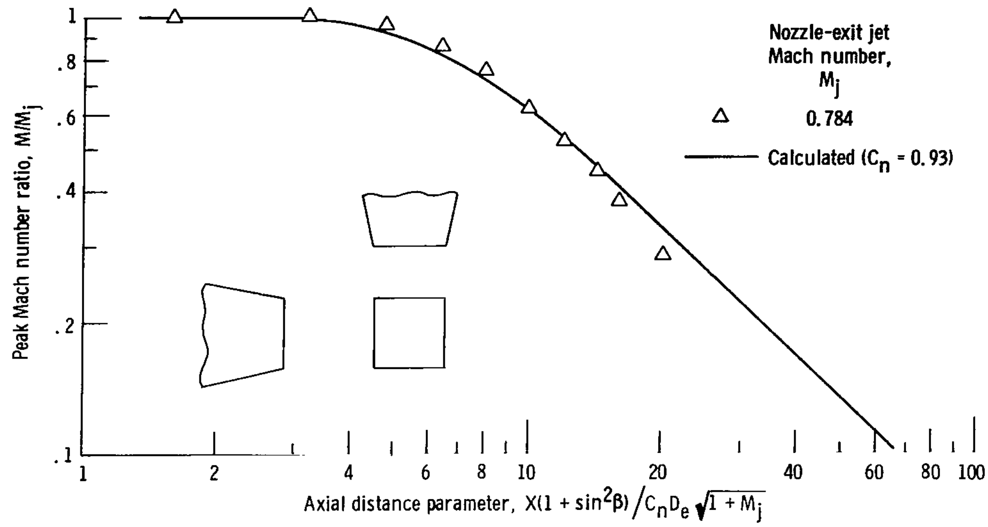

Figure 25. - Peak axial Mach number decay of 6.75-centimeter by 6.75-centimeter square convergent nozzle. Configuration 25; equivalent diameter, D_e, 7.62 centimeters; wall divergence angle, β, 0°. (From ref. 10; nozzle 5.)

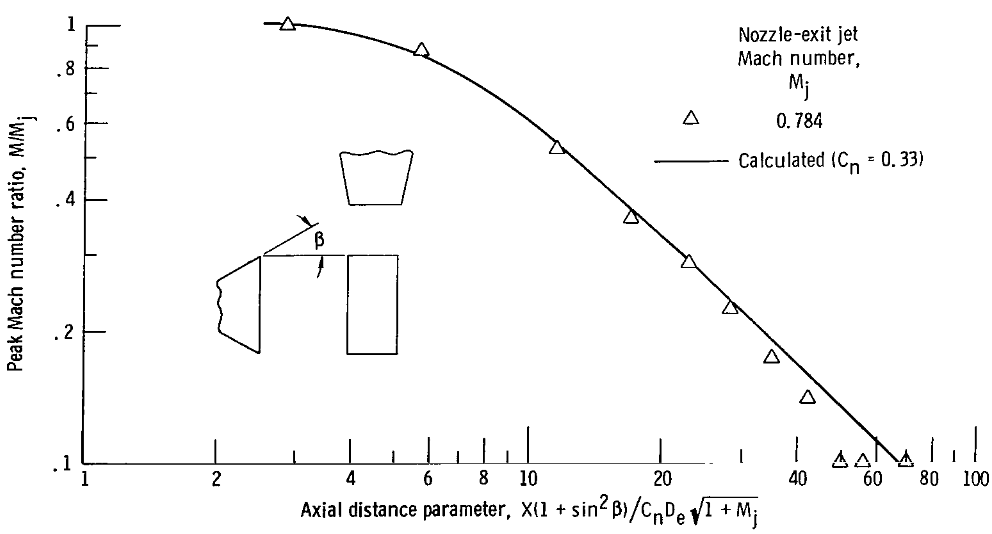

Figure 26. - Peak axial Mach number decay of 4.775-centimeter by 9.55-centimeter rectangular nozzle. Configuration 26; equivalent diameter, D_e, 7.62 centimeters; aspect ratio, AR, 2; wall divergence angle, β, 30°. (From ref. 10; nozzle 7.)

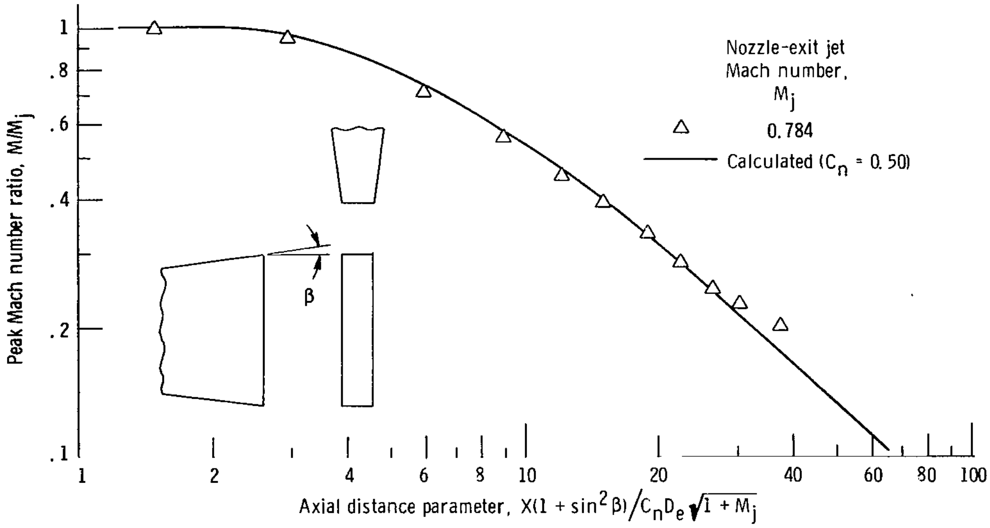

Figure 27. - Peak axial Mach number decay of 3.02-centimeter by 15.1-centimeter rectangular nozzle. Configuration 27; equivalent diameter, D_e, 7.62 centimeters; aspect ratio, AR, 5; wall divergence angle, β, 5°. (From ref. 10; nozzle 8.)

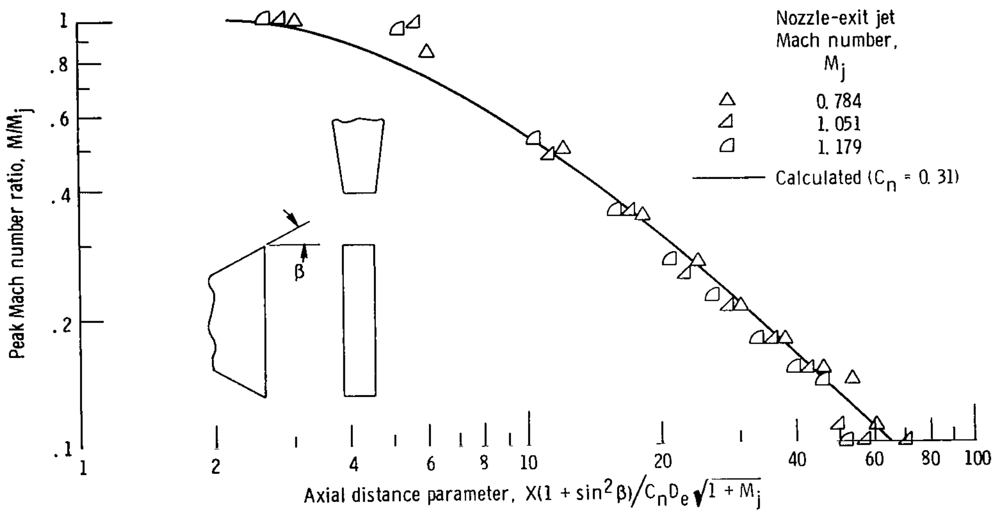

Figure 28. - Peak axial Mach number decay of 3.02-centimeter by 15.1-centimeter rectangular nozzle. Configuration 28; equivalent diameter, D_e, 7.62 centimeters; aspect ratio, AR, 5; wall divergence angle, β, 30°. (From ref. 10; nozzle 9.)

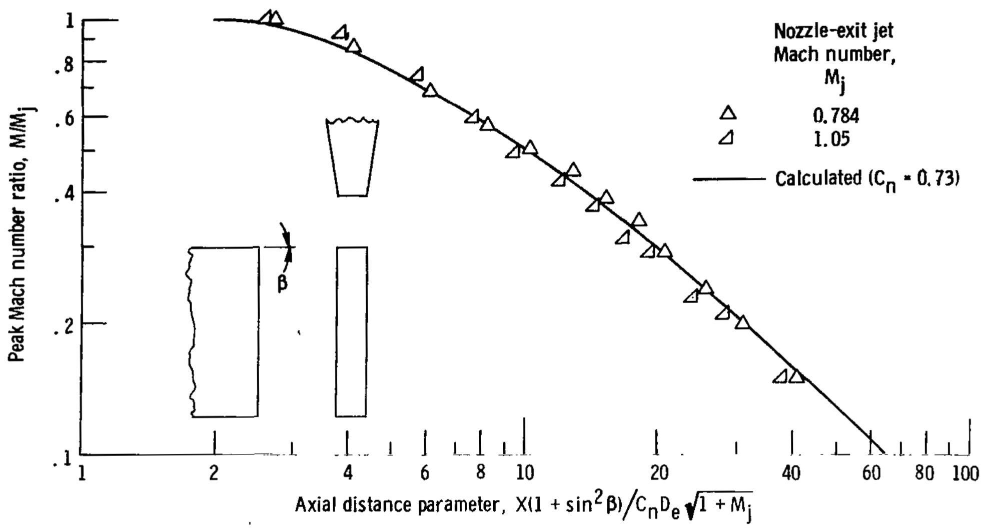

Figure 29. - Peak axial Mach number decay of 2.74-centimeter by 16.55-centimeter rectangular nozzle. Configuration 29; equivalent diameter, D_e, 7.62 centimeters; aspect ratio, AR, 6; wall divergence angle, β, 0°. (From ref. 10; nozzle 6.)

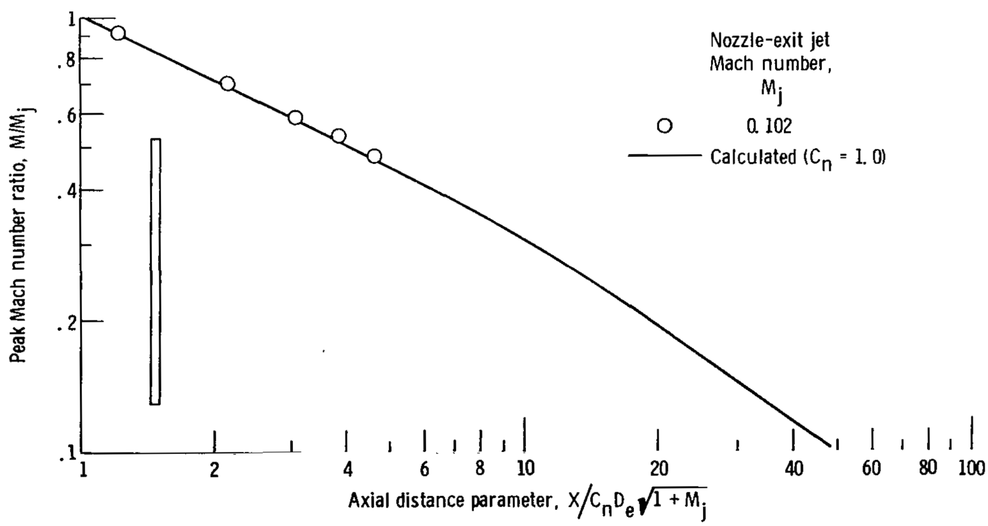

Figure 30. - Peak axial Mach number decay of 3-centimeter by 65-centimeter rectangular nozzle. Configuration 30; equivalent diameter, D_e, 15.75 centimeters; aspect ratio, AR, 21.7. (From ref. 8.)

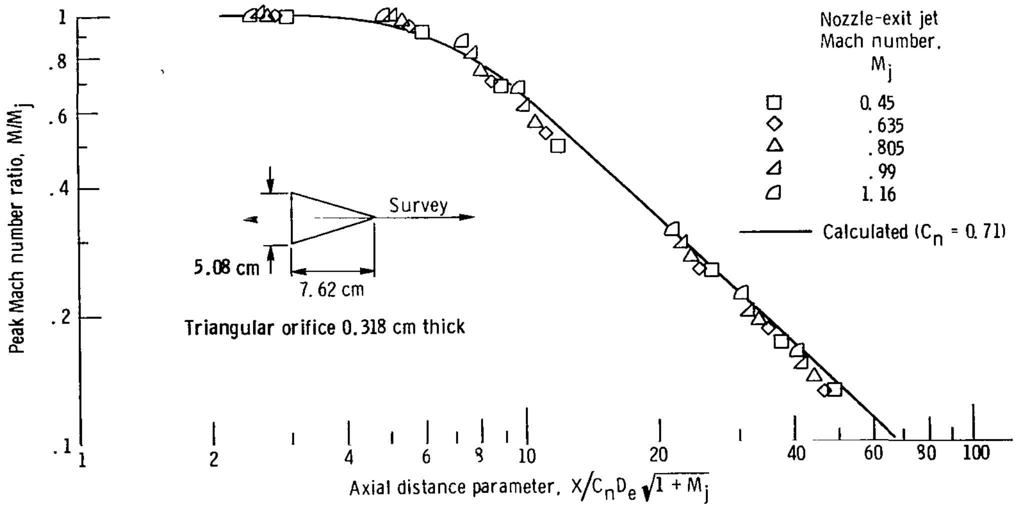

Figure 31. - Peak axial Mach number decay of 5.08-centimeter by 7.62-centimeter triangular sharp-edge orifice. Configuration 31; equivalent diameter, D_e, 4.96 centimeters.

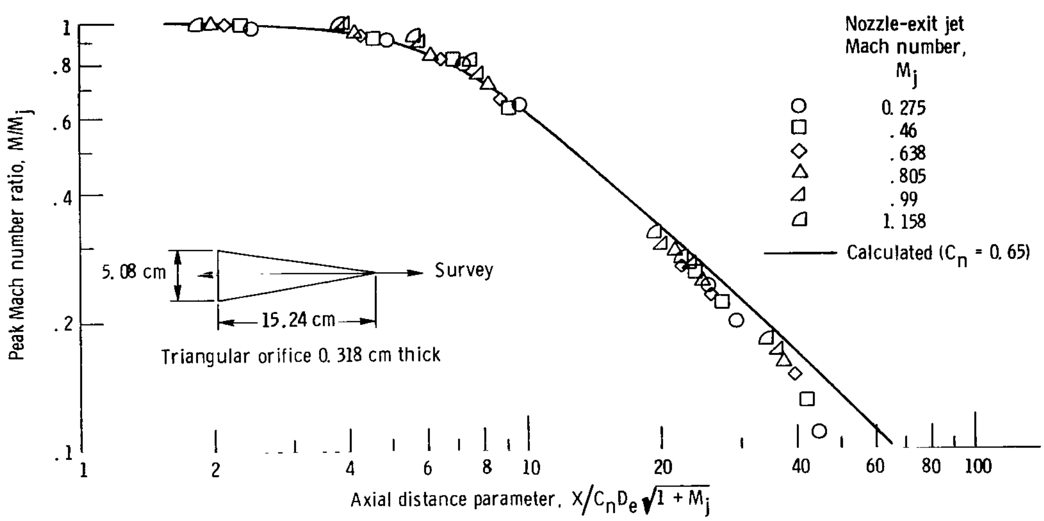

Figure 32. - Peak axial Mach number decay of 5.08-centimeter by 15.24-centimeter triangular sharp-edge orifice. Configuration 32; equivalent diameter, D_e, 7.03 centimeters.

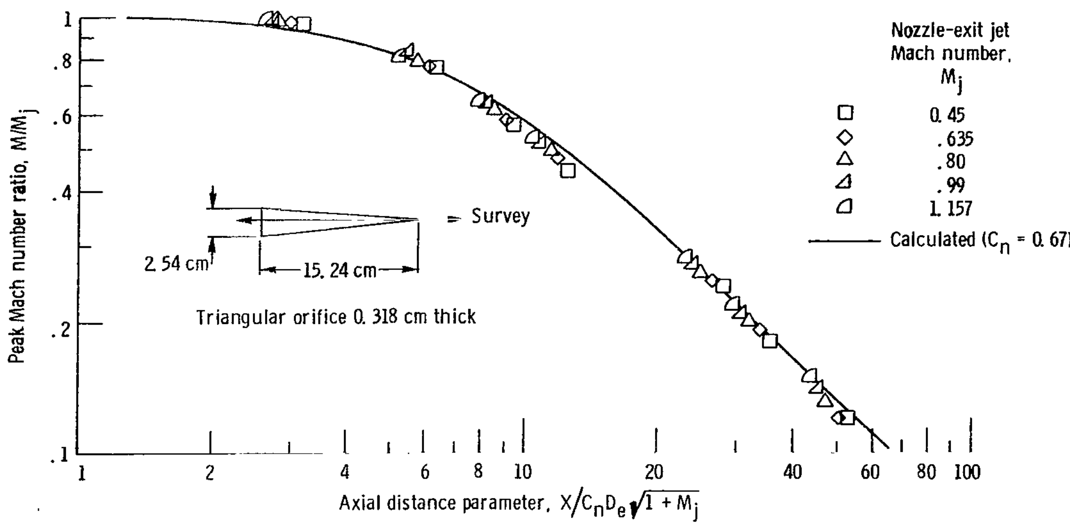

Figure 33. - Peak axial Mach number decay of 2.54-centimeter by 15.24-centimeter triangular sharp-edge orifice. Configuration 33; equivalent diameter, D_e, 4.96 centimeters.

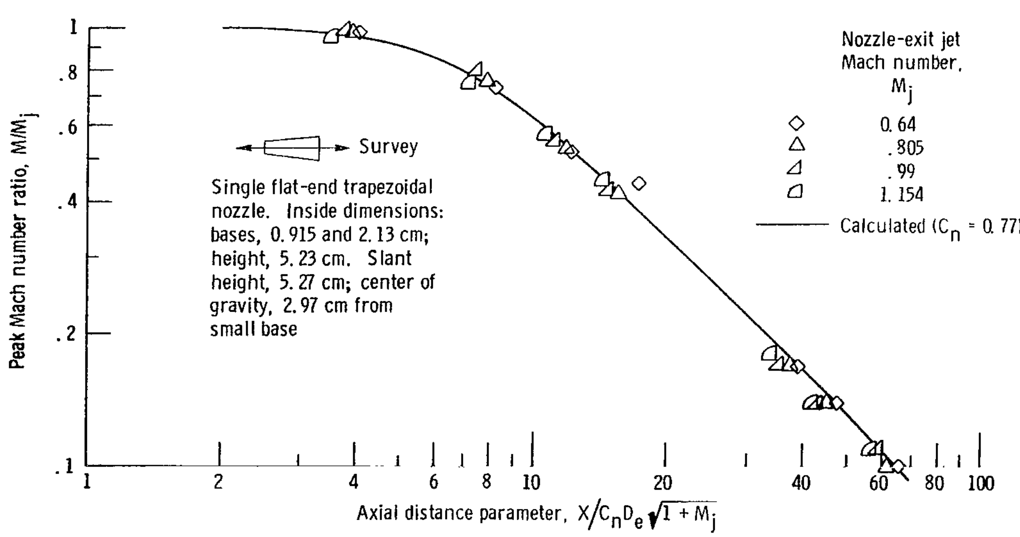

Figure 34. - Peak axial Mach number decay of flat-end trapezoidal nozzle. Configuration 34 (single nozzle of configuration 94); equivalent diameter, D_e, 3.19 centimeters.

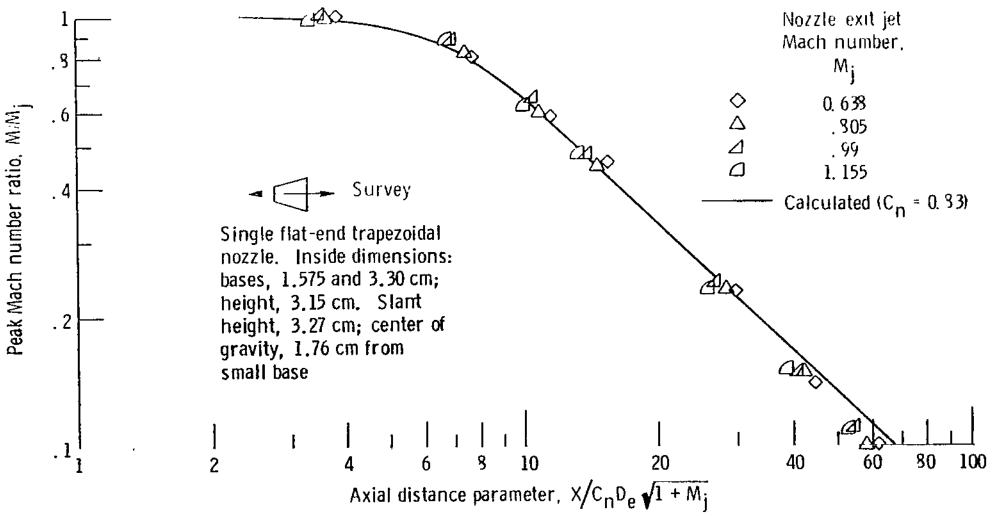

Figure 35. - Peak axial Mach number decay of flat-end trapezoidal nozzle. Configuration 35 (single nozzle of configuration 95); equivalent diameter, D_e, 3.125 centimeters.

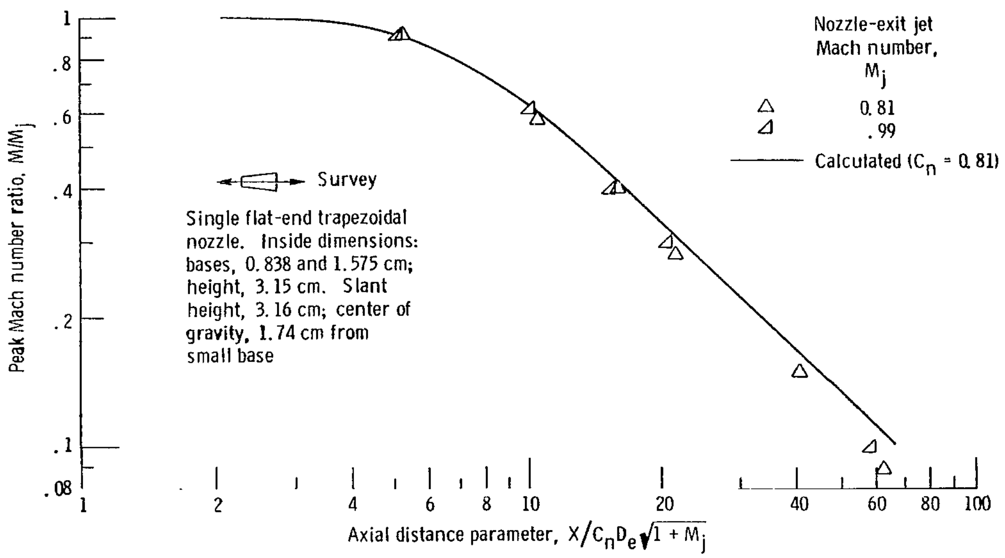

Figure 36. - Peak axial Mach number decay of flat-end trapezoidal nozzle. Configuration 36 (single nozzle of configuration 96); equivalent diameter, D_e, 2.20 centimeters.

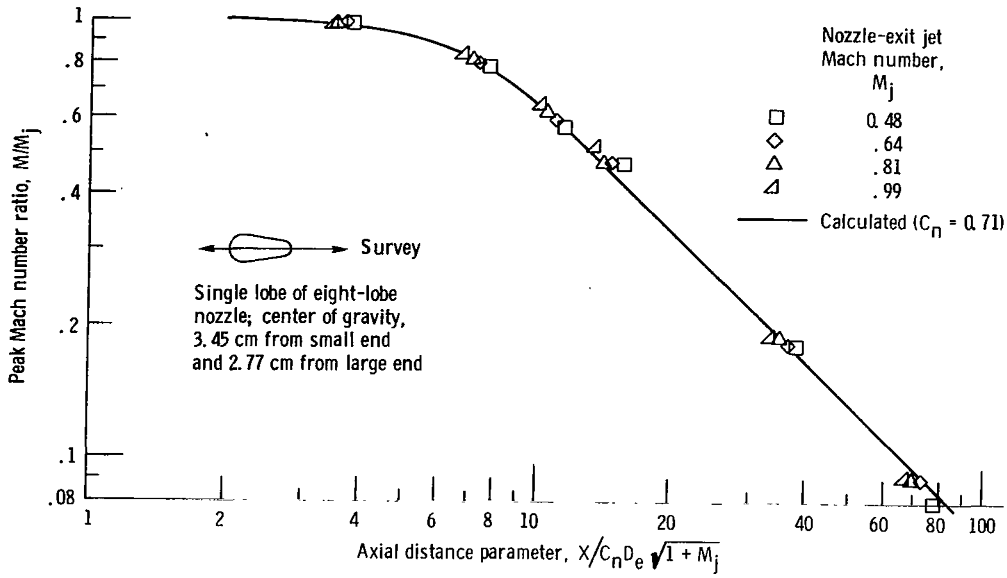

Figure 37. - Peak axial Mach number decay of round-end trapezoidal nozzle. Configuration 37 (single nozzle of configurations 97, 98, 99, 100, 101, and 102); equivalent diameter, D_e, 3.81 centimeters.

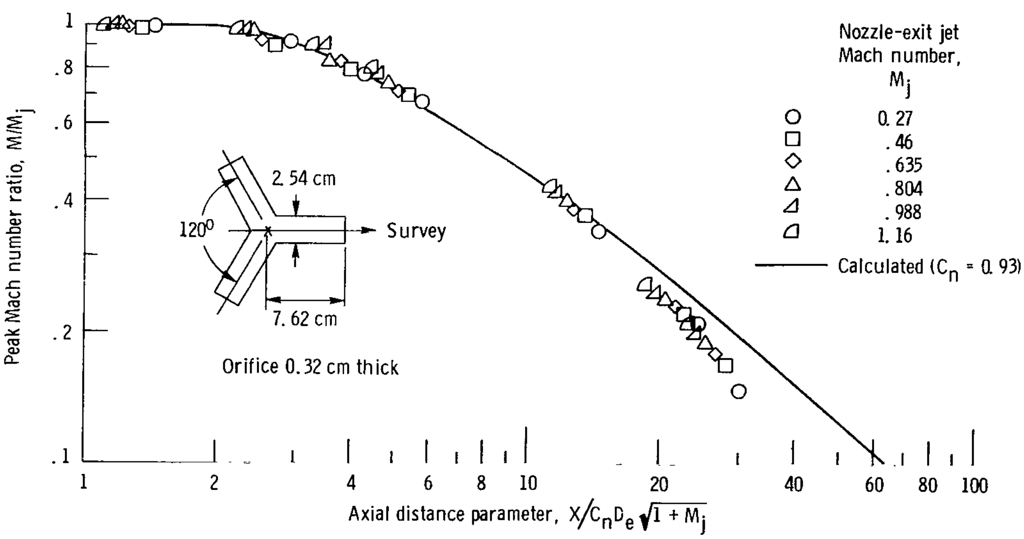

Figure 38. - Peak axial Mach number decay of a Y-shape sharp-edge orifice. Configuration 38; equivalent diameter, D_e, 8.40 centimeters.

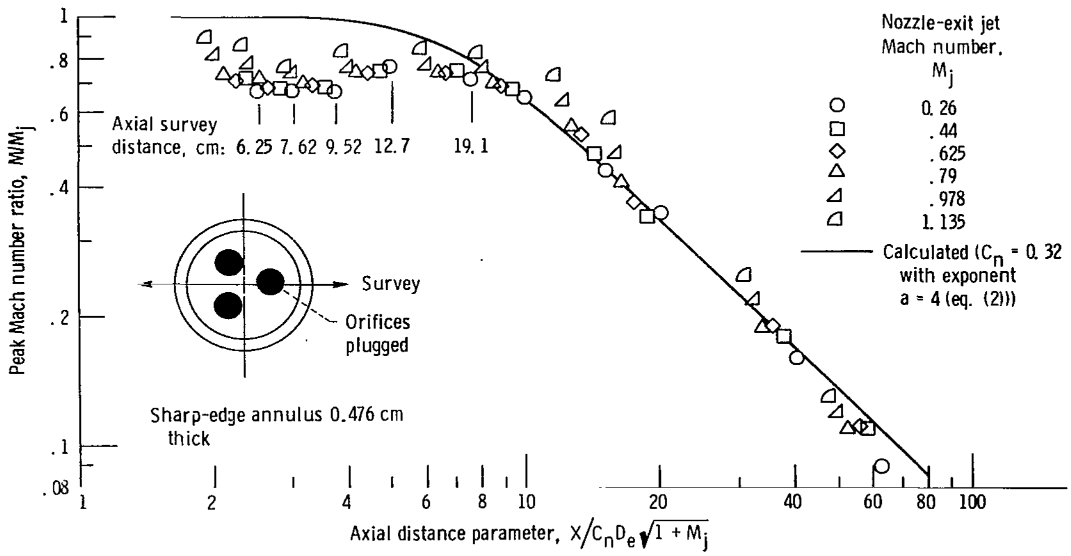

Figure 39. - Peak axial Mach number decay of 1.016-centimeter-wide sharp-edge annulus 13.21 centimeters in outside diameter by 11.18 centimeters in inside diameter. Configuration 39 (used on configurations 108, 109, 110, 111, 112, and 113); equivalent diameter, D_e, 7.05 centimeters. (Inner surface (jet) pumped subatmospheric for first 7.62 cm.)

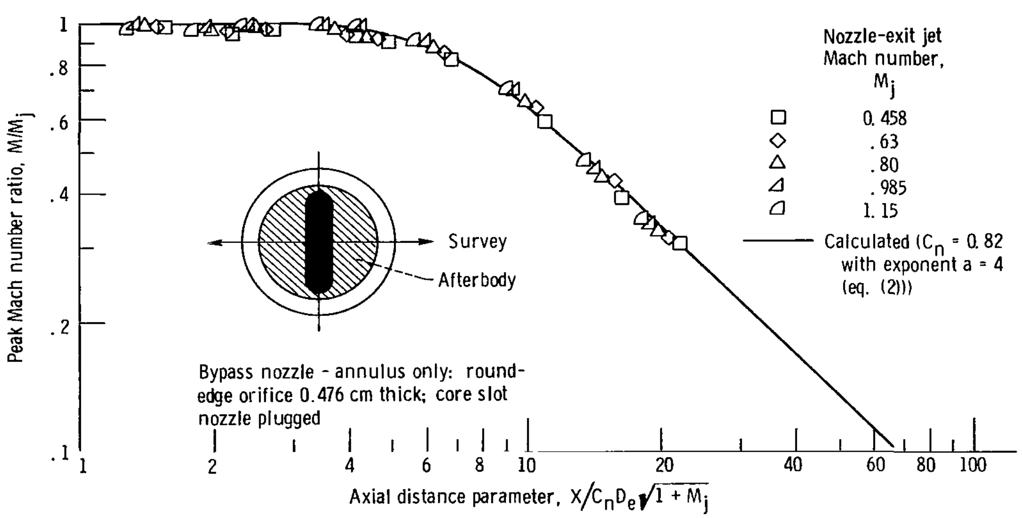

Figure 40. - Peak axial Mach number decay of 1.663-centimeter-wide round-edge annulus 14.78 centimeters in outside diameter by 11.44 centimeters in inside diameter. Configuration 40 (used on configurations 114, 115, 116, and 117); equivalent diameter, D_e, 9.37 centimeters.

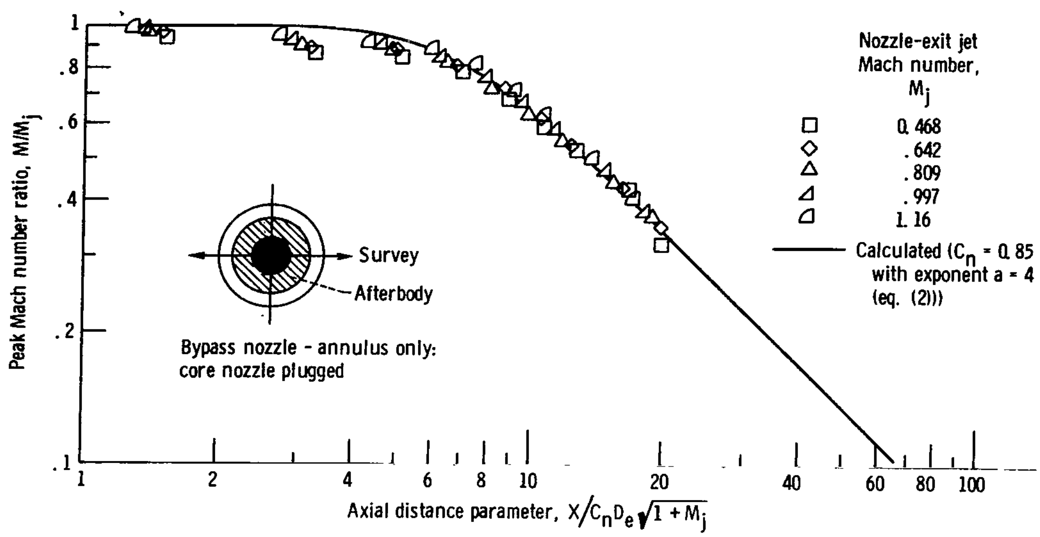

Figure 41. - Peak axial Mach number decay of bypass-nozzle convergent annulus only, 10.23 centimeters in outside diameter by 7.92 centimeters in inside diameter. Configuration 41 (used on configurations 118, 119, and 120); equivalent diameter, D_e, 6.472 centimeters.

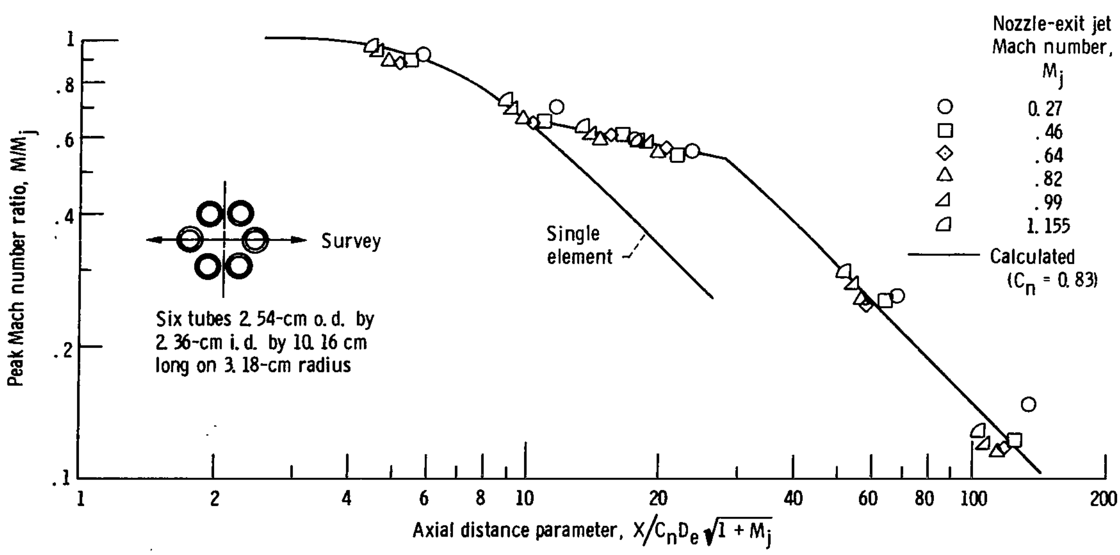

Figure 42. - Peak axial Mach number decay of 0-6-0 multitube nozzle with spacing ratio s_1/d_1 of 0.345. Configuration 42; equivalent diameter, D_e, 2.36 centimeters.

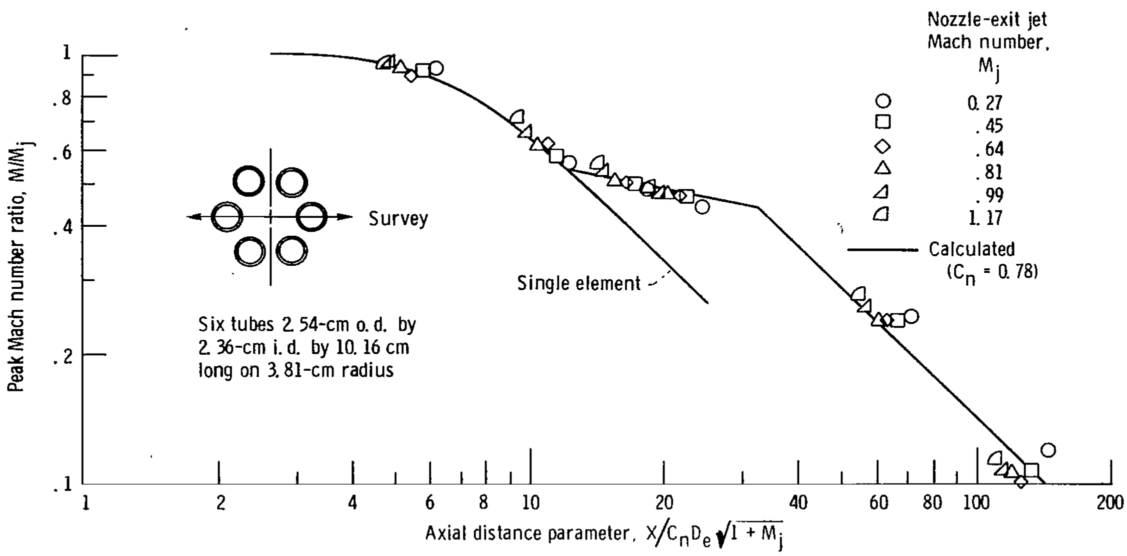

Figure 43. - Peak axial Mach number decay of 0-6-0 multitube nozzle with spacing ratio s_1/d_1 of 0.613. Configuration 43; equivalent diameter, D_e, 2.36 centimeters.

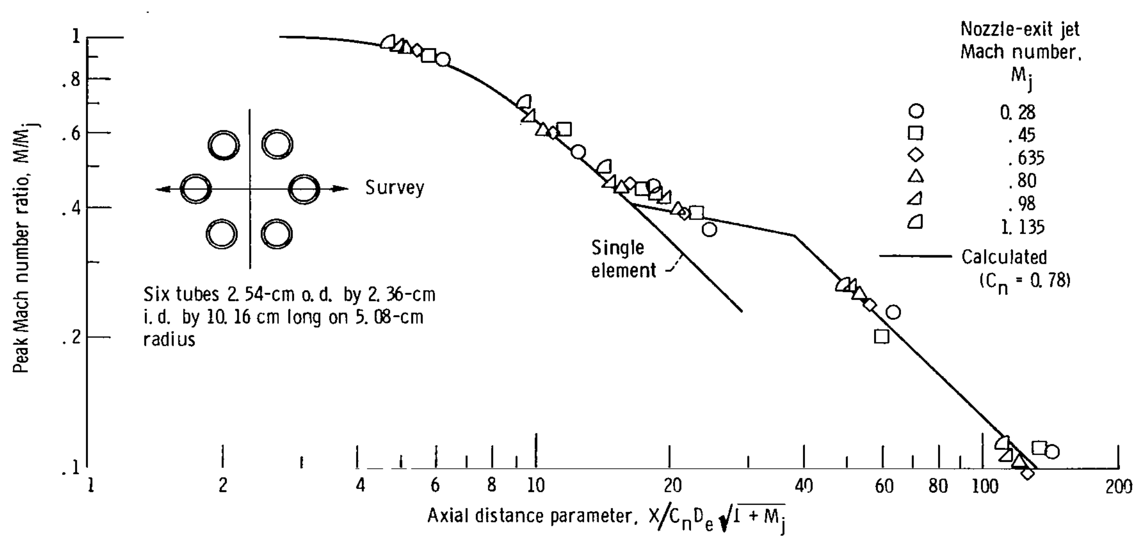

Figure 44. - Peak axial Mach number decay of 0-6-0 multitube nozzle with spacing ratio s_1/d_1 of 1.152. Configuration 44: equivalent diameter, D_e, 2.36 centimeters.

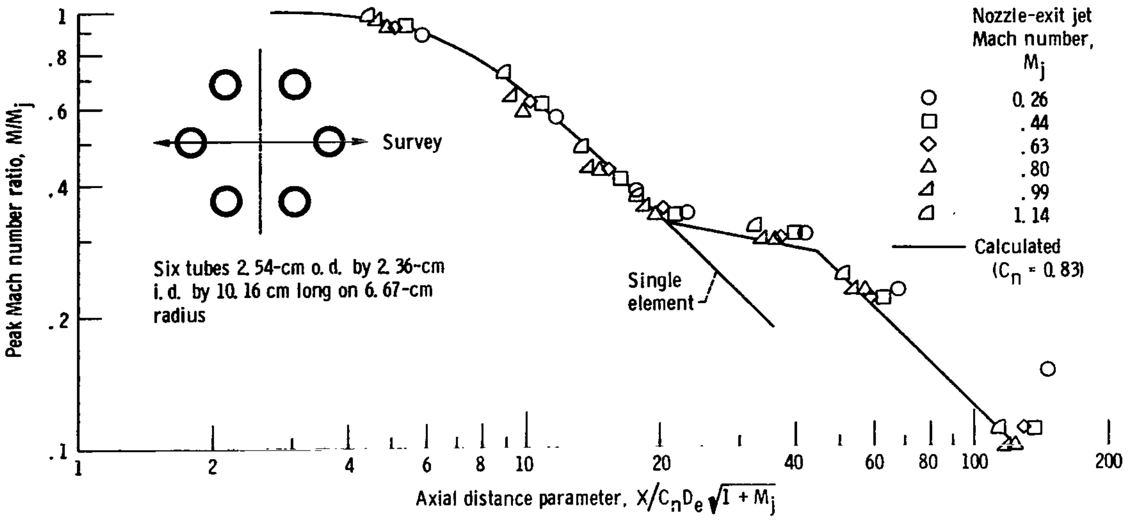

Figure 45. - Peak axial Mach number decay of 0-6-0 multitube nozzle with spacing ratio s_1/d_1 of 1.825. Configuration 45; equivalent diameter, D_e, 2.36 centimeters.

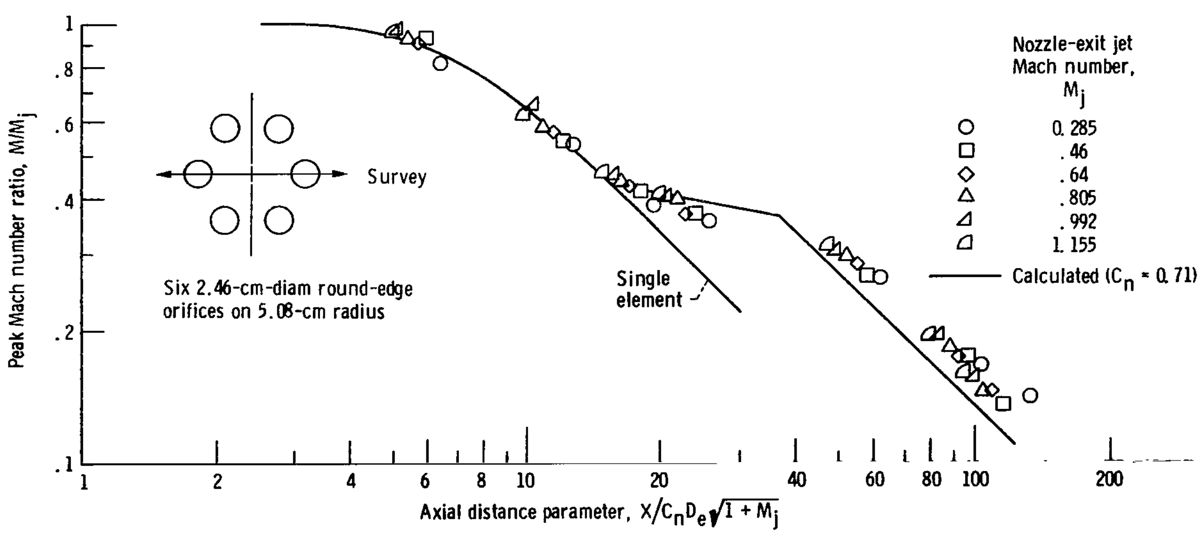

Figure 46. - Peak axial Mach number decay of 0-6-0 multiorifice (round edge) nozzle with spacing ratio s_1/d_1 of 1.064. Configuration 46; equivalent diameter, D_e, 2.46 centimeters.

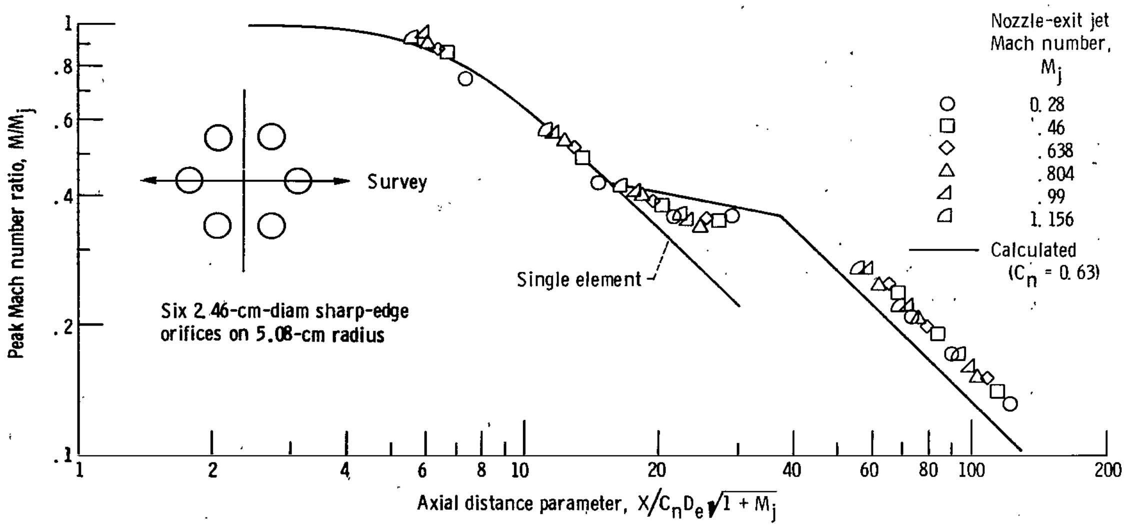

Figure 47. - Peak axial Mach number decay of 0-6-0 multiorifice (sharp edge) nozzle with spacing ratio s_1/d_1 of 1.064. Configuration 47; equivalent diameter, D_e, 2.46 centimeters.

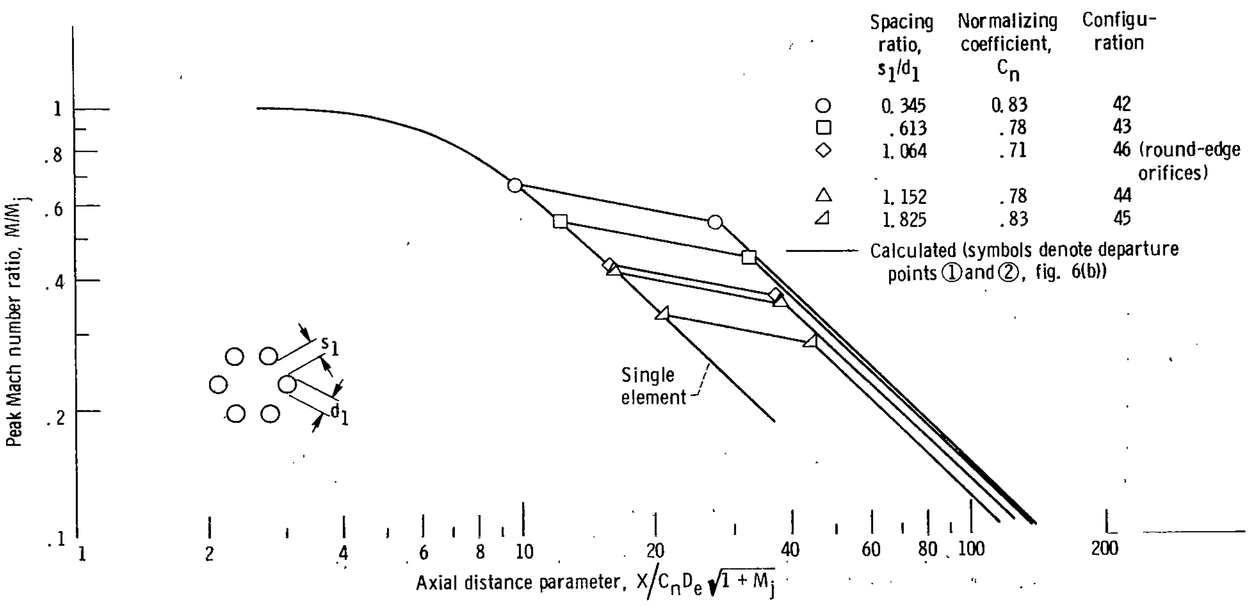

Figure 48. - Effect of circumferential spacing on peak axial Mach number decay for 0-6-0 multitube or multiorifice nozzles.

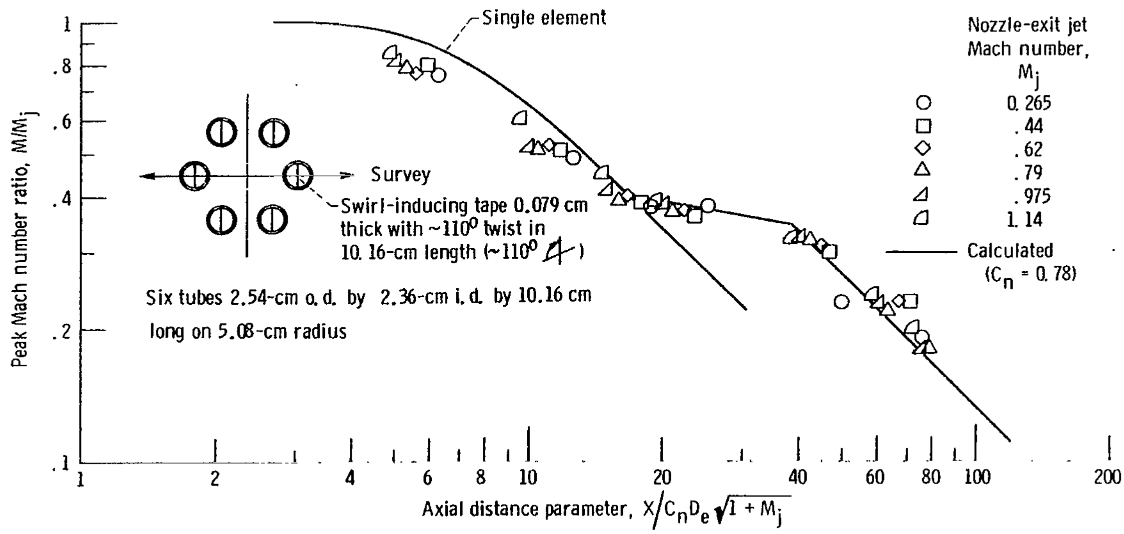

Figure 49. - Peak axial Mach number decay of 0-6-0 multitube nozzle with spacing ratio s_1/d_1 of 1.152 and swirl-inducing tape in each tube. Configuration 48 (configuration 44 with swirl tapes).

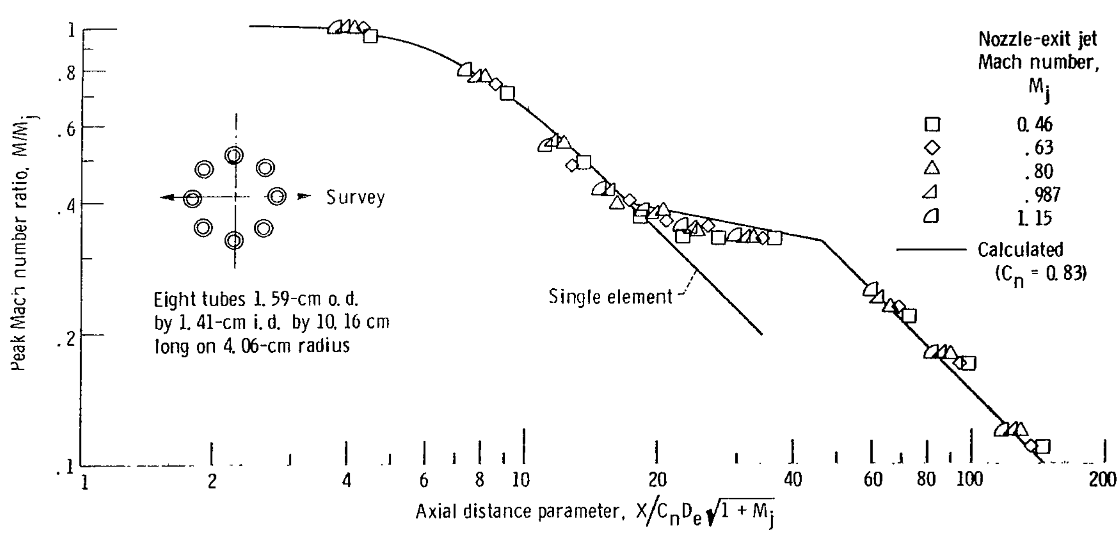

Figure 50. - Peak axial Mach number decay of 0-8-0 multitube nozzle with spacing ratio s_1/d_1 of 1.25. Configuration 49 (core nozzle of configurations 103, 104, and 108 to 111).

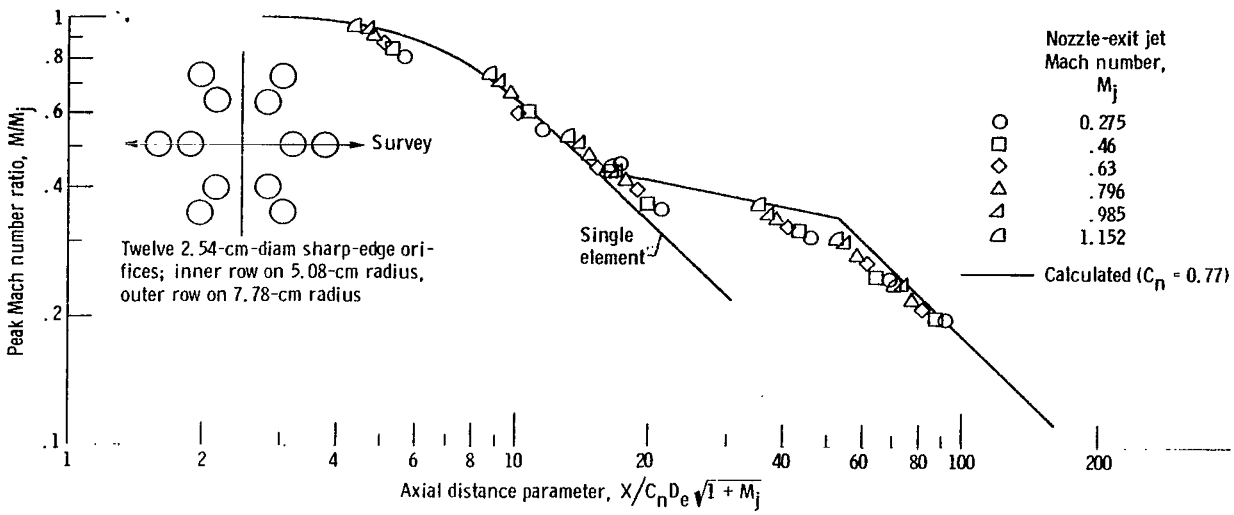

Figure 51. - Peak axial Mach number decay of 0-6-6 multiorifice (sharp edge) nozzle with spacing ratios $r_2/s_2 = 0.0304$ and $s_1/d_1 = 1.0$. Configuration 50; equivalent diameter, D_e, 2.54 centimeters.

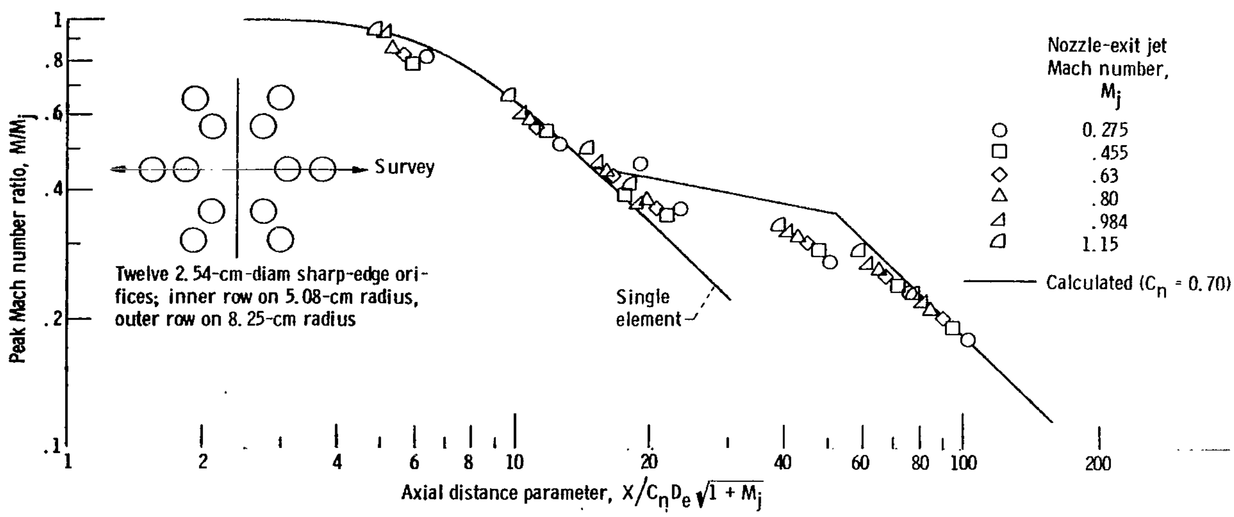

Figure 52. - Peak axial Mach number decay of 0-6-6 multiorifice (sharp edge) nozzle with spacing ratios $r_2/s_2 = 0.111$ and $s_1/d_1 = 1.0$. Configuration 51; equivalent diameter, D_e, 2.54 centimeters.

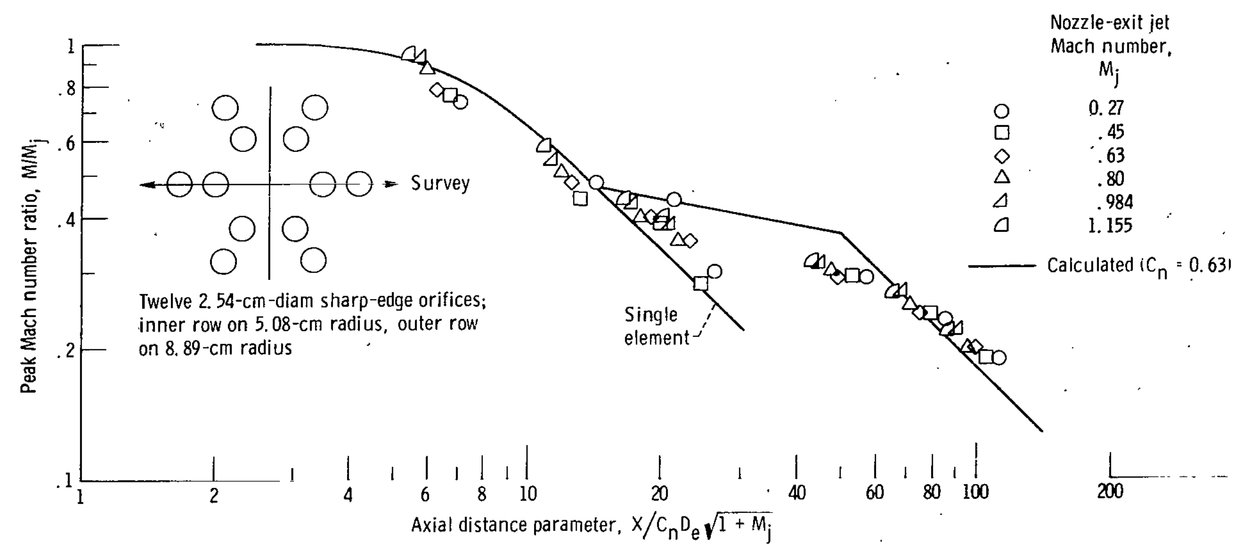

Figure 53. - Peak axial Mach number decay of 0-6-6 multiorifice (sharp edge) nozzle with spacing ratios r_2/s_2 = 0.200 and s_1/d_1 = 1.0. Configuration 52; equivalent diameter, D_e, 2.54 centimeters.

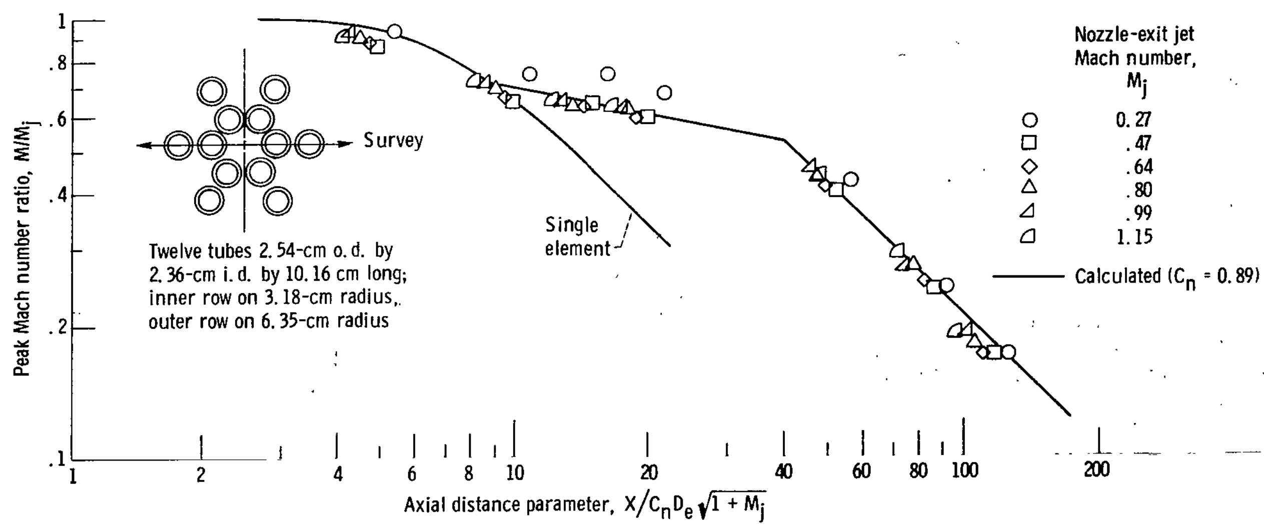

Figure 54. - Peak axial Mach number decay of 0-6-6 multitube nozzle with spacing ratios r_2/s_2 = 0.204 and s_1/d_1 = 0.345. Configuration 53; equivalent diameter, D_e, 2.36 centimeters.

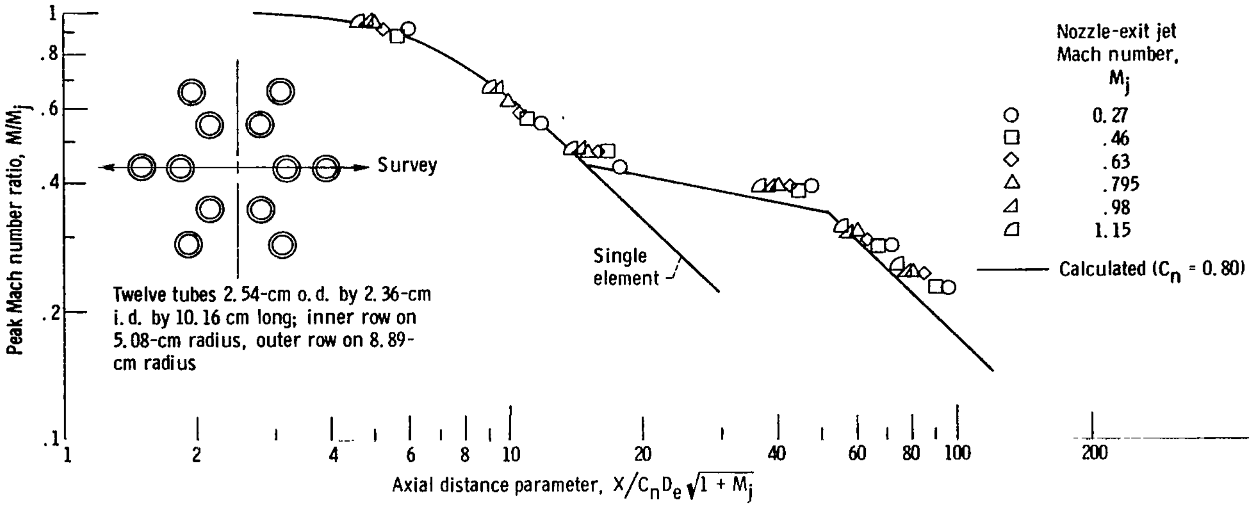

Figure 55. - Peak axial Mach number decay of 0-6-6 multitube nozzle with spacing ratios $r_2/s_2 = 0.222$ and $s_1/d_1 = 1.152$. Configuration 54; equivalent diameter, D_e, 2.36 centimeters.

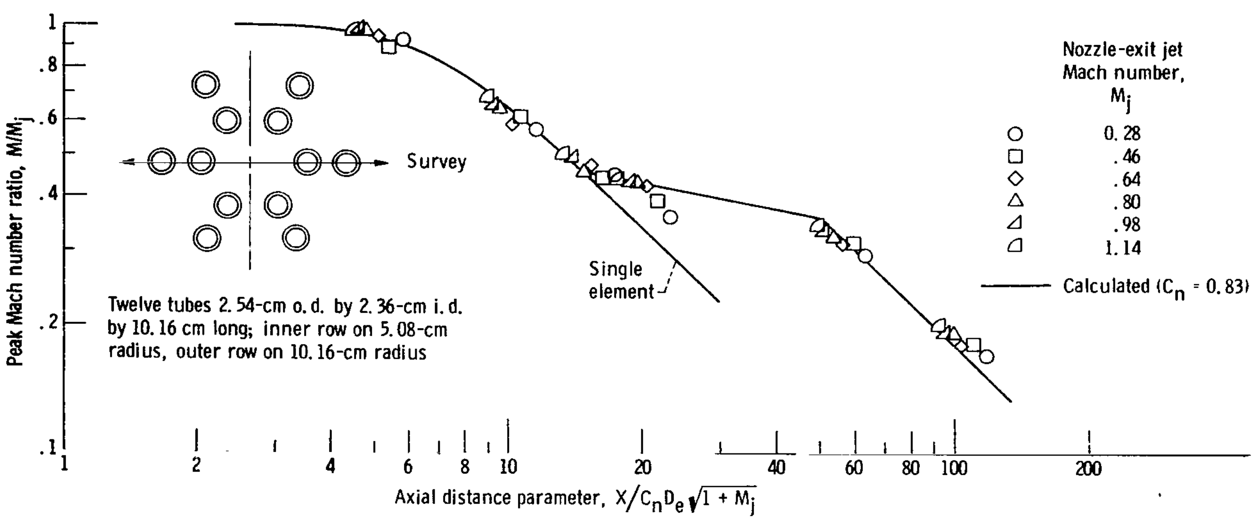

Figure 56. - Peak axial Mach number decay of 0-6-6 multitube nozzle with spacing ratios $r_2/s_2 = 0.349$ and $s_1/d_1 = 1.152$. Configuration 55; equivalent diameter, D_e, 2.36 centimeters.

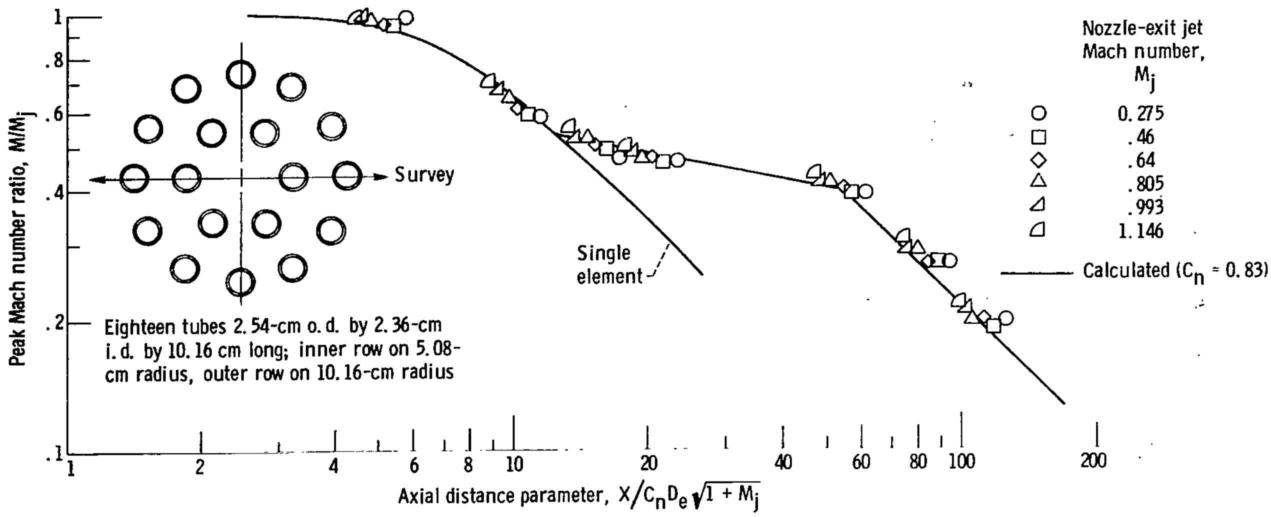

Figure 57. - Peak axial Mach number decay of 0-6-12 multitube nozzle with spacing ratios $r_2/s_2 = 0.938$ and $s_1/d_1 = 1.152$. Configuration 56; equivalent diameter, D_e, 2.36 centimeters.

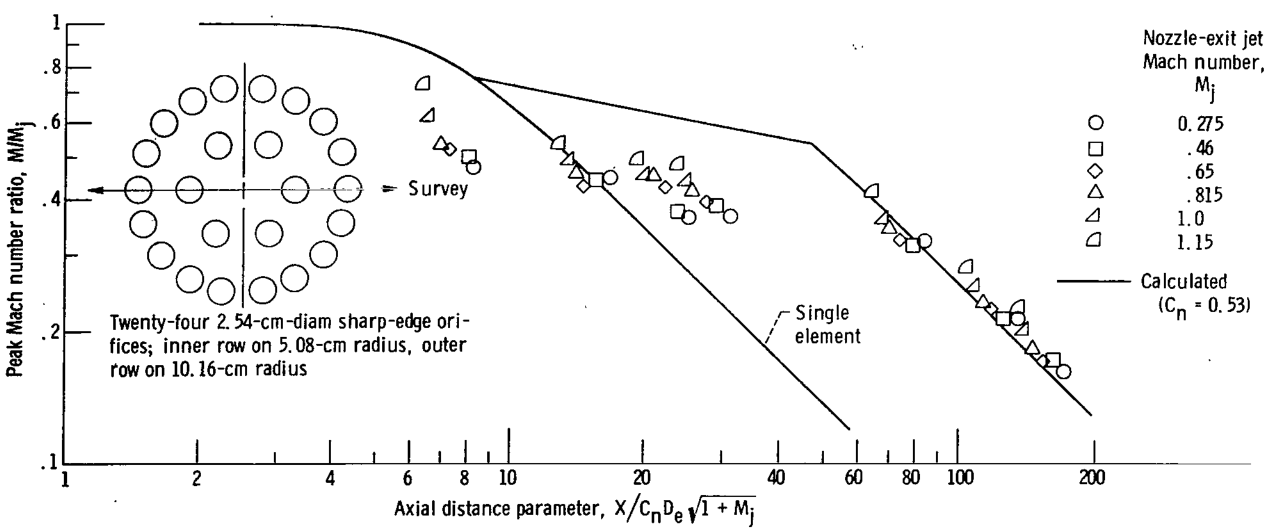

Figure 58. - Peak axial Mach number decay of 0-6-18 multiorifice (sharp edge) nozzle with spacing ratios $r_2/s_2 = 2.56$ and $s_1/d_1 = 1.0$. Configuration 57; equivalent diameter, D_e, 2.54 centimeters; spaces between orifices pumped subatmospheric.

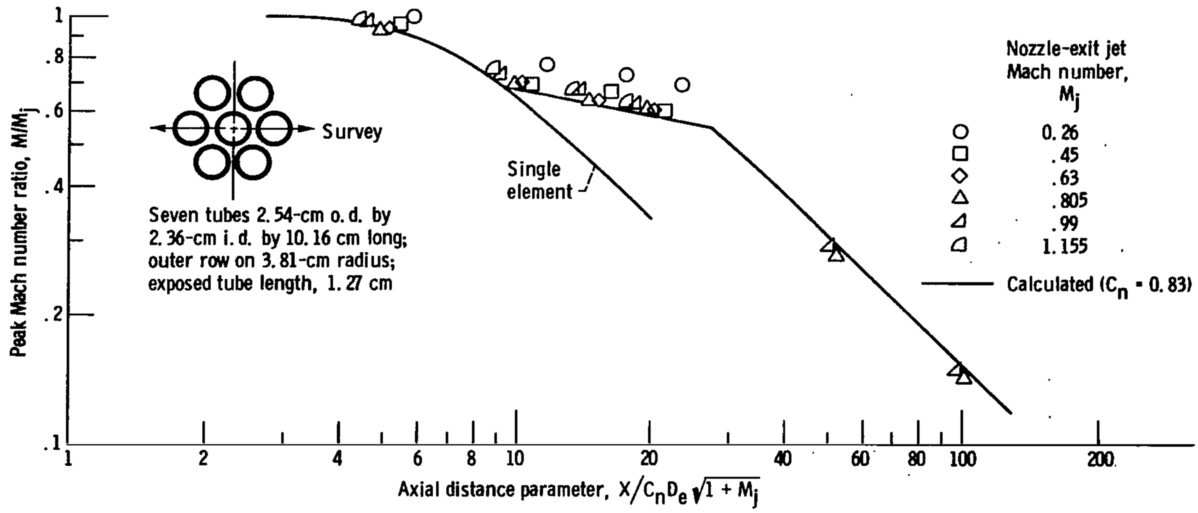

Figure 59. - Peak axial Mach number decay of 1-6-0 multitube nozzle with spacing ratios $r_1/s_1 = 1.0$ and $s_1/d_1 = 0.613$. Configuration 58; equivalent diameter, D_e, 2.36 centimeters.

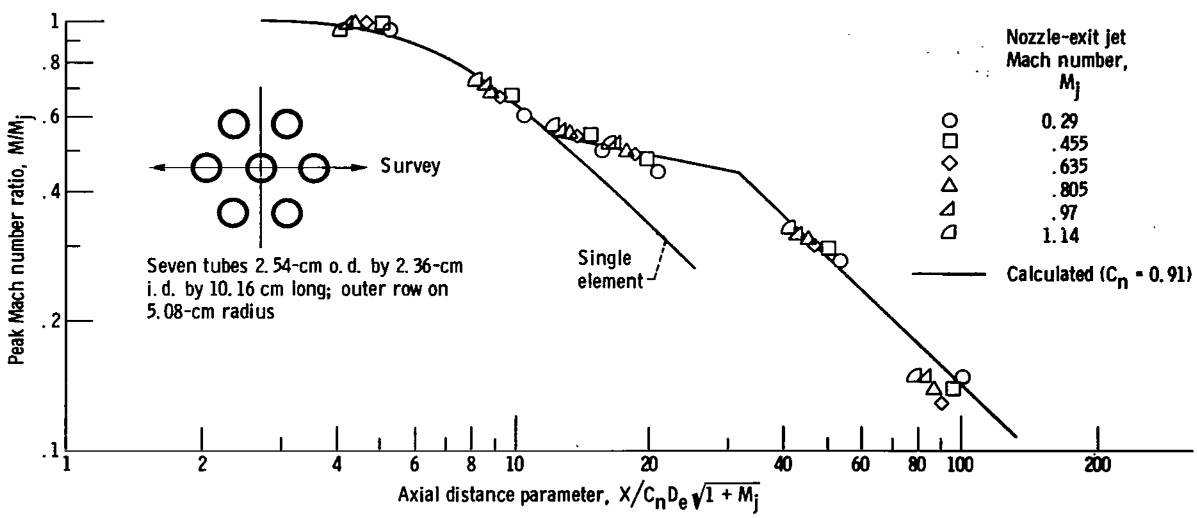

Figure 60. - Peak axial Mach number decay of 1-6-0 multitube nozzle with spacing ratios $r_1/s_1 = 1.0$ and $s_1/d_1 = 1.152$. Configuration 59; equivalent diameter, D_e, 2.36 centimeters.

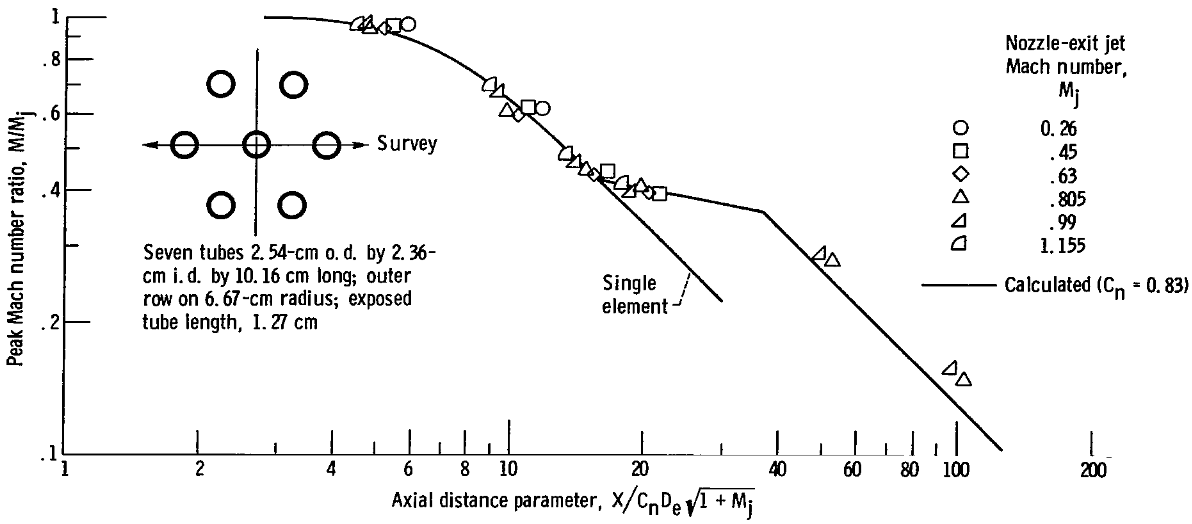

Figure 61. - Peak axial Mach number decay of 1-6-0 multitube nozzle with spacing ratios $r_1/s_1 = 1.0$ and $s_1/d_1 = 1.83$. Configuration 60; equivalent diameter, D_e, 2.36 centimeters.

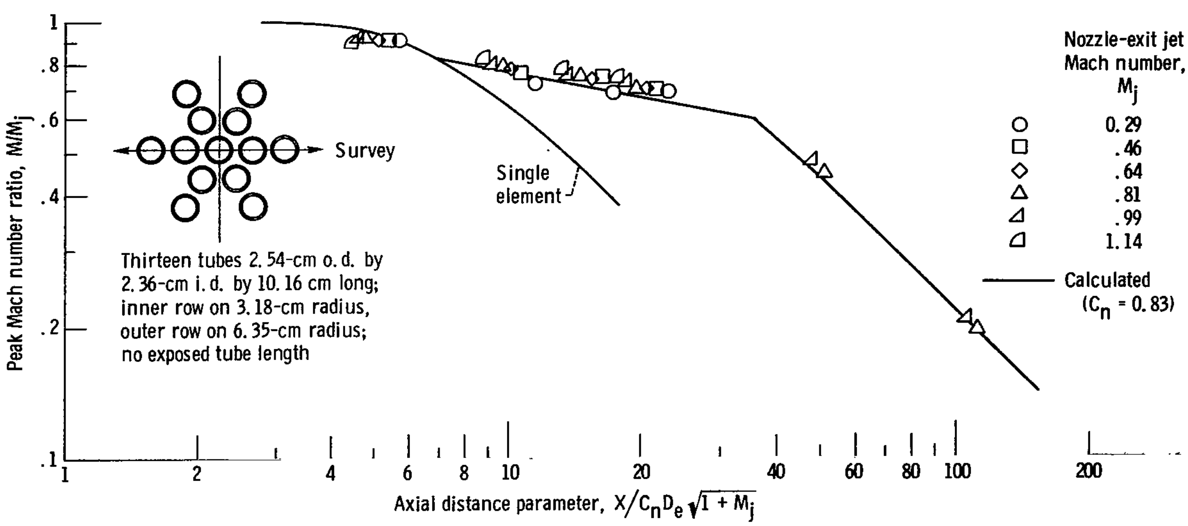

Figure 62. - Peak axial Mach number decay of 1-6-6 multitube nozzle with spacing ratios $r_1/s_1 = 1.0$ and $s_1/d_1 = 0.344$. Configuration 61; equivalent diameter, D_e, 2.36 centimeters.

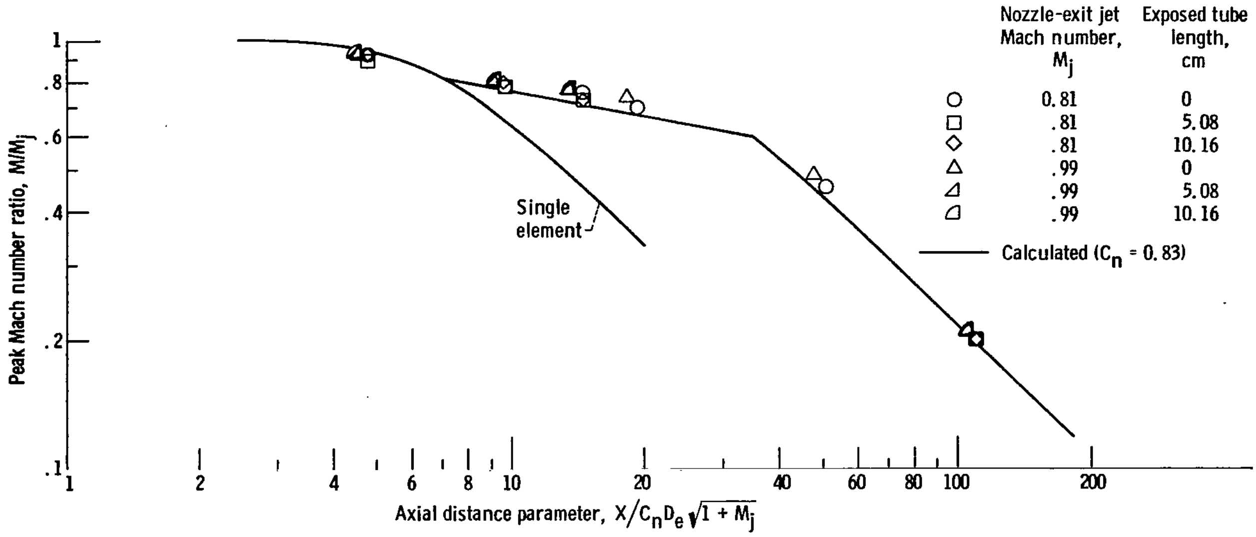

Figure 63. - Effect of exposed nozzle tube length on peak axial Mach number decay of 1-6-6 multitube nozzle with spacing ratios r_1/s_1 = 1.0 and s_1/d_1 = 0.344. Configuration 61; equivalent diameter, D_e, 2.36 centimeters.

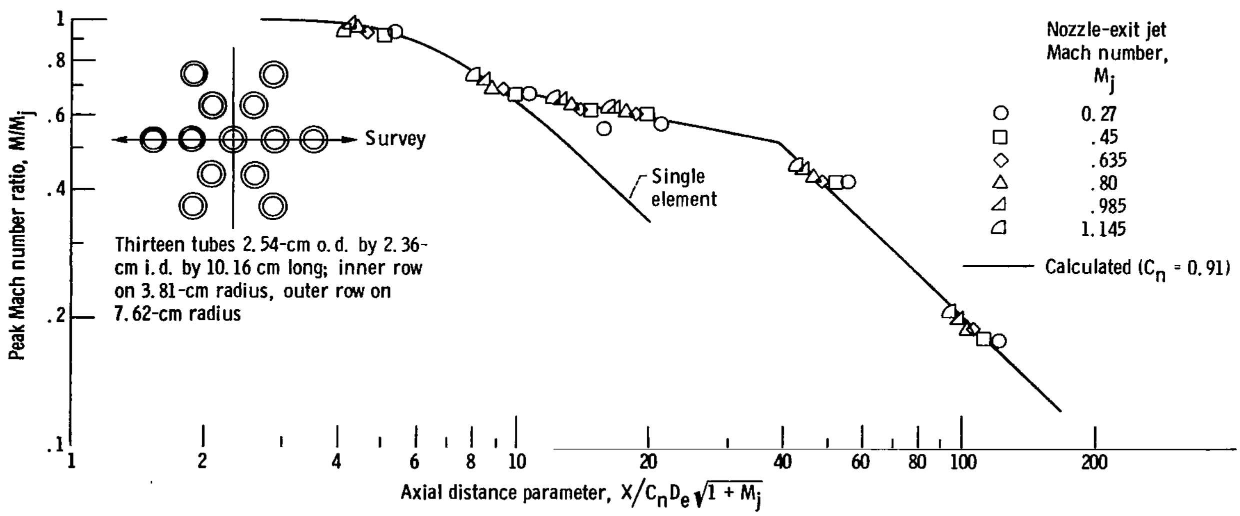

Figure 64. - Peak axial Mach number decay of 1-6-6 multitube nozzle with spacing ratios r_1/s_1 = 1.0 and s_1/d_1 = 0.613. Configuration 62; equivalent diameter, D_e, 2.36 centimeters.

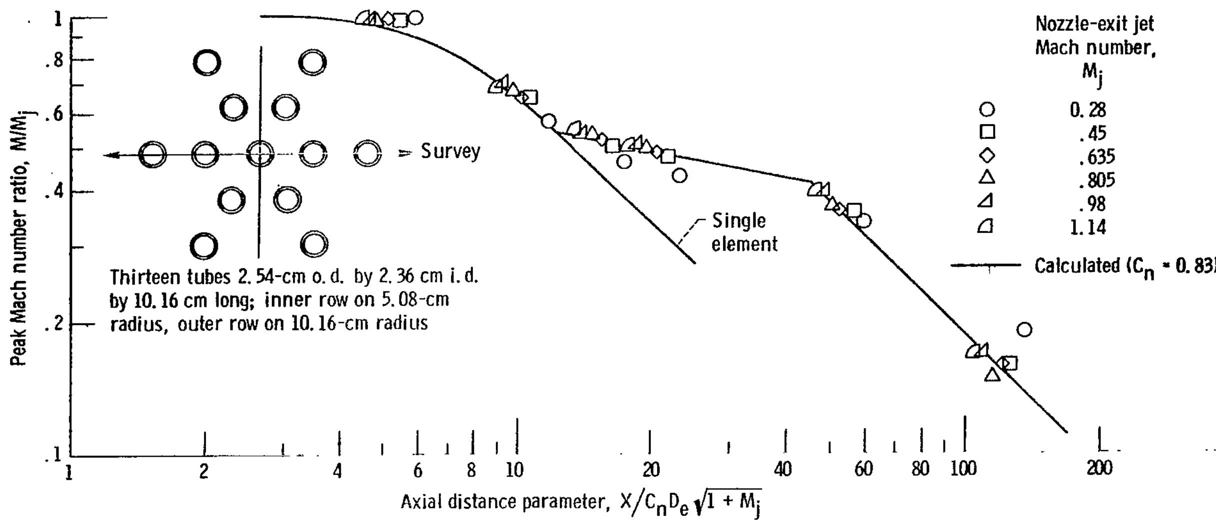

Figure 65. - Peak axial Mach number decay of 1-6-6 multitube nozzle with spacing ratios $r_1/s_1 = 1.0$ and $s_1/d_1 = 1.152$. Configuration 63; equivalent diameter, D_e, 2.36 centimeters.

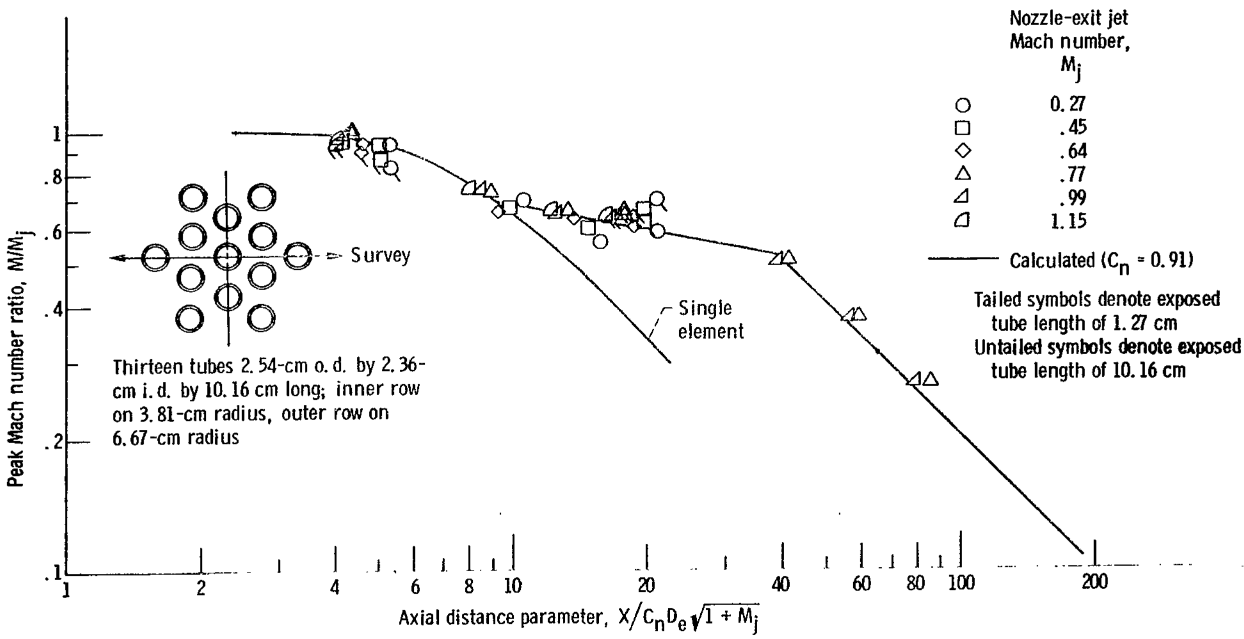

Figure 66. - Effect of exposed nozzle tube length on peak axial Mach number decay of 1-6-6 multitube nozzle with spacing ratios $r_1/s_1 = 1.0$ and $s_1/d_1 = 0.613$. Configuration 64; equivalent diameter, D_e, 2.36 centimeters.

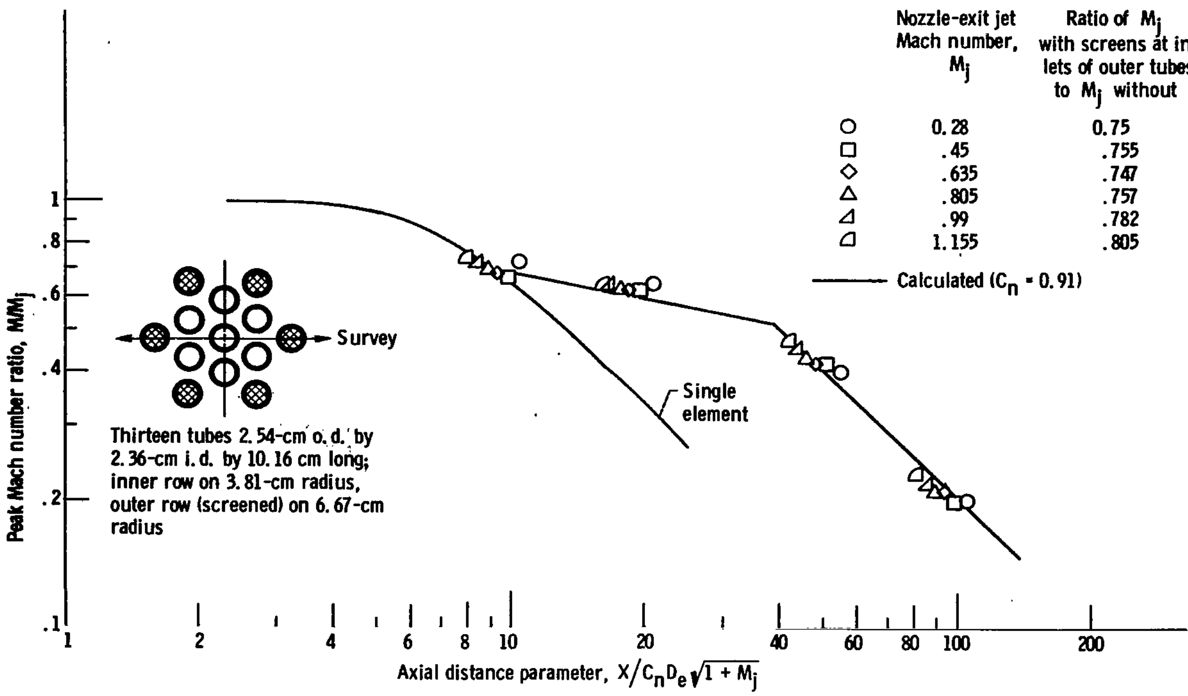

Figure 67. - Effect of screens at inlets of outer tubes on peak axial Mach number decay of 1-6-6 multitube nozzle with spacing ratios $r_1/s_1 = 1.0$ and $s_1/d_1 = 0.613$. Configuration 65; equivalent diameter, D_e, 2.36 centimeters; all tubes 10.16 centimeters long.

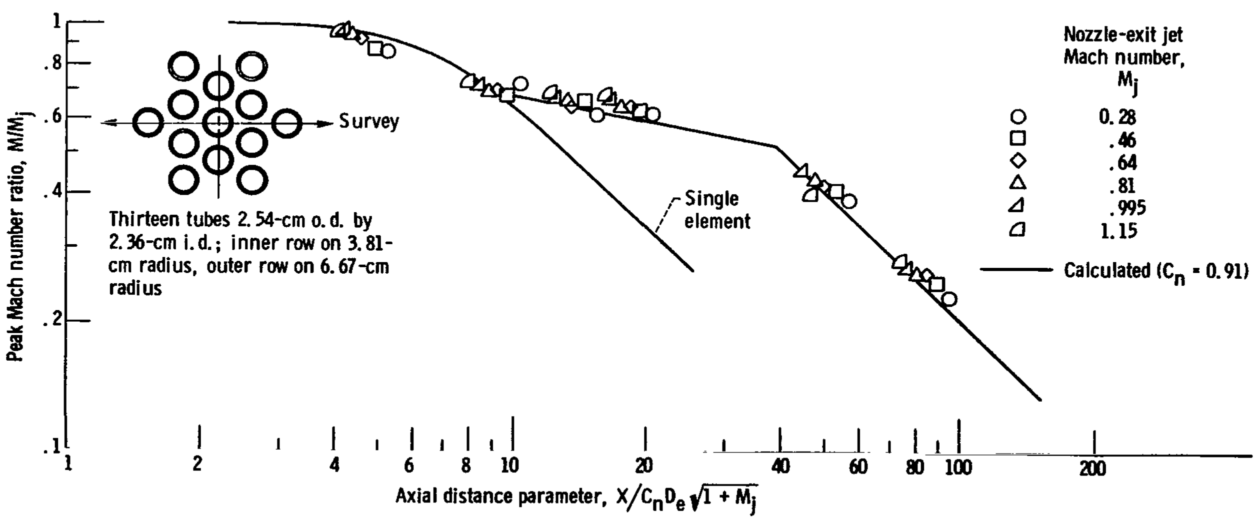

Figure 68. - Effect of tube length on peak axial Mach number decay of 1-6-6 multitube nozzle with spacing ratios $r_1/s_1 = 1.0$ and $s_1/d_1 = 0.613$ - six outer tubes, 3.81 centimeters long; all other tubes, 10.16 centimeters long. Configuration 66; equivalent diameter, D_e, 2.36 centimeters.

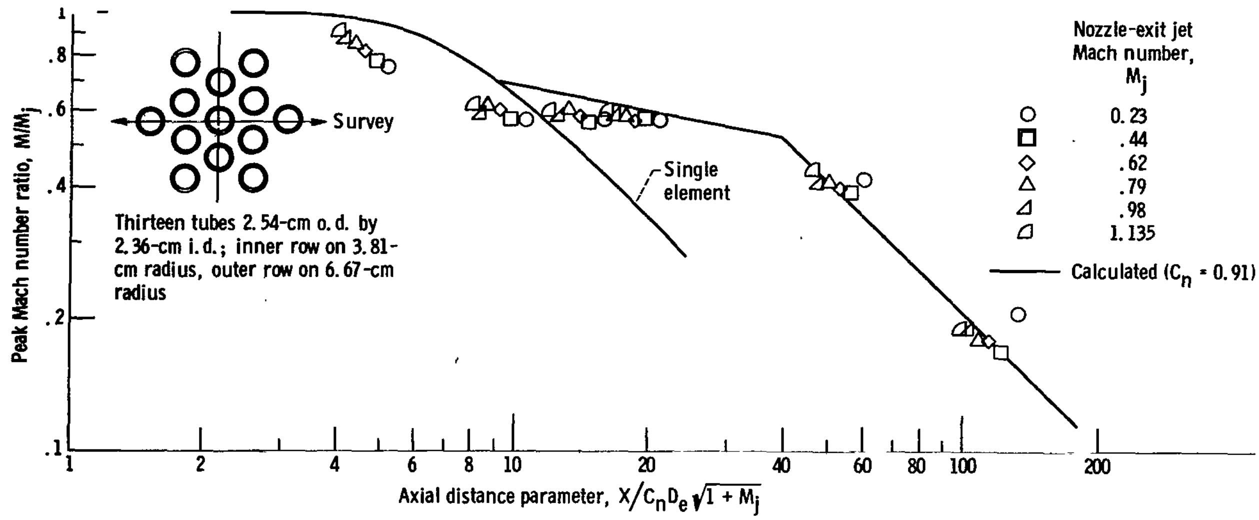

Figure 69. - Effect of tube length on peak axial Mach number decay of 1-6-6 multitube nozzle with spacing ratios r_1/s_1 = 1.0 and s_1/d_1 = 0.613 - nozzle centerline tube, 1.27 centimeters long; six inner tubes, 6.35 centimeters long; six outer tubes, 10.16 centimeters long. Configuration 67; equivalent diameter, D_e, 2.36 centimeters.

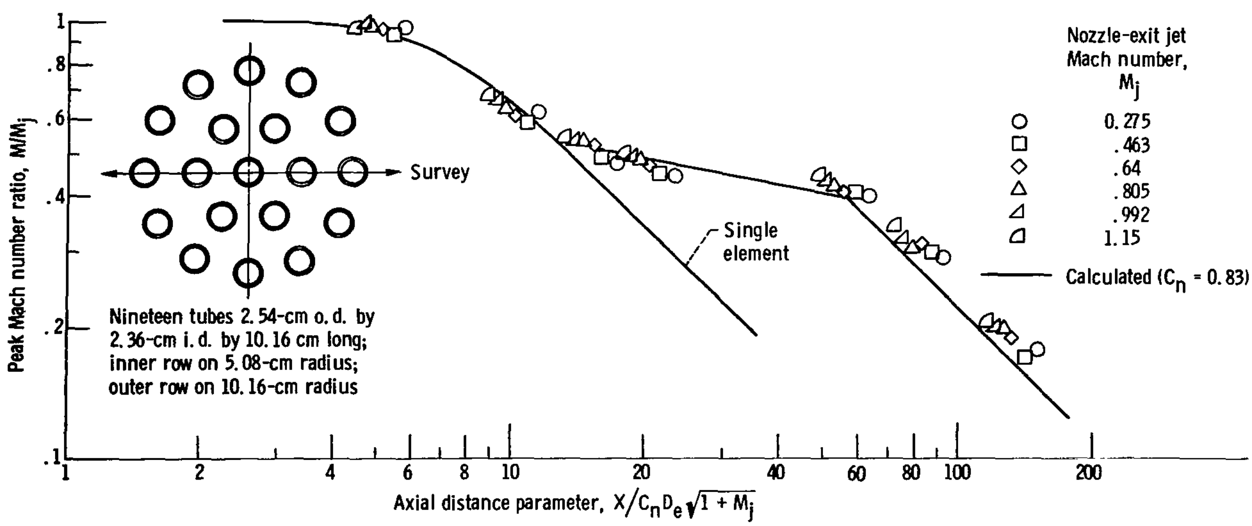

Figure 70. - Peak axial Mach number decay of 1-6-12 multitube nozzle with spacing ratios r_1/s_1 = 1.0 and s_1/d_1 = 1.152. Configuration 68; equivalent diameter, D_e, 2.36 centimeters.

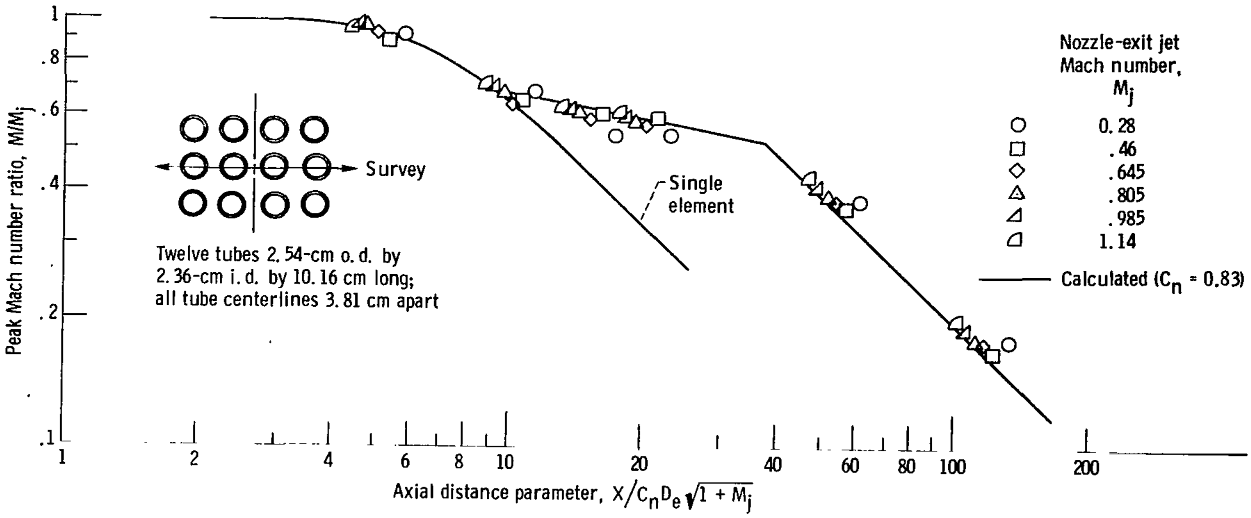

Figure 71. - Peak axial Mach number decay of 12-tube rectangular-array nozzle (4 tubes by 3 tubes) with spacing ratio s_1/d_1 = 0.613. Configuration 69; equivalent diameter, D_e, 2.36 centimeters.

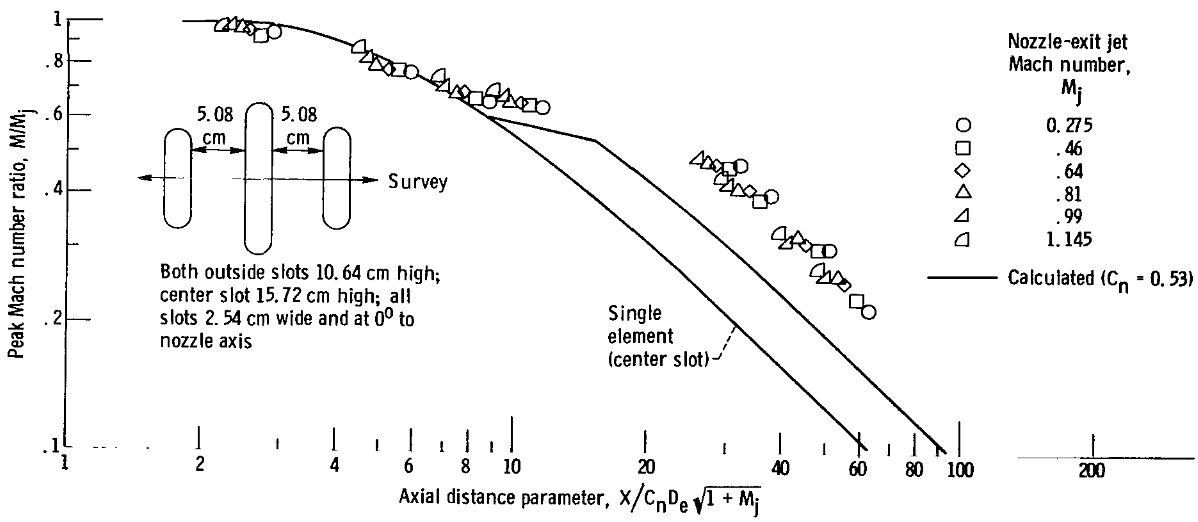

Figure 72. - Peak axial Mach number decay of nozzle composed of three round-end rectangular slots - all slots at 0° to nozzle axis. Configuration 70; equivalent diameter, D_e, 7.25 centimeters (center slot); spaces between slots pumped slightly subatmospheric.

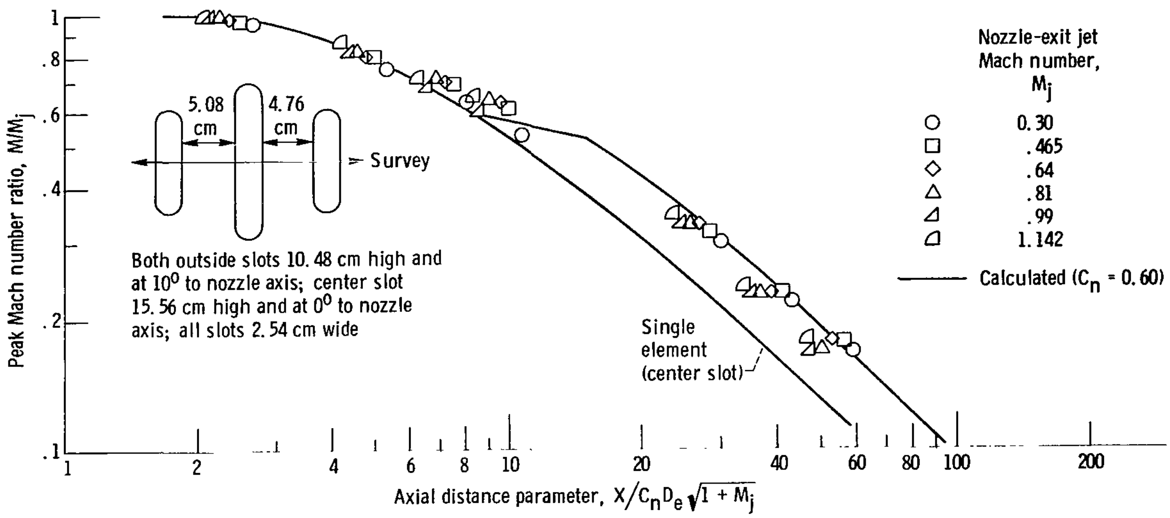

Figure 73. - Peak axial Mach number decay of nozzle composed of three round-end rectangular slots - both outside slots at 10° to nozzle axis. Configuration 71; equivalent diameter, D_e, 6.96 centimeters (center slot).

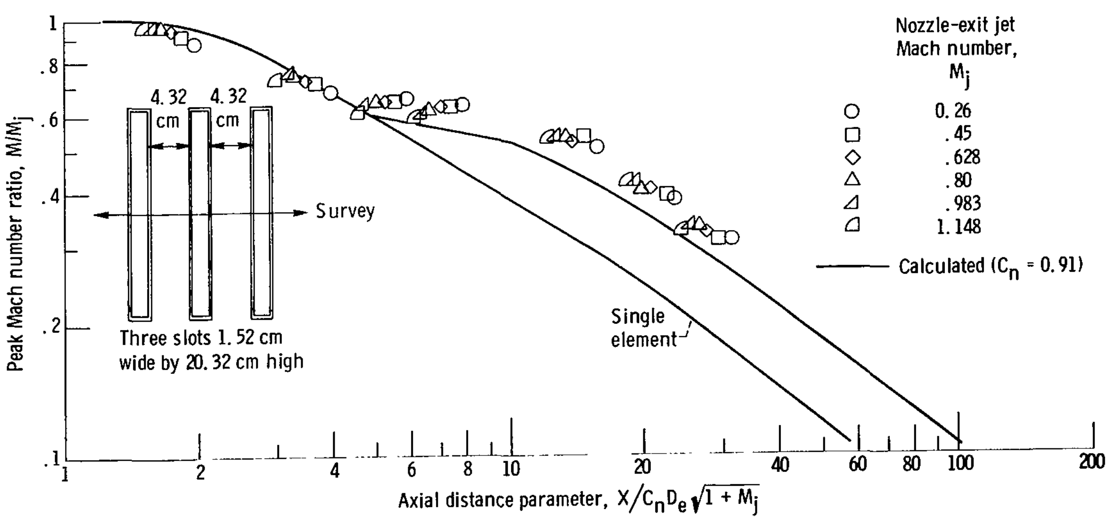

Figure 74. - Peak axial Mach number decay of three-slot convergent nozzle with spacing ratio s_1/w = 2.83. Configuration 72 (single element, configuration 23); equivalent diameter, D_e, 6.27 centimeters.

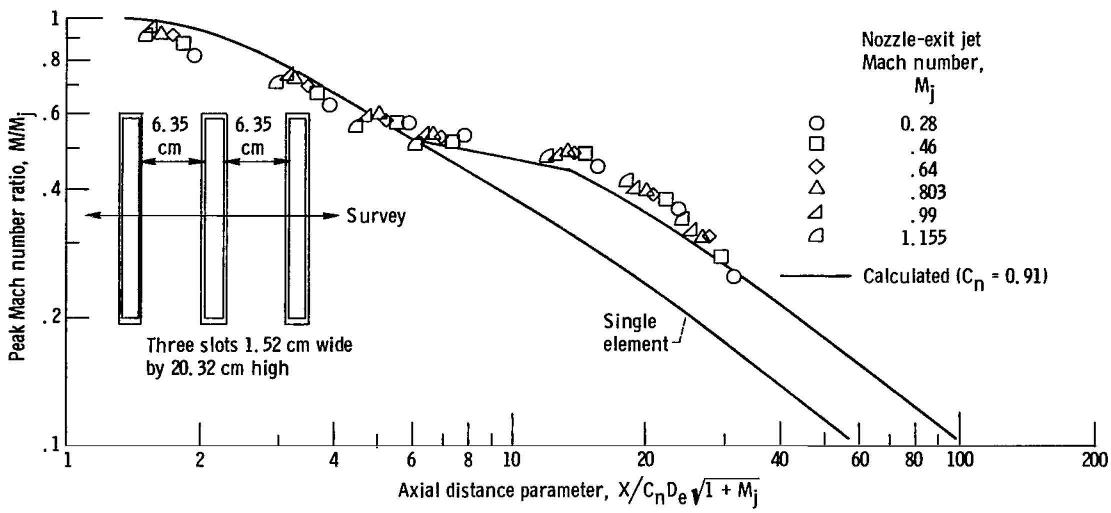

Figure 75. - Peak axial Mach number decay of three-slot convergent nozzle with spacing ratio $s_1/w = 4.17$. Configuration 73 (single element, configuration 23); equivalent diameter, D_e, 6.27 centimeters.

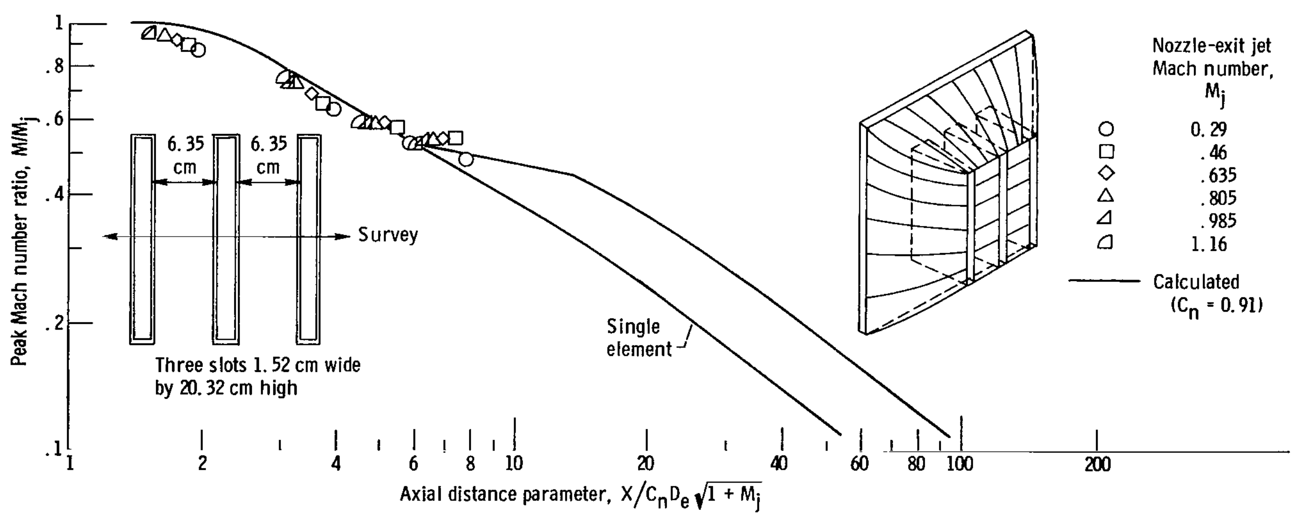

Figure 76. - Peak axial Mach number decay of three-slot convergent nozzle (configuration 73) with hemispherical afterbody flush with nozzle exits. Configuration 74; equivalent diameter, D_e, 6.27 centimeters.

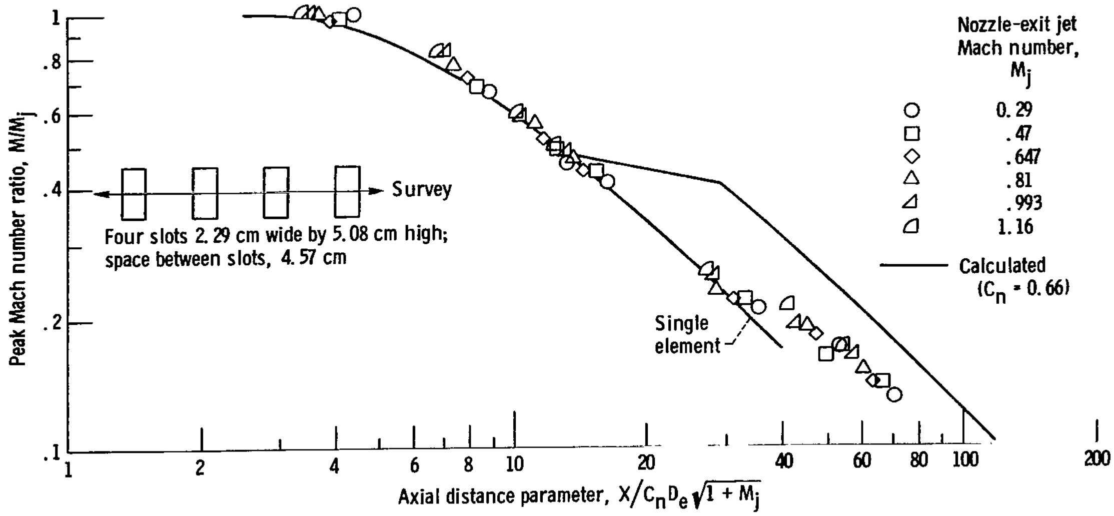

Figure 77. - Peak axial Mach number decay of four-slot, sharp-edge-orifice nozzle with spacing ratio s_1/w = 2.0. Configuration 75 (single element, configuration 15); equivalent diameter, D_e, 3.85 centimeters.

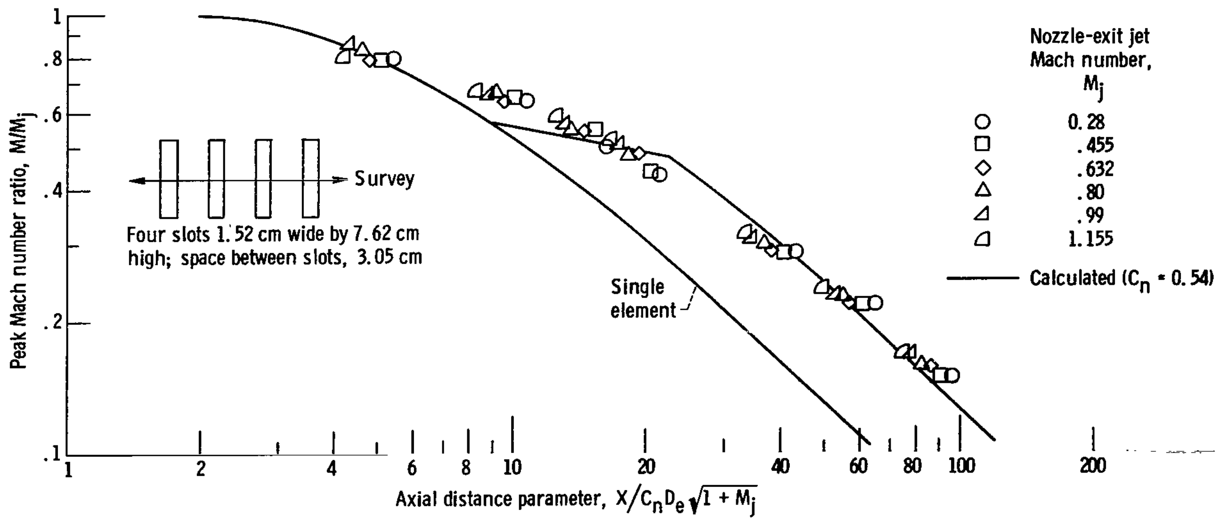

Figure 78. - Peak axial Mach number decay of four-slot, sharp-edge-orifice nozzle with spacing ratio s_1/w = 2.0. Configuration 76 (single element, configuration 16); equivalent diameter, D_e, 3.85 centimeters; spaces between slots pumped slightly subatmospheric.

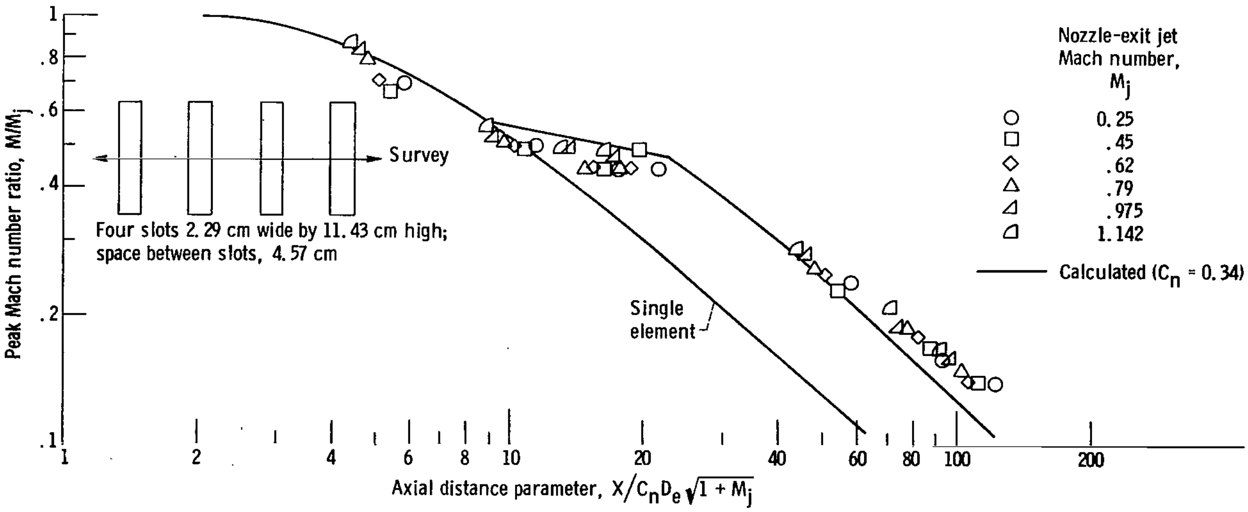

Figure 79. - Peak axial Mach number decay of four-slot, sharp-edge-orifice nozzle with spacing ratio s_1/w = 2.0. Configuration 77 (single element, configuration 17); equivalent diameter, D_e, 5.76 centimeters.

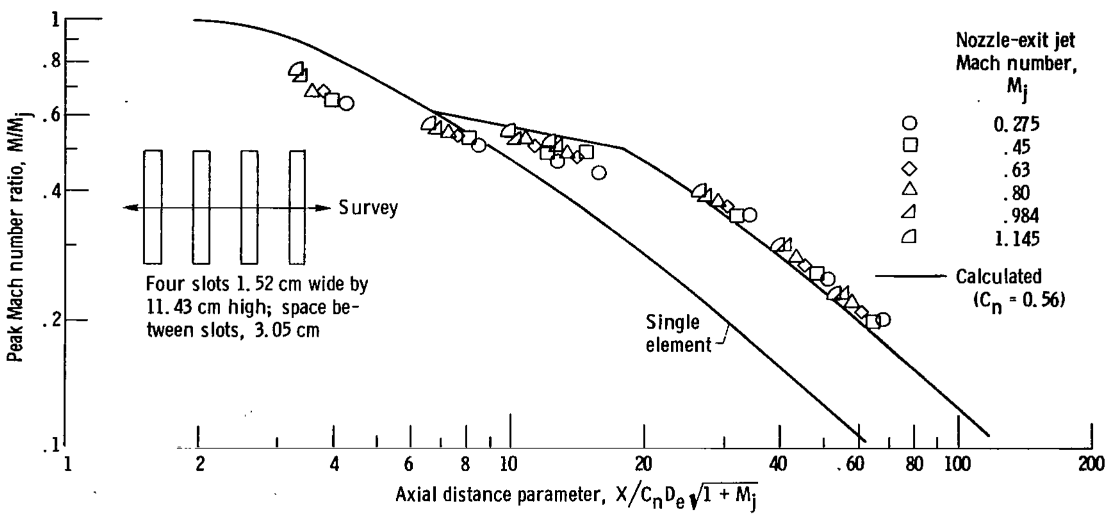

Figure 80. - Peak axial Mach number decay of four-slot, sharp-edge-orifice nozzle with spacing ratio s_1/w = 2.0. Configuration 78 (single element, configuration 18); equivalent diameter, D_e, 4.71 centimeters; spaces between slots pumped slightly subatmospheric at 0.32-centimeter survey location.

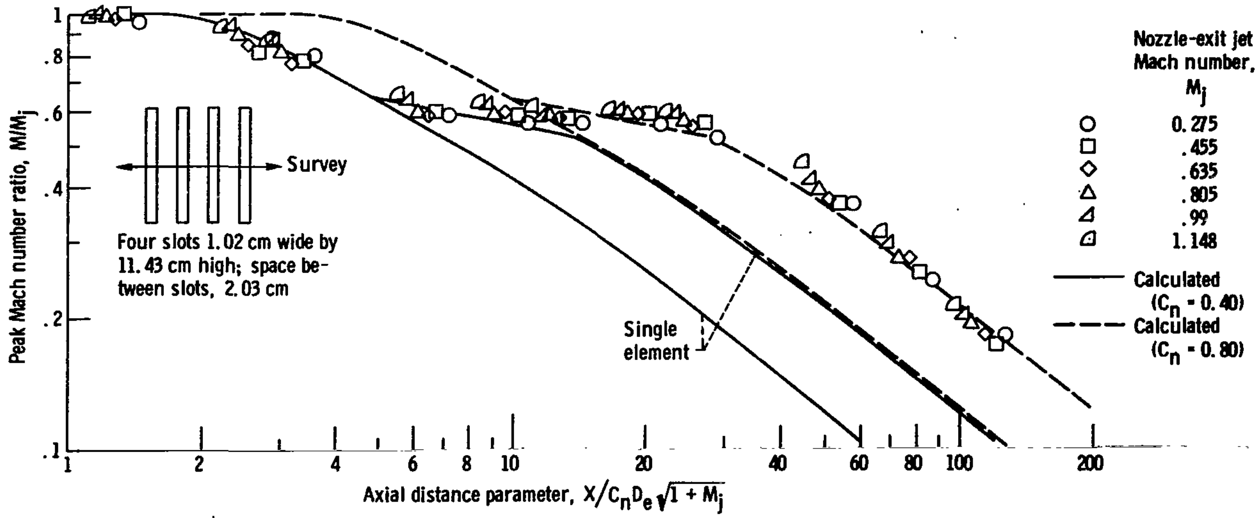

Figure 81. - Peak axial Mach number decay of four-slot, sharp-edge-orifice nozzle with spacing ratio s_1/w = 2.0. Configuration 79 (single element, configuration 19); equivalent diameter, D_e, 3.85 centimeters; spaces between slots pumped subatmospheric at 0.32-centimeter and 2.54-centimeter survey stations.

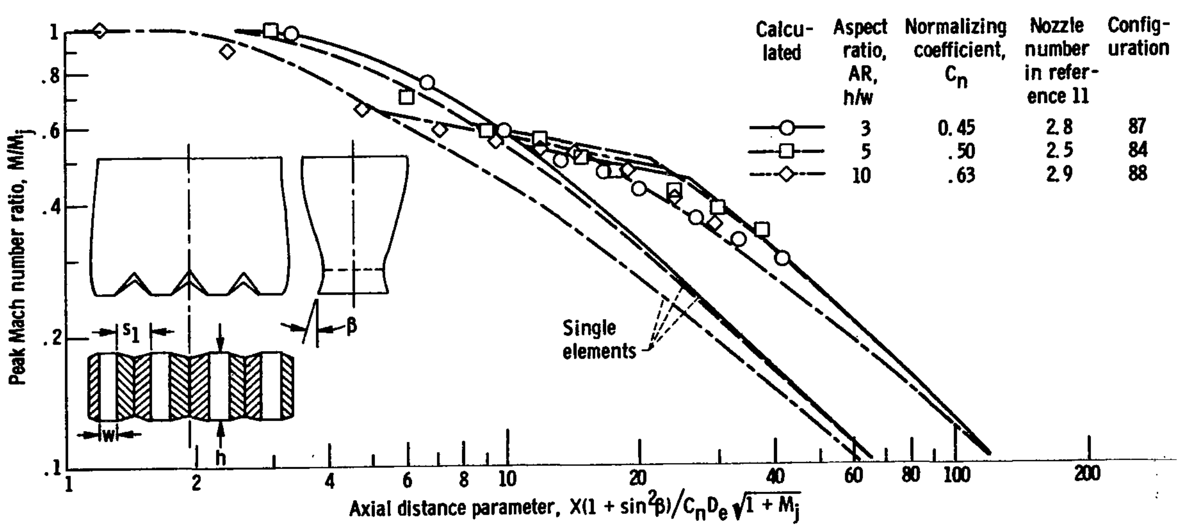

Figure 82. - Effect of aspect ratio on peak axial Mach number decay of four-slot convergent rectangular nozzle. Spacing ratio, s_1/w, 2.0; wall divergence angle, β, 15°; nozzle-exit jet Mach number, M_j, 1.05. (From ref. 11.)

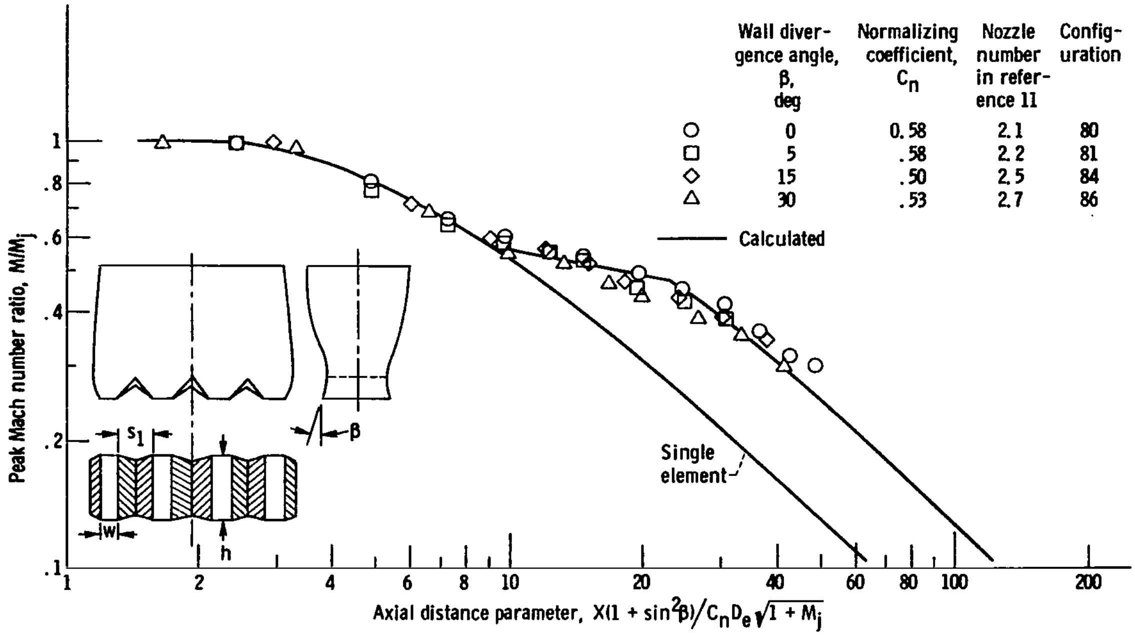

Figure 83. - Effect of wall divergence angle on peak axial Mach number decay of four-slot convergent rectangular nozzle. Spacing ratio, s_1/w, 2.0; aspect ratio, AR, 5; nozzle-exit jet Mach number, M_j, 1.05. (From ref. 11.)

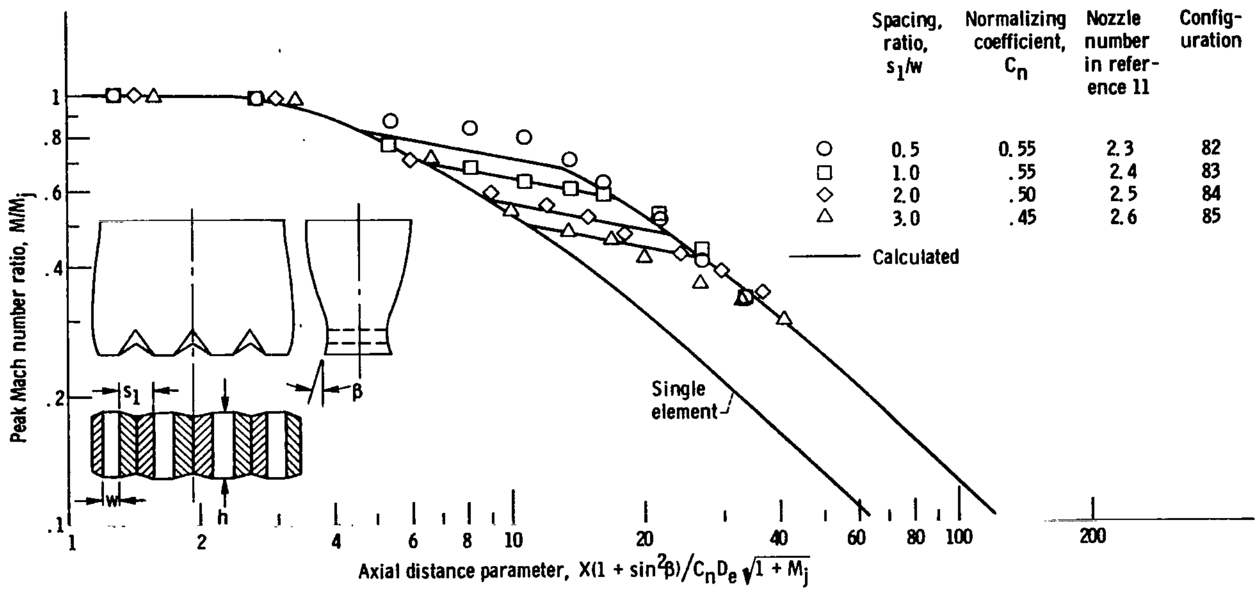

Figure 84. - Effect of spacing ratio s_1/w on peak axial Mach number decay of four-slot convergent rectangular nozzle. Aspect ratio, AR, 5; wall divergence angle, β, 15°; nozzle-exit jet Mach number, M_j, 1.05. (From ref. 11.)

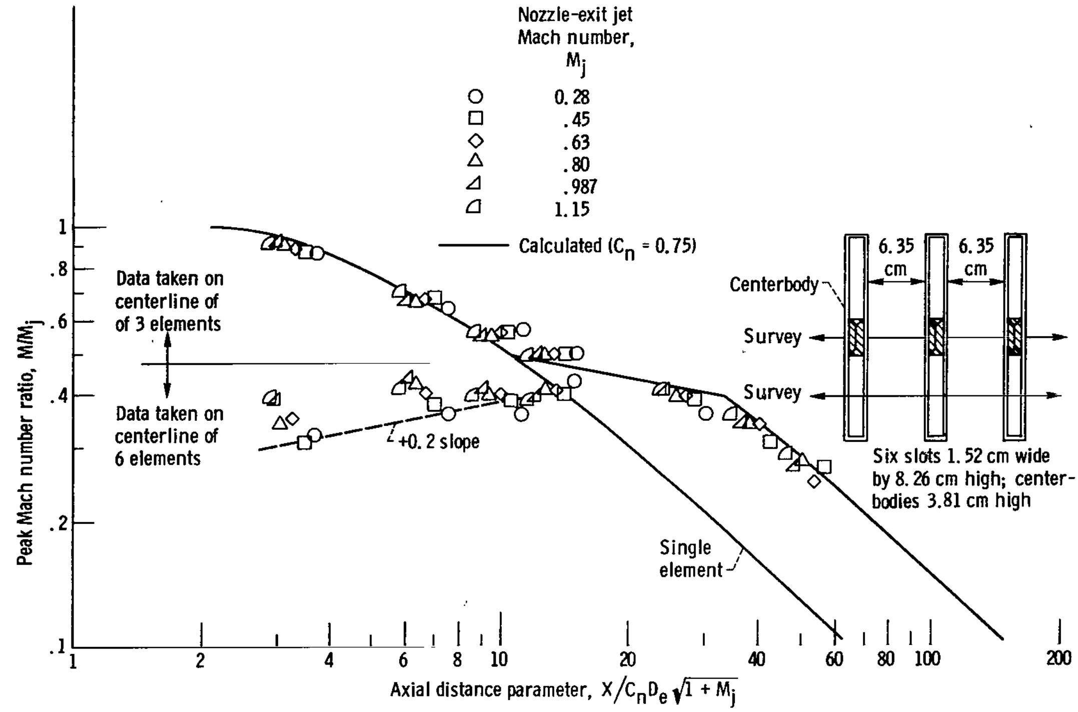

Figure 85. - Peak axial Mach number decay of six-slot ventilated convergent nozzle. Height-width ratio, h/w, 5.42; radial spacing, r_1, 3.81 centimeters. Configuration 89 (single element, configuration 21); equivalent diameter, D_e, 4.00 centimeters.

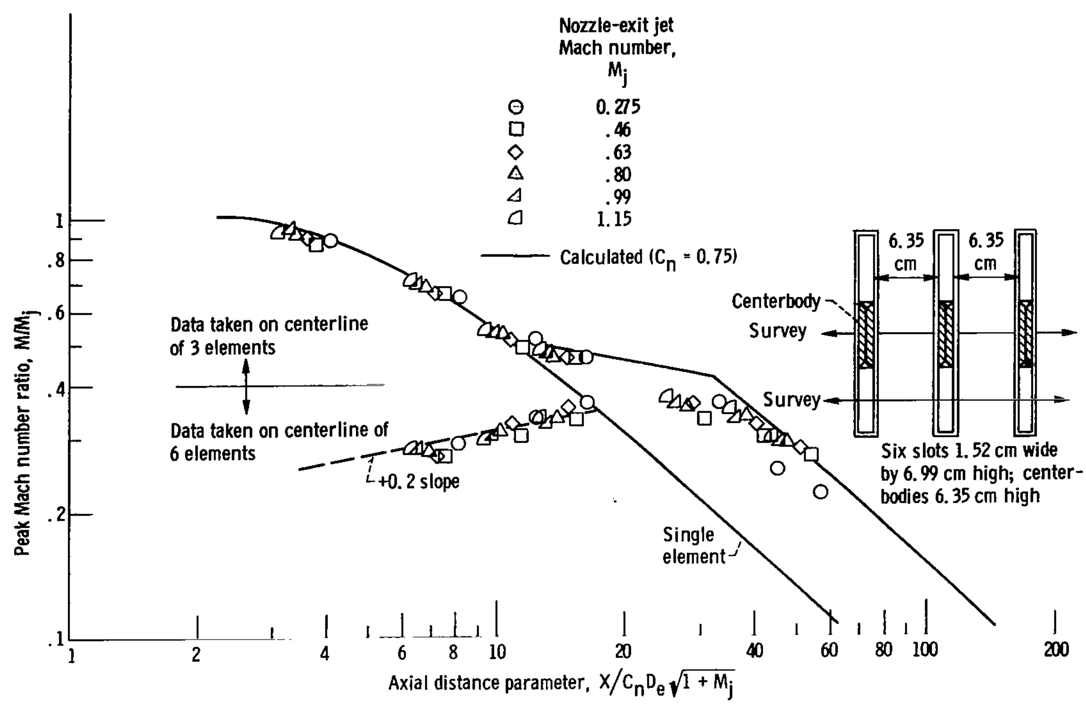

Figure 86. - Peak axial Mach number decay of six-slot ventilated convergent nozzle. Height-width ratio, h/w, 4.58; radial spacing, r_1, 6.35 centimeters. Configuration 90 (single element, configuration 20); equivalent diameter, D_e, 3.67 centimeters.

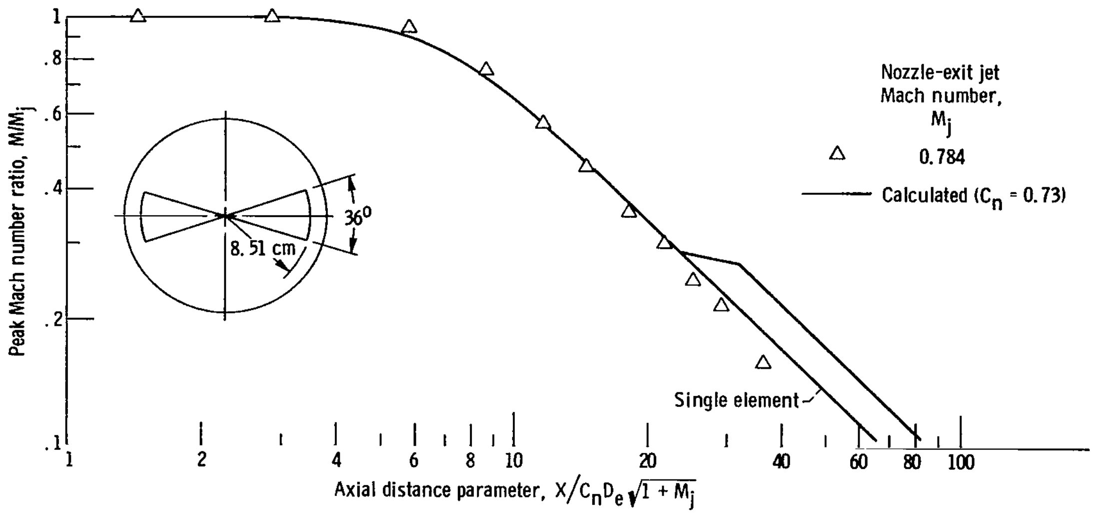

Figure 87. - Peak axial Mach number decay of two-lobe triangular convergent nozzle with circumferential spacing ratio s_l/w_l of 3.08 centimeters. Configuration 91; equivalent diameter, D_e, 5.40 centimeters. (From ref. 10.)

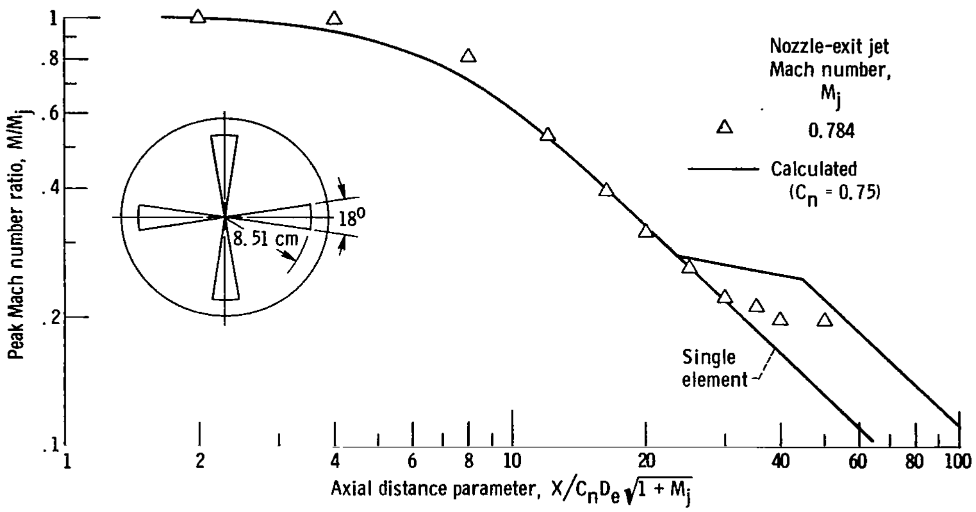

Figure 88. - Peak axial Mach number decay of four-lobe triangular convergent nozzle with circumferential spacing ratio s_l/w_l of 3.76. Configuration 92; equivalent diameter, D_e, 3.81 centimeters. (From ref. 10.)

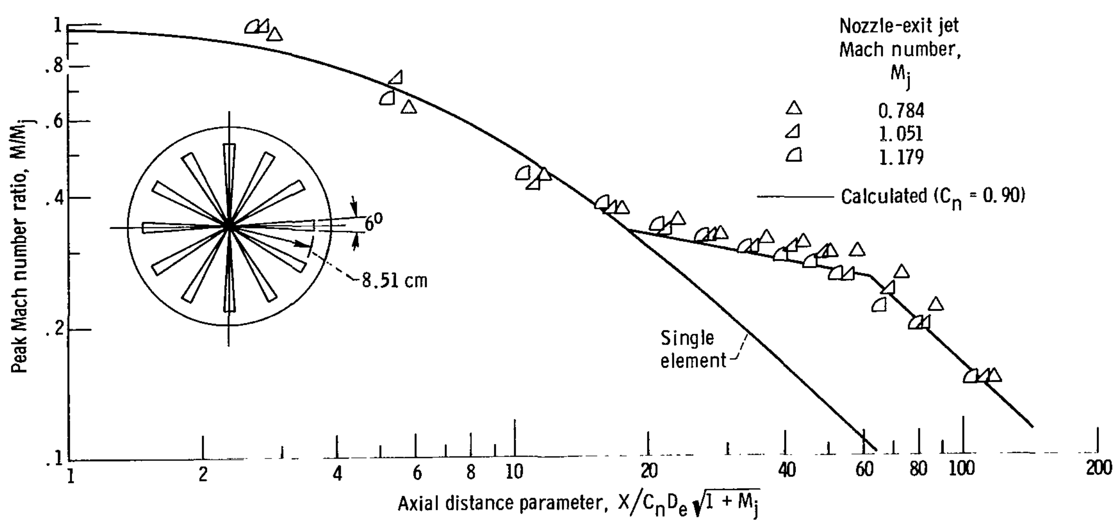

Figure 89. - Peak axial Mach number decay of 12-lobe triangular convergent nozzle with circumferential spacing ratio s_l/w_l of 3.98. Configuration 93; equivalent diameter, D_e, 2.20 centimeters. (From ref. 10.)

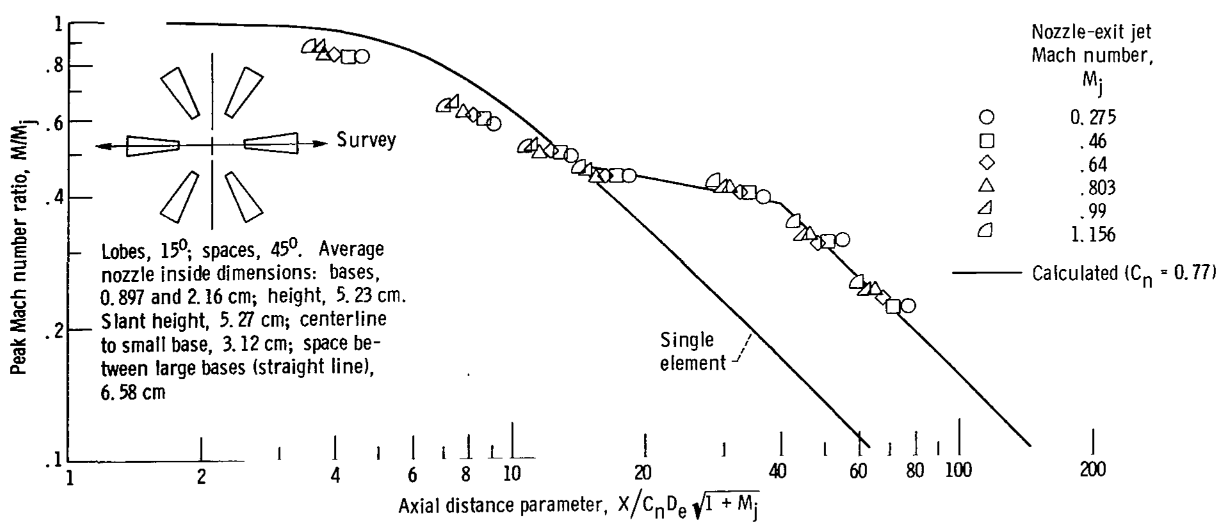

Figure 90. - Peak axial Mach number decay of six-lobe, flat-end trapezoidal nozzle with circumferential spacing ratio s_l/w_l of 3.06. Configuration 94 (single element, configuration 34); equivalent diameter, D_e, 3.20 centimeters.

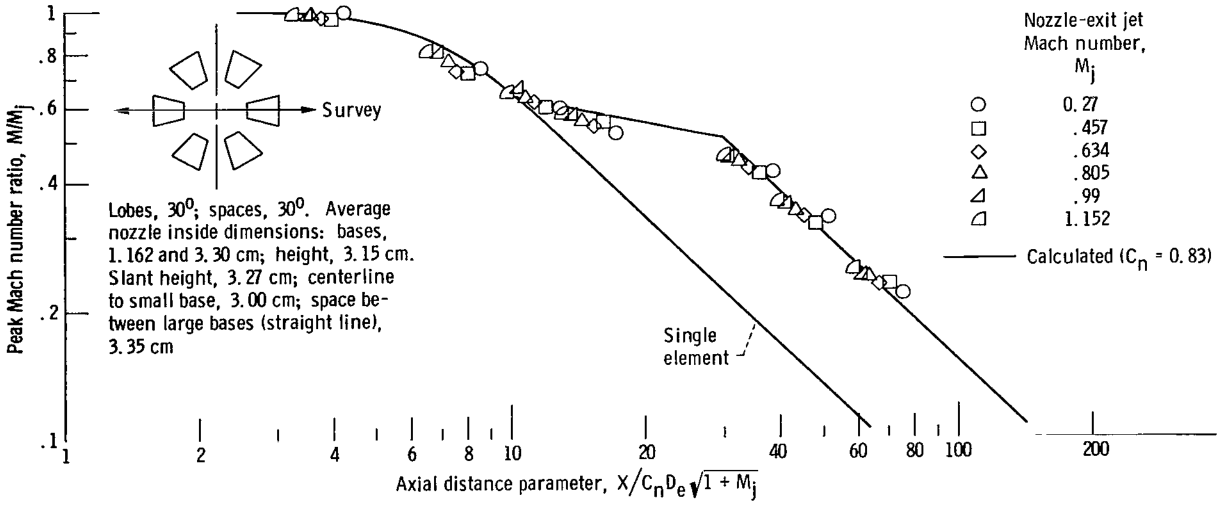

Figure 91. - Peak axial Mach number decay of six-lobe, flat-end trapezoidal nozzle with circumferential spacing ratio s_l/w_l of 1.014. Configuration 95 (single element, configuration 35); equivalent diameter, D_e, 3.15 centimeters.

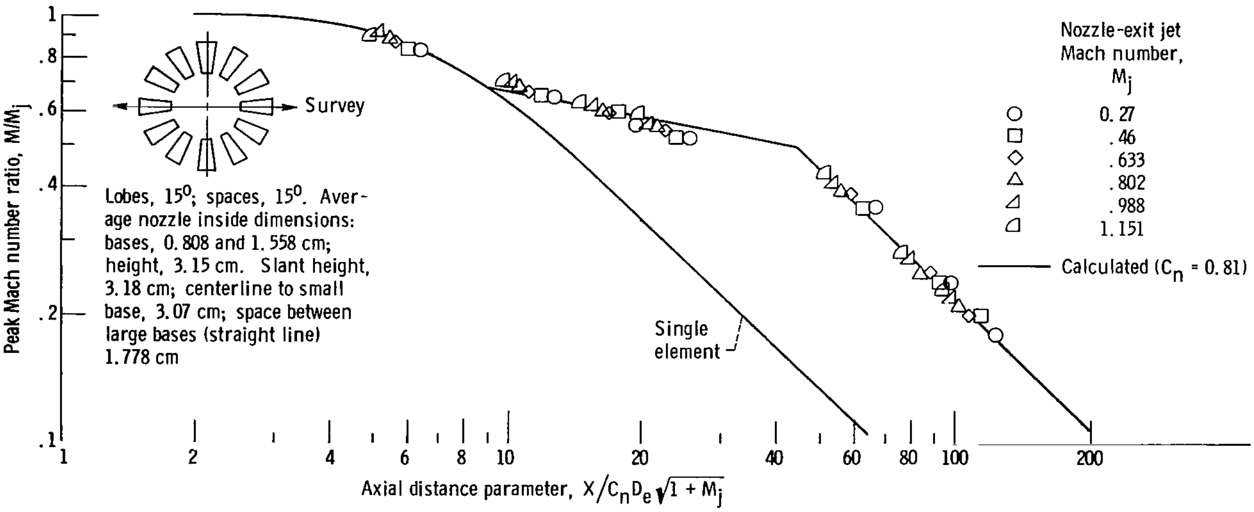

Figure 92. - Peak axial Mach number decay of 12-lobe, flat-end trapezoidal nozzle with circumferential spacing ratio, s_l/w_l of 1.14. Configuration 96 (single element, configuration 36); equivalent diameter, D_e, 2.18 centimeters.

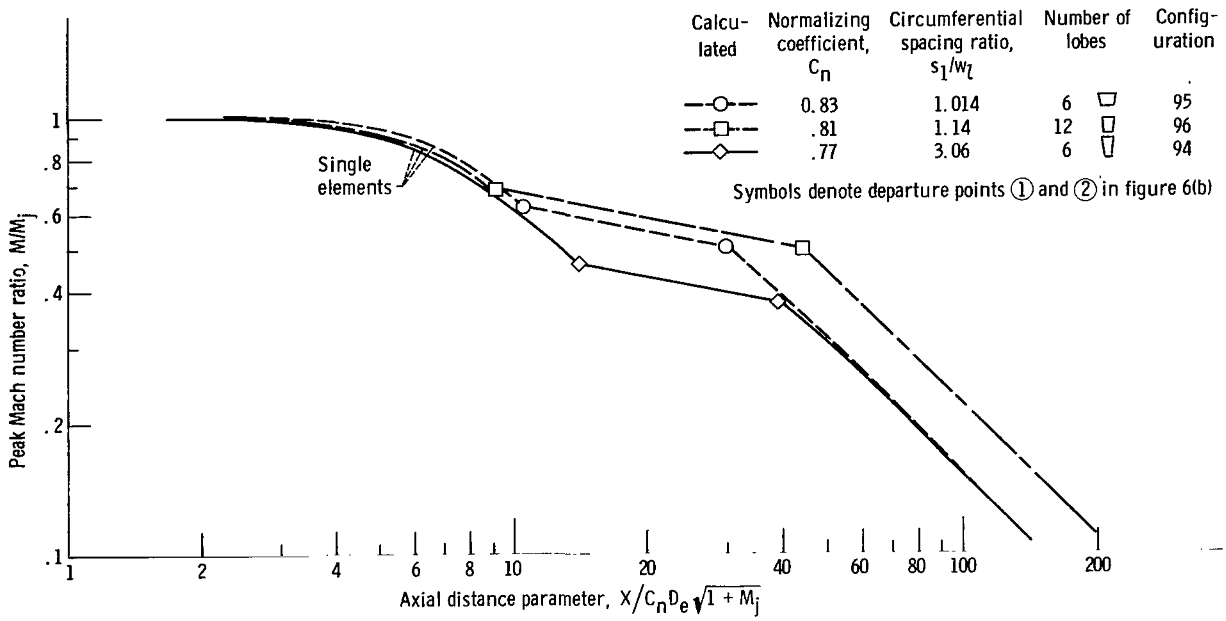

Figure 93. - Comparison of calculated peak axial Mach number decay of multilobed flat-end trapezoidal nozzles.

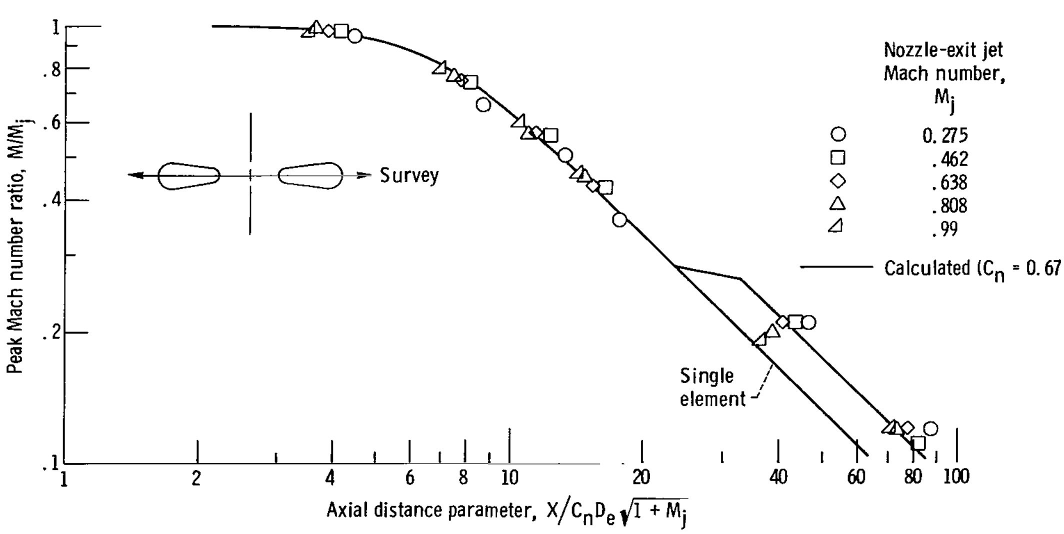

Figure 94. - Peak axial Mach number decay of two-lobe, round-end trapezoidal nozzle - both lobes at 0° to nozzle axis. Configuration 97 (single element, configuration 37); equivalent diameter, D_e, 3.81 centimeters.

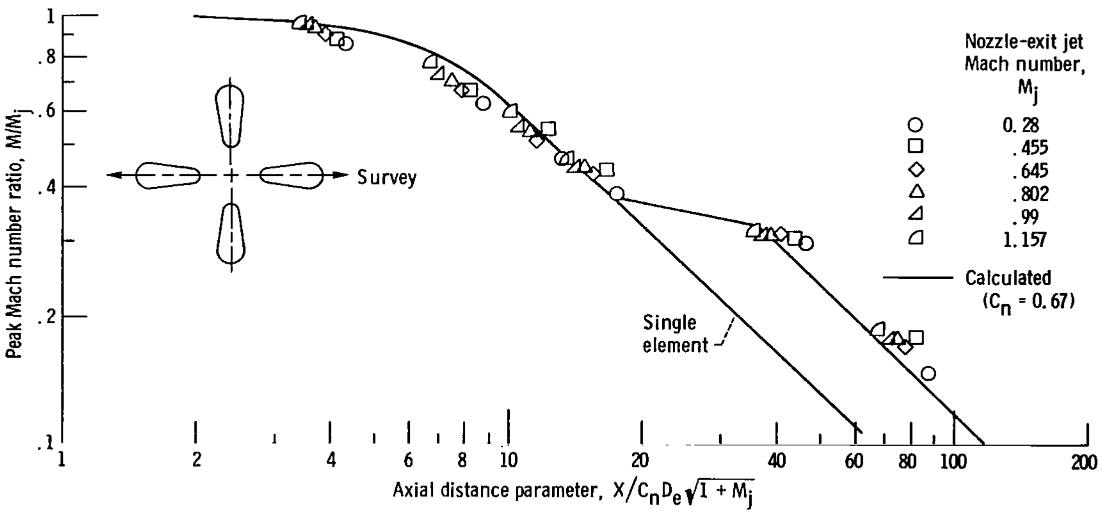

Figure 95. - Peak axial Mach number decay of four-lobe, round-end trapezoidal nozzle - all lobes at 0^{0} to nozzle axis. Configuration 98 (single element, configuration 37); equivalent diameter, D_e, 3.81 centimeters.

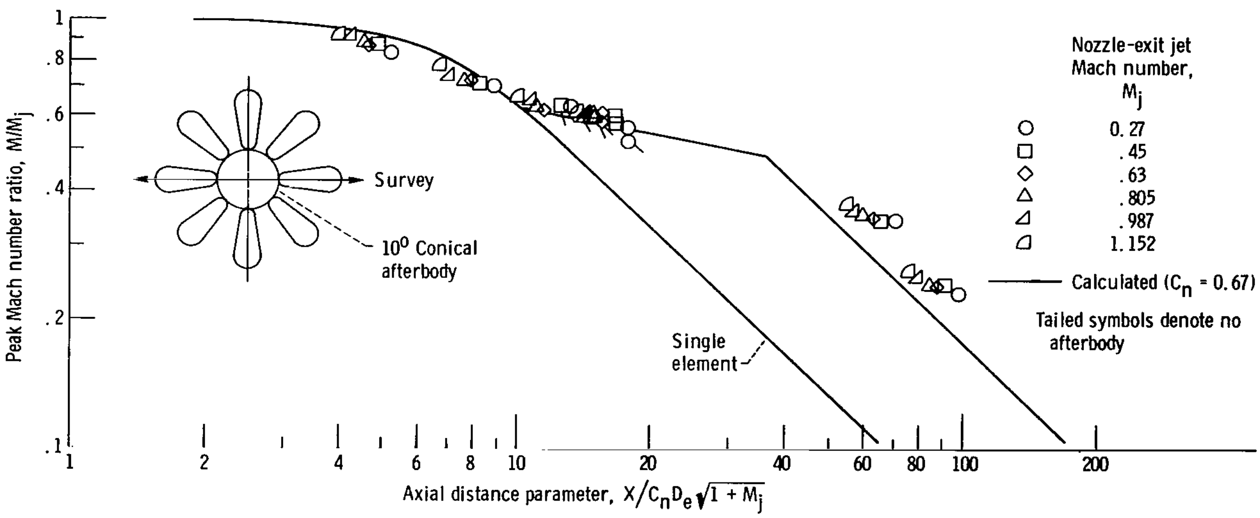

Figure 96. - Peak axial Mach number decay of eight-lobe, round-end trapezoidal nozzle with 10^{0} conical afterbody - all lobes at 0^{0} to nozzle axis. Configuration 99 (single element, configuration 37); equivalent diameter, D_e, 3.81 centimeter.

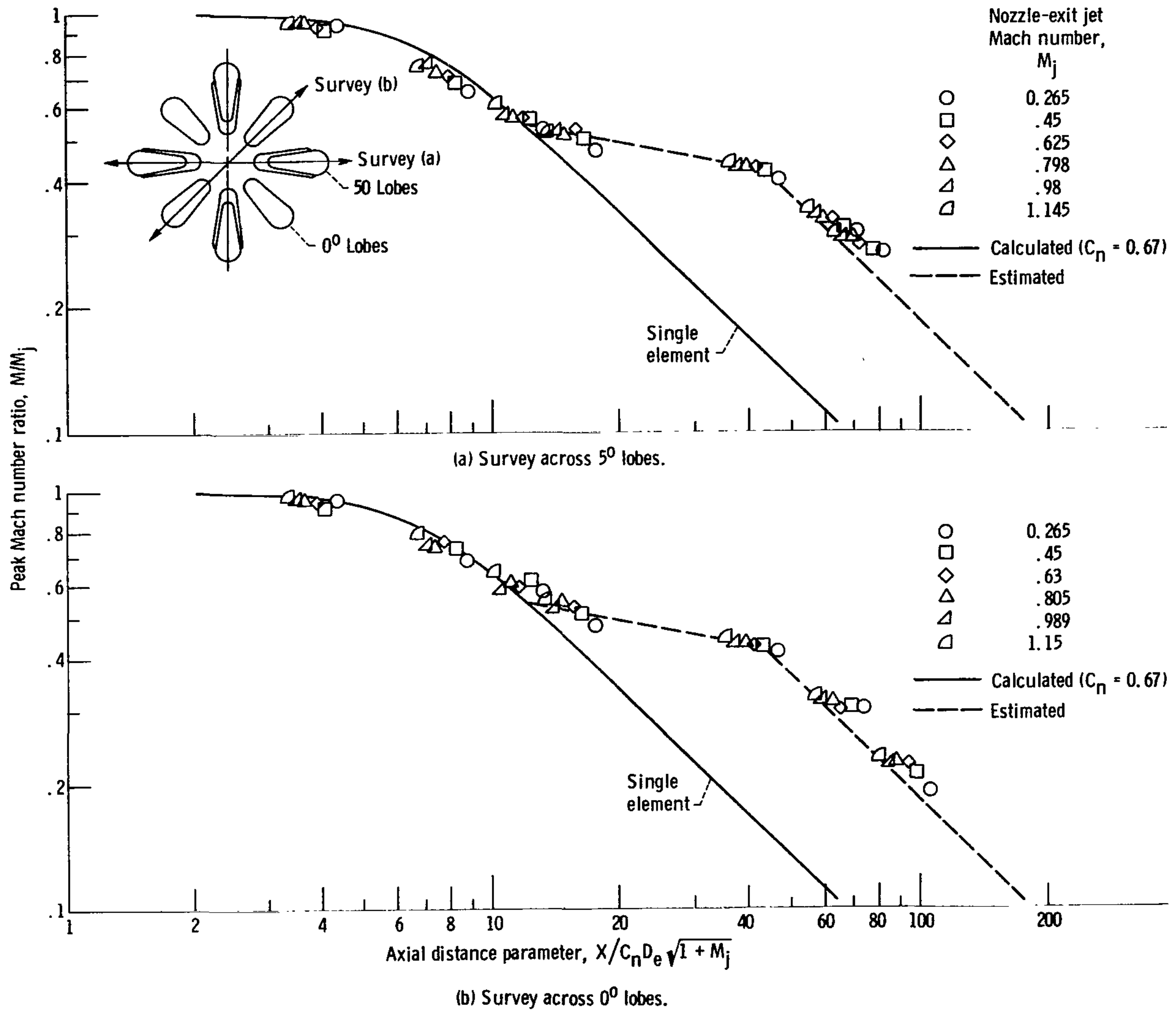

Figure 97. - Peak axial Mach number decay of eight-lobe, round-end trapezoidal nozzle - four lobes at 0° and four alternate lobes at 5° to nozzle axis. Configuration 100 (single element, configuration 37); equivalent diameter, D_e, 3.81 centimeters.

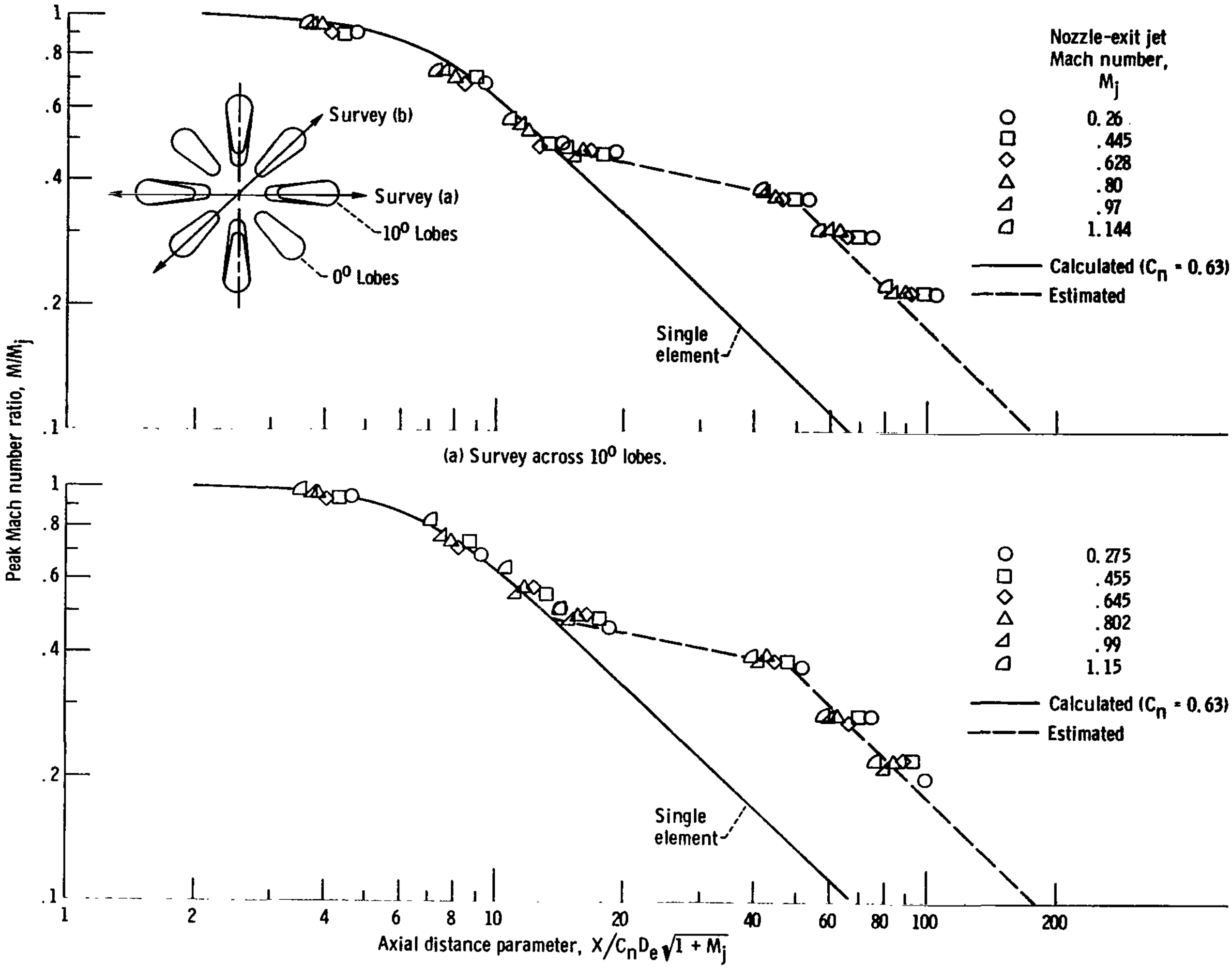

(b) Survey across 0° lobes.

Figure 98. - Peak axial Mach number decay of eight-lobe, round-end trapezoidal nozzle - four lobes at 0° and four alternate lobes at 10° to nozzle axis. Configuration 101 (single element, configuration 37); equivalent diameter, D_e, 3.81 centimeters.

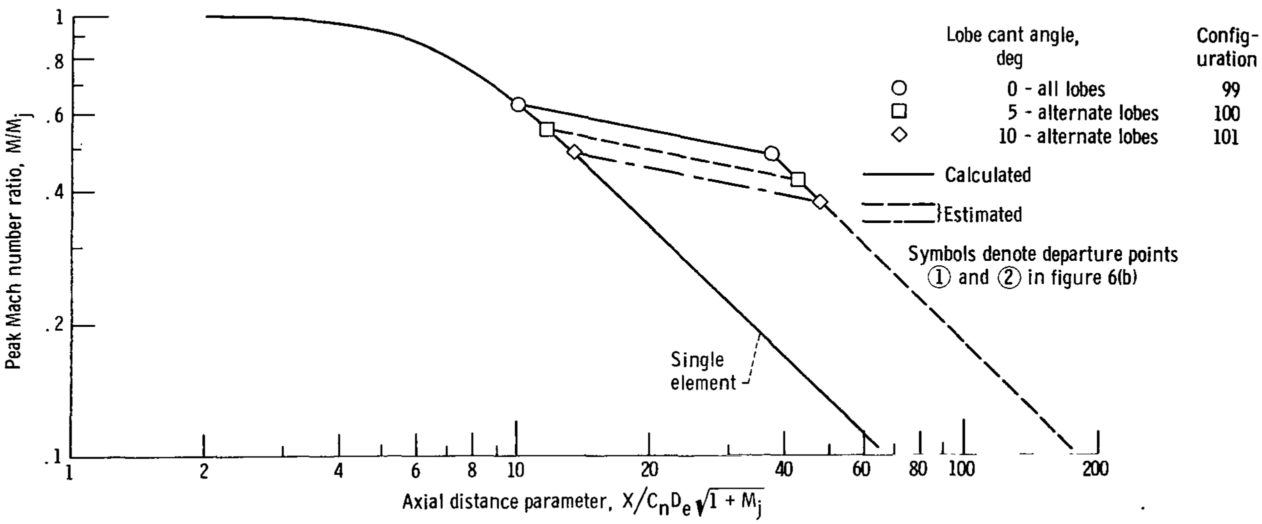

Figure 99. - Comparison of effect of canting alternate lobes of eight-lobe, round-end trapezoidal nozzle.

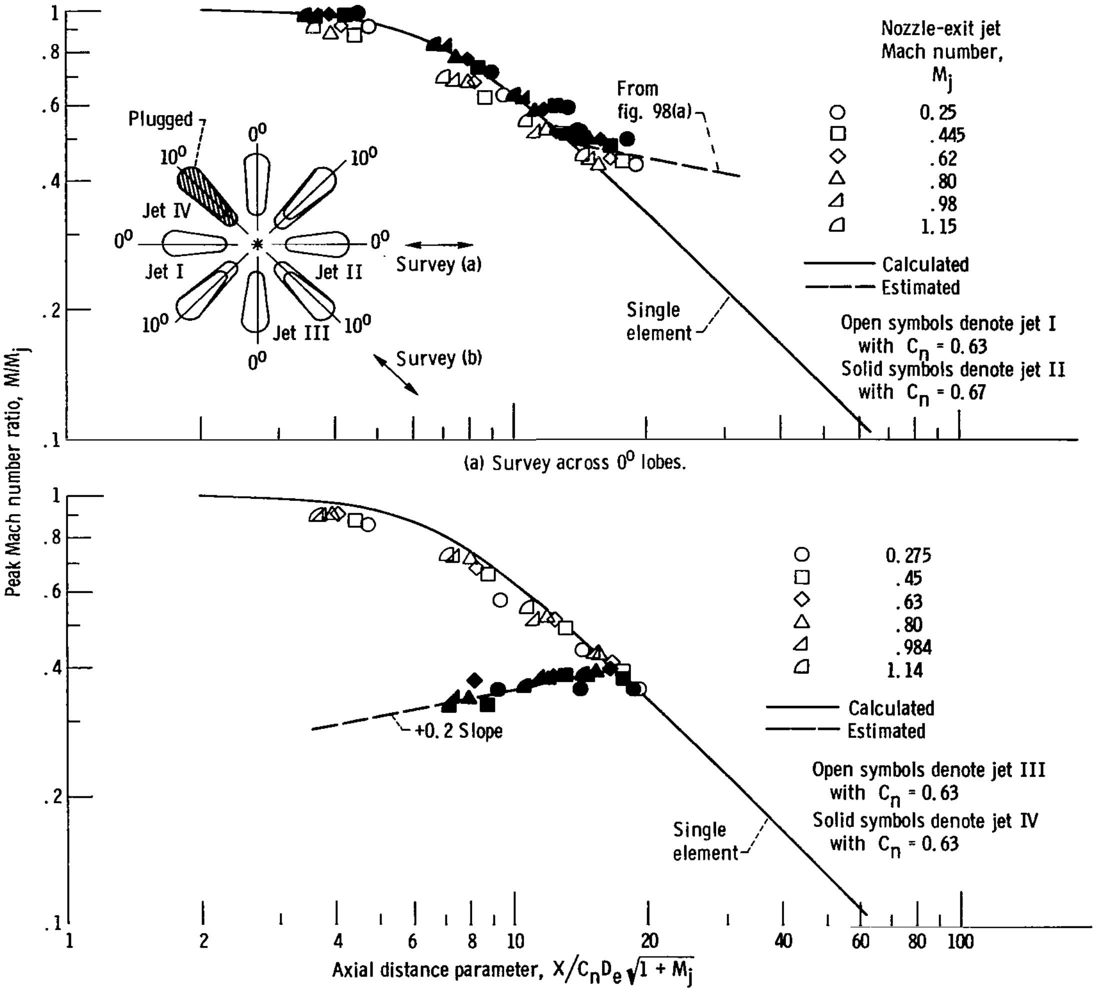

(a) Survey across 0° lobes.

(b) Survey across plugged lobe and one 10° lobe. Survey traces at 12.7 centimeters are atmospheric and/or slightly subatmospheric.

Figure 100. - Peak axial Mach number decay of seven-lobe, round-end trapezoidal nozzle - eight-lobe nozzle with four lobes at 0°, three alternate lobes at 10°, and one lobe plugged. Configuration 102 (single element, configuration 37); equivalent diameter, D_e, 3.81 centimeters.

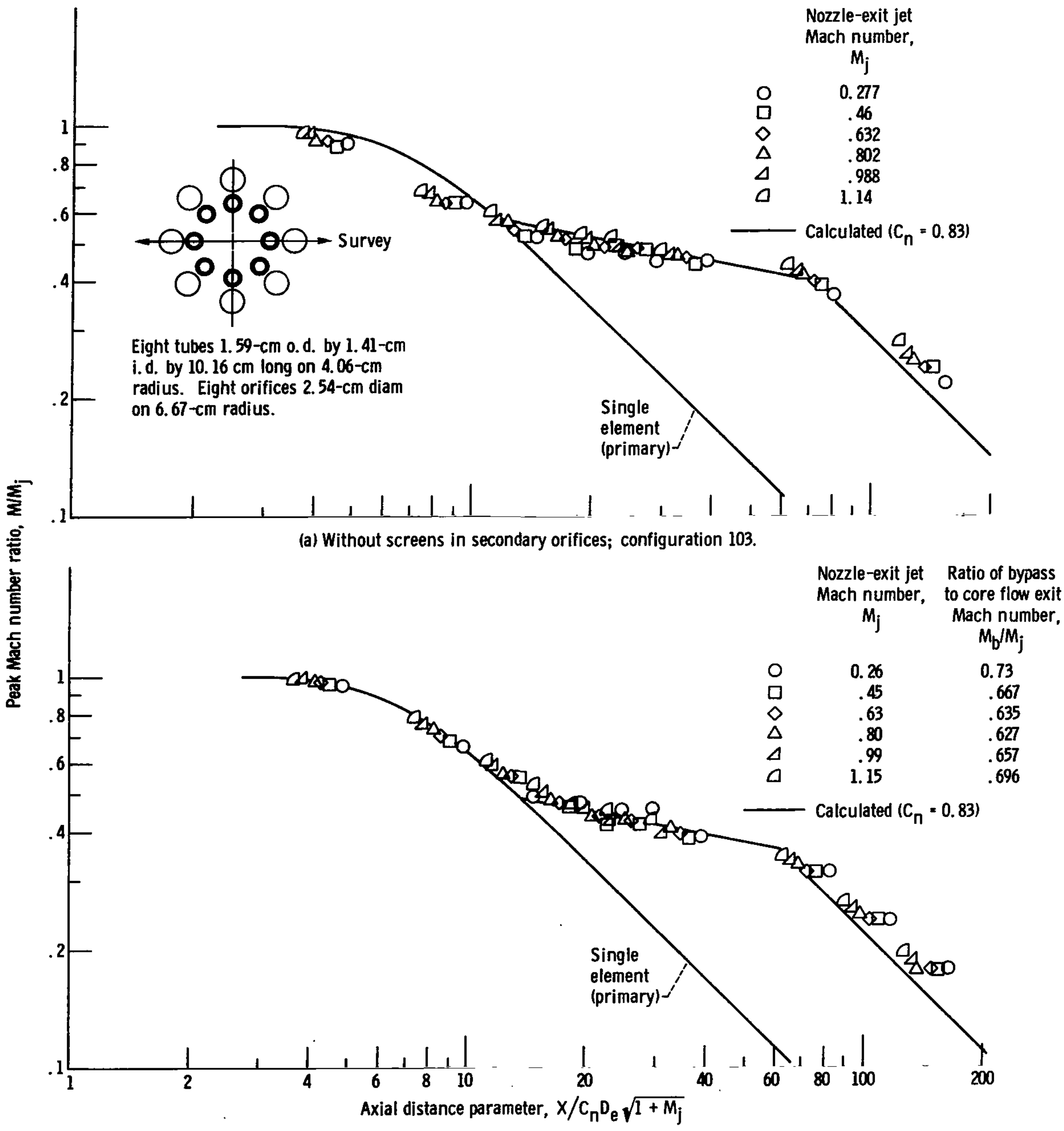

(b) With screens in secondary orifices; configuration 104.

Figure 101. - Peak axial Mach number decay of nonplanar multielement nozzle - primary, eight tubes; secondary, eight round-edge orifices. Equivalent diameter (primary), D_e, 1.41 centimeters.

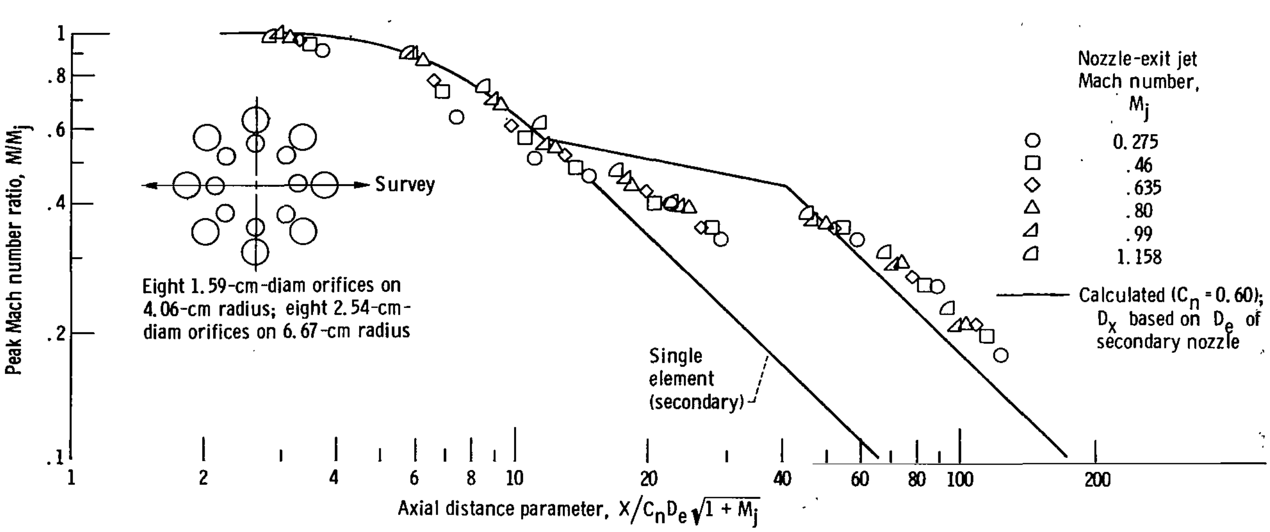

Figure 102. - Peak axial Mach number decay of planar multielement nozzle - primary, eight sharp-edge orifices; secondary, eight sharp-edge orifices. Configuration 105; equivalent diameter (secondary), D_e, 2.54 centimeters.

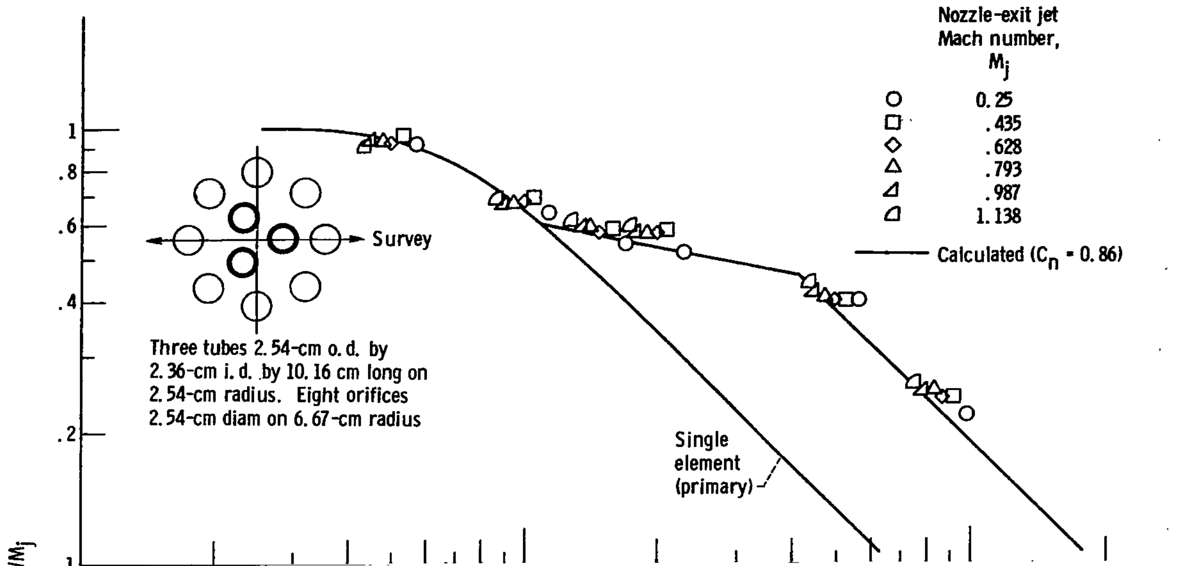

(a) Without screens in secondary orifices; configuration 106.

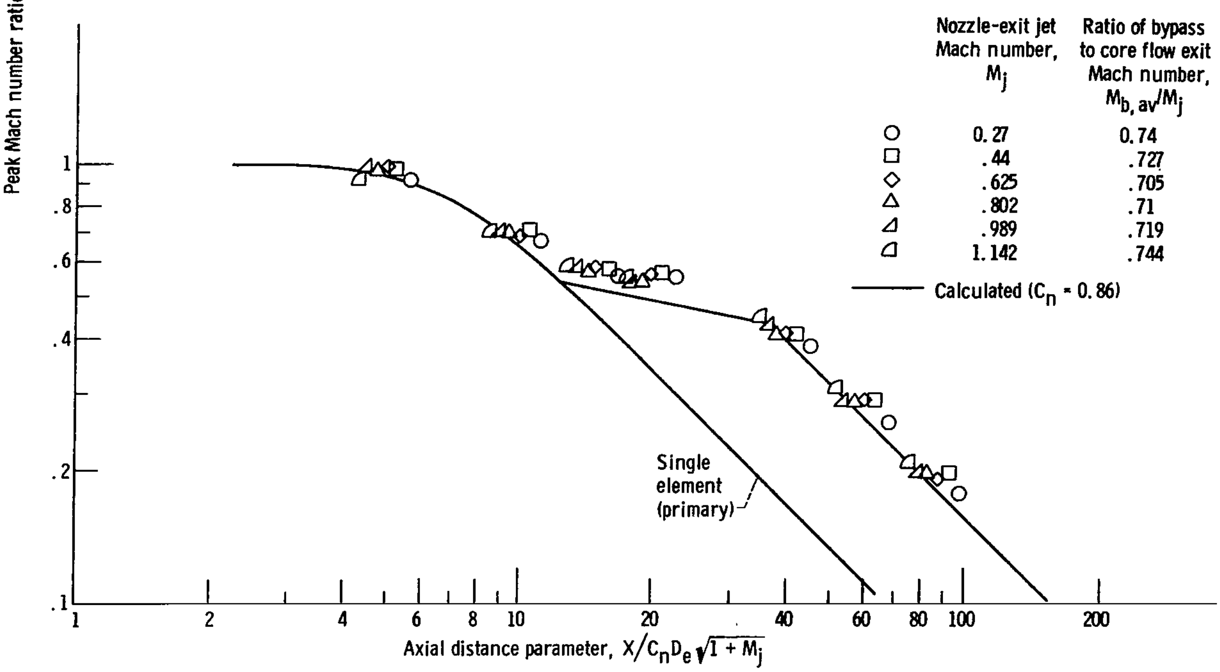

(b) With screens in secondary orifices; configuration 107.

Figure 103. - Peak axial Mach number decay of nonplanar multielement nozzle - primary, three tubes; secondary, eight round-edge orifices. Equivalent diameter (primary), D_e, 2.36 centimeters.

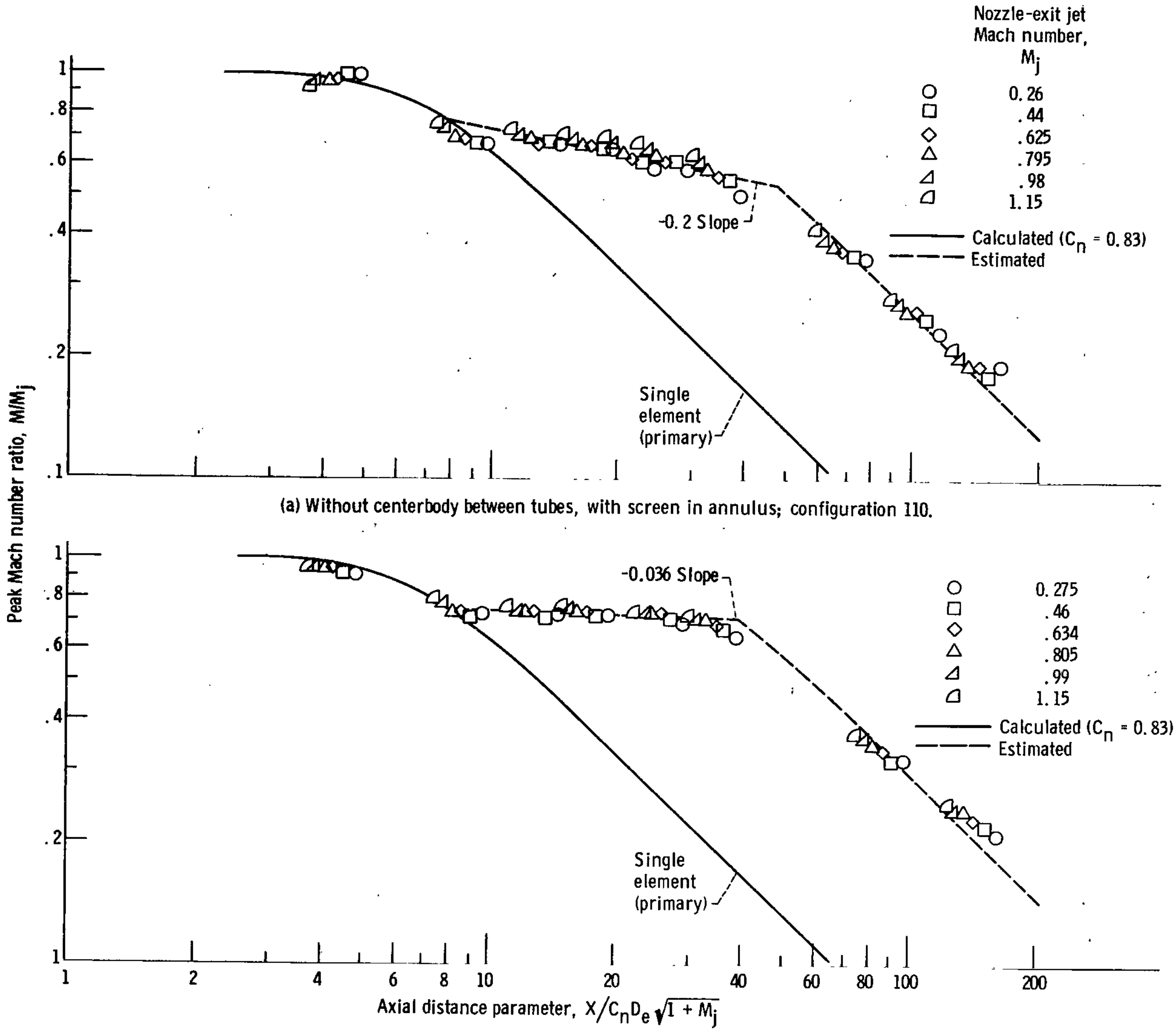

(b) With centerbody between tubes, with screen in annulus; configuration 111.

Figure 104. - Peak axial Mach number decay of nonplanar bypass nozzle - primary, eight tubes; secondary, 1.02-centimeter-wide sharp-edge annulus. Equivalent diameter, D_e, 1.41 centimeters.

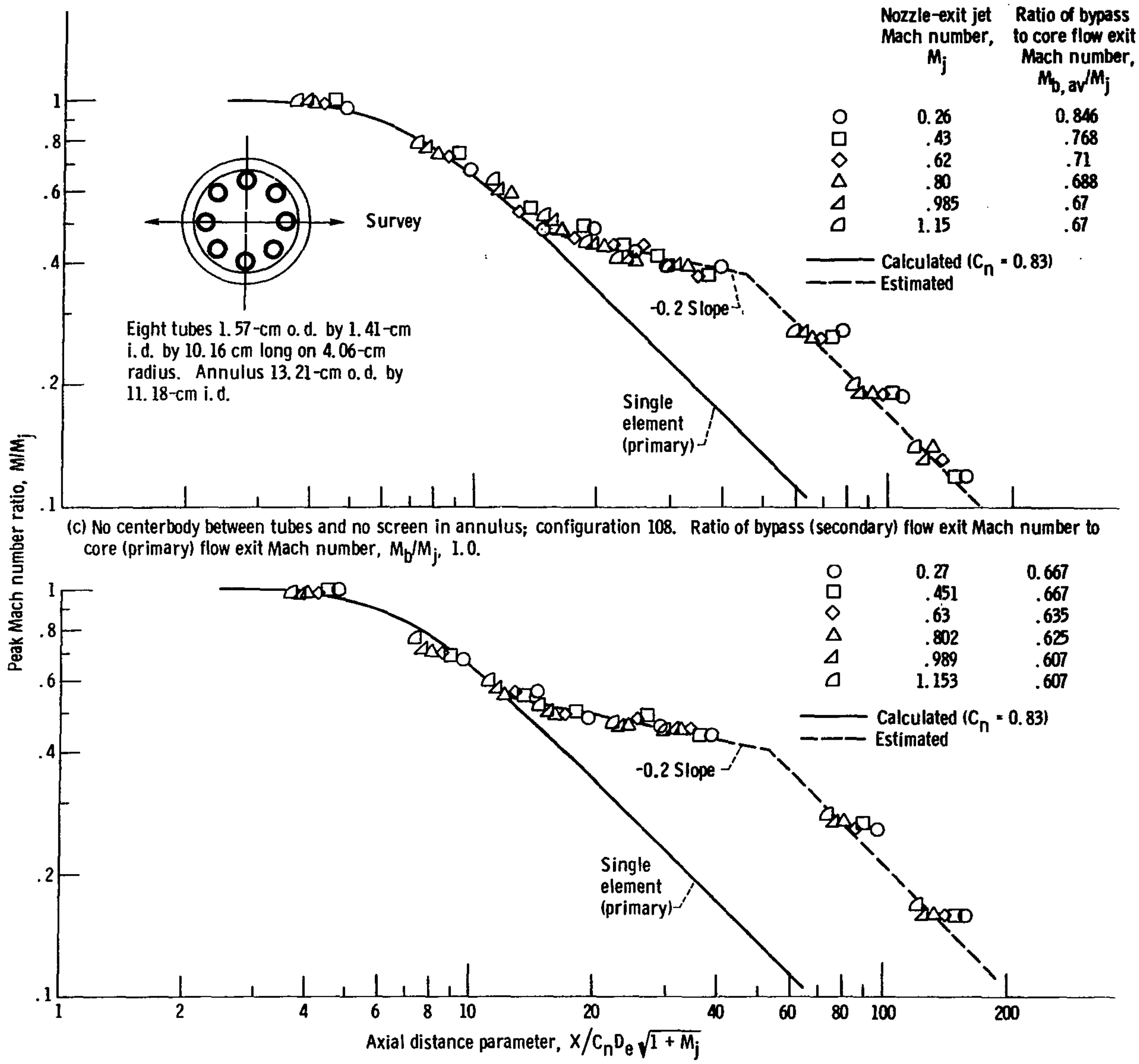

(c) No centerbody between tubes and no screen in annulus; configuration 108. Ratio of bypass (secondary) flow exit Mach number to core (primary) flow exit Mach number, M_b/M_j, 1.0.

(d) With centerbody between tubes and no screen in annulus; configuration 109. Ratio of bypass (secondary) flow exit Mach number to core (primary) flow exit Mach number, 1.0.

Figure 104. - Concluded.

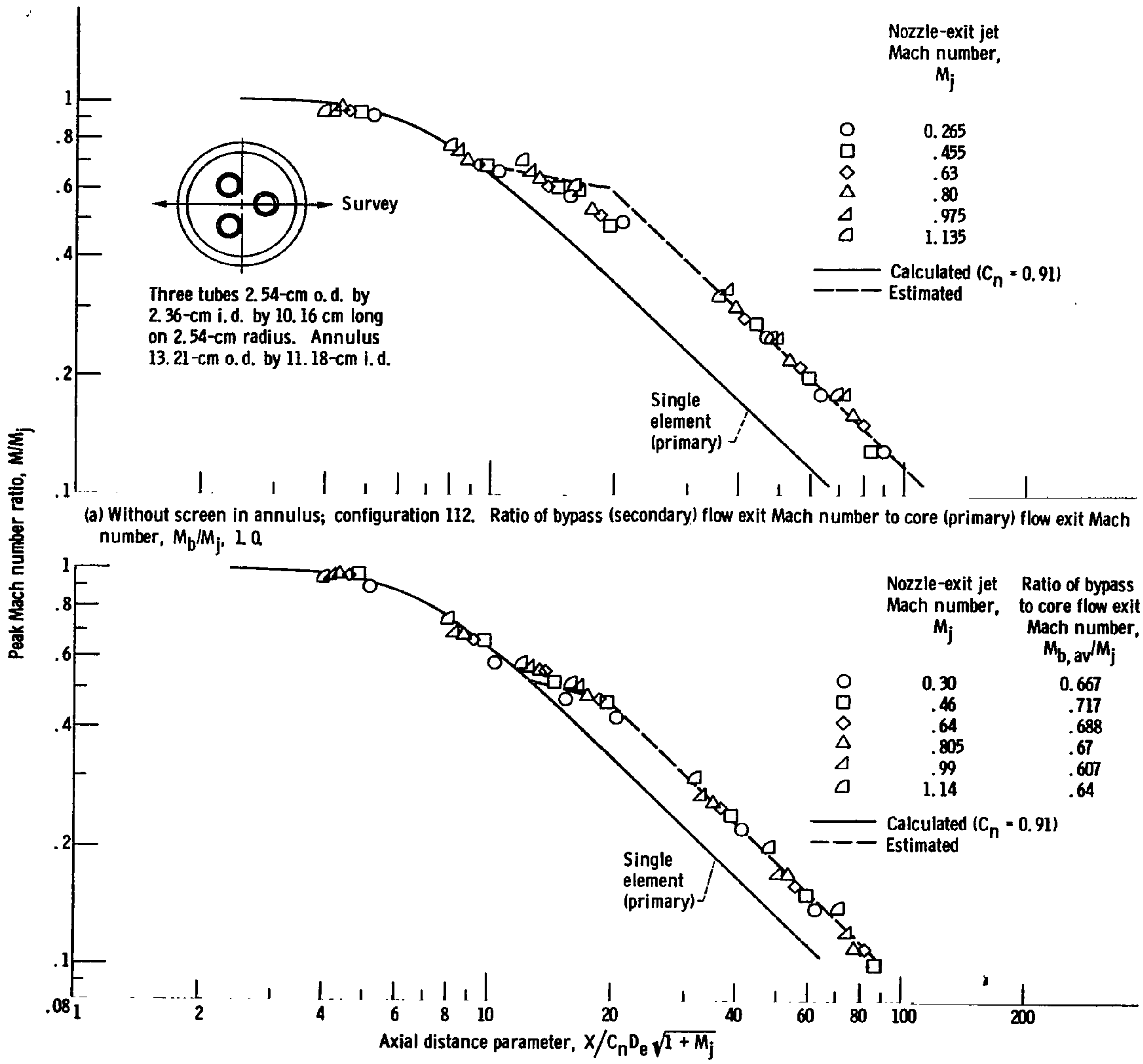

(a) Without screen in annulus; configuration 112. Ratio of bypass (secondary) flow exit Mach number to core (primary) flow exit Mach number, M_b/M_j, 1.0.

(b) With screen in annulus; configuration 113.

Figure 105. - Peak axial Mach number decay of nonplanar bypass nozzle - primary, three tubes; secondary, 1.02-centimeter-wide sharp-edge annulus. Equivalent diameter, D_e, 2.36 centimeters.

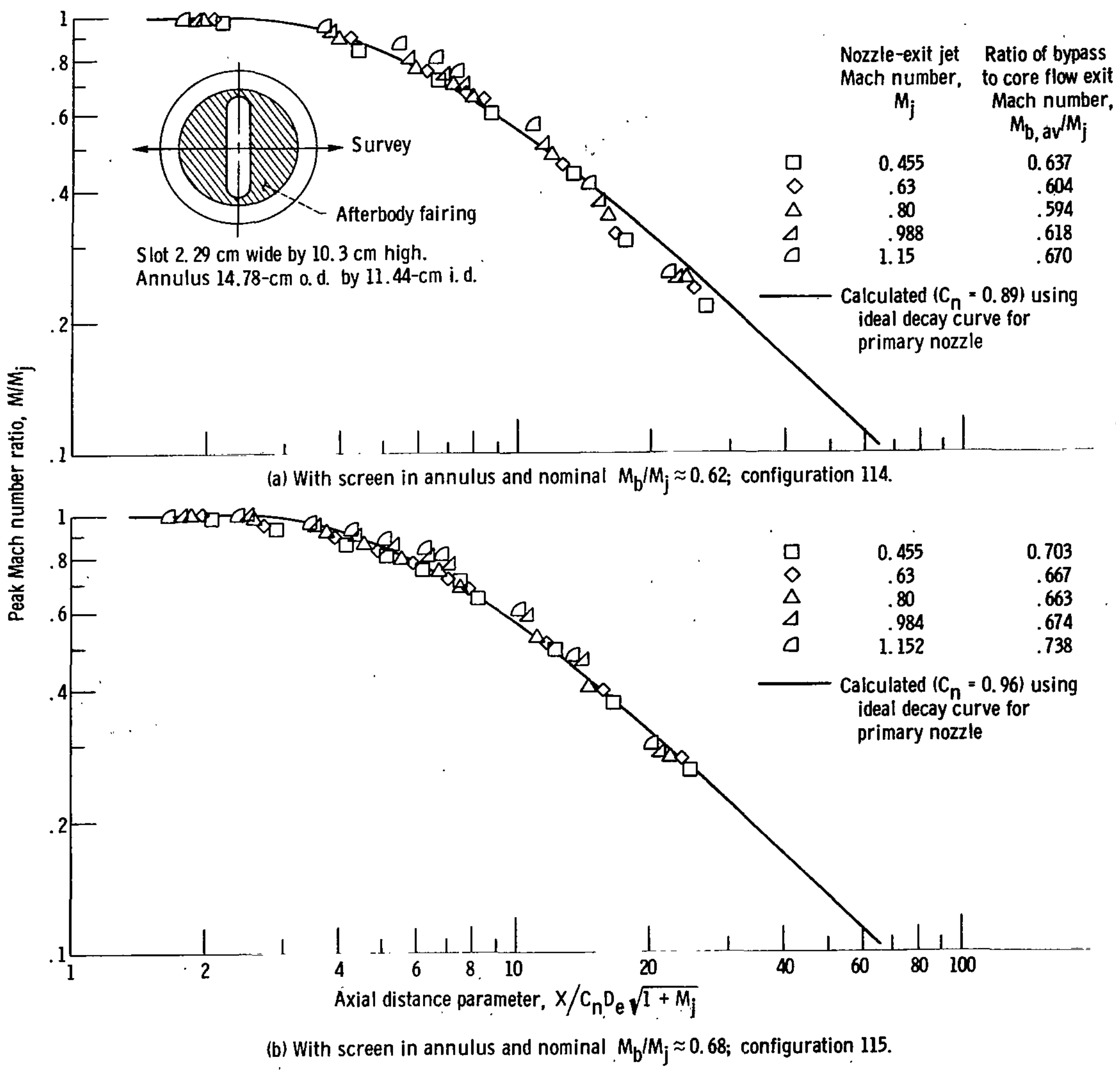

Figure 106. - Peak axial Mach number decay of nonplanar bypass nozzle - primary, 4.76-aspect-ratio slot nozzle (configuration 22); secondary, 1.664-centimeter-wide round-edge annulus. Equivalent diameter, D_e, 5.32 centimeters.

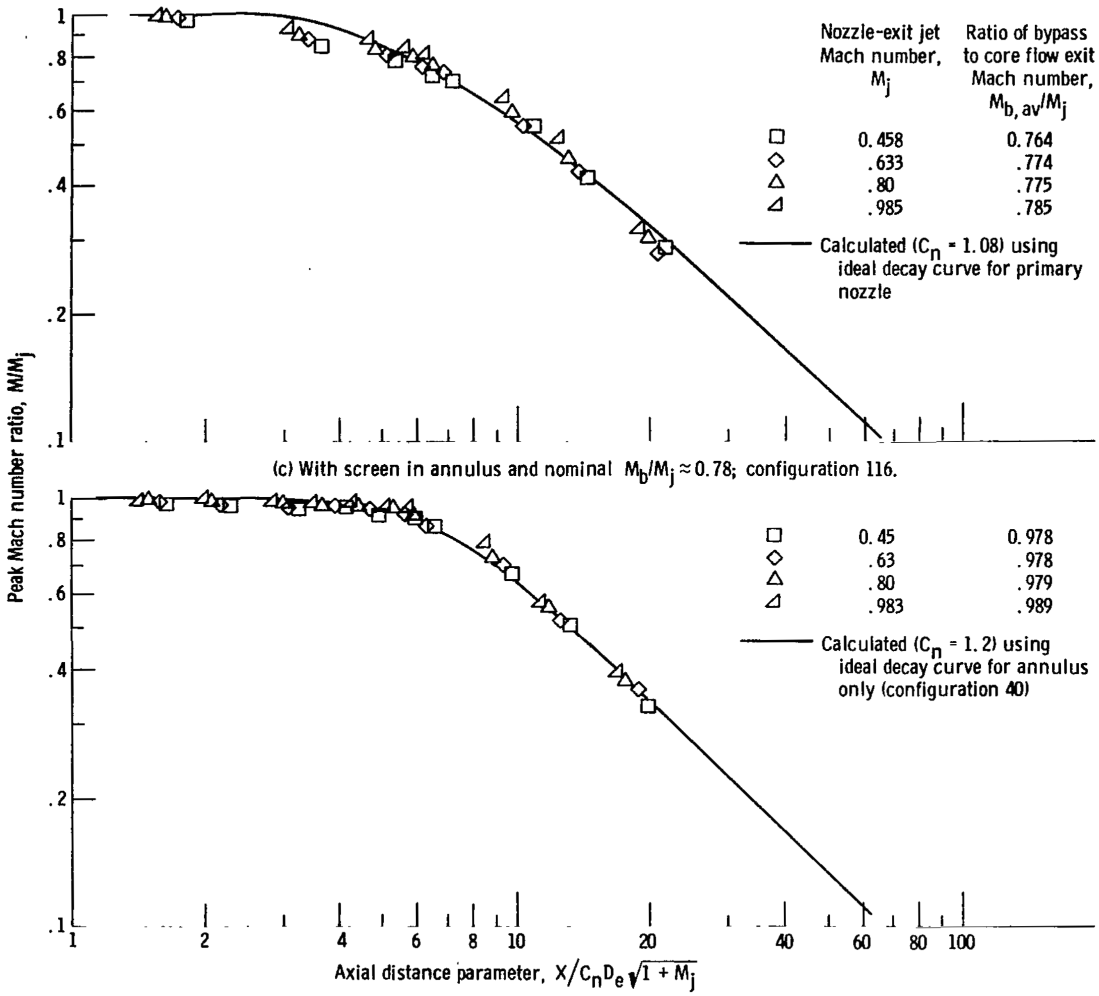

(c) With screen in annulus and nominal $M_b/M_j \approx 0.78$; configuration 116.

(d) Without screen in annulus and with nominal $M_b/M_j \approx 0.98$; configuration 117.

Figure 106. - Concluded.

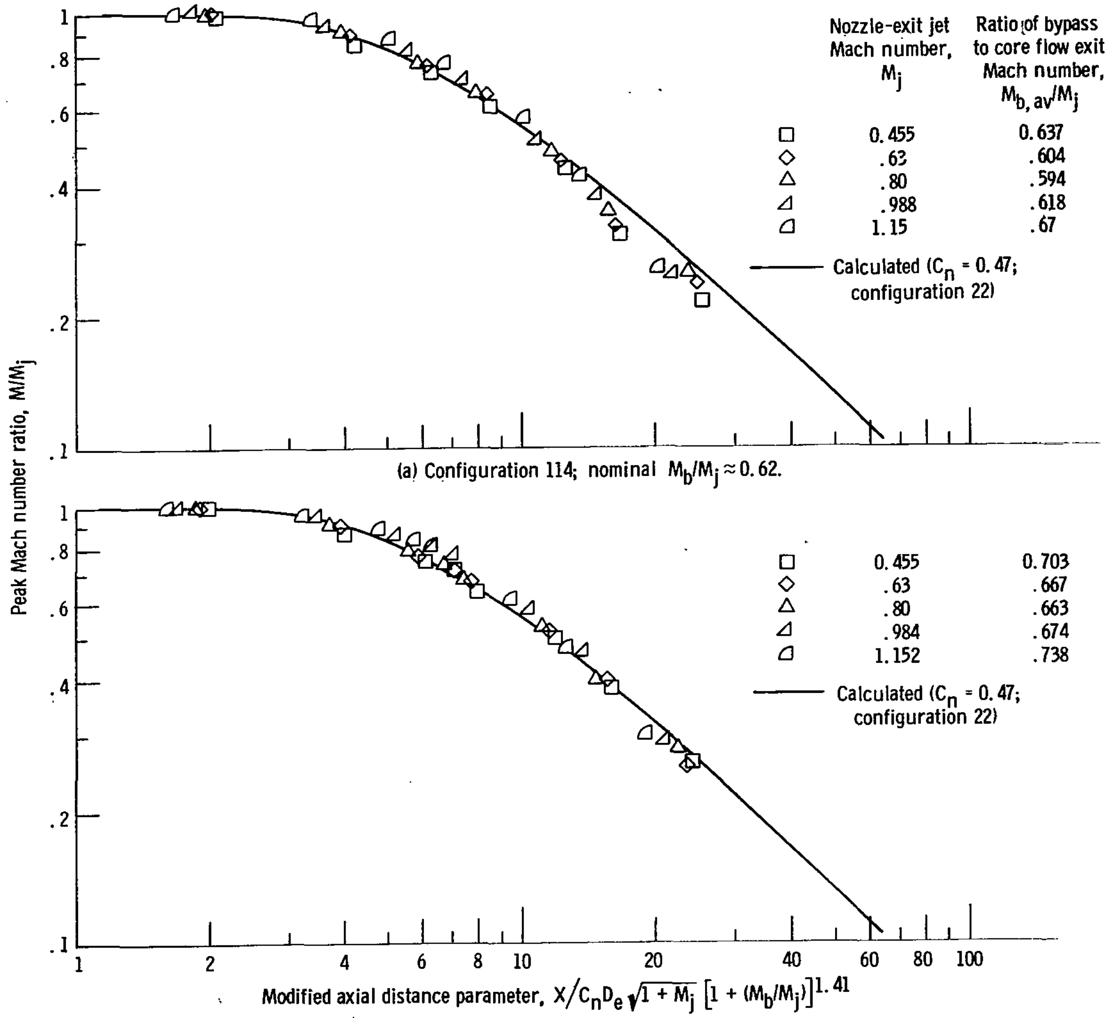

(a) Configuration 114; nominal $M_b/M_j \approx 0.62$.

(b) Configuration 115; nominal $M_b/M_j \approx 0.67$.

Figure 107. - Normalization of effect of secondary-flow Mach number on bypass-nozzle peak axial Mach number decay. Primary, 4.76-aspect-ratio slot nozzle (configuration 22); secondary, 1.664-centimeter-wide round-end annulus; equivalent diameter, D_e, 5.32 centimeters.

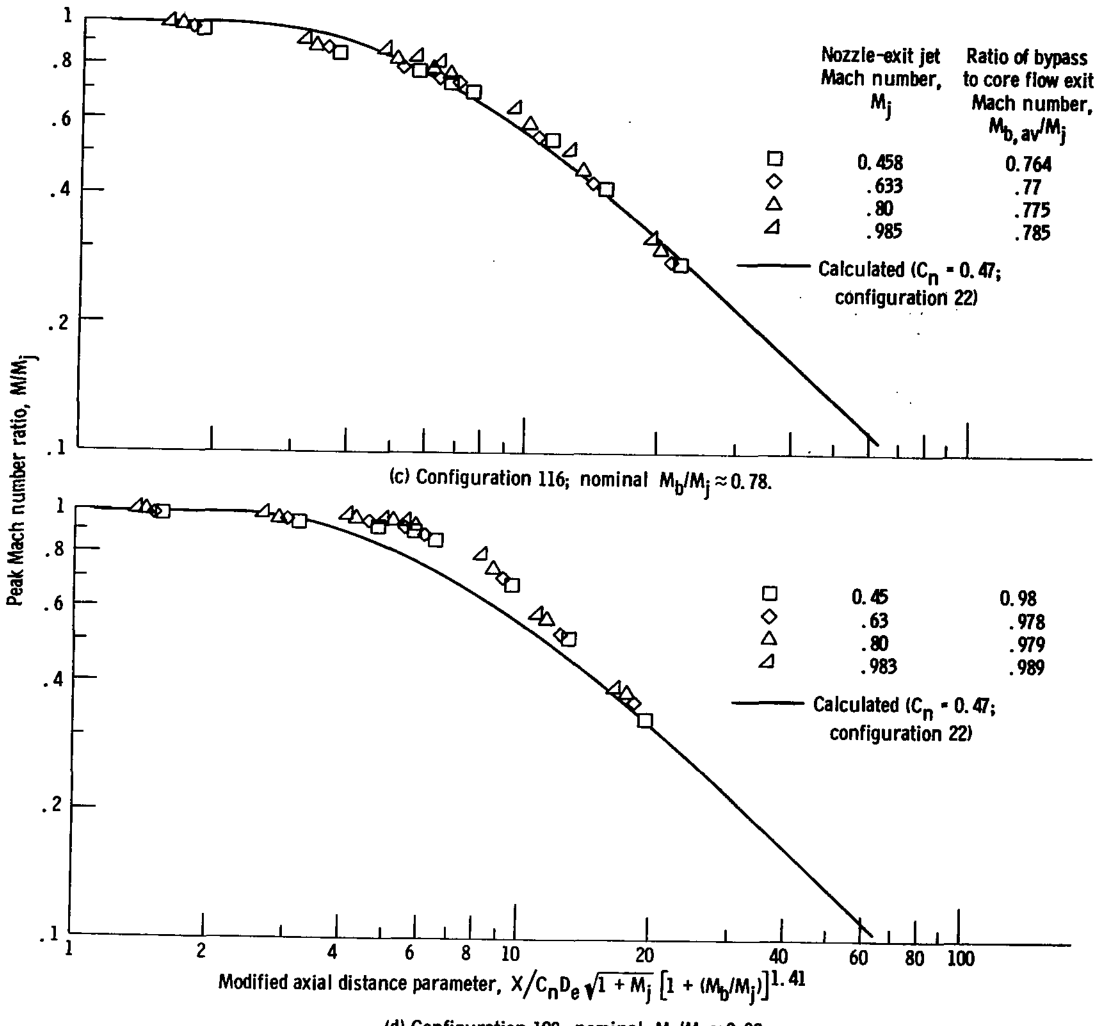

Figure 107. - Concluded.

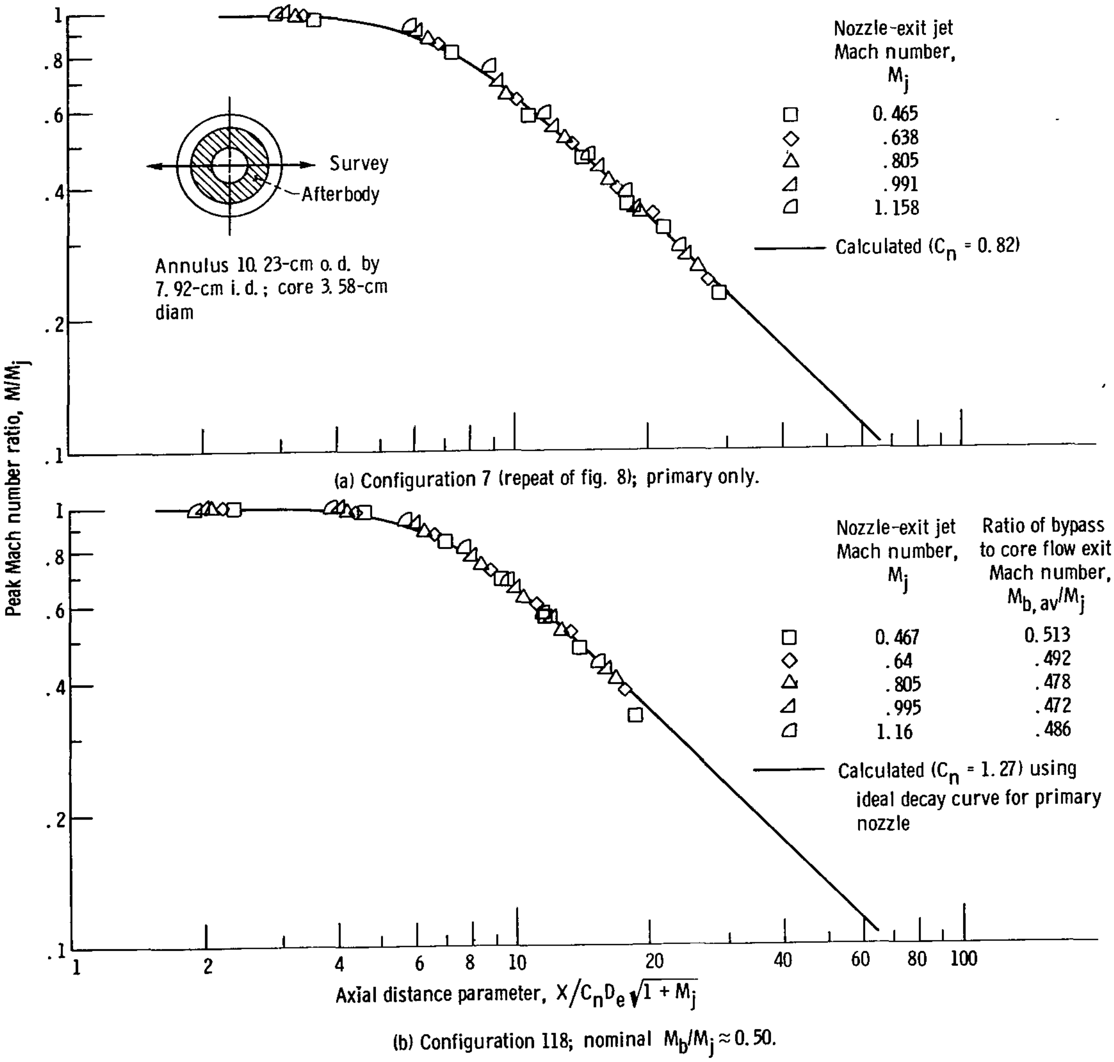

Figure 108. - Peak axial Mach number decay of nonplanar small bypass nozzle - primary, 3.58-centimeter-diameter circular convergent nozzle; secondary, 1.15-centimeter-wide convergent annulus. Equivalent diameter, D_e, 3.58 centimeters.

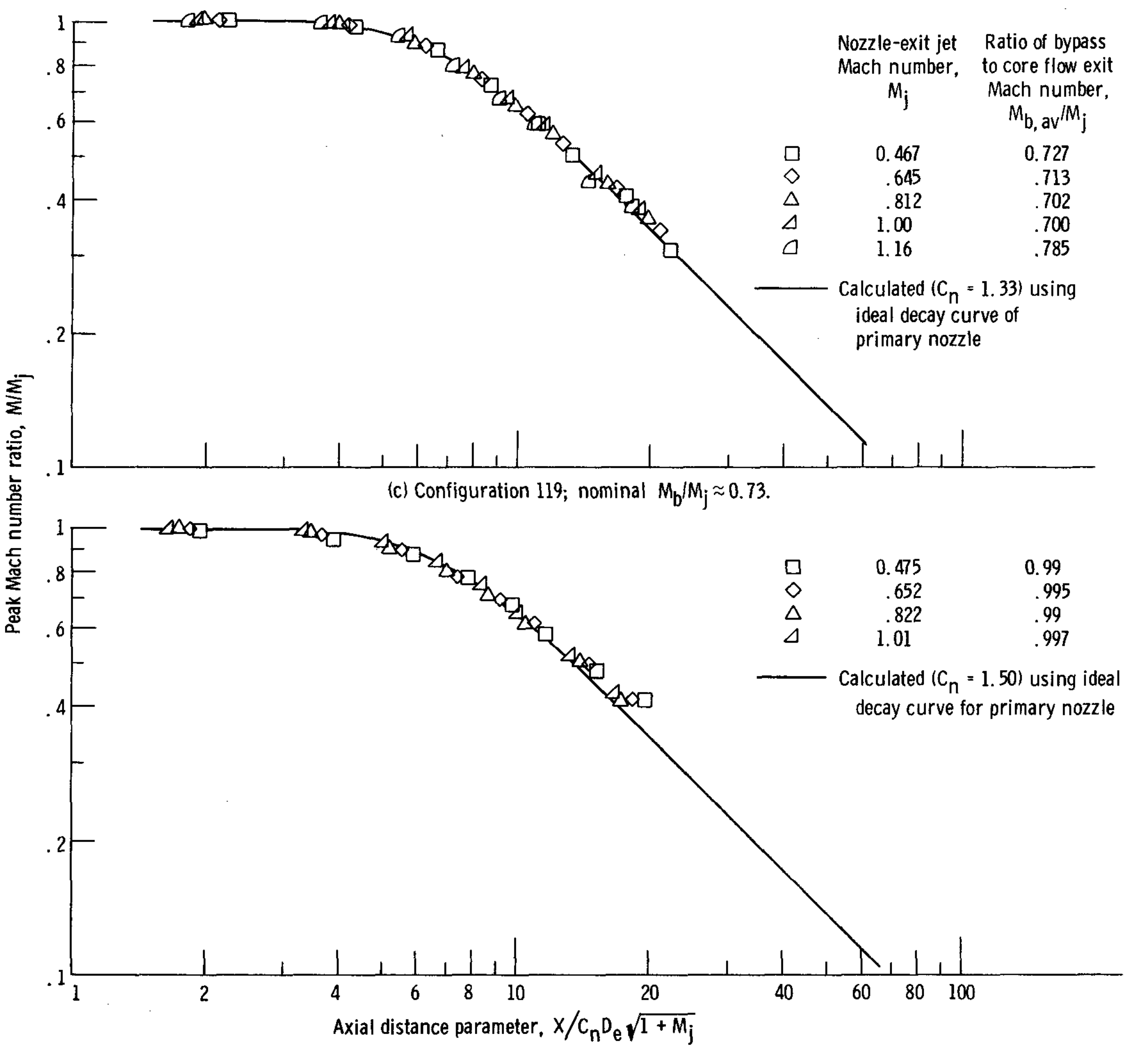

(c) Configuration 119; nominal $M_b/M_j \approx 0.73$.

(d) Configuration 120; nominal $M_b/M_j \approx 1.0$.

Figure 108. - Concluded.

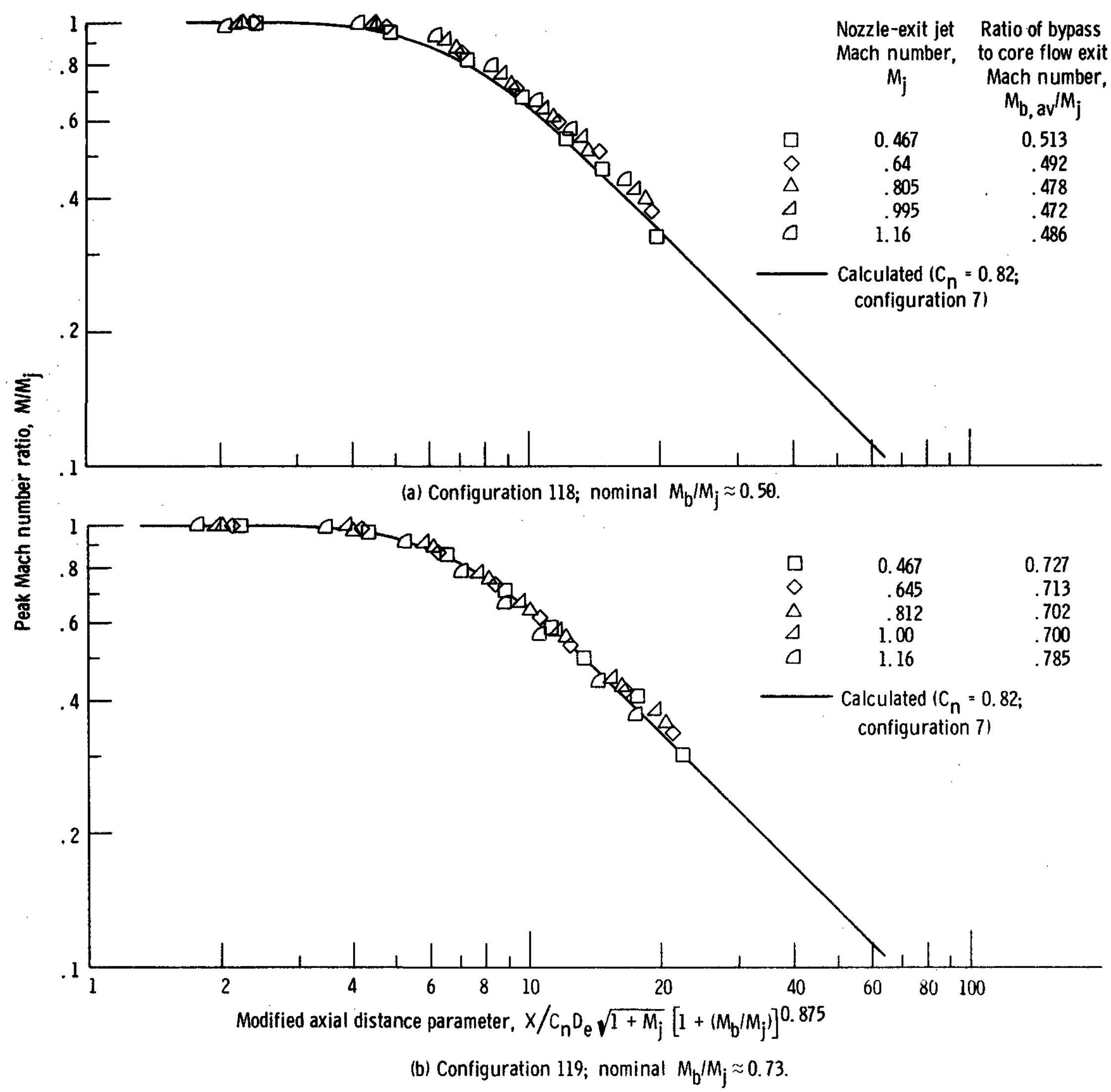

Figure 109. - Normalization of effect of secondary-flow Mach number on small-bypass-nozzle peak axial Mach number decay Primary, 3.58-centimeter-diameter circular convergent nozzle (configuration 7); secondary, 1.15-centimeter-wide convergent annulus; equivalent diameter, D_e, 3.58 centimeters.

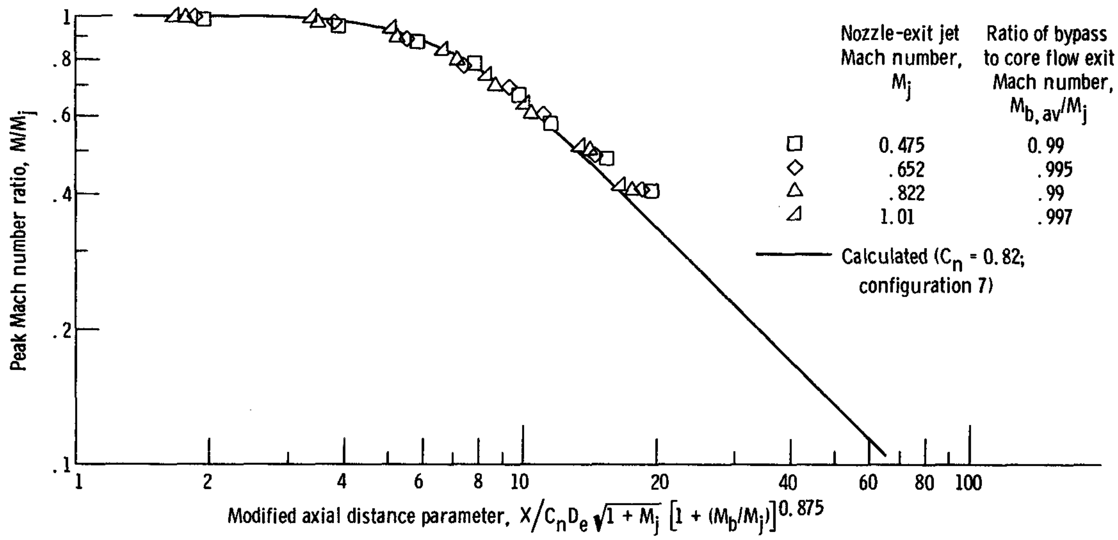

(c) Configuration 120; nominal $M_b/M_j \approx 1.0$.

Figure 109. - Concluded.

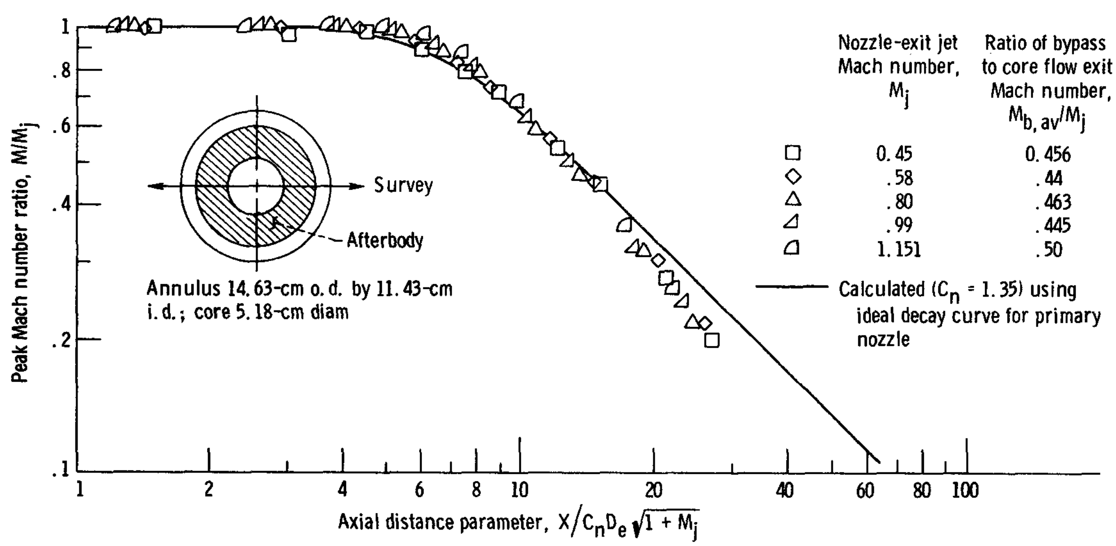

(a) Configuration 121; nominal $M_b/M_j \approx 0.46$.

Figure 110. - Peak axial Mach number decay of nonplanar large bypass nozzle - primary, 5.18-centimeter-diameter circular convergent nozzle; secondary, 1.60-centimeter-wide convergent annulus. Equivalent diameter, D_e, 5.18 centimeters.

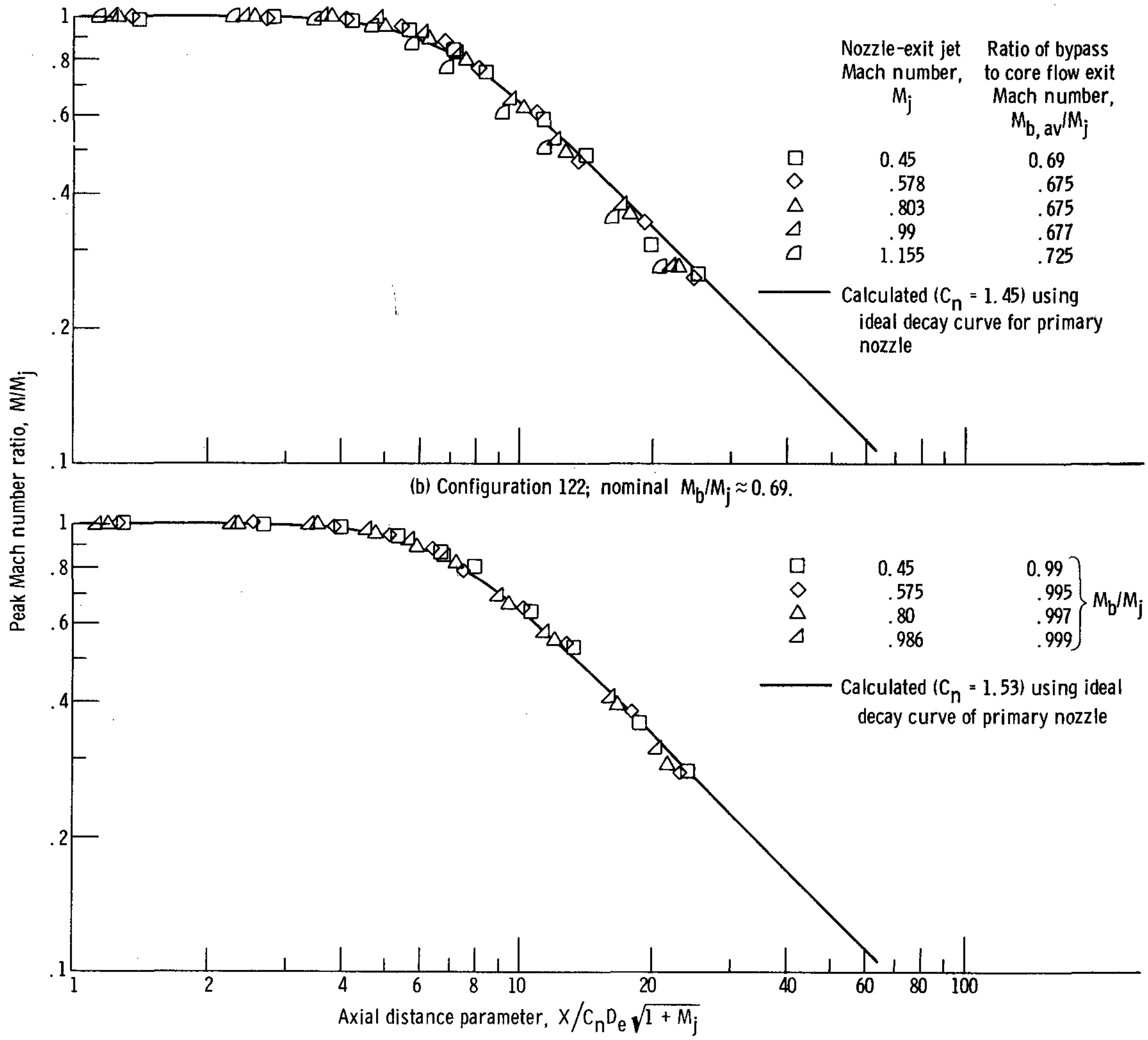

(b) Configuration 122; nominal $M_b/M_j \approx 0.69$.

(c) Configuration 123; nominal $M_b/M_j \approx 1.0$.

Figure 110. - Concluded.

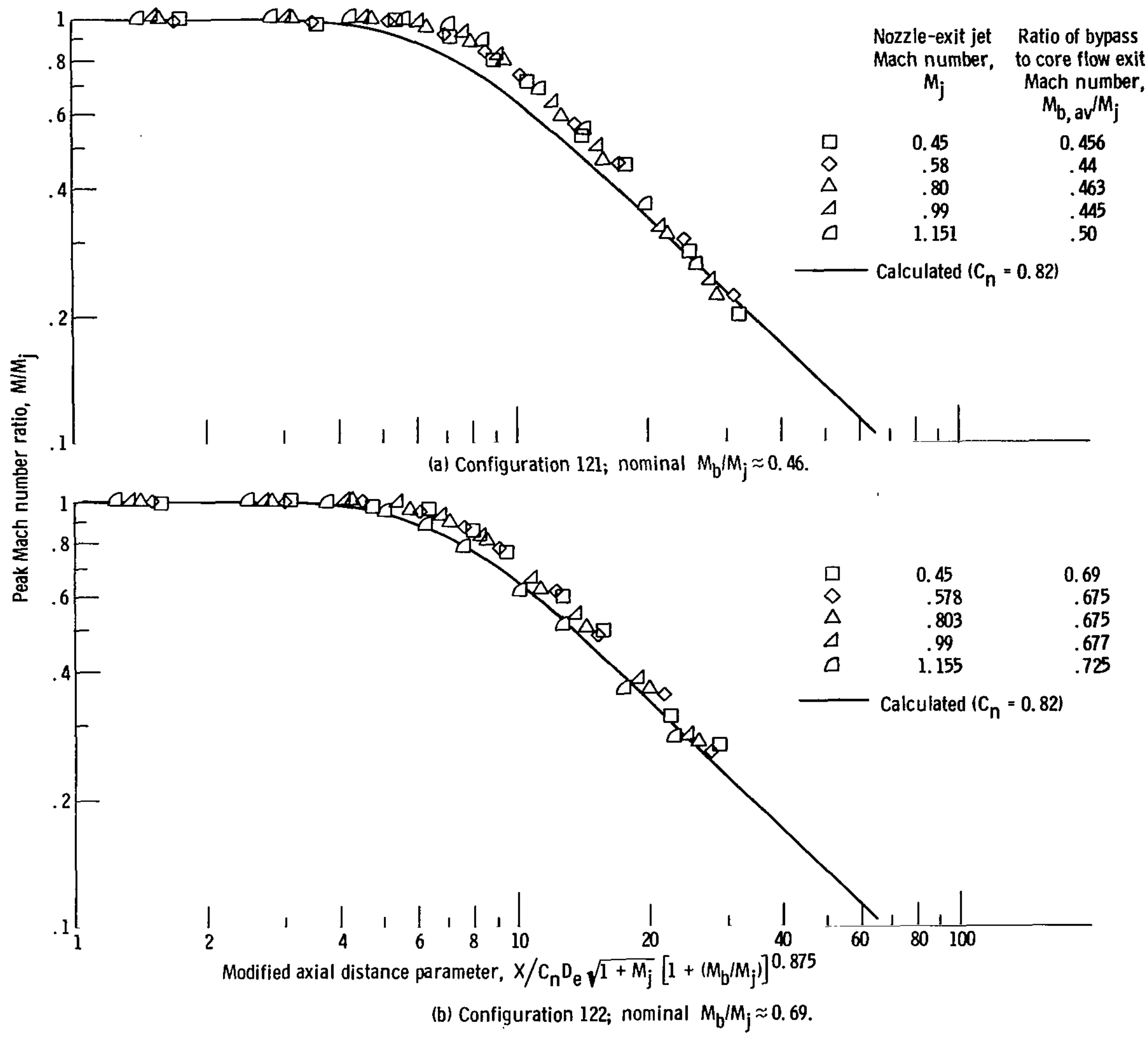

Figure 111. - Normalization of effect of secondary-flow Mach number on large-bypass-nozzle peak axial Mach number decay. Primary, 5.18-centimeter-diameter circular convergent nozzle; secondary, 1.60-centimeter-wide convergent annulus; equivalent diameter, D_e, 5.18 centimeters.

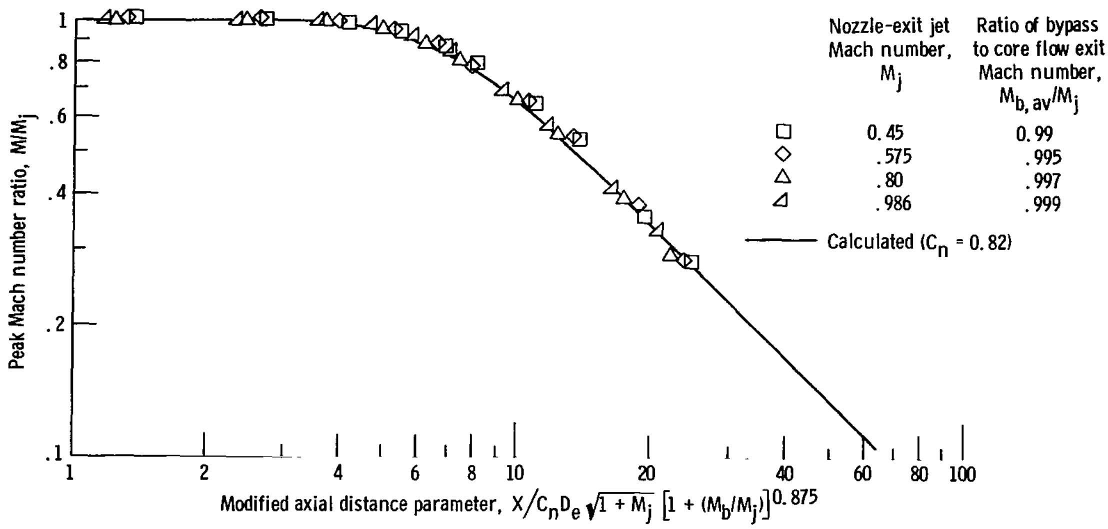

(c) Configuration 123; nominal $M_b/M_j \approx 1.0$

Figure 111. - Concluded.

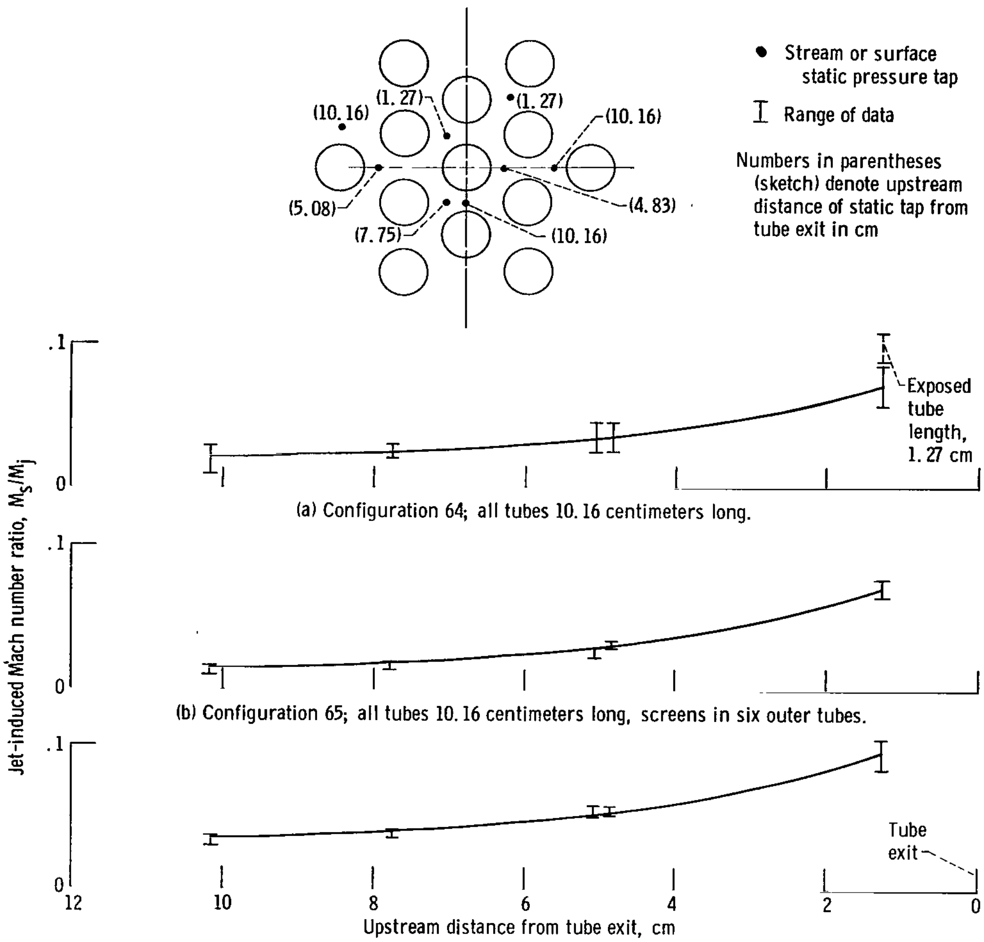

(c) Configuration 66; six outer tubes 3.81 centimeters long, seven inner tubes 10.16 centimeters long.

Figure 112. - Jet-induced Mach number ratios between tubes of multitube nozzles. Nozzle-exit jet Mach number, $0.64 < M_j < 1.15$.

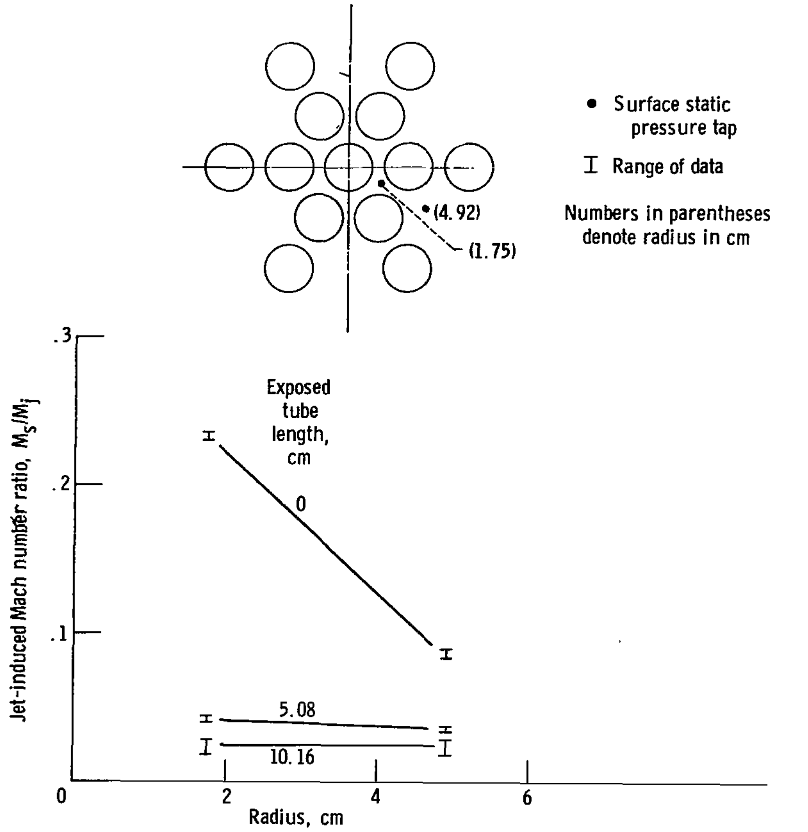

Figure 113. - Effect of exposed tube length of multitube nozzle on jet-induced base-surface Mach number ratio. Nozzle-exit jet Mach number, $0.81 < M_j < 0.99$; configuration 61.

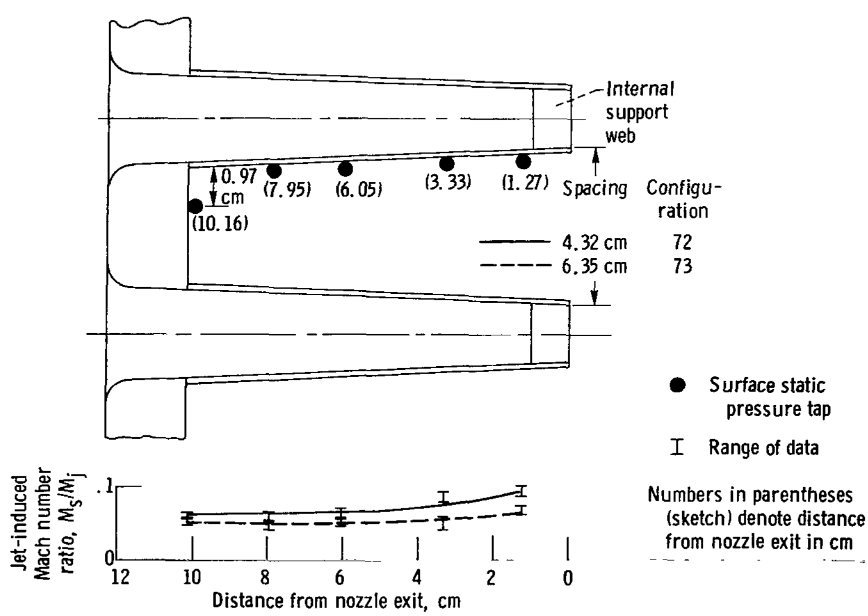

Figure 114. - Effect of three-slot nozzle spacing on jet-induced surface Mach number ratios between slots. Nozzle-exit jet Mach number, $0.45 < M_j < 1.148$.

APPENDIX A

JET MACH NUMBER DECAY CONTOURS

The nozzle-exit jet Mach number profiles are given for all the configurations reported in figures 115 to 218. The configurations are presented in the same order as they are discussed in the text and listed in tables I to III.

The Mach number decay contours of all the configurations have been nondimensionalized for both velocity and axial downstream distance. Lines of constant ratios of downstream local Mach number M_l to nozzle-exit jet Mach number M_j are shown as a function of axial distance divided by the equivalent diameter of a single element of the nozzle. The contours are all for a nominal M_j of 0.99.

These contours can be used to estimate the jet profile at downstream distances of interest.

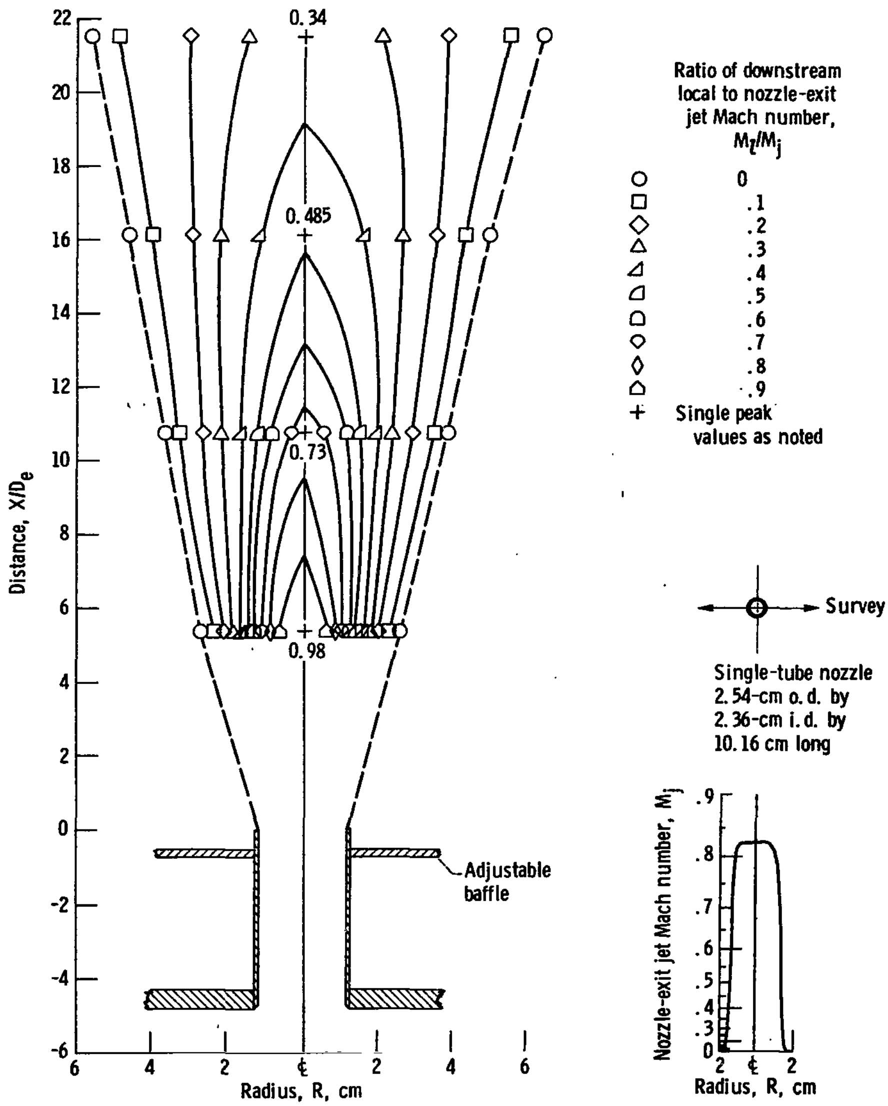

Figure 115. - Configuration 1. Nozzle-exit jet Mach number, M_j, 0.825; equivalent diameter, D_e, 2.36 centimeters; exposed tube length, 1.27 centimeters.

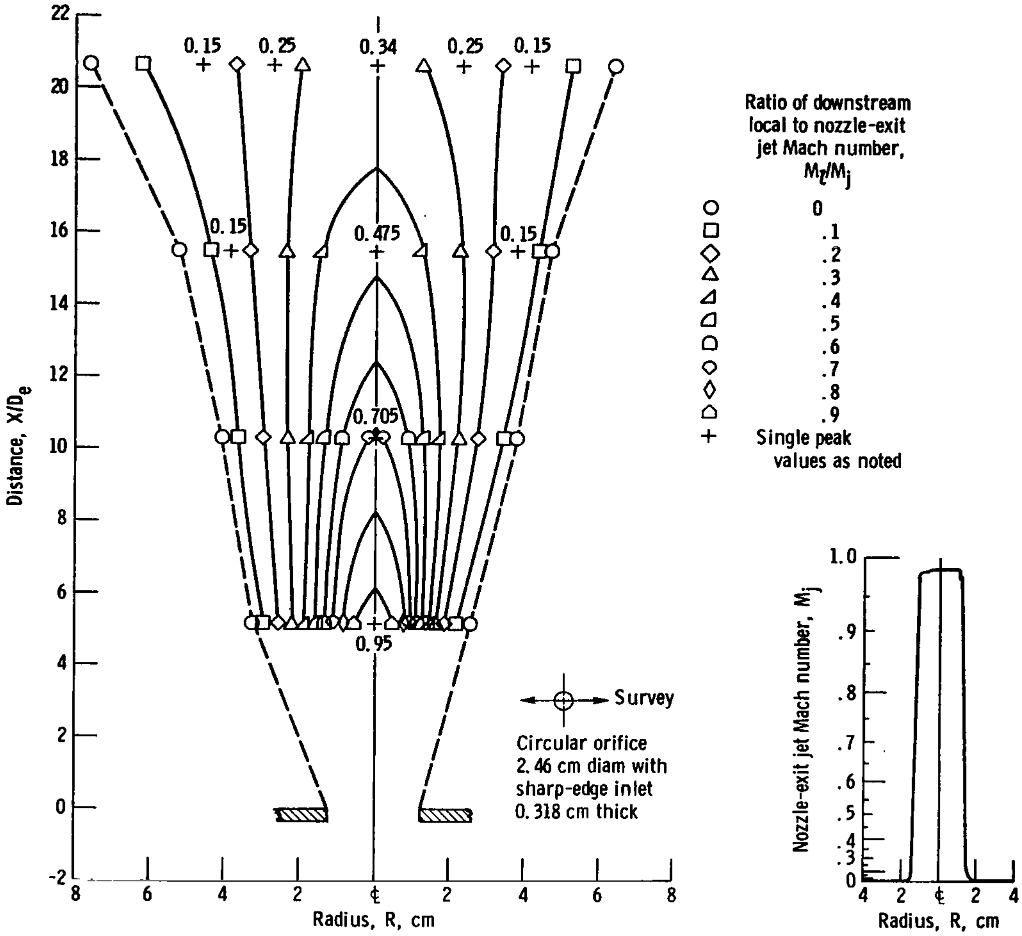

Figure 116. - Configuration 2. Nozzle-exit jet Mach number, M_j, 0.985; equivalent diameter, D_e, 2.46 centimeters.

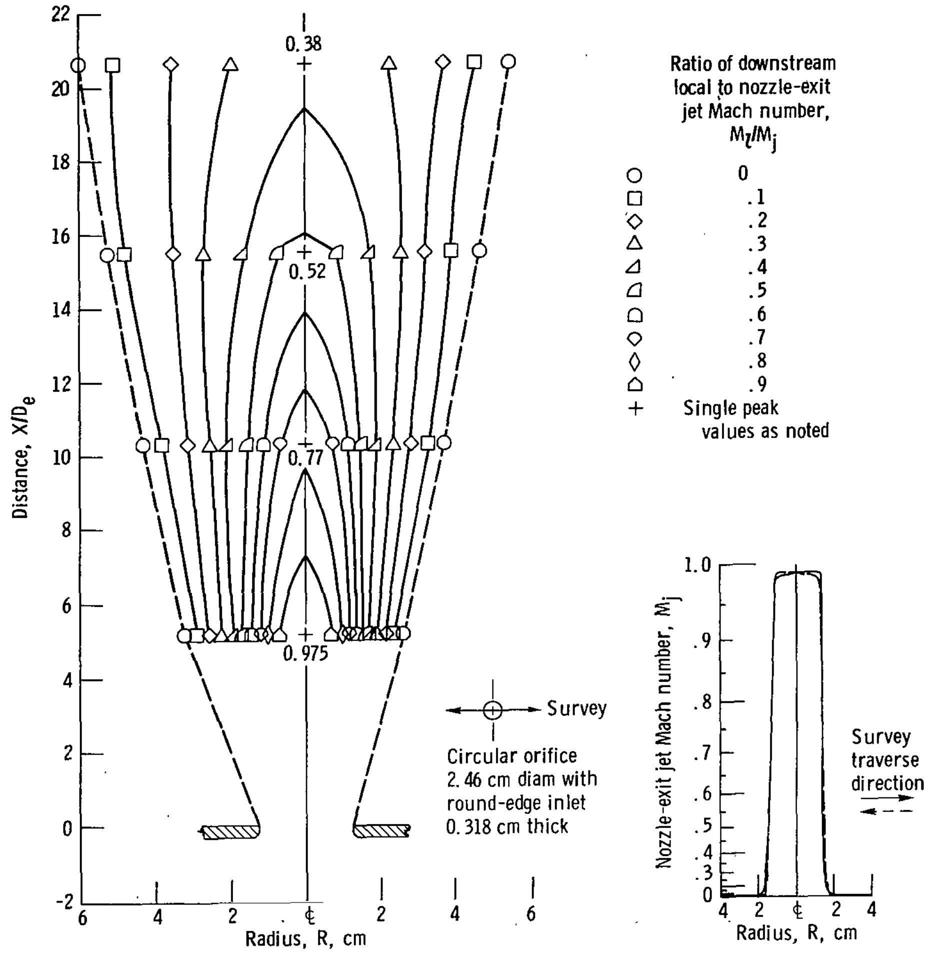

Figure 117. - Configuration 3. Nozzle-exit jet Mach number, M_j, 0.99; equivalent diameter, D_e, 2.46 centimeters.

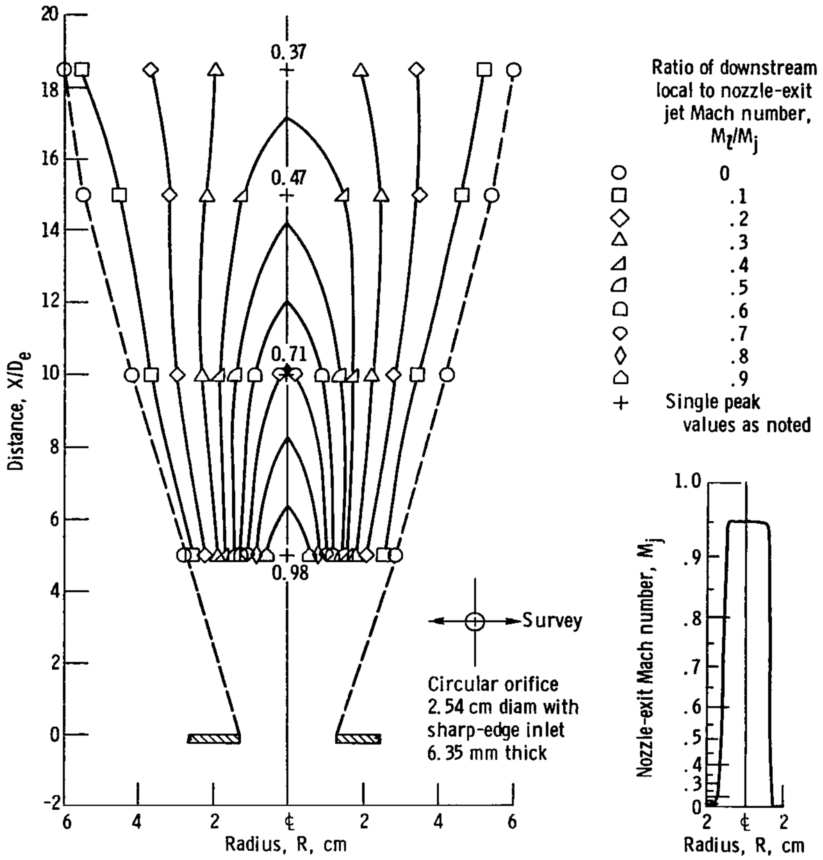

Figure 118. - Configuration 4. Nozzle-exit jet Mach number, M_j, 0.952; equivalent diameter, D_e, 2.54 centimeters.

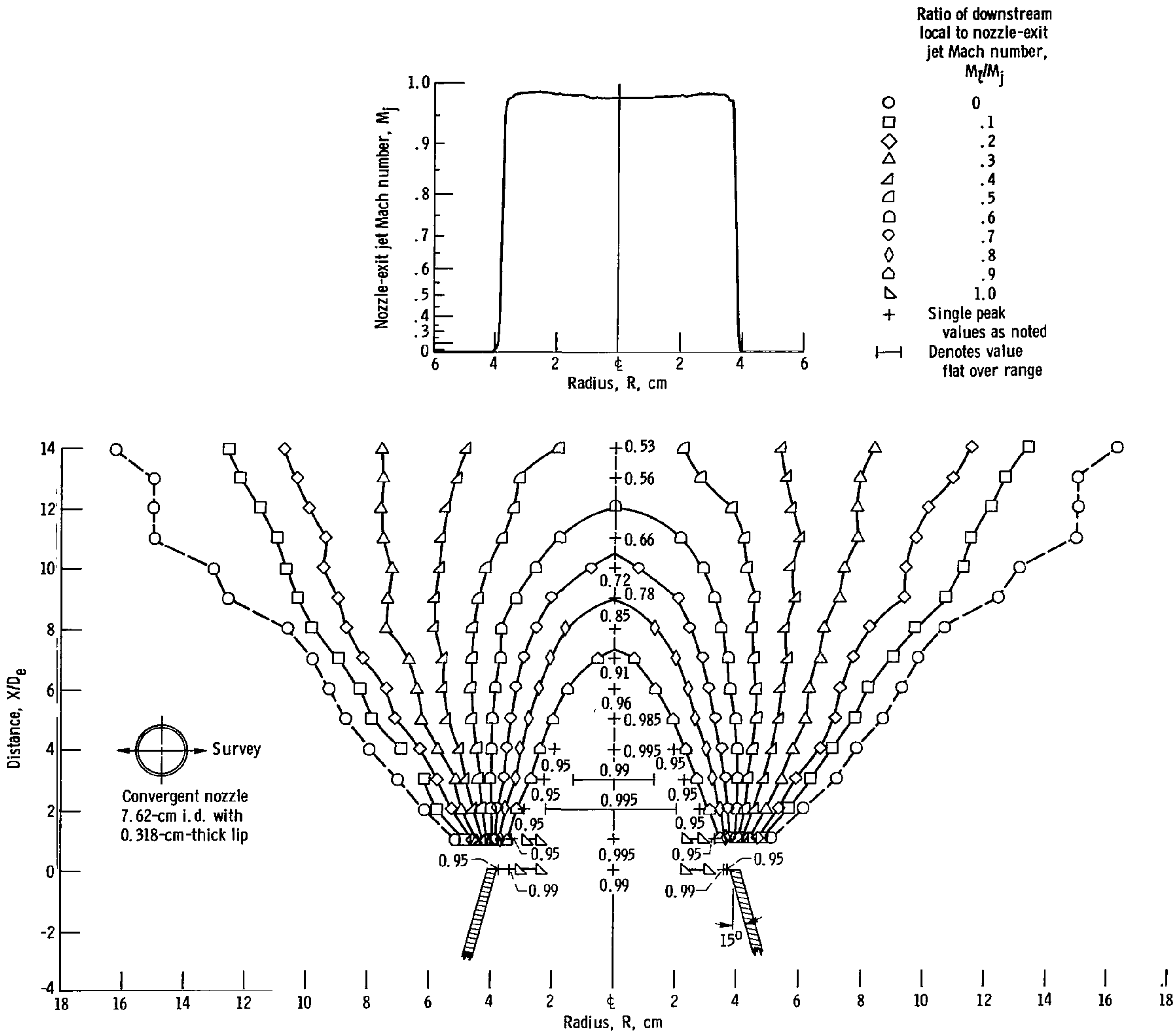

Figure 119. - Configuration 5. Nozzle-exit jet Mach number, M_j, 0.985; equivalent diameter, D_e, 7.62 centimeters.

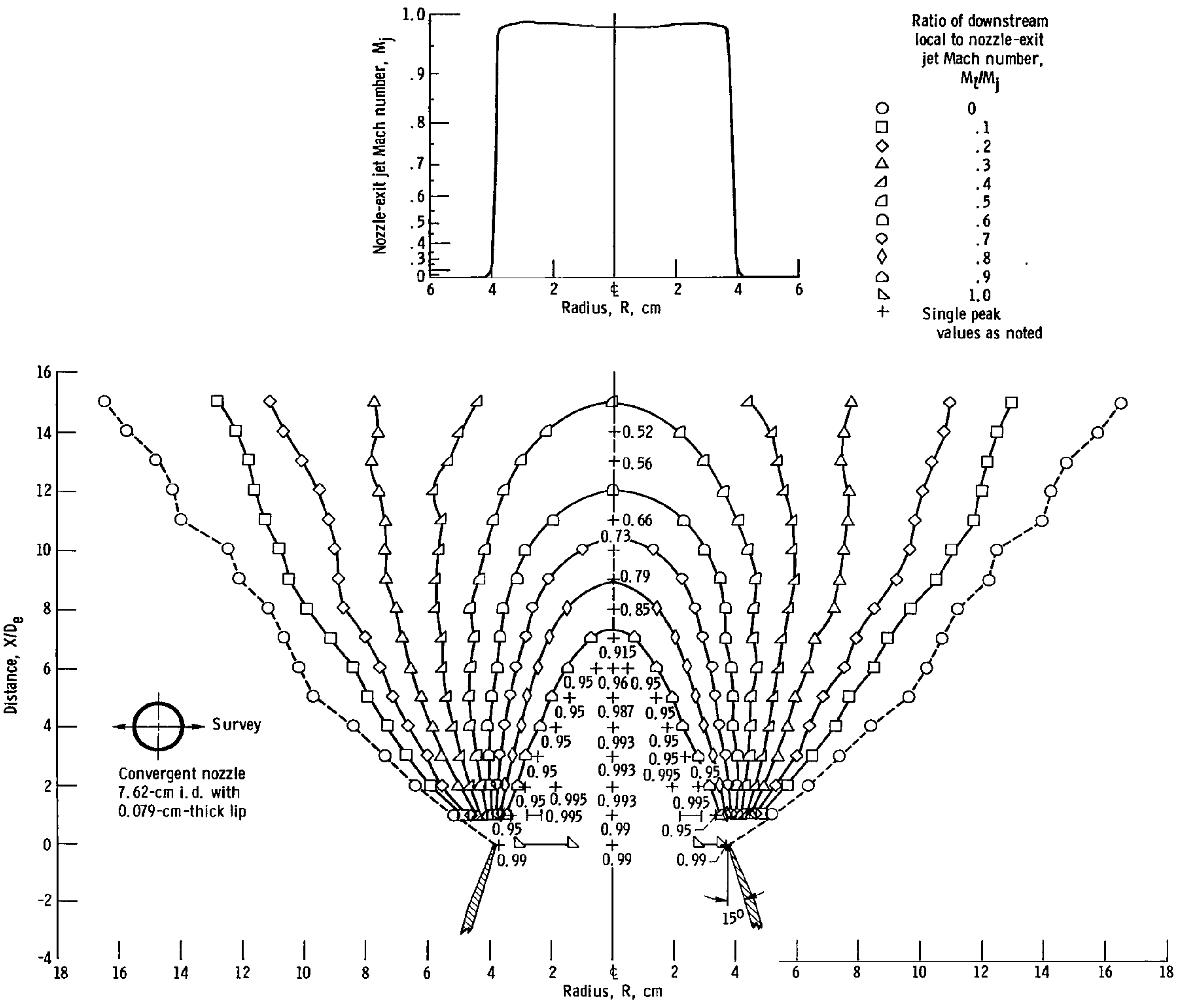

Figure 120. - Configuration 6. Nozzle-exit jet Mach number, M_j, 0.985; equivalent diameter, D_e, 7.62 centimeters.

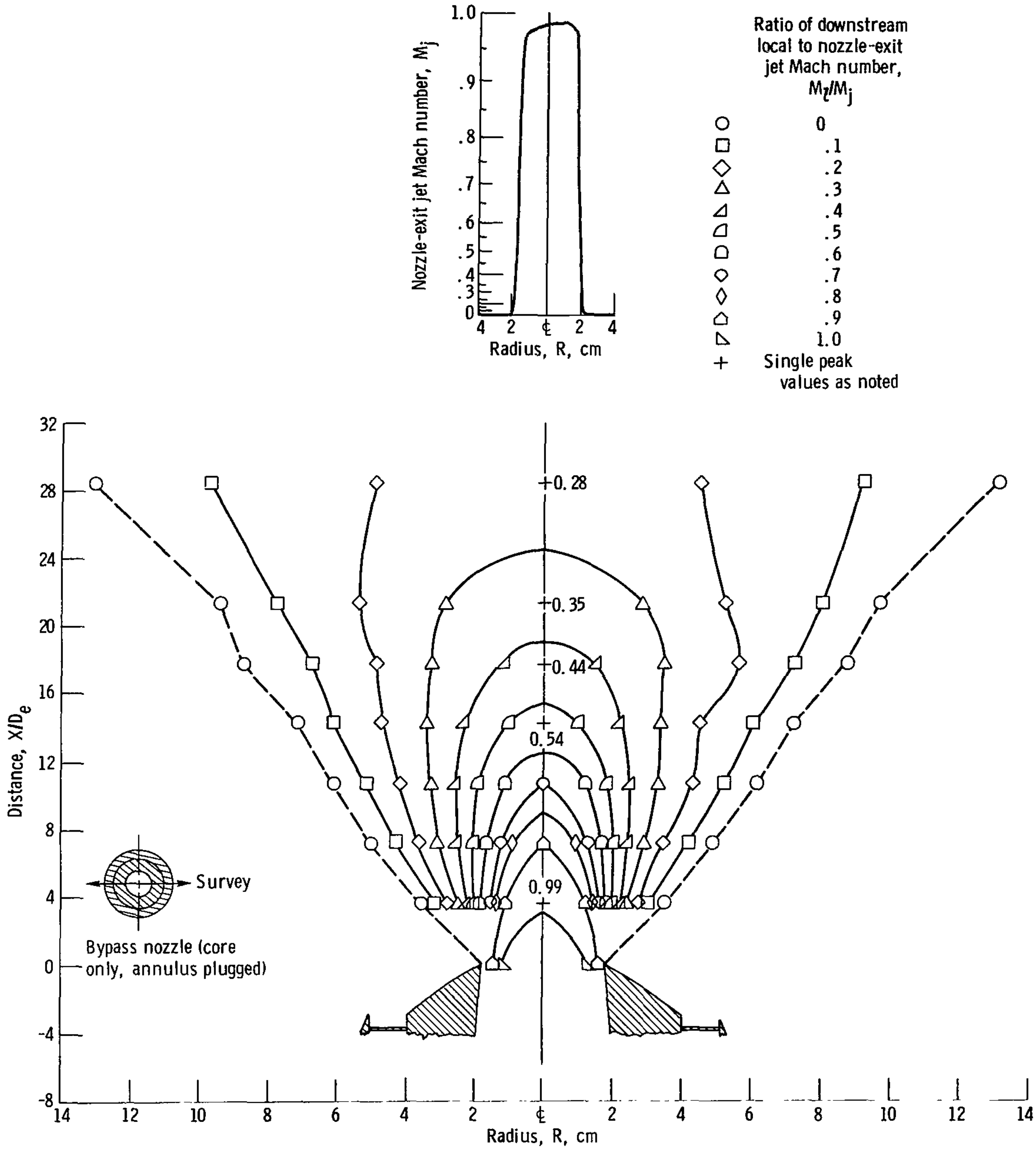

Figure 121. - Configuration 7. Nozzle-exit jet Mach number, M_j, 0.991; equivalent diameter, D_e, 3.58 centimeters.

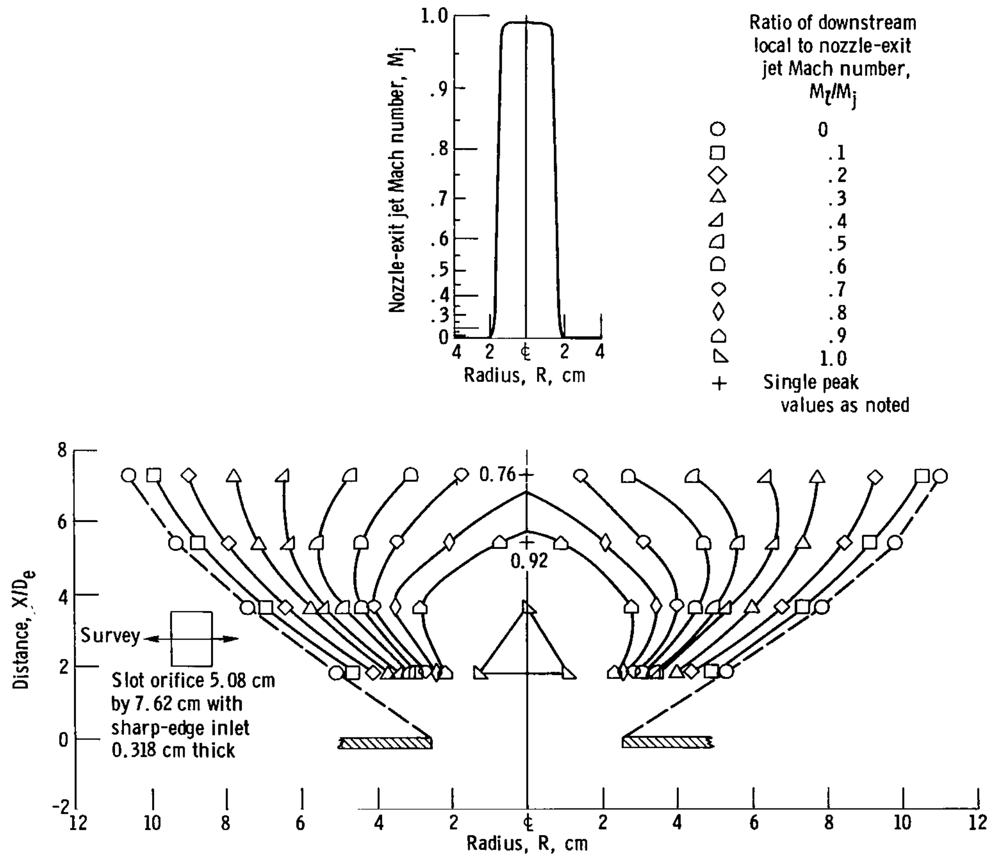

Figure 122. - Configuration 9. Nozzle-exit jet Mach number, M_j, 0.99; equivalent diameter, D_e, 7.03 centimeters.

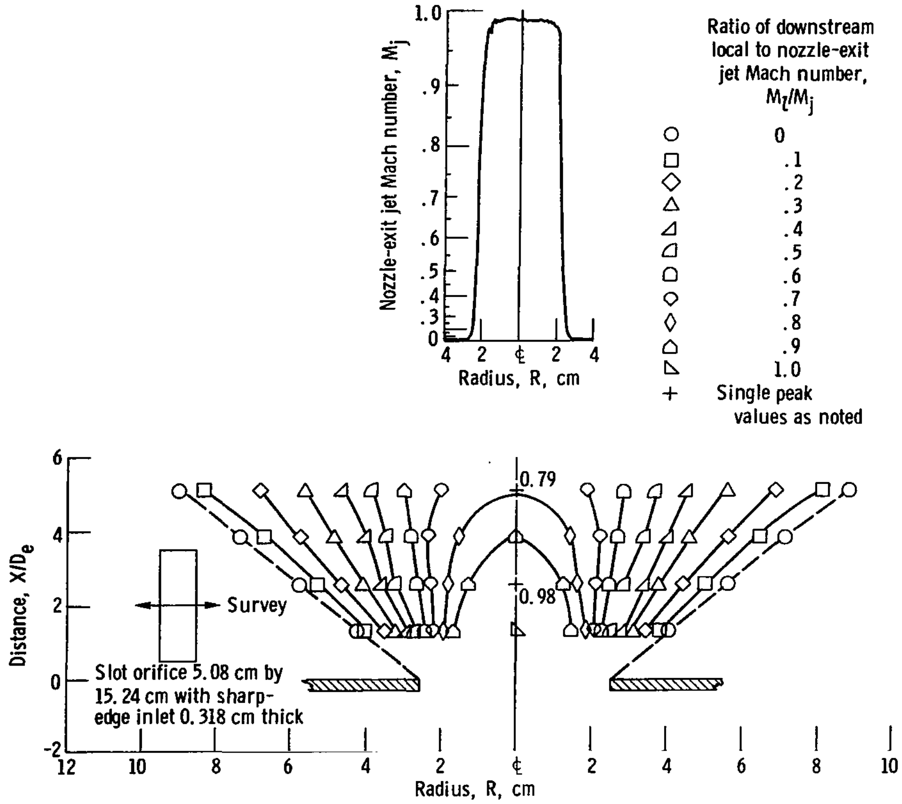

Figure 123. - Configuration 10. Nozzle-exit jet Mach number, M_j, 0.99; equivalent diameter, D_e, 9.94 centimeters.

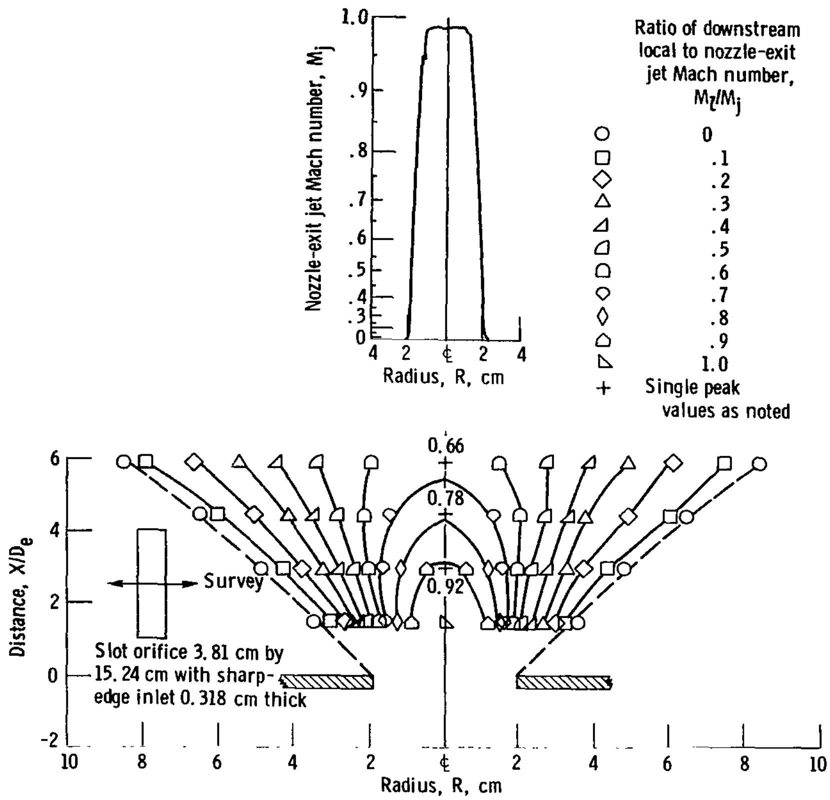

Figure 124. - Configuration 11. Nozzle-exit jet Mach number, M_j, 0.99; equivalent diameter, D_e, 8.6 centimeters.

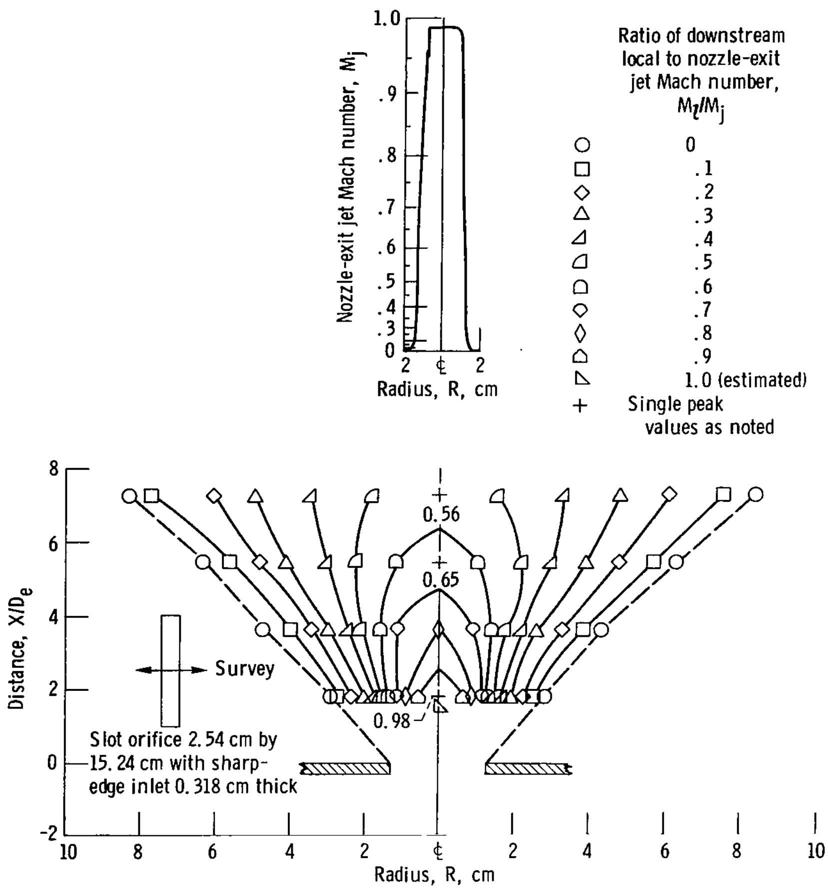

Figure 125. - Configuration 12. Nozzle-exit jet Mach number, M_j, 0.99; equivalent diameter, D_e, 7.03 centimeters.

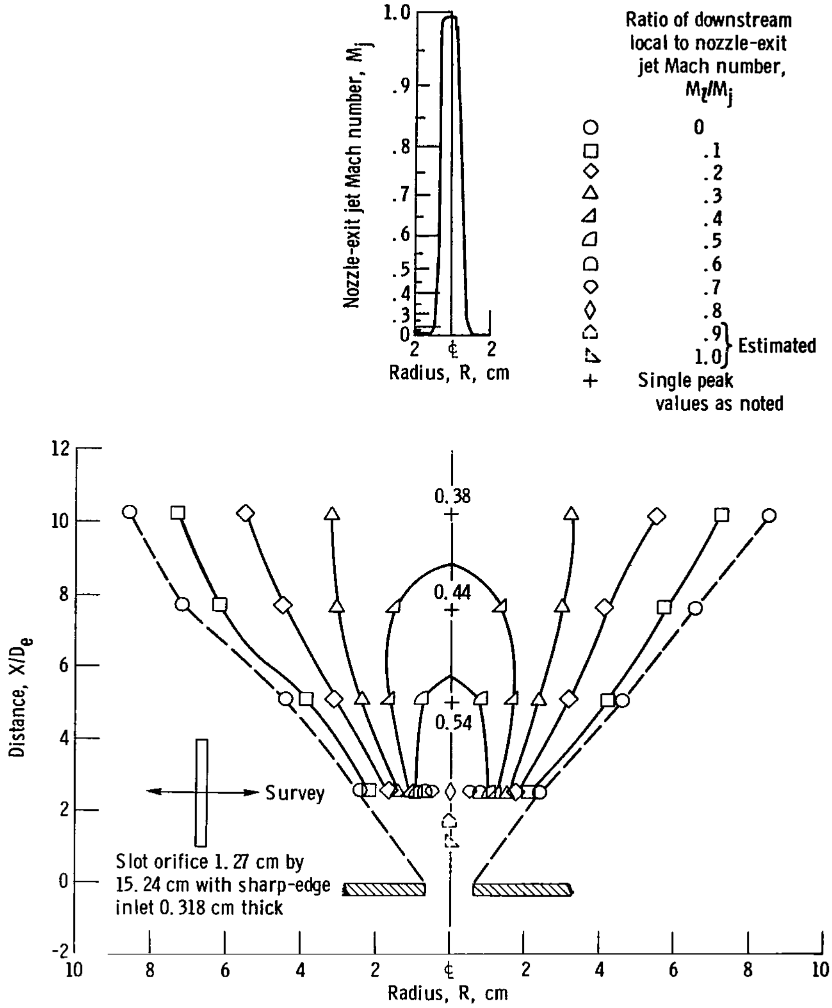

Figure 126. - Configuration 13. Nozzle-exit jet Mach number, M_j, 0.99; equivalent diameter, D_e, 4.96 centimeters.

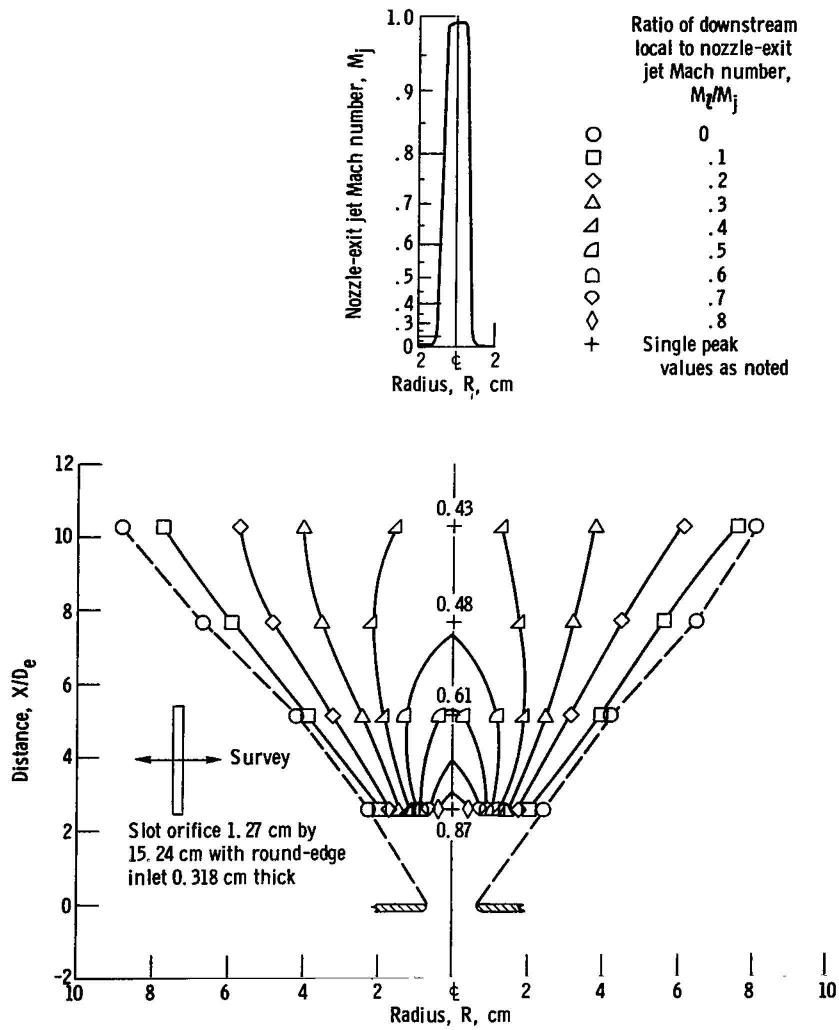

Figure 127. - Configuration 14. Nozzle-exit jet Mach number, M_j, 0.99; equivalent diameter, D_e, 4.96 centimeters.

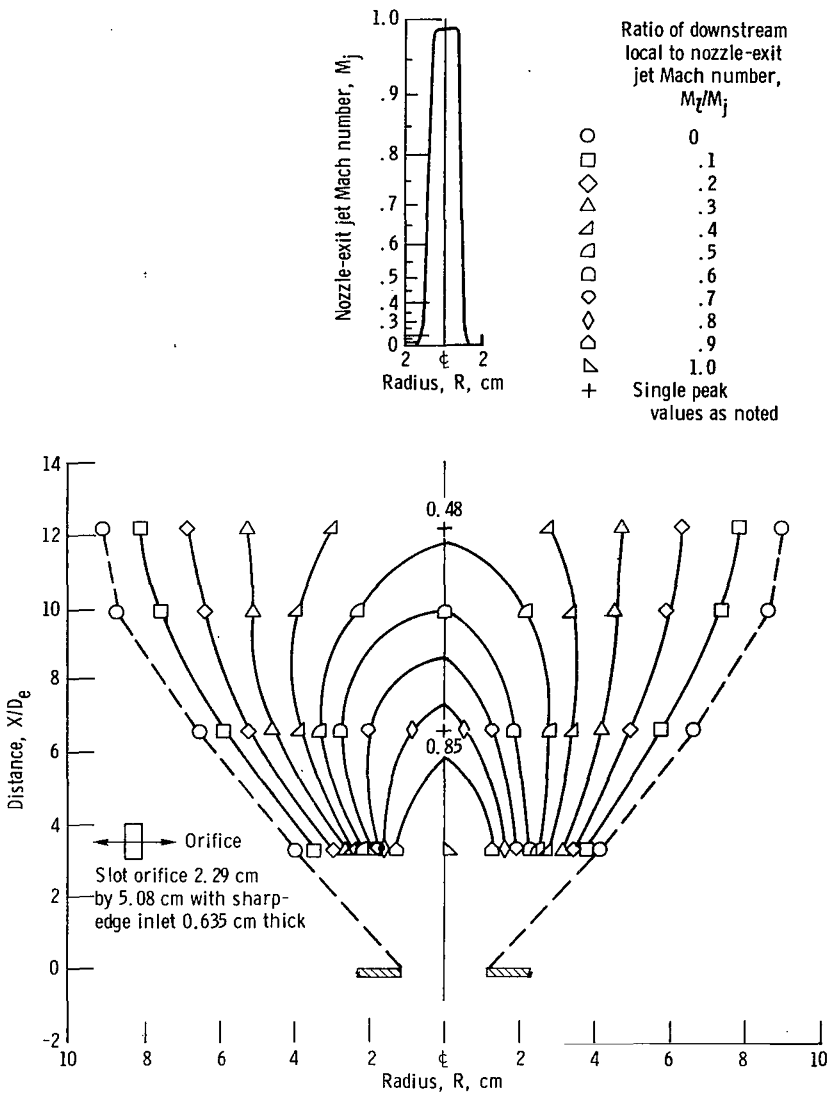

Figure 128. - Configuration 15. Nozzle-exit jet Mach number, M_j, 0.985; equivalent diameter, D_e, 3.84 centimeters.

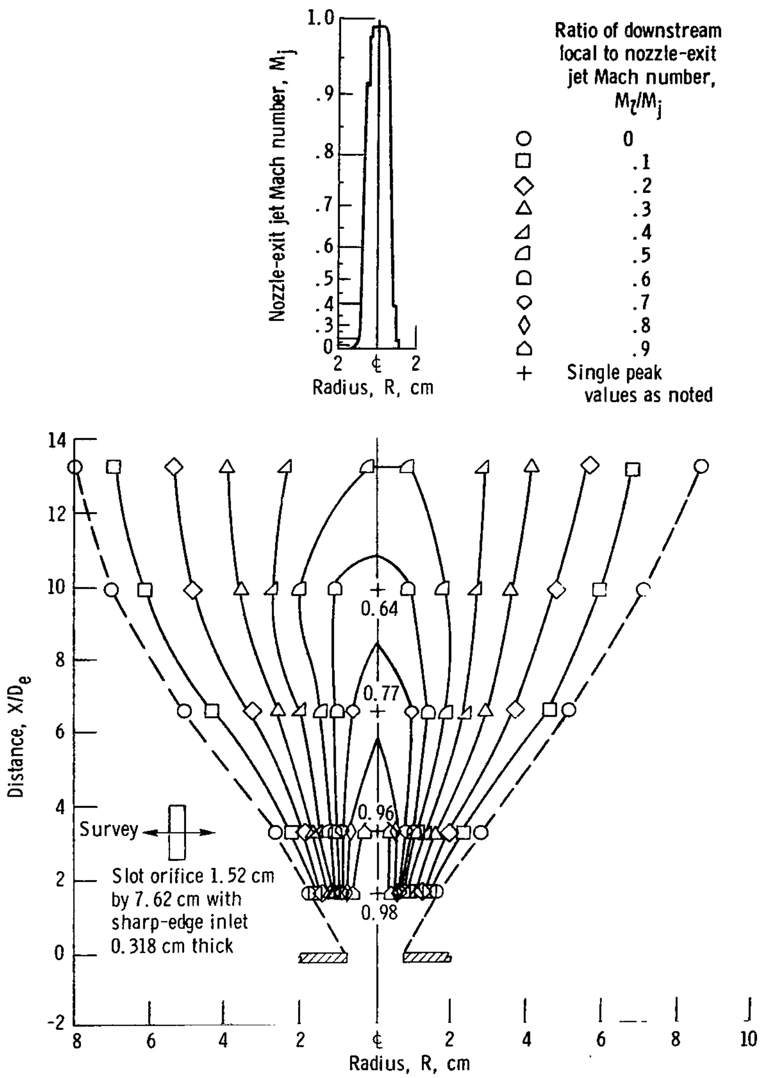

Figure 129. - Configuration 16. Nozzle-exit jet Mach number, M_j, 0.99; equivalent diameter, D_e, 3.84 centimeters.

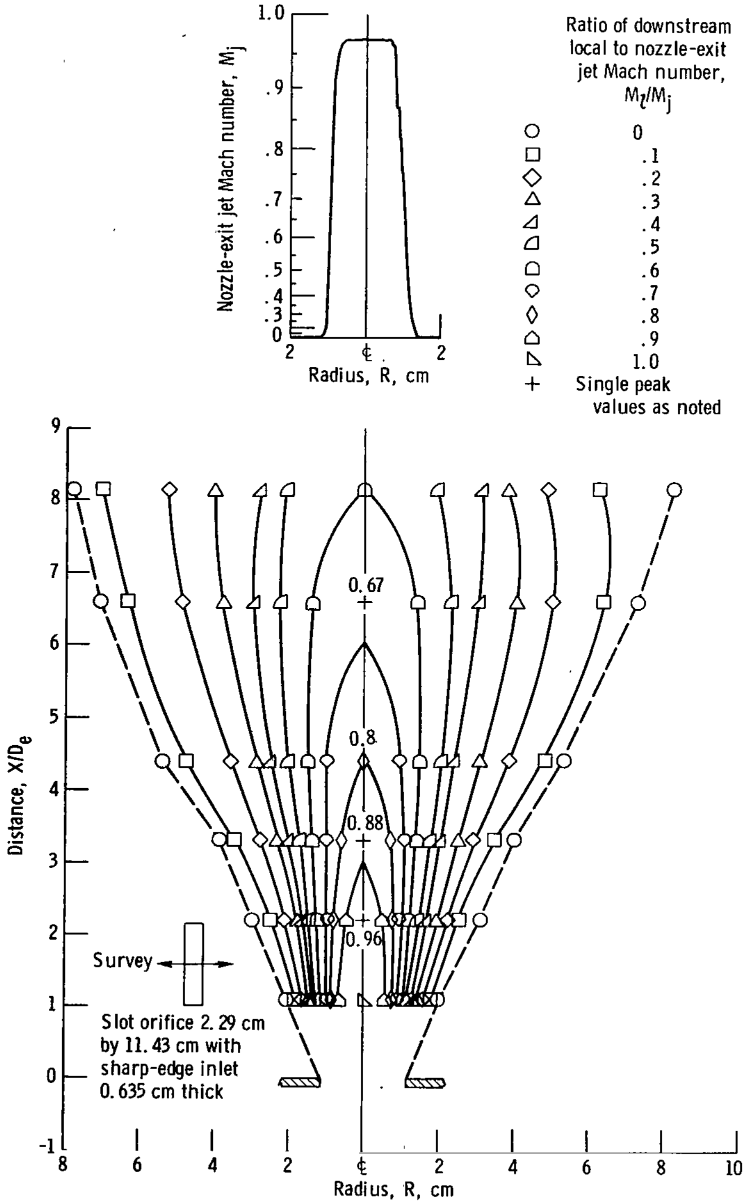

Figure 130. - Configuration 17. Nozzle-exit jet Mach number, M_j, 0.97; equivalent diameter, D_e, 5.76 centimeters.

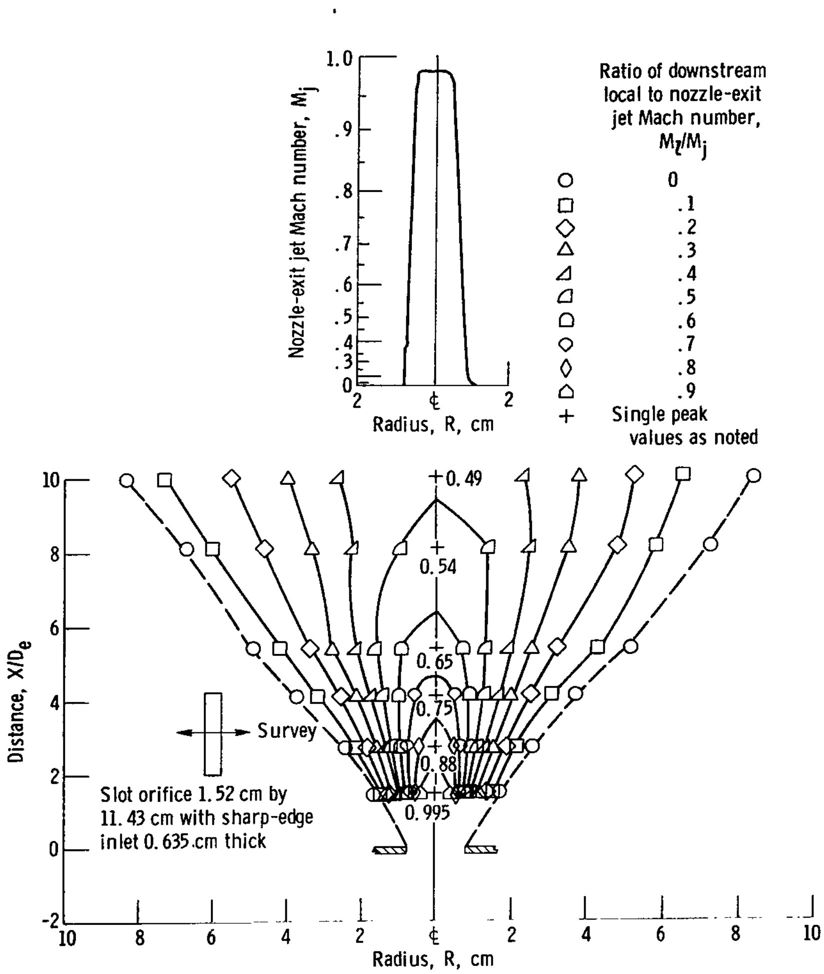

Figure 131. - Configuration 18. Nozzle-exit jet Mach number, M_j, 0.98; equivalent diameter, D_e, 4.71 centimeters.

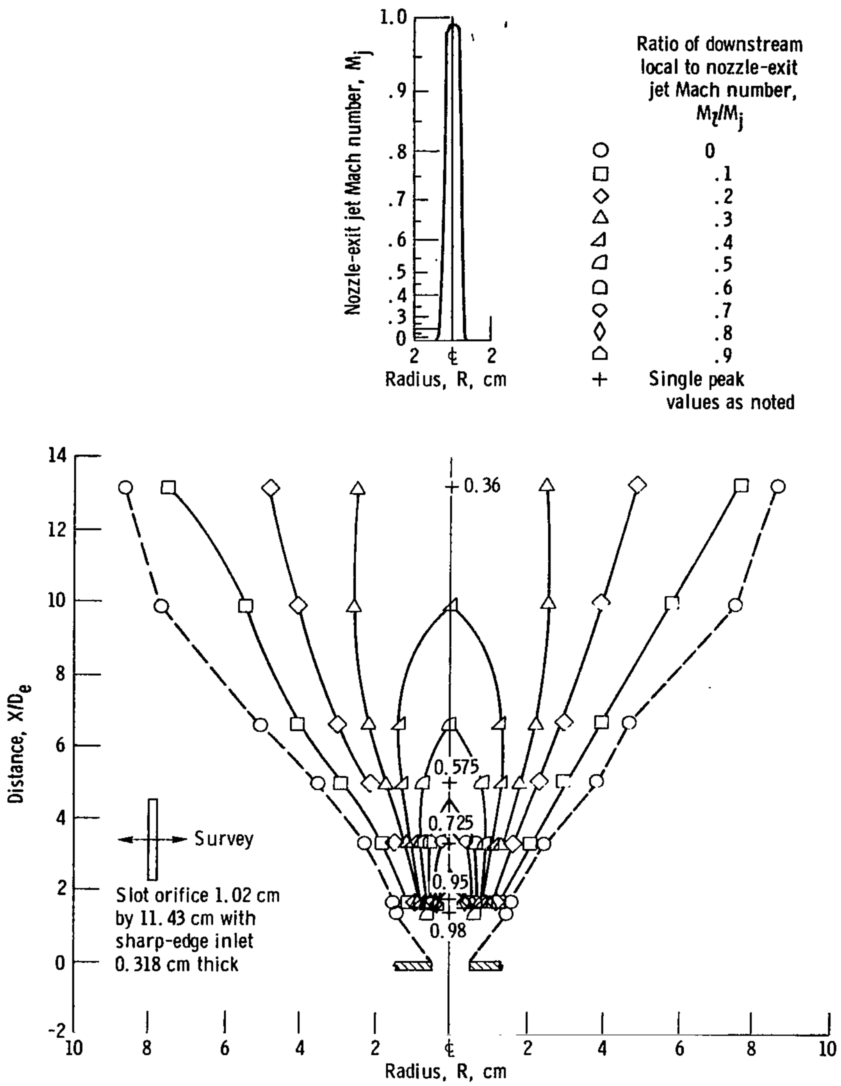

Figure 132. - Configuration 19. Nozzle-exit jet Mach number, M_j, 0.99; equivalent diameter, D_e, 3.84 centimeters.

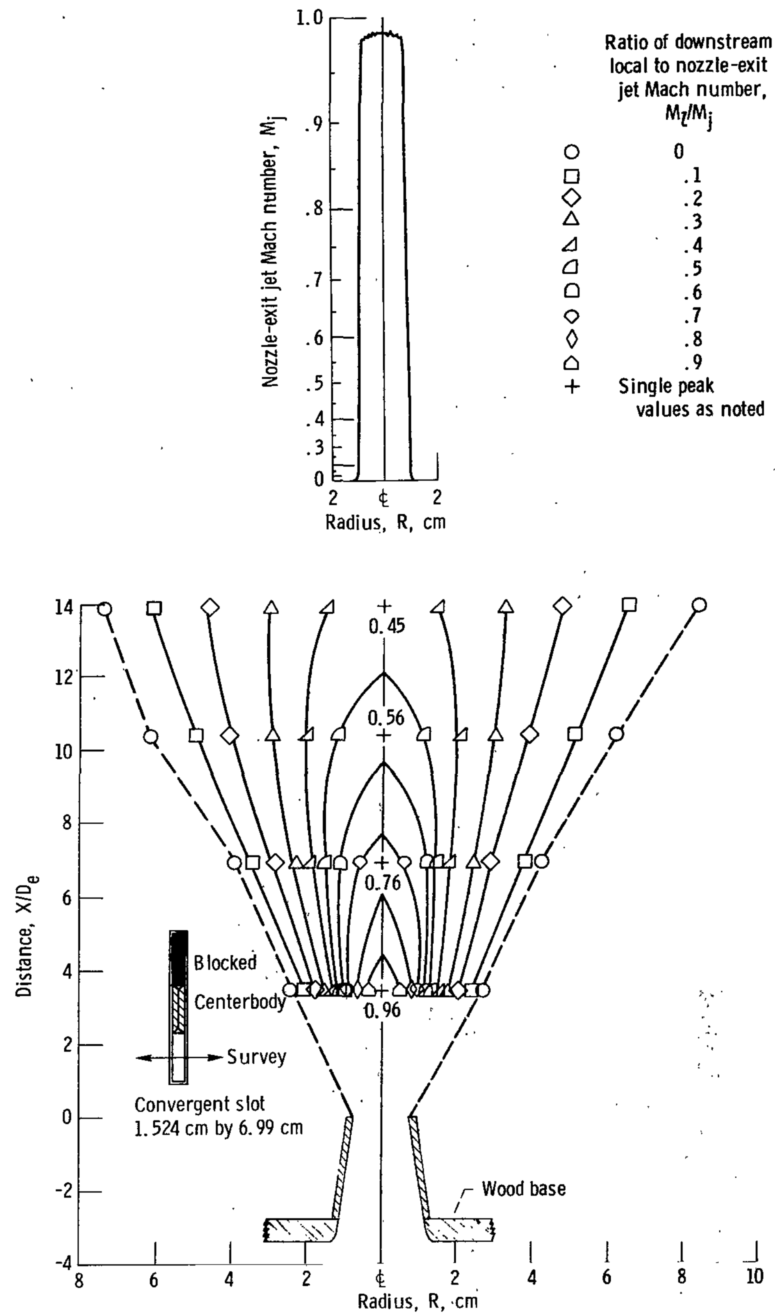

Figure 133. - Configuration 20. Nozzle-exit jet Mach number, M_j, 0.985; equivalent diameter, D_e, 3.68 centimeters.

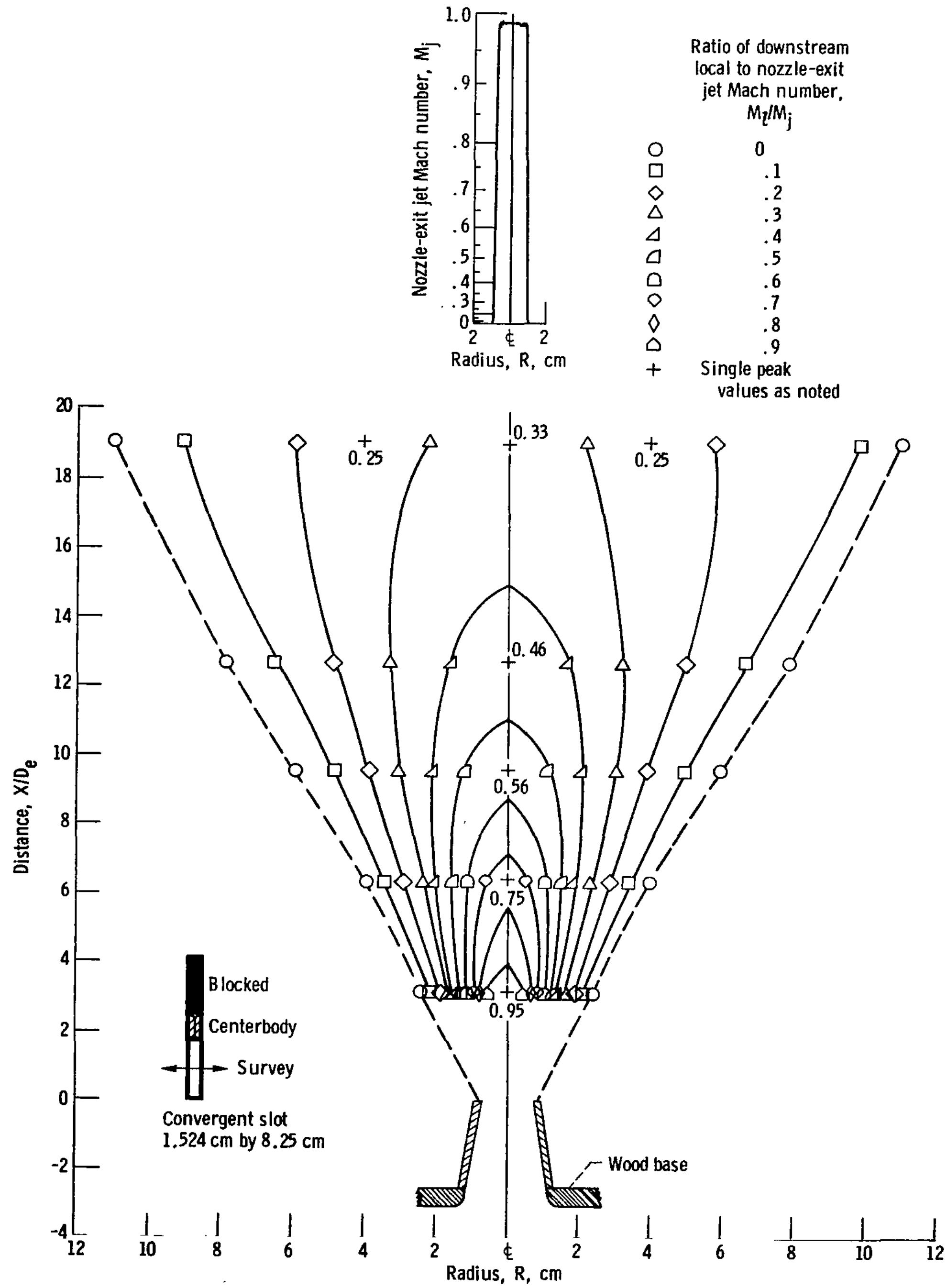

Figure 134. - Configuration 21. Nozzle-exit jet Mach number, M_j, 0.99; equivalent diameter, D_e, 4.00 centimeters.

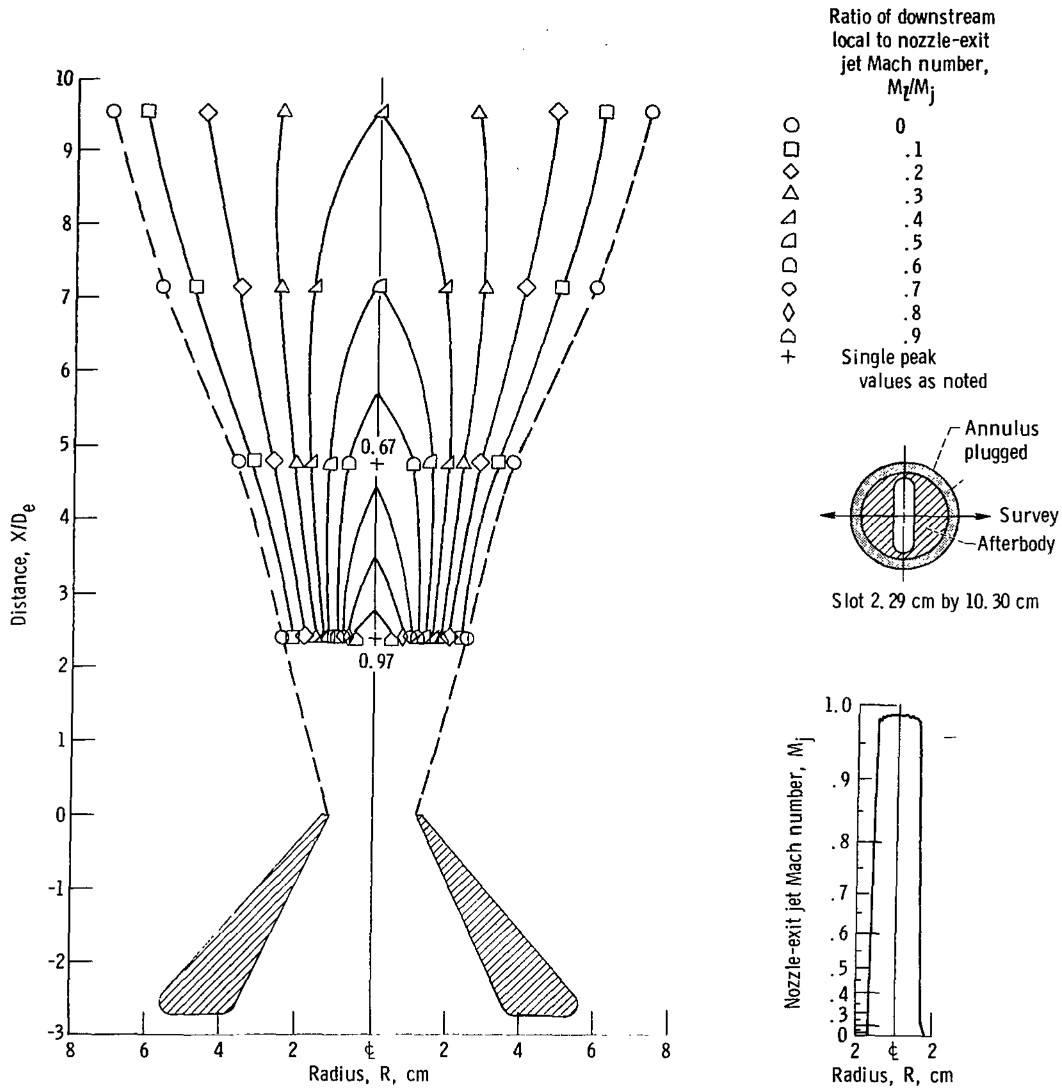

Figure 135. - Configuration 22 (slot nozzle vertical). Nozzle-exit jet Mach number, M_j, 0.987; equivalent diameter, D_e, 5.32 centimeters.

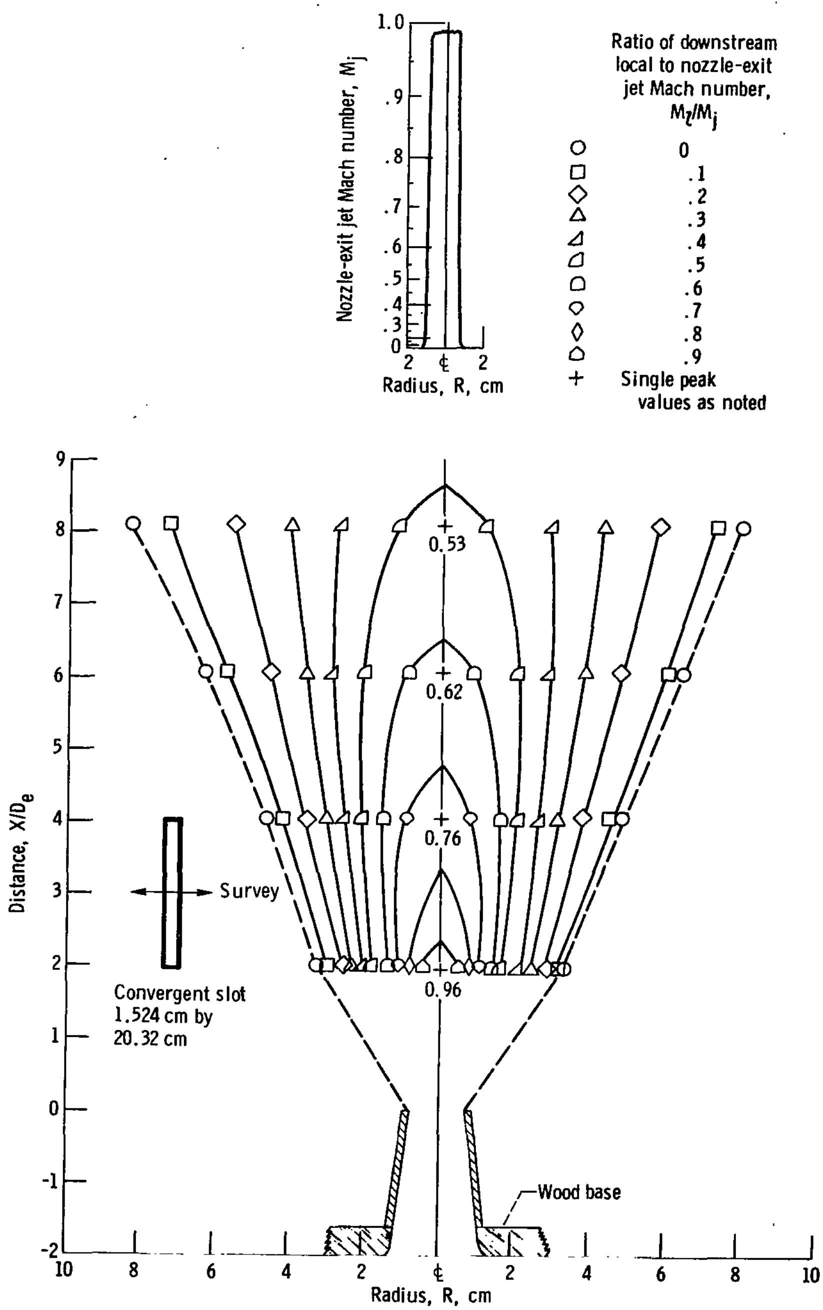

Figure 136. - Configuration 23. Nozzle-exit jet Mach number, M_j, 0.99; equivalent diameter, D_e, 6.28 centimeters.

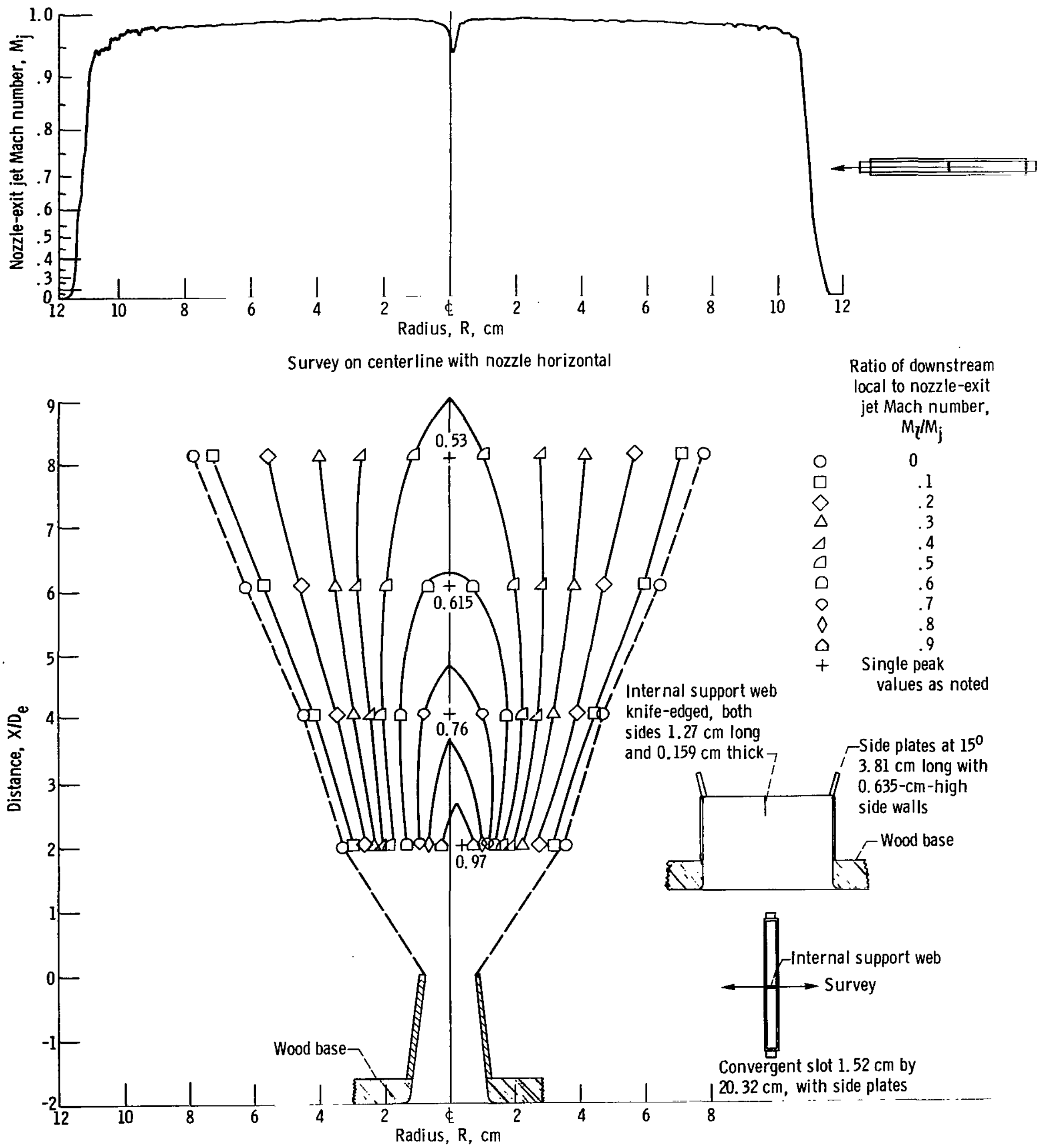

(a) Survey on nozzle centerline; nozzle vertical.

Figure 137. - Configuration 24. Nozzle-exit jet Mach number, M_j, 0.99; equivalent diameter, D_e, 6.28 centimeters.

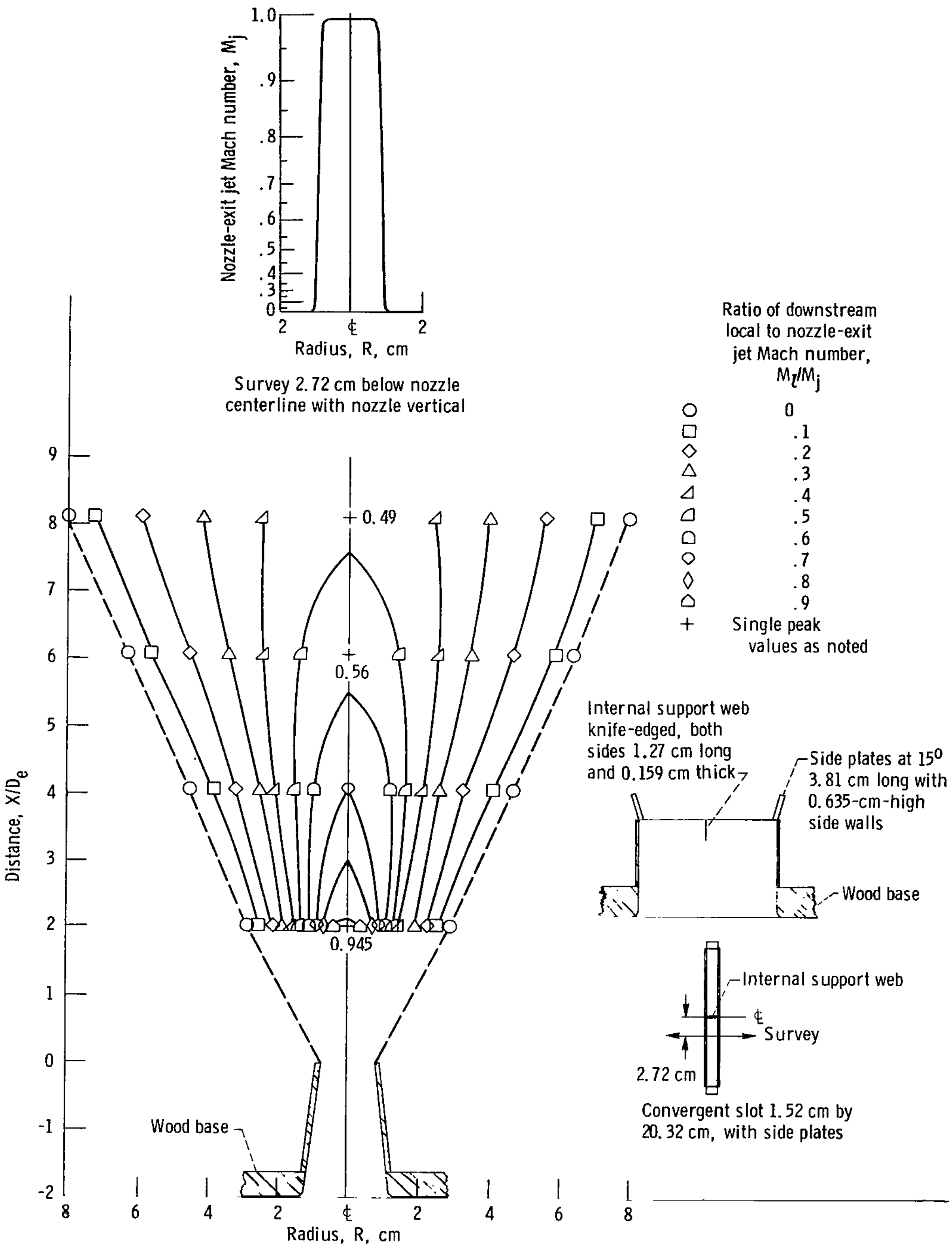

(b) Survey below nozzle centerline; nozzle vertical.

Figure 137. - Concluded.

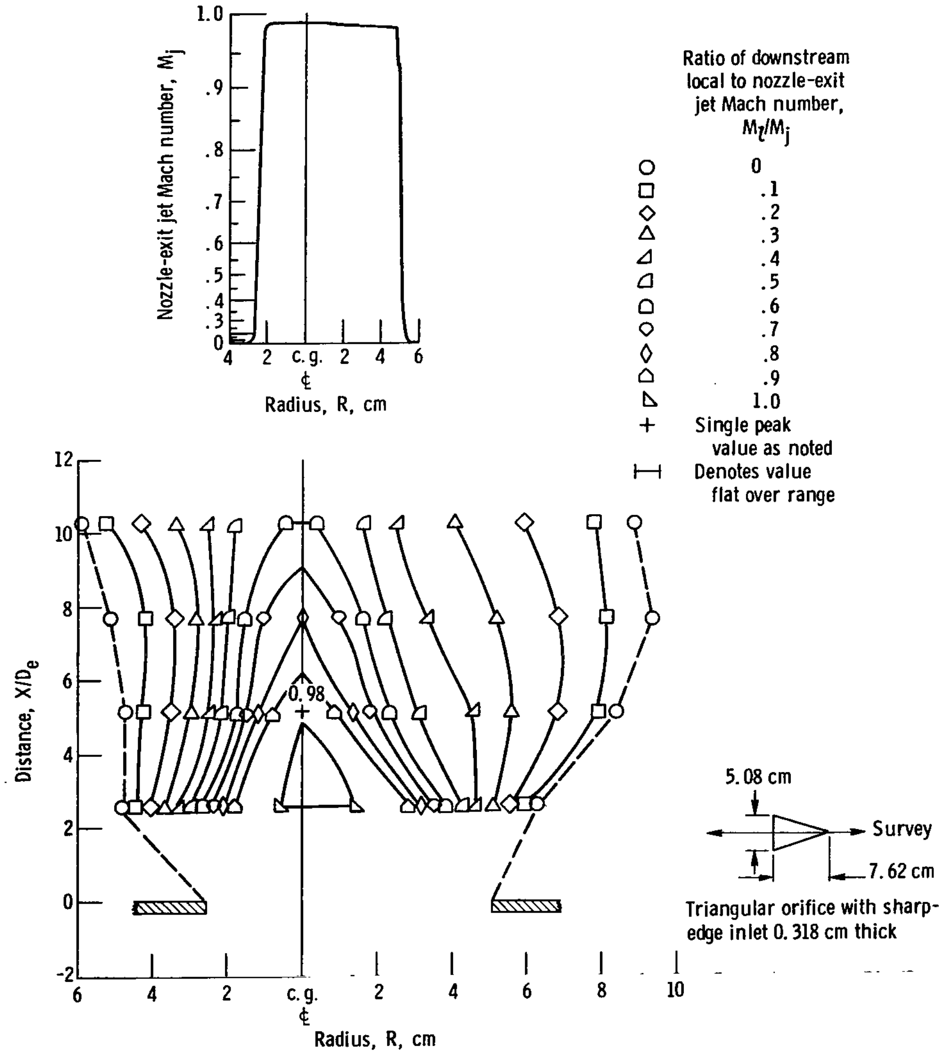

Figure 138. - Configuration 31. Nozzle-exit jet Mach number, M_j, 0.99; equivalent diameter, D_e, 4.96 centimeters.

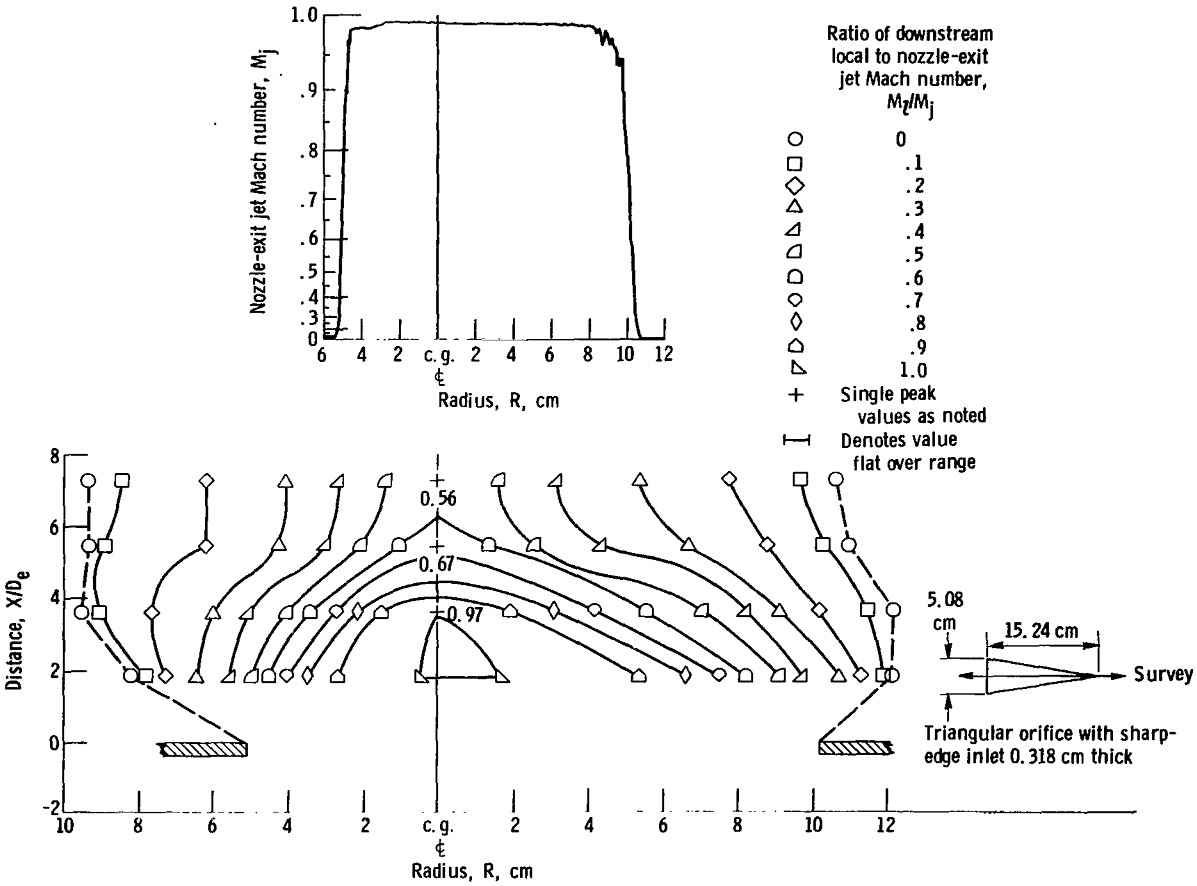

Figure 139. - Configuration 32. Nozzle-exit jet Mach number, M_j, 0.99; equivalent diameter, D_e, 7.03 centimeters.

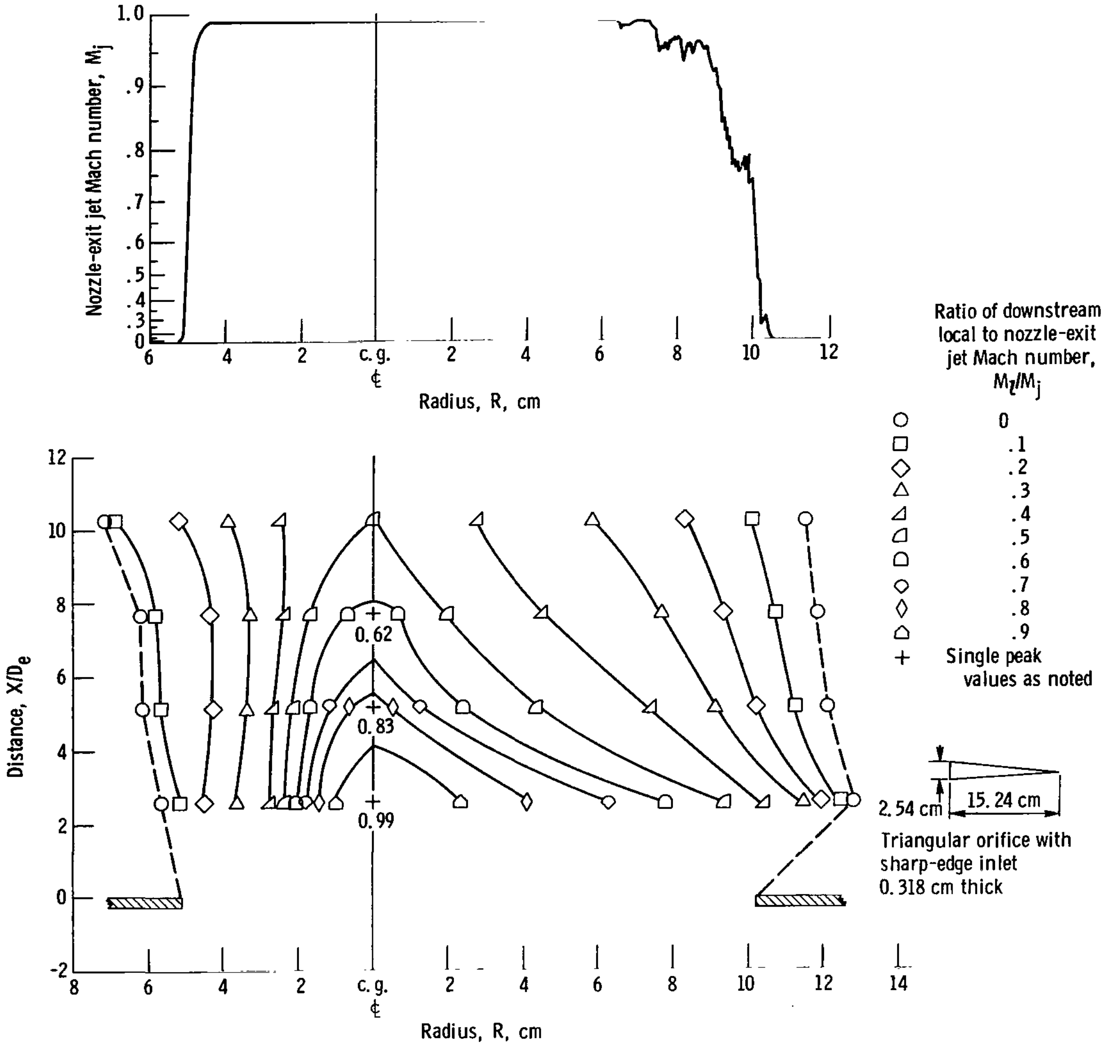

Figure 140. - Configuration 33. Nozzle-exit jet Mach number, M_j, 0.99; equivalent diameter, D_e, 4.96 centimeters.

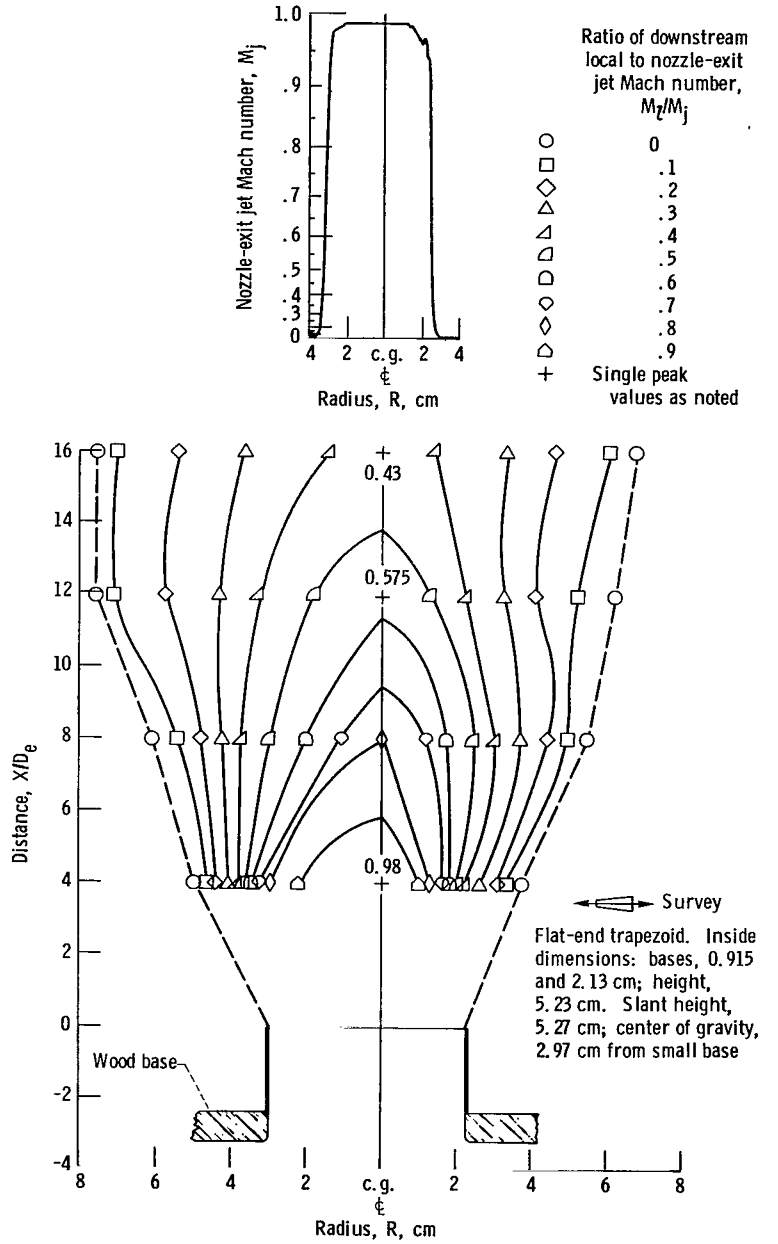

Figure 141. - Configuration 34. Nozzle-exit jet Mach number, M_j, 0.99; equivalent diameter, D_e, 3.19 centimeters.

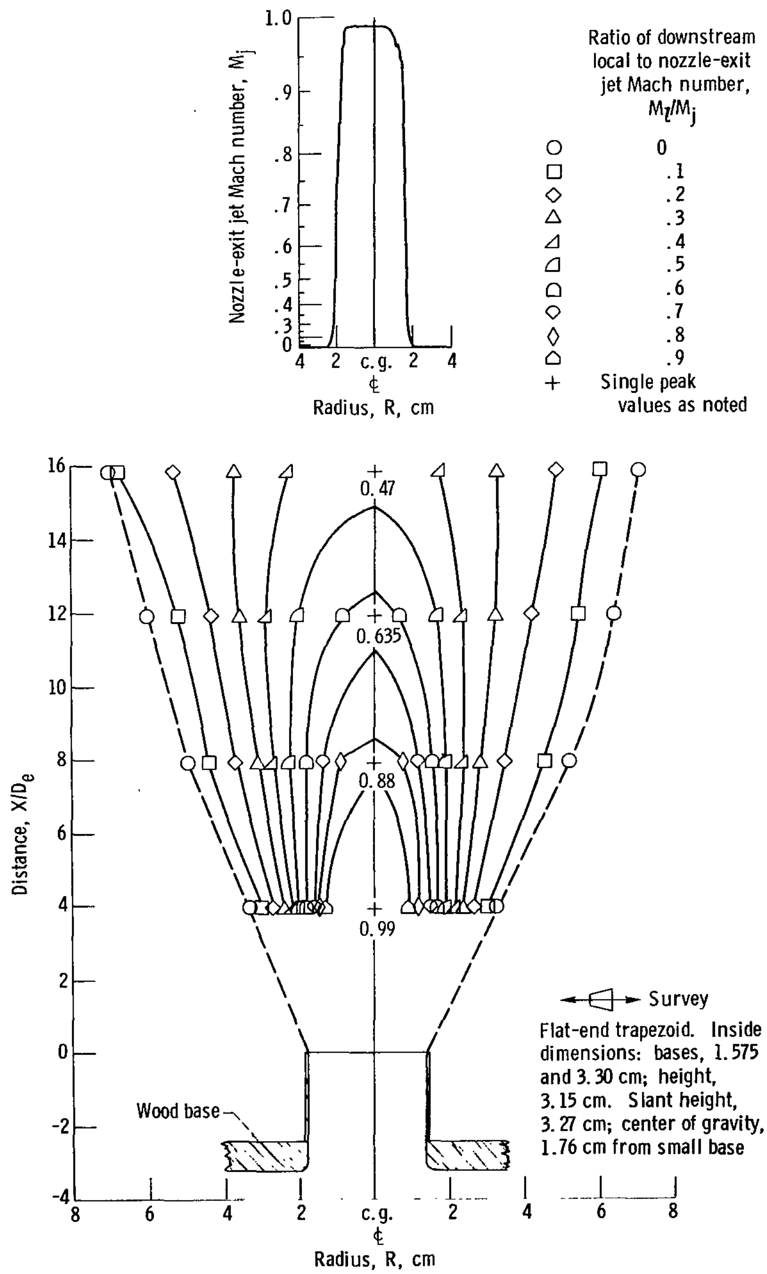

Figure 142. - Configuration 35. Nozzle-exit jet Mach number, M_j, 0.99; equivalent diameter, D_e, 3.125 centimeters.

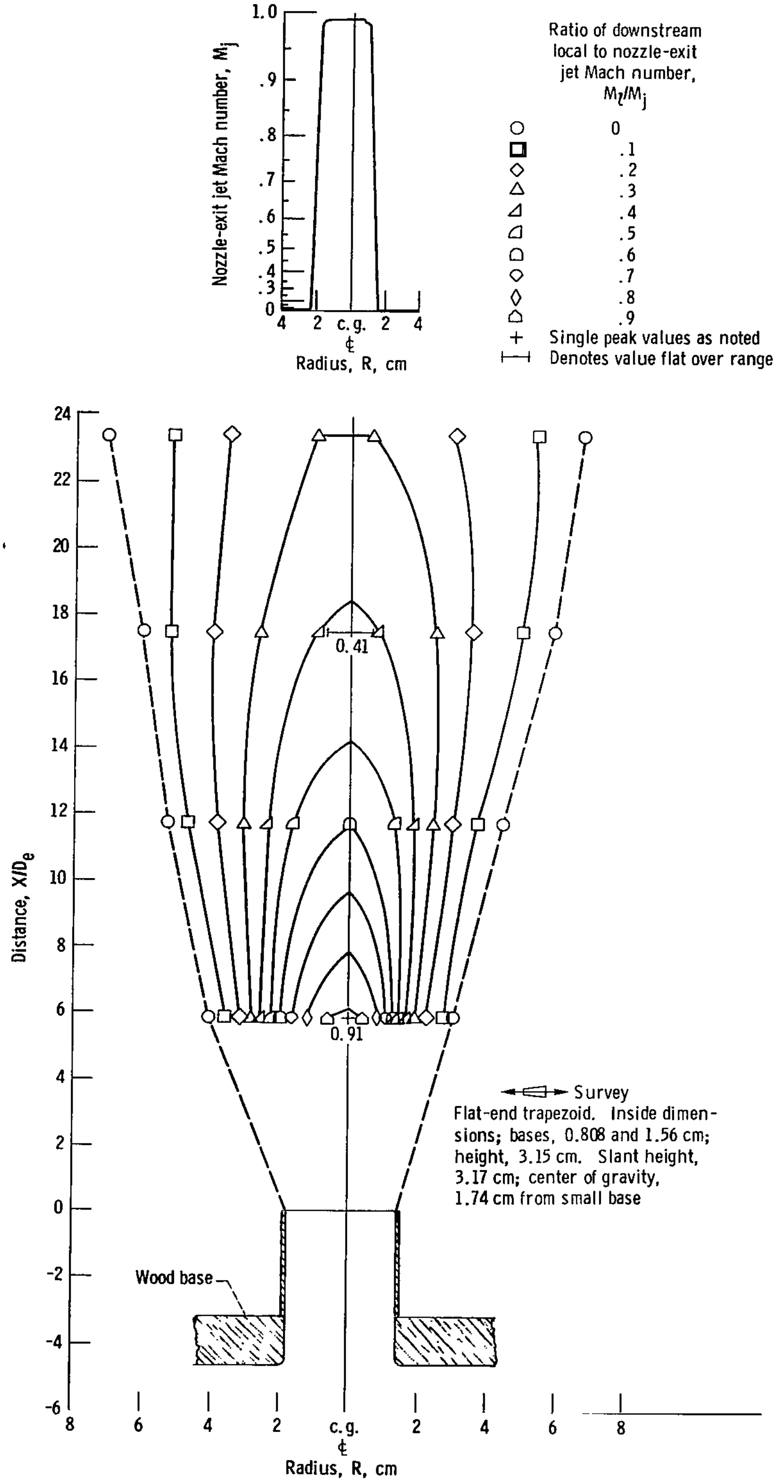

Figure 143. - Configuration 36. Nozzle-exit jet Mach number, M_j, 0.99; equivalent diameter, D_e, 2.20 centimeters.

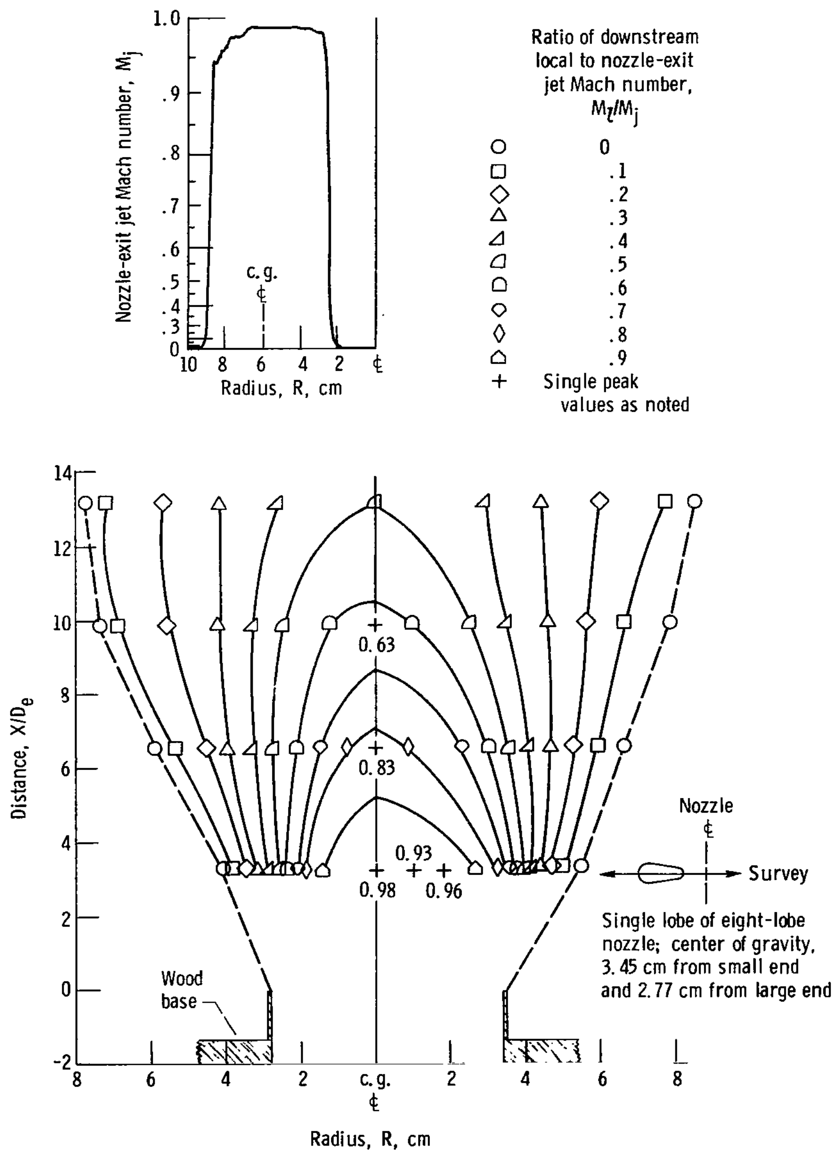

Figure 144. - Configuration 37. Nozzle-exit jet Mach number, M_j, 0.99; equivalent diameter, D_e, 3.81 centimeters.

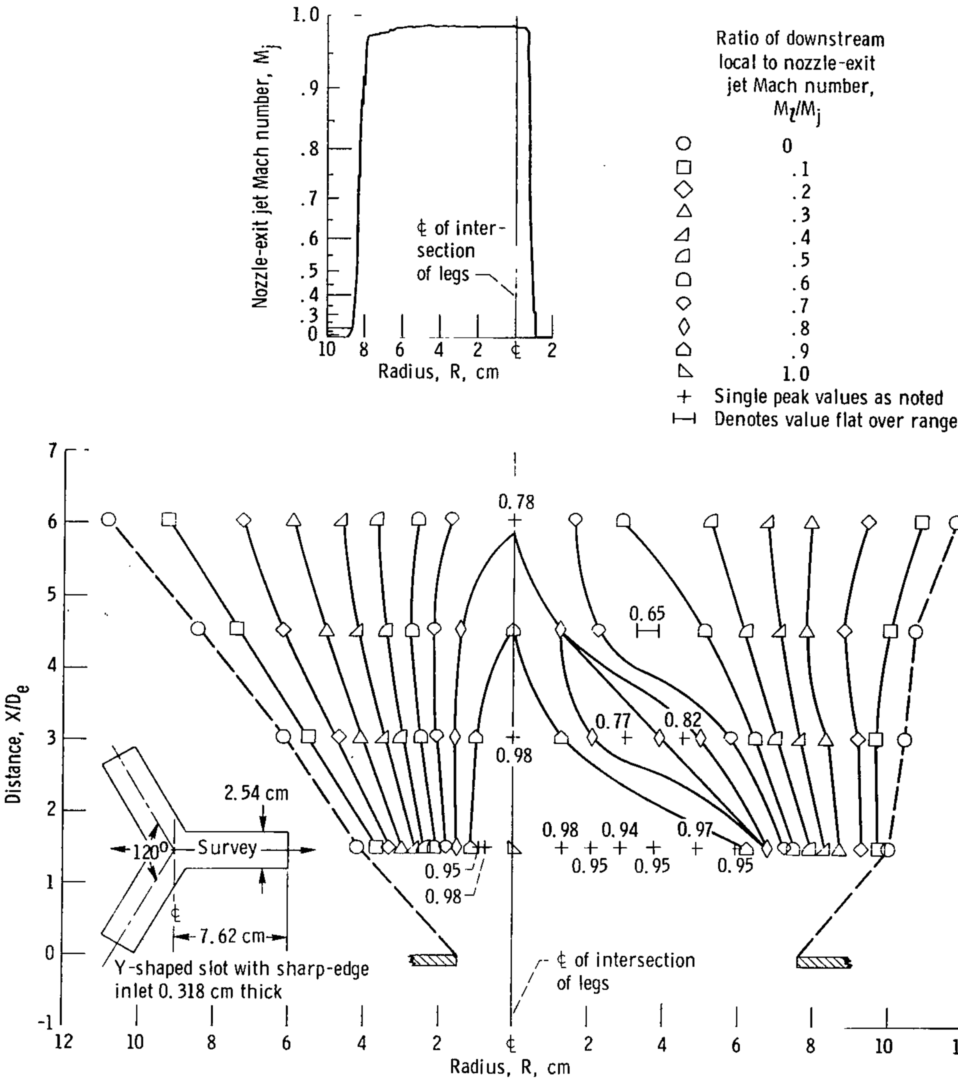

Figure 145. - Configuration 38. Nozzle-exit jet Mach number, M_j, 0.988; equivalent diameter, D_e, 8.4 centimeters.

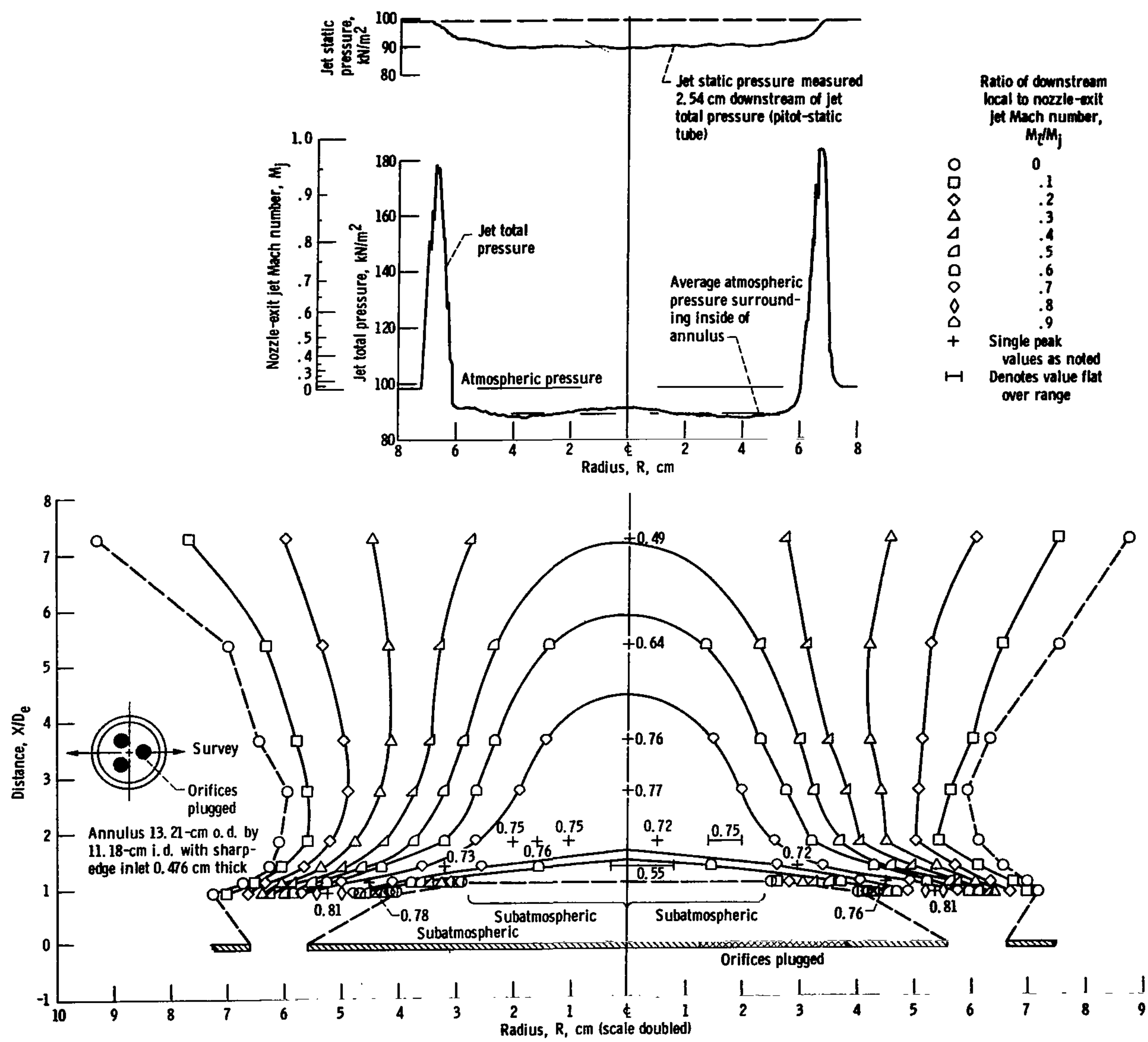

Figure 146. - Configuration 39. Nozzle-exit jet Mach number, M_j, 0.978; equivalent diameter, D_e, 7.05 centimeters.

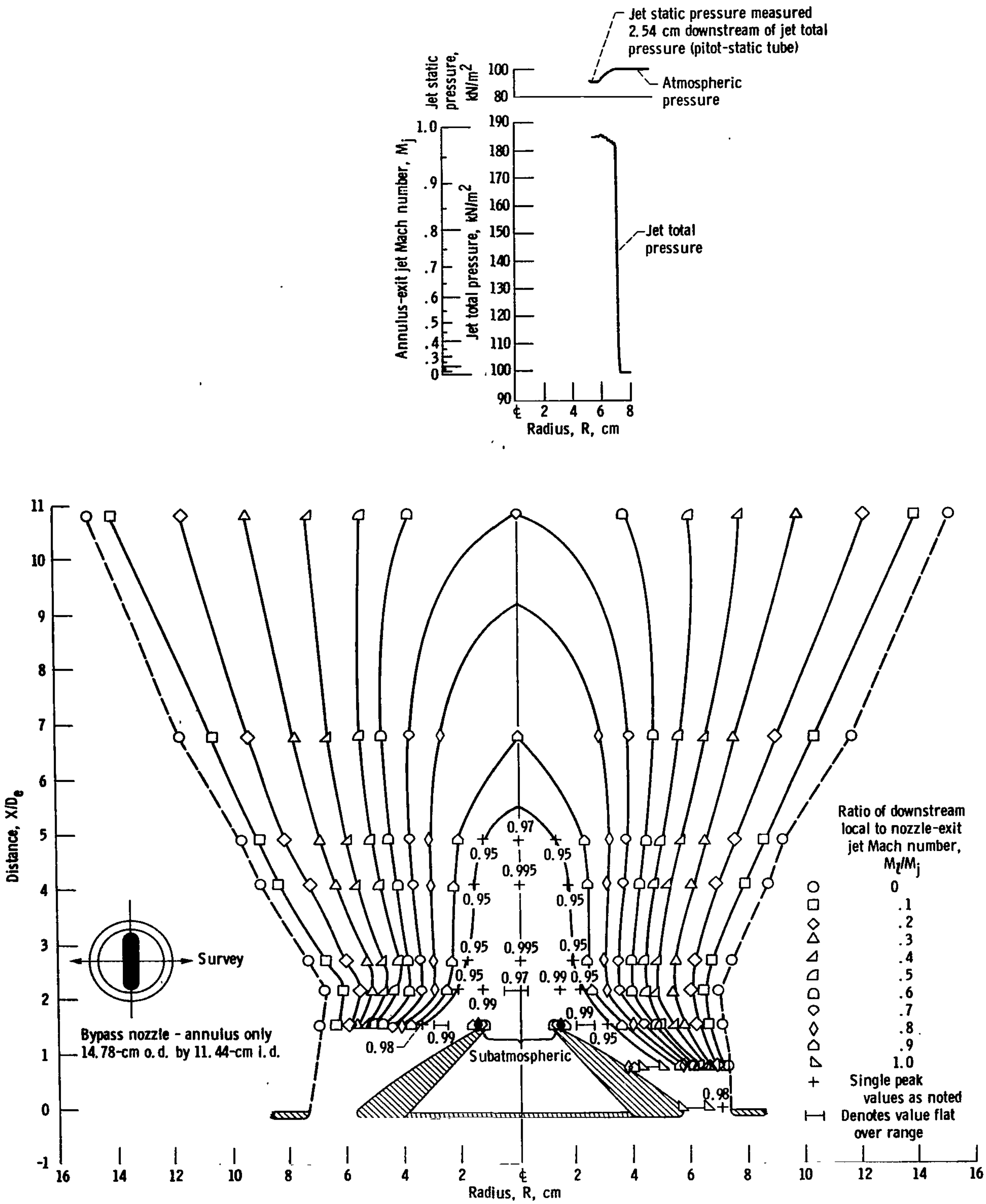

Figure 147. - Configuration 40 (core slot nozzle plugged). Nozzle-exit jet Mach number, M_j, 0.985; equivalent diameter, D_e, 9.37 centimeters.

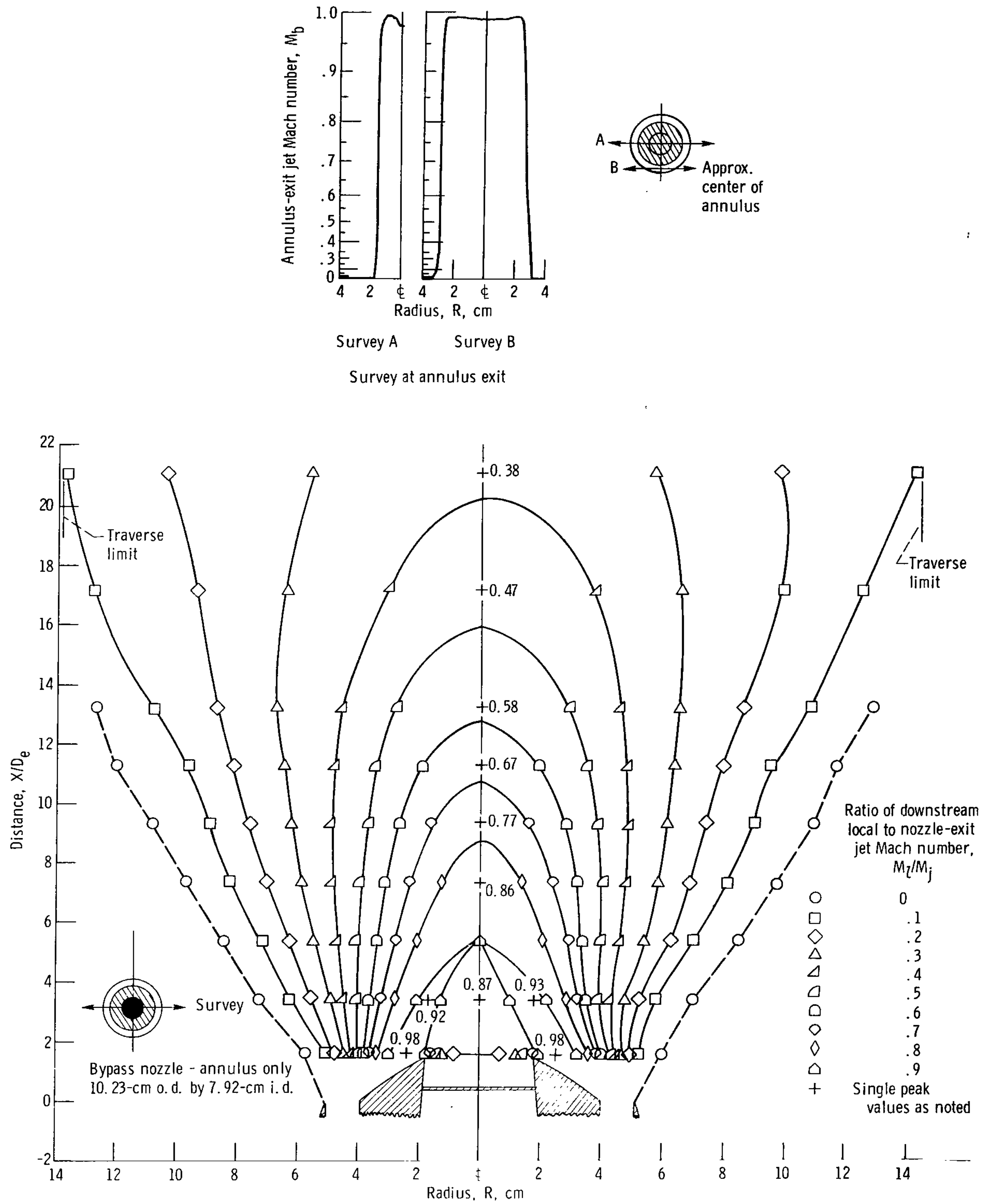

Figure 148. - Configuration 41 (core nozzle (3.58 cm diam) plugged). Nozzle-exit jet Mach number, M_j, 0 997; equivalent diameter, D_e, 6.47 centimeters.

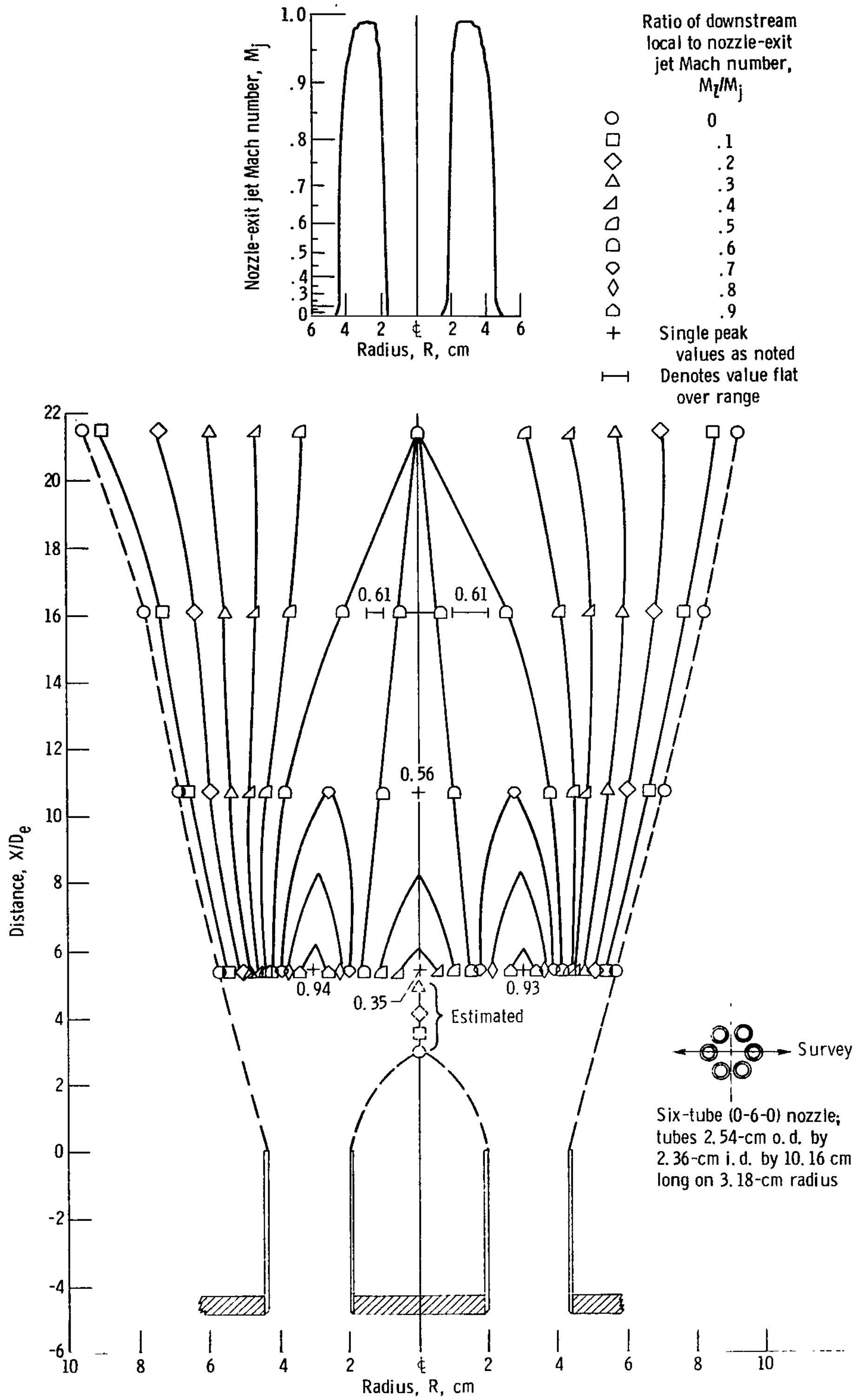

Figure 149. - Configuration 42. Nozzle-exit jet Mach number, M_j, 0.99; equivalent diameter, D_e, 2.36 centimeters.

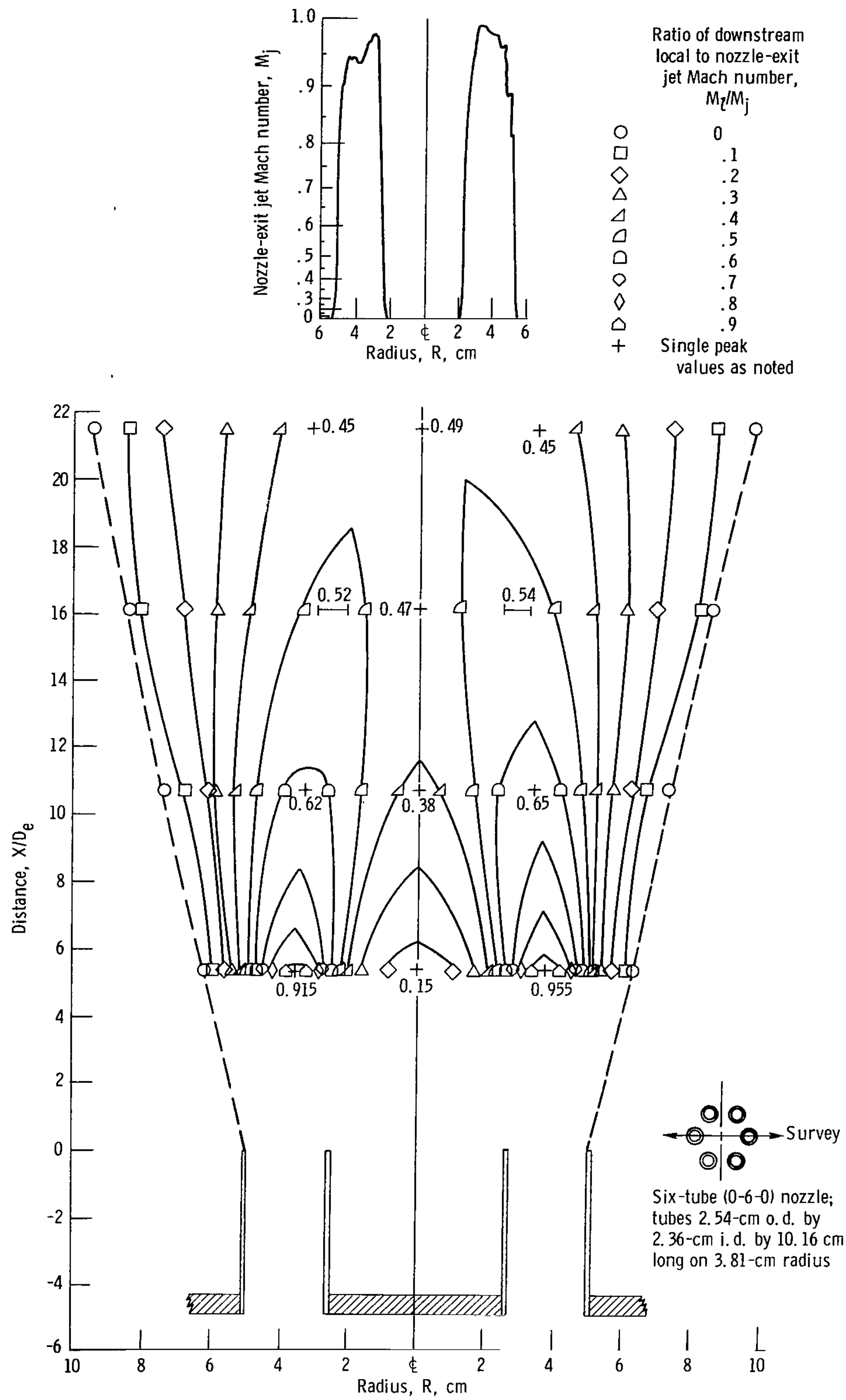

Figure 150. - Configuration 43. Nozzle-exit jet Mach number, M_j, 0.99; equivalent diameter, D_e, 2.36 centimeters.

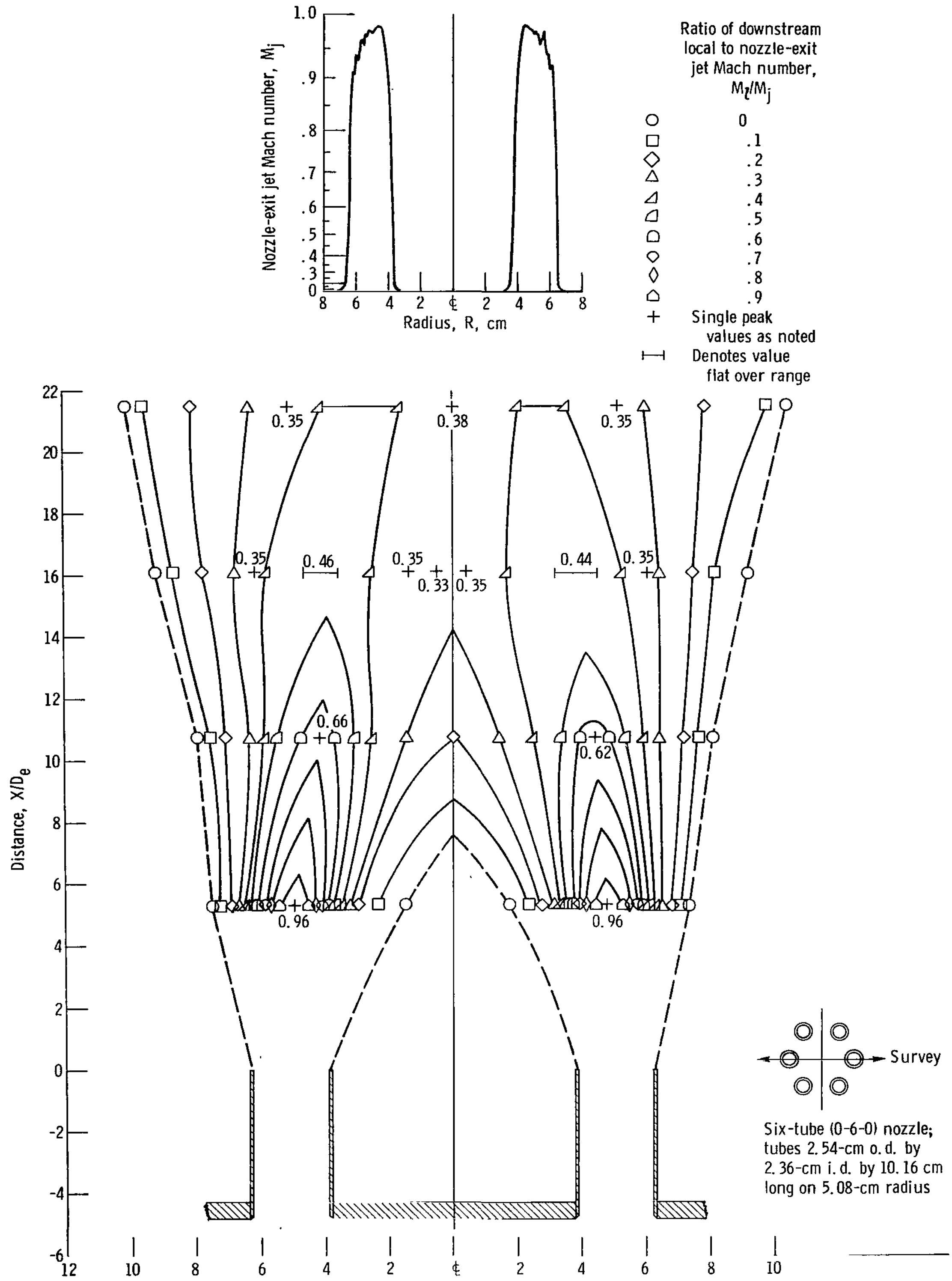

Figure 151. - Configuration 44. Nozzle-exit jet Mach number, M_j, 0.98; equivalent diameter, D_e, 2.36 centimeters.

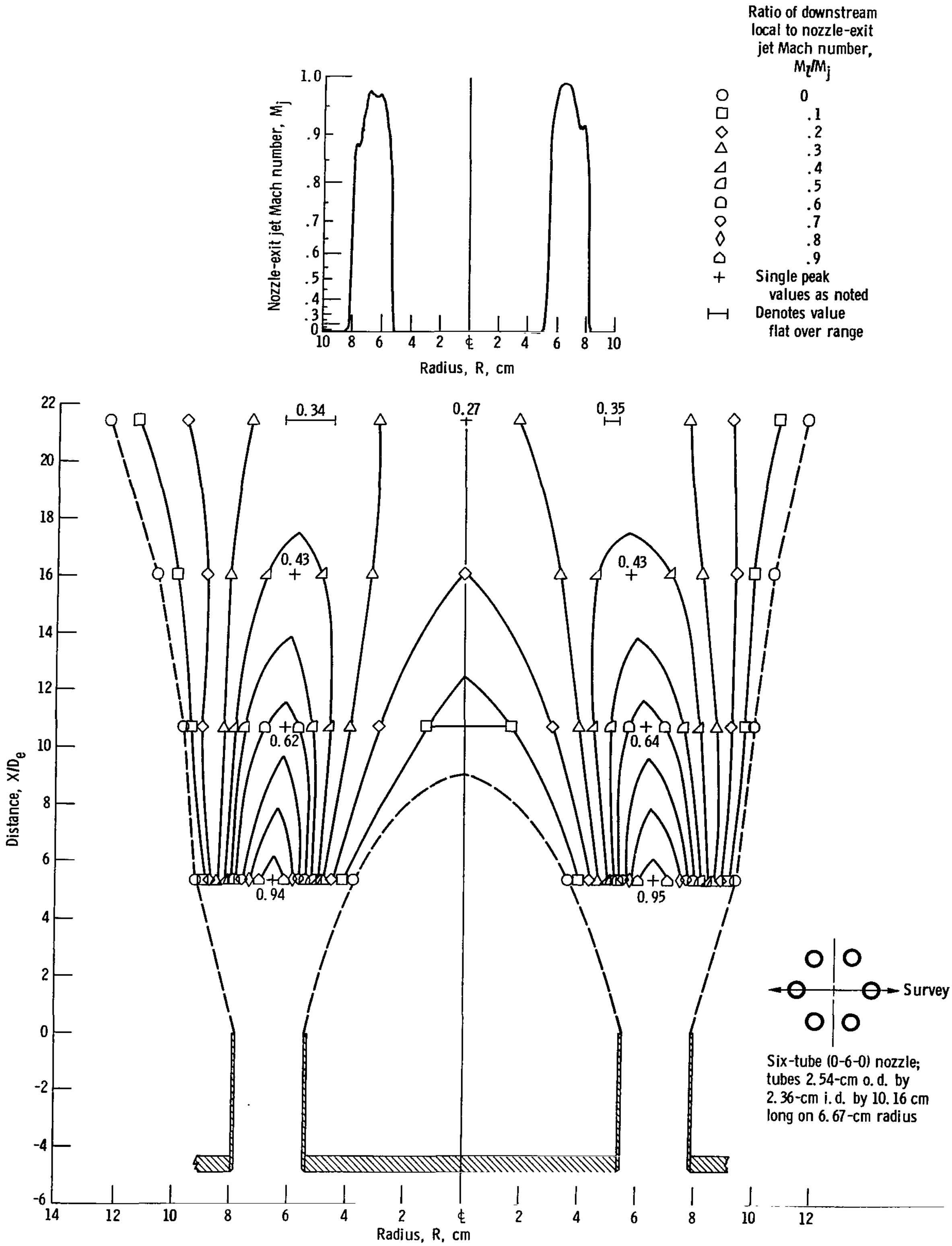

Figure 152. - Configuration 45. Nozzle-exit jet Mach number, M_j, 0.99; equivalent diameter, D_e, 2.36 centimeters.

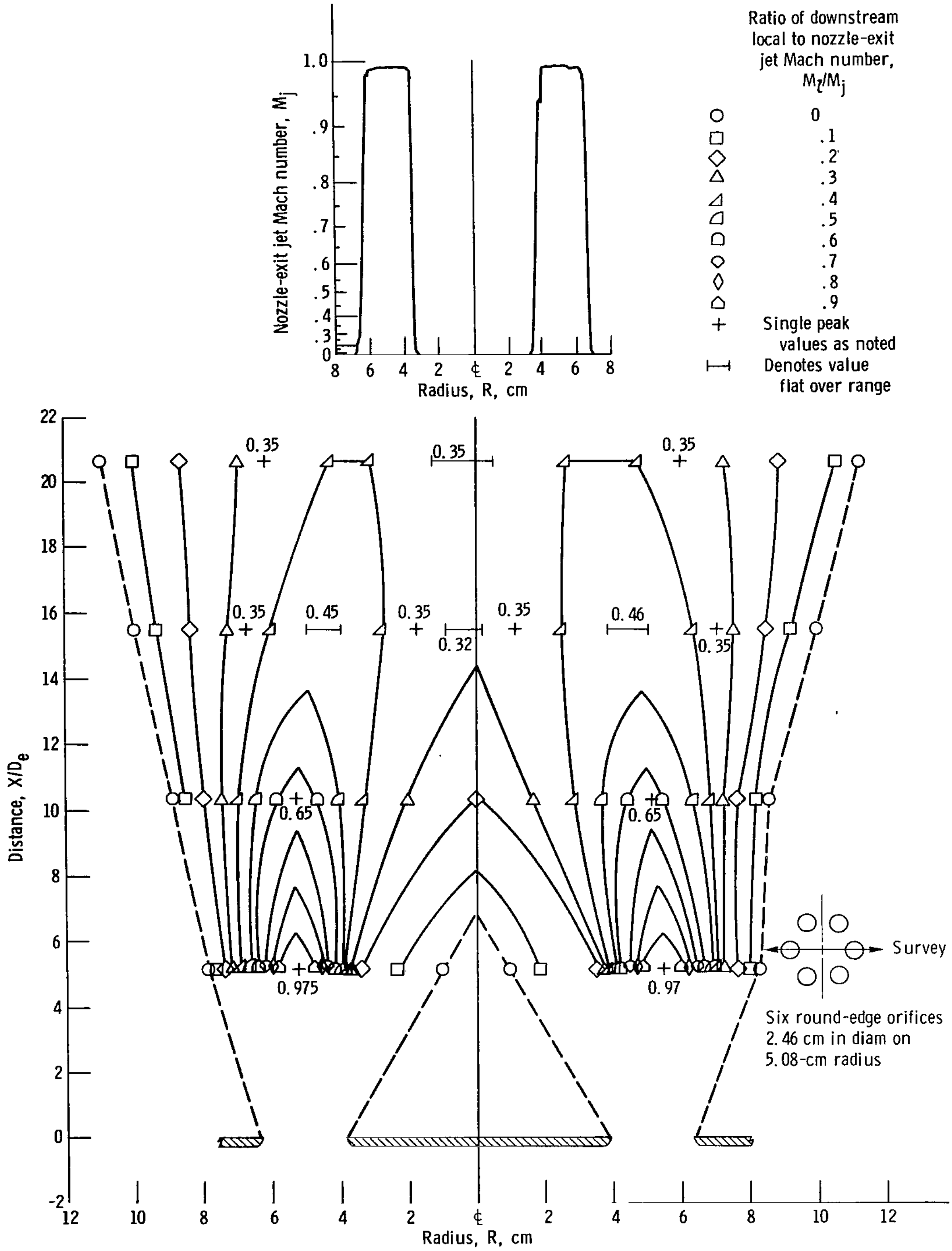

Figure 153. - Configuration 46. Nozzle-exit jet Mach number, M_j, 0.992; equivalent diameter, D_e, 2.46 centimeters.

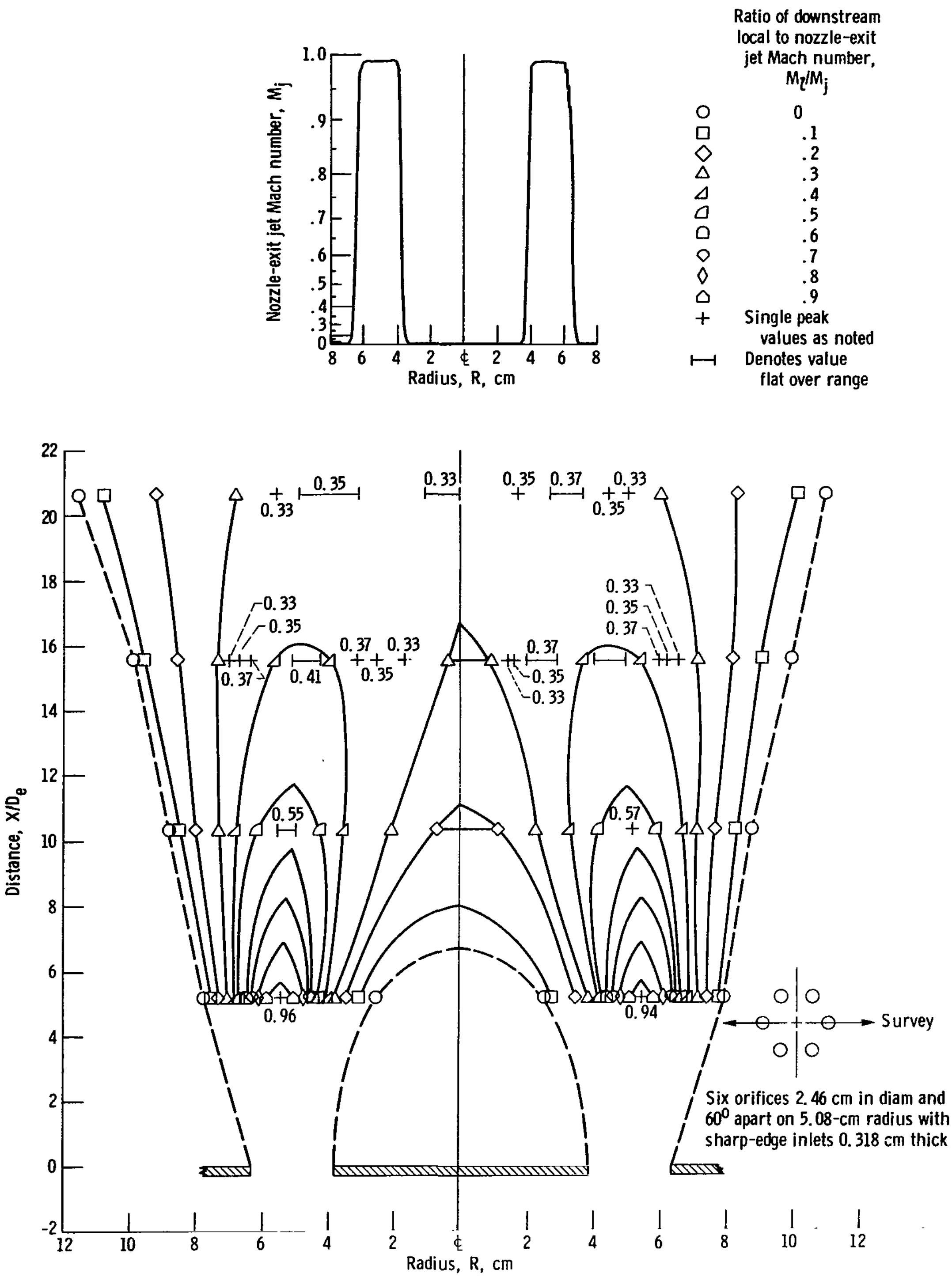

Figure 154. - Configuration 47. Nozzle-exit jet Mach number, M_j, 0.99; equivalent diameter, D_e, 2.46 centimeters.

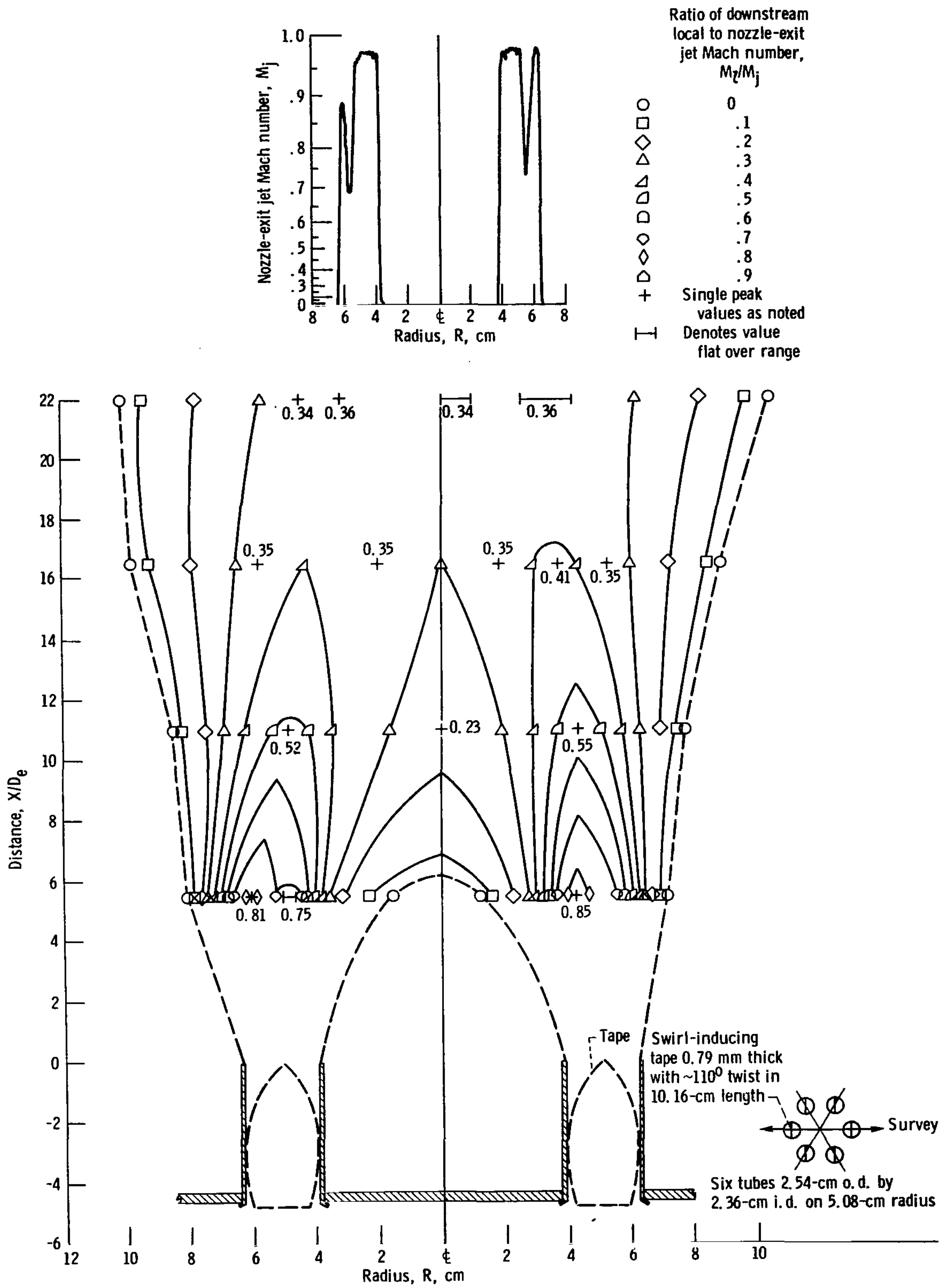

Figure 155. - Configuration 48. Nozzle-exit jet Mach number, M_j, 0.975; equivalent diameter, D_e, 2.31 centimeters.

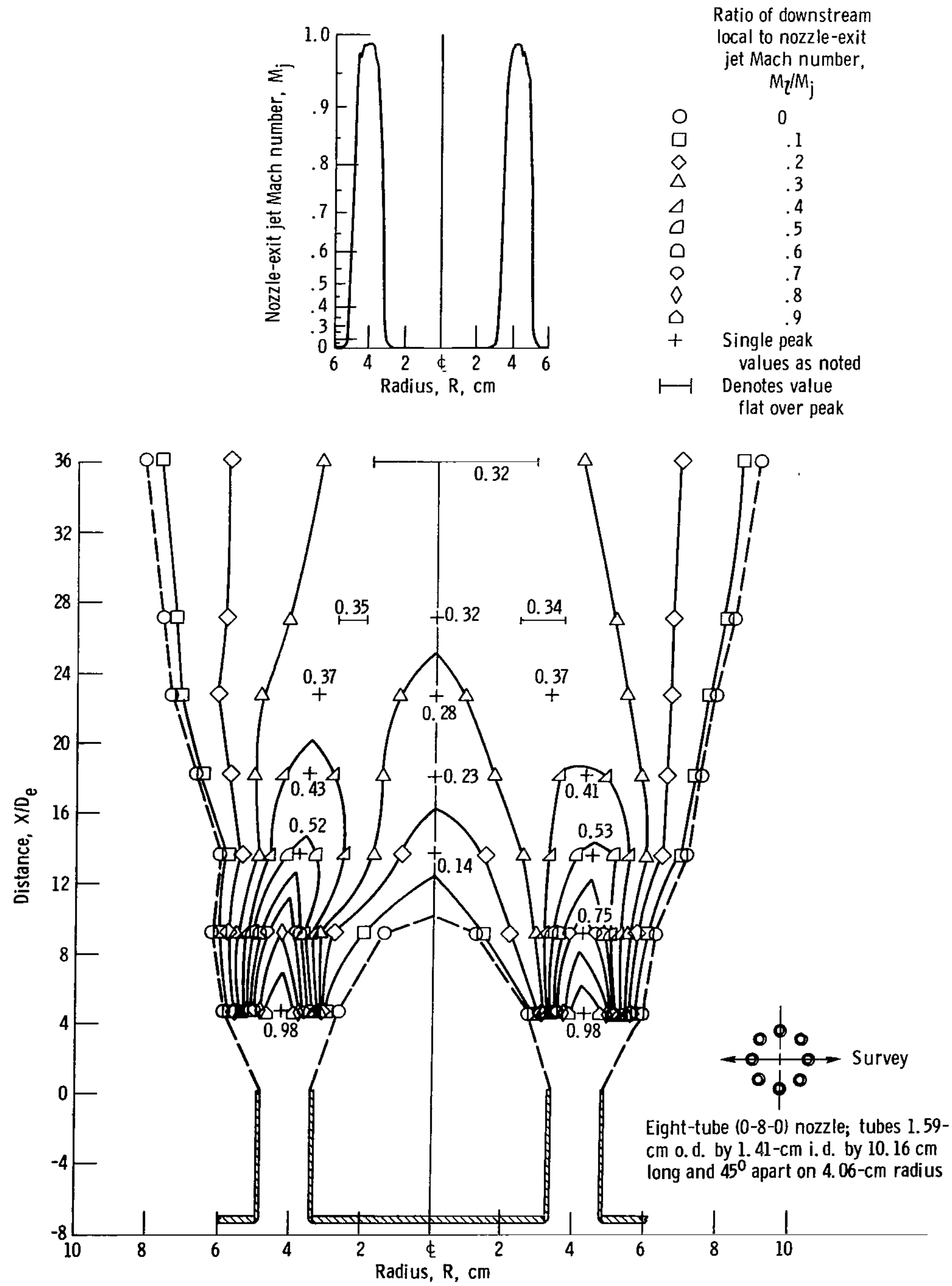

Figure 156. - Configuration 49. Nozzle-exit jet Mach number, M_j, 0.99; equivalent diameter, D_e, 1.41 centimeters.

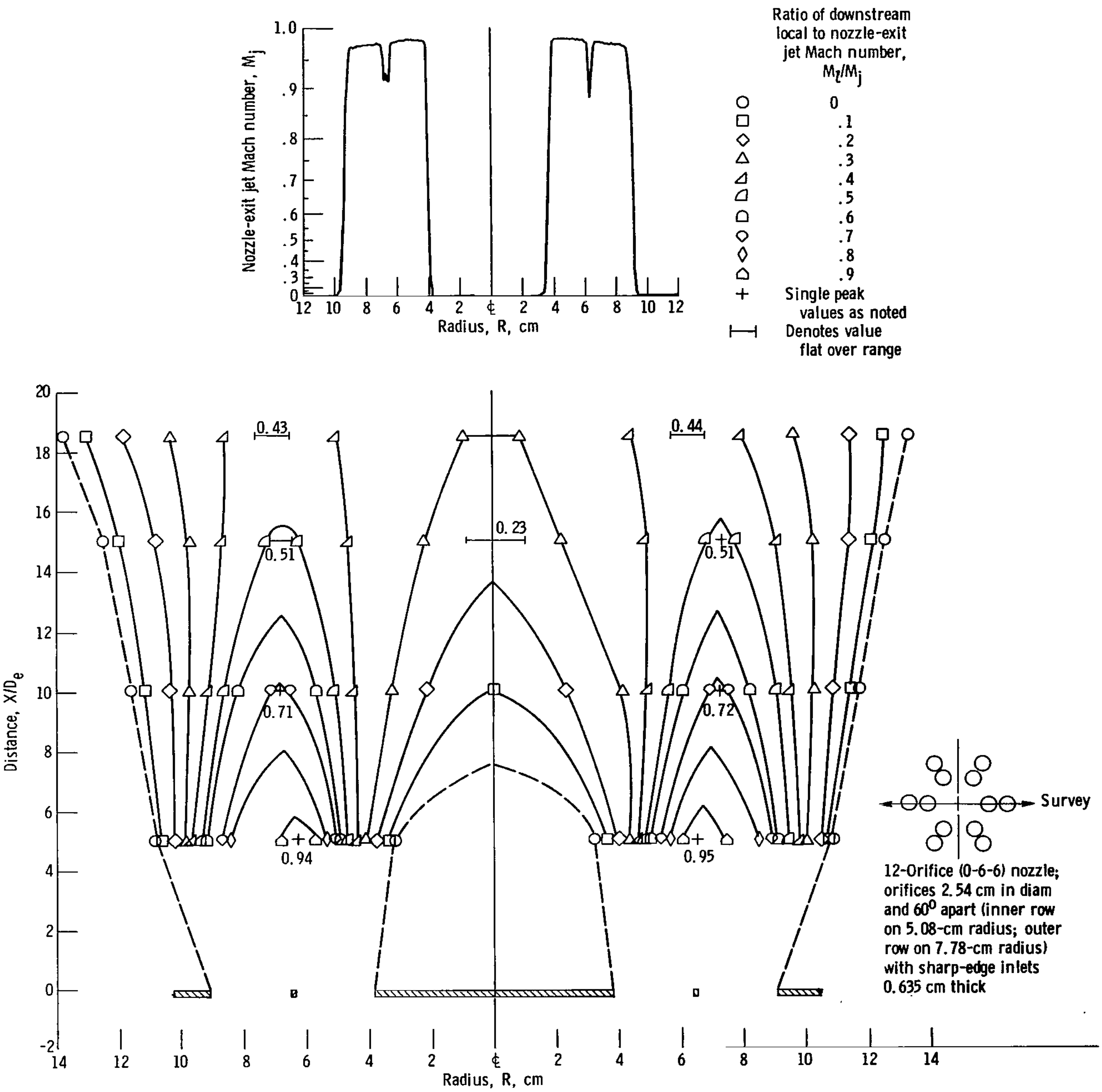

Figure 157. - Configuration 50. Nozzle-exit jet Mach number, M_j, 0.985; equivalent diameter, D_e, 2.54 centimeters.

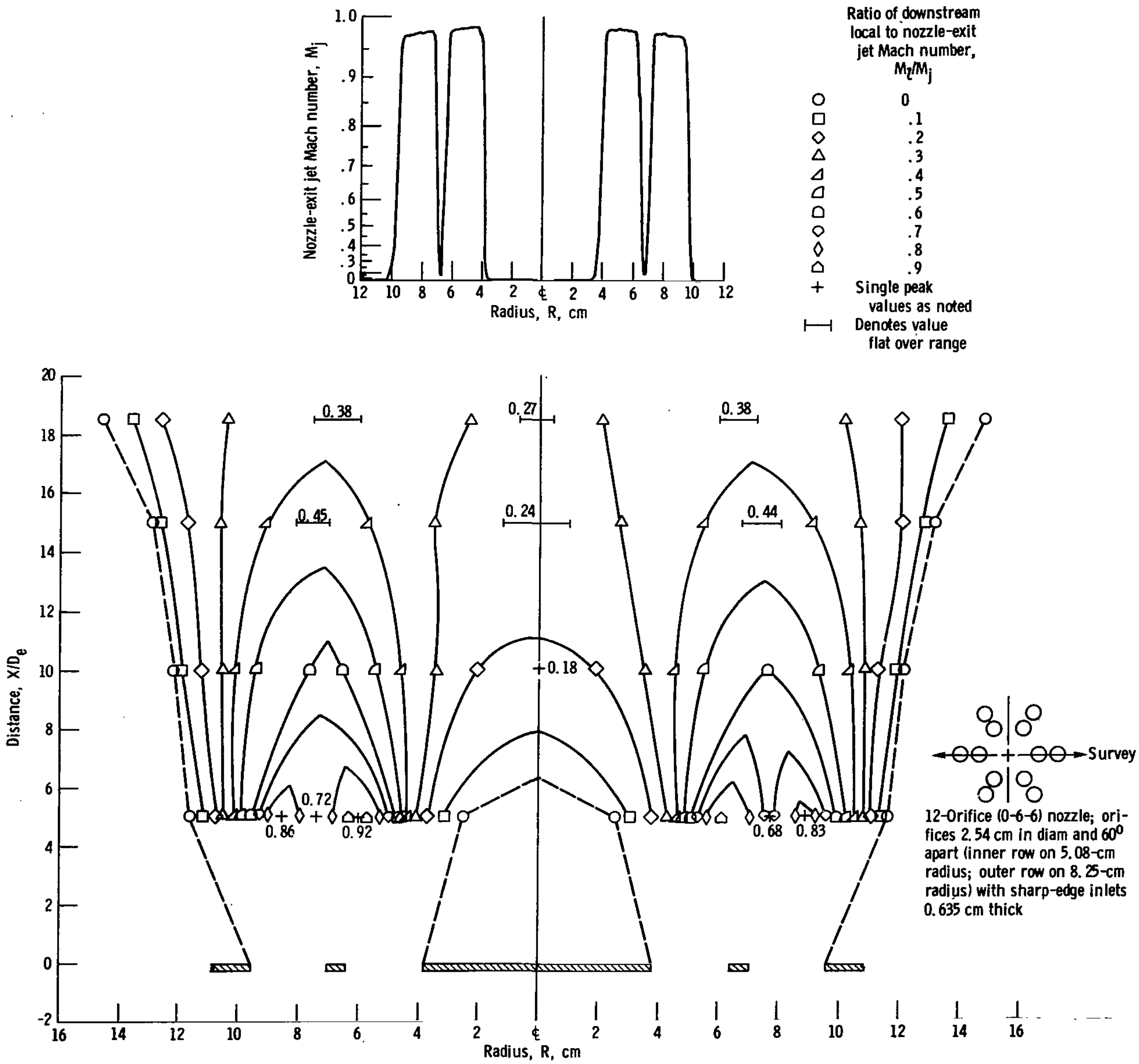

Figure 158. - Configuration 51. Nozzle-exit jet Mach number, M_j, 0.984; equivalent diameter, D_e, 2.54 centimeters.

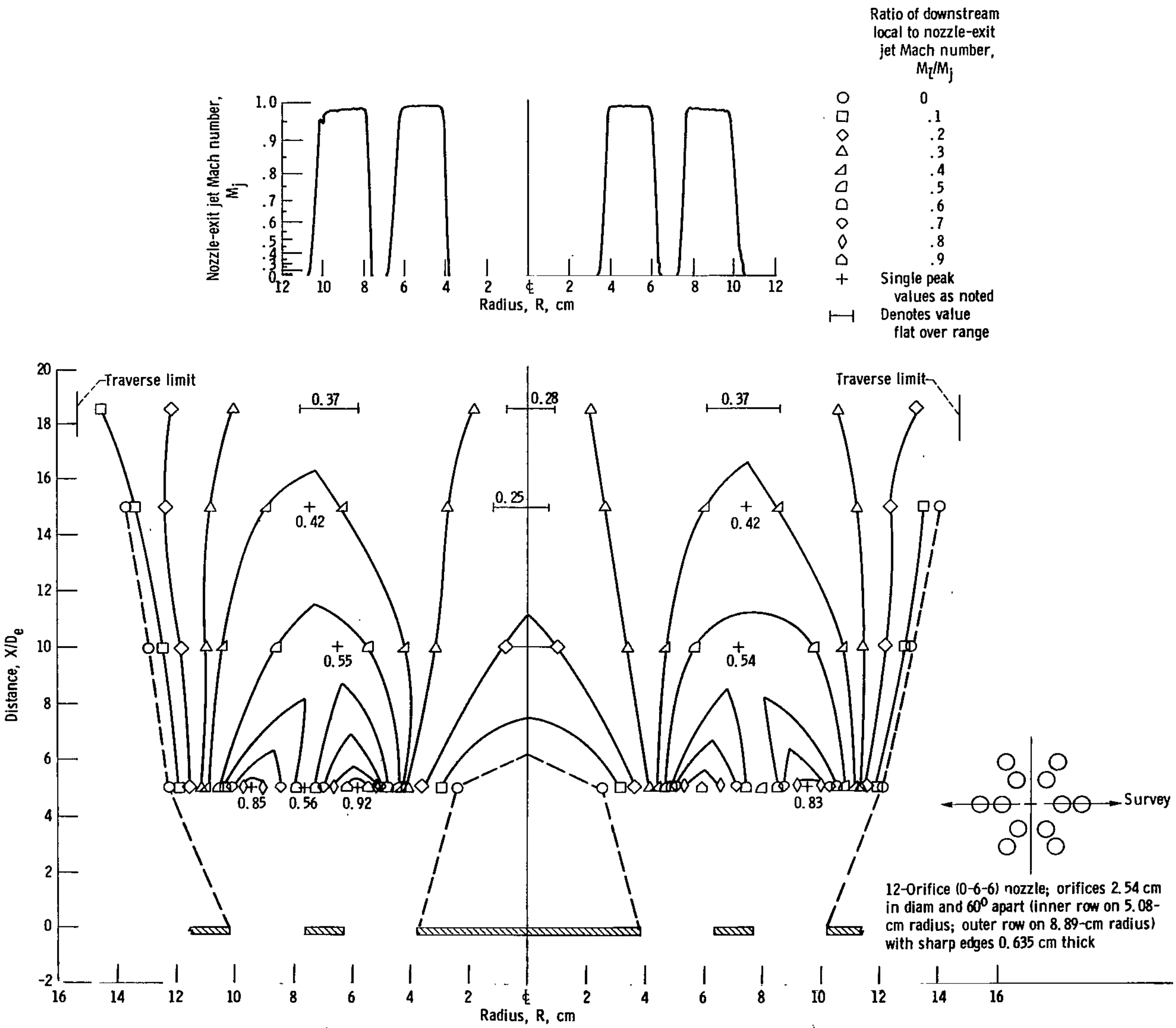

Figure 159. - Configuration 52. Nozzle-exit jet Mach number, M_j, 0.985; equivalent diameter, D_e, 2.54 centimeters.

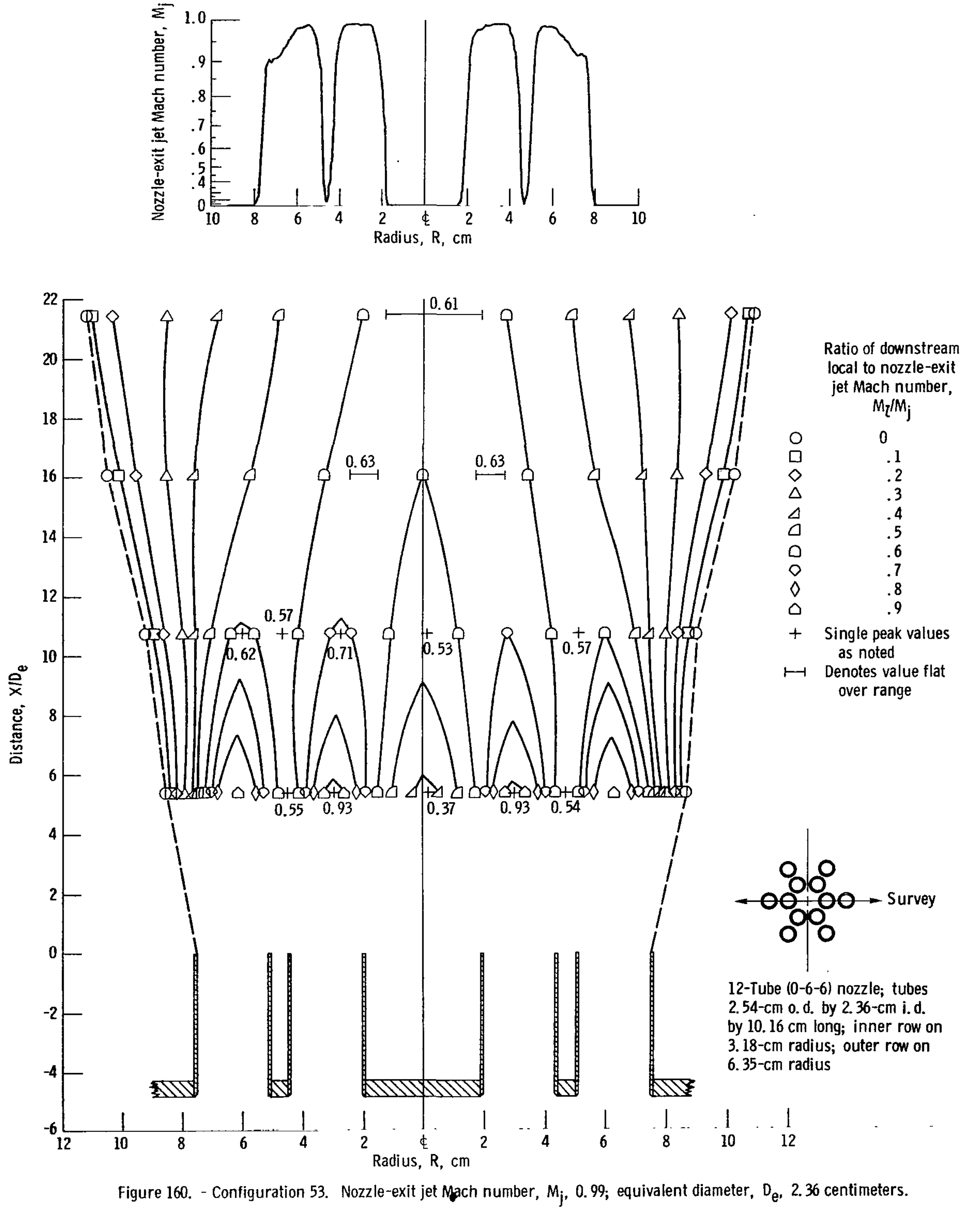

Figure 160. - Configuration 53. Nozzle-exit jet Mach number, M_j, 0.99; equivalent diameter, D_e, 2.36 centimeters.

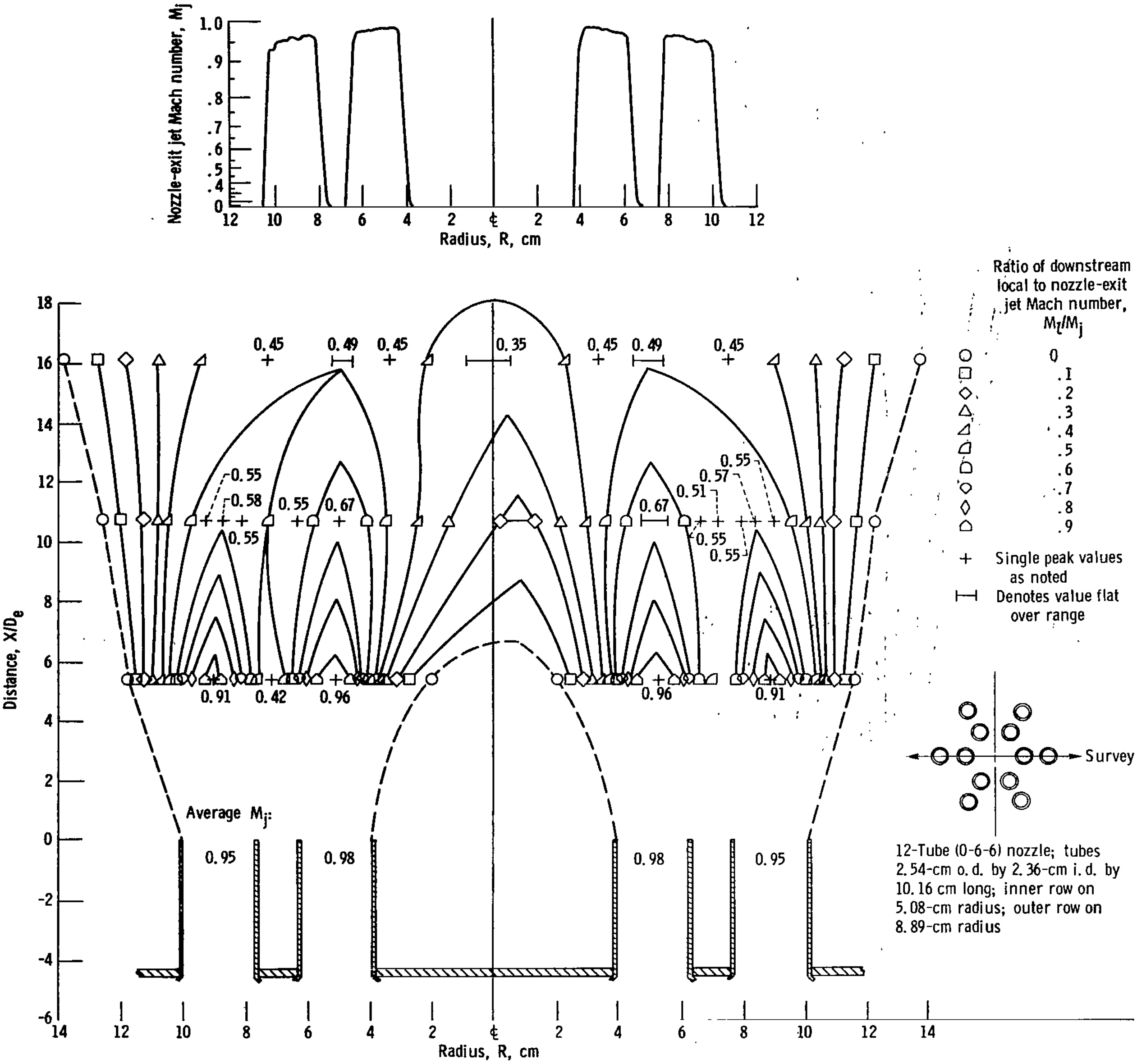

Figure 161. - Configuration 54. Nozzle-exit jet Mach number, M_j, 0.98; equivalent diameter, D_e, 2.36 centimeters.

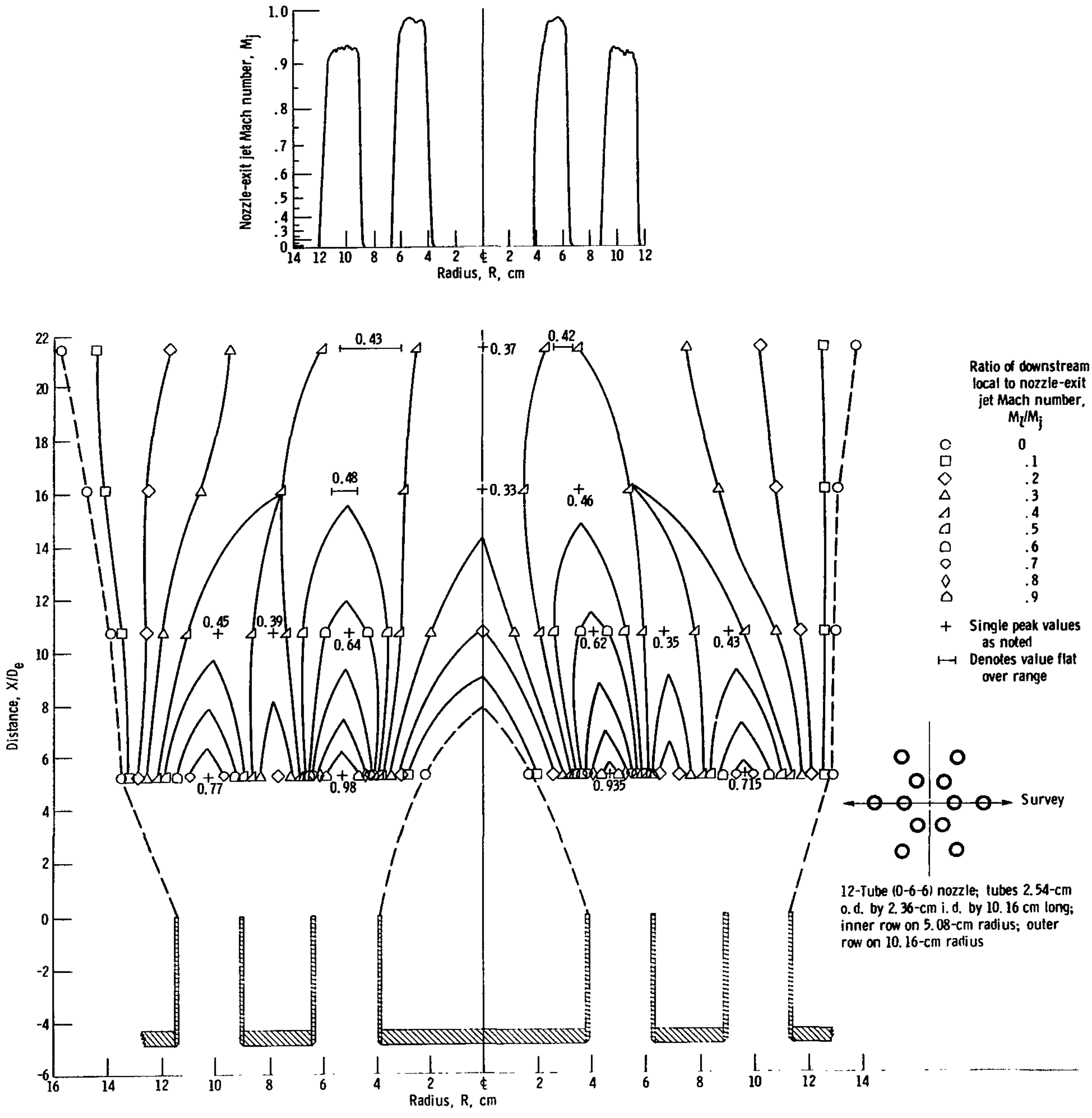

Figure 162. - Configuration 55. Nozzle-exit jet Mach number, M_j, 0.98; equivalent diameter, D_e, 2.36 centimeters.

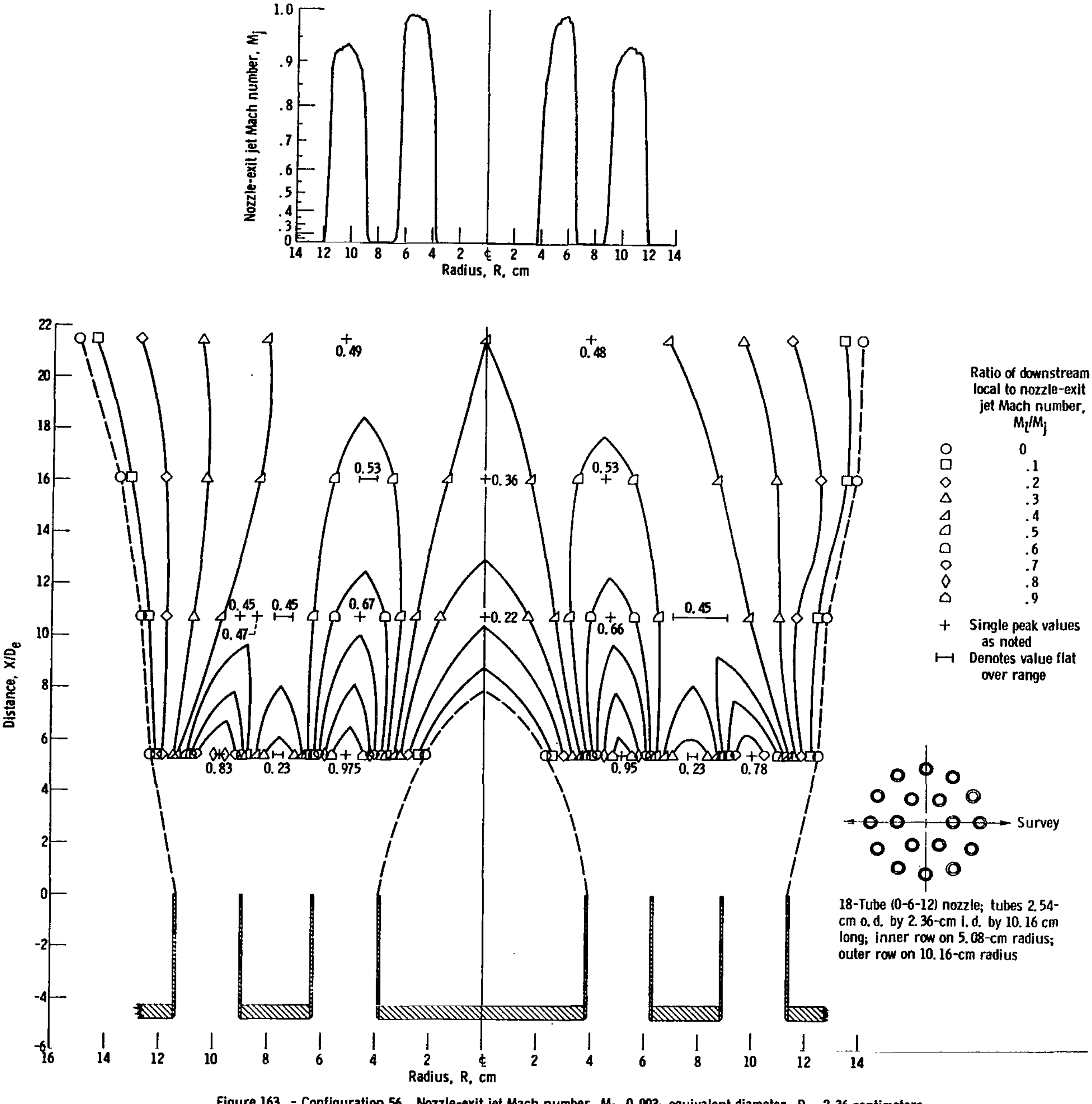

Figure 163. - Configuration 56. Nozzle-exit jet Mach number, M_j, 0.993; equivalent diameter, D_e, 2.36 centimeters.

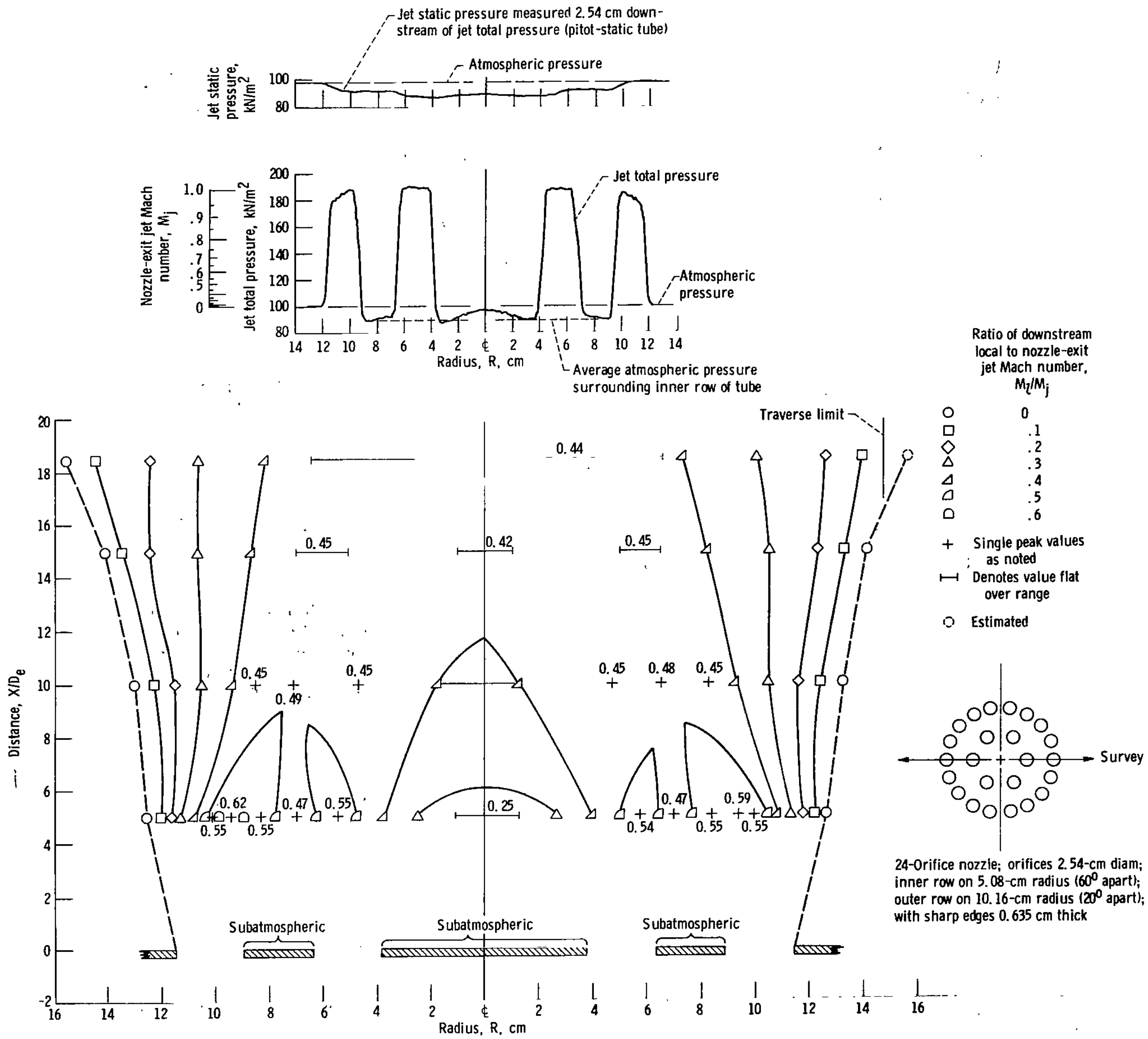

Figure 164. - Configuration 57. Nozzle-exit jet Mach number, M_j, 1.0; equivalent diameter, D_e, 2.54 centimeters.

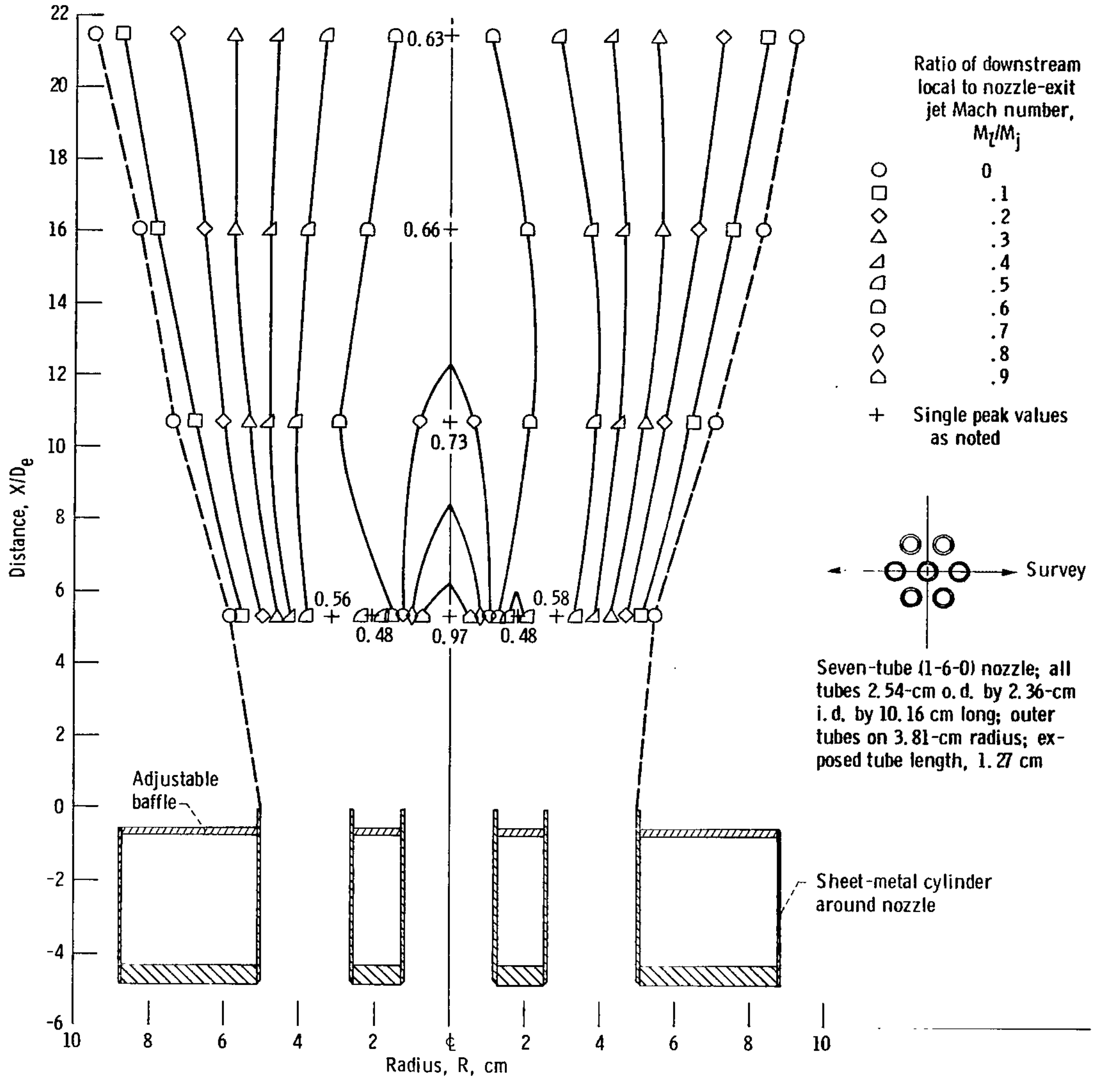

Figure 165. - Configuration 58. Nozzle-exit jet Mach number, M_j, 0.99; equivalent diameter, D_e, 2.36 centimeters. (No exit survey.)

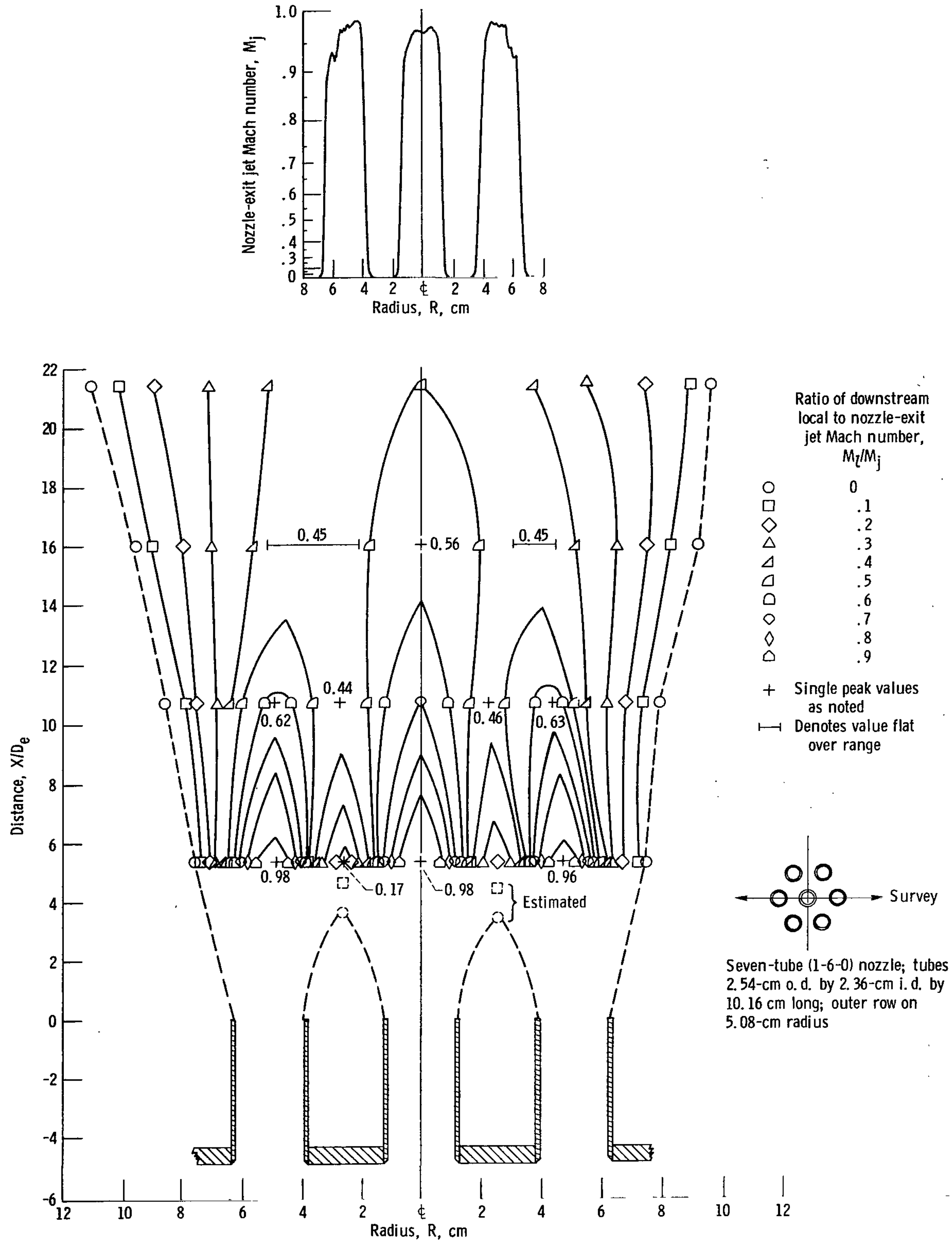

Figure 166. - Configuration 59. Nozzle-exit jet Mach number, M_j, 0.97; equivalent diameter, D_e, 2.36 centimeters.

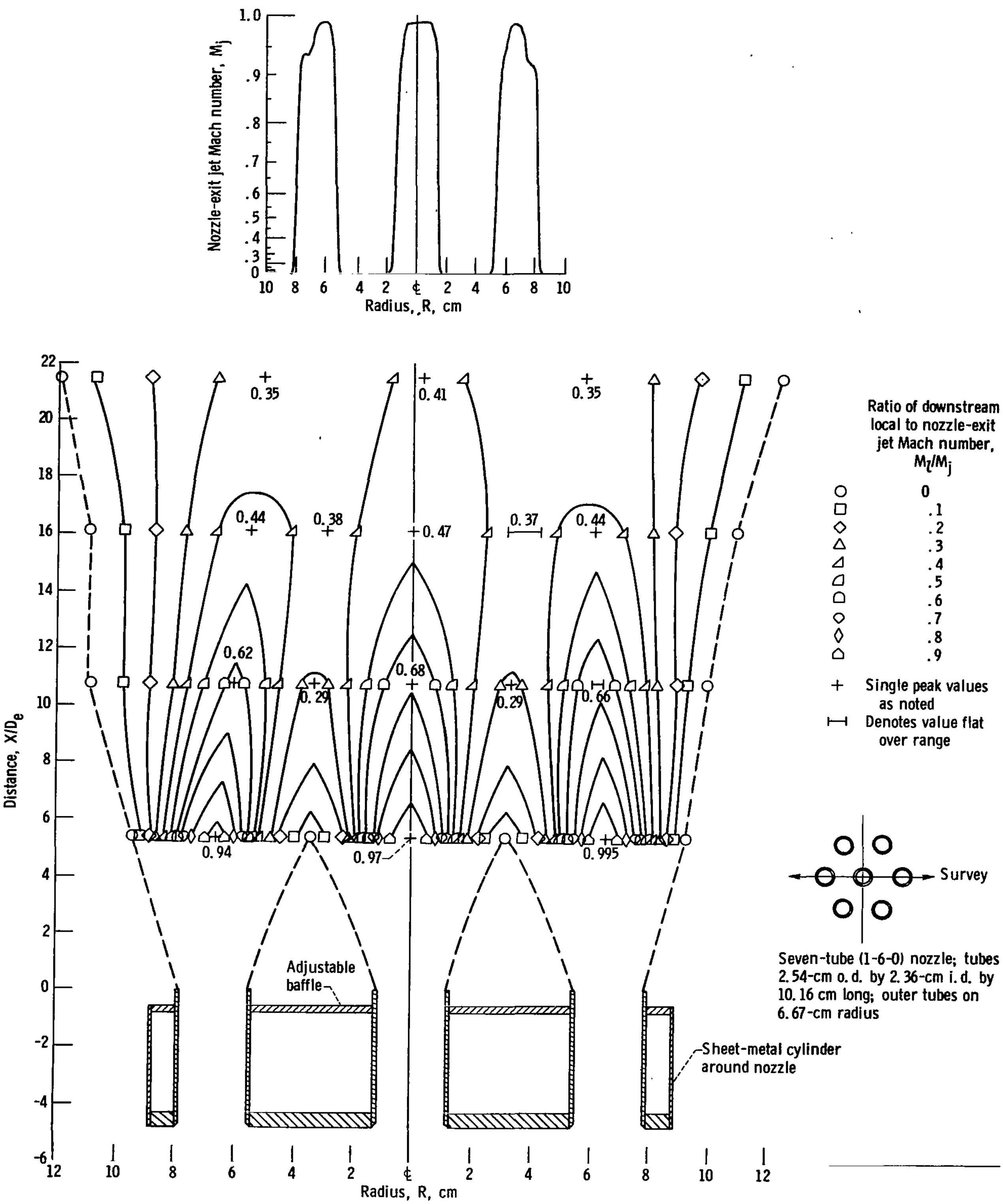

Figure 167. - Configuration 60. Nozzle-exit jet Mach number, M_j, 0.99; equivalent diameter, D_e, 2.36 centimeters; exposed tube length, 1.27 centimeters.

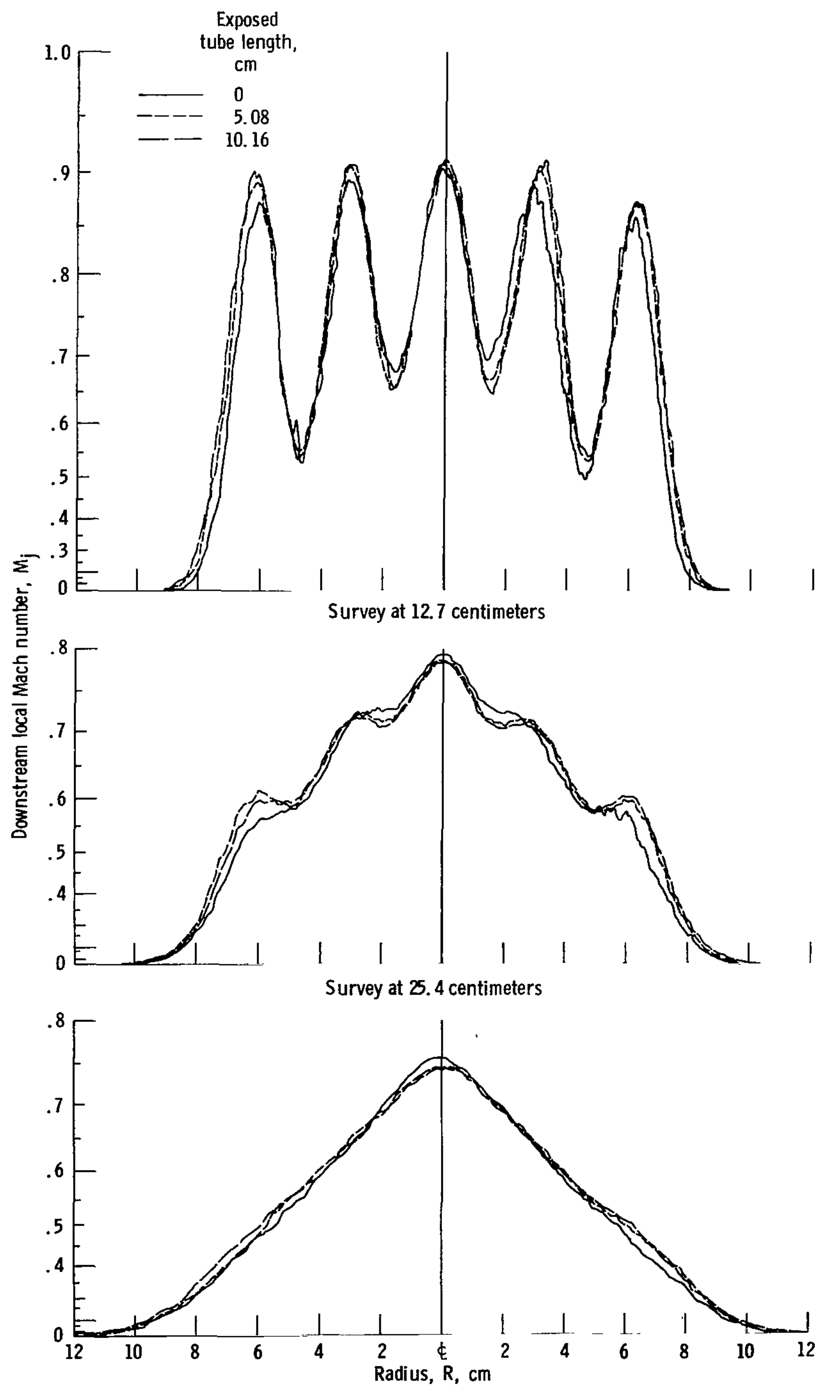

Survey at 38.1 centimeters

Figure 168. - Configuration 61. Nozzle-exit jet Mach number, M_j, 0.99;

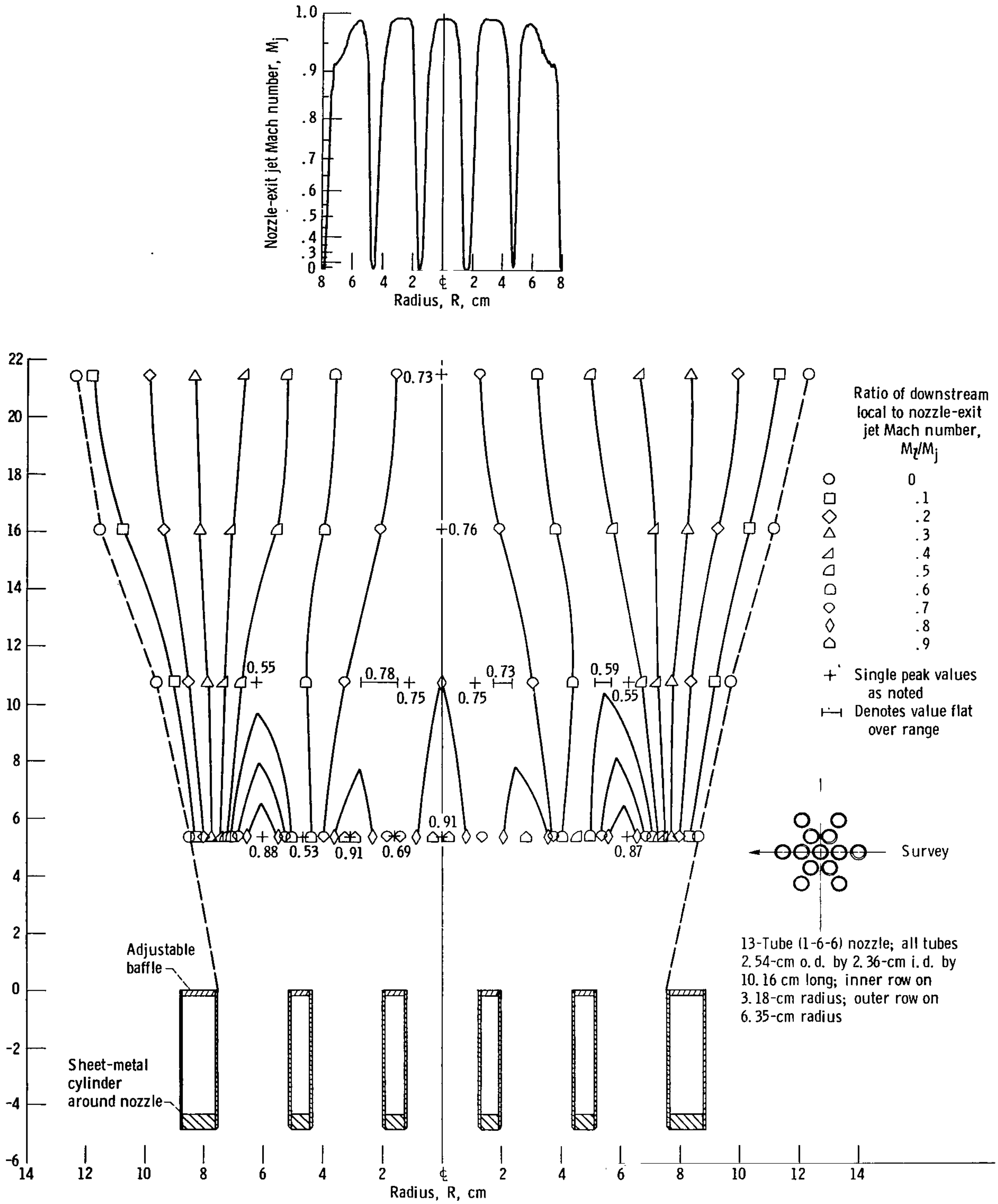

equivalent diameter, D_e, 0.93 centimeter. (Adjustable baffle at end of tubes for exposed tube length of zero.)

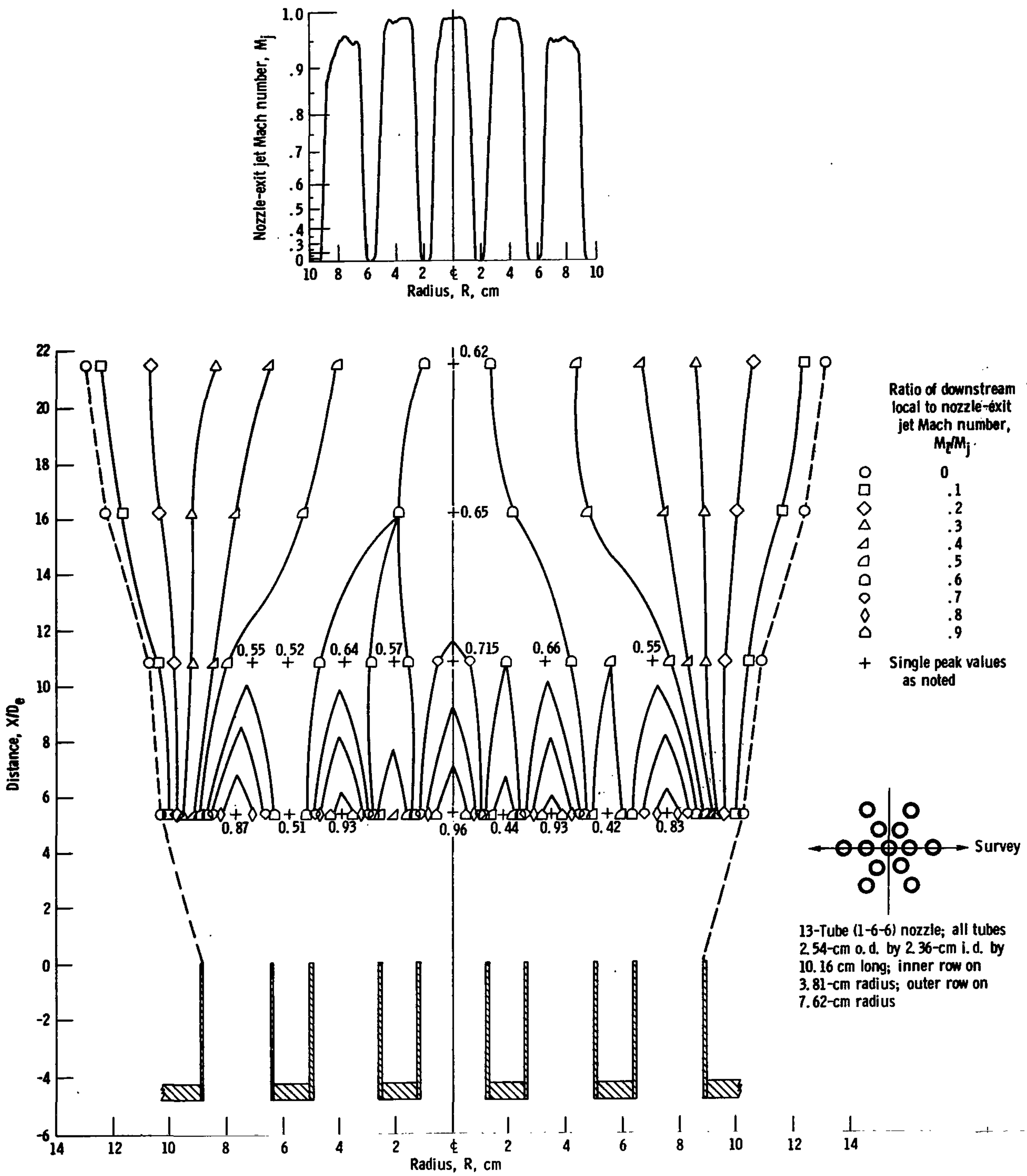

Figure 169. - Configuration 62. Nozzle-exit jet Mach number, M_j, 0.985; equivalent diameter, D_e, 2.36 centimeters.

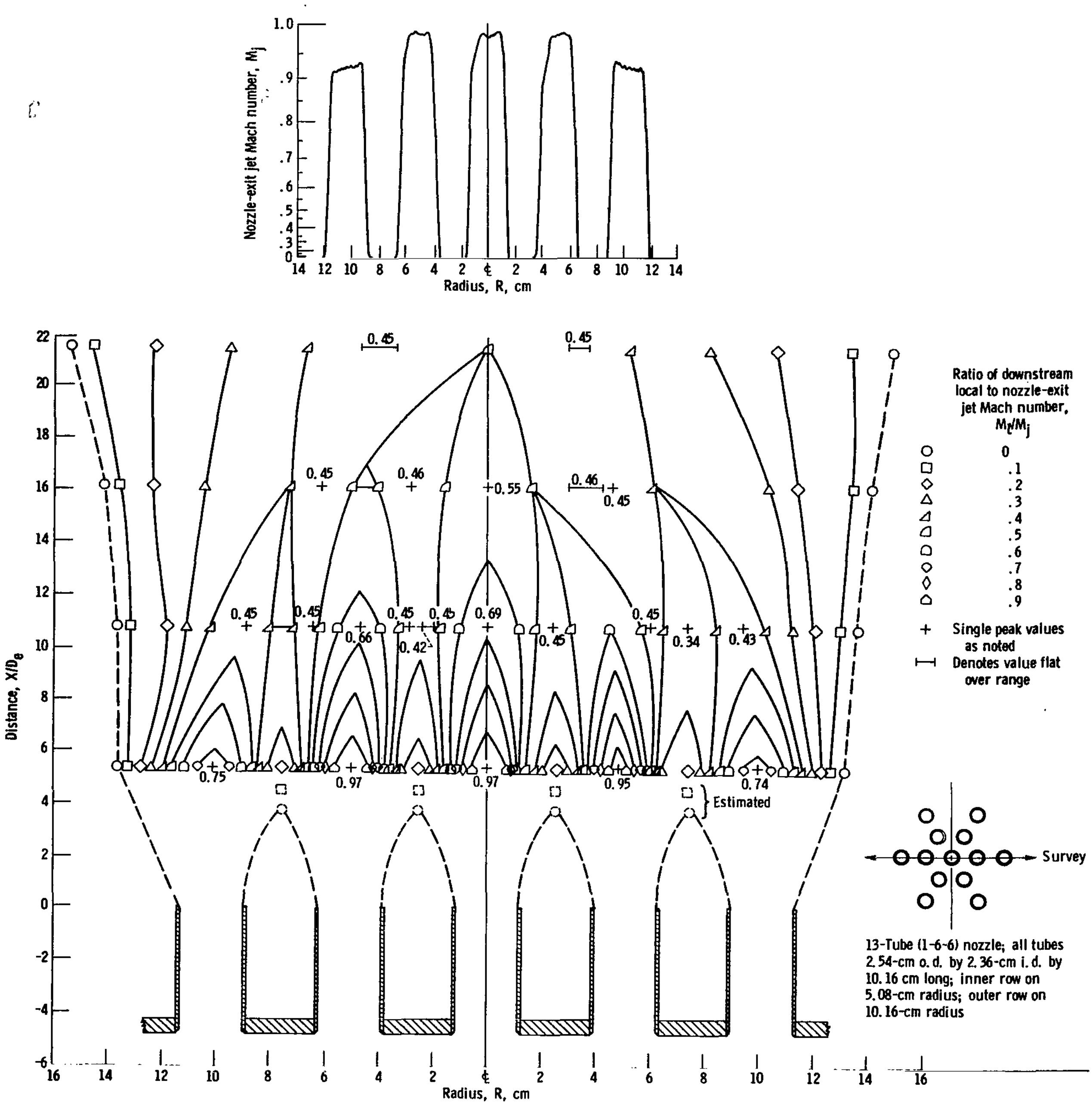

Figure 170. - Configuration 63. Nozzle-exit jet Mach number, M_j, 0.98; equivalent diameter, D_e, 2.36 centimeters.

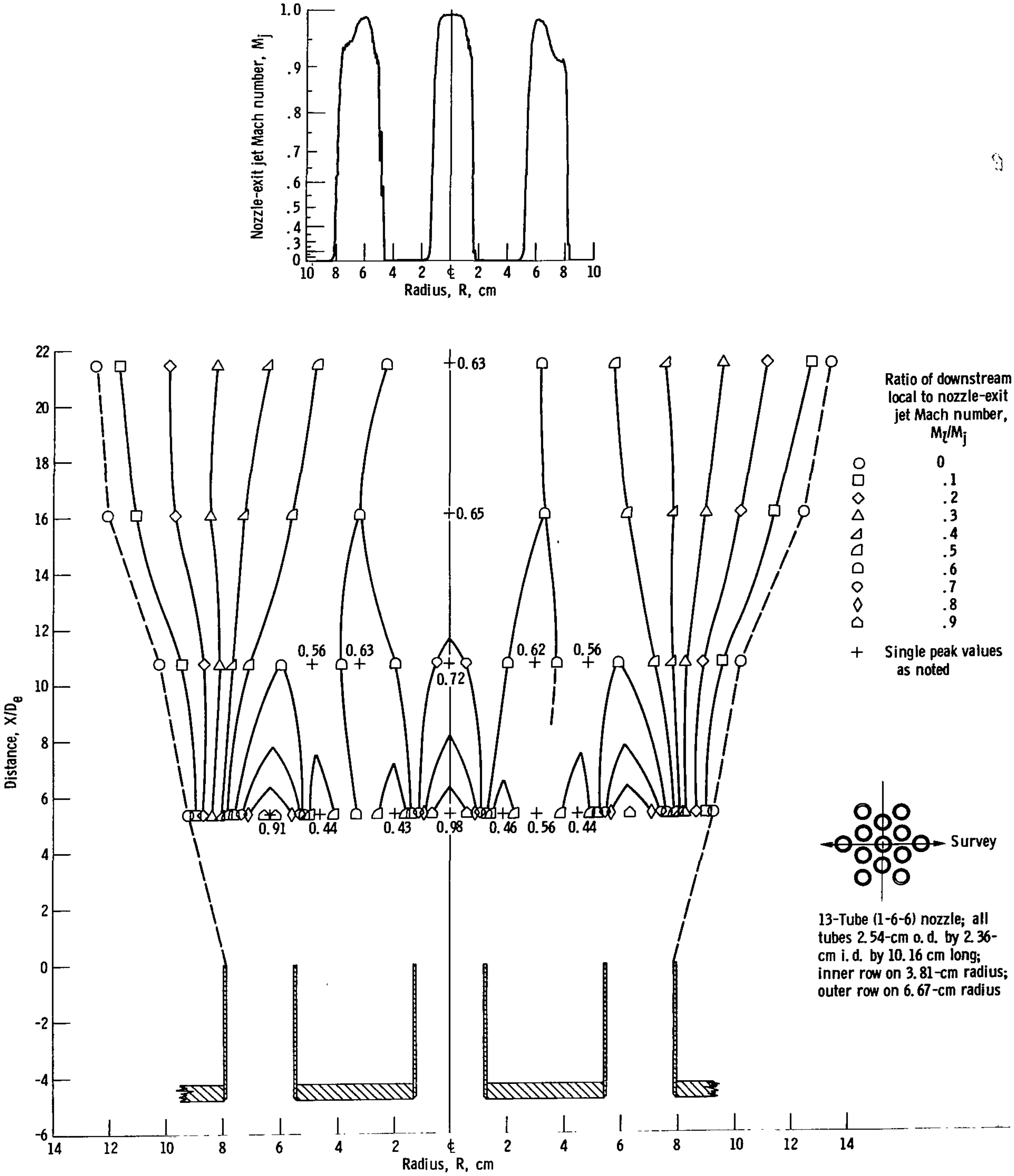

Figure 171. - Configuration 64. Nozzle-exit jet Mach number, M_j, 0.99; equivalent diameter, D_e, 2.36 centimeters.

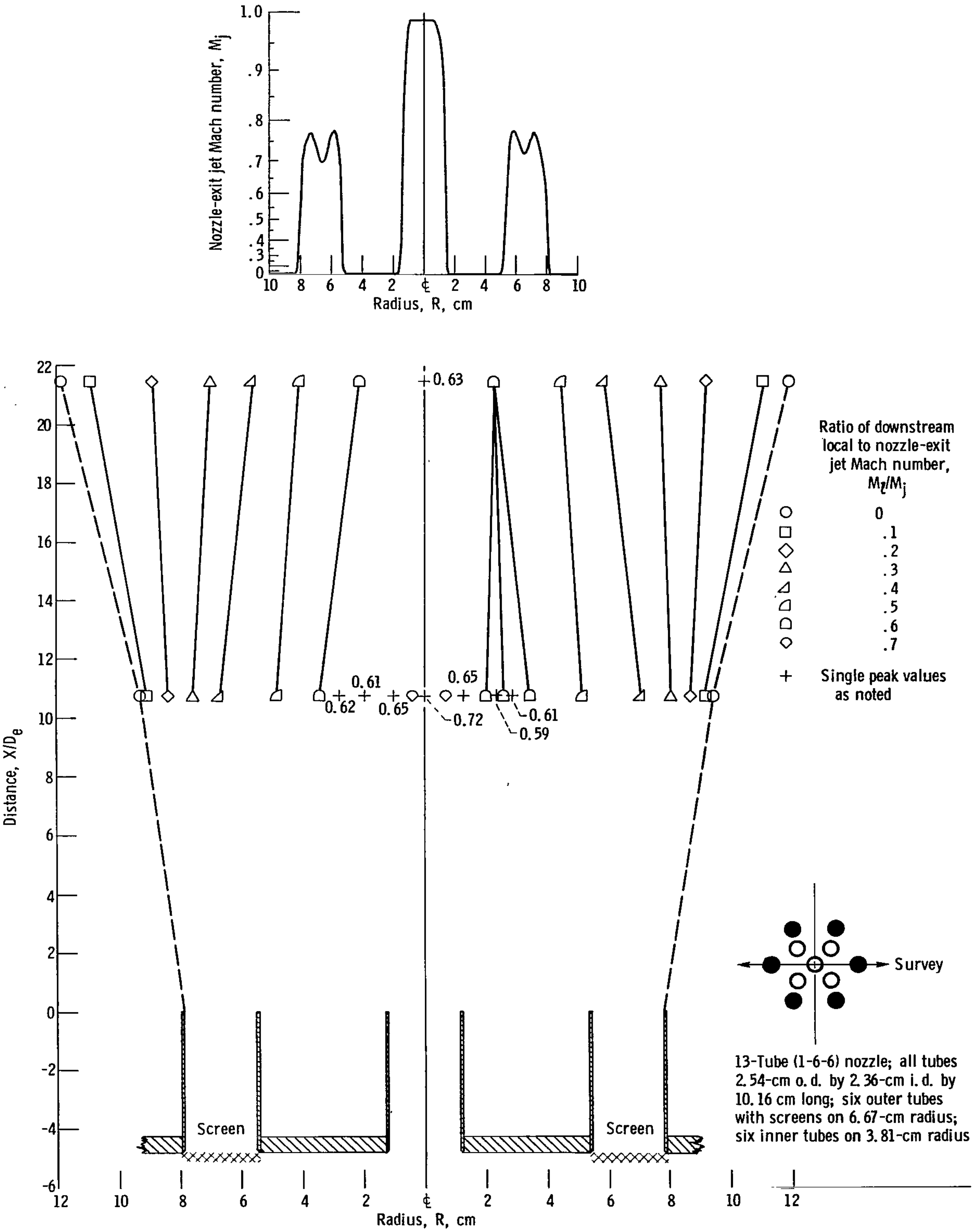

Figure 172. - Configuration 65. Nozzle-exit jet Mach number, M_j, 0.99; equivalent diameter, D_e, 2.36 centimeters; ratio of bypass (secondary) flow exit Mach number to core (primary) flow exit Mach number, M_b/M_j, 0.738.

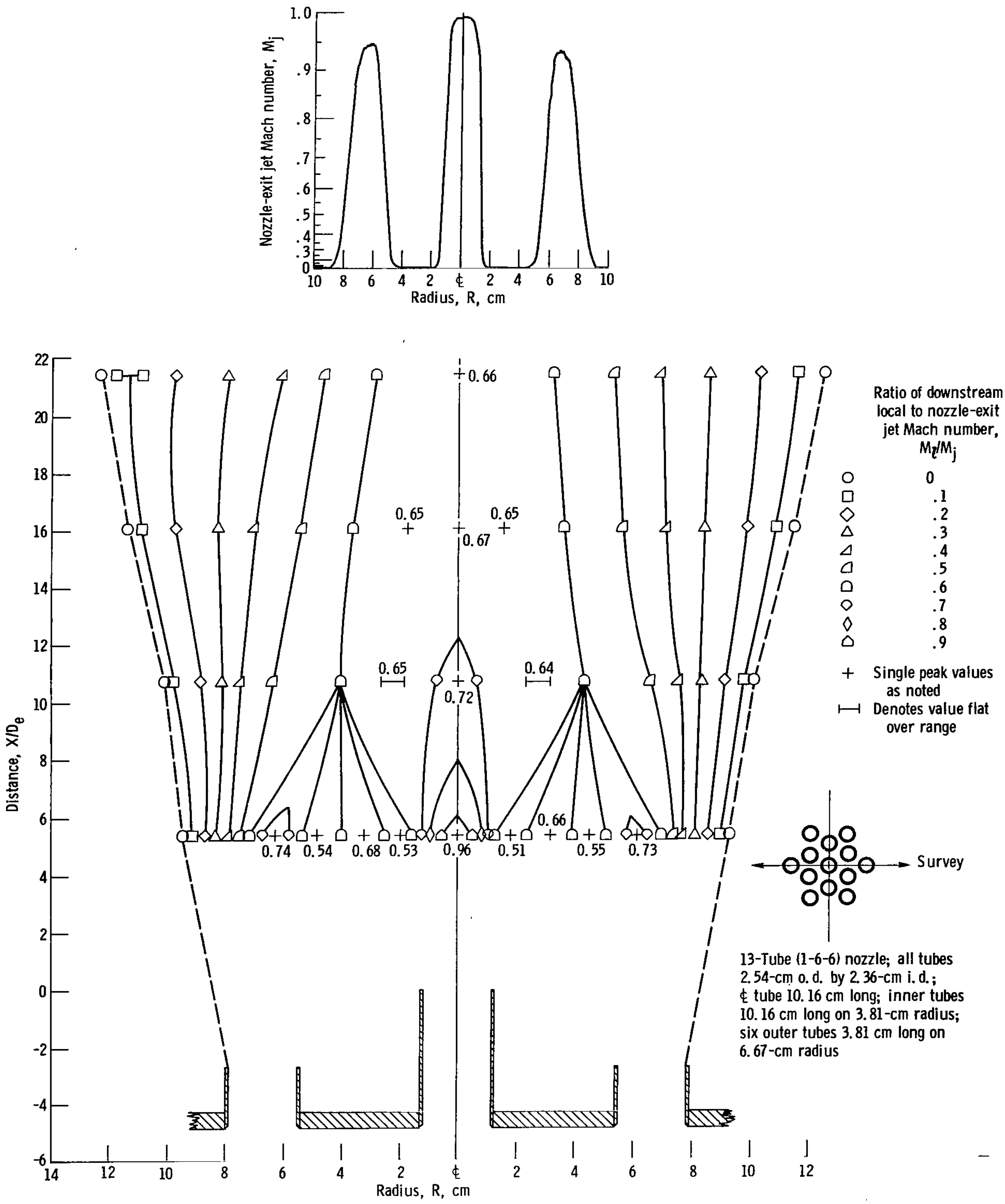

Figure 173. - Configuration 66. Nozzle-exit jet Mach number, M_j, 0.995; equivalent diameter, D_e, 2.36 centimeters.

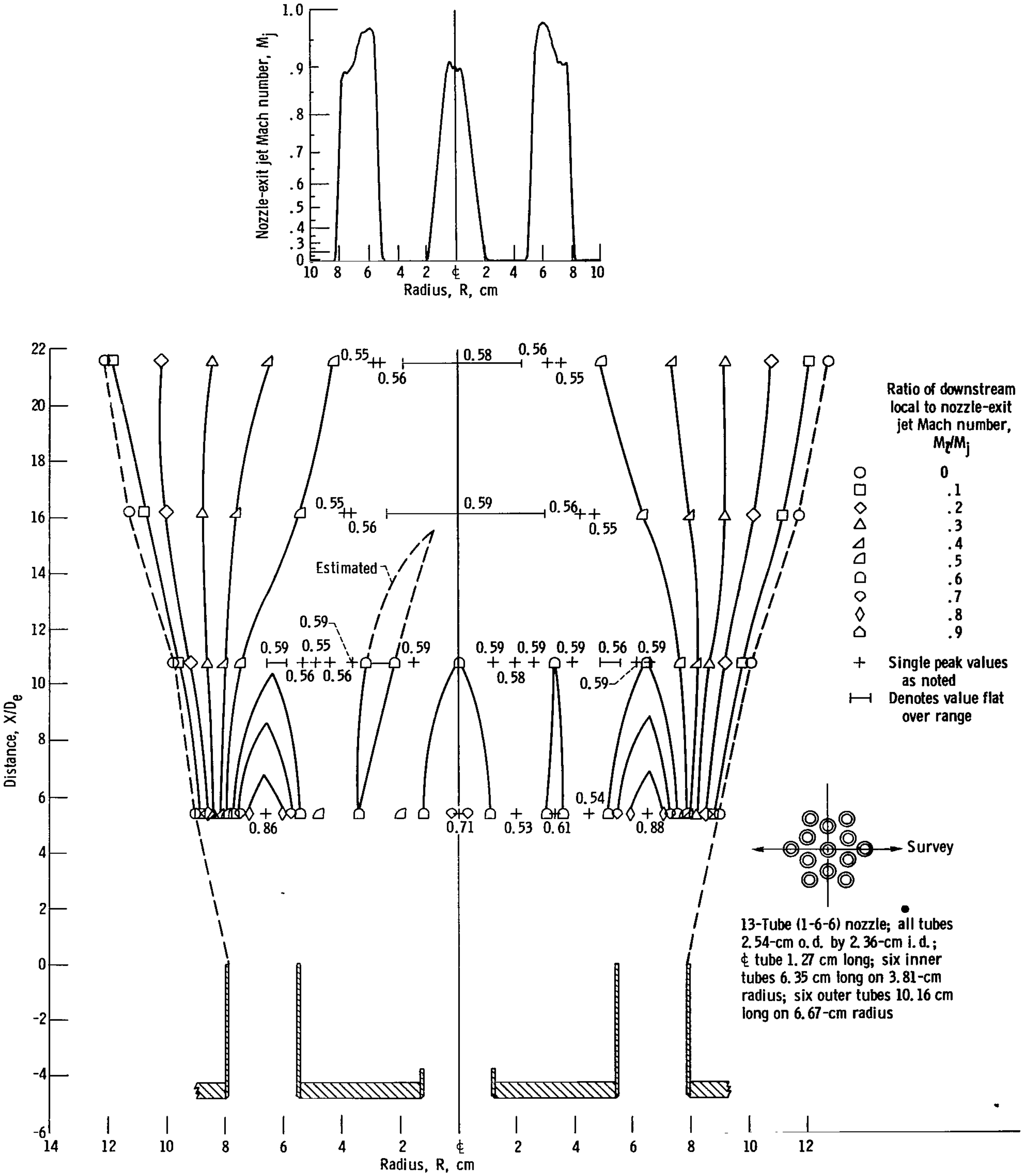

Figure 174. - Configuration 67. Nozzle-exit jet Mach number, M_j, 0.98; equivalent diameter, D_e, 2.36 centimeters.

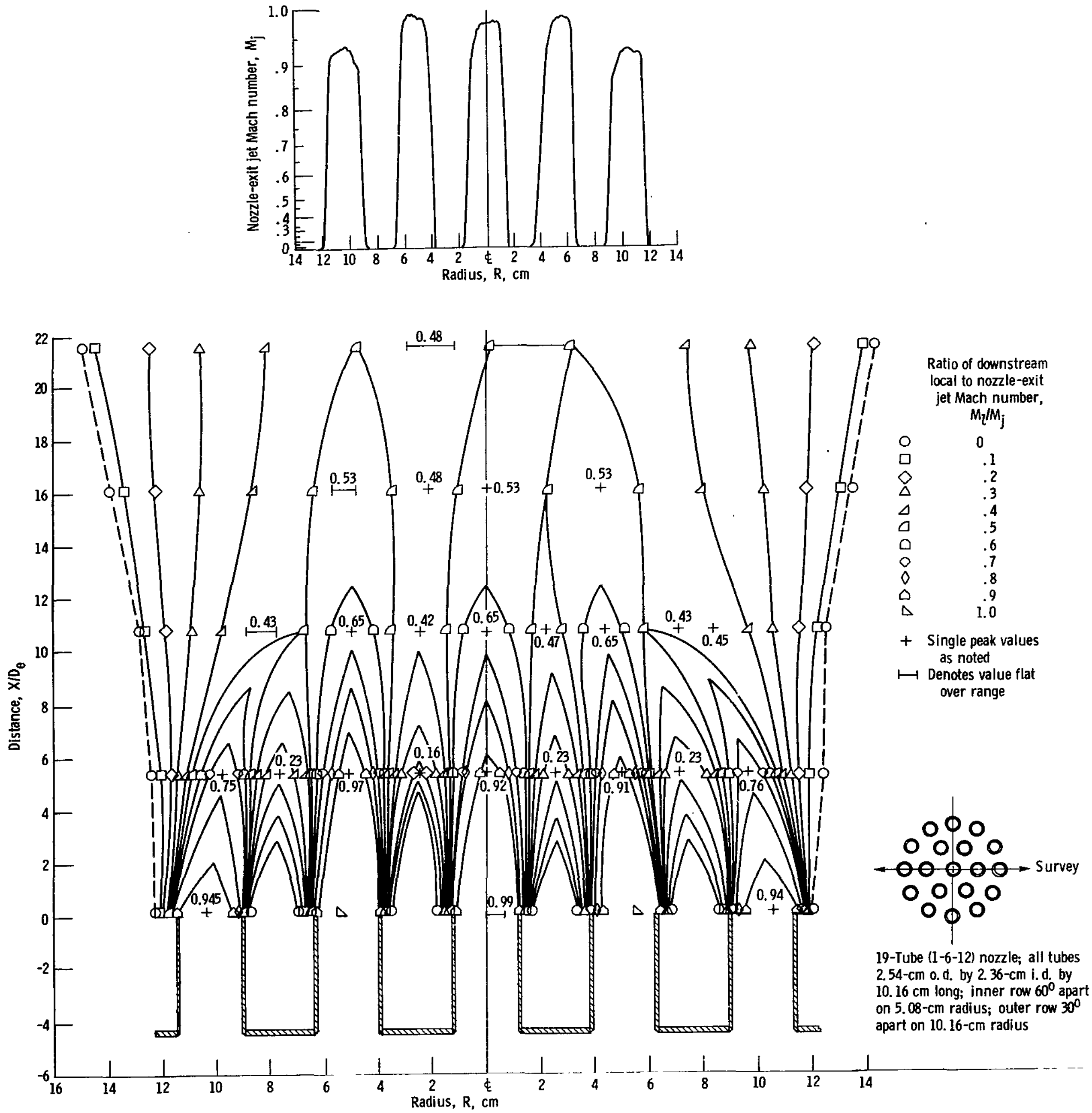

Figure 175. - Configuration 68. Nozzle-exit jet Mach number, M_j, 0.99; equivalent diameter, D_e, 2.36 centimeters.

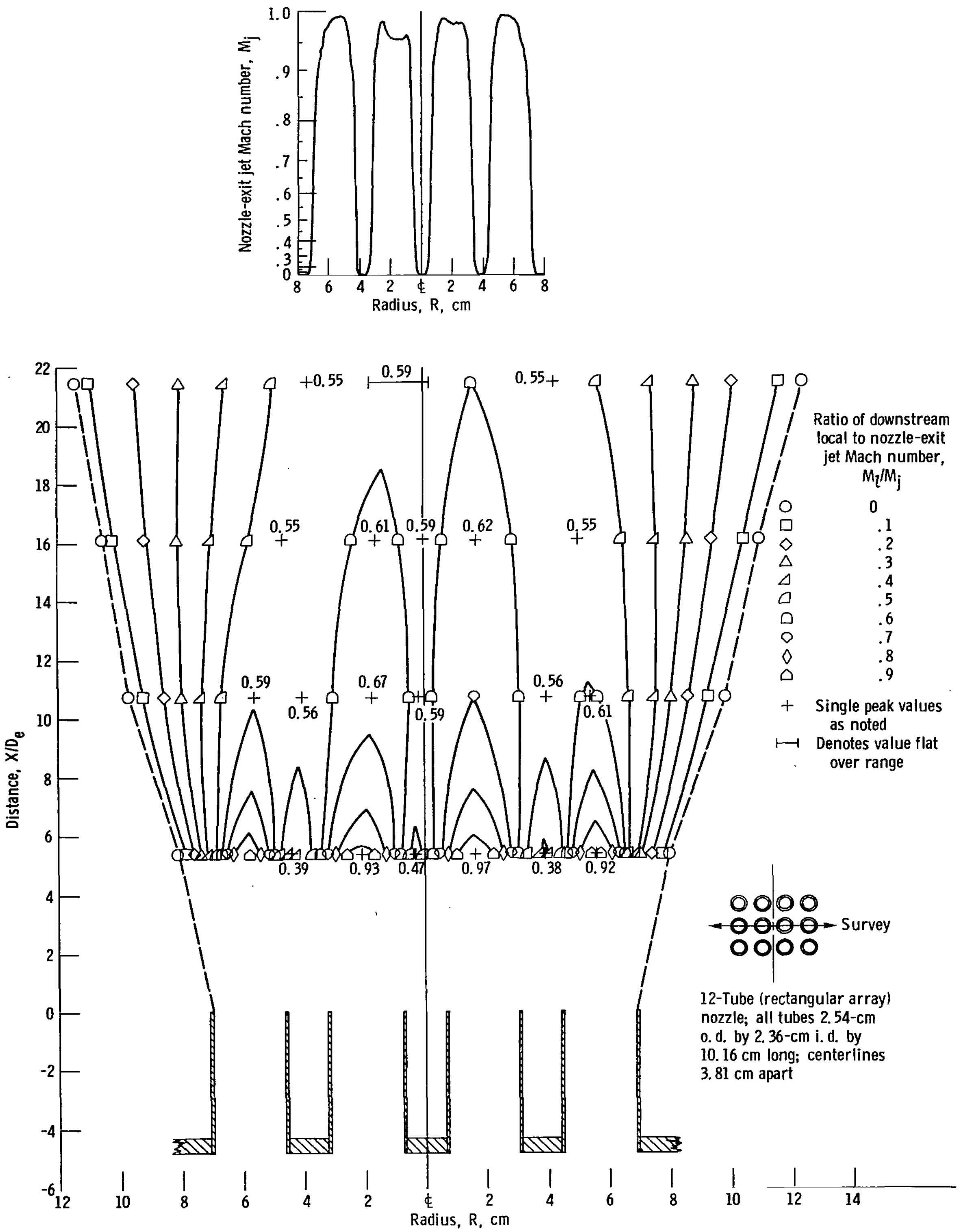

(a) Survey across center row of tubes.

Figure 176. - Configuration 69. Nozzle-exit jet Mach number, M_j, 0.985; equivalent diameter, D_e, 2.36 centimeters.

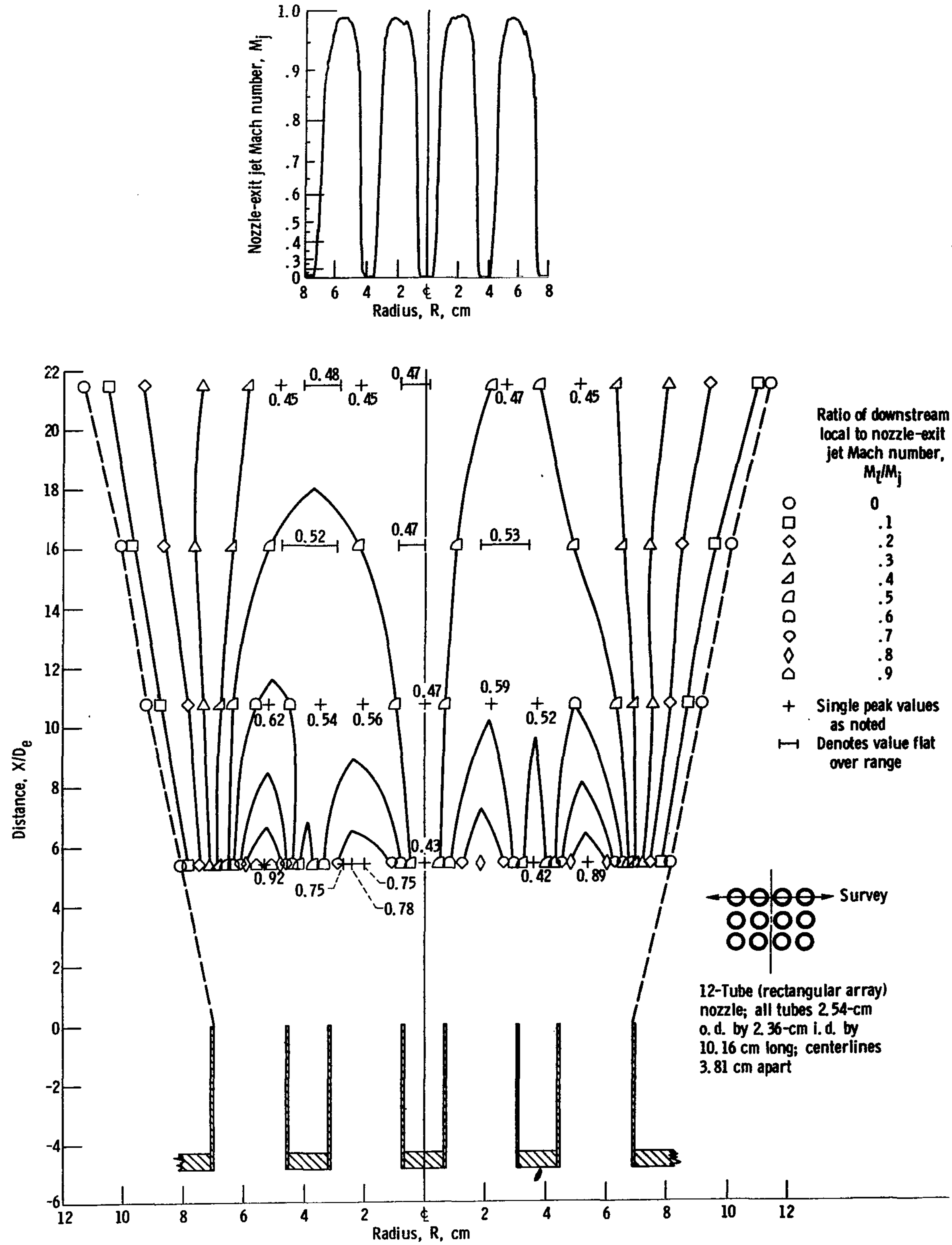

(b) Survey across top row of tubes.

Figure 176. - Concluded.

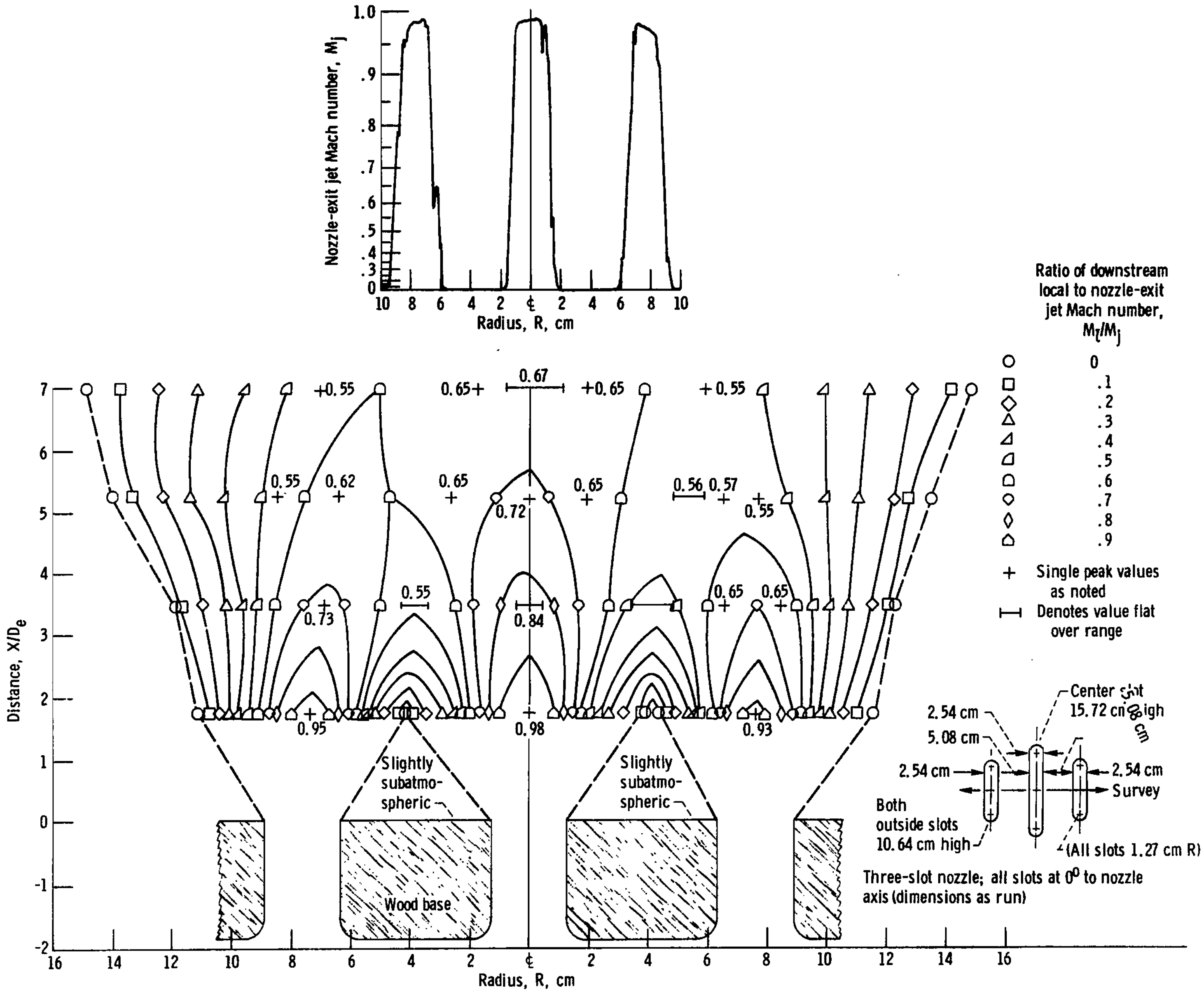

Figure 177. - Configuration 70. Nozzle-exit jet Mach number, M_j, 0.99; equivalent diameter (center slot), D_e, 7.25 centimeters.

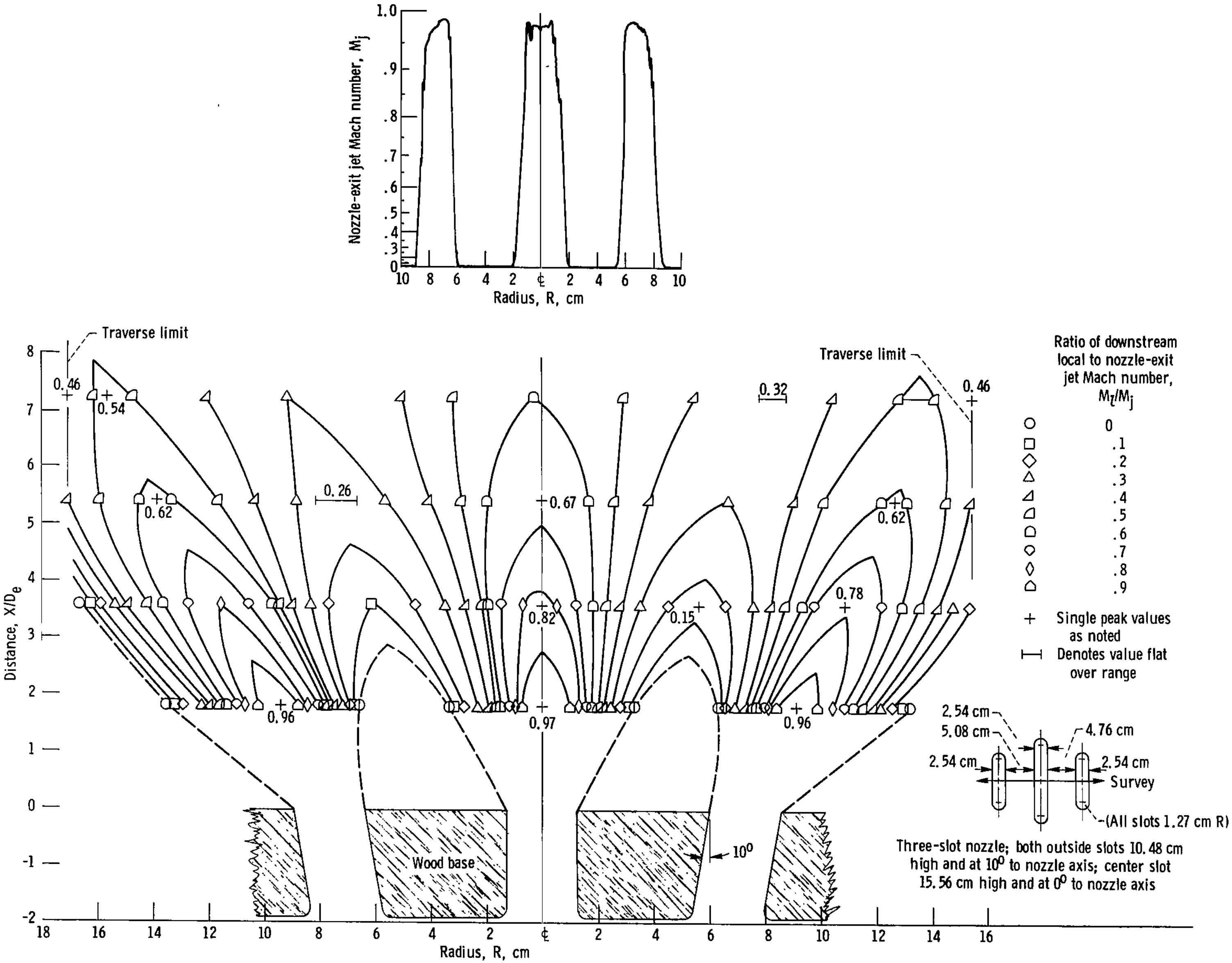

Figure 178. - Configuration 71. Nozzle-exit jet Mach number, M_j, 0.99; equivalent diameter (center slot), D_e, 6.96 centimeters.

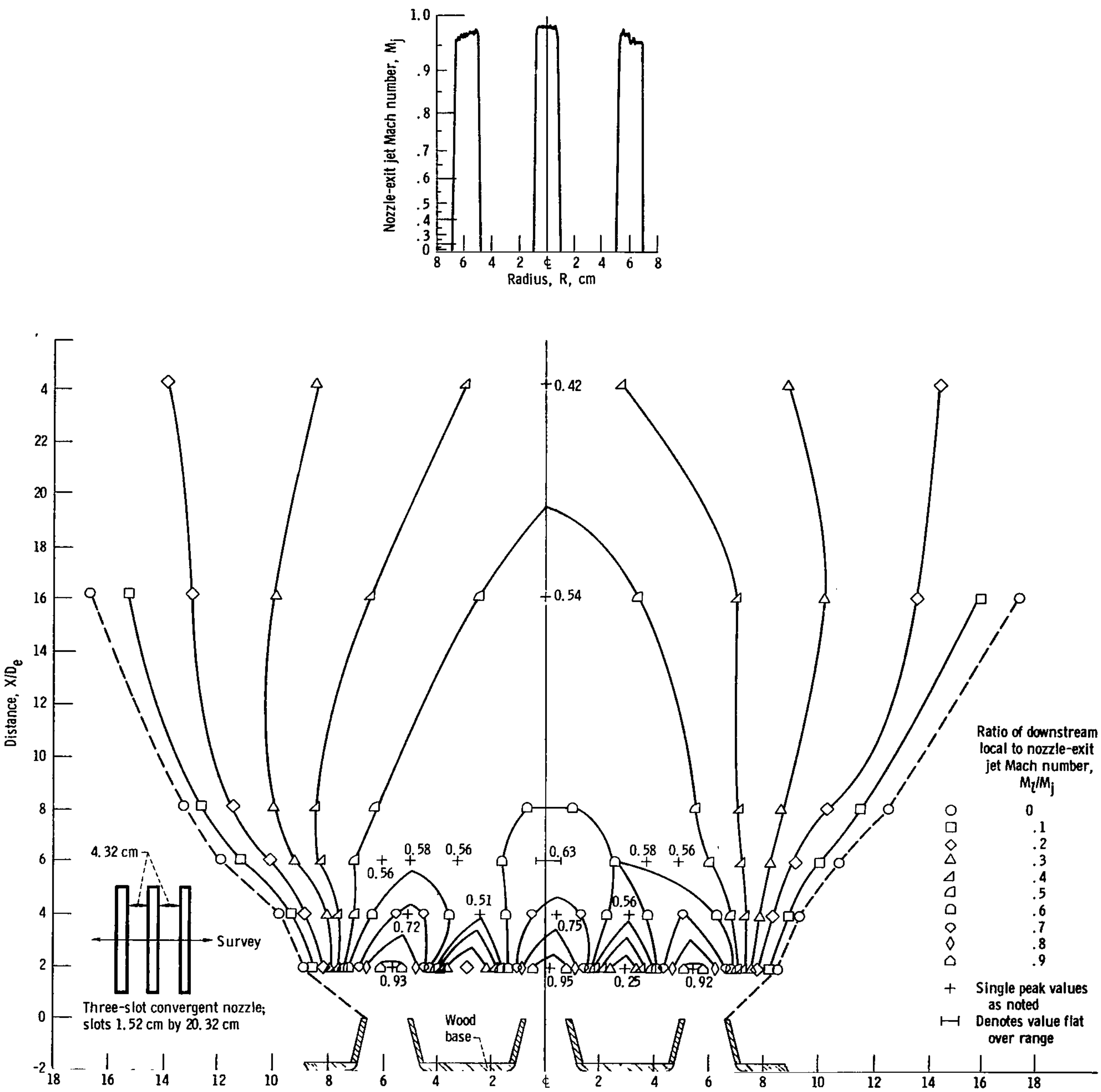

Figure 179. - Configuration 72. Nozzle-exit jet Mach number, M_j, 0.983; equivalent diameter, D_e, 6.28 centimeters.

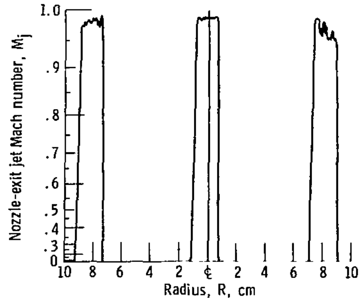

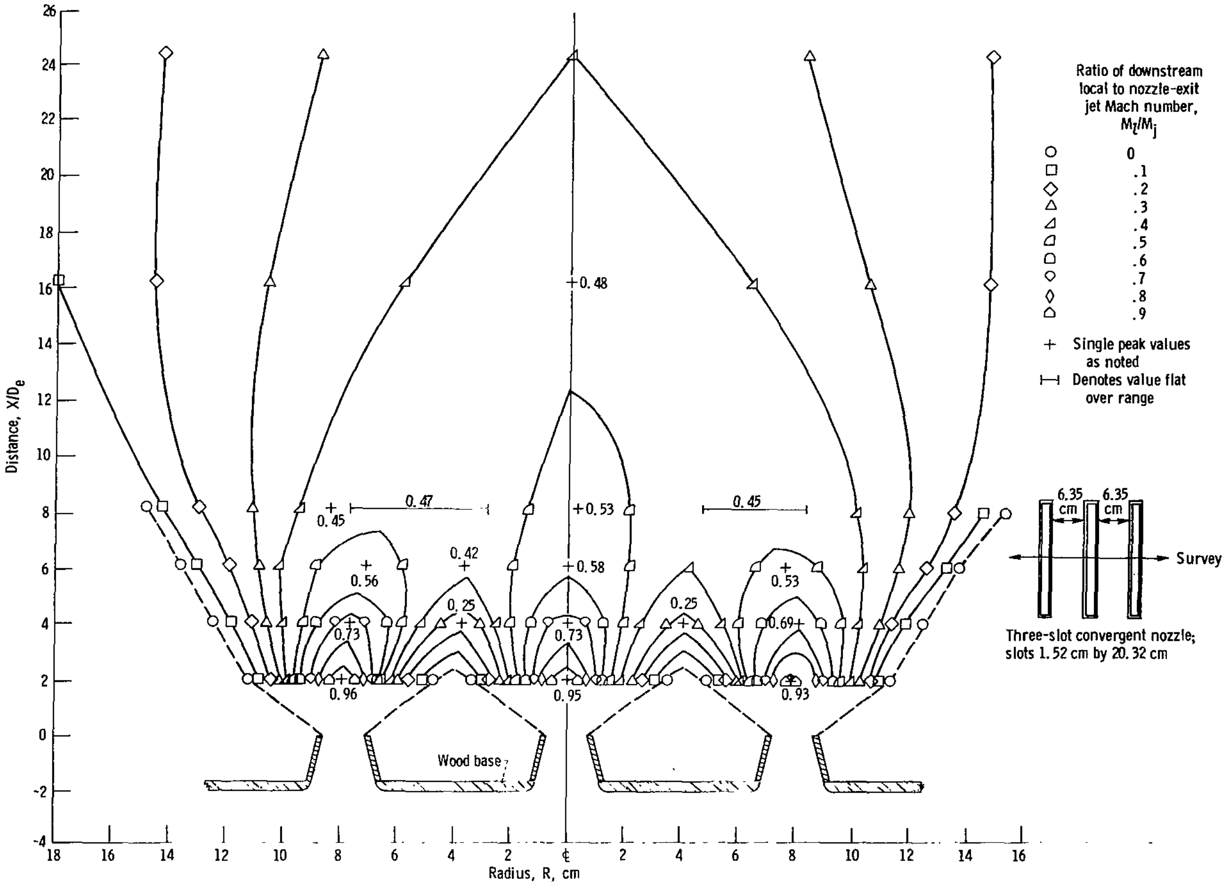

Figure 180. - Configuration 73. Nozzle-exit jet Mach number, M_j, 0.99; equivalent diameter, D_e, 6.28 centimeters.

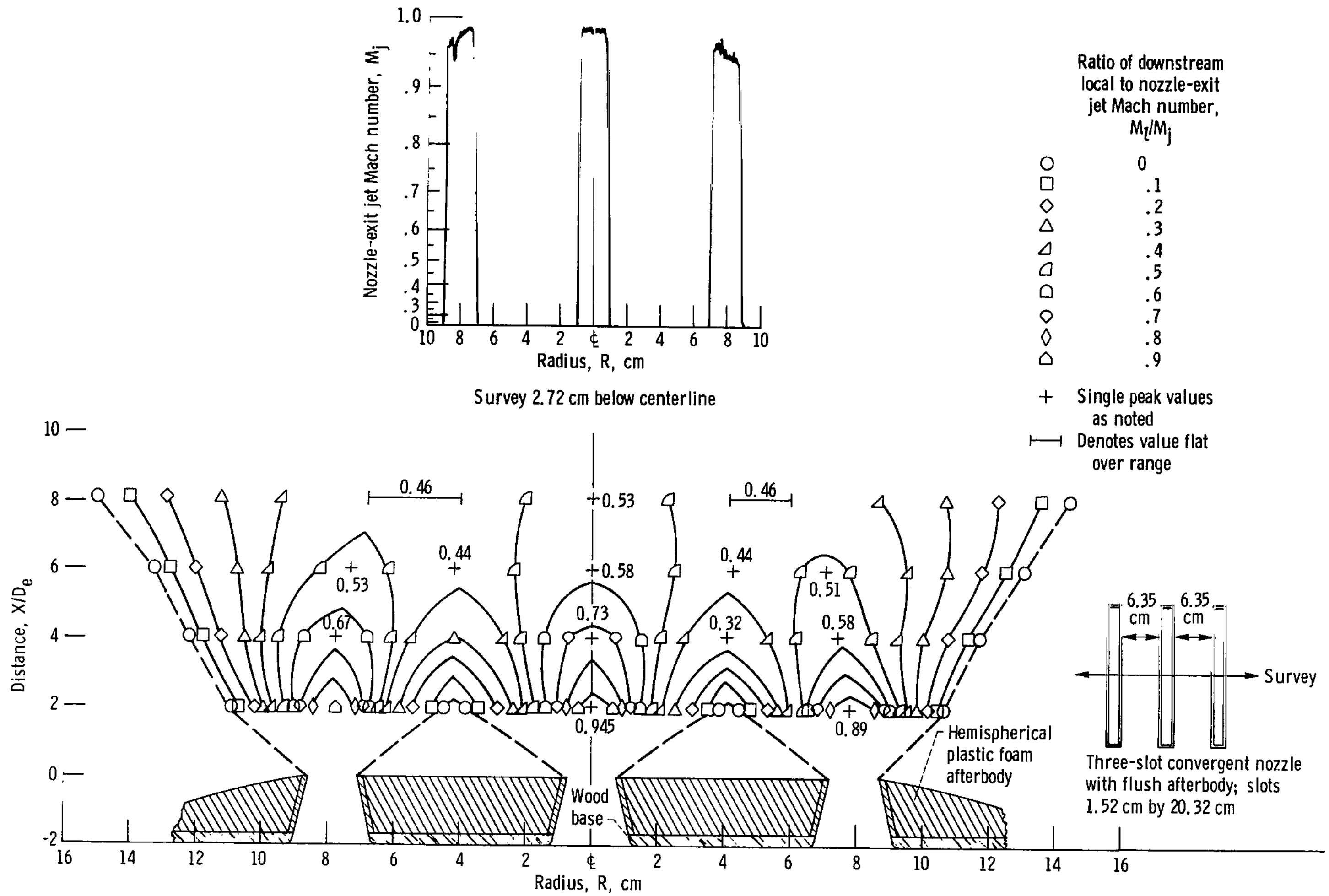

Figure 181. - Configuration 74. Nozzle-exit jet Mach number, M_j, 0.985; equivalent diameter, D_e, 6.28 centimeters.

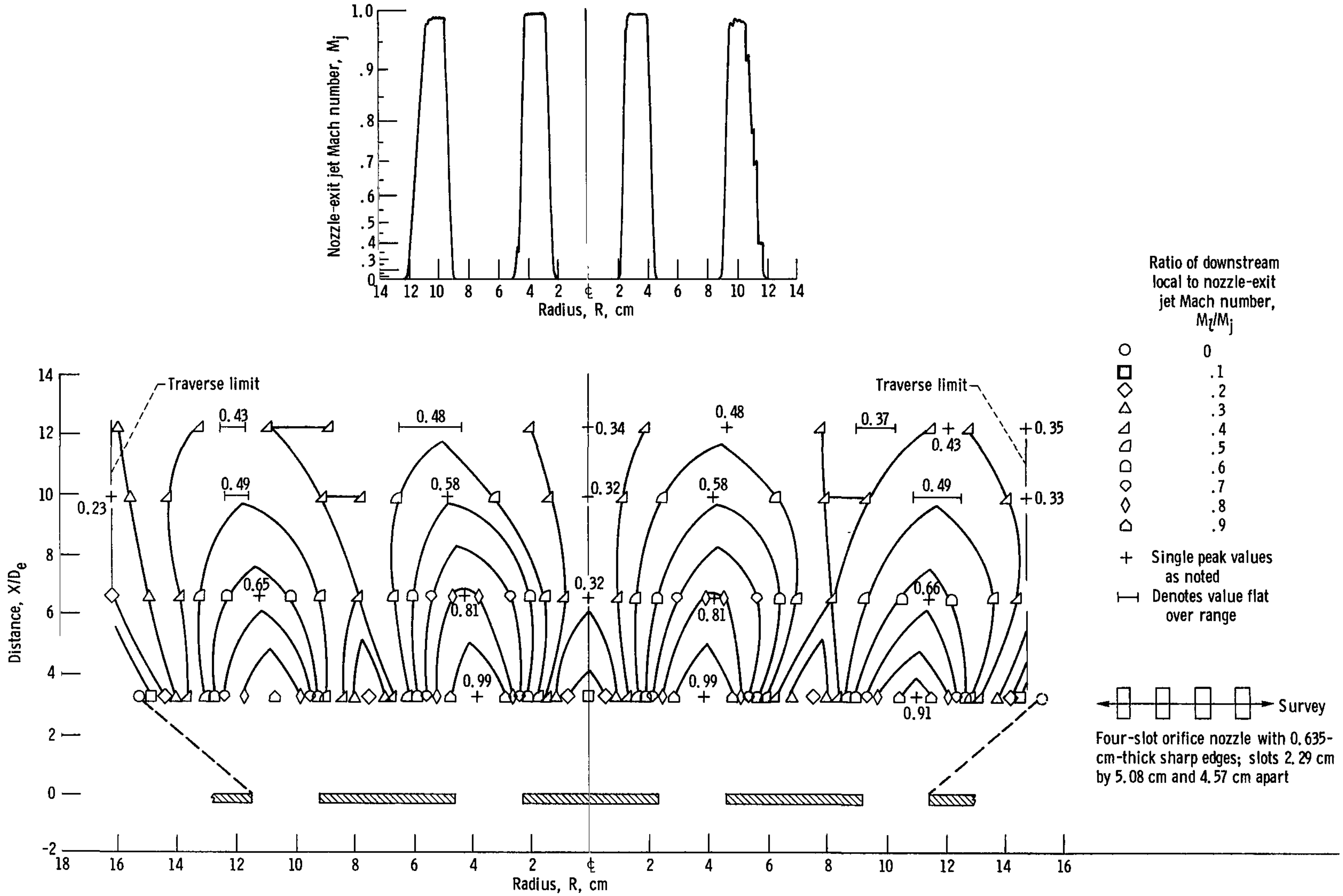

Figure 182. - Configuration 75. Nozzle-exit jet Mach number, M_j, 0.993; equivalent diameter, D_e, 3.84 centimeters.

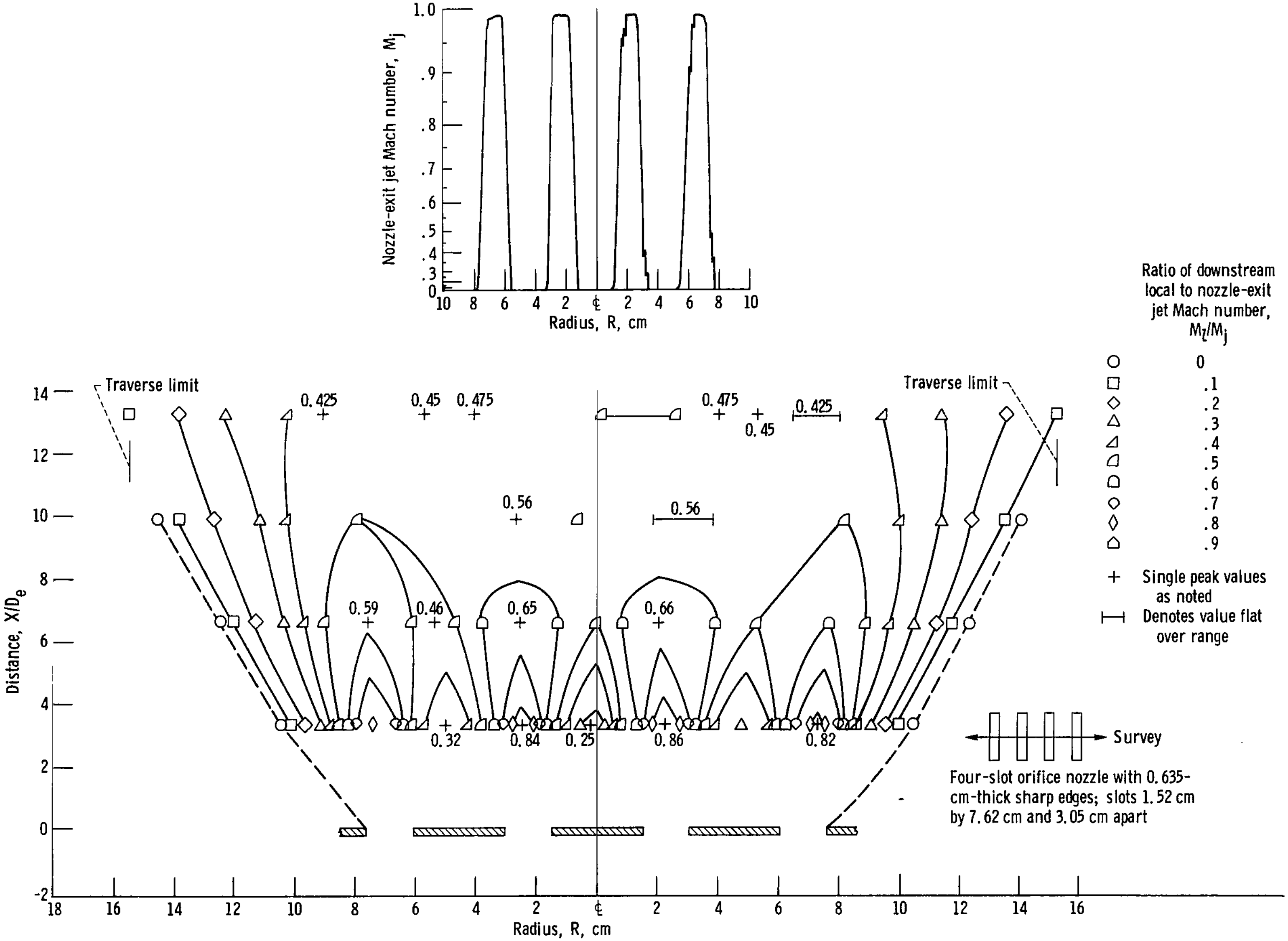

Figure 183. - Configuration 76. Nozzle-exit jet Mach number, M_j, 0.99; equivalent diameter, D_e, 3.84 centimeters.

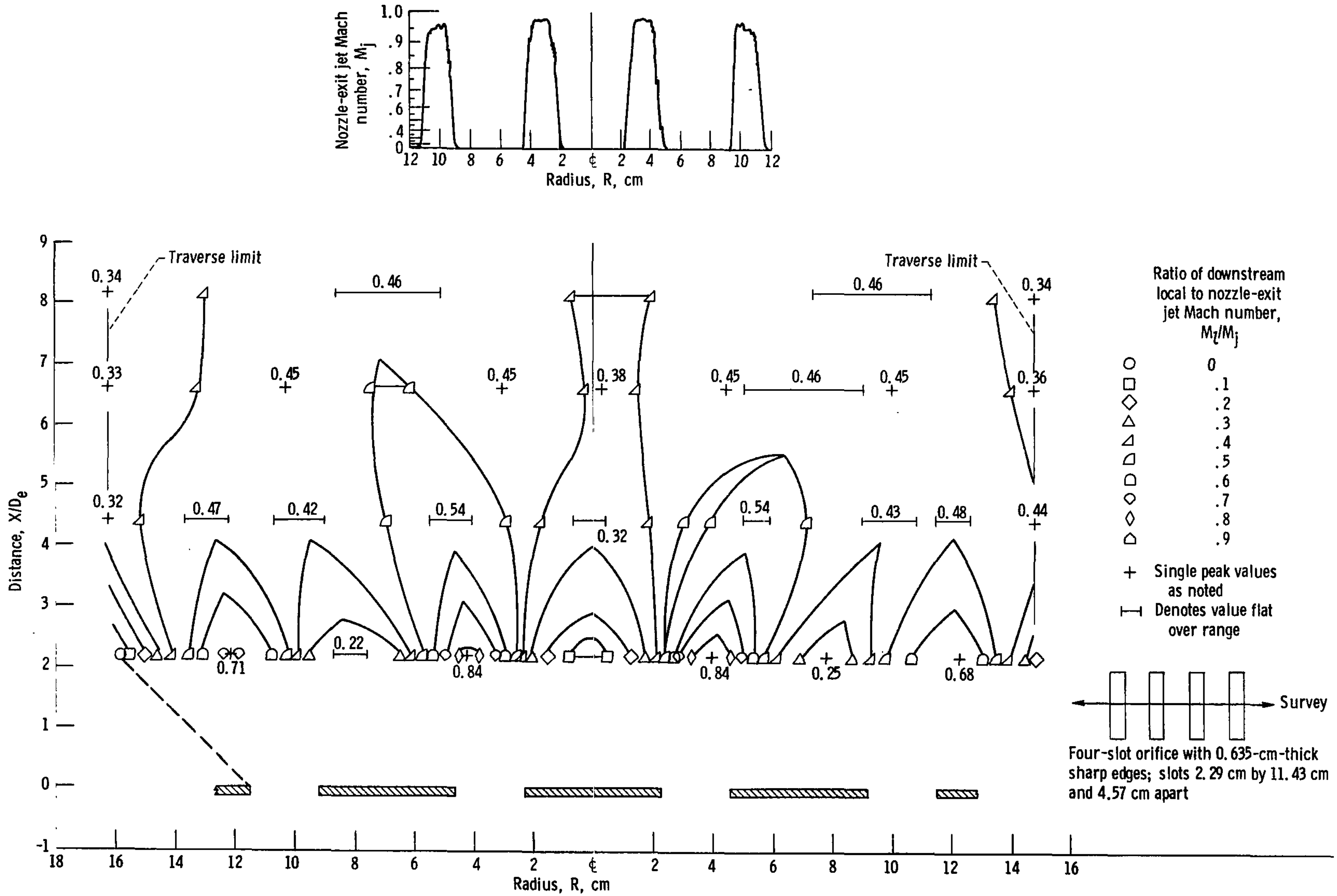

Figure 184. - Configuration 77. Nozzle-exit jet Mach number, M_j, 0.975; equivalent diameter, D_e, 5.76 centimeters.

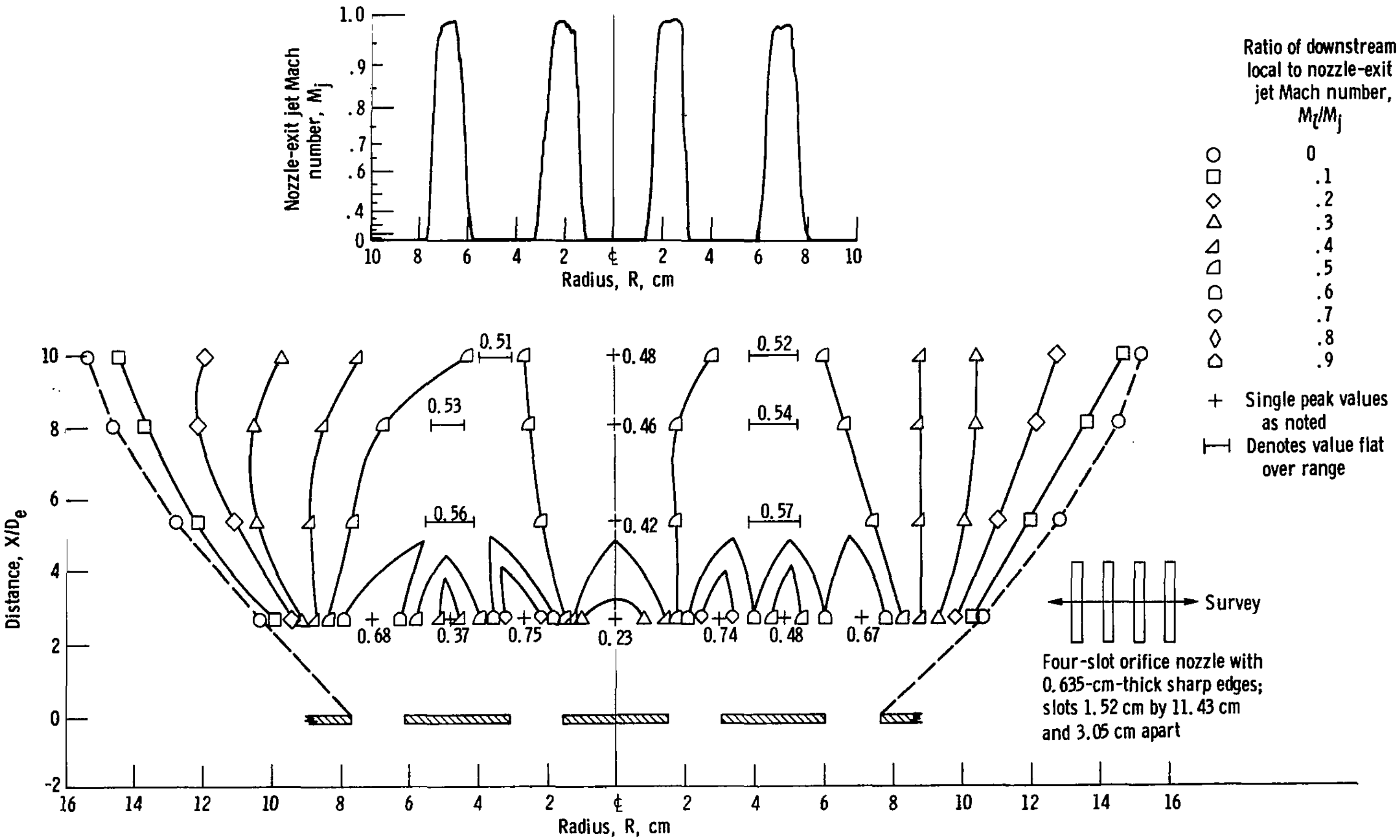

Figure 185. - Configuration 78. Nozzle-exit jet Mach number, M_j, 0.984; equivalent diameter, D_e, 4.71 centimeters.

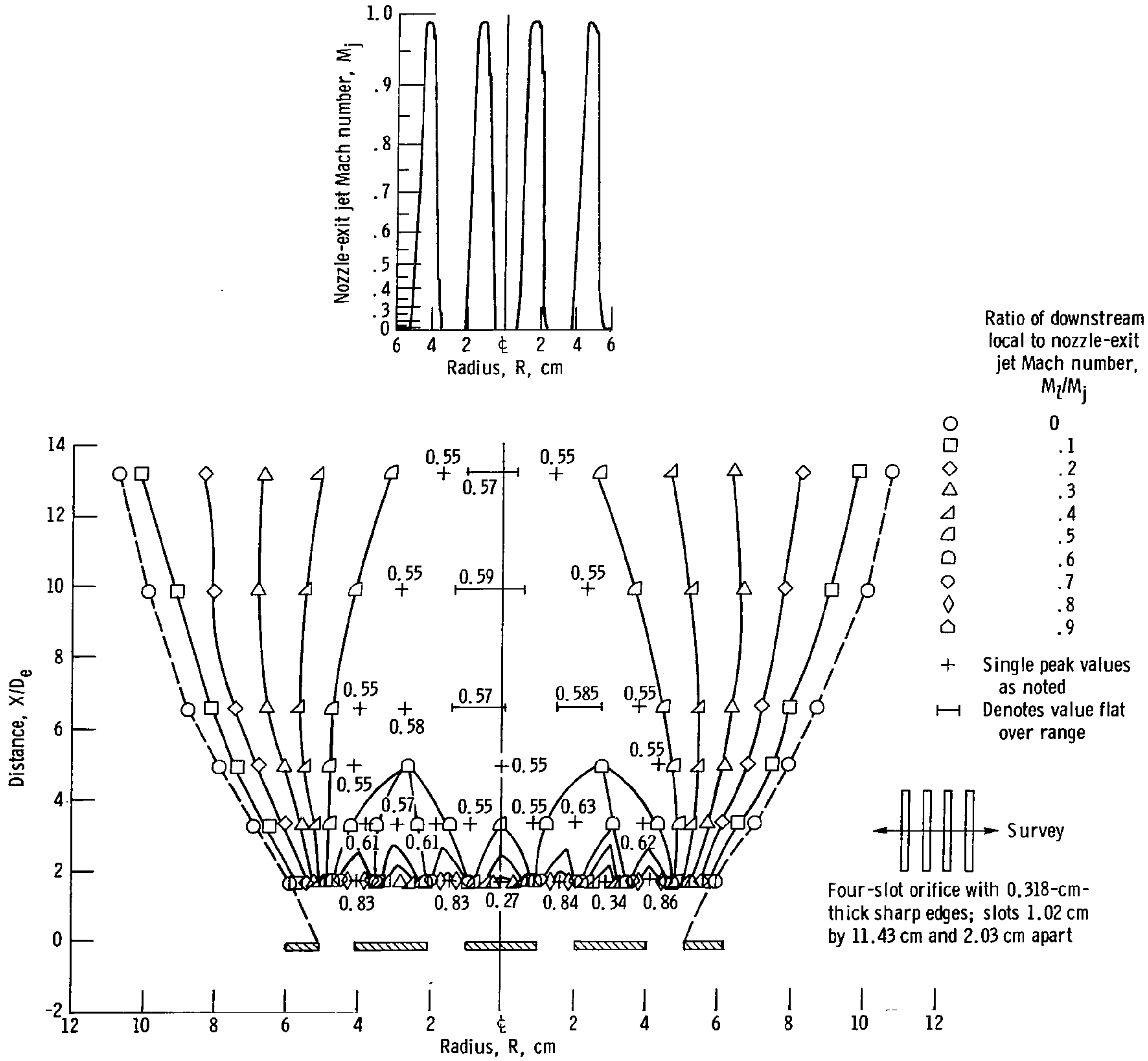

Figure 186. - Configuration 79. Nozzle-exit jet Mach number, M_j, 0.99; equivalent diameter, D_e, 3.84 centimeters. (Spaces between slots pumped slightly subatmospheric for 2.54 cm downstream.)

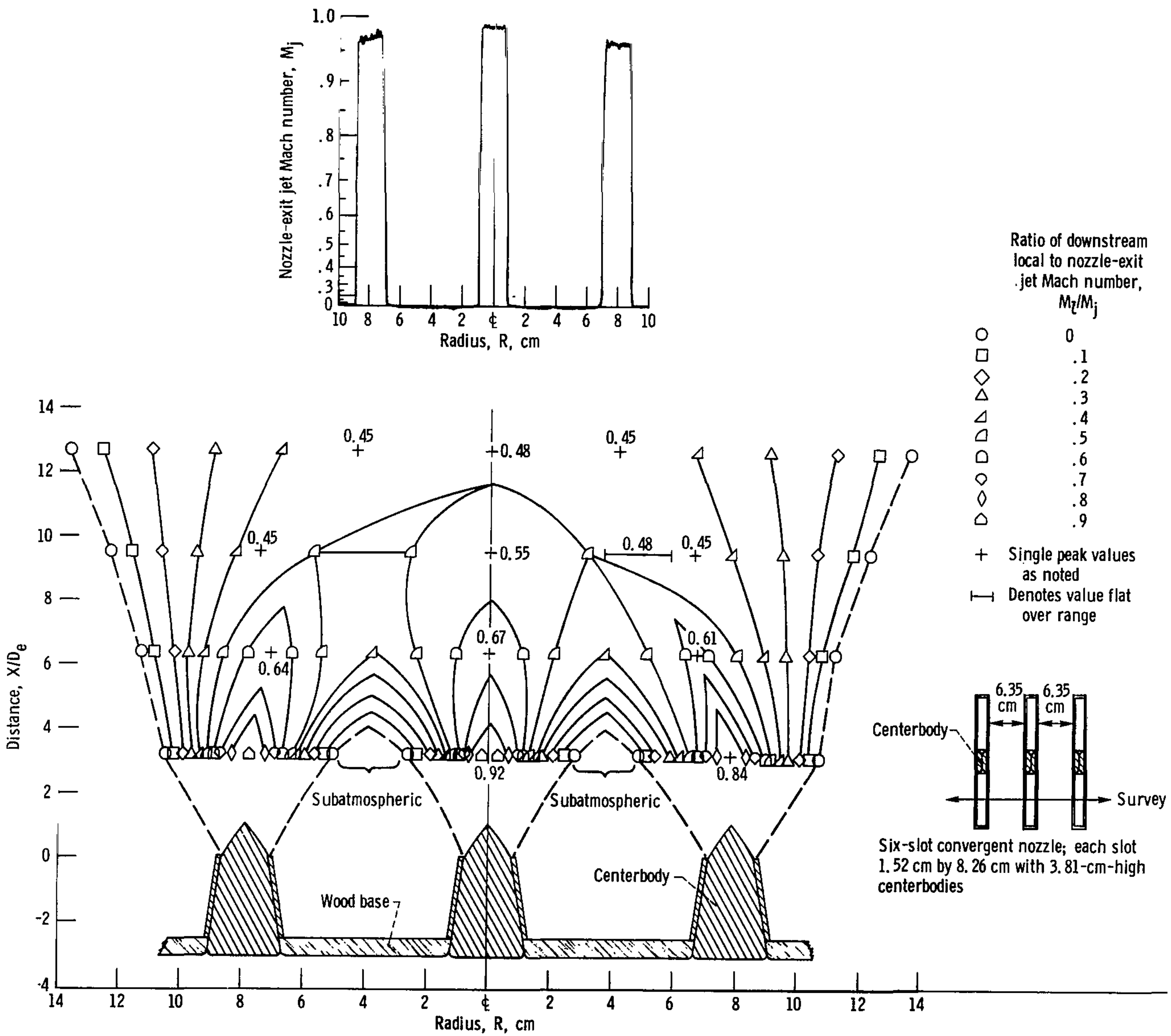

(a) Survey on centerline of lower slots.

Figure 187. - Configuration 89. Nozzle-exit jet Mach number, M_j, 0.987; equivalent diameter, D_e, 4.00 centimeters.

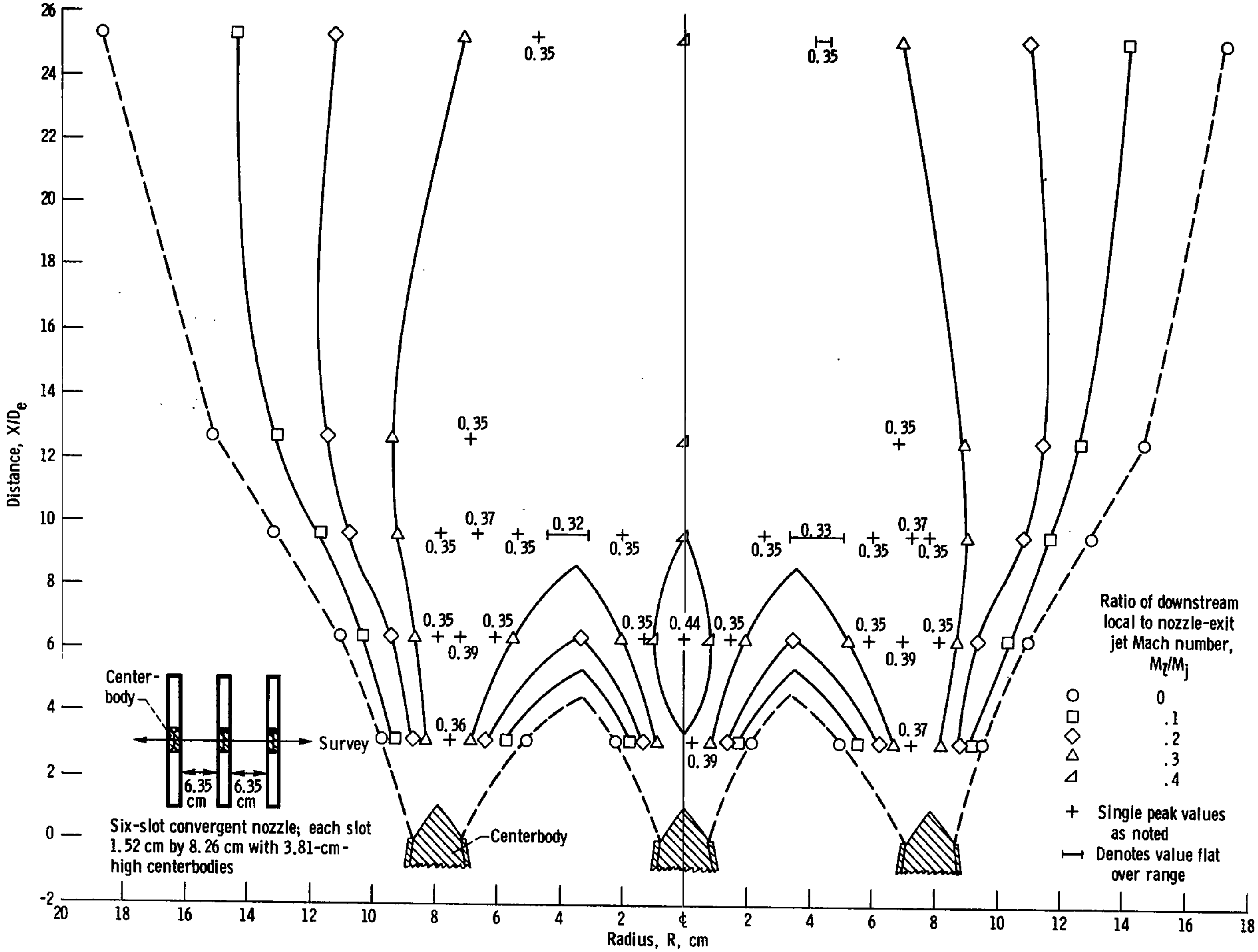

(b) Survey on nozzle centerline.

Figure 187. - Concluded.

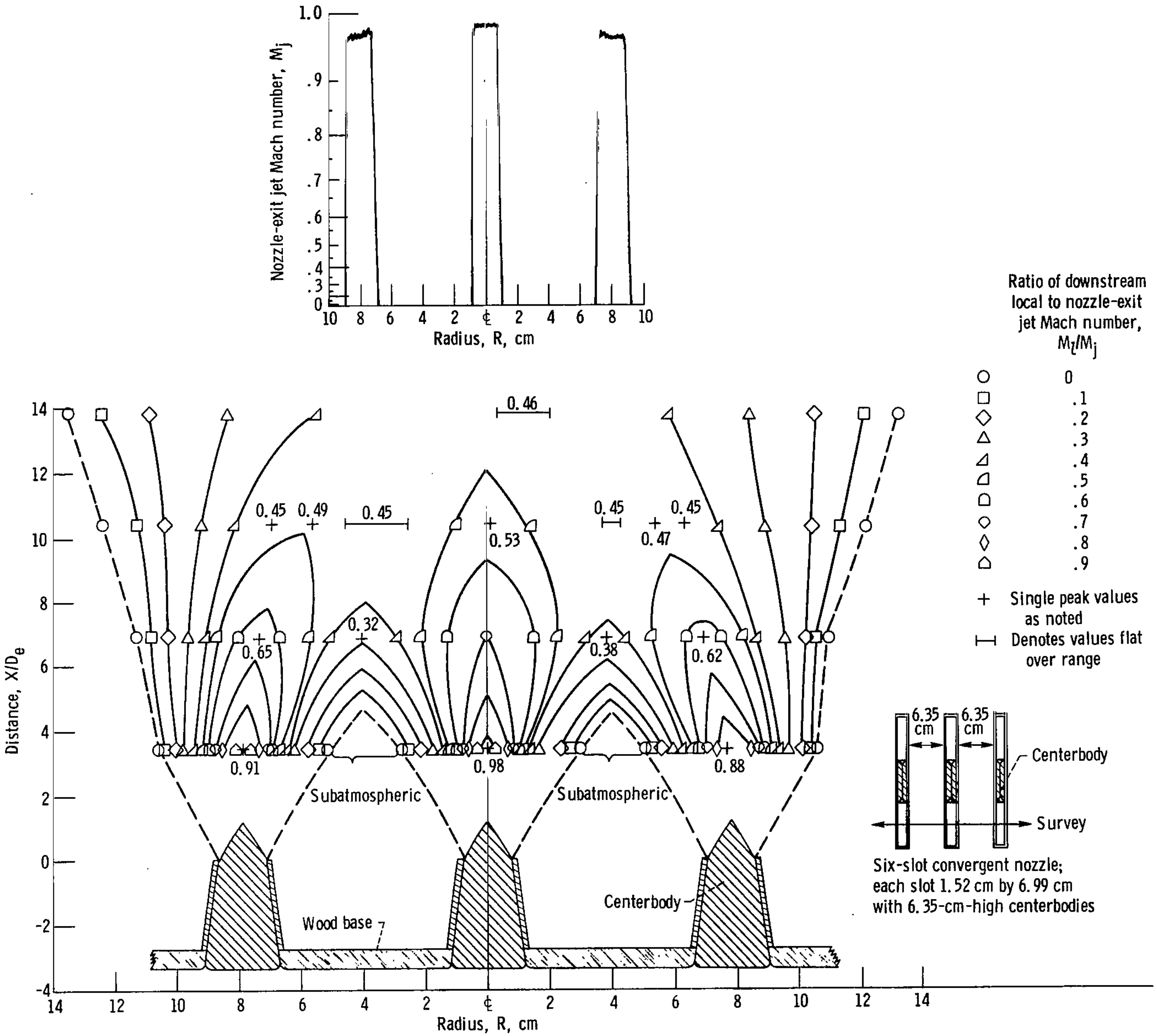

Figure 188. - Configuration 90. Nozzle-exit jet Mach number, M_j, 0.99; equivalent diameter, D_e, 3.68 centimeters.

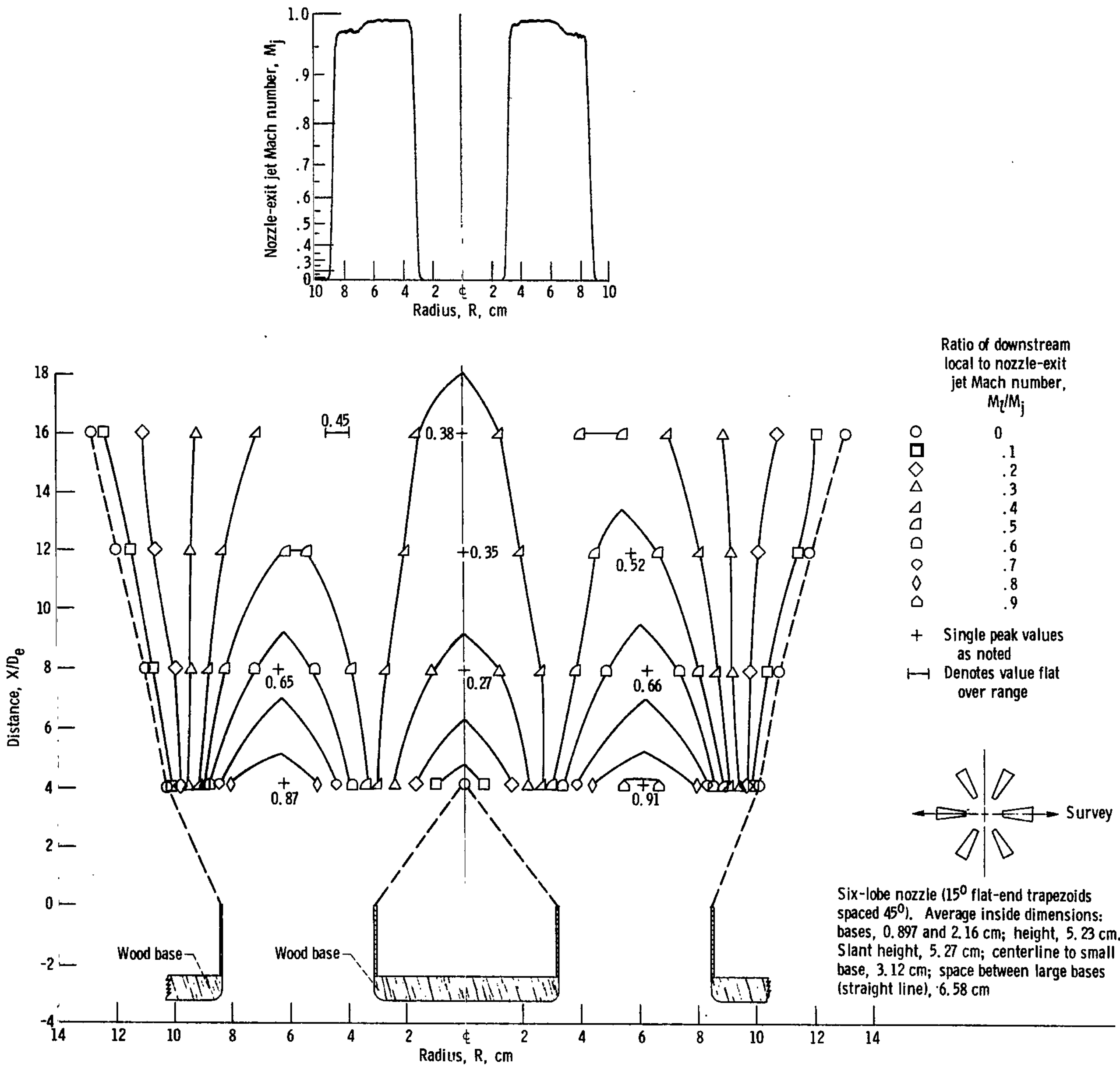

Figure 189. - Configuration 94. Nozzle-exit jet Mach number ratio, M_j, 0.99; equivalent diameter, D_e, 3.20 centimeters.

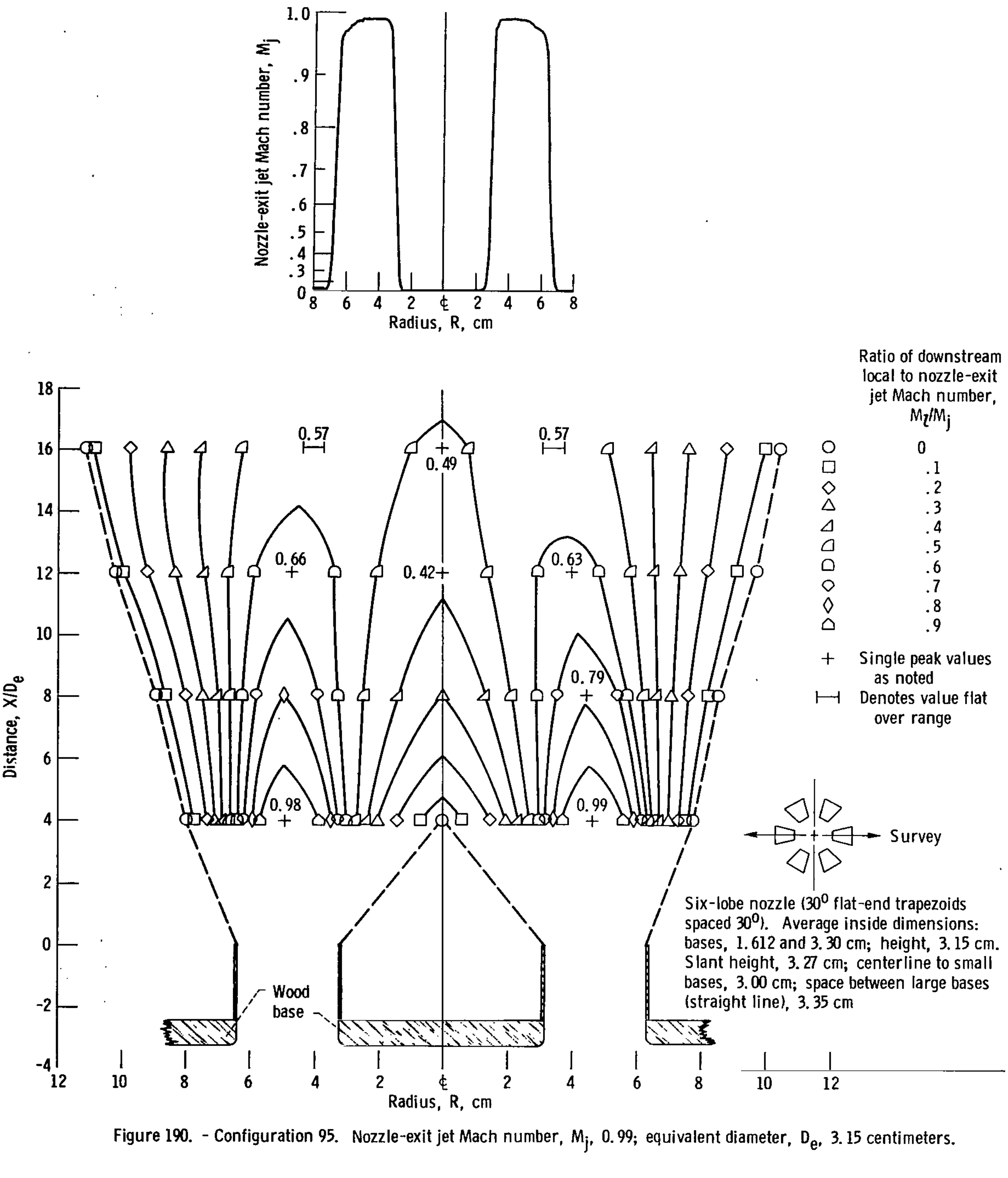

Figure 190. - Configuration 95. Nozzle-exit jet Mach number, M_j, 0.99; equivalent diameter, D_e, 3.15 centimeters.

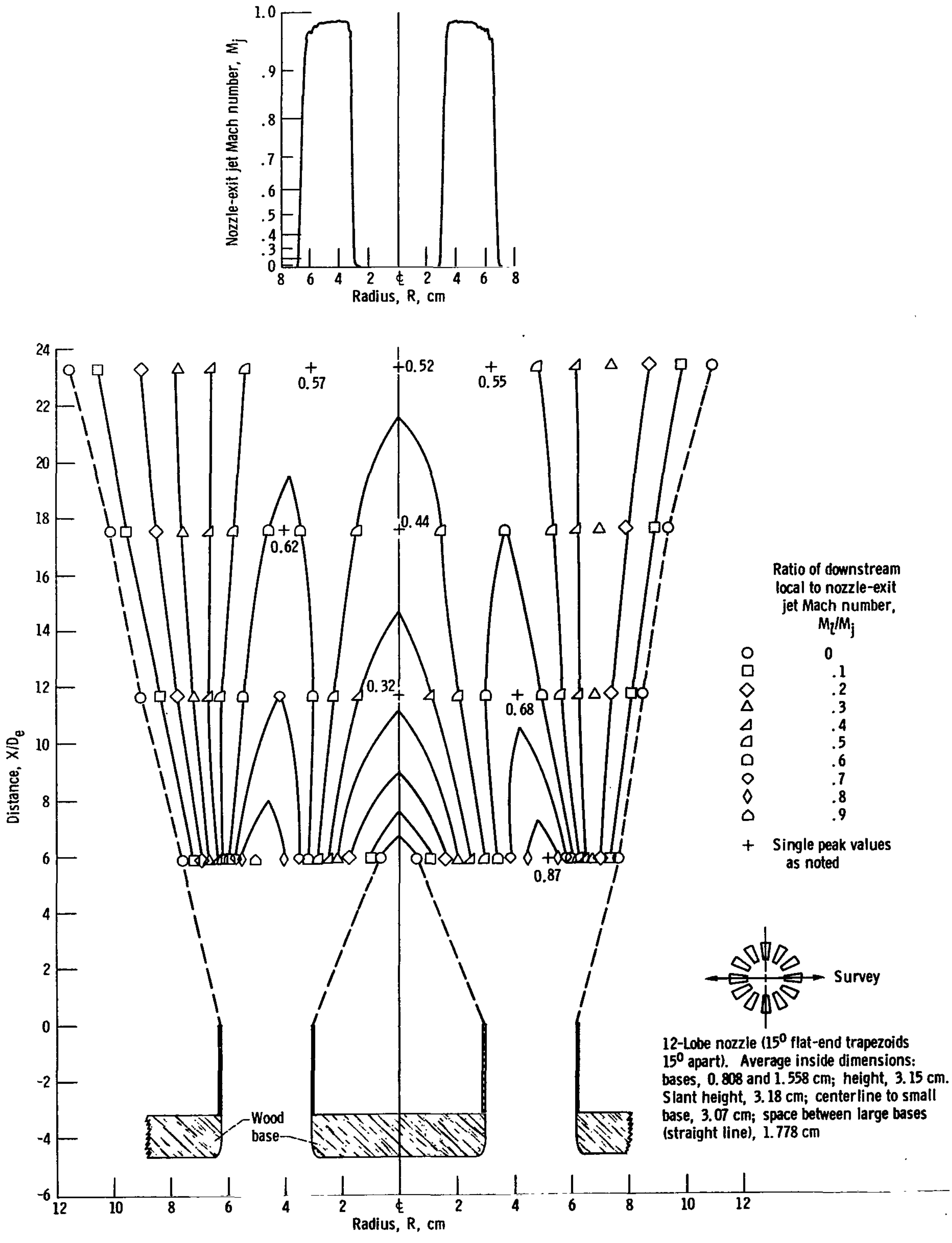

Figure 191. - Configuration 96. Nozzle-exit jet Mach number, M_j, 0.99; equivalent diameter, D_e, 2.18 centimeters.

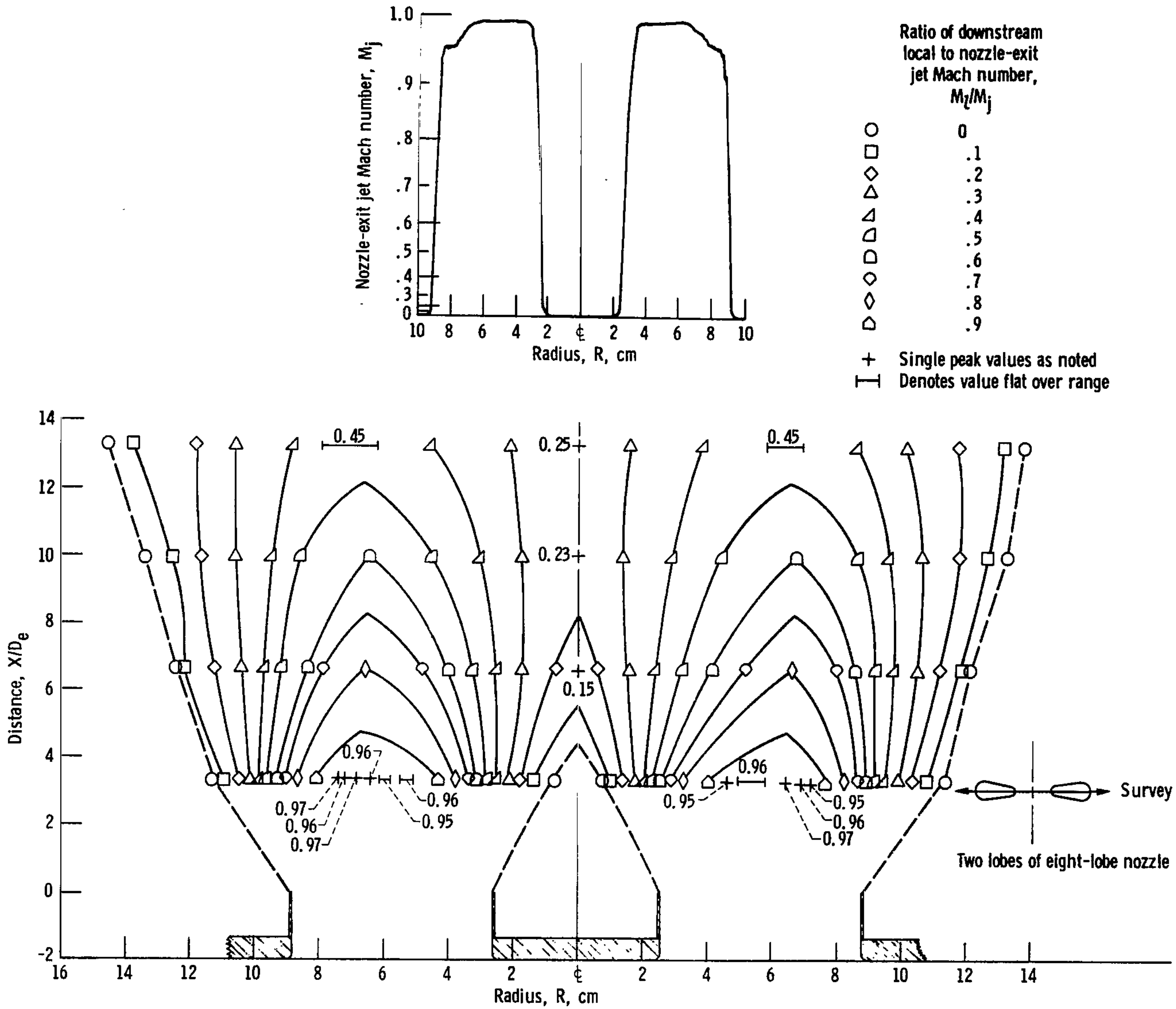

Figure 192. - Configuration 97. Nozzle-exit jet Mach number, M_j, 0.99; equivalent diameter, D_e, 3.81 centimeters.

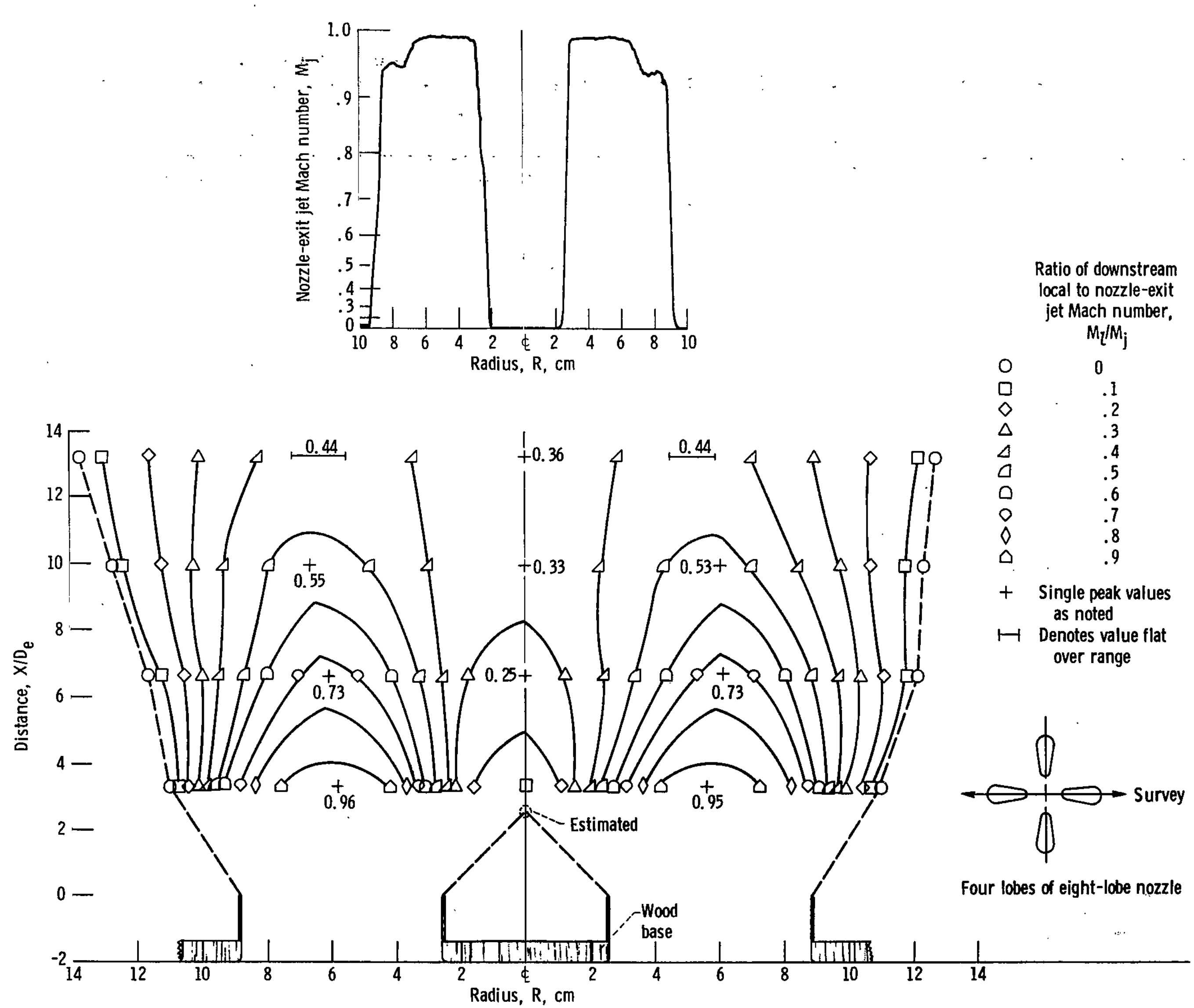

Figure 193. - Configuration 98. Nozzle-exit jet Mach number, M_j, 0.99; equivalent diameter, D_e, 3.81 centimeters.

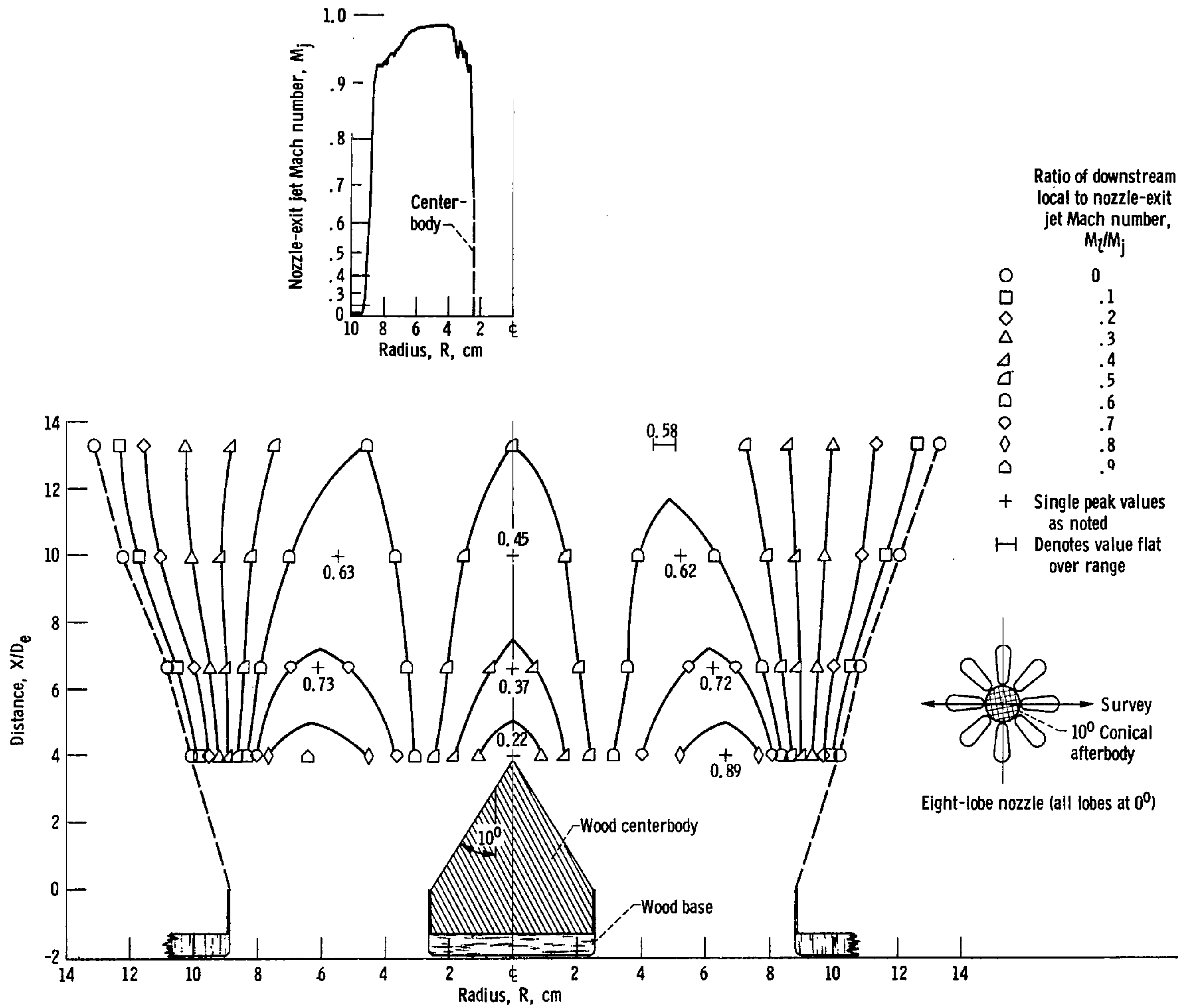

Figure 194. - Configuration 99. Nozzle-exit jet Mach number, M_j, 0.987; equivalent diameter, D_e, 3.81 centimeters. (No visible difference in contour run at X/D_e = 13.3 without afterbody in nozzle.)

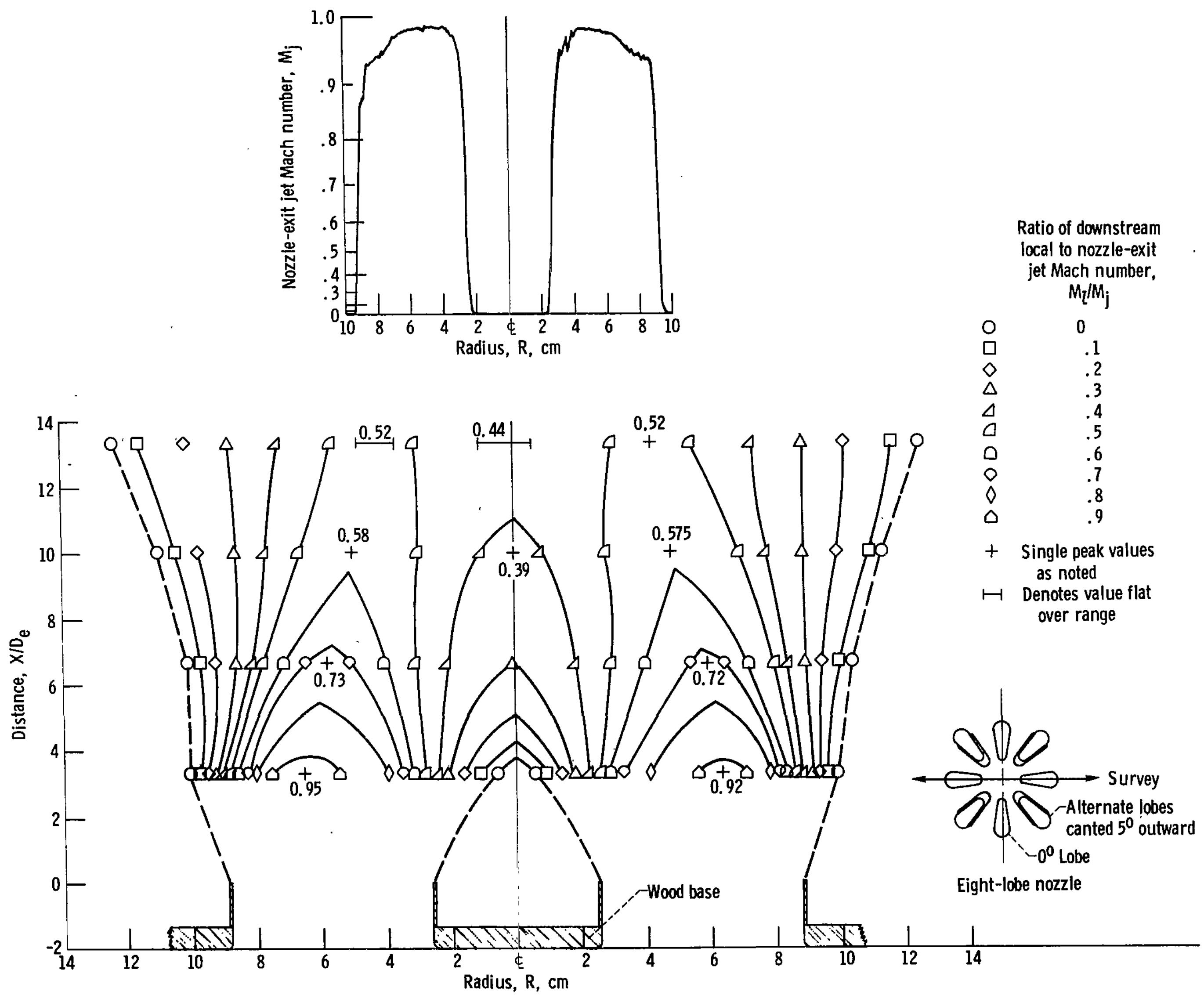

(a) Survey across 0° lobes; nozzle-exit jet Mach number, M_j, 0.989.

Figure 195. - Configuration 100. Equivalent diameter, D_e, 3.81 centimeters.

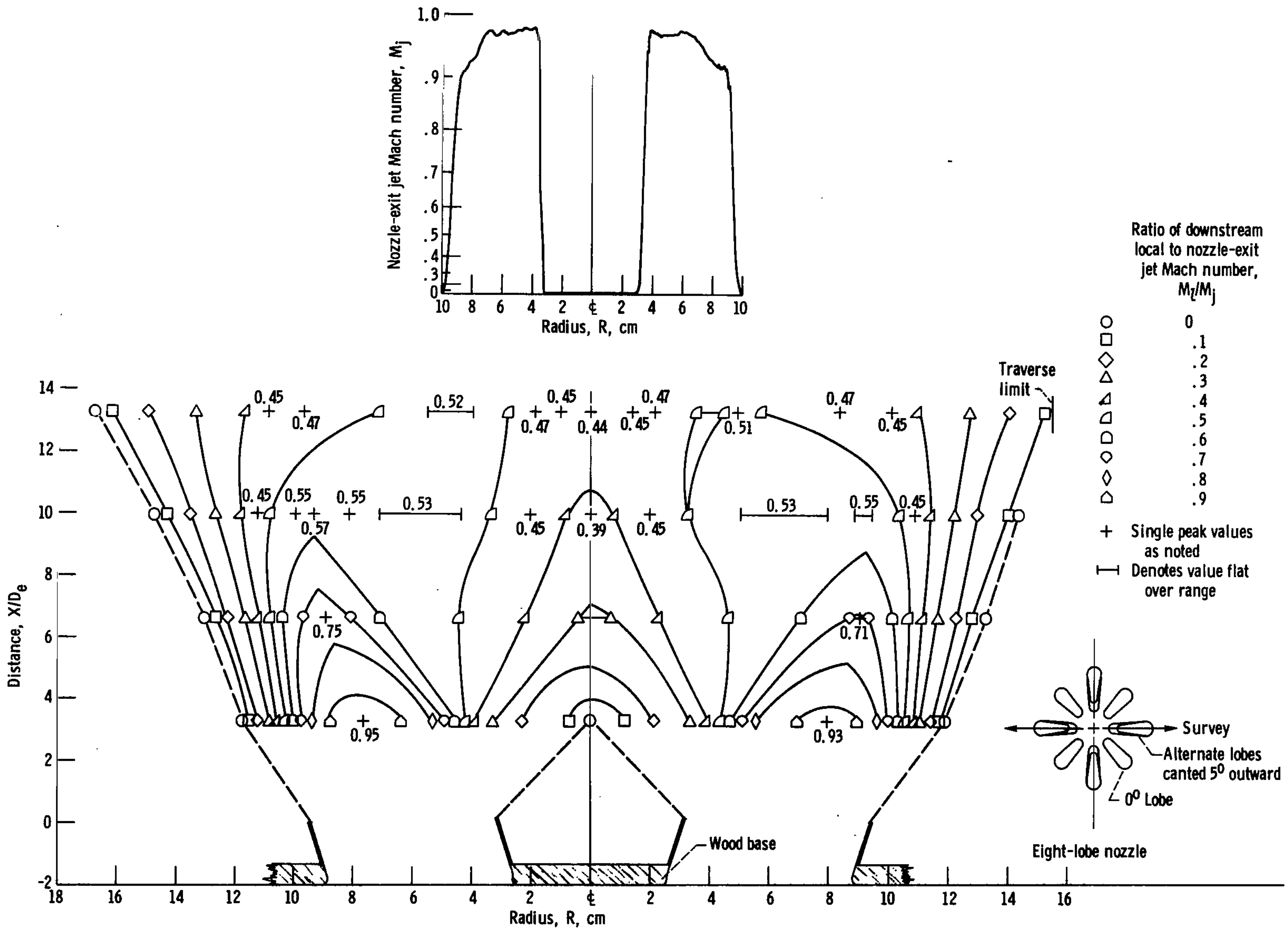

(b) Survey across 5° lobes; nozzle-exit jet Mach number, M_j, 0.98.

Figure 195. - Concluded.

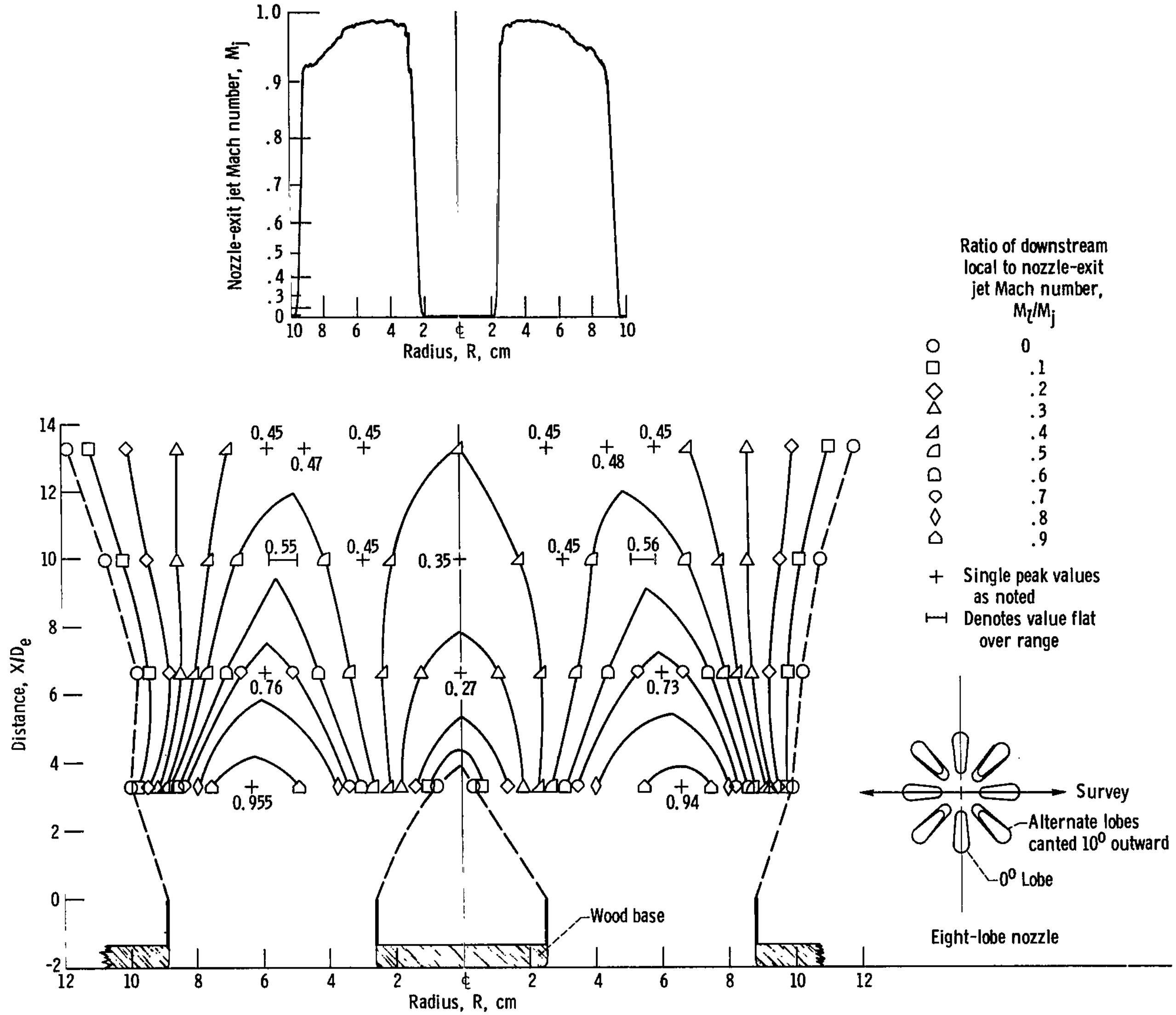

(a) Survey across 0° lobes; nozzle-exit jet Mach number, M_j, 0.99.

Figure 196. - Configuration 101. Equivalent diameter, D_e, 3.81 centimeters.

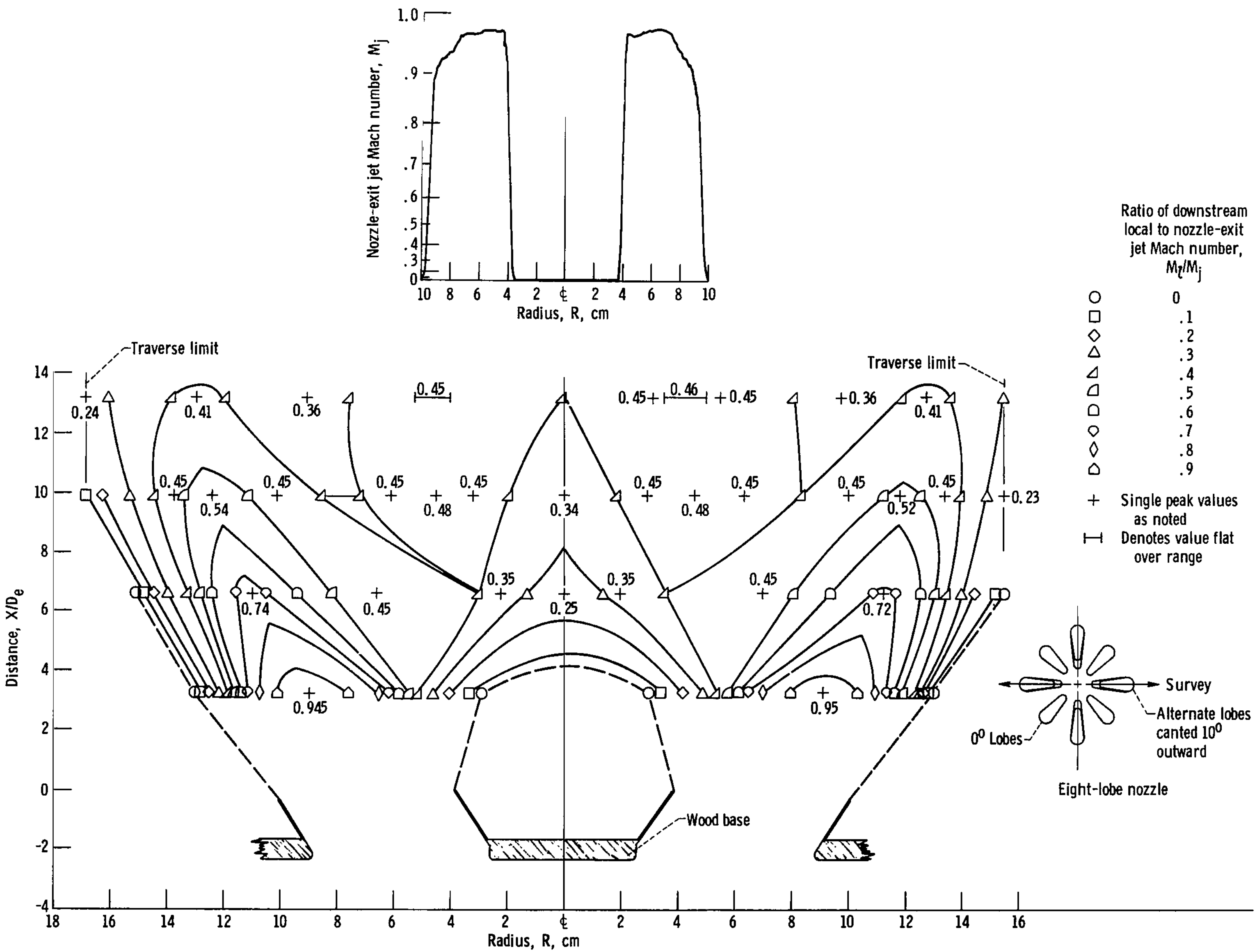

(b) Survey across 10° lobes; nozzle-exit jet Mach number, M_j, 0.97.

Figure 196. - Concluded.

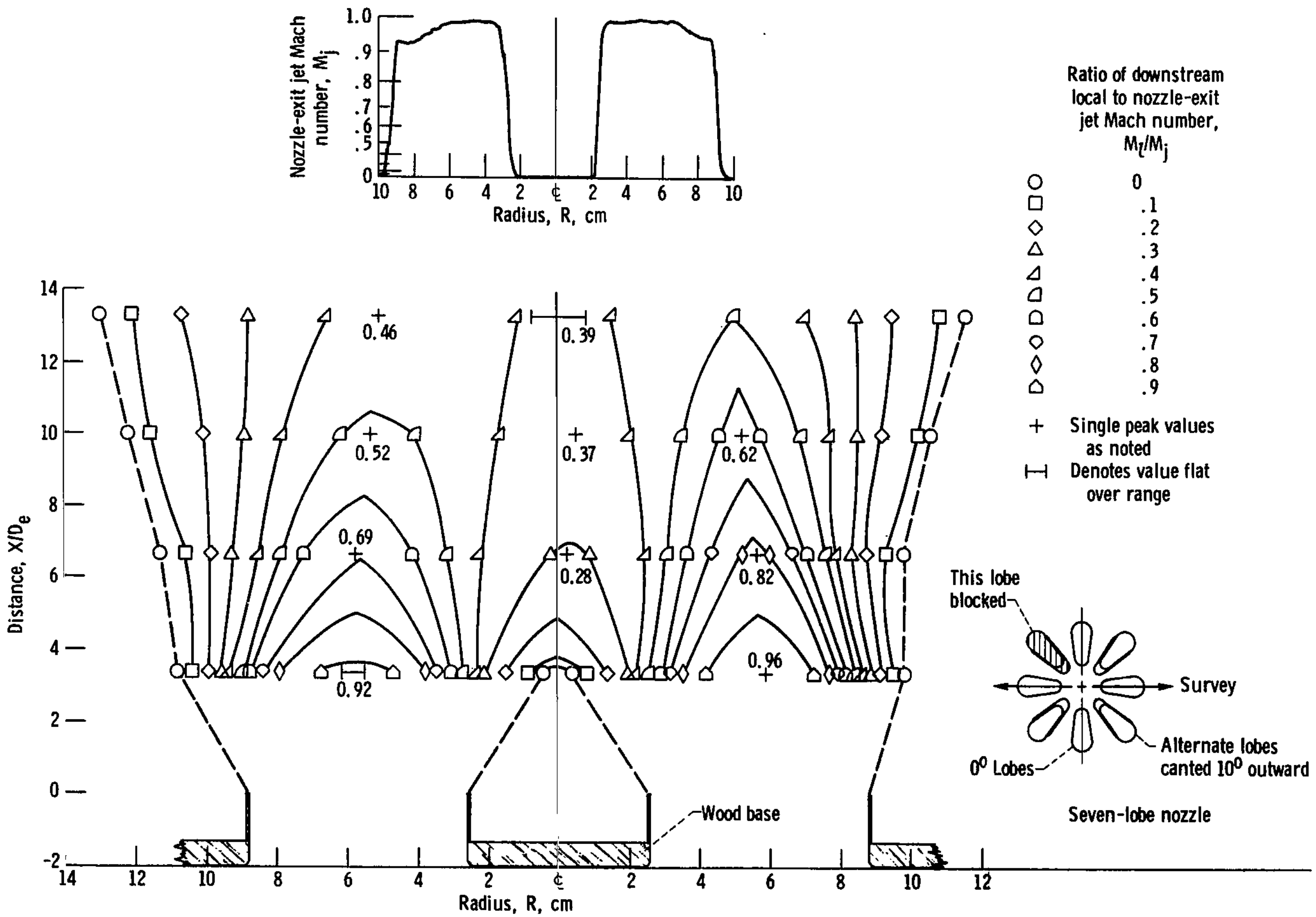

(a) Survey across 0° lobes.

Figure 197. - Configuration 102. Nozzle-exit jet Mach number, M_j, 0.98; equivalent diameter, D_e, 3.81 centimeters.

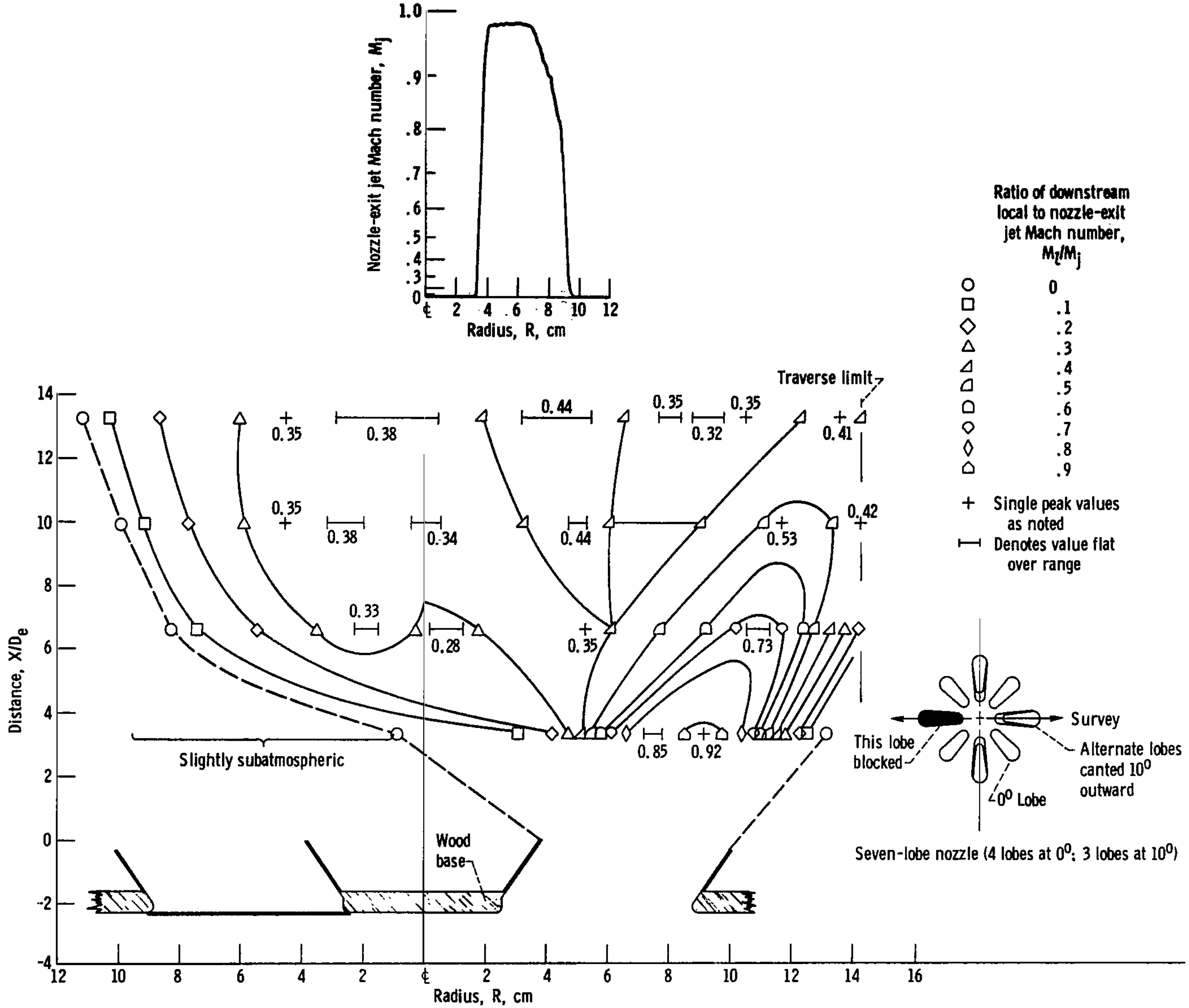

(b) Survey across 10° lobes (one blocked).

Figure 197. - Concluded.

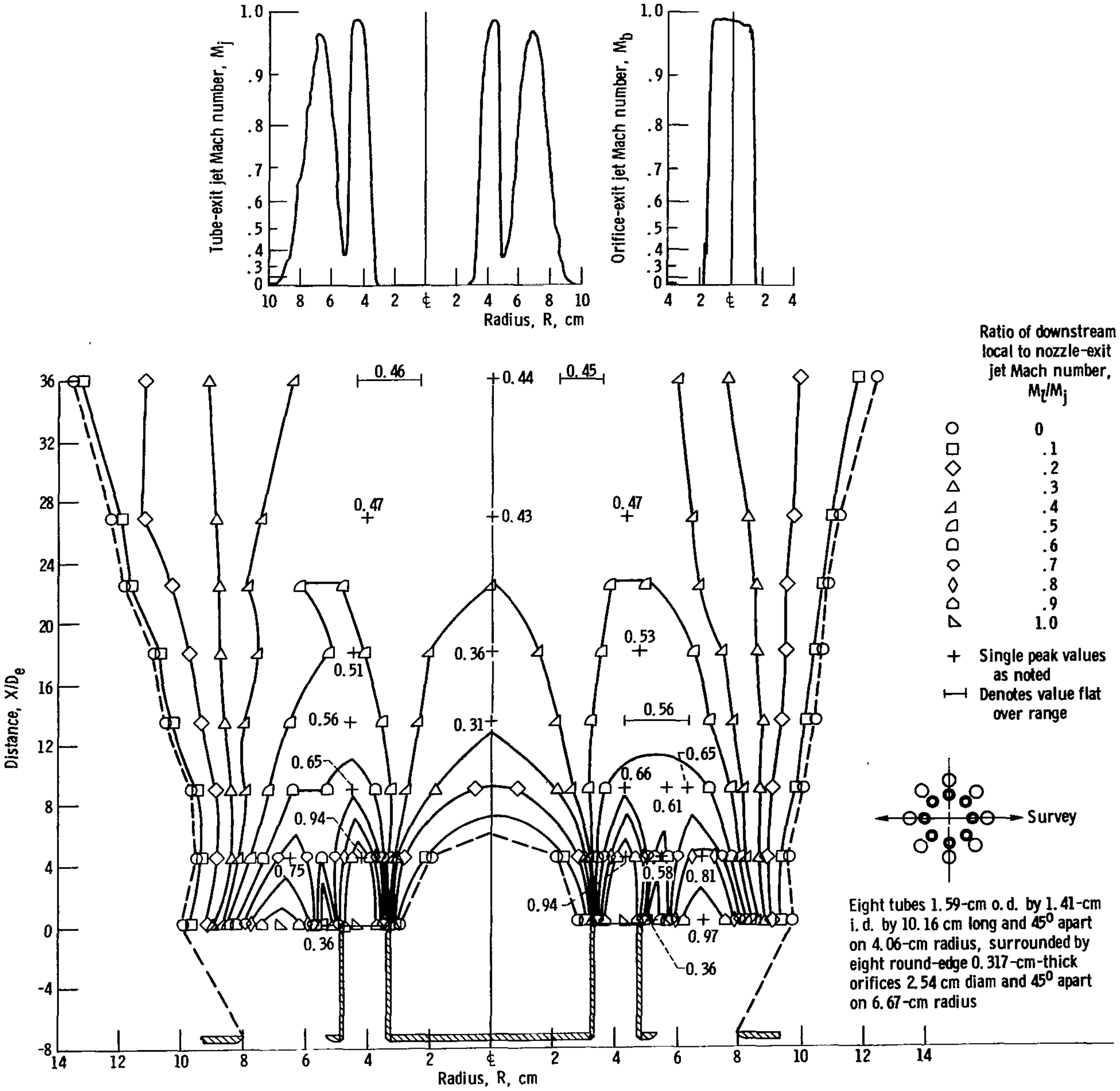

Figure 198. - Configuration 103. Nozzle-exit jet Mach number, M_j, 0.99; equivalent diameter, D_e, 1.41 centimeters; ratio of bypass (secondary) flow exit Mach number to core (primary) flow exit Mach number, M_b/M_j, 1.0.

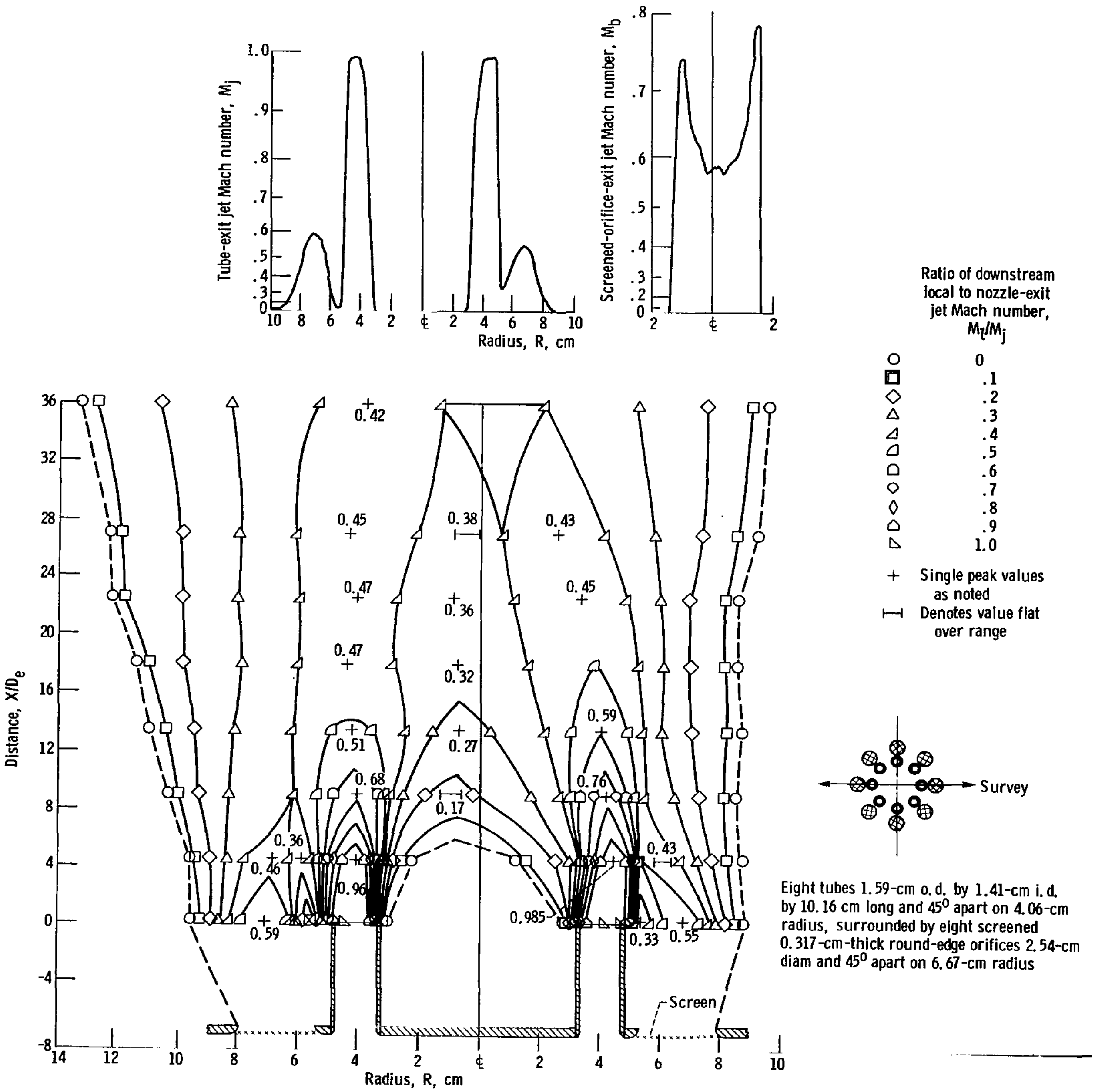

Figure 199. - Configuration 104. Nozzle-exit jet Mach number, M_j, 0.99; equivalent diameter, D_e, 1.41 centimeters; ratio of bypass (secondary) flow exit Mach number to core (primary) flow exit Mach number, M_b/M_j, 0.657.

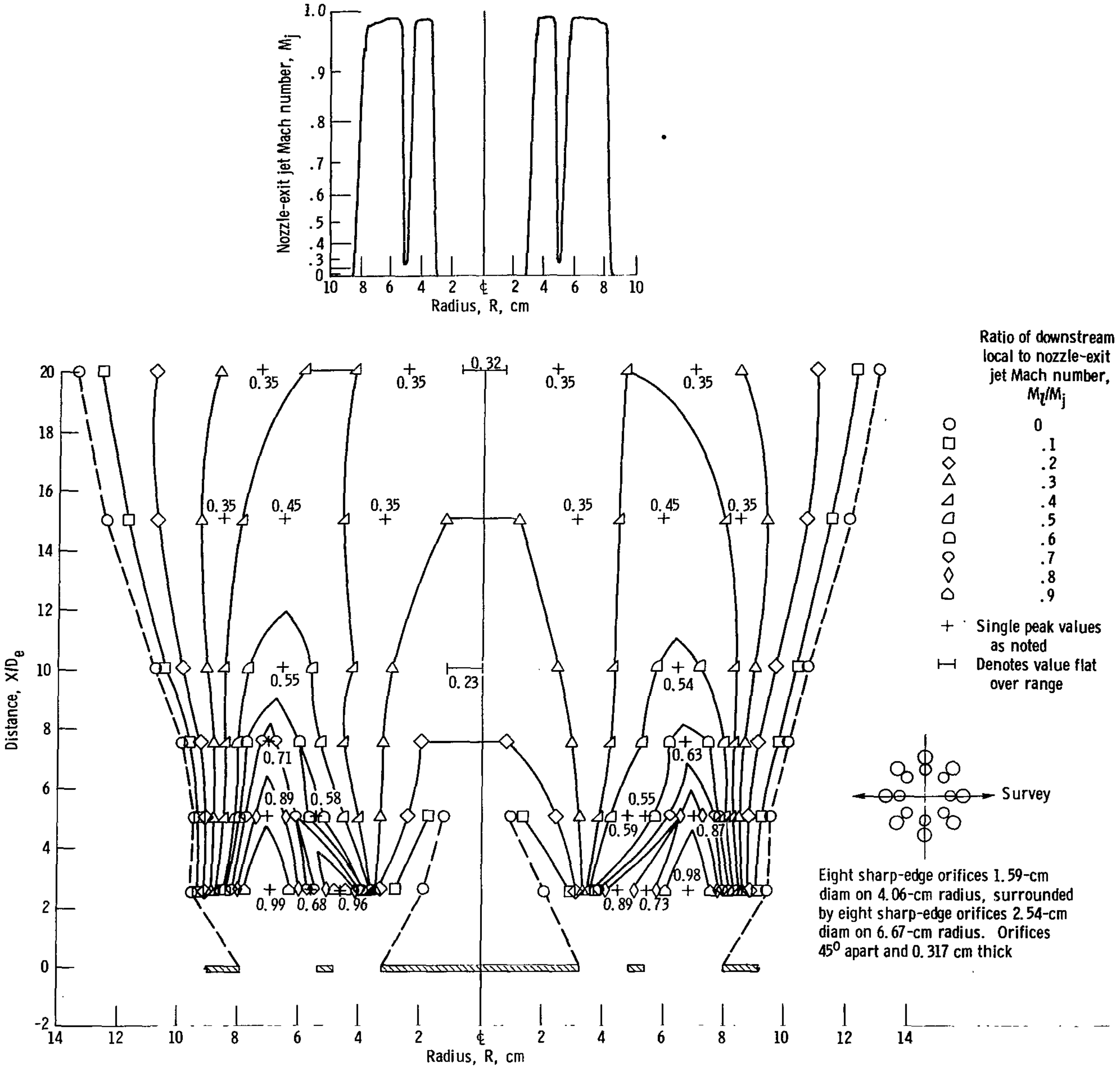

Figure 200. - Configuration 105. Nozzle-exit jet Mach number, M_j, 0.99; equivalent diameter, D_e, 2.54 centimeters.

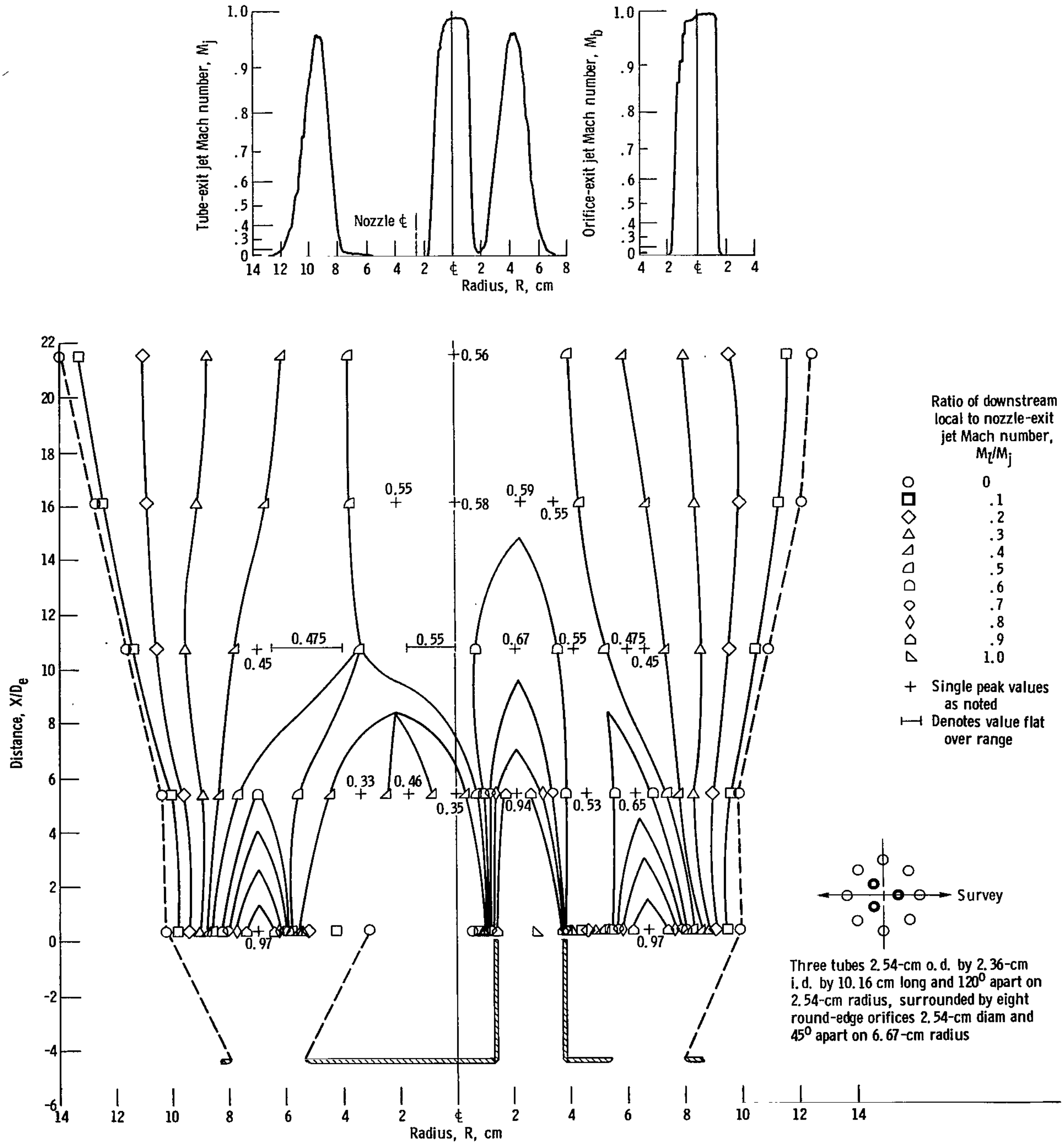

Figure 201. - Configuration 106. Nozzle-exit jet Mach number, M_j, 0.987; equivalent diameter, D_e, 2.36 centimeters; ratio of bypass (secondary) flow exit Mach number to core (primary) flow exit Mach number, M_b/M_j, 1.0. (Survey between two tubes left of centerline.)

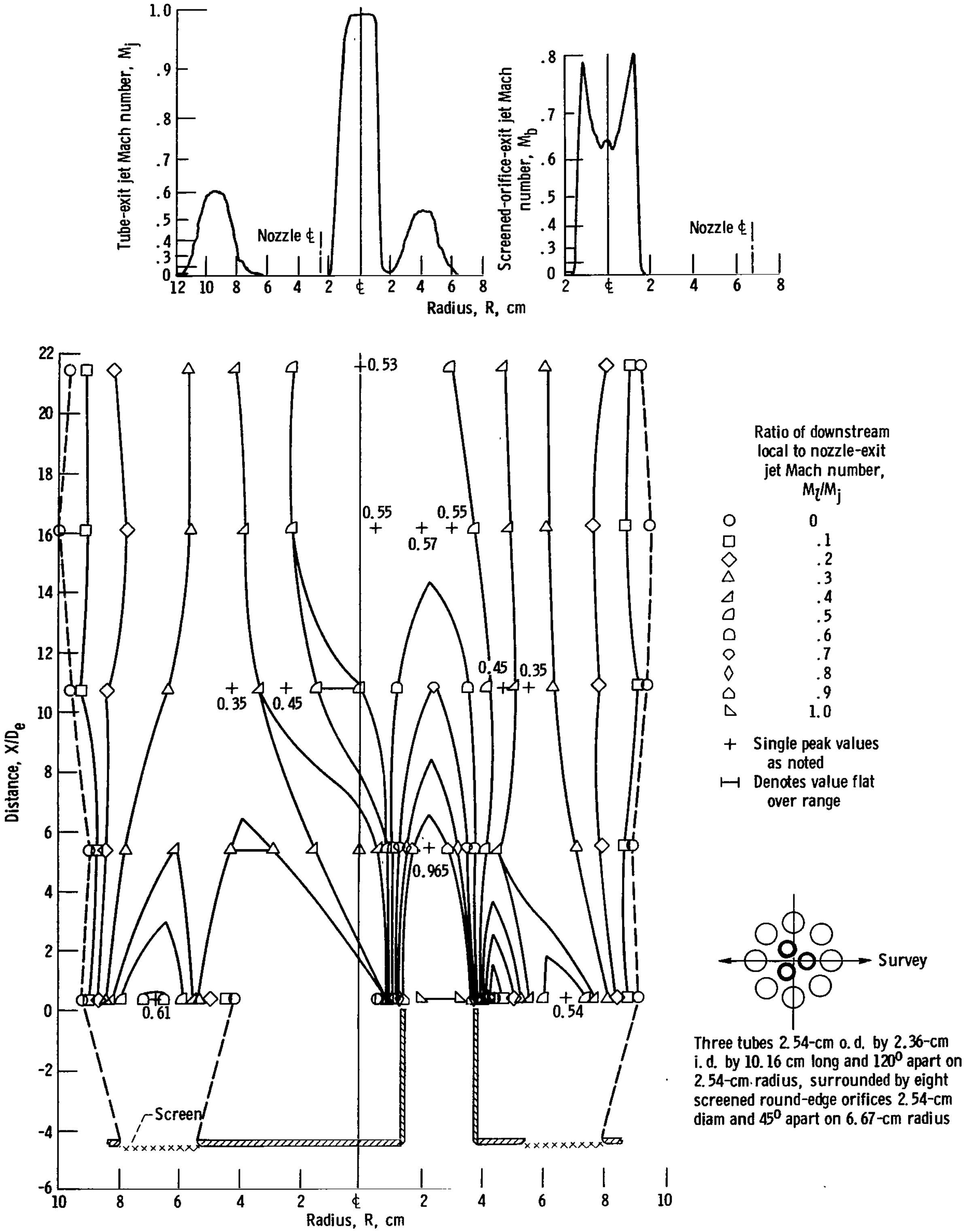

Figure 202. - Configuration 107. Nozzle-exit jet Mach number, M_j, 0.989; equivalent diameter, D_e, 2.36 centimeters; ratio of bypass (secondary) flow exit Mach number to core (primary) flow exit Mach number, M_b/M_j, 0.719. (Survey between two tubes left of centerline.)

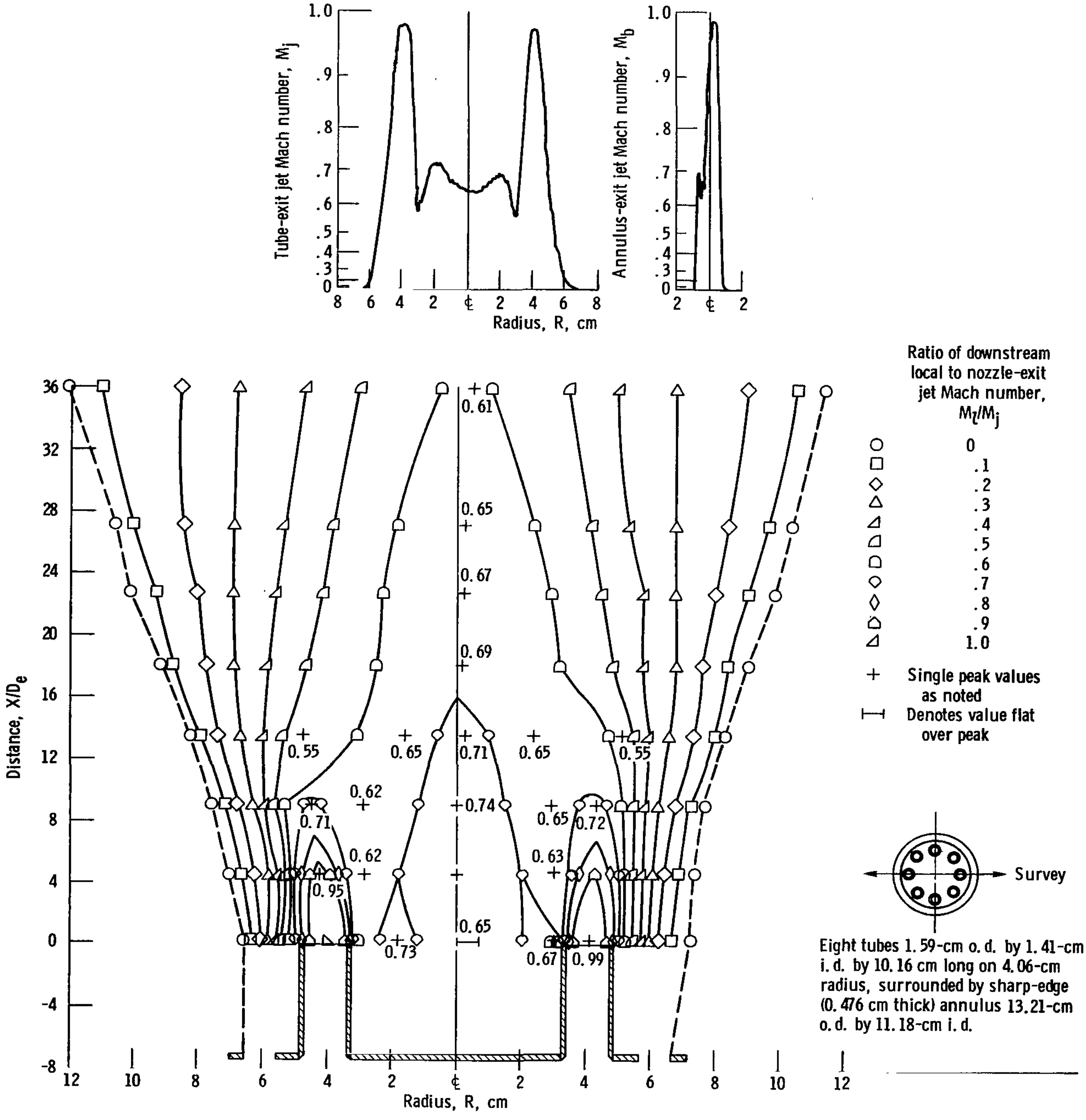

Figure 203. - Configuration 108. Nozzle-exit jet Mach number, M_j, 0.98; equivalent diameter, D_e, 1.41 centimeters; ratio of bypass (secondary) flow exit Mach number to core (primary) flow exit Mach number, M_b/M_j, 1.0.

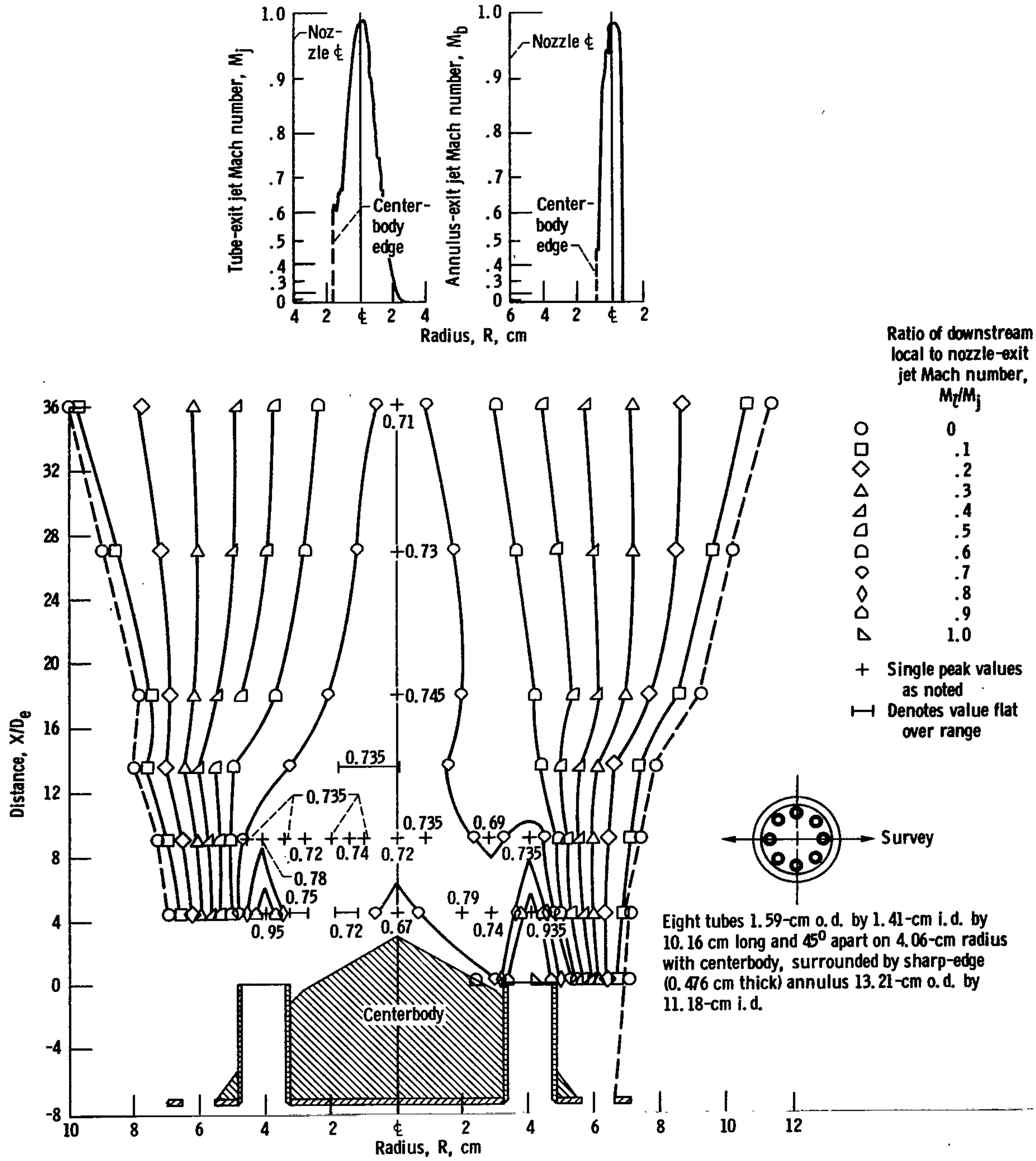

Figure 204. - Configuration 109. Nozzle-exit jet Mach number, M_j, 0.99; equivalent diameter, D_e, 1.41 centimeters; ratio of bypass (secondary) flow exit Mach number to core (primary) flow exit Mach number, M_b/M_j, 1.0.

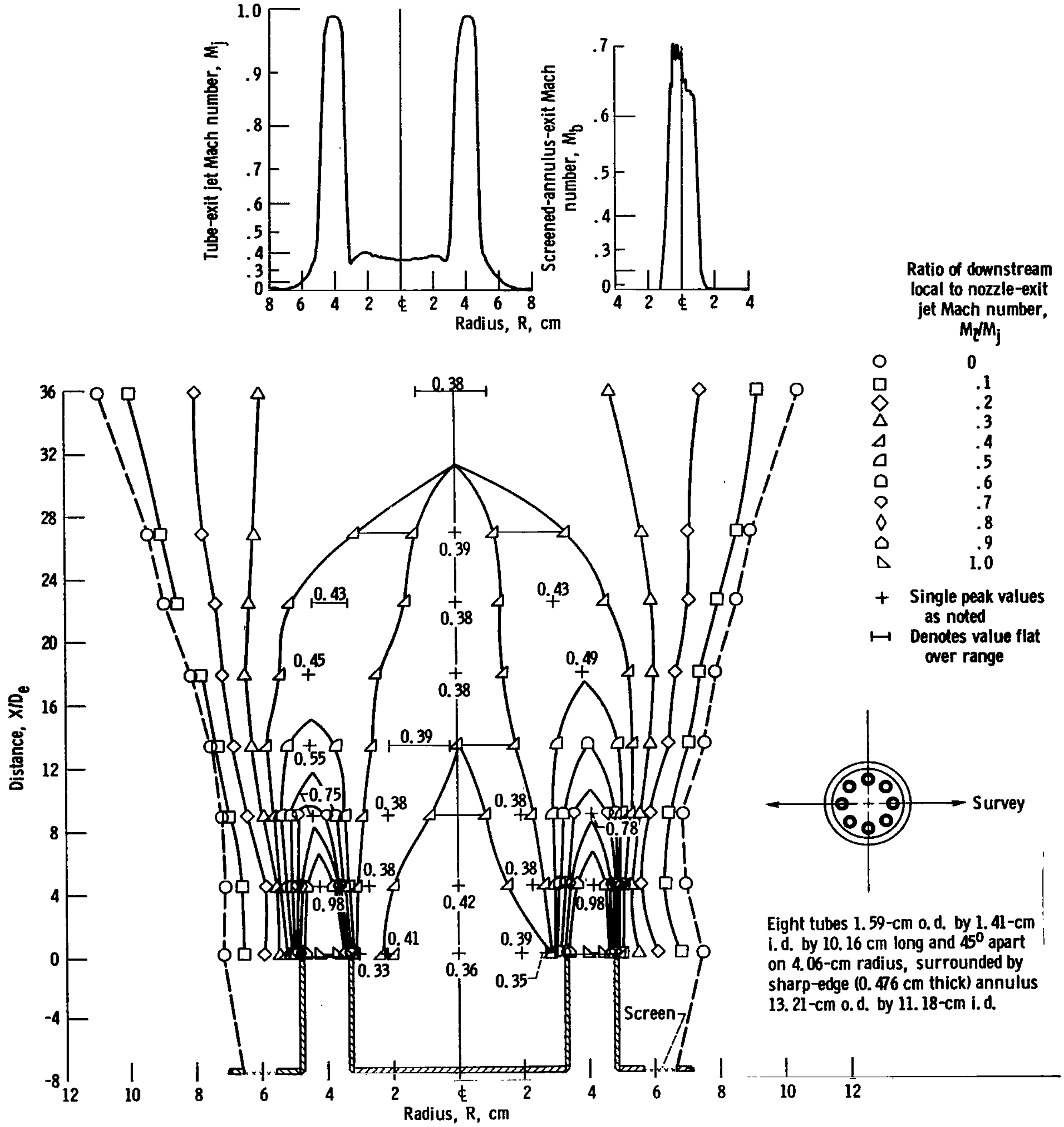

Figure 205. - Configuration 110. Nozzle-exit jet Mach number, M_j, 0.985; equivalent diameter, D_e, 1.41 centimeters; ratio of bypass (secondary) flow exit Mach number to core (primary) flow exit Mach number, M_b/M_j, 0.67.

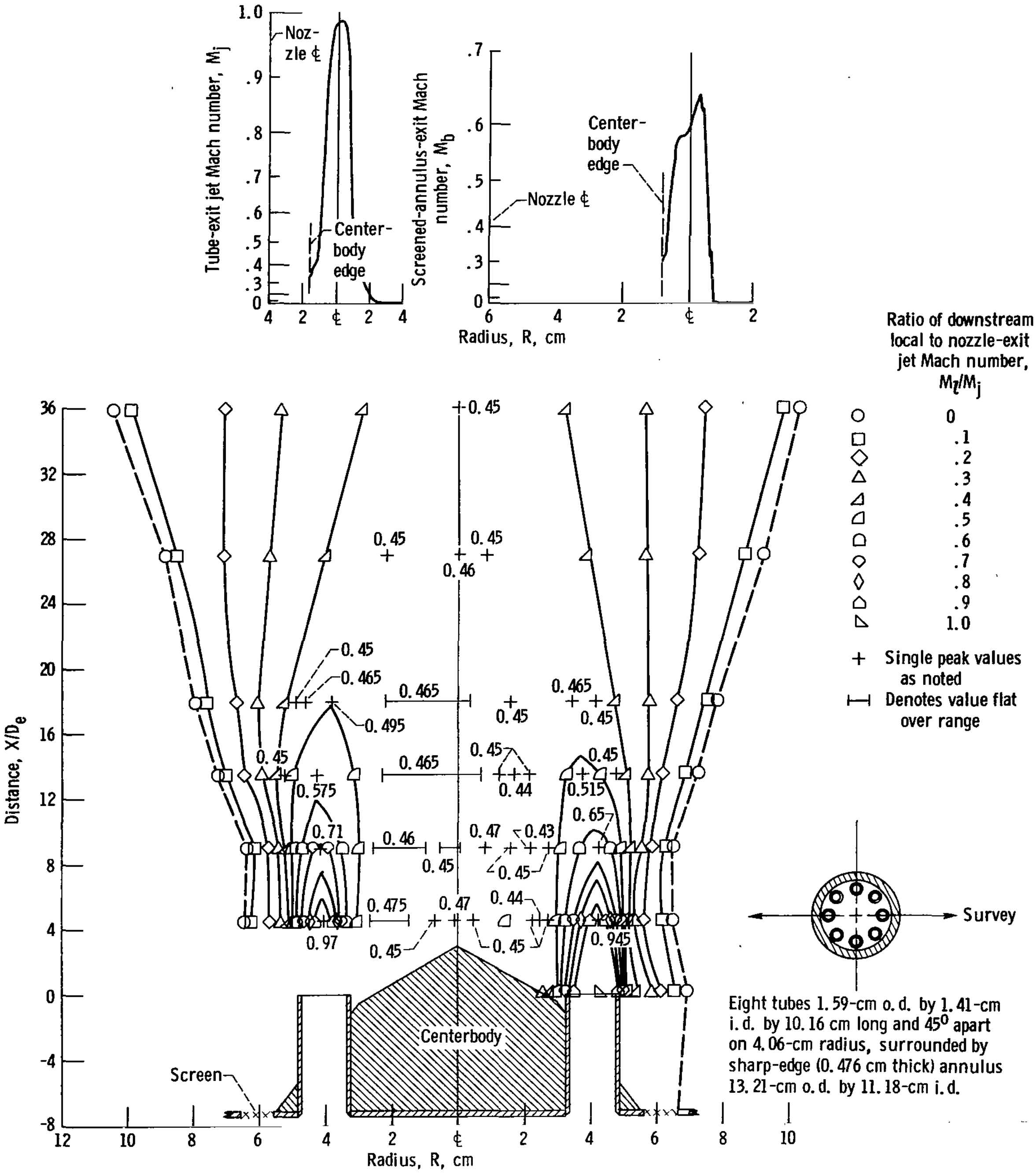

Figure 206. - Configuration 111. Nozzle-exit jet Mach number, M_j, 0.989; equivalent diameter, D_e, 1.41 centimeters; ratio of bypass (secondary) flow exit Mach number to core (primary) flow exit Mach number, M_b/M_j, 0.607.

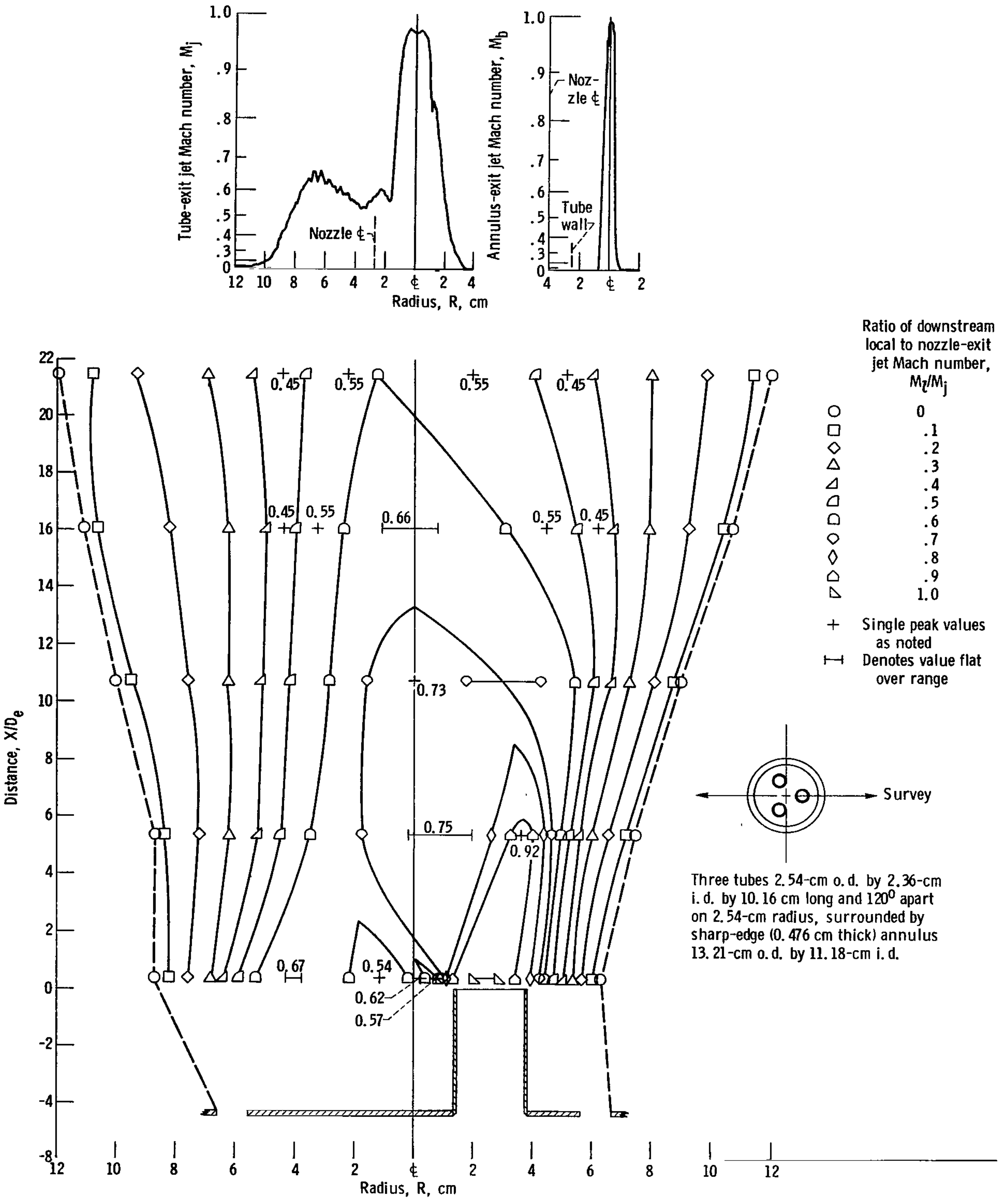

Figure 207. - Configuration 112. Nozzle-exit jet Mach number, M_j, 0.975; equivalent diameter, D_e, 2.36 centimeters; ratio of bypass (secondary) flow exit Mach number to core (primary) flow exit Mach number, M_b/M_j, 1.0. (Survey between two tubes left of centerline.)

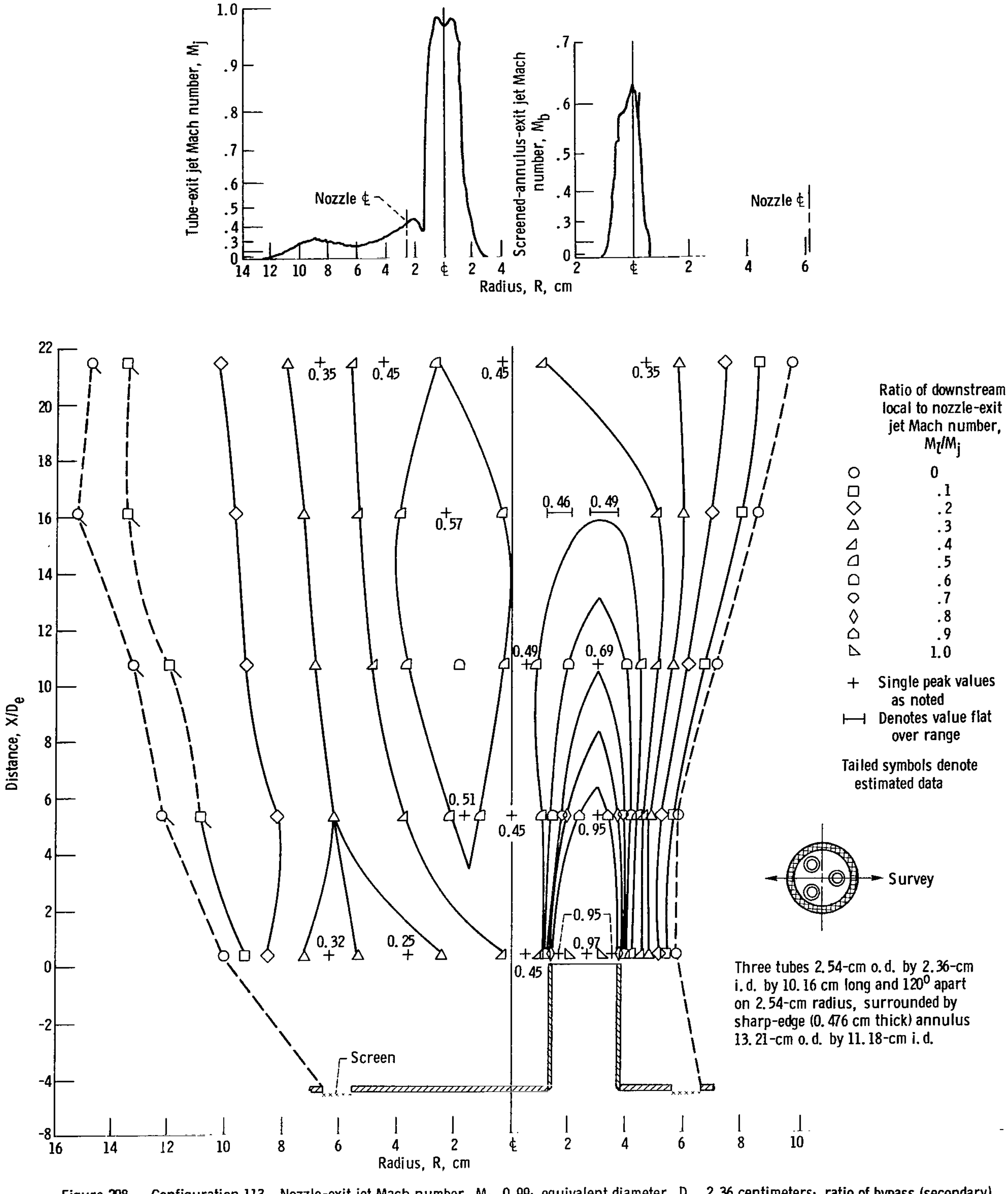

Figure 208. - Configuration 113. Nozzle-exit jet Mach number, M_j, 0.99; equivalent diameter, D_e, 2.36 centimeters; ratio of bypass (secondary) flow exit Mach number to core (primary) flow exit Mach number, M_b/M_j, 0.61.

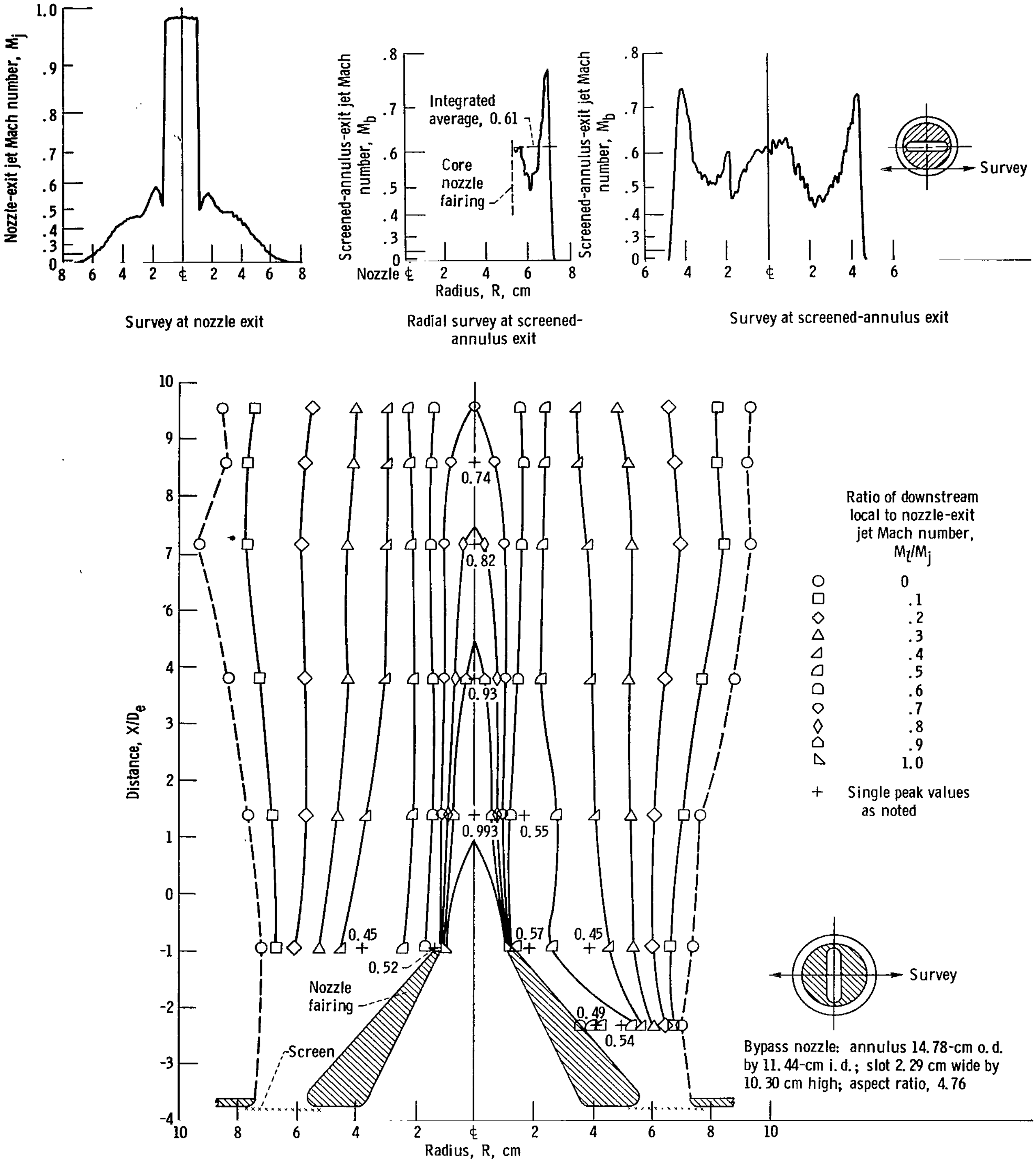

Figure 209. - Configuration 114 (core slot nozzle vertical). Nozzle-exit jet Mach number, M_j, 0.988; equivalent diameter, D_e, 5.32 centimeters; ratio of bypass (secondary) flow exit Mach number to core (primary) flow exit Mach number, M_b/M_j, 0.618.

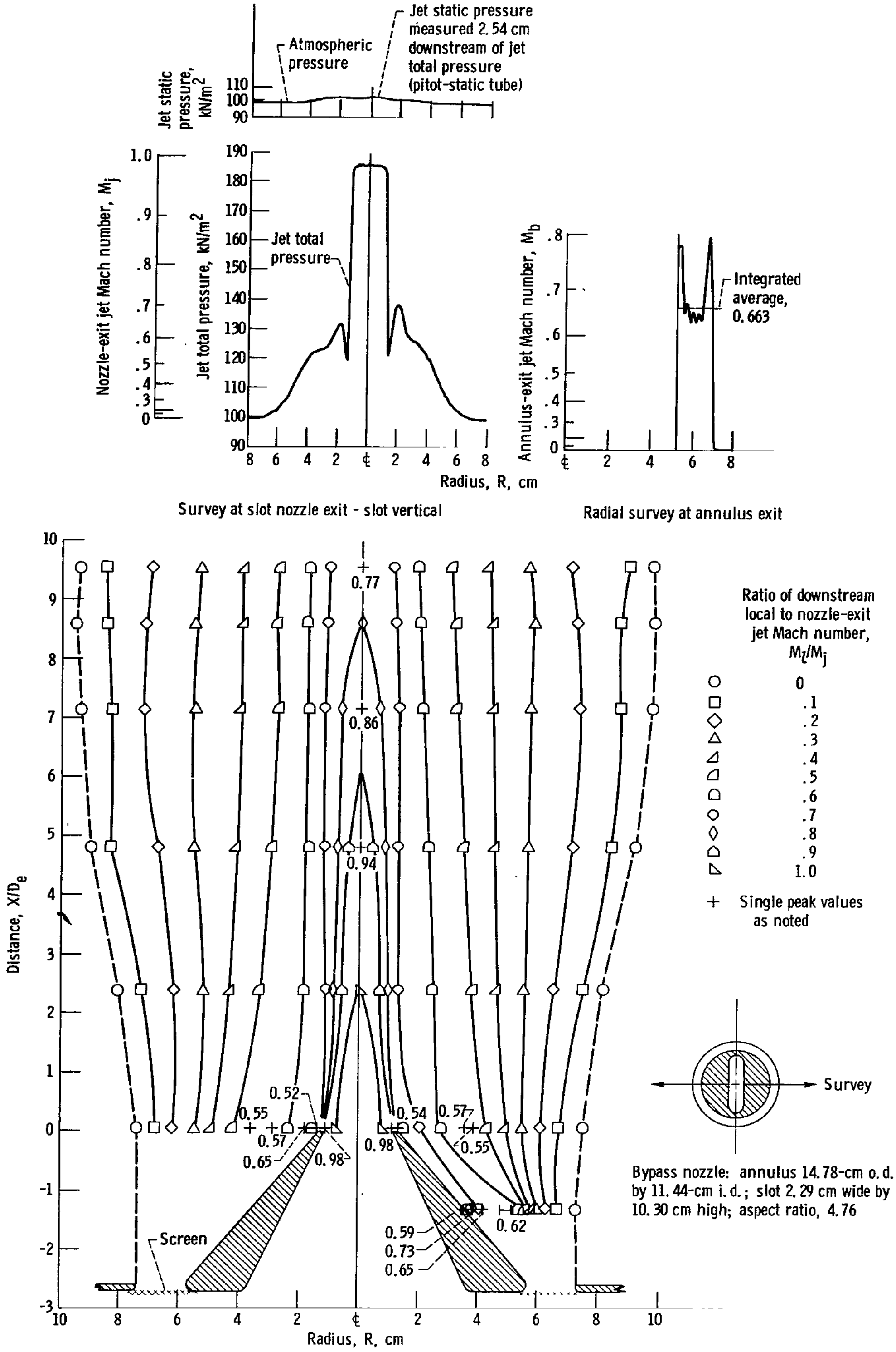

(a) Core slot nozzle vertical.

Figure 210. - Configuration 115. Nozzle-exit jet Mach number, M_j, 0.984; equivalent diameter, D_e, 5.32 centimeters; ratio of bypass (secondary) flow exit Mach number to core (primary) flow exit Mach number, M_b/M_j, 0.674.

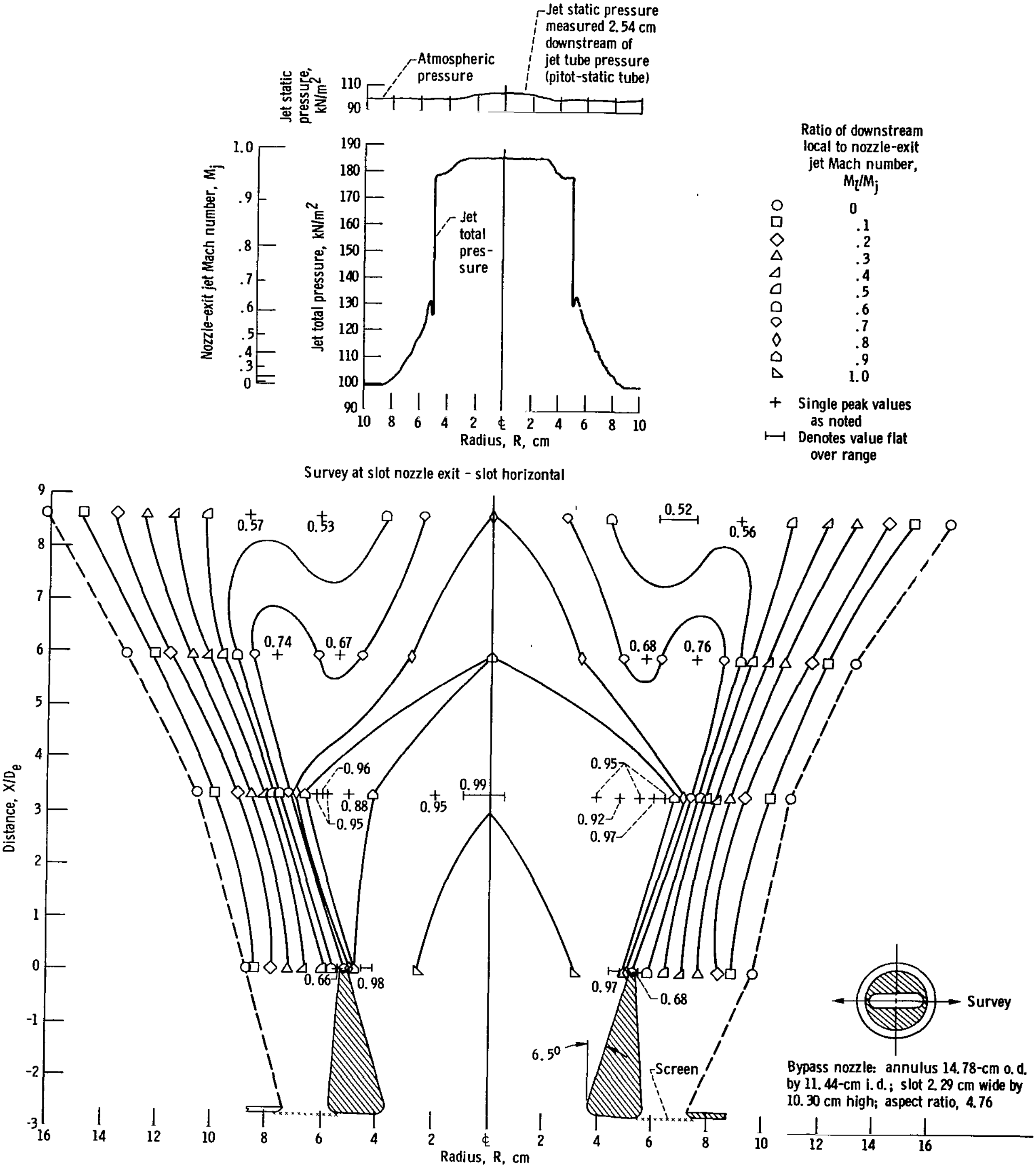

(b) Core slot nozzle horizontal.

Figure 210. - Concluded.

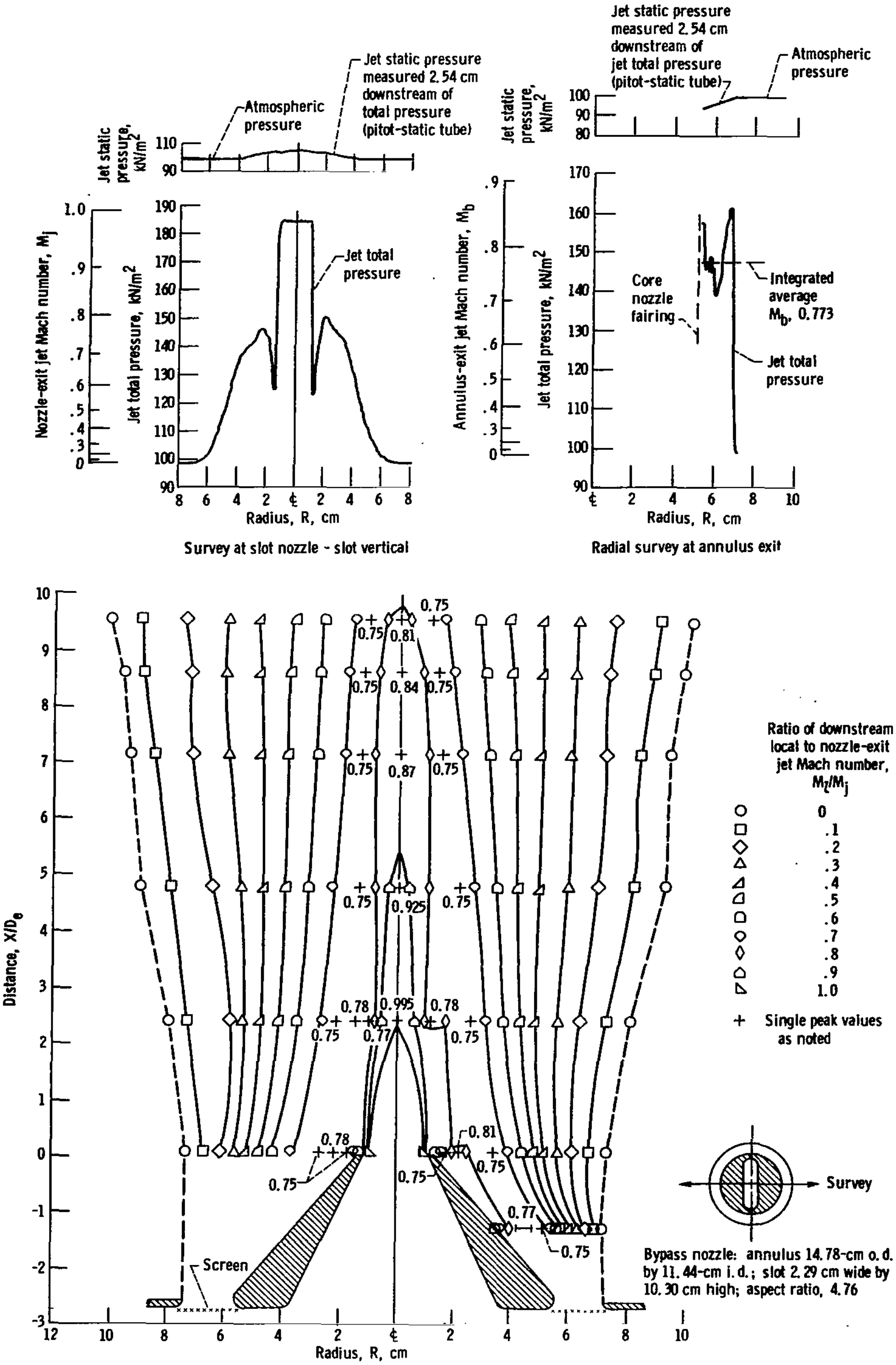

(a) Core slot nozzle vertical.

Figure 211. - Configuration 116. Nozzle-exit jet Mach number, M_j, 0.985; equivalent diameter, D_e, 5.32 centimeters; ratio of bypass (secondary) flow exit Mach number to core (primary) flow exit Mach number, M_b/M_j, 0.785.

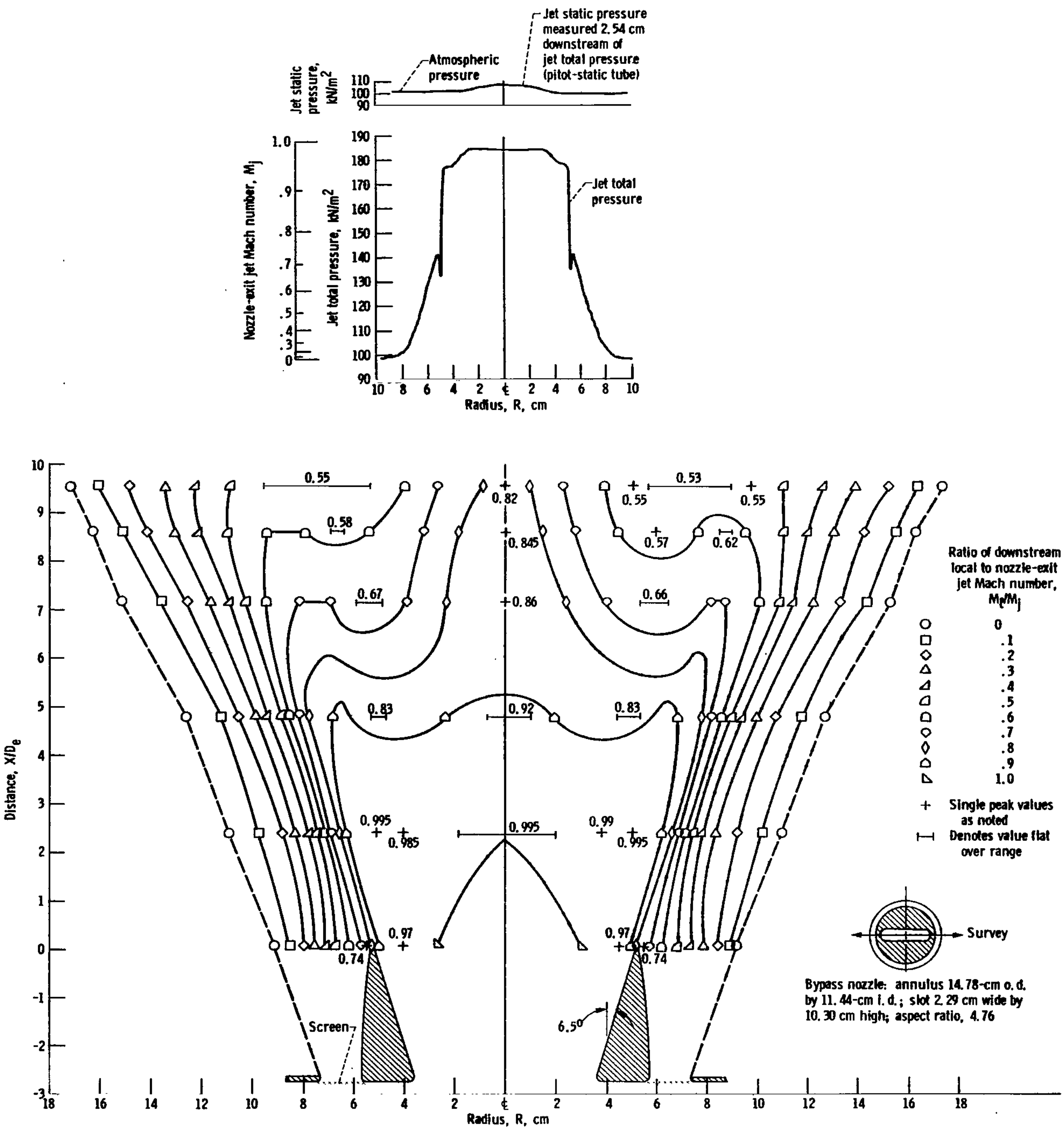

(b) Core slot nozzle horizontal.

Figure 211. - Concluded.

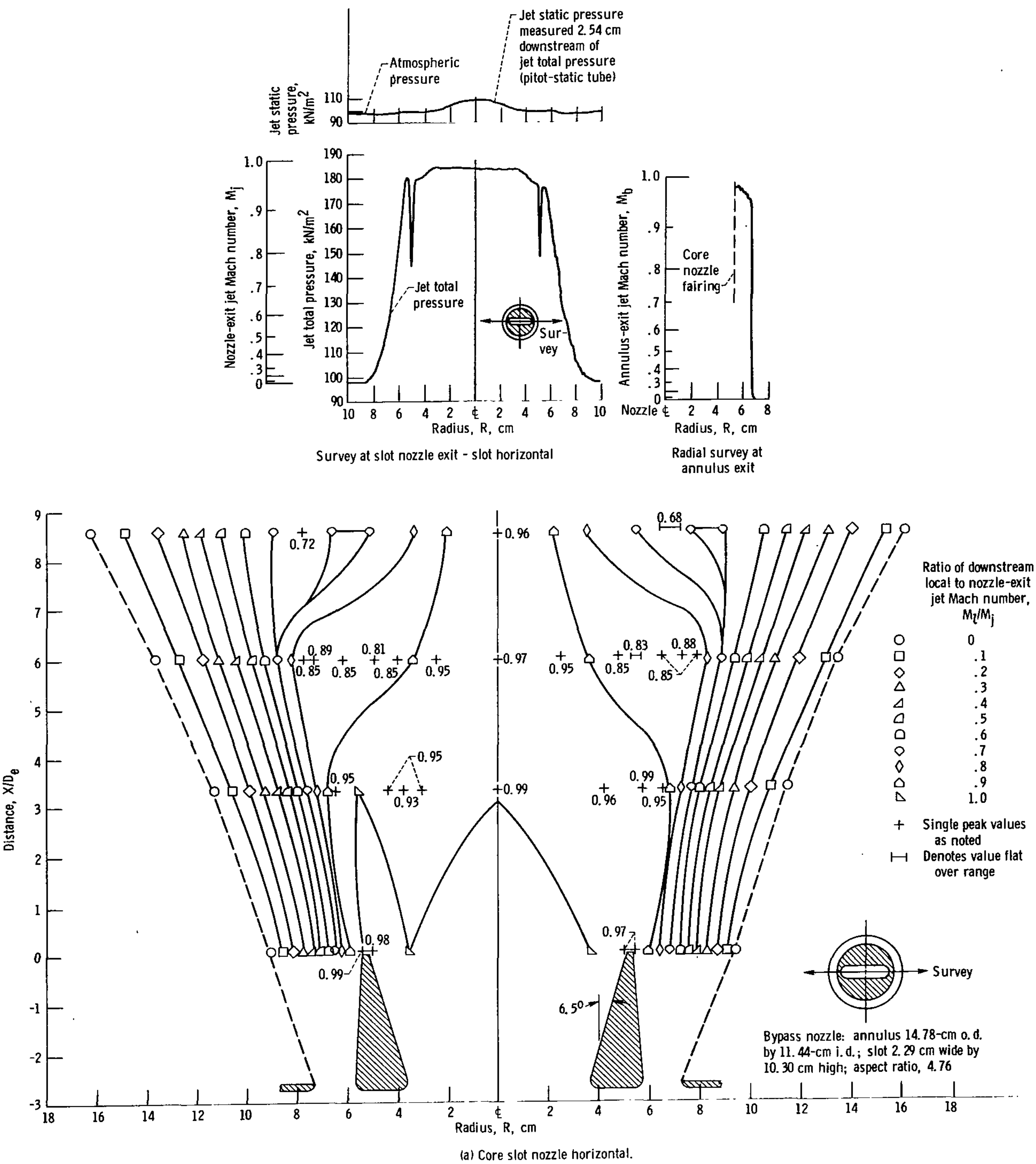

(a) Core slot nozzle horizontal.

Figure 212. - Configuration 117. Nozzle-exit jet Mach number, M_j, 0.983; equivalent diameter, D_e, 5.32 centimeters; ratio of bypass (secondary) flow exit Mach number to core (primary) flow exit Mach number, M_b/M_j, 0.989.

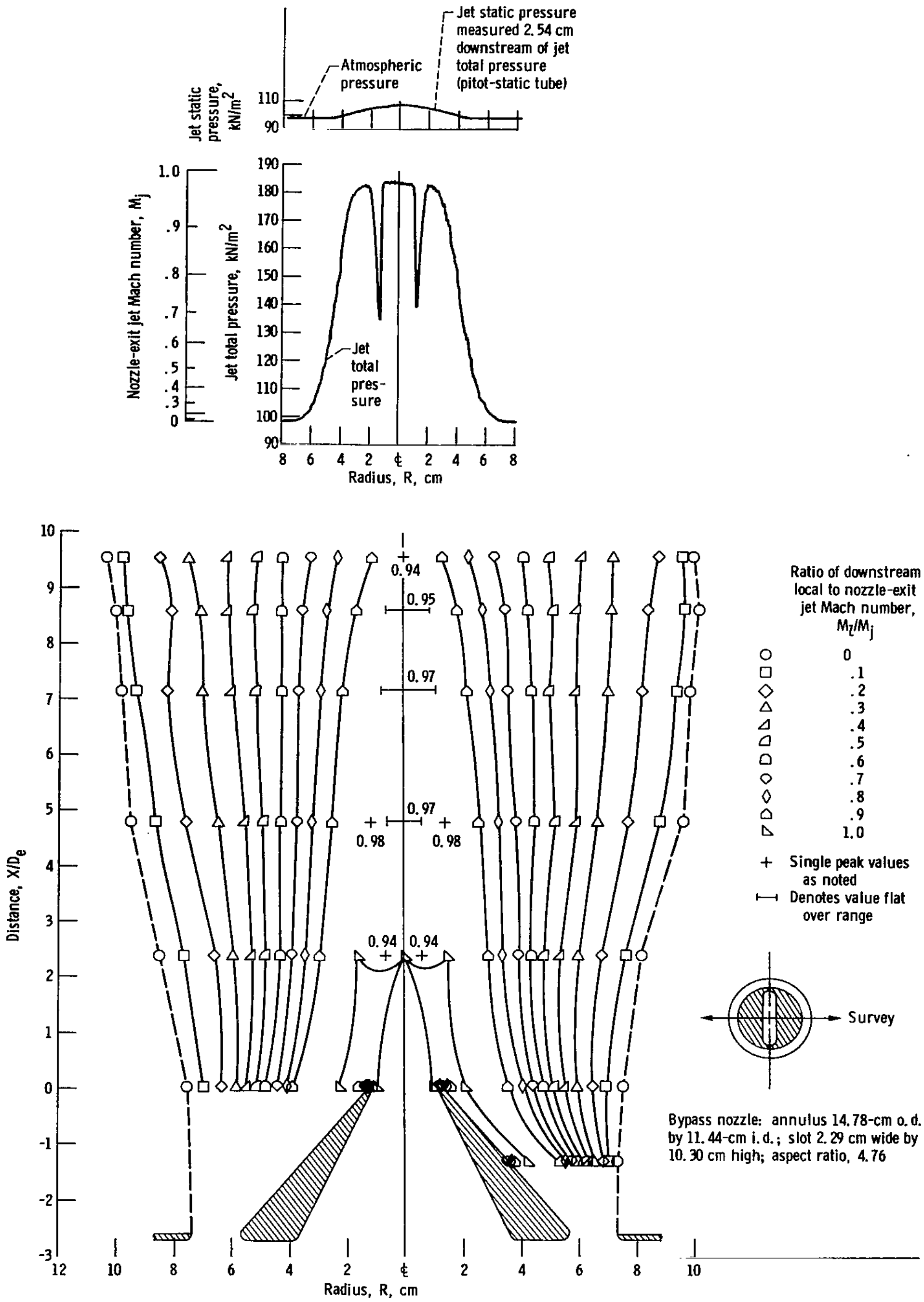

(b) Core slot nozzle vertical.

Figure 212. - Concluded.

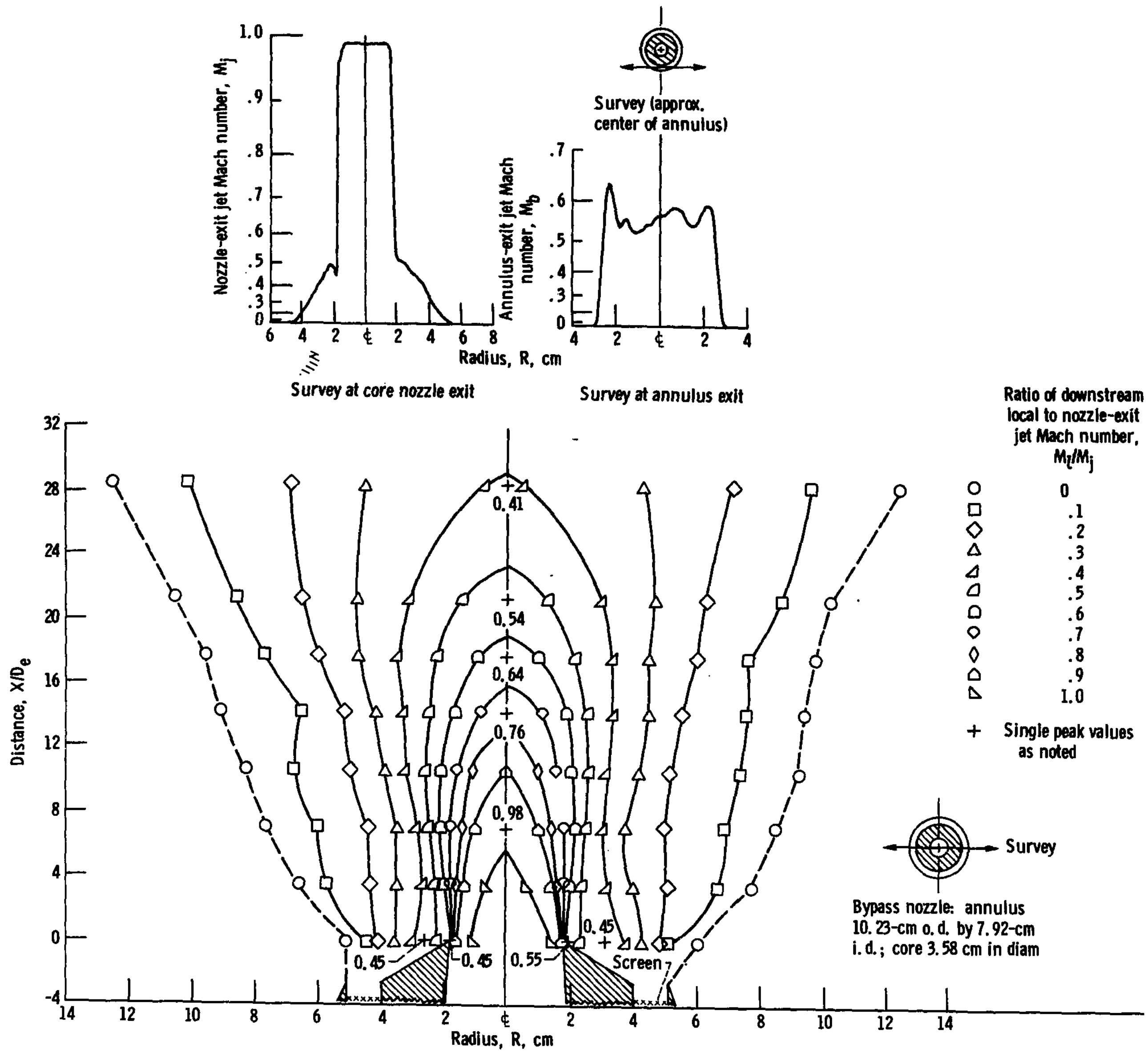

Figure 213. - Configuration 118. Nozzle-exit jet Mach number, M_j, 0.995; equivalent diameter, D_e, 3.58 centimeters; ratio of bypass (secondary) flow exit Mach number to core (primary) flow exit Mach number, M_b/M_j, 0.472.

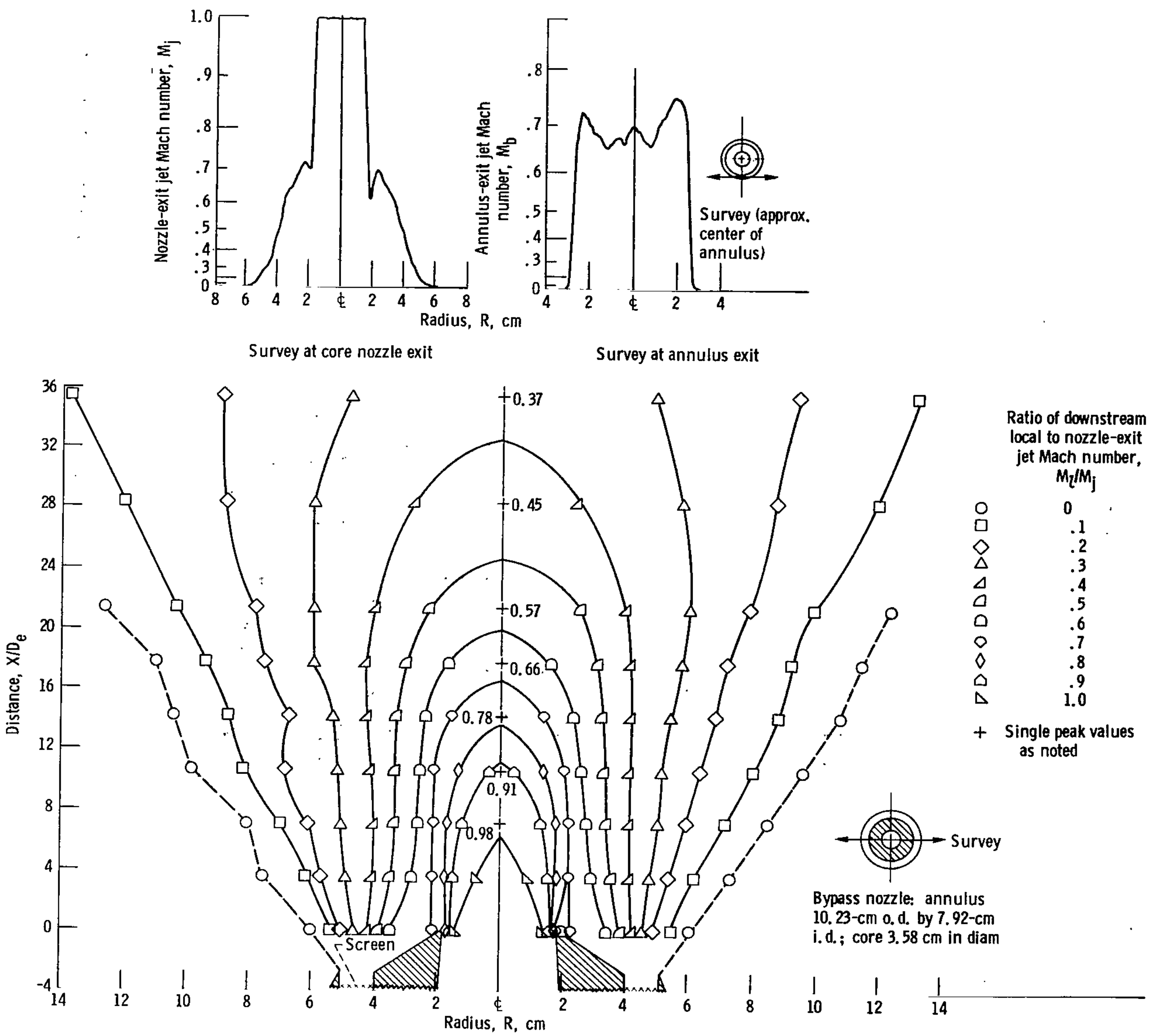

Figure 214. - Configuration 119. Nozzle-exit jet Mach number, M_j, 1.0; equivalent diameter, D_e, 3.58 centimeters; ratio of bypass (secondary) flow exit Mach number to core (primary) flow exit Mach number, M_b/M_j, 0.7.

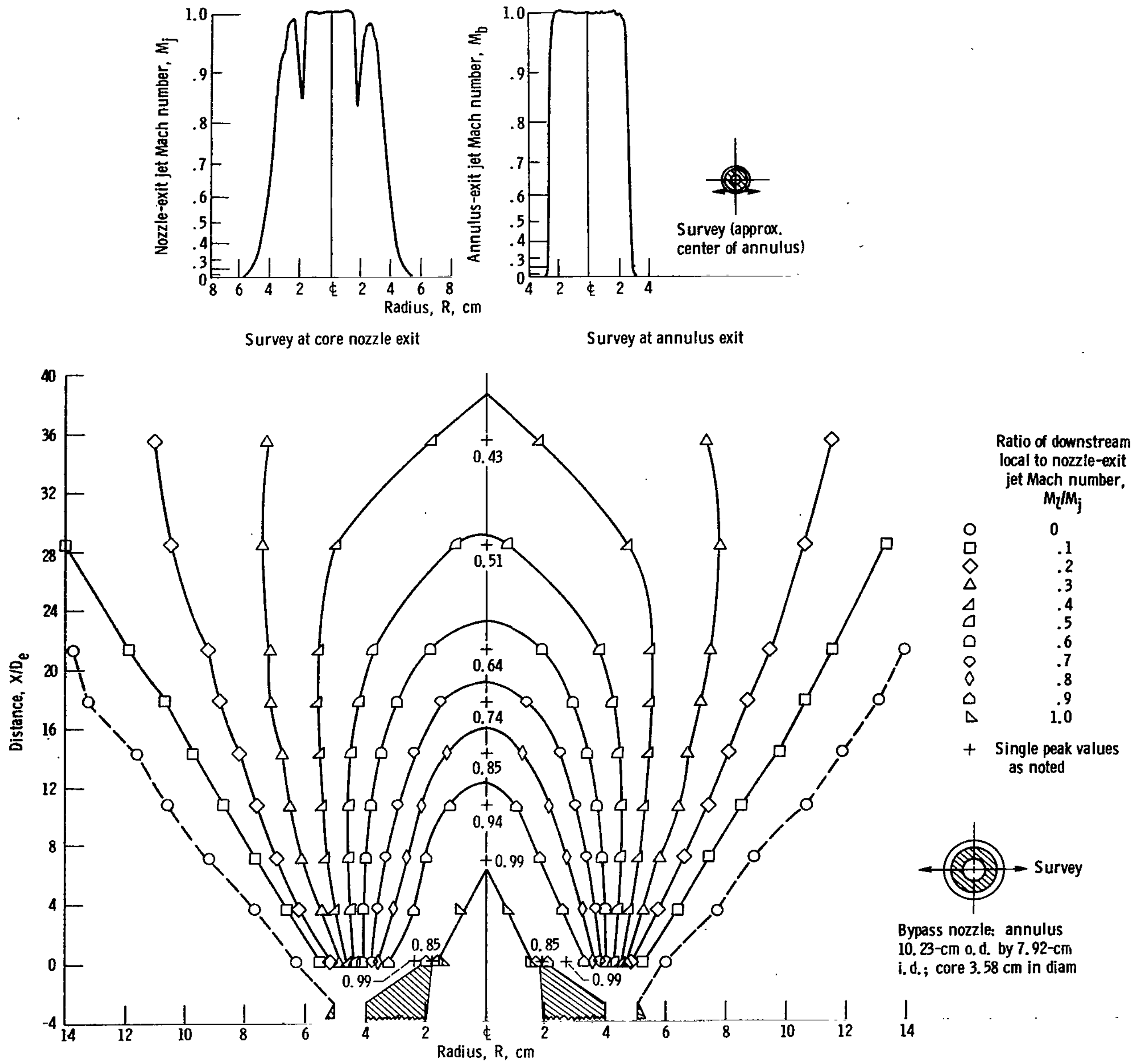

Figure 215. - Configuration 120. Nozzle-exit jet Mach number, M_j, 1.0; equivalent diameter, D_e, 3.58 centimeters; ratio of bypass (secondary) flow exit Mach number to core (primary) flow exit Mach number, M_b/M_j, 0.997.

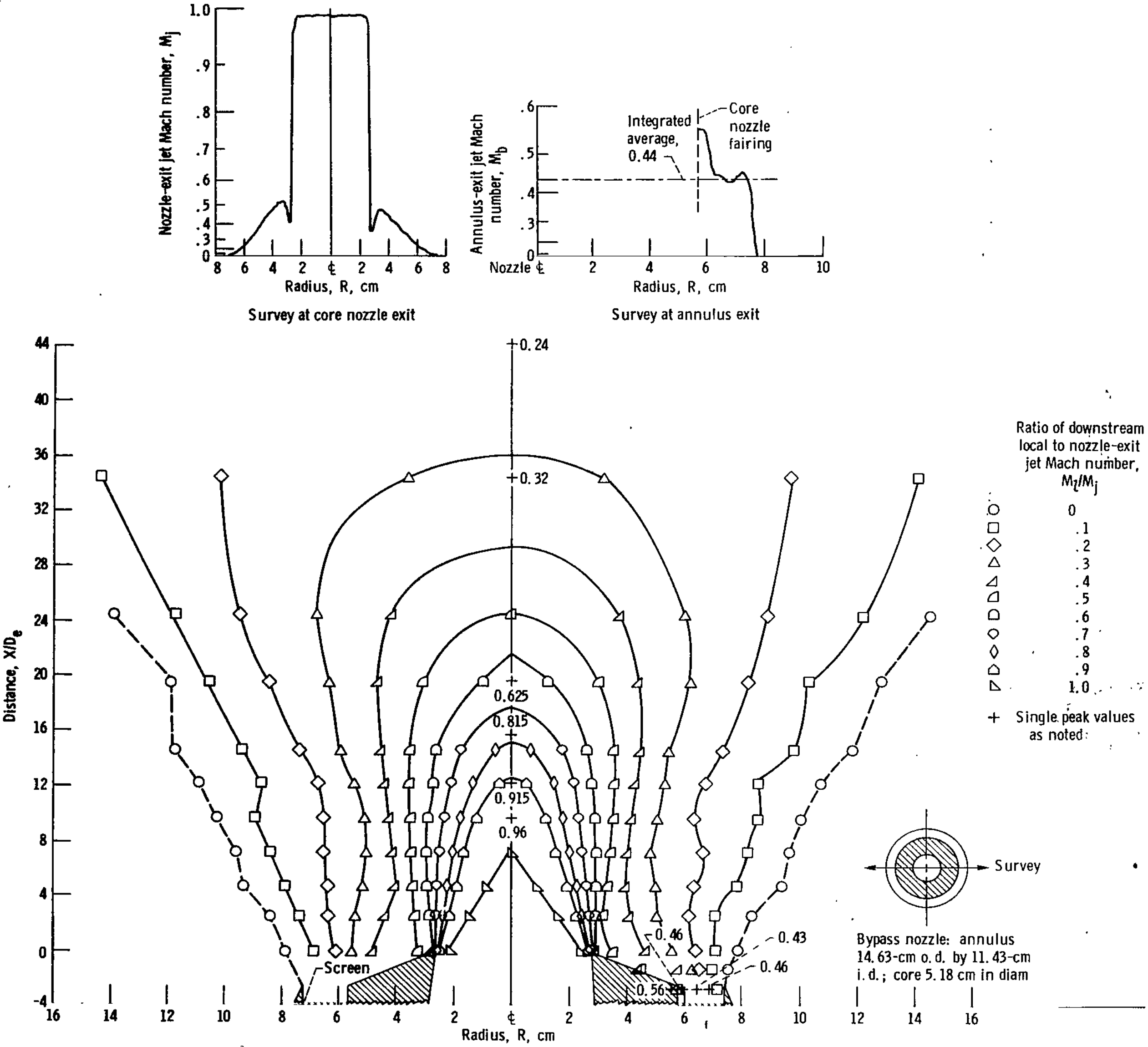

Figure 216. - Configuration 121. Nozzle-exit jet Mach number, M_j, 0.99; equivalent diameter, D_e, 5.18 centimeters; ratio of bypass (secondary) flow exit Mach number to core (primary) flow exit Mach number, M_b/M_j, 0.445.

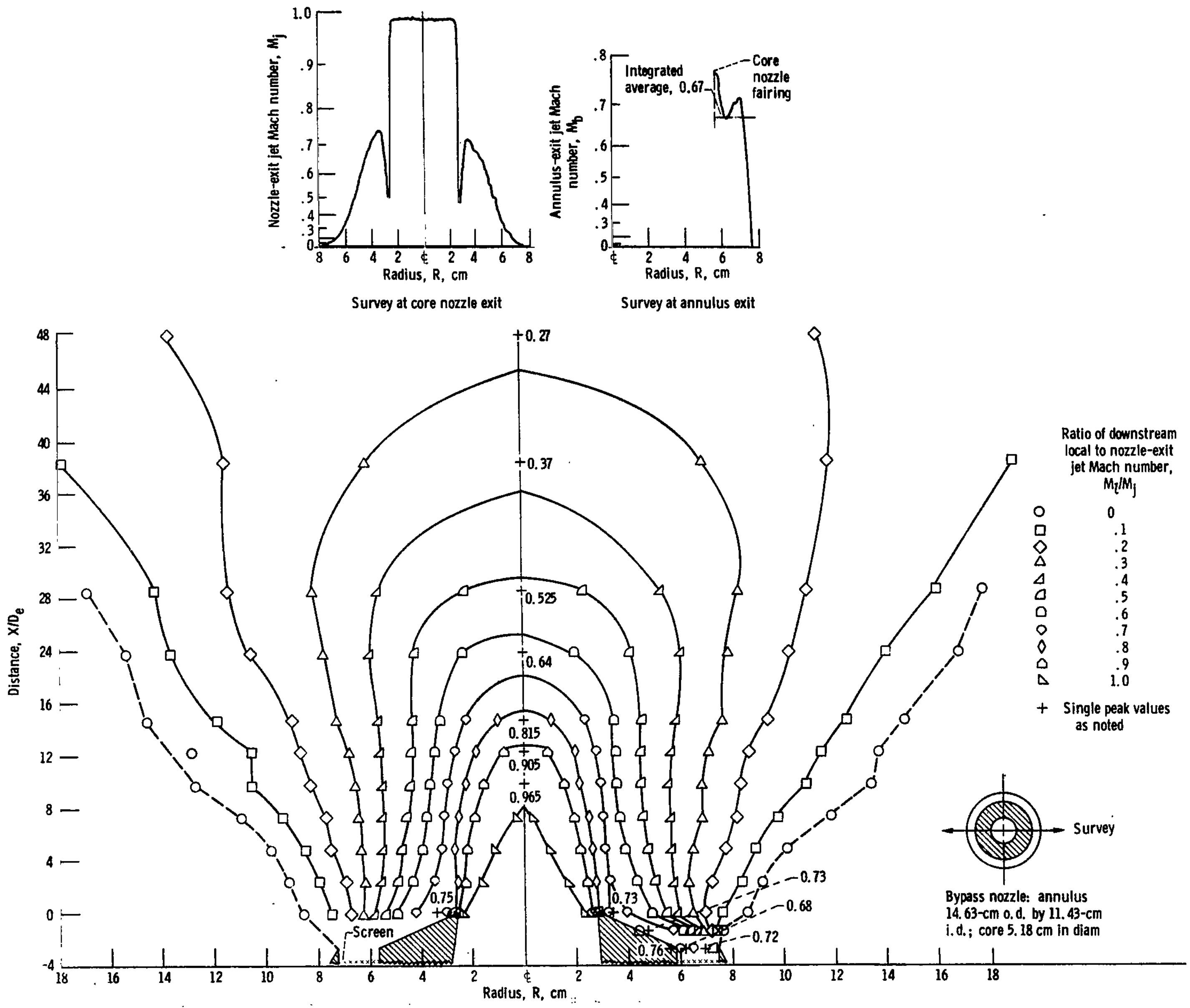

Figure 217. - Configuration 122. Nozzle-exit jet Mach number, M_j, 0.99; equivalent diameter, D_e, 5.18 centimeters; ratio of bypass (secondary) flow exit Mach number to core (primary) flow exit Mach number, M_b/M_j, 0.677.

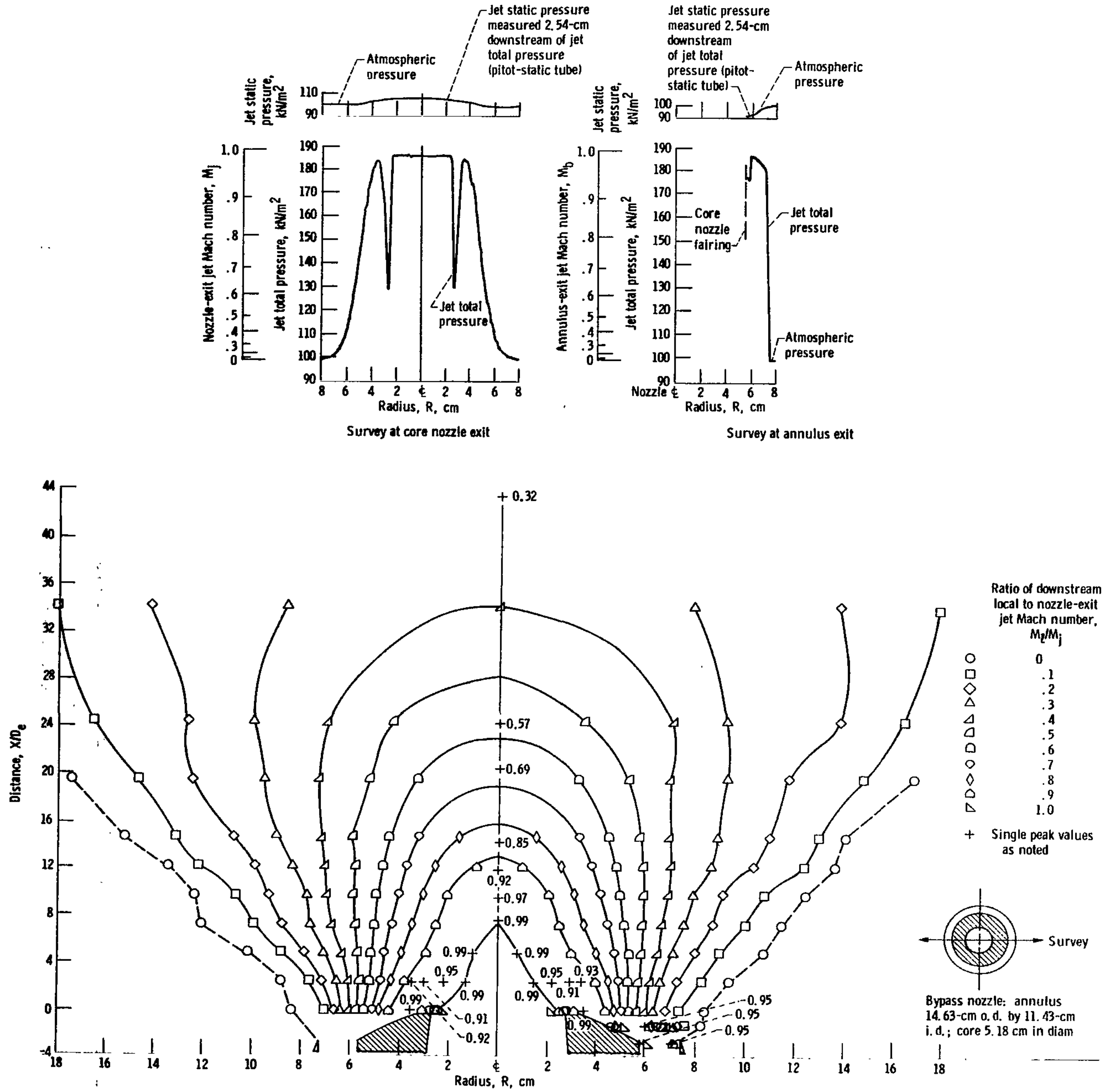

Figure 218. - Configuration 123. Nozzle-exit jet Mach number, M_j, 0.986; equivalent diameter, D_e, 5.18 centimeters; ratio of bypass (secondary) flow exit Mach number to core (primary) flow exit Mach number, M_b/M_j, 0.999.

APPENDIX B

SYMBOLS

A_b	area of secondary (bypass) nozzle, cm^2
A_c	area of primary (core) nozzle, cm^2
A_e	area of single nozzle element, cm^2
A_n	total nozzle area, cm^2
AR	aspect ratio, h/w or h^2/area
C_n	nozzle (or orifice) normalizing coefficient
D_e	equivalent diameter of circular nozzle with exit area equal to that of noncircular single element (D_e for circular nozzle equals nozzle diameter), cm
$D_{e,T}$	equivalent diameter of circular nozzle with exit area equal to total nozzle-exit area, cm
D_h	hydraulic diameter of nozzle element, 4(area)/perimeter, cm
D_x	analytical displacement parameter, dimensionless
d	circular element diameter or annulus height, cm
h	noncircular element height, cm
l	nozzle axial length; or thickness of orifice plate, cm
M	downstream peak Mach number
M_b	bypass flow (secondary) exit Mach number
M_j	nozzle-exit peak jet Mach number
M_l	downstream local Mach number
M_s	induced flow Mach number determined from surface or stream static pressures
M_b/M_j	ratio of bypass (secondary) flow exit Mach number to core (primary) flow exit Mach number
P_n	nozzle-inlet total pressure, kN/m^2 gage
p_s	stream or surface static pressure, kN/m^2
p_0	atmospheric pressure, kN/m^2
R	radius, cm

R_n	overall nozzle radius, cm
R_1	centerline radius of first ring of tubes
R_2	centerline radius of second ring of tubes; or inside radius of an annulus, cm
r	local jet radius, cm
r_{max}	jet radius where downstream local Mach number M_l equals zero
r_1, r_2	actual radial spacing between adjacent jets (including nozzle wall thickness), cm
s_1, s_2	actual circumferential spacing between adjacent jets (including nozzle wall thickness), cm
W_n	nozzle mass flow rate, kg/sec
w	noncircular element width, cm
w_l	larger width of variable-width element, cm
w_s	smaller width of variable-width element, cm
w_s/w_l	ratio of smaller width to larger width of a variable-width (trapezoidal) nozzle element
X	axial distance downstream of nozzle-exit plane, cm
$\dfrac{X}{C_n D_e \sqrt{1 + M_j}}$	axial distance parameter
$Z_{①}$	value of axial distance parameter $X/\left(C_n D_e \sqrt{1 + M_j}\right)$ at departure point of coalescing core from single-element decay curve
β	wall divergence angle (refs. 10 and 11), deg

Subscripts:

av	average
b	bypass
i	inner
id	ideal
o	outer
0,1,2	center, first ring, second ring, respectively (table II)

REFERENCES

1. Dorsch, R. G.: Externally Blown Flap Noise Research. SAE Paper 740468, Apr. 1974.

2. Goodykoontz, Jack H.; Dorsch, Robert G.; and/Groesbeck, Donald E.: Noise Tests of a Mixer Nozzle Externally Blown Flap System. NASA TN D-7236, 1973.

3. Aircraft Engine Noise Reduction. NASA SP-311, 1972, pp. 259-290.

4. Groesbeck, D.; Huff, R.; and von Glahn, U.: Peak Axial-Velocity Decay with Mixer-Type Exhaust Nozzles. NASA TM X-67934, 1971.

5. Groesbeck, D. E.; von Glahn, U. H.; and Huff, R. G.: Peak Axial-Velocity Decay with Multi-Element Rectangular and Triangular Nozzles. NASA TM X-68047, 1972.

6. von Glahn, U. H.; Groesbeck, D. E.; and Huff, R. G.: Peak Axial-Velocity Decay with Single- and Multi-Element Nozzles. AIAA Paper 72-48, Jan. 1972.

7. Schubauer, Galen B.; and Tchen, C. M.: Turbulent Flow. Princeton Aeronautical Paperbacks, No. 9, Coleman duP. Donaldson, ed., Princeton Univ. Press, 1961, Sec. B., pp. 87-90.

8. Förthmann, E.: Turbulent Jet Expansion (Uber Turbulente Strahlausbreitung). Ingenieur-Archiv, vol. 5, 1934, pp. 42-54 (Translated as NACA TM 789).

9. Landis, F.; and Shapiro, A. H.: The Turbulent Mixing of Co-Axial Gas Jets. Proceedings of Heat Transfer and Fluid Mechanics Institute, Stanford Univ. Press, 1951, pp. 133-148.

10. Higgins, C. C.; and Wainwright, T. W.: Dynamic Pressure and Thrust Characteristics of Cold Jets Discharging from Several Exhaust Nozzles Designed for VTOL Downwash Suppression. NASA TN D-2263, 1964.

11. Higgins, C. C.; Kelley, D. P.; and Wainwright, T. W.: Exhaust Jet Wake and Thrust Characteristics of Several Nozzles Designed for VTOL Downwash Suppression. NASA CR-373, 1966.

*U.S. GOVERNMENT PRINTING OFFICE: 1977 - 735-004/12

"The aeronautical and space activities of the United States shall be conducted so as to contribute . . . to the expansion of human knowledge of phenomena in the atmosphere and space. The Administration shall provide for the widest practicable and appropriate dissemination of information concerning its activities and the results thereof."

—NATIONAL AERONAUTICS AND SPACE ACT OF 1958

NASA SCIENTIFIC AND TECHNICAL PUBLICATIONS

TECHNICAL REPORTS: Scientific and technical information considered important, complete, and a lasting contribution to existing knowledge.

TECHNICAL NOTES: Information less broad in scope but nevertheless of importance as a contribution to existing knowledge.

TECHNICAL MEMORANDUMS: Information receiving limited distribution because of preliminary data, security classification, or other reasons. Also includes conference proceedings with either limited or unlimited distribution.

CONTRACTOR REPORTS: Scientific and technical information generated under a NASA contract or grant and considered an important contribution to existing knowledge.

TECHNICAL TRANSLATIONS: Information published in a foreign language considered to merit NASA distribution in English.

SPECIAL PUBLICATIONS: Information derived from or of value to NASA activities. Publications include final reports of major projects, monographs, data compilations, handbooks, sourcebooks, and special bibliographies.

TECHNOLOGY UTILIZATION PUBLICATIONS: Information on technology used by NASA that may be of particular interest in commercial and other non-aerospace applications. Publications include Tech Briefs, Technology Utilization Reports and Technology Surveys.

Details on the availability of these publications may be obtained from:

SCIENTIFIC AND TECHNICAL INFORMATION OFFICE

NATIONAL AERONAUTICS AND SPACE ADMINISTRATION

Washington, D.C. 20546